NUREG/CR-3224
LA-9716-MS

Los Alamos National Laboratory is operated by the University of California for the United States Department of Energy under contract W-7405-ENG-36.

An Assessment of CRBR Core Disruptive Accident Energetics

Los Alamos National Laboratory
Los Alamos, New Mexico 87545

Edited by N. N. Sheheen

Available from

GPO Sales Program
Division of Technical Information and Document Control
US Nuclear Regulatory Commission
Washington, DC 20555

and

National Technical Information Service
Springfield, VA 22161

Printed copy price: $8.50

NUREG/CR-3224
LA-9716-MS

An Assessment of CRBR Core Disruptive Accident Energetics

T. G. Theofanous*
C. R. Bell

Report Issue Date: March 1983
Date published: March 1984

Prepared for
CRBR Program Office
Office of Nuclear Reactor Regulation
US Nuclear Regulatory Commission
Washington, DC 20555

NRC FIN No. A7271

*Consultant at Los Alamos. Purdue University, School of Nuclear Engineering, West Lafayette, IN 47907.

Los Alamos National Laboratory
Los Alamos, New Mexico 87545

NOTICE

Availability of Reference Materials Cited in NRC Publications

Most documents cited in NRC publications will be available from one of the following sources:

1. The NRC Public Document Room, 1717 H Street, N.W.
   Washington, DC 20555
2. The NRC/GPO Sales Program, U.S. Nuclear Regulatory Commission,
   Washington, DC 20555
3. The National Technical Information Service, Springfield, VA 22161

Although the listing that follows represents the majority of documents cited in NRC publications, it is not intended to be exhaustive.

Referenced documents available for inspection and copying for a fee from the NRC Public Document Room include NRC correspondence and internal NRC memoranda; NRC Office of Inspection and Enforcement bulletins, circulars, information notices, inspection and investigation notices; Licensee Event Reports, vendor reports and correspondence; Commission papers; and applicant and licensee documents and correspondence.

The following documents in the NUREG series are available for purchase from the NRC/GPO Sales Program: formal NRC staff and contractor reports, NRC-sponsored conference proceedings, and NRC booklets and brochures. Also available are Regulatory Guides, NRC regulations in the *Code of Federal Regulations*, and *Nuclear Regulatory Commission Issuances*.

Documents available from the National Technical Information Service include NUREG series reports and technical reports prepared by other federal agencies and reports prepared by the Atomic Energy Commission, forerunner agency to the Nuclear Regulatory Commission.

Documents available from public and special technical libraries include all open literature items, such as books, journal and periodical articles, and transactions. *Federal Register* notices, federal and state legislation, and congressional reports can usually be obtained from these libraries.

Documents such as theses, dissertations, foreign reports and translations, and non-NRC conference proceedings are available for purchase from the organization sponsoring the publication cited.

Single copies of NRC draft reports are available free upon written request to the Division of Technical Information and Document Control, U.S. Nuclear Regulatory Commission, Washington, DC 20555.

Copies of industry codes and standards used in a substantive manner in the NRC regulatory process are maintained at the NRC Library, 7920 Norfolk Avenue, Bethesda, Maryland, and are available there for reference use by the public. Codes and standards are usually copyrighted and may be purchased from the originating organization or, if they are American National Standards, from the American National Standards Institute, 1430 Broadway, New York, NY 10018.

AN ASSESSMENT OF CRBR CORE DISRUPTIVE ACCIDENT ENERGETICS

by

T. G. Theofanous and C. R. Bell

Contributors

W. R. Bohl (Los Alamos)

L. B. Luck (Los Alamos)

T. R. Wehner (Los Alamos)

H. H. Hummel (ANL)

P. A. Pizzica (ANL)

M. Asprey (Los Alamos)

T. A. Butler (Los Alamos)

R. E. Baars (Los Alamos)

ABSTRACT

The results of an independent assessment of core disruptive accident energetics for the Clinch River Breeder Reactor are presented in this document. This assessment was performed for the Nuclear Regulatory Commission under the direction of the CRBR Program Office within the Office of Nuclear Reactor Regulation. It considered in detail the accident behavior for three accident initiators that are representative of three different classes of events; unprotected loss of flow, unprotected reactivity insertion, and protected loss of heat sink. The primary system's energetics accommodation capability was realistically, yet conservatively,

determined in terms of core events. This accommodation capability was found to be equivalent to an isentropic work potential for expansion to one atmosphere of 2550 MJ or a ramp rate of about 200 $/s applied to a classical two-phase disassembly. This accommodation capability was contrasted to the potential for energetic behavior, which, due to the heterogeneous CRBR core design, was shown to arise only in the advanced core disruption states (gravity driven recriticalities). The core-disruption behavior was assessed through integral analyses to establish an overall viewpoint; through separate, bounding evaluations of recriticality severity at various states of disruption; and through separate, conservative estimates of fuel removal during disruption. The accident behavior was found to be dominated by neutronic activity that was bounded conservatively by 100-$/s events. This neutronic activity effectively terminated itself by promoting the necessary fuel removal from the active core, and it did so before a homogenized whole-core pool formed, thereby avoiding the regime of highest ramp rates. Even the whole-core pool was found to produce energetics levels within the system's accommodation capability. Based on a qualitative probabilistic approach, we concluded that massive failure of the reactor head with associated early challenge to the containment building is physically unreasonable.

CONTENTS

ACRONYMS

ACRS	Advisory Committee on Reactor Safeguards
ANL	Argonne National Laboratory
BNL	Brookhaven National Laboratory
CB	Core Barrel
CSS	Core Support Structure
CDA	Core Disruptive Accident
CRBR	Clinch River Breeder Reactor
FAI	Fauske and Associates Inc.
FFP	Fuel Failure Propagation
FFTF	Fast Flux Test Facility
FPS	Full Power Seconds
FTR	Fast Test Reactor
GE	General Electric Co.
HCDA	Hypothetical Core Disruptive Accident
HEDL	Hanford Engineering Development Laboratory
IKE	Impact Kinetic Energy
IRP	Intermediate Rotating Plug
IWP	Impact Work Potential
LMFBR	Liquid Metal Fast Breeder Reactor
LOFA	Loss-of-Flow Accident

LOF-d-TOP	Loss-of-Flow Driven Transient Overpower
LOHS	Loss-of-Heat-Sink Accident
LOPI	Loss of Piping Integrity
LWR	Light Water Reactor
NRC	Nuclear Regulatory Commission
PDE	Postdisassembly Expansion
PRA	Probabilistic Risk Assessment
RES	Office of Nuclear Regulatory Research
S/A	Subassembly
SAS3D	Computer Code for Initiating Phase Analysis
SBTF	Sodium Boiling Test Facility
SIMMER-II	Computer Code for Generalized CDA Analyses
SE	Severe Earthquake
SSE	Safe Shutdown Earthquake
SMBDB	Structural Margin Beyond the Design Basis
SNL	Sandia National Laboratory
TER	Technical Evaluation Report
TOP	Transient Overpower Accident
TREAT	The TREAT Test Reactor
UCS	Upper Core Structure
UIS	Upper Internal Structures
ULOHS	Unprotected LOHS
UWP	Ultimate Work Potential
VHS	Vessel Head Structure

0. EXECUTIVE SUMMARY

This report contains the results of our independent assessment of the energetic behavior resulting from postulated CDAs in the CRBR heterogeneous core design. The objective was to define in a reasonably conservative fashion the magnitude of the mechanical energy releases against which the integrity of primary system, and of the reactor vessel head in particular, should be assessed. The effort began with a detailed review and evaluation of the Applicants' positions and their technical bases and evolved, over a period of nearly 15 months, into a completely independent study with original elements on one or more of the following aspects: (a) accidents, phenomena, or effects taken into account; (b) analysis methods utilized; and (c) experimental evidence brought to bear. The results of the independent assessment are briefly summarized in this section and the details are provided in the body of this report. Similar structure and cross-referencing are utilized in this summary and in the main body to facilitate the search for additional details.

1. Overall Technical Approach

Depending upon whether reactor shutdown has been achieved, core disruption may initiate at powers ranging from nearly normal to decay levels. The corresponding heating rates vary by two orders of magnitude and define the first major classification of CDAs into "unprotected" and "protected" respectively. Mechanistically, a protected CDA results from sustained failure to remove decay heat and is commonly referred to as the LOHS. In the unprotected CDA case, initial core disruption may occur due to either an undercooling or an overpower condition. Mechanistically, the undercooling would result from loss of coolant flow, which is known as the LOFA, and the overpower would result from uncontrolled reactivity insertion, which is commonly referred to as the TOP. In general terms, these three accidents exemplify the generic behavior over the whole range of the CDA spectrum of circumstances, hence, they can be used to adequately characterize the spectra of energetic consequences.

Another class of CDA initiators, fuel failure propagation, also has been identified and extensively studied in the past. The evidence is conclusive now that the attainment of whole core disruption through such a mechanism can be neglected. Finally, various combinations of function failure events (TOP/LOF, etc.) and/or of structural failures (due to extreme external events such as earthquakes beyond the SSE yielding core support failures, loss of piping integrity, etc.) have also occasionally been considered. Our

review of these areas indicates that those few cases, for which severe energetic behavior cannot be precluded at this time (TOP/LOF, etc.), have sufficiently low probability that they need not be considered further.

Our approach consisted of realistically following each one of the three generic CDA initiators through the core-disruption phases until accident termination. These so-called mechanistic CDA analyses provided an overall framework against which the potential for energetic phenomena was assessed with due regard for the controlling physical processes. In terms of actual licensing cases, the first efforts along these lines were made during the Regulatory review of the FFTF CDA energetics assessment. The approach further matured with the initial (homogeneous core) CRBR application and licensing review.

It would be in error, however, to expect that such mechanistic analyses can, at this time, predict uniquely the complete evolution of a postulated CDA from initiation to termination. There is considerable complexity in the underlying physical processes that has not yet been modeled appropriately. We believe that such limitations may alter the overall timing of some events and may even affect the actual character and sequence of the intermediate states. However, we also believe that these uncertainties can be handled adequately within a properly oriented overall effort. With this in mind we did not attempt to associate a simple outcome to a given initiator. Rather, we attempted to establish a "range of phenomenology" consistent with experience and known physical principles. Within this range we searched for energetically-prone circumstances, we identified the important mechanisms, and we quantified the intensity of energy release in a reasonably conservative manner (avoiding excessive and clearly nonphysical conservatisms). Similarly, we scrutinized for termination-favoring phenomena, we identified the important mechanisms, and we quantified the approach to termination by the fraction of fuel removed from the core region (at approximately 40% removal, permanent subcriticality is achieved). Based on these results we completed the assessment by synthesizing sequences and respective likelihoods.

These analyses were carried out by means of the system codes SAS3D (and, to a limited extent, the most recent version, SAS4A) and SIMMER-II. These codes were used as "integrators" of the technical base and their results were guided, scrutinized, and/or augmented by special-purpose analytical techniques, in-pile experimental data, and out-of-pile simulant experiments as appropriate. As in all safety studies, the synthesis of experimental data and analysis techniques to produce a quantified basis for the conclusions requires approximations, involves uncertainties, and must be appropriately focused. Engineering judgement was utilized to provide overall guidance in this regard.

As an initial step in our independent assessment effort, we made the judgement that, among all core-disruptive accidents, the LOFA should be

chosen as the subject of our most detailed considerations. The basis was: (a) the LOFA phenomenology spans the range of energetically significant CDA behavior; (b) within the LOFA sequences our previous review effort identified specific and significant areas of concern; and (c) exploratory examination of all other CDAs indicated an energetically benign behavior compared to that projected for the LOFA. Furthermore, this emphasis was to reflect the relative complexity of the LOFA sequence compared to that of the TOP and LOHS accidents, rather than the neglect of the unique aspects of these other CDA initiators. Indeed, these unique aspects also were studied in detail. After all the assessments were complete, we found that the choice of this distribution of effort was appropriate.

2. The Loss of Flow Accident

- Generalities

From the initiation of core disruption (initial clad melting), the LOFA will evolve through a continuum of gradually escalating core disruption states until complete disruption (melting of all materials found within the original core confines, also known as a whole-core pool) occurs. Energetically, this progression is important for as long as a sufficient fraction of the initially present fuel (approximately 60% for the CRBR) remains within the active core region. Neutronically active states are then possible through a variety of rearrangements of driver, blanket, structural, control, and coolant materials. Permanent subcriticality, or "termination" (termination of energetic concerns) may occur from any point along the continuum of core-disruption states. When the relocation of the appropriate quantity of driver fuel occurs in a forceful manner, we speak of "energetic termination" or hydrodynamic "disassembly." When this relocation is benign we speak of "mild termination" or simply "dispersal." Our overall objective was to determine the relative likelihood of these two termination paths as a function of the degree of core disruption and to quantify the damage potential of the energetic ones.

Energetic behavior is the consequence of rapid reactivity insertion. For the present CRBR design such reactivity increases only result from sizable (large mass flux), and generally compactive, fuel motions. When such motions occur from fuel in the process of undergoing disruption we speak of "initiating-phase energetics." When such motions occur due to compaction from highly, but temporarily, dispersed fuel states, they are called "recriticalities." The character of these two energetic phenomena fundamentally differ both in reactivity-yielding mechanisms and in resulting damage potential. The structural capability of the system provides an appropriate perspective against which the damage potential of a given energetic event must be viewed.

- Structural Capability of CRBR

The levels of energetics required to produce significant structural damage in the CRBR were evaluated (Section II.2) taking into account an "inner containment" formed by the CB/UIS/CSS envelope. In addition, the pressure transmission characteristics of the two-phase, expanding core medium and other materials found within this envelope were taken into account. These characteristics have important implications on the resulting short-term loading of the local structures (CB and CSS). This mitigating behavior is the result of a compliant core state (distributed voids), and it must be taken into account, particularly since such compliance is one of the crucial prerequisites for highly energetic behavior. Our structural analyses indicated that a level of energetics in the range of 1130 MJ (isentropic expansion yield to one atmosphere) would be required to breach this inner containment. That is, minimal energetic release against the boundary of the primary system can be expected for energetics below this level.

At still higher levels, upward displacement of the UIS and a longer-term expansion against the sodium pool occurs. For the heterogeneous CRBR core this is the only sequence that could provide the opportunity for large-scale, fuel-coolant interactions. Experimental evidence indicates that, under these specific contact conditions, this interaction would not yield pressure augmentation, and that the energy conversion process would be controlled by two-phase choking and minimal fuel/coolant heat transfer. Evaluations of the long-term expansion phenomena indicated that an energetic event of nearly twice the above magnitude, approximately 2550 MJ, would be required to produce a slug-impact kinetic energy close to the vessel-head design capability of 75 MJ. The 1130 and 2550 MJ energetic levels correspond approximately to 100 and 200 $/s disassemblies, respectively, occurring in the two-phase regime.

- Initiating Phase Energetics

A number of SAS3D analyses covering broad ranges of the important parameters were carried out to characterize the range of initiating-phase LOFA behavior (Section II.3). With the lower coolant void reactivity of the heterogeneous CRBR core, the LOF-d-TOP, which was a major energetic problem area [1] for the previous homogeneous CRBR core design, is avoided. This LOF-d-TOP situation arises only when high overpower conditions develop leading to pin failures in unvoided subassemblies. If such failures occur at the core midplane, which cannot be excluded based on available evidence, potentially autocatalytic behavior may result from the rapid in-pin fuel motion toward the failure location (core midplane).

Although our analyses revealed insufficient power augmentation to reach the LOF-d-TOP condition, even those cases calculated with the parameter choices favoring a "slow" accident exhibit substantial neutronic activity

(overpower condition). This activity is caused by extended fuel motions (following the initial tendency to disperse due to pressure from retained fission gas) and gives rise to a process we call codisruption. Codisruption is the result of accelerated core disruption such that there is insufficient time for the molten cladding to separate from the fuel prior to core-wide fuel disruption. Codisruption favors dispersal since it implies higher (steel) vapor pressures, increased penetration potential into axial blanket areas, and remeltable blockages.

Plenum fission-gas-induced fuel compaction has been proposed as another mechanism for initiating-phase energetics [2]. In the presence of plenum pressure, the fuel pin is subjected to unbalanced forces at the time of fuel disruption resulting in rapid downward ejection of the blanket and undisrupted driver fuel pellets. The Applicant analyzed this mechanism in response to questioning during this review process and concluded that there would be adequate time for the plenum fission gas to escape prior to fuel disruption. Based on the results of our own analyses we could not agree with this conclusion (Section II.4). We were able to bound realistically the reactivity insertion rates from the fuel compaction process per se at approximately 50 $/s, which, as previously indicated, represents a tolerable level of energetics. However, at the time of this energetic event, only one-half of the core would be voided and the resulting high overpower could induce an LOF-d-TOP event in the other half. Such a combination of energetic events was judged as highly undesirable. Even on purely philosophical grounds the unmitigated manifestation of these high pressures at the core boundary cannot be tolerated. We recommended, therefore, that steps be taken to limit the action of these pressures during the initiating phase of the LOFA.

- Recriticality Energetics

The general behavior of the post-initiation period was examined (Section II.5) both in terms of a SIMMER-II integral system calculation as well as in terms of generic ad hoc evaluations of relevant physical processes.

The integral calculation was a continuation of one of the SAS3D analyses. The overlapping portions of these two calculations were in excellent agreement. The results depict a generally active sequence, with regular power bursts corresponding to fuel reassembly motions. Some evidence of progressive coherence or "tuning" is noted, however. The power oscillations in the early portion appear to be substantially damped. The effect of the associated pressurization transients is to force molten fuel (and steel mixture) away from the core region through the axial blankets and, upon melting of subassembly walls that are adjacent to internal blankets, through intersubassembly gaps. The modeling allowed for freezing and plugging of such paths, and indeed such behavior is observed in the results. Merging of the S/A-scale pools (annular pool geometry) and destruction of the internal blanket barriers (whole-core pool) occur successively within only a few seconds. Upon

attainment of a large two-dimensional pool, the power oscillations amplify because of increasingly severe sloshing pool motions. However, homogenization of the internal blanket regions develops slowly; hence, radially focused sloshes are inhibited, the system's total available reactivity is well below that of a homogeneous pool, and the associated power bursts are nonenergetic. This delay is sufficient to allow removal of the fuel required for termination prior to the formation of a homogeneous whole-core pool, even though the inter-assembly gap escape paths of the radial blankets were, conservatively, not modeled in this calculation.

Recognizing that this integral calculation is one of a few ever attempted, the above detailed results must not and were not taken at face value. The mild termination potential was evaluated (Section II.6) in terms of separate-effects calculations that model in great detail the flow path, the flow constituents, and thermal interactions including freezing and plugging phenomena. Prototypic experimental data were utilized to benchmark these calculations. Even under modest pressures (compared to those expected from the continuing neutronic activity), adequate fuel removal is estimated to assure permanent neutronic termination prior to the formation of a homogeneous whole-core pool.

Gravity-driven recriticalities were examined for amplification potential (Section II.7). For the S/A-scale and annular pool phases under power-burst perturbations, the fuel column separates initially into a compact lower mass and a distributed upper segment of approximately equal material quantity. Reassembly under conditions of reduced fuel inventory or low heat losses (minimal boilup) produces a growing lower liquid puddle within which the peak of the axial power distribution occurs. Hence, reassembly energetics are mitigated strongly by single-phase liquid expansion feedback during the power transient. Reassembly under conditions of high inventory or high heat losses (large-scale boilup), however, produces low ramp rates and therefore is effectively controlled by two-phase dispersal during the power transient. In addition, the S/A phase cannot have core-wide coherence because the time interval to S/A wall disintegration permits only a few power cycles that are insufficient to complete the "tuning" of the fluid dynamics. Thus, reassembly ramp rates would be small. However, even if we assume complete core-wide coherence, maximum ramp rates of less than 100 $/s are obtained. Therefore, no physically reasonable threat to the vessel head structures can be seen from these first two stages of disruption.

For the whole-core, homogeneous pool an amplification mechanism was calculated. Under perfectly symmetric conditions (geometry and power distribution), a radially focused sloshing action was observed that, under certain conditions of material configuration, produced high reactivity insertion rates. In those cases single-phase disassemblies dominated and negligible energetics resulted. For example, in one such case considered, an in-slosh

with a 300 $/s ramp at prompt critical yielded quick, single-phase thermal expansion shutdown and produced negligible energy release. However, there is also a range of conditions over which substantial energy releases can be calculated. This is particularly so when two-phase regions exist. For example, in one high-inventory case considered, prompt criticality was obtained earlier in the in-slosh, while a two-phase condition dominated the central portion of the pool. The resulting reactivity insertion rate of 125 $/s produced an energy approximately equivalent of the 100 $/s two-phase disassembly considered in our structural evaluation. The importance of symmetry in such evaluations is highlighted by the integral SIMMER-II calculation of core disruption. This calculation did enter the whole-core pool phase and it did indicate radial sloshing and amplification. However, due to the system's nonhomogeneity in the early stages of this phase, a noncentered power distribution resulted, hence, radial focusing was absent and non-energetic behavior was observed. Before homogenization of the internal blanket material occurred, permanent termination of neutronic activity by fuel removal was indicated.

3. The Transient Overpower Accident

The TOP-unique behavior (Section III) develops during the very early stages of the initiating phase. As a result of the assumed reactivity insertion, the power rises quickly and produces fuel melting and pin failure well before coolant and cladding overheating. For a postulated midplane failure location, pin-internal fuel motion can have a significant reactivity augmentation effect, and unless it is moderated by an equally rapid dispersal of the fuel that is ejected into the coolant channels, an autocatalytic behavior potentially could develop.

The Applicant provided extensive analyses for a variety of core burnup states and reactivity insertion rates. Our assessment focused, therefore, on more closely defining the margins for autocatalytic behavior for assumed midplane failures. This behavior is controlled by the competition between pin-internal fuel motion and pin-external dispersal (usually referred to as sweepout). The relevant time scale is determined by the core-wide coherence of such pin failures which, in turn, is affected by the core configuration and the imposed reactivity ramp rate (coherence increases with ramp rate). For the CRBR, the EOC-3 core with the replacement of the six high power driver fuel assemblies with blanket assemblies is the most coherent. On the basis of failure modes and effects analysis of the reactor control system, we concluded that ramp rates of 10-12 ¢/s are more than one order of magnitude less probable than those of 2 ¢/s or 5-8 ¢/s. Furthermore 15-20 ¢/s ramps are more than three orders of magnitude less likely than those of 10-12 ¢/s. Therefore, we selected the 10-12 ¢/s TOP as a conservative upper limit for this investigation.

The EOC-3 TOP accident was simulated with the PLUTO2/SAS4A computer code. A failure incoherence (time between failures) of more than 300 ms was deduced for the first six groups of subassemblies. The PLUTO2 sweepout calculation was adjusted to experimental data from the L8 TREAT TOP test. The calculated sweepout was seen to cancel successfully pin-internal fuel motion reactivity (and a small amount of sodium voiding reactivity) and to produce shutdown.

Thus, even under the most limiting conditions of core coherence and pin failure location, no energetic behavior could be found for TOPs of up to 10-12 ¢/s. For TOPs with higher ramp rates, energetic behavior cannot be precluded; however, such events are of sufficiently low probability that they can be excluded from consideration.

4. The Loss of Heat Sink Accident

The LOHS-unique circumstances (Section IV) originate from core disruption at very low power and in the absence of sodium coolant. The absence of coolant is required since natural convection boiling has been shown to be adequate to remove heat at decay power levels. Core uncovery may occur either due to coolant boiloff or due to reactor vessel failure at the high temperature LOHS environment. The actual failure mechanism is not important, affecting only the disruption-stage power level, which, in any case, is very small and much more dependent upon the other aspects of the accident scenario. Characteristically, however, disruption would not occur until many hours into the accident, indicating significant margins for recovery.

At the characteristically low heating rates, all steel within the core melts, relocates downward, and forms a plug in the lower axial blanket region. The system remains subcritical, but continues to heat slowly until fuel settling occurs either due to softening of the pellets (as the melting point is approached) or simply due to toppling and compaction to a lower porosity. The initial porosity is approximately 65% and a porosity of approximately 50% is required to approach criticality. Criticality accelerates the melting rate, thus producing, at most, a moderate recriticality estimated at approximately 60 $/s. Such an event would disperse the core into the vessel and provide permanent neutronic termination. A smaller recriticality, however (approximately 10-20 $/s), is considered more likely under these circumstances and would be insufficient to provide termination. A whole-core pool with homogenization of all internal, axial, and radial blankets results in this case. The resulting dilution is adequate to render the system permanently subcritical even after steel and control rod materials eventually separate out.

Furthermore, in the absence of the sodium pool, even the most severe recriticalities could provide no challenge to the reactor vessel head integrity.

As an example we used the 200 $/s transient, discussed in the LOFA assessment as the energetic level required to challenge the vessel head integrity, to obtain loads in the LOHS environment. The expansion forces on the UIS, assuming the absence of significant resistance by its support columns, and on the vessel head were evaluated using the SIMMER-II code. An upper-bound UIS kinetic energy (in the upward direction) of approximately 5 MJ was thus estimated. Such a missile is of little mechanical consequence to the reactor vessel head. The direct expansion loads on the head were approximately equivalent to a quasistatic pressure (decays rapidly by condensation and leakage) of 2 MPa which is well below the head failure pressure even at this elevated temperature condition.

5. Conclusions

- We have systematically evaluated the possible progression of all three classes of CDAs as exemplified by the LOF, TOP, and LOHS accidents. Non-negligible energetic circumstances were identified only within the LOFA sequences and, assuming that the plenum fission gas fuel compaction mechanism becomes inoperative through redesign as recommended, only as a consequence of recriticalities.

- Recriticality events in the S/A-scale and annular pool phases cannot be excluded. However, their magnitudes are limited to the order of 50 $/s or less because of incoherence and the absence of significant amplification. Neutronic activity throughout both of these stages of core disruption is substantial and contributes to pressurization and fuel dispersal away from the core region. Thus, benign termination prior to entering the whole-core, homogeneous, pool phase is projected even under restrictive assumptions for fuel removal path availability and fuel removal mechanics.

- Whole-core pool recriticalities exhibit a narrow regime of significant energetic behavior. This energetic regime is associated with idealized, perfectly symmetric geometry and completely homogeneous pools. The amplification is the result of radial sloshing following a centrally peaked and symmetrically distributed power pulse. Even so, the resulting levels of energetics do not exceed the structural capability of the primary-system boundary.

- The levels of energetics required to produce significant structural damage in the CRBR were evaluated, taking into account for the first time, the structural enclosure formed by the CB/UIS/CSS and the pressure transmission characteristic of the expanding core medium and other materials within the enclosure. We conclude that an accident with a mechanical energy yield in the range of 1130 MJ (expressed as the isentropic work potential for expansion to one atmosphere) would be required to fail this inner structure, and an accident with a mechanical energy yield in the range of 2550 MJ would

be required to challenge substantially the reactor vessel head structure, that is, produce a slug impact kinetic energy close to the CRBR vessel head design value of 75 MJ. These levels of energetics roughly correspond to two-phase whole-core disassemblies with 100 $/s and 200 $/s driving reactivity ramp rates.

- Based on these results, we conclude that a CDA-induced energetic vessel head failure is physically unreasonable.

- Further, based on the projected absence of significant energetic events, we conclude that the Applicant's energetic source term of 661 MJ (75 MJ slug impact kinetic energy) is adequate, as applied by the Applicant for evaluating the structural margin beyond design basis.

6. References

1. J. F. Meyer, L. Lois, J. L. Carter, and T. P. Speis, "An Analysis and Evaluation of the Clinch River Breeder Reactor Core Disruptive Accident Energetics," Nuclear Regulatory Commission report NUREG-0122 (March 1977).

2. T. G. Theofanous, "Multiphase Transients with Coolant and Core Materials in LMFBR Core Disruptive Accident Energetics Evaluations," Purdue University report NUREG/CR-0224, (July 1978).

I. INTRODUCTION

Although excluded from the design basis, core-melt accidents in Liquid Metal Fast Breeder Reactors (LMFBRs) have claimed a prominent role in licensing even when relatively little attention was devoted to such accidents in Light Water Reactors (LWRs) (pre-Three Mile Island era). Clearly, the probability of such events is very low in both cases. However, in the LMFBR case upon meltdown and loss of the original core geometry, configurations of higher reactivity are possible. Thus, the theoretical possibility of achieving very high temperatures and pressures with direct and potentially severe consequences on the containment barriers gives rise to an LMFBR-generic safety issue, that of "energetics." As we experience the current up-stepping (post-Three Mile Island era) of licensing efforts in the beyond the design-basis accidents for LWRs, it is important to remember that the LMFBR safety community in general, and our regulatory system in particular, has maintained a balanced overall approach to risk assessments throughout these early stages of LMFBR technology development. Furthermore, just as important differences in system behavior led to an early recognition of the "energetics" issue, similarly important differences point to the expectation of significantly lower probability of core-melt accidents in LMFBRs [1]. It is for these reasons that all energetics considerations must be viewed in the proper probabilistic perspective.

In this report we are concerned with the impact of such accidents given their initiation. That is, we will assume the occurrence of gross power/cooling mismatch or the loss of decay heat removal from the primary system. Such conditions lead to overheating of core and coolant materials and eventual melting and relocation. Typically, the reactivity changes associated with such core material relocations yield power transients such that even in the absence of energetics, major core disruption and dispersal away from the original geometric configuration must occur before permanent subcriticality can be achieved. It is for these reasons that core-melt accidents in LMFBRs are more commonly known as Core Disruptive Accidents (CDAs). Available experience indicates that CDA energetics depend strongly on the particular reactor design. In this report we will assess the CDA energetic behavior of Clinch River Breeder Reactor (CRBR) heterogeneous core design described in Reference 2.

In the initial licensing application [3], the blanket material was arranged to surround the driver fuel region, this being referred to today as the homogeneous core design. The assessment [4] of CDA energetics for this design was initially carried out by the General Electric Company (GE). These analyses were superseded by two Argonne National Laboratory (ANL) studies

[5, 6] which were in turn further extended by another GE study [7]. Meanwhile, the licensing review by the Nuclear Regulatory Commission (NRC) staff, which considered the then-available original GE and the first of the ANL studies [5], was discontinued in 1976. The status of the review at that time as summarized in the Denise to Caffey letter [8] indicated a significant divergence of opinion between the NRC staff and Applicant on the subject of energetics. The Applicant's best-estimate assessment indicated a negligible level of energetics, while certain "pessimistic" estimates were still insufficient to challenge the structural integrity of the primary system (reactor vessel head). The NRC staff, on the other hand, reached the conclusion that a level of energetics of roughly twice the magnitude chosen by the Applicant as the structural design basis "should be included in the specification of functional requirements for features to protect containment integrity." The basis for this conclusion was documented in Reference 9. It appears that the concerns over a potentially energetic process referred to as Loss-of-Flow driven Transient Over Power (LOF-d-TOP) (see Section II.4) provided the main impetus for this assessment.

In 1981 the licensing process for CRBR was reactivated. The core design was changed to include blanket material within the driver fuel region. This is known as the heterogeneous CRBR core design. In this arrangement the reactivity increase due to coolant voiding from the core is significantly smaller than that in the homogeneous design. As a consequence the propensity for certain CDAs to yield the LOF-d-TOP condition is significantly decreased. The Applicant's CDA analysis [10] again argued for negligible energetics in the best-estimate case and showed that certain pessimistic ones were well below the 75 MJ slug impact kinetic energy (the whole sodium pool accelerated to a velocity corresponding to a kinetic energy of 75 MJ) which represents the structural design basis [11] for the CRBR.

The renewed NRC staff licensing review effort evolved in two distinct phases. The first phase involved a team of consultants (see Table 1) from Los Alamos National Laboratory (Los Alamos), Sandia National Laboratory (SNL), and Universities under the general direction of C. Allen, cognizant engineer for energetics in NRC's CRBR Program Office. This effort took just over six months (12/81-6/82) and was predominantly review oriented. With the help of several technical exchange meetings, the NRC consultants endeavored to comprehend and scrutinize the assessment presented by the Applicant. This review effort culminated with the documentation of a rather comprehensive enumeration of their areas of concern in a Technical Evaluation Report (TER) that was authored by the Los Alamos members but included the concerns of all the review team participants. Subsequently, these concerns were summarized in the form of eight questions (see Table 2) which on 6/15/82 were officially transmitted to the CRBR Project Office. At this time it became evident that an independent probing of these eight areas of concern (which spanned the whole range of accident analyses performed by the Applicant) by the reviewers would be beneficial in sharpening their own

TABLE 1
LIST OF CONSULTANTS IN THE
INITIAL REVIEW EFFORT

M. E. Asprey
Los Alamos National Laboratory

R. E. Baars
Los Alamos National Laboratory

C. R. Bell
Los Alamos National Laboratory

W. R. Bohl
Los Alamos National Laboratory

C. A. Erdman
Texas A&M University

T. Ginsberg
Brookhaven National Laboratory

H. H. Hummel
Argonne National Laboratory

M. S. Kazimi
Massachusetts Institute of Tech.

L. B. Luck
Los Alamos National Laboratory

P. K. Mast
Sandia National Laboratory

P. Pickard
Sandia National Laboratory

P. A. Pizzica
Argonne National Laboratory

J. Scott
Los Alamos National Laboratory

T. G. Theofanous
Purdue University

T. R. Wehner
Los Alamos National Laboratory

TABLE 2
THE EIGHT AREAS OF CONCERN

1. Can TOPs become prompt-critical in such a way that internal fuel motion in lower power channels is the key factor in the energetics determination? Is such an event possible only for mid-plane failures with low sweepout? How is the degree of sweepout determined? What is the effect of intrasubassembly incoherence on sweepout?

2. An LOF-d-TOP might still occur if the sodium void worth is 50-60 percent higher and internal fuel motion in the pins of TOP type channels can occur. What are the reactivity uncertainties for sodium void, Doppler, axial expansion and lead channel fuel motion? How do you interpret the significance of these uncertainties?

3. What is the potential for autocatalysis due to plenum fission gas acting on the fuel column to force axial compaction as disruption occurs in the initiating phase of the LOF?

4. To what extent can steel blockages form throughout the core to prevent fuel removal through normal axial blanket flow channels during the early phase of the LOF? What is the location and character of the steel blockages in these channels?

5. What is the basis for maintaining continuous subcriticality in the high heat loss environment of the early meltout phase? What are the fuel losses (quantified) taking into account uncertainties in removal path geometries, driving pressures, and freezing mechanisms?

6. What degree of subcriticality is required to prevent pool recriticality from thermal- and fluid-dynamics upset conditions? What is your position on the potential for small recriticalities to amplify? What is the justification for your position?

7. In assessing benign termination from the boiled-up pool (upward removal), justify the fuel removal mechanisms and rates. In particular, assess the potential for upper pool sodium entry via rapid condensation of steel vapor pressure.

8. What is your estimate of the force required to produce a mechanically induced relief path via upper internals structures displacement?

ability to sort out the important aspects from the details. Thus, the second phase of the review was initiated.

This independent assessment effort involved, by-and-large, the same NRC review team (to be referred to as the Team) under the direction of a Management Group (to be referred to as the Group) consisting of T. G. Theofanous (Purdue) and C. R. Bell (Los Alamos). The purpose of the Group was to focus the technical efforts of the Team such that an independent position on CRBR energetics could be completed under the tight time constraints specified. This effort took roughly six months and it culminated with the publication of the present report.

For clarity and continuity, this report is focused on our independent assessment efforts. However, important differences or similarities with the Applicant's methods and/or results are briefly mentioned as appropriate. Additional details on our views of the Applicant's assessment may be found in our TER mentioned above. This TER and a massive quantity of other material developed during both phases of the review have been compiled under one cover and are available upon request. It is intended that this "Compendium" will make our technical effort scrutable in all its detail. References to particular sections of this Compendium and to specific pages of the TER frequently will be made.

The remainder of this Introduction provides a perspective on the magnitude and depth of the overall effort. Thus, in addition to presenting our overall technical approach, we discuss certain organizational and management aspects. In the concluding section of the Introduction, the structure of the report is explained and some guidance is offered to facilitate the task of obtaining particular information by audiences with various interests.

1. Scope and Management of the Independent Assessment

The charge given to the Group by the NRC staff, CRBR Program Office, was to develop and document, by March 4, 1983, an independent position on the CRBR energetics issue. This position was to be considered, together with the Applicant's updated assessments, by the NRC staff in making the necessary licensing decisions. In this licensing context the charge amounts to providing an assessment of the magnitude of CDA energetic events to be "expected" as well as the resulting potential to violate the containment barriers provided in the CRBR.

Toward this goal, the major task of the Group was to manage, focus, and integrate the technical activities of the Team members. Complementary to the above efforts, however, the Group elicited additional data and technical contributions from the Applicant. Thus, in parallel with the independent assessment activities, the review effort continued as these additional materials were provided by the Applicant over the same time frame. The essential

aspects of this review work also are included in this report. Finally, the Group maintained a close interaction with the NRC staff and its on-going licensing activities. The Group interactions with the Applicant were carried out through H. K. Fauske of Fauske and Associates Inc. (FAI) who at about the same time was appointed to manage the Applicant's energetics licensing efforts. These main organizational interfaces are schematically illustrated in Figure 1.

In pursuing its task, the Group sought the advice and criticisms of the Team and of the NRC staff of the CRBR Program Office on a continuing basis. In addition, the Group formally requested comments and criticisms from these two "internal" organizations as well as from the "outside." These formal requests were issued on three occasions. The first was addressed to the Team and to the NRC staff of the CRBR Program Office upon completion of the detailed definition and scheduling of the technical tasks comprising the independent assessment effort. The responses received were compiled in Section 1 of the Compendium. The second request was issued following the formulation of a preliminary independent assessment position as documented in Reference 12. This was prepared for a status report presentation to the Advisory Committee on Reactor Safeguards (ACRS) CRBR subcommittee (on 11/19/82) by the Group [13]. The final formal request was issued upon the completion of the final draft of the present document. The second and third formal requests were intended to cover the US LMFBR safety community at

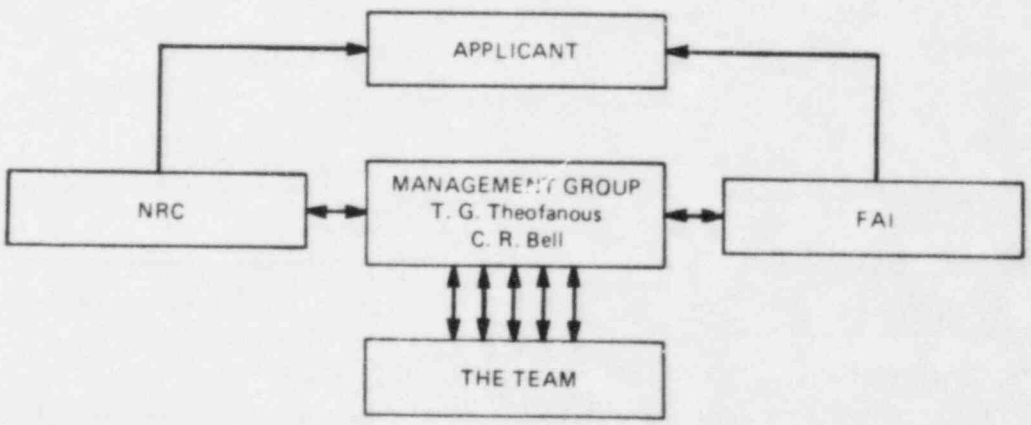

Fig. 1.
Organizational interfaces for the independent assessment.

large. That is, in addition to the ACRS, the Team, and the NRC staff of the CRBR Program Office, these requests for feedback were addressed to the Applicant and the Managements of the NRC's Office of Nuclear Regulatory Research (RES) and of all National Laboratories engaged in LMFBR energetics research (Los Alamos, SNL, BNL, ANL, and HEDL). Comments from appropriate members of their respective organizations were solicited. These two subject documents [12, 14], the responses received, and our disposition of the points raised are now part of the record and available upon request as Section 2 of the Compendium.

Based upon the level of involvement and their eventual contributions toward this document, Team members are identified as "contributors" and as "consultants" as shown in Table 3. All written contributions received by the "contributors" and "consultants" have been compiled in Section 3 of the Compendium.

TABLE 3
THE INDEPENDENT ASSESSMENT TEAM

Contributors

P. A. Pizzica
Argonne National Laboratory

H. H. Hummel
Argonne National Laboratory

W. R. Bohl
Los Alamos National Laboratory

M. E. Asprey
Los Alamos National Laboratory

T. A. Butler
Los Alamos National Laboratory

R. E. Baars
Los Alamos National Laboratory

T. R. Wehner
Los Alamos National Laboratory

L. B. Luck
Los Alamos National Laboratory

Consultants

T. Ginsberg
Brookhaven National Laboratory

C. A. Erdman
Texas A&M University

P. K. Mast
Sandia National Laboratory

2. Philosophy of the Overall Technical Approach

In the early considerations of LMFBR energetics, the term Hypothetical Core Disruptive Accidents (HCDAs) was in common use. This was not only to connote the extremely low probability of initiation of such accidents, but also the tentative nature of our understanding of their behavior and resulting consequences. Certain out-of-context (Hypothetical?) situations were postulated for the purpose of analytically realizing an energetic behavior and thus attempting to establish "bounds of severity." After nearly twenty years of intensive research and development, it appears that there is no longer reason to resort to such examinations of hypothetical circumstances. Rather, a CDA initiator can be realistically followed through the core disruption phases until accident termination. These so-called mechanistic CDA analyses provide an overall framework against which the potential for energetic phenomena may be assessed with due regard for the controlling physical processes. In terms of actual licensing cases, the first efforts along these lines were made during the Regulatory review of the FFTF CDA energetics. The approach further matured with the initial (homogeneous core) CRBR application and licensing review.

It would be in error, however, to expect that such mechanistic analyses can, at this time, predict uniquely the complete evolution of a postulated core disruptive accident from initiation to termination. There is considerable complexity in the underlying physical processes that has not yet been appropriately modeled. We believe that such limitations may alter the overall timing of some events and may even affect the actual character and sequence of the intermediate states. However, we also believe that these uncertainties can be adequately handled within a properly oriented overall effort. With this in mind we did not attempt to associate a single outcome to any given initiator. Rather, we attempted to establish a "range of phenomenology" consistent with experience and known physical principles. Within this range we searched for energetically-prone circumstances, we identified the important mechanisms, and we quantified the intensity of energy release in a reasonably conservative manner (avoiding excessive and clearly nonphysical conservatism). Similarly, we scrutinized for termination-favoring phenomena, we identified the important mechanisms, and we quantified the approach to termination by the fraction of fuel removed from the core region (at approximately 40%, permanent subcriticality and termination are achieved). Based on these results we completed the assessment by synthesizing sequences and respective likelihoods.

For these assessments we used the system codes SAS3D [23] and SIMMER-II [24]. These codes were used as "integrators" of the technical base and their results were guided, scrutinized, and augmented by employing special-purpose analytical techniques, in-pile experimental data, and out-of-pile simulant experiments as appropriate. "Engineering judgement" was a very important ingredient of these activities and since the term is so often misused and/or misinterpreted, we would like to elaborate on our usage.

First, judgement was required in identifying the priorities and level of detail (or effort) for assessing the variously initiated CDAs and particular aspects of each. In addition, judgement was applied to synthesize through various code calculations (including sensitivity studies), through auxiliary analyses, and through considerations of the available experimental evidence, the nominal range of expected accident progression (ranges of relevant phenomenology). Further, and perhaps most importantly, judgement was utilized in searching within this broad range for energetic-prone circumstances and adequately enveloping their consequences. Finally, judgement was required to synthesize sequences and likelihoods in a manner usable in the licensing context. The implication is that no single element (code, analysis, or experiment) is a sufficiently capable, or in our opinion, even desirable tool for addressing safety concerns associated with CDA energetics. We approached this task with the recognition that judgement in the above sense would be the central element of our efforts.

3. Structure of the Technical Management Plan

Among the variously initiated core disruptive accidents, those resulting from an unprotected LOFA (loss of pumping power in all sodium recirculation pumps with failure of the protection system to scram the reactor) or from an unchecked TOP (control rod withdrawal with failure of the protection system to scram the reactor) attracted almost exclusive attention in previous LMFBR safety assessments [3,9,10,19]. Also, historically, the LOFAs seem to have dominated in terms of concerns for energetically-prone mechanisms as well as severity of projected consequences [15,16,17,18]. The propagation of local faults, that is, Fuel Failure Propagation (FFP), as a mechanism leading to CDAs has been the subject of persistent investigations although with consistently negative results. The remaining CDA initiator possibilities arise from severe external events, that is, earthquakes beyond the safe shutdown design limit (SSE) or a variety of Loss-of-Heat-Sink (LOHS) accidents. A persistent LOHS event, although powered at decay heat levels only (protected accident), leads to coolant boil-off and a CDA eventually, nonetheless. A very severe earthquake, in addition to causing failures leading to any combination of the above initiators (for example, shearing off all primary recirculation lines and causing a LOHS situation), could also introduce core structural perturbations with associated reactivity changes. None of these other possibilities seems to have been the subject of serious study previously. Of particular interest in this regard is the call for attention to the LOHS accident expressed in a recent SNL study [20]. Based on the fact that LOHS accidents (as do all protected accidents) have a significantly higher probability of occurrence, as compared to the unprotected ones (LOFA, TOP), and on the findings of previous BNL work [21, 22] indicating the potential for recriticality in the CDA sequence of the LOHS, the SNL study concluded that such accidents dominate the risk.

As an initial step in our independent assessment effort, we made the judgement that among all CDAs, the LOFA should be chosen as the subject of our detailed considerations. This was based on the following: (a) the LOFA phenomenology spans the range of energetically significant CDA behavior; (b) within the LOFA sequences our previous review effort identified specific and significant areas of concern; and (c) preliminary scoping examination of all other CDAs, including the LOHS accident, indicated an energetically benign behavior as compared to that projected for the LOFA.

On this basis our technical management plan was formulated in terms of two more-or-less distinct portions. One was concerned with the in-depth study of the LOFA and the other dealt with all other CDAs, including probabilistic aspects of the respective initiators, a broad but realistic scoping of the relevant phenomenologies, and an evaluation of the consequences and/or of the available recovery margins. Detailed analyses on unique and important aspects of these accidents were to be conducted as needed.

A set of technical tasks and associated completion milestones was defined for each of these two portions. The definition and structure of the tasks in the LOFA portion were keyed to a generic visualization of the progression of CDAs, and of the LOFA in particular, as illustrated in Figure 2. In contrast to severe LWR accidents, the energetically significant portion of CDAs (with the possible exception of certain LOHS accidents, which are protected and hence evolve over a considerable period) is of a very short duration, that is, less than one minute for the LOFA. As a result there is no means or opportunity for such accidents to be complicated by external actions and typically they will evolve from initiation to termination on their own accord. As a result, a simple and generic structure as shown in Figure 2 indeed exists.

From the initiation of core disruption (initial cladding melting), the accident will evolve through a continuum of gradually escalating core disruption states until complete disruption (melting of all materials within the original core) occurs. Energetically, this progression is important for as long as a sufficient fraction of the initially present driver fuel (typically more than 60% for the CRBR) remains within the core region. Neutronically active states are then possible through a variety of rearrangements of driver, blanket, structural, control, and coolant materials. When such states are obtained by fuel compaction in supercritical configurations following highly but temporarily dispersed fuel states (subcritical), they are called "recriticalities." Permanent subcriticality, or "termination" (termination of energetic concerns), on the other hand, may occur from any point along the continuum of core disruption states. When the relocation of the appropriate quantity of driver fuel occurs in a forceful manner we speak of "energetic termination" or "hydrodynamic disassembly," or simply "disassembly." When this relocation is benign we speak of "mild termination" or simply "dispersal." Our overall objective is to determine the relative likelihood of these two termination paths (processes) as a function of the

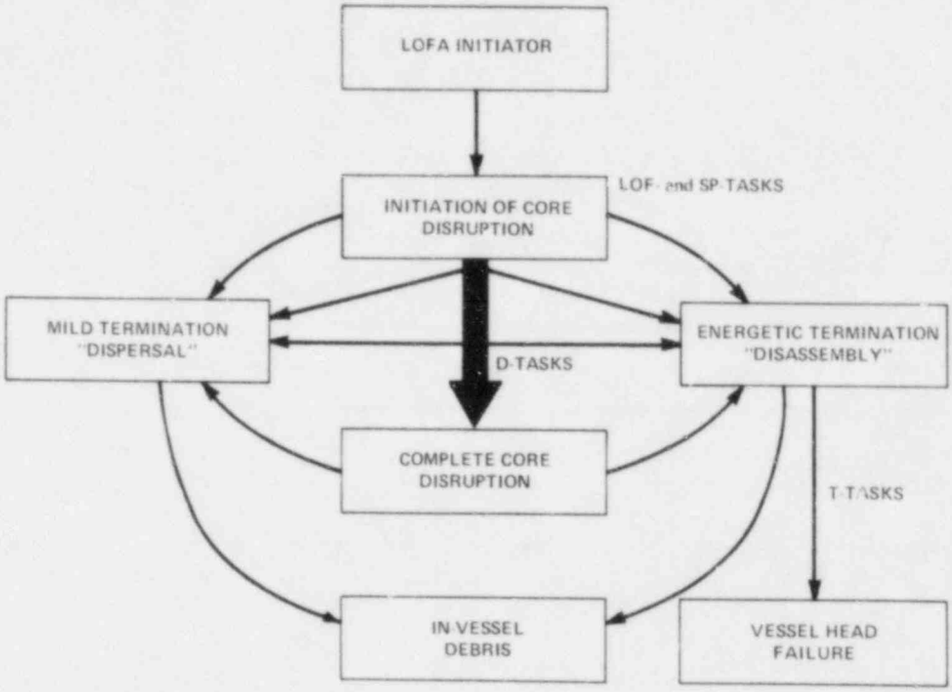

Fig. 2.
Generic progression of LOF CDAs and associated management structure.

degree of core disruption and to quantify the damage potential of the energetic ones.

This dependence on degree of core disruption is taken into account explicitly by assessing at each major stage of core disruption the likelihood of achieving termination against the likelihood of progressing into the next stage. Two groups of tasks (LOF- and SP-) addressing questions relevant to the initial stages of disruption and one group (D-) addressing questions in all subsequent disruption states were identified as shown on Figure 2. The initial stages of disruption are defined to extend through significant loss of fuel pin (rod) structure. The LOF- tasks pertain to events and phenomena typical of the classical LOFA and the SP- tasks address special (new) areas of concern. The technical basis for judging the damage potential of the energetic termination path against the capability of the CRBR primary system is developed in the group of T- tasks. With the exception of the dual-scope TOP- tasks, all other tasks are keyed specifically to the LOFA sequences. The adequacy of this approach, including the definition and resolution of any unique circumstances from other CDA initiators, is developed within the group of I- tasks.

The listing of all tasks is shown in the form of our milestone chart in Table 4. The vertical arrows indicate lines of feedback and/or continuing interaction. The Group was responsible for these integration activities. For each task, a reasonably detailed definition in the format of Table 5 was

TABLE 4
TASK MILESTONE CHART

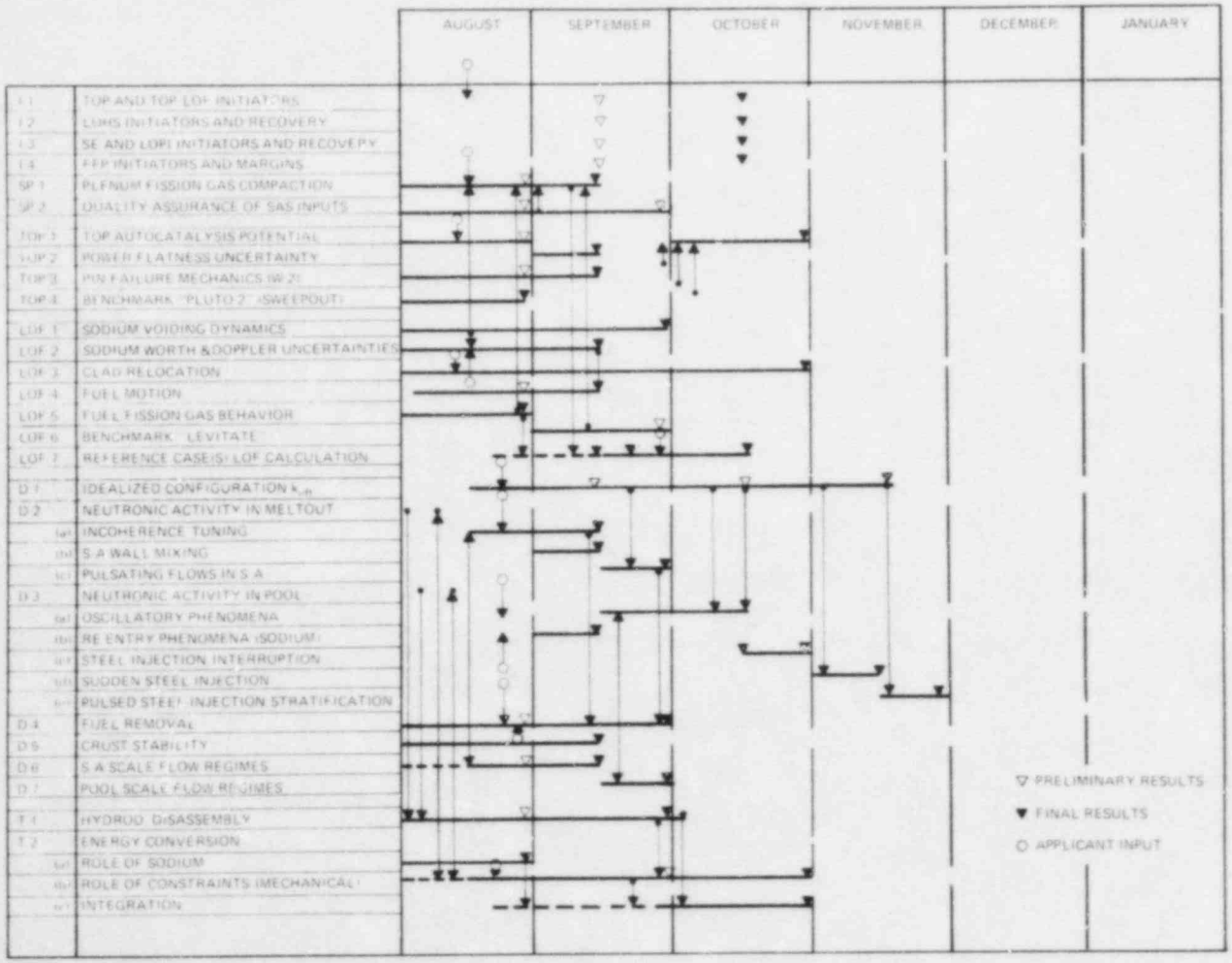

prepared. These tasks then were matched to individual Team members according to interest and specialty. The list of these assignments, together with the corresponding task definitions and other organizational details contained in the transmittal letter, has been compiled in Section 4 of the Compendium. Responses to our formal request for feedback on this technical plan did not indicate any area of difficulty, disagreements, or omissions.

Finally, it would appear proper to comment on the positive phrasing, "show that autocatalytic behavior is extremely unlikely," utilized in the sample task definition of Table 5, as well as in several of the other task definitions. This is not to be perceived as a biased outlook from the outset! Rather, it should convey the thought that in July 1982 the Group did not embank on an openly defined "research project" to be completed six months later; but rather it undertook to complete an assessment of a case for which it had a reasonably good understanding already (in addition to the first-phase six-month review effort, some of the Team members had been involved in the CRBR CDA energetics evaluations since the original application almost a decade ago!). Furthermore, a few independent studies were conducted by the Team during the review period. Thus, for the particular example of Table 5, such studies explored expressly for autocatalytic behavior and found none. Last, but not least, the general working atmosphere within the Team was to encourage the pursuit of any aspects for which potential difficulties could be suspected. Indeed, this mode of operation resulted in a number of new elements (as listed in Section 5) that significantly contributed to our understanding of CRBR CDA energetics.

4. Chronology of the Review and Independent Assessment Activities

The essential elements of the review and independent assessment phases of the CRBR energetics evaluations were discussed in the previous sections. A better appreciation of the interrelationships among these different activities and their relative timing may be gained with the help of Figures 3 and 4.

We hope that these figures clearly indicate our special efforts to seek "internal" as well as "external" feedback throughout the independent assessment phase for which we were responsible.

5. Major Accomplishments

Our independent-assessment studies ranged from simple parametric evaluations conducted within the context of the Applicant's analyses to completely new studies that are original in one or more of the following elements: (a) phenomena or effects taken into account, (b) analysis methods, and (c) experimental evidence. An effort is made in the technical presentation to identify the nature of the contribution on a topic-by-topic basis as the

TABLE 5
SAMPLE TASK DEFINITION

SP-1 Plenum F.G. Compaction

Objectives

Show that autocatalytic behavior is extremely unlikely. Establish a range of realistic LOFA initiating-phase power history outcomes.

Scope

Consider in detail fission gas inventories, blowdown constraints and accident timing margins. Consider incoherent core behavior. Consider the effect of fuel motion history (early). Take into account Na worth uncertainties. Consider R8 experimental information.

Output

Provide initiating phase power histories and enthalpy distributions for a range of conditions. Document one or two cases in detail adequate to visualize the scenario and sequence of processes. Highlight remaining areas of uncertainty.

Schedule

Preliminary assessment August 30. Final report September 15.

Resources

SAS3D, LEVITATE (SAS4A)

Inputs

LOF-2, LOF-5, SP-2, LOF-6

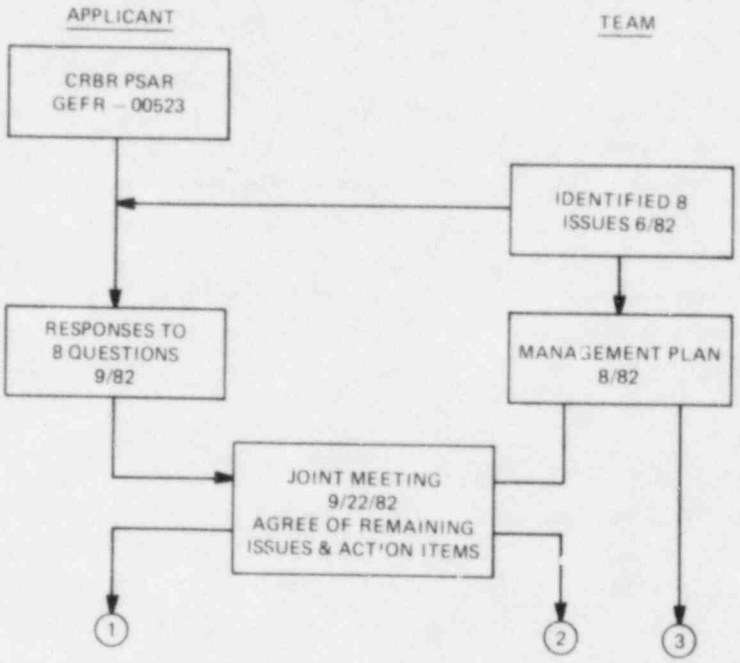

Fig. 3.
Review phase of the CRBR energetics evaluation.

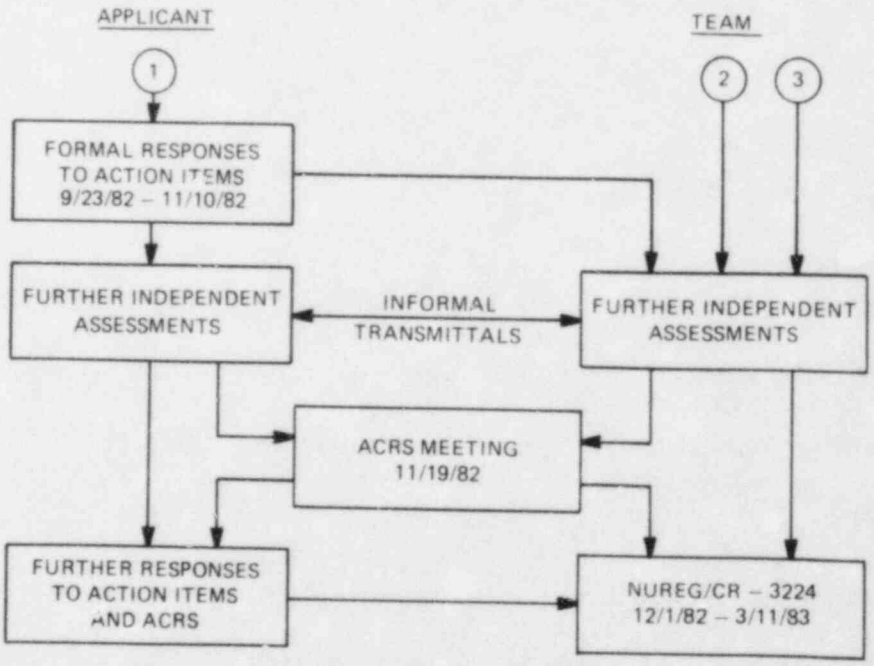

Fig. 4.
Independent assessment phase of the CRBR energetics evaluation.

case may be. For now we would like to offer, from our perspective, in summary form the major technical contributions made. The nature of these contributions is identified in the listing of Table 6 where reference to the appropriate report section is made for additional details.

A brief statement on each item on this table is given below.

(a) As a result of the eight questions, the Applicant revised upward the best-estimate value of the sodium void reactivity worth. This revision had a significant impact on the whole LOFA sequence and hence on the energetics potential.

(b) A new mechanism for energetic behavior in the LOFA was brought to the attention of the Applicant as a result of our review. This mechanism involves the compaction of fuel columns by the gas pressures in the fission gas plena, following loss of fuel pin integrity (occurring typically around the core axial midplane). This mechanism was accepted and eventually addressed also by the Applicant.

(c) Results of original calculations provided important new perspectives on the origin and possible magnitude of recriticalities.

(d) New analyses of recriticalities provided important new insights on the effects of fuel inventory and configuration (especially of the existence of single-phase regions) on the magnitude of the resulting energetics.

TABLE 6
MAJOR REVIEW ACCOMPLISHMENTS

- Revision of Sodium-Void-Worth Values (AII.3)
- Consideration of Plenum Fission-Gas Compaction (II.4)
- Detailed Consideration of Recriticality Potential (II.7)
- Inventory and Configuration Effects on Recriticalities (II.7)
- Energetics Mitigating Mechanisms due to Internal Structures (II.2)
- Consideration of the LOHS Accident (IV)
- Relative Likelihood of LOFA Evolution Paths (II.8)

(e) We identified and quantified significant energetics mitigating mechanisms in the mechanical constraints provided by the Upper Internal Structure (UIS) and Core Barrel (CB), that is, core "cage."

(f) Our evaluation of the LOHS accident (the Applicant did not submit such evaluations) indicates the absence of significant energetic behavior.

(g) It is our judgement that our evaluation of CRBR energetics has reached a level of confidence sufficient to allow a first attempt to quantify realistically the probability of energetically induced vessel failure.

6. Structure of this Report

The technical portion of this report is arranged under three major headings. Section II covers the detailed evaluation of the LOFA, Section III covers the evaluation of the TOP, and Section IV covers the evaluation of the LOHS.

The LOFA is treated according to the "generic structure" and the "philosophy of the overall technical approach" discussed above. With reference to Figure 2, the basis for the whole treatment is provided by establishing a range of expected phenomenology through the successive core-disruption states. This is done in Sections II.3 and II.5 for the initial and for all the advanced core-disruption states, respectively. Plenum fission-gas-induced fuel compaction (relevant during the initial stages of core disruption) and gravity-driven fuel compaction (relevant during the advanced stages of core disruption) were identified as dominant energetics-yielding mechanisms during these projected stages of accident evolution. Our assessments of the energetics potentially resulting from these mechanisms are found in Sections II.4 and II.7, respectively. The relationship between the magnitude of the reactivity excursion and resulting damage potential is developed in Section II.2. Considerations of termination by mild fuel removal from any one state in the core-disruption sequence are presented in Section II.6. Finally, the overall framework for converting all these assessments into a quantitative collective judgement is introduced in Section II.1 and is completed in Section II.8.

The other CDAs are handled similarly except not at the same level of detail. Here, emphasis is given to the identification and treatment of any unique circumstances (as compared to the LOFA sequences). The probabilistic aspects of CDA initiator intensity (rate of control rod withdrawal) and of available recovery margins (recovery from a LOHS event) also are considered.

As already mentioned, this document is focused on our independent assessment effort. However, important aspects of the Applicant's positions [10,11,25] are given in the introductory, "objectives and overview,"

subsection of each major section, together with references to documents and locations where the positions on the particular topic may be found in original form. We also reference our Draft TER [26] that contain our detailed evaluations of these positions. References to our supplemental TER [27] containing our evaluations of the Applicant's responses to the eight questions also are made as appropriate.

In the presentation of the technical material, several levels of detail are utilized to facilitate the communication at the level of detail chosen by the reader. The "Executive Summary" presents a non-technical abstract of our main results and conclusions. The "main body" of this report provides a technical presentation emphasizing the essence of the technical arguments and the results obtained. The details of the analysis methods and their bases are covered in the "Appendixes." Still more detail, including computer program listings, outputs, data, or other auxiliary material, may be found in the Compendium.

The report is organized in a "unit" format. Each unit is self-contained and independent with respect to all Appendixes, References, Nomenclature, Figures, Tables, and pagination. The set of units corresponds to the main report Sections (I, III, IV, V, VI) and subsections of Section II (II.1, II.2, . . ., II.8). The Appendixes are placed to follow the particular main text unit to which they refer and are named by prefixing the letters A, B, C, . . . to the number of this main text unit. The page numbering contains as a prefix the unit number such that with a glance at the Table of Contents the ordering of the units may be visualized and hence any unit may be quickly located through the page identification.

7. References

1. E. R. Copus, "Estimated Recurrence Frequencies for Initiating Accident Categories Associated with the Clinch River Breeder Reactor Plant Design," Sandia National Laboratory report NUREG/CR-2681 (April 1982).

2. "CRBRP Preliminary Safety Analysis Report," As Amended for the Heterogeneous Core Design, Project Management Corporation, Docket No. 50-537.

3. "CRBR Preliminary Safety Analysis Report," Project Management Corporation, Docket No. 50-537.

4. "CRBR Preliminary Safety Analysis Report," Appendix F, Project Management Corporation, Docket No. 50-537.

5. W. R. Bohl, H. K. Fauske, D. R. Ferguson, R. J. Henninger, and R. W. Ostensen, "An Analysis of Transient Undercooling and Transient Overpower Accidents without Scram in the Clinch River Breeder Reactor," Argonne National Laboratory report ANL/RAS 75-29 (July 1975).

6. W. R. Bohl, J. E. Cahalan, and D. R. Ferguson, "An Analysis of the Unprotected Loss-of-Flow Accident in the Clinch River Breeder Reactor with an End-of-Equilibrium-Cycle Core," Argonne National Laboratory report ANL/RAS 77-15 (May 1977).

7. J. L. McElroy, D. M. Switich, N. W. Brown, F. M. Chou, W. P. Damerow, and F. C. Rodgers, "Clinch River Breeder Reactor Plant: An Analysis of Hypothetical Core Disruptive Events in the Clinch River Breeder Reactor Plant," General Electric Company report CRBRP-GEFR-00103 (April 1978).

8. R. P. Denice ltr. to L. W. Caffey, "Design Safety Approach, Site Suitability Source Term, and Core Disruptive Accidents," U.S. Nuclear Regulatory Commission (May 6, 1976).

9. J. F. Meyer, L. Lois, J. L. Carter, and T. P. Speis, "An Analysis and Evaluation of the Clinch River Breeder Reactor Core Disruptive Accident Energetics," Nuclear Regulatory Commission report NUREG-0122 (March 1977).

10. S. K. Rhow, D. M. Switick, J. L. McElroy, and B. W. Joe, "An Assessment of HCDA Energetics in the CRBR Heterogeneous Reactor Core," General Electric Company report CRBRP-GEFR-00523 (December 1981).

11. "Hypothetical Core Disruptive Accident Considerations in CRBRP, Vol. 1: Energetics and Structural Margins Beyond the Design Base," Clinch River Breeder Reactor Project report CRBRP-3, Rev. 4 (March 1982).

12. "Compendium to NUREG/CR-3224, An Assessment of CRBR Core Disruptive Accident Energetics," Section 2, Nuclear Regulatory Commission Document (March 1983).

13. Official Transcript Proceedings Before the Nuclear Regulatory Commission Advisory Committee on Reactor Safeguards, Washington, D.C., November 19, 1982, T-1152.

14. T. G. Theofanous and C. R. Bell, "An Assessment of CRBR Core Disruptive Accident Energetics," Draft Los Alamos National Laboratory report NUREG/CR-3224 (March 4, 1983).

15. "Proceedings of the Fast Reactor Safety Meeting, Beverly Hills, CA, April 2-4, 1974," CONF-740401.

16. "Proceedings of the Fast Reactor Safety Meeting, Chicago, IL, October 5-8, 1976," CONF-761001.

17. "Proceedings of the Fast Reactor Safety Meeting, Seattle, WA, August 19-23, 1979."

18. "Proceedings of the Fast Reactor Safety Meeting, Lyon, France, July 19-23, 1982."

19. "Preliminary Safety Analysis Report, Fast Flux Test Facility," Westinghouse document (1970).

20. D. C. Williams, J. A. Sholtis, F. W. Sciacca, D. W. Varela, M. Rios, P. W. Conrad, E. R. Copus, M. J. Clauser and P. S. Pickard, "LMFBR Accident Delineation Study, Phase I Final Report," Sandia National Laboratory report NUREG/CR-1507, SAND 80-1267 (November 1980).

21. R. A. Bari, H. Ludewig, W. T. Pratt, and Y. H. Sun, "Material Relocation and Recriticality Assessment for the Loss-of-Heat Sink Accident in an LMFBR," Brookhaven National Laboratory report BNL-NUREG-23432 (November 1977).

22. R. A. Bari, H. Ludewig, W. T. Pratt, and Y. H. Sun, "Accident Progression for a Loss of Heat Sink with Scram in an LMFBR," Brookhaven National Laboratory report BNL-NUREG-50910 (October 1978).

23.[a] J. E. Cahalan and D. R. Ferguson, "A Preliminary User's Guide to Version 1.0 of the SAS3D LMFBR Accident Analysis Computer Code," Argonne National Laboratory informal document included with code (1977).

24. L. L. Smith, "SIMMER-II: A Computer Program for LMFBR Disrupted Core Analysis," Los Alamos National Laboratory report NUREG/CR-0453, LA-7515-M (June 1980).

25. "Compendium to NUREG/CR-3224, An Assessment of CRBR Core Disruptive Accident Energetics," Section 6, Nuclear Regulatory Commission document (March 1983).

26. "Compendium to NUREG/CR-3224, An Assessment of CRBR Core Disruptive Accident Energetics," Section 5, Nuclear Regulatory Commission document (March 1983).

27. "Compendium to NUREG/CR-3224, An Assessment of CRBR Core Disruptive Accident Energetics," Section 7, Nuclear Regulatory Commission document (March 1983).

[a] Address requests for this document to: F. X. Gavigan, Director, Office of Breeder Demonstration Projects (NE-50), U.S. Department of Energy, Washington, DC 20545, Telephone (301) 353-3134.

II. THE LOSS-OF-FLOW ACCIDENT

II.1. QUALITATIVE PROBABILISTIC FRAMEWORK

1. Objectives and Overview

This section lays the framework for quantifying the relative likelihoods of the various LOFA paths and outcomes (particularly those that challenge the vessel head). Such quantification, of course, can be done at various levels of detail and with varying degrees of rigor. For the results to be of adequate reliability, and thus useful, these choices must be made with a realistic appreciation of the available state of technology vis-a-vis accident sensitivities. At this time no well-established procedures or guidelines exist. In fact, the available experience in this area is very limited (see next section). Still, there seems to be little disagreement that the high end of the LMFBR risk spectrum is dominated by the energetics of CDAs. Notwithstanding the above difficulties, therefore, it appeared to us essential that our effort include a serious attempt in this direction. As it turned out, our studies revealed a generally insensitive CRBR energetic behavior, relative to the specified vessel structural capability, such that our final results are in fact considerably "cleaner" (of less ambiguity) than initially expected.

2. Previous Work

Previous attempts in this direction were made as portions of overall Probabilistic Risk Assessments (PRAs) and seem to have been overwhelmed by the magnitude of these efforts. Thus, in the recent SNR-300 PRA [1], the treatment of CDA energetics occupies approximately 50 out of the 815 pages of the study. The quantitative aspects on the CDA portion were synthesized from the responses of 18 internationally selected LMFBR safety experts who were polled by mail on certain aspects of the LOFA scenario. The available CRBR PRA [2] was done for the original homogeneous core design and also contains an abbreviated treatment of CDA energetics. The pivotal point in this work was a perceived (and well accepted until now) sensitivity of the energetic outcome to small variations in the assumed, or estimated, disassembly-driving conditions, beyond a low range considered insignificant for the structural design. The approach, therefore, consisted of arguing that any energetic behavior above a certain low value (approximately 30 $/s) would be a low probability event. Thus, for initiating-phase energetics, several SAS-3A parametrics for the LOFA were conducted to address the question ". . . to what extent conservative assumptions have to be

compounded . . ." for an energetic disassembly outcome. That is, recognizing the absence of experimental information in the LOF-d-TOP, a threshold (on-off) approach was utilized, rather than one discriminating on the level of resulting damage. Similarly, recriticalities were judged to be low probability events on the basis of the compaction-resistant nature of the volumetrically boiling CRBR core at decay heat levels. Based on these considerations, probability split fractions for three damage levels were assigned to the outcome of each CDA initiator. For the LOFA, for example, values of 10^{-1} and 10^{-2} were assigned for "moderate" and "massive" reactor vessel head seal failure, respectively. The energy level ranges of 300-800 MJ (around the design value of 661 MJ) and of 800-1500 MJ "or higher" were chosen to correspond to these two damage levels. These engineering-judgement probability assignments were intended to be conservative and the method included a review ". . . by a number of people who are knowledgeable about the current state of LMFBR accident analysis technology." The most recent Applicant position on the heterogeneous CRBR design contained in CEFR-00523 [4] is that "best-estimate" CDAs terminate in a benign fashion, and that energetic terminations are comparatively low probability events. No attempt was made, however, to quantify this judgement.

At the other extreme we find the Sandia LMFBR Accident Delineation Study [3]. The major emphasis here is in laying out the currently available understanding of the CDA phenomenological sequences in the PRA event-tree formalism. A detailed elaboration of much of the pertinent literature is given, and eventually the study loses itself in its own detail. In fact, the quantitative assessment of CDA energy yields, which is the source of all consequence analysis, is bypassed altogether in the single "quantitative" example given at the end. The LOFA for the CRBR heterogeneous core is chosen for this example. A qualitative discussion of the accident phenomenology concludes with, "For purposes of this illustrative example and its continuation into the Post-Accident Phenomenology Area, it is assumed [emphasis added] that the disassembly causes moderate damage to the vessel head but no secondary containment damage." Presumably the authors did not feel that the state of technology allowed at that time a quantification of the phenomena in terms of their methodology. However, qualitative approaches are not always more "forgiving" than quantitative ones. Two important issues will be mentioned in this regard. One concerns the judgement made in this example that initiating-phase energetics in the CRBR heterogeneous core design are negligible. The other, concerning the conclusion (presumably one of the major ones) made in this delineation study that for LMFBR in general and CRBR in particular, the LOHS accident represents the dominant CDA contributor to the risk (from energetics). We sharply disagree with both of these two judgements (see Sections II.4 and IV, respectively).

3. Present Procedure

3.1. Generic Structure of Accident Evolution

The essential elements of the LOFA CDA sequence as discussed previously (see Section I.3) are shown in Figure 1. Here the continuum of intermediate core-disruption states is discretized into two generic configurations. One is characterized by extensive fuel disruption although the subassembly (S/A) walls are still largely intact, that is, many S/A-scale pools. The other acknowledges the existence of core-internal blanket subassemblies as illustrated in Figure 2. Because of the low power level in these internal blankets, their disruption from their own internal heating would lag substantially behind the disruption of all driver fuel. In fact, such a time-lag would be substantially longer than the time required to melt the walls of the internal blanket subassemblies by the surrounding driver fuel. Hence, the formation of an annular pool is envisioned to precede the state of complete disruption, also known as a whole-core pool. It is our view that more detailed considerations, including additional intermediate disruption states, are unnecessary and beyond the level of detail considered reasonably predictable. However, the assessment proposed here is feasible even though the projected high neutronic activity (power transients) in the postinitiation period introduces a strong element of nondeterminism (randomness) that results in a chaotic, "long-term" character to the transient along the locus of highly disrupted core states.

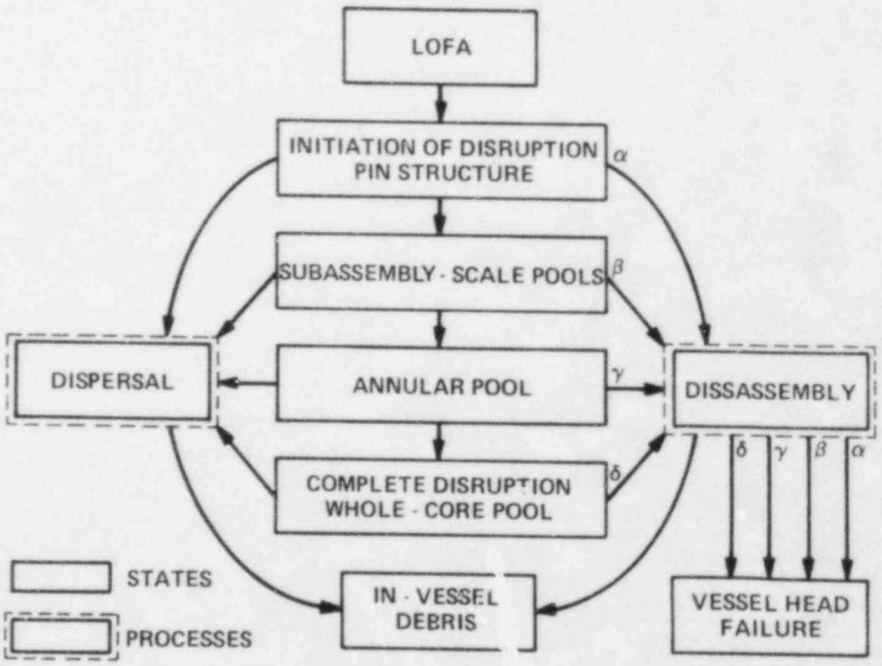

Fig. 1.
Qualitative probabilistic framework.

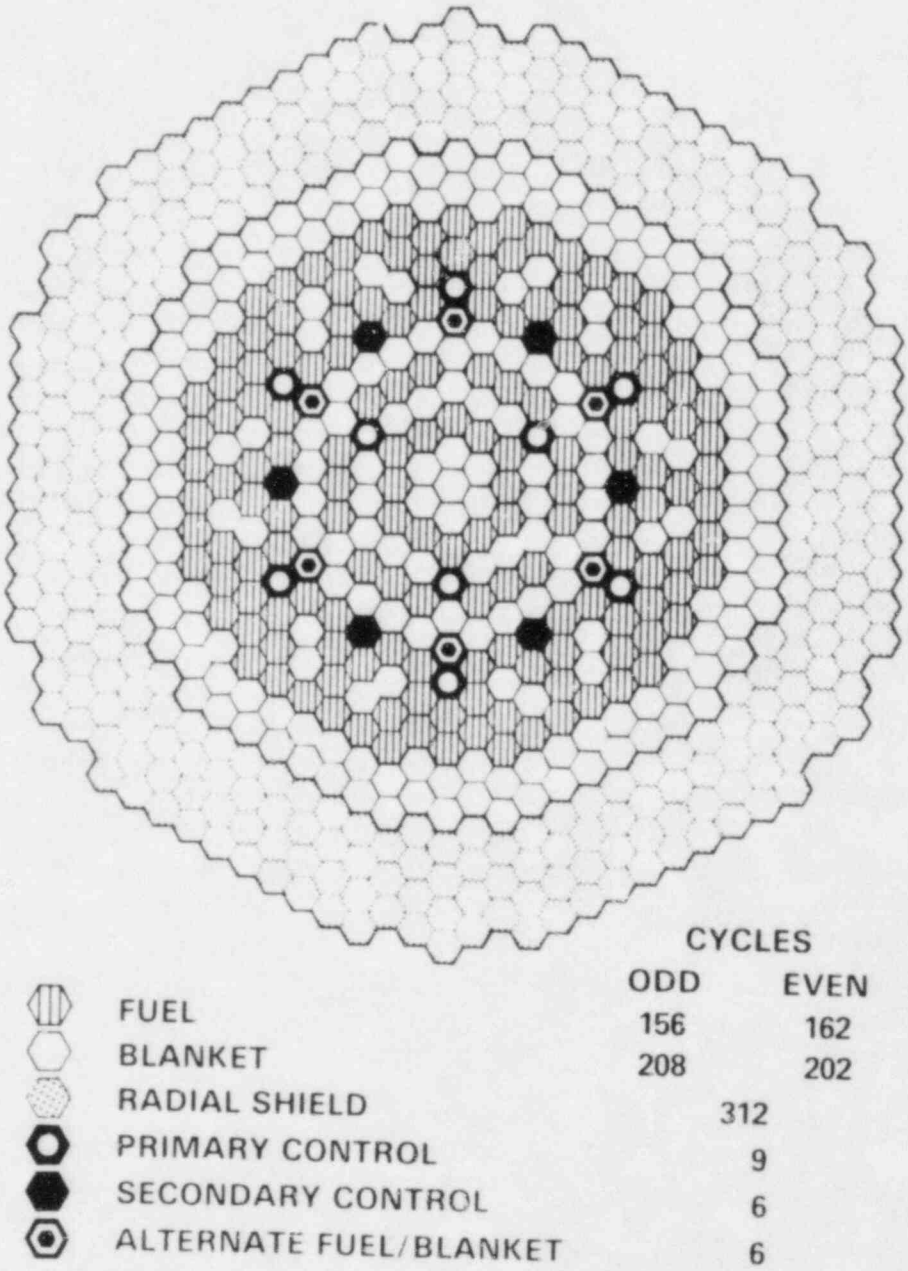

Fig. 2.
CRBR core configuration.

Both the mechanisms and the character of the potential energetic events change as we proceed from the initial stages of core disruption (often called "initiating phase") to the whole-core pool stage (named "transition phase" [5]). In particular, for all but the initiating-phase stages, this character is an important function of the fuel inventory (see sections II.5 and II.7). As shown in Figure 1, termination via mild dispersal can occur from any stage along the disruption path. Similarly, "partial" (insufficient to yield termination) dispersals also can occur. Such dispersals will continue to reduce the core fuel inventory, thus affecting the character of all subsequent stages. Therefore, a "long-term" memory effect is implied.

A detailed appreciation of this "dual character" of the core disruption process provides the key to the quantitative understanding of the potential energetic consequences. Our approach is to bound separately and conservatively the "inventory" effects as well as the magnitude of energetic events at each step along the disruption path. This is accomplished by enveloping the non-deterministic nature of the sequence by a priori deterministic calculations. This procedure is possible because

(a) the core fuel inventory depends mainly on the integral of the power history rather than on its detailed shape; and as the level of disruption increases, the fuel dispersal process is dominated by the increasing availability of the escape paths (intersubassembly gaps), thus becoming less dependent on pressure driving forces; and

(b) at each stage, recriticalities are best bounded not in terms of a precisely interphased calculation of a detailed core disruption history, but rather in terms of a priori specifications of recriticality geometries that span the range of physically possible behavior.

The quantitative aspects of this procedure are found in sections II.5, II.6, and II.7.

By comparison to the nondeterminism introduced by the extended fuel motions in the various advanced core-disruption states mentioned above, the early stages of core disruption including coolant voiding, clad melting, and initial fuel disruption (initiating phase) may be viewed as reasonably deterministic. Yet uncertainties in phenomenological behavior (material motions) give rise, also here, to a need for viewing this early sequence in terms of a range rather than as a single or even a few discrete outcomes. Our approach is to identify energetic mechanisms that can occur within this range and bound the energetic results. The quantitative aspects of this procedure are found in Sections II.3 and II.4. The core fuel inventory aspects of this phase are assessed in Section II.6.

3.2. Definitions and Probabilistic Concepts

In the next few sections we will develop the basis for assigning probability split fractions to each of the transitions shown in Figure 1. In a complete probabilistic study, the transition probabilities would be dependent upon the probability distributions of the various important parameters and, in principle, could be obtained from them through a series of calculations and classification of outcomes according to the definitions taken for each transition path. In addition, by considering the uncertainty ranges in these distributions, uncertainty bounds could be placed on the transition probabilities.

However, this process is not practical for the problem at hand. Several reasons may be cited: (a) the detailed probability distributions for individual parameters that control the processes are not known; (b) the probability distributions of the deviations of the various analytical (model) predictions from the corresponding reactor behavior are not known; and (c) the sensitive and hence nondeterministic character of the core disruption sequences cannot be quantified probabilistically. Furthermore, it is unlikely that these difficulties could be eliminated at any time in the foreseeable future. As it turns out, all these details can be made unnecessary in characterizing the energetic behavior of the CRBR heterogeneous core.

This is accomplished by aiming to quantify the high (in severity) ends of the probability spectra rather than the complete distributions. That is, at each transition we aim to bound the energetic consequences from above and the dispersal behavior from below. The result is a high confidence level, upper bound, vessel failure probability. Clearly, some judgement is required in developing the technical base and in assigning the actual numbers for each transition. The role of such judgements and the associated level of confidence can be appreciated only after a careful study of Sections II.2 to II.6.

Probability levels are assigned on an order of magnitude basis according to the following definitions. A transition with 10^{-1} chance is one with an overall behavior within known trends (adequately characterized by a set of parameters) but obtainable only at the "edge of spectrum" of the parameter values. A transition with 10^{-2} chance represents a behavior that cannot be positively excluded, although its occurrence would be clearly "outside the spectrum of reason." As a consequence of these two definitions, an outcome with a 10^{-3} chance represents the in-series occurrence of an off-spectrum and an edge-of-spectrum event and should be characterized as "physically unreasonable." The dispersal transitions are examined against the 40% core fuel inventory reduction required for permanent subcriticality. The vessel failure transitions are judged by comparing the estimated upper-bound mechanical energy releases (measured as sodium slug kinetic energy impacting the vessel head) against the specified design capability of 75 MJ. The disassembly transitions include only those that have the potential for significant vessel head loading. All these definitions are summarized in Table 1.

TABLE 1
DEFINITION OF PROBABILITY SPLIT LEVELS

1/10	Behavior within known trends but obtainable only at the edge-of-spectrum parameter values.
1/100	Behavior cannot be positively excluded but outside the spectrum of reason.
1/1000	Physically unreasonable behavior violating well-known reality and its occurrence can be argued against positively.

3.3. Probabilistic Assessment Procedure

The procedure involves three major steps. In the first step we characterize the accident progression along the various core-disruption states (Figure 1), without particular regard for termination processes. The aim is to identify and characterize the range of possible behavior in certain important respects. Power behavior, blockage formation, and timing between successive disruption states represent some of these important aspects. This task is accomplished in two segments, Sections II.3 and II.5, for the initiating and all other disrupted-core states, respectively.

The second step is focused on the termination processes. The path of core-succession states previously established is now searched to identify and quantify (bound) the occurrence of energetic events. The two such mechanisms identified are treated in Sections II.4 and II.7 for the two segments of analysis mentioned above, respectively. Similarly, fuel dispersal rates at the various stages along the disruption path are estimated to scope the benign termination potential (Section II.6). Based on the outcome of these studies, a dominant behavior along either of the two termination paths or toward the next disruption state is identified at each transition in core-disruption state. The remaining two paths then are identified as edge-of-spectrum or off-spectrum events.

Finally, in the third step the disassembly paths are assessed analytically for their mechanical consequences (Section II.2). Conservative bounds are again established and vessel failure probabilities are assigned to each path based on previous definitions according to the implied violation of (or margin from) the design limit.

4. References

1. Gesellschaft Fuer Reaktorsicherheit, "Risk Oriented Analysis on the SNR-300 Reactor," GRS-A-700, Vol. 1 and 2 (April 1982).

2. "CRBR Risk Assessment Report," Clinch River Breeder Reactor Project report CRBRP-1 (March 1977).

3. D. C. Williams, J. A. Sholtis, F. W. Sciacca, D. W. Varela, M. Rios, P. W. Conrad, E. R. Copus, M. J. Clauser, and P. S. Pickard, "LMFBR Accident Delineation Study, Phase I Final Report," Sandia National Laboratory report NUREG/CR-1507, SAND 80-1267 (November 1980).

4. S. K. Rhow, D. M. Switick, J. L. McElroy, B. W. Joe, "An Assessment of HCDA Energetics in the CRBR Heterogeneous Reactor Core," General Electric Company report CRBRP-GEFR-00523 (December 1981).

5. J. F. Jackson, M. G. Stevenson, J. F. Marchaterre, R. H. Sevy, R. Avery, and K. O. Ott, "Trends in LMFBR Hypothetical-Accident Analysis," Proceedings of the Fast Reactor Safety Meeting, Beverly Hills, CA, April 2-4, 1974, CONF-740401.

II.2. CRBR STRUCTURAL CAPABILITY

1. Overview and Objectives

Because of the dispersive character of matter under high heating rates (thermal expansion and vapor pressures), the high pressure characteristic of disassemblies must develop in short (millisecond) time scales. These high pressures are possible at sufficiently high reactivity insertion rates such that super-prompt criticality and the associated extremely high power levels are maintained for a sufficiently long time (typically 1-2 milliseconds) to produce the necessary energy before the self-limiting character (Doppler, rapid outward displacements due to high internal pressures) of these excursions yields neutronic shutdown.

High reactivity insertion rates or ramp rates require rapid material relocations. As we will see in Section II.7, the actual relationship between these two quantities and with the associated energy release is a strong function of the quantity and configuration of the materials involved. Typically for vapor-pressure disassemblies (disassemblies occurring in the two-phase regime), a ramp rate of approximately 30 $/s would be required to produce pressures in excess of a few atmospheres. For purposes of this discussion, we will use this ramp rate level to define, roughly, the onset of energetic behavior. In conjunction with material reactivity worths, the corresponding material relocation requirements for energetic behavior may be identified.

Thus, for the CRBR heterogeneous core with a maximum sodium void worth below 2$, the coherent voiding of the whole core in less than 0.07 s would be required to achieve energetic behavior. In fact, some very early LMFBR LOFA analyses considered such a direct disassembly mechanism, which was postulated to occur by highly superheating and suddenly flashing the core sodium into vapor. Today we know that except in highly controlled laboratory environments such high superheating and associated rapid sodium voiding is truly physically unreasonable and we cite it as an example of our 1/1000 probability category. In fact, we will see (Section II.3) that sodium voiding, in an intact pin geometry, is roughly one order of magnitude slower than required for energetic behavior. However, sodium voiding in the presence of or because of fuel pin disruption may be substantially faster. In the CRBR heterogeneous core design, such situations arise only under a very particular set of circumstances (see Section II.4); and, in any case the overall reactivity transient is dominated by fuel motion.

The core cladding worth is approximately 5 $ and its complete removal in less than 0.17 s could yield the onset of energetic behavior. Again, such behavior is physically unreasonable. Even if all cladding could become mobile (molten) within this time (this in itself being impossible), the forces and mechanisms for such rapid relocations simply do not exist (see Section II.3). Furthermore, such massive relocations, should they be postulated, would be self-terminating by freezing and plugging of the core exit paths.

Finally, a uniform, core-wide fuel compaction by approximately 0.01 m would insert a reactivity of approximately 1$. Uniform compaction velocities in excess of 0.30 m/s would be required for energetic behavior through this mechanism, in CRBR. Alternatively, higher velocities and smaller core fractions could be equally effective. These situations cannot be excluded a priori in the simple manner just done for the sodium and cladding cases and will have to be considered, therefore, in detail.

The essential conclusion is that only substantial fuel compactions are relevant to energetics concerns. Cladding and sodium relocations (and associated neutronic feedbacks and thermal effects), however, also are significant in setting the stage for these all-important fuel motions during the initial phases of core disruption. The negative reactivity feedbacks from Doppler, fuel axial expansion (in pin geometry, prior to disruption), and retained (within the fuel) fission gas and vapor pressures that help moderate positive reactivity insertions also should be mentioned here. Further, because of the non-uniformity in power and coolant flow distributions, considerable variations develop in the timing of material motions across the core. Such space-time distributions in voiding and cladding relocation processes directly affect the early accident evolution, particularly in promoting fuel motion incoherencies and hence moderating any resulting positive reactivity insertion rates from such motion.

These considerations on the onset of energetic behavior, together with the level required to produce "significant mechanical damage," form a perspective against which the search for energetics must be made. The objective of this section is to quantify this latter aspect. As shown in Figure 1, two structures are relevant in this regard; hence the discussion is presented in terms of the two levels of energetics that roughly correspond to the onset of potential mechanical damage for these two structures, respectively. From a risk standpoint, the integrity of the Vessel Head Structure (VHS) is significant. Failures in this structure would allow the release of coolant directly into the containment atmosphere with the possibility for spray fires and containment overpressurization. At the extreme of catastrophic failure, one might even be concerned about missile generation and hence direct challenge to the containment boundary integrity. The significance of the "cage" defined by the UIS/CB/CSS enclosure (the term cage is used rather than bottle to signify the leaky character of this enclosure), however, is in providing an "intermediate containment" so to speak with substantial

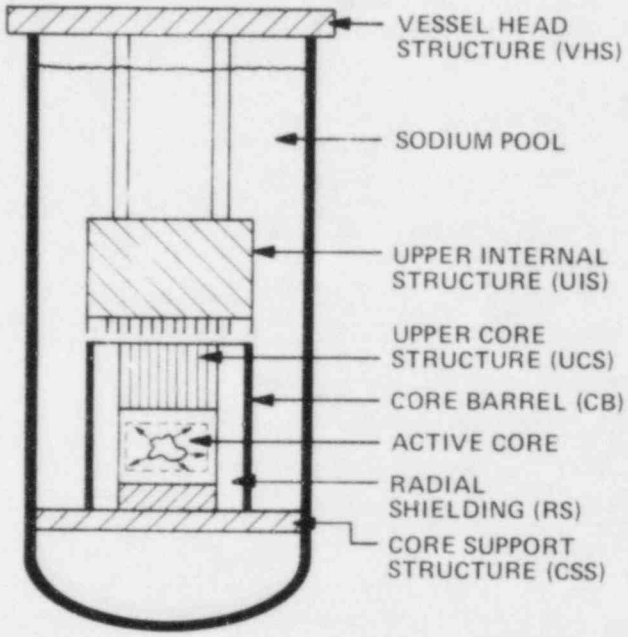

Fig. 1.
Important structures in evaluation of CRBR energetics.

dissipative qualities (mitigating VHS loadings). The analysis is conducted in two steps.

We begin with the immediate postdisassembly stage (Section 2), that is, with the power excursion terminated, but before any significant expansion (only slight displacements are required for neutronic shutdown) of the high pressure core materials. For the purpose of this discussion, this state will be characterized by the work produced through a packet-by-packet adiabatic expansion to a final pressure of one atmosphere and will be related to a reactivity ramp rate through a vapor-pressure-driven (two-phase) disassembly. This ideal work production is associated with an uncontained (free) expansion, hence it will be called "Ultimate Work Potential" (UWP). An expansion to the cover gas volume, however, is a more appropriate measure of the potential for VHS damage and will be called "Impact Work Potential" (IWP). The effect of material quantity and configuration on the energy yield and the relation to the cases chosen here will be covered in Section II.7. In the first analysis step (Section 3.1), the expansion is allowed to proceed only within the UIS/CB/CSS cage. With the boundaries of this enclosure fixed, we can estimate loading histories and thus evaluate the structural response. This portion we call "short-term expansion." The second step (Section 3.2) consists of continuing the expansion into the sodium pool. This portion we call "long-term expansion." Clearly, this second expansion is relevant only in the event of substantial failure of the cage boundary. The long-term expansion then would be forceful, yielding sodium pool acceleration and,

eventually, pool impact with the VHS. This impact kinetic energy (IKE) defines the forcing function against which the structural capability of the VHS is assessed [1].

The Applicant has taken the position that significant energetic behavior is of extremely low probability. Hence, the quantitative aspects of excursion yields and energy conversions (damage potential) were not emphasized. The Structural Margin Beyond the Design Basis (SMBDB) was based on an arbitrarily defined pressure-volume (fuel vapor expansion) curve with an UWP of 661 MJ, and an IWP of 100 MJ. The role of the UIS in constraining this expansion was neglected (subsequently in response to our Question #8, see Table 2 of Section I, the Applicant estimated [11] that the UIS columns would buckle at a pressure of approximately 10 MPa); however, a relatively small degree of energy absorption into the CB was taken into account to yield a slug IKE of approximately 75 MJ. One initiating-phase (assumed for a TOP sequence) disassembly for 43 $/s was analyzed [2] yielding an UWP of 111 MJ and an IWP of 33 MJ which was well below the SMBDB of the VHS. The Applicant estimated that ramp rates of approximately 80 $/s and of 90-100 $/s for initiating-phase and recriticality disassemblies, respectively, would be required to produce mechanical energy releases approaching the system's structural capability. Our detailed comments on the Applicant's documentation in this area may be found in Reference 3.

2. Energy Yield Characteristics

The two-step analysis method mentioned above was employed here for disassemblies representative of 100 $/s and 200 $/s. The actual results presented are for 110 $/s and 220 $/s, respectively, as obtained by ideally imposed material motions in a two-phase, disrupted core. These two levels were chosen as roughly indicative of the energy required to approach the structural capability limits of the UIS/CB/CSS cage and of the VHS, respectively, and with no regard for the actual attainability of such conditions. Their relationship to any projected CRBR energetic events will be discussed in Section II.7.

The energetic characterization of these two disassemblies, made according to the methods and results of Section II.7, is graphically depicted in Figures 2 to 4. The work potential results are not very sensitive to the equation of state utilized, as long as consistency is maintained in the usage between disassembly and expansion calculations; hence they are convenient in expressing in a very loose way the "severity" of the excursion. The temperature distributions, Figure 3, however, are useful for understanding the magnitude of the core internal pressure gradients as shown in Figure 4. The adiabatic, packet-by-packet expansions that have been traditionally utilized [4] to obtain the UWP and IWP values and the loadings (shown in Figure 5 for the two cases at hand) on the immediate structures (CB in

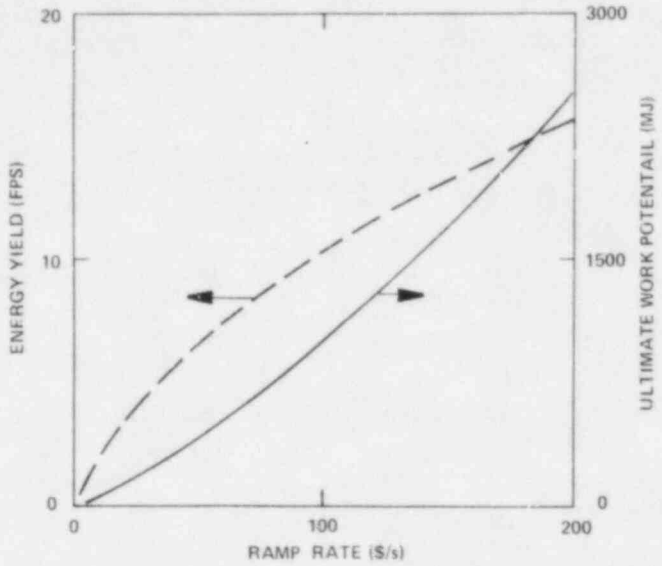

Fig. 2.
Yield characteristics of disassemblies at various ramp rates.

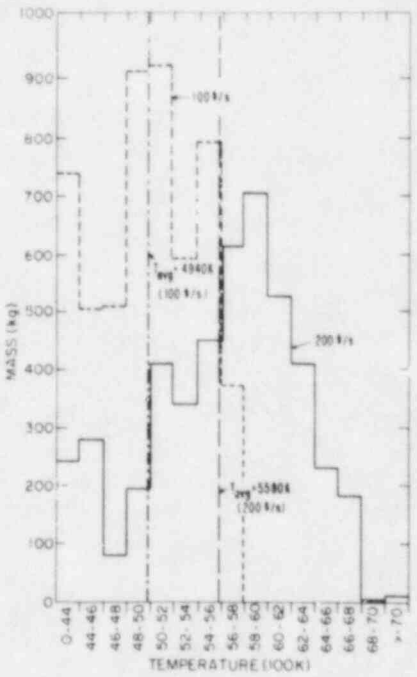

Fig. 3.
Nonuniform energy generation characteristics from disassemblies.

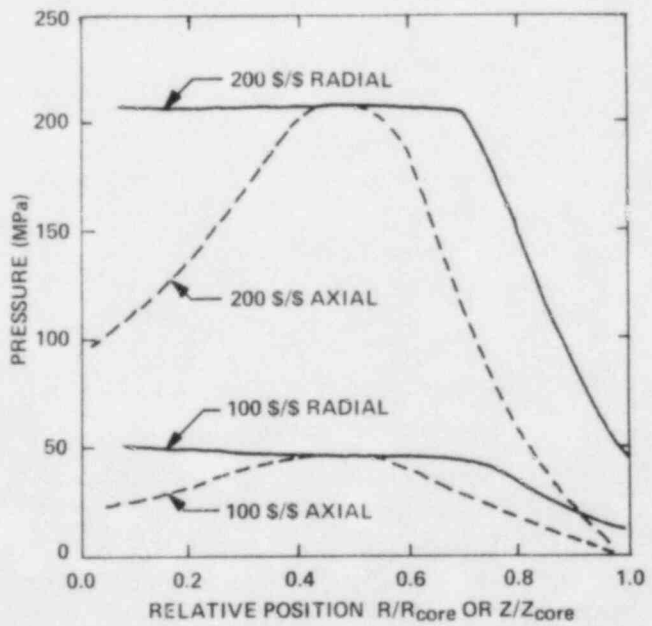

Fig. 4.
Nonuniform pressure characteristics from disassemblies.

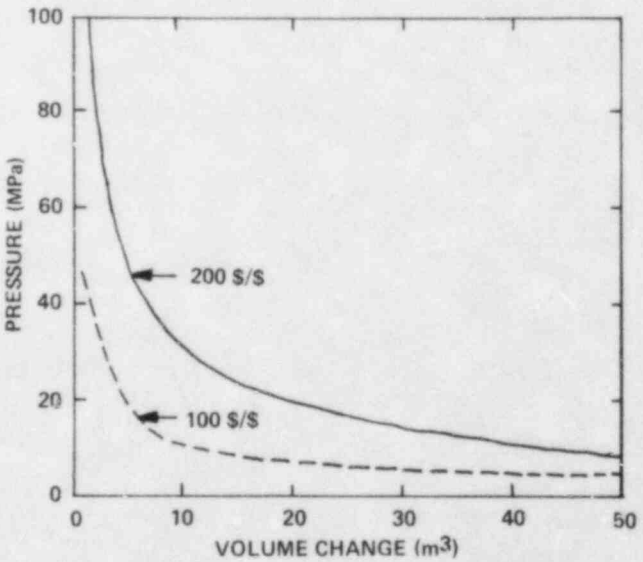

Fig. 5.
Pressure vs. volume change for isentropic expansions.

particular) disregard these internal gradients, and hence the associated dissipative effects.

The mitigating character of these internal pressure gradients results from the existence of void space both within the expanding core and within the surrounding material that will eventually transmit the loading to the adjacent structural boundary (the UIS/CB/CSS cage). The core-internal void allows rapid decay of the peak pressures of Figure 4 by a succession of local expansions before these pressures can be transmitted to the boundary. The recognition of this mechanism is important, particularly in view of the crucial role of such internal voids (and the associated compliance) in allowing the development of high energetic yields in the first place, as compared to low void single-phase systems (see Section II.7).

3. Energy Conversions and Damage Potential

3.1. Short-Term Expansion

The objective of this first portion of the analysis is to quantify the structural response of the UIS/CB/CSS cage subjected to the forces resulting from the relaxation of the thermal energy states depicted in Figure 3. These loads are highly dynamic and a rigorous computation must consider simultaneously the fluid with the structure dynamics. In the absence of an adequate computational tool in this regard, we proceed to decouple the problem and obtain an approximate solution.

First we considered the fluid-dynamic loads resulting from an expansion constrained within an assumed rigid-boundary enclosure or cage. This assumption eliminates pressure relief from the displacement of these boundaries; hence, it should provide a conservative load definition. The detailed description of the SIMMER-II model utilized in these analyses is given in Appendix A. Briefly, a core-internal void of 1.0 m^3 (approximately 30%) more or less uniformly distributed, and a surrounding material void of approximately 7 m^3 has been utilized as shown schematically in Figure 6. Of this surrounding void the major portion is found within the Upper Core Structure (UCS) region (fission gas plena). These surrounding regions were assumed to freely "crush" (void collapse) against the rigid boundaries constrained only by their own inertia. Based upon this calculated pressure field, a preliminary estimation of the CB strain was made according to the procedure discussed in the next paragraph. A second and more realistic calculation of the pressure field then was made by repeating the expansion described above but with an allowance for CB boundary displacement, taken as a conservative fraction of the estimated CB strains as shown in Figure 6. These second-iteration pressure transients, at several key locations within the enclosure, are shown in Figures 7 and 8 for the 100 \$/s and the 200 \$/s

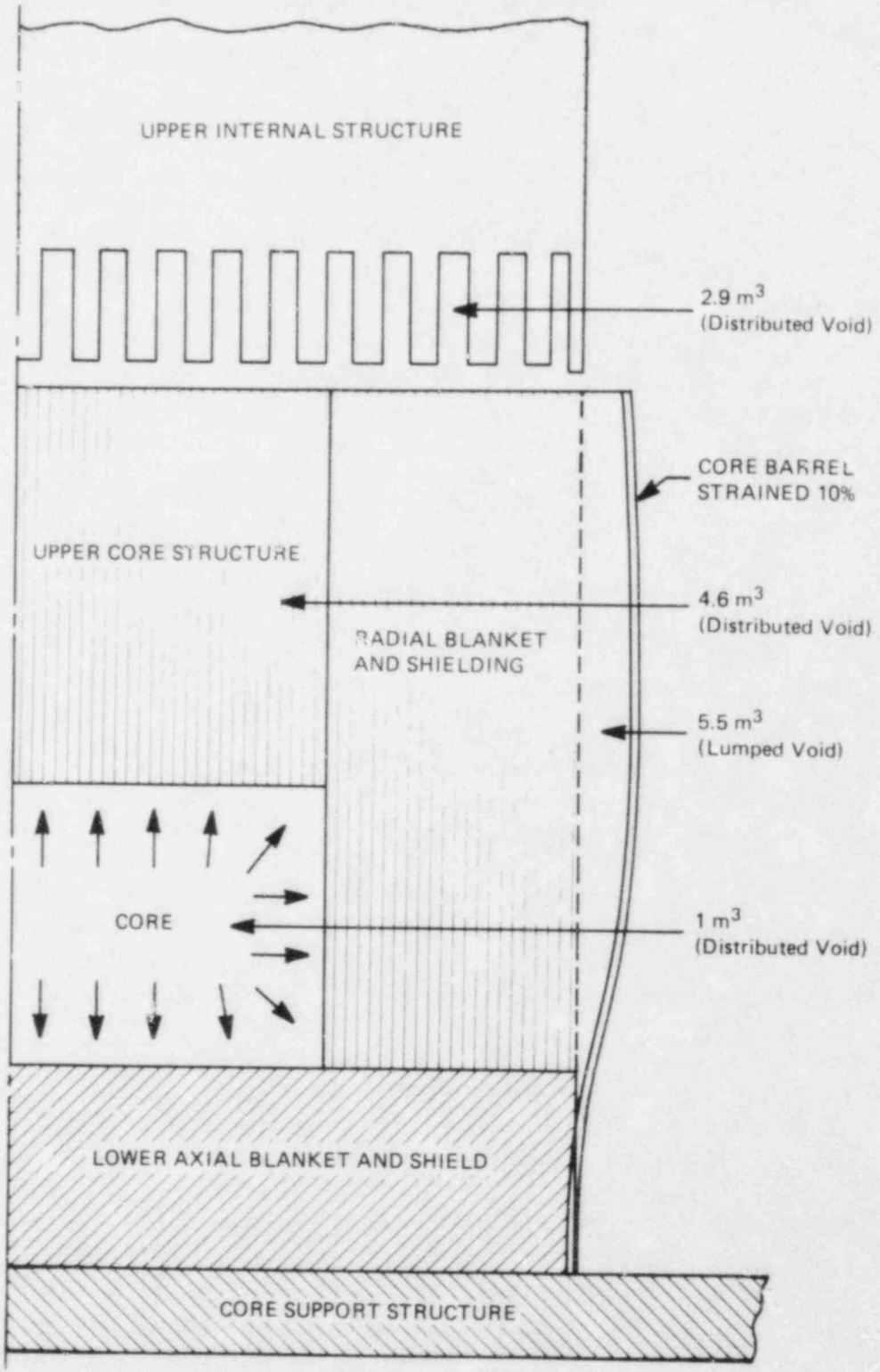

Fig. 6.
Short-term expansion configuration.

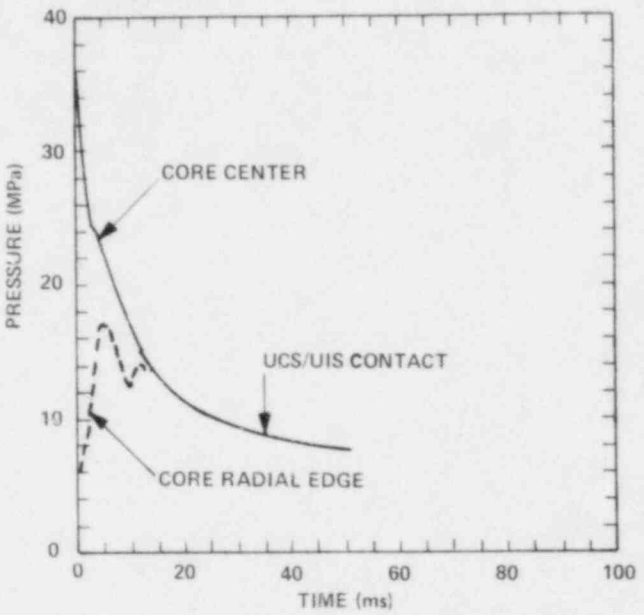

Fig. 7.
In-core pressure transients for the 100 $/s short-term expansion.

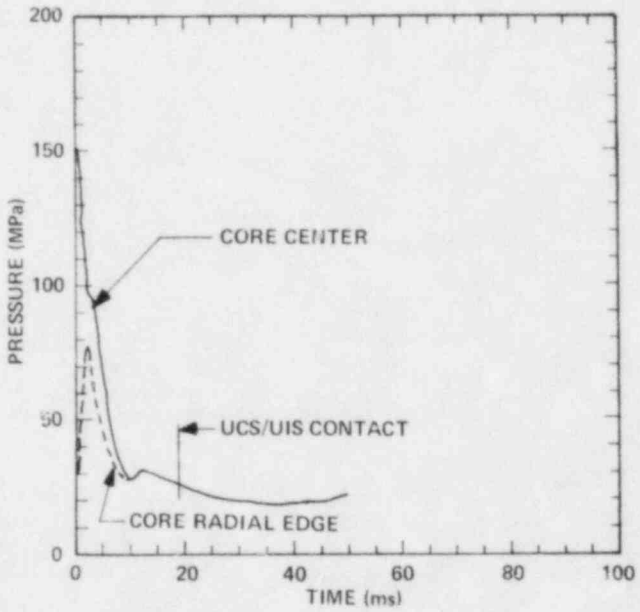

Fig. 8.
In-core pressure transients for the 200 $/s short-term expansion.

cases, respectively. Especially note that the radial, CB, loads would be grossly overestimated if the peak pressure was used rather than the pressure at the edge of the core. The detailed results may be found in Appendix A.

The structural responses of the CB and UIS under the dynamic loads defined above were determined with the help of the finite-element model described in Appendix B. The actual calculations were performed following a successful benchmarking exercise against the SRI CRBR model tests [5] and a REXCO calculation [4].

The calculated UIS displacement histories for the two cases considered are shown in Figure 9. We can see that for the 200-$/s case the UIS boundary clearly fails, while a small but measureable (indicating the approach to failure) total displacement was found in the 100-$/s case. As may be seen in Figures 7 and 8, the quasistatic UIS loading pressures for the corresponding cases were approximately 20 MPa and 8 MPa, respectively, hence our results are in good agreement with the 10 MPa failure threshold provided by the Applicant. Taking into account the additional dynamic loading from the impact of the accelerated UCS (free crushing assumption) with the UIS, the 100-$/s case would indicate UIS failure based on simple momentum and energy considerations.

The UIS failure threshold also can be approached from another limit, that is, assuming that the UCS and CB do not strain. The results of Figures

7 and 9 indicate that quasistatic pressures in the range of 8 to 10 MPa would be required for failure. Taking into account, in this limit, an expansion into the internal voids (approximately 1 m^3) only to achieve these quasistatic loading conditions (with no major structural displacements), we estimate that an energetic event of 9.5 FPS (or approximately 90 \$/s) would be required. Thus, it is seen that the UIS failure threshold is approached and surpassed within a narrow range of ramp rates around 100 \$/s.

The calculated CB displacement histories are shown in Figure 10. Again, the 100 \$/s loads are clearly contained, while the 200 \$/s case indicates strains well within the failure range of approximately 10-20%. The CB strain allowed in the expansion seems to have converged for the 100 \$/s; however, the 10% allowance (see Figure 6) made in the 200-\$/s expansion still is conservative. Furthermore, at these high strains, the vessel would establish contact with and expand against the guard vessel; therefore an additional stiffening effect should be considered. Considering everything, we judge that the CB failure conditions under a 200 \$/s disassembly are only marginally met.

The net result of this short-term expansion is to degrade the work potential greatly while little kinetic energy is manifested in the sodium pool. For the 200-\$/s case with the free-crushing assumption, 520 MJ of mechanical energy was released. This corresponds well with the isentropic work, 535 MJ, for an equivalent expansion, indicating that numerical dissipation in our

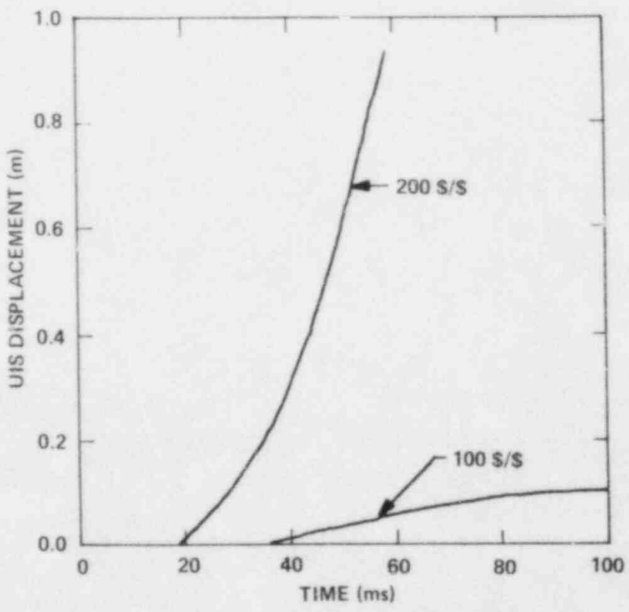

Fig. 9.
UIS displacement histories during the short-term expansion.

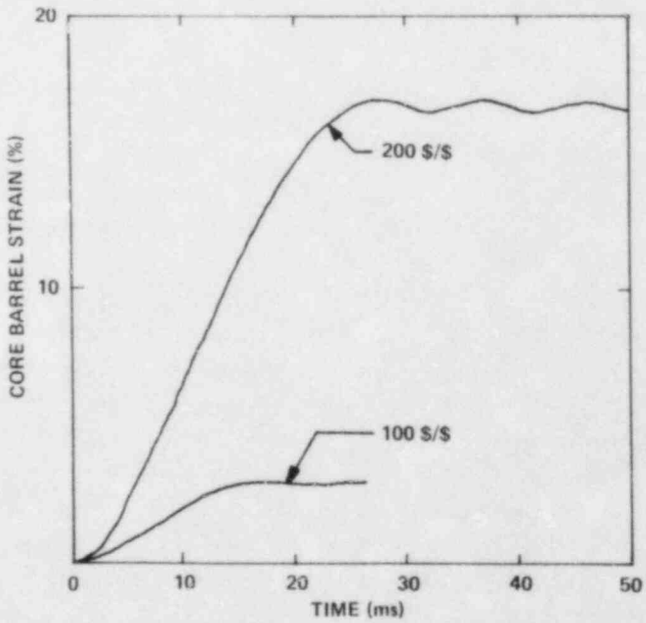

Fig. 10.
Core barrel strain histories during the short-term expansion.

dynamic calculations was minimal. Of that, approximately 180 MJ is used in straining the core barrel and vessel and dissipated by expansion into the core internal voids. The other 340 MJ is manifested first as kinetic energy in the UCS. After UCS/UIS impact, most of it is dissipated in the inelastic interaction between these two bodies. At most about 85 MJ is given to the UIS. This kinetic energy cannot be effectively given to the pool to augment the head impact loads. This kinetic energy is dissipated by column crushing, sodium slug rebound after impact with the VHS, and delayed interaction with the head. Our assessment of the UIS/VHS impact using simple analytical models and SRI model test data [5] indicates that this would be a decoupled event relative to sodium pool impact and, therefore, of little consequence to the VHS integrity. This delayed impact is damped substantially by the intervening sodium and UIS columns.

The impact of our approach for assessing CB behavior may be surmised by comparison with the results of Reference 4. The 5400 K CRBR case of Table I of Reference 4 corresponds to approximately 10 Full Power Seconds (FPS) or approximately 10000 MJ. This case is close to our 100-$/s case and was estimated to yield a 12.5% CB strain. Our estimated strain for this case is much lower (approximately 2.5%). In fact, the pressure transient utilized in loading the CB in Reference 4, as shown in their Figure 2, seems to correspond qualitatively to our 200-$/s case (see Figure 8) and indeed produces CB strains very similar to those we calculated, that is, 12.5% vs 18%. It is clear, therefore, that the structural portion of our analysis method is consistent with previous work, while the substantial discrepancy in final results lies in differences in the definition of the forcing functions.

In the SIMMER-II expansions reported herein, the heat exchange among the different constituents of the expanding core region were neglected. With the exception of the sodium coolant, which would be absent in the post-initiating-phase, recriticality-type energetics of interest here (see Sections II.3, II.4, and II.5), these constituents include steel and, depending on the circumstances, blanket materials. These discrete materials will remain essentially "cold" during the extremely short duration of the power burst, hence, they will represent substantial heat sinks in the post-disassembly expansion period. Owing to the complex nature of the underlying physical processes and the variability in the material quantities and configurations involved, the actual quantification of this effect is not straightforward. However, the generally mitigative character of such thermal interactions was established through parametric SIMMER-II calculations [6] and, for now, we will let this effect represent an unquantified conservative element in the adiabatic expansion results reported herein.

3.2. Long-Term Expansion

For as long as the structural envelope of the UIS/CB/CSS system remains largely intact, an effective "throttling" of the expansion process is achieved with essentially no VHS damage potential. However, the massive failure of this "intermediate" containment envelope would release a high-pressure expanding fluid at the base of the sodium pool, causing its upward acceleration until vessel head impact. Our objective here is to quantify both the pressure release and energy conversion processes.

Again, an idealized conceptual model, as shown in Figure 11, was utilized for this purpose. A fixed UIS position, displaced by 0.5 m, was chosen to minimize the radial flow area restriction and hence any interference with the blowdown process. As may be seen from the UIS displacement transients, the time for achieving this displacement is of the same order as that for long-term expansion. Thus, in reality the area would be restricted partially and the long-term expansion would be throttled somewhat. The calculation was initialized at the quasistatic core conditions achieved at the end of the constrained, short-term, expansion just discussed. Again, the expansion was modeled as an adiabatic process. Other details of the SIMMER-II simulations, including references to similar model applications to relevant experimental data, are provided in Appendix C.

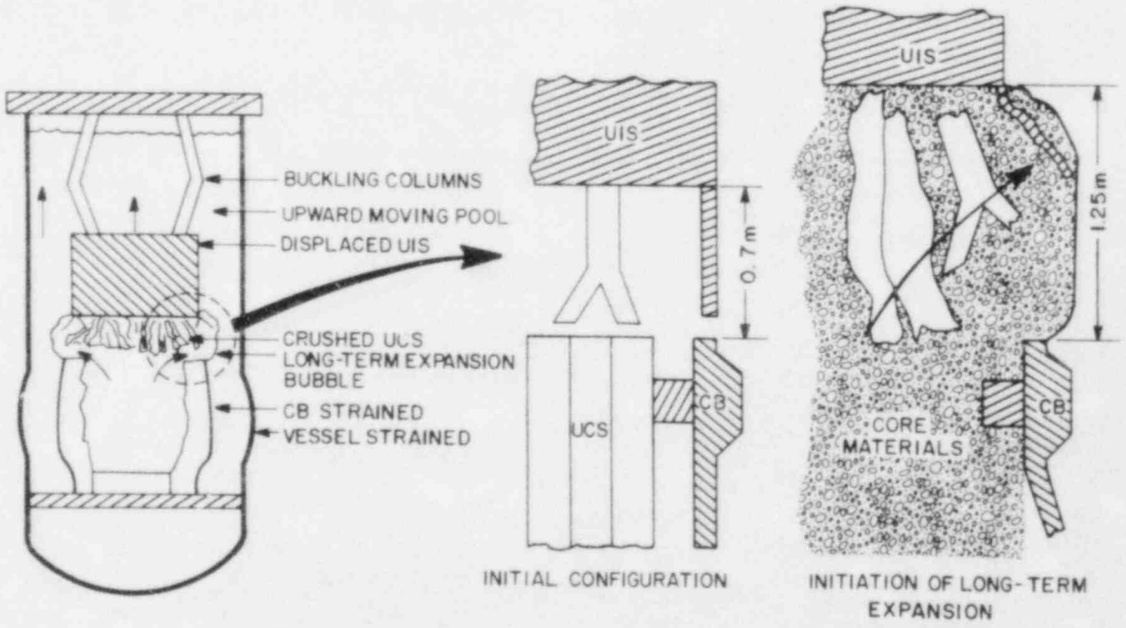

Fig. 11.
Transition between short-term and long-term expansions.

The 200-$/s case yielded slug velocities in the 30-40 m/s range with an impact kinetic energy of approximately 80 MJ. The core and bubble pressures that produced these accelerations are shown in Figure 12. These pressure traces indicate, again, a significant nonuniformity within the expansion volume. The reason for this behavior, which also has been observed experimentally [7, 8] in simulant-material tests, is due to two-phase choking phenomena. Because of its low speed of sound, the two-phase expansion (into the vapor bubble) cannot keep up with the rapid rate of bubble growth (pool displacement); hence a rapid pressure decay occurs, as shown in Figure 12, and an associated reduction in pool acceleration with time results, as shown in Figure 13. The impact of this effect in limiting the magnitude of the generated IKE may be readily visualized. In a uniform expansion with an "average" core pressure of approximately 17.5 MPa through an expansion of approximately 15 m^3 (cover gas volume at the time of cage failure), an IKE of 260 MJ would be generated. With an "average" bubble pressure of approximately 7 MPa (see Figure 12), on the other hand, expansion over the same volume would generate only approximately 105 MJ. The actual computed slug impact energy is somewhat lower than this order-of-magnitude estimate because of deviations from one-dimensional behavior. A more detailed presentation of the results may be found in Appendix C.

As we have seen in the previous section, the 100-$/s expansion is near the threshold of cage failure in the short-term expansion. It is interesting to determine the long-term energy release resulting from a postulated UIS failure. An order-of-magnitude estimate may be obtained from the quasistatic pressures of Figure 7 in the simple manner employed above. An average quasistatic pressure of approximately 6 MPa implies an "average" bubble pressure of approximately 2.5 MPa, which for an expansion of approximately 15 m^3, translates to an IKE of approximately 35 MJ. Indeed, a ratio of results from SIMMER-II calculations for this situation yields approximately 30 MJ, which is a value well below the VHS design specification (SMBDB).

Finally, we must consider the potential augmentation of the long-term expansion pressures from thermal interactions between the fuel and steel bubble contents and the relatively volatile sodium pool. This problem was first considered by Cho and Epstein [9] using a simple parametric pool-entrainment model. They concluded that for an "optimum" entrainment rate, a maximum augmentation of pool kinetic energy by a factor of two could be obtained. The available experimental evidence is preliminary at this time [8, 10], however, it does indicate that pool volatility promotes adiabatic expansions rather than any augmentation processes. Similarly, parametric SIMMER-II simulations allowing for sodium entrainment and heat transfer did not provide evidence for any major effects. In any case, it is important to emphasize that this situation does not even arise below the 100 $/s energetics level.

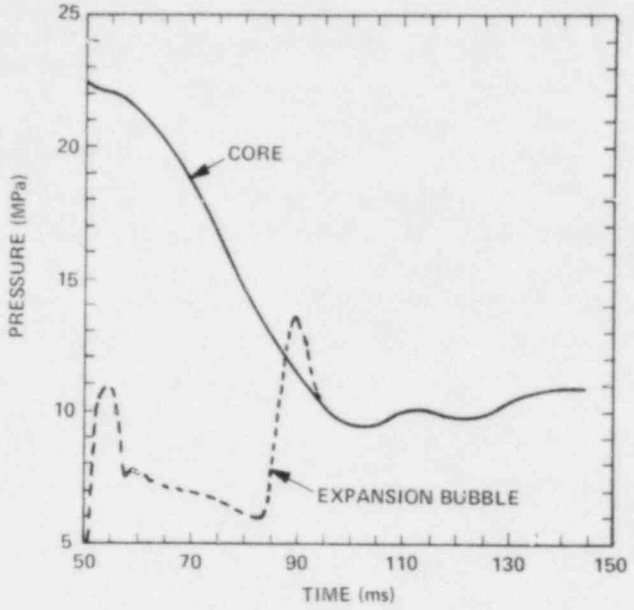

Fig. 12.
Core and expansion bubble pressures during the 200 $/s long-term expansion.

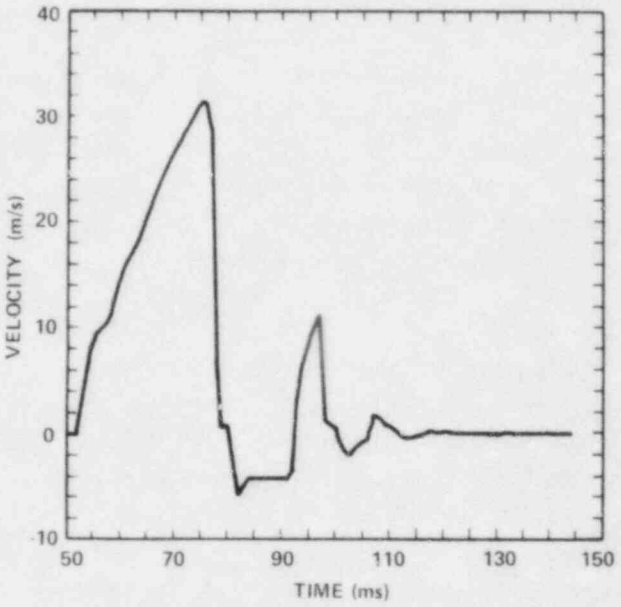

Fig. 13.
Sodium pool surface velocity history during the 200 $/s long-term expansion.

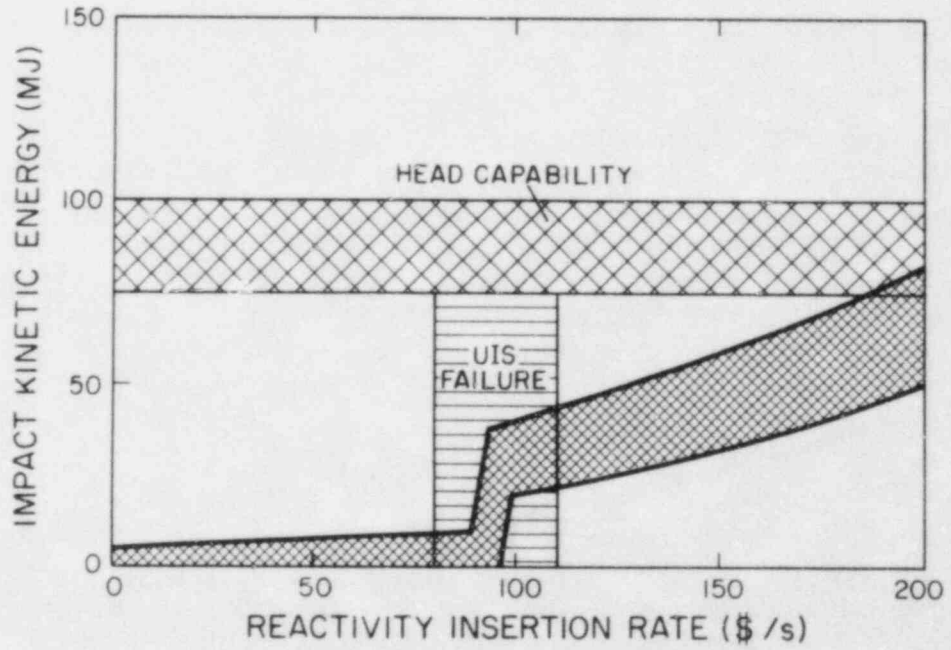

Fig. 14.
Summary results for impact kinetic energy vs. ramp rate.

4. Summary

The potential for incipient structural damage was keyed to two levels of recriticality energetics. At the 100-$/s level (UWP approximately 1130 MJ), the UIS/CB/CSS structural envelope remains largely intact. However, the approach to the UIS failure threshold is evident. At the 200-$/s level (UWP approximately 2550 MJ), a pool kinetic energy near the SMBDB is obtained. Large failure displacements for the UIS and substantial CB strains are noted, again in the failure range. The essence of these conclusions is graphically depicted in Figure 14. The relationship to potential CRBR energetic events is made in Section II.7.

The Applicant's analysis of these damage levels in relation to the originating power excursions (reactivity ramp rates) appears overly conservative in three areas: (a) the mitigating role of the high compliance of the core during the short-term expansion was neglected, that is, the centrally originating high vapor pressures were applied directly to the CB structural boundary; (b) the value of the UIS/CB/CSS structural envelope in "throttling" the high- pressure, long-term expansion also was neglected; and (c) the moderation in pool acceleration from nonuniform expansion (choking effects) was not taken into account. Because these mitigating circumstances were neglected, the Applicant's 661 MJ accident corresponds, roughly, to our 2550 MJ (200 $/s) energetics level in terms of CB strains and slug impact kinetic energy.

Our own analysis is conservative in the following areas: (a) the energy yields of the disassemblies utilized in our analysis were biased upwards because motions were restricted to one-dimension and because a "soft" system (uniformly distributed, high void fraction) was assumed; (b) we utilized 20% lower than expected Doppler; (c) we neglected quenching effects of in-core steel and blankets; (d) during the post disassembly expansion we neglected loss of core material into surrounding structures and, also, we utilized the whole-core inventory (neglecting amounts dispersed prior to the occurrence of the energetic event); (e) we neglected the time-dependent throttling effects during the upward UIS displacement; and (f) we utilized a downward biased value of CB strain during the short-term expansion.

5. References

1. "Hypothetical Core Disruptive Accident Considerations in CRBRP, Vol. 1: Energetics and Structural Margins Beyond the Design Base," Clinch River Breeder Reactor report CRBRP-3, Vol. 1, Rev. 4 (March 1982).

2. S. K. Rhow, D. M. Switick, J. L. McElroy, and B. W. Joe, "An Assessment of HCDA Energetics in the CRBR Heterogeneous Reactor Core," General Electric Company report CRBRP-GEFR-00523 (December 1981).

3. "Compendium to NUREG/CR-3224, An Assessment of CRBR Core Disruptive Accident Energetics," Section 5, Nuclear Regulatory Commission document (March 1983).

4. J. Marchaterre, T. Marciniak, J. Bratis, and H. Fauske, "Work-Energy Characterization for Core Disruptive Accident," Proceedings of the Fast Reactor Safety Meeting, Chicago, IL, October 5-8, 1976, CONF-761001.

5. "CRBRP Structural Response of CRBRP Scale Models to a Simulated Hypothetical Core Disruptive Accident," Westinghouse report WARD-D-218 (October 1978).

6. "Compendium to NUREG-CR-3224, An Assessment of CRBR Core Disruptive Accident Energetics," Section 12, Nuclear Regulatory Commission document (March 1983).

7. R. J. Tobin and D. J. Cagliostio, "Effects of Vessel Internal Structures on Simulated HCDA Bubble Expansion," SRI International Technical Report 5 (November 1978).

8. J. J. Simpson, M. Saito, and T. G. Theofanous, "The Termination Phase of Core Disruptive Accidents in LMFBRS," Purdue University report PNE-81-151 (June 1981).

9.[a] D. H. Cho and M. Epstein, "Work Potential Resulting From a Mechanical Disassembly of the Voided FFTF Core," Argonne National Laboratory report ANL/RAS 74-17 (August 1974).

10. R. J. Tobin, "Effects of Coolant Volaticity on Simulated HCDA Bubble Expansions," SRI International Technical Report 10 (September 1980).

11. "Compendium to NUREG-CR-3224, An Assessment of CRBR Core Disruptive Accident Energetics," Section 6, Nuclear Regulatory Commission report (March 1983).

[a] Address requests for this document to: F. X. Gavigan, Director, Office of Breeder Demonstration Projects (NE-50), U.S. Department of Energy, Washington, DC 20545, Telephone (301) 353-3134.

APPENDIX A
SHORT-TERM EXPANSION

1. Introduction

This Appendix provides the detailed analysis of the short-term expansion of the high-temperature fuel following core disassembly transients of 100 and 200 $/s. We describe the geometric model used, the assumptions made, and the results. Isentropic work potentials also are developed for reference.

2. Geometric Model

The first phase of the Post Disassembly Expansion (PDE) begins directly after disassembly and continues until quasistatic conditions develop within the enclosure comprized of the UIS, CB, and CSS. This defines the geometric region of interest.

The calculational mesh for this first phase or short-term expansion is shown in Figure 1. The core region mesh was identical to that used the disassembly calculations (Section II.7). This permitted the thermal/physical data from the disassembly to be used directly in the expansion. Because the early PDE pressures are very large, we assumed that the structural resistance from intact driver subassembly walls to radial flow within the core could be neglected.

Initially the UIS does not directly feel the core pressure. The load transfer from the core is mitigated because of the crushability of the plena within the subassemblies of the UCS. To simulate this delayed UIS loading, the inertial constraints produced by the UCS mass (approximately 17000 kg), and the volume available for core expansion, the materials in the upper axial blanket and gas plena regions were modeled as solid particulates. The residual sodium in the region above the subassemblies was removed based on its easy access to escape paths.

The materials in radial blankets and shielding also were modeled as particulates. When CB strain was assumed, an equivalent volume was placed between the radial reflector and CB as shown on Figure 1. The particles then represent the radial inertia. For these expansions the downward direction was assumed blocked and rigid.

A special modification to SIMMER-II was required to prevent the radial blanket and radial reflector "particulates" from convecting axially. As

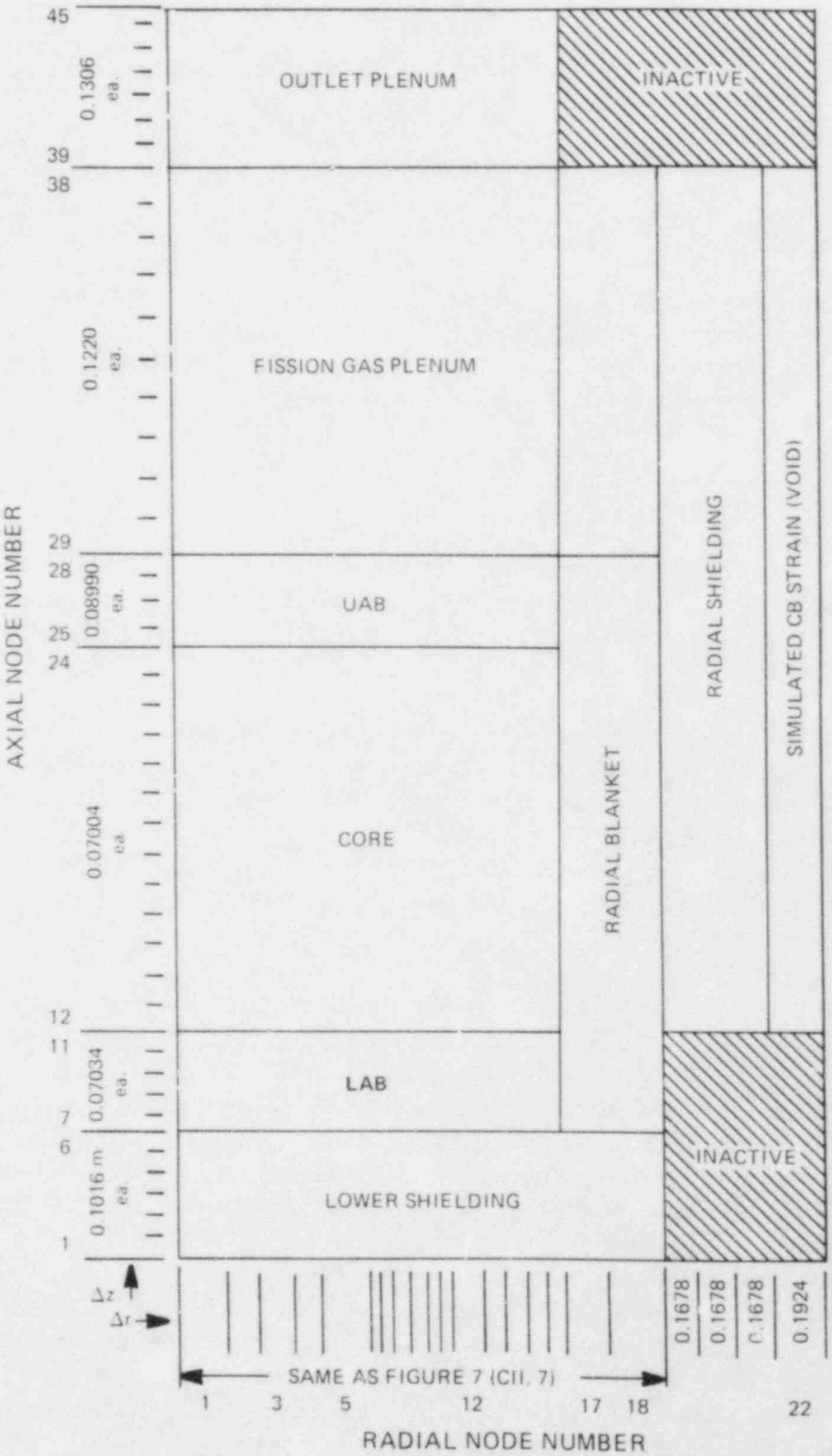

Fig. 1.
SIMMER-II geometric model for the short-term expansion analysis.

structural members they should move only in the radial direction. The modification simply introduced an artificial resistance into the axial momentum equation in these regions.

3. Assumptions

As a result of initial expansions with no assumed CB strain and the analysis of strains from these expansions, second-iteration strains of 10% and 2.5% were selected to size the radial void for the 200 $/s and 100 $/s cases, respectively. All heat transfer except between fuel and its vapor was eliminated to provide an adiabatic limit. Standard momentum coupling between the liquids, vapors, and particles was assumed.

4. Results

200 $/s Adiabatic

The initial core temperature distribution for this short-term post-disassembly expansion is given in Figure 3 of Section II.2. The average value of 5580 K must be interpreted carefully and in the context of the equation of state used when comparing with mechanical energy yields in the literature. For our assessment this average temperature represents a very high energy state, 87% of T_{crit}. The short-term expansion led to the temperature reduction shown in Figure 2. The energy change associated with this temperature reduction produced the vapor that drove the expansion.

The massive vaporization of fuel associated with the adiabatic expansion is shown in Figures 3 and 4. The final total volume within the UIS/CB/CSS enclosure that fuel and its vapor could occupy was about 15 m^3. Of this, 5.5 m^3 is associated with the assumed CB strain of 10%, 4.6 m^3 is within the UCS, 2.9 m^3 is above the UCS and below the UIS, and 2 m^3 is in the active core. Thus, this was a relatively large expansion (of the order of the cover gas volume) and was the reason for the large quantity of vapor generated (37% of fuel mass).

The change in the volume provided inside the CB to simulate its strain is shown on Figure 5 as it collapsed from radial blanket and shield motions. Note that it was completely collapsed at the same time as the UIS was loaded. This coincidence is appropriate because the upper CB does not see pressure until the UCS is crushed upward.

The pressure histories of interest are shown on Figures 6 through 8, for the core center, upper core surface, and outer core surface. The latter two curves are average pressures over the surfaces of interest. The pressure transient in Figure 7 drove the UCS upward and ultimately loaded the UIS;

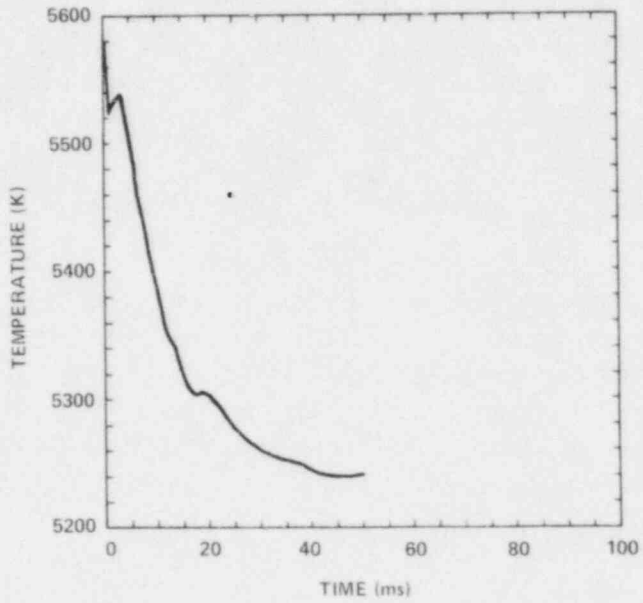

Fig. 2.
Average temperature of liquid fuel during the 200 $/s short-term expansion.

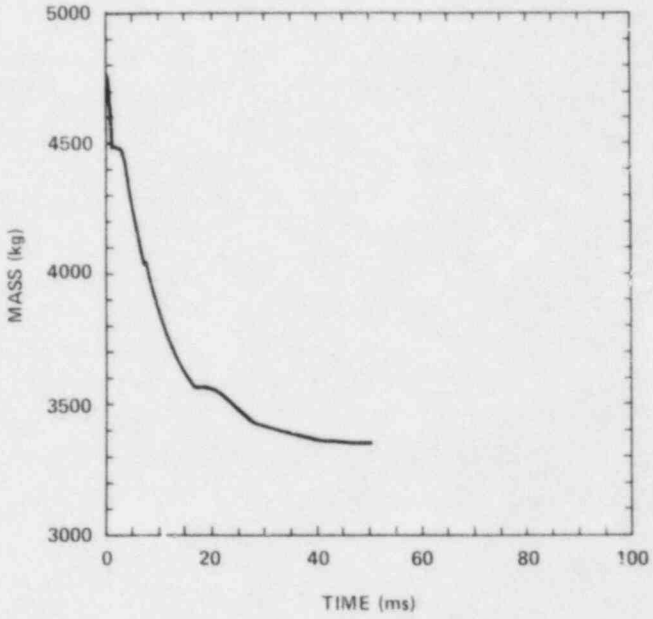

Fig. 3.
Mass of liquid fuel during the 200 $/s short-term expansion.

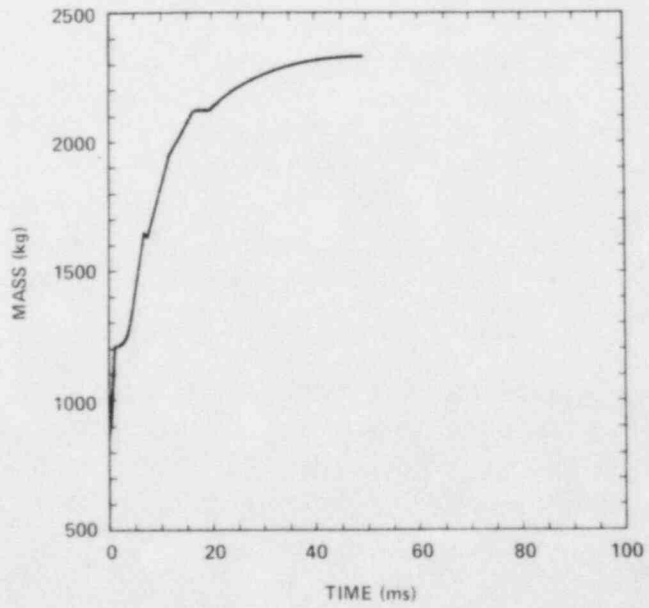

Fig. 4.
Mass of fuel vapor during the 200 $/s short-term expansion.

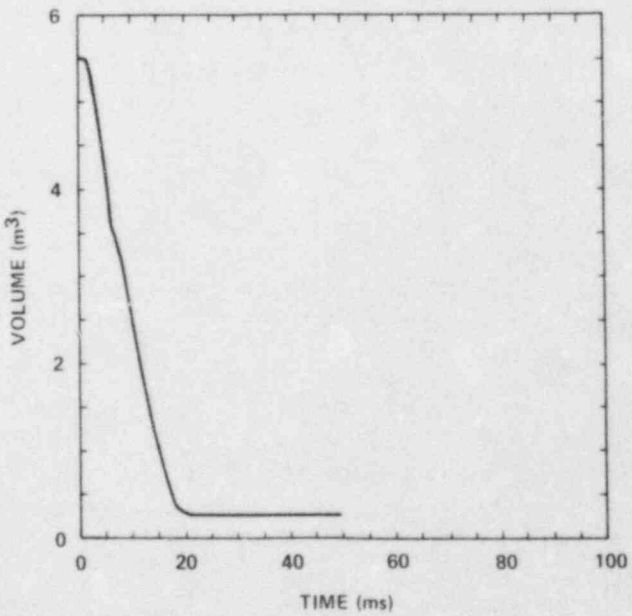

Fig. 5.
Collapse of the CB strain volume during the 200 $/s short-term expansion.

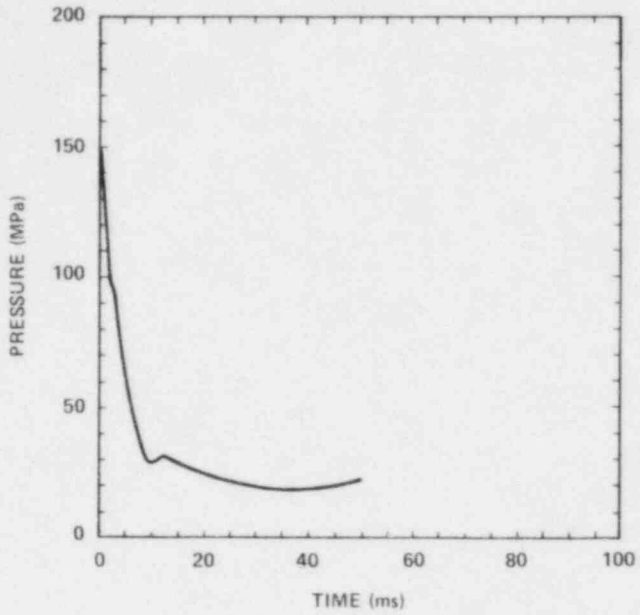

Fig. 6.
Peak core pressure during the 200 $/s short-term expansion.

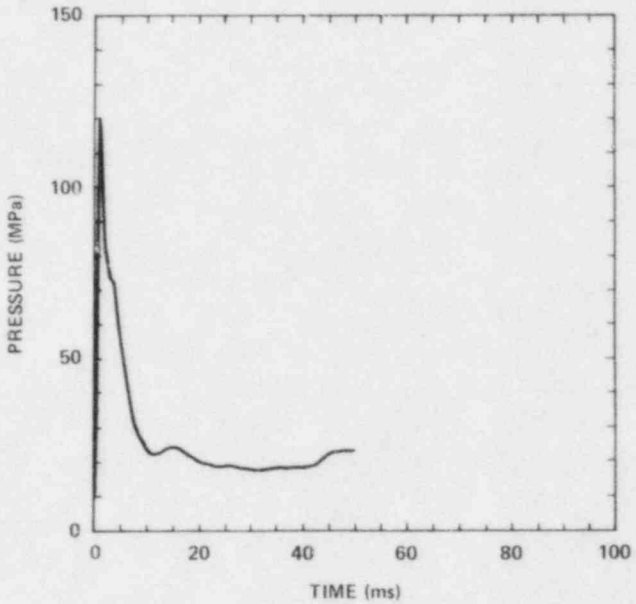

Fig. 7.
Average pressure at the core top boundary during the 200 $/s short-term expansion.

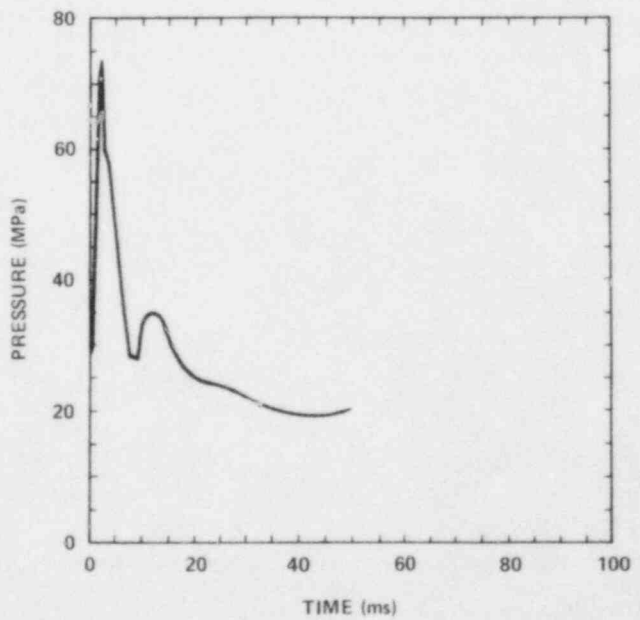

Fig. 8.
Average pressure at the core outer boundary during the 200 $/s short-term expansion.

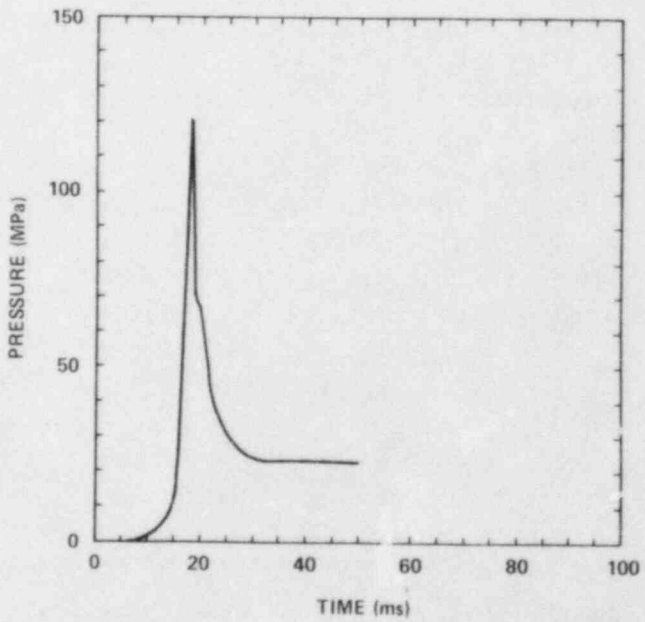

Fig. 9.
Pressure history at the UIS during the 200 $/s short-term expansion.

and that shown in Figure 8 loaded the CB with an appropriate reduction for the radial inertia and cylindrical geometry. Figure 9 shows the time of UIS engagement based on the UCS crushability assumption. This pressure spike is associated with the assumed fluid nature of the UCS and therefore is somewhat artificial.

The development of the expansion can be seen with the series of three-dimensional plots for vapor volume fraction (Figures 10 through 15) and liquid volume fraction (Figures 16 through 21). Figure 11 shows the early movement of material radially opposite the core (radial is to the right and vertical is up to the left--volume fraction is the ordinate). The void grew rapidly upward in the core and the initial void in the UCS collapsed by this upward movement as time increased. At 0.020 s (Figure 14) the CB void was gone and the UCS was against the upper boundary or UIS. The liquid volume fraction plots simply give a different perspective of the same transient.

The capability to perform an isentropic expansion was developed as part of this assessment. The isentropic results for the 200-$/s case are shown on Figure 22. At the end of this first phase of expansion ($\Delta V \approx 14$ m^3), 535 MJ of work potential have been expended. This is in good agreement with our SIMMER-II results. If the calculated expansion is truly adiabatic, this work potential should be manifested. In Appendix B the core barrel energy absorption was developed per inch of core barrel at 10% strain. Using the utilized strains for both the core barrel and vessel wall and taking the core barrel length as 2.5 m (for strain purposes we used the length from the bottom of the active core to the top of the CB), we obtained about 80 MJ. Consider now the work done against the UCS. The UCS contacted the UIS after about 0.02 s. The upper axial blanket must be displaced about 2 m in this time, requiring an average velocity of 100 m/s; but because of the nearly constant acceleration, the impact velocity would be about 200 m/s. The kinetic energy in the UCS at impact is then 0.5 x (17,000 kg) x (200 m/s)^2, or 340 MJ. When we add this value to the strain energy and to that dissipated in early in-core expansion (~100 MJ), we obtain 520 MJ which agrees very well with the isentropic value.

The 340 MJ imparted to the UCS for the 200-$/s case is dissipated by inelastic impact with the UIS. The mass ratio of these two bodies is about 3:1, UIS:UCS. The final velocity of the combined masses would be 25% of the impact value or about 50 m/s if no further crushing occurred and the interaction were truly inelastic. The final kinetic energy would be reduced also to 25% or 85 MJ for these assumptions. There is a loss of work or damage potential of at least 255 MJ in this collision process. The UIS columns and control rod drives absorb some of the remaining kinetic energy as strain energy. This is estimated to be approximately 6 MJ for a buckling strain of about 5%. The slug impact pressure transient will act downward on the UIS to further reduce its residual kinetic energy. Even if it did reach the head,

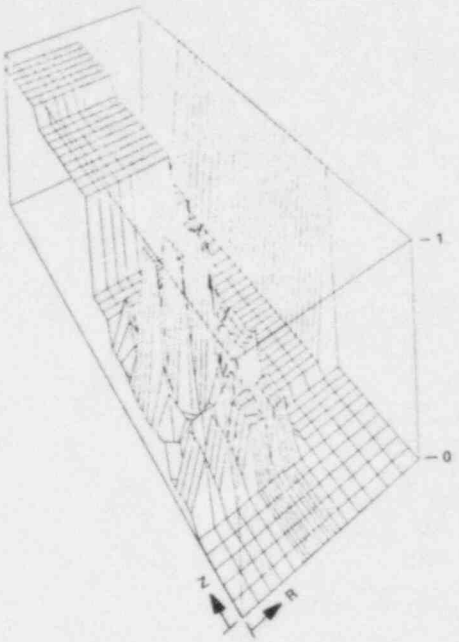

Fig. 10.
Vapor volume fraction distribution at 0 ms for the 200 $/s short-term expansion.

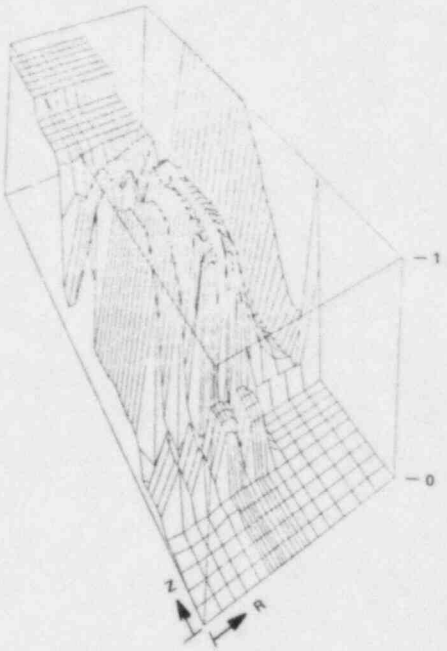

Fig. 11.
Vapor volume fraction distribution at 5 ms for the 200 $/s short-term expansion.

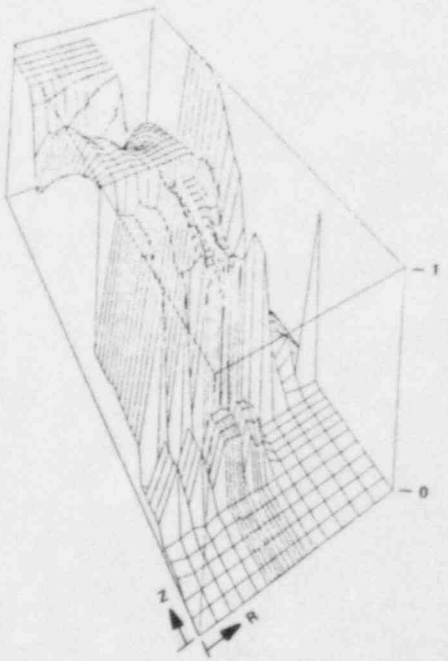

Fig. 12.
Vapor volume fraction distribution at 10 ms for the 200 $/s short-term expansion.

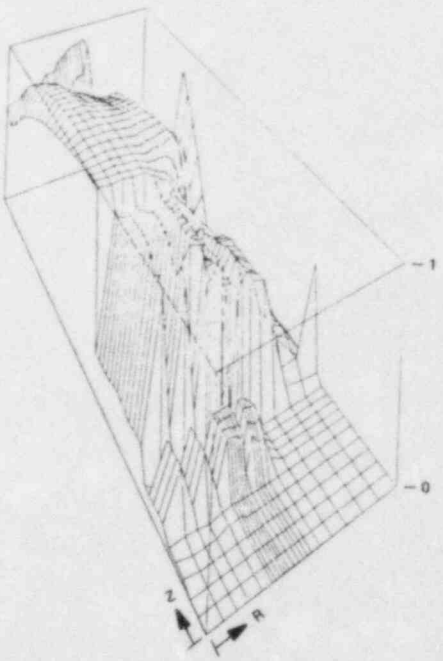

Fig. 13.
Vapor volume fraction distribution at 15 ms for the 200 $/s short-term expansion.

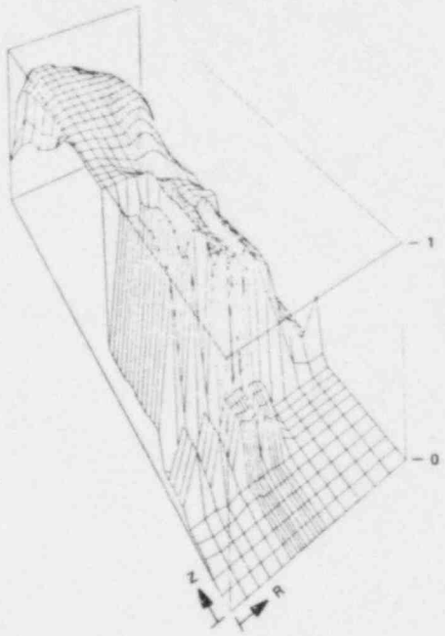

Fig. 14.
Vapor volume fraction distribution at 20 ms for the 200 $/s short-term expansion.

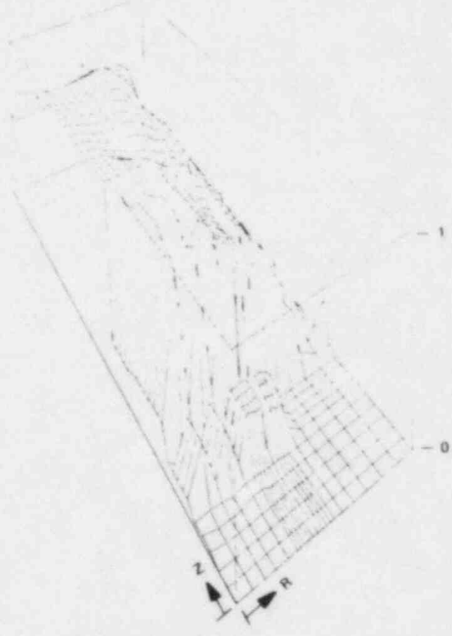

Fig. 15.
Vapor volume fraction distribution at 25 ms for the 200 $/s short-term expansion.

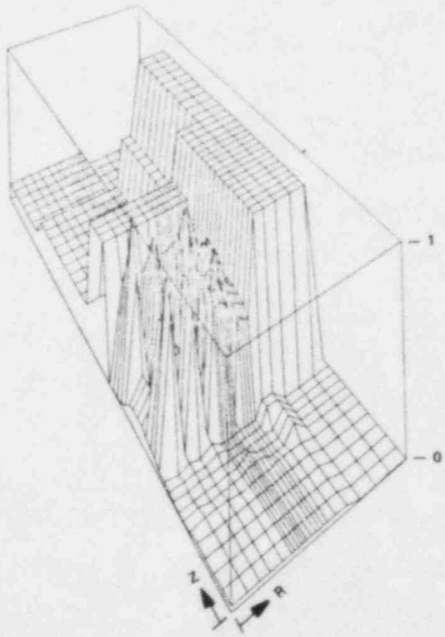

Fig. 16.
Liquid volume fraction distribution at 0 ms for the 200 $/s short-term expansion.

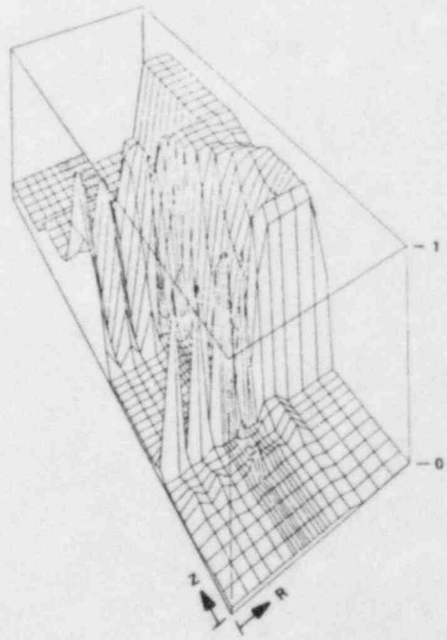

Fig. 17.
Liquid volume fraction distribution at 5 ms for the 200 $/s short-term expansion.

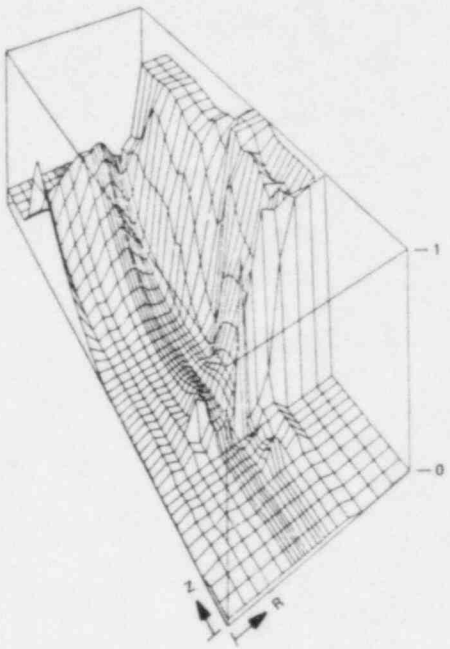

Fig. 18.
Liquid volume fraction distribution at 10 ms for the 200 $/s short-term expansion.

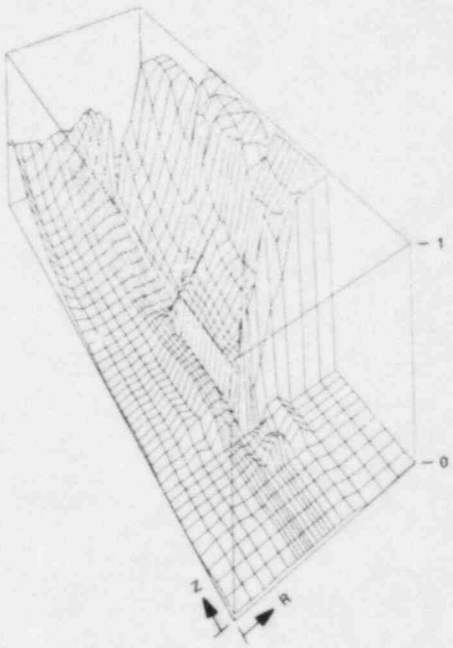

Fig. 19.
Liquid volume fraction distribution at 15 ms for the 200 $/s short-term expansion.

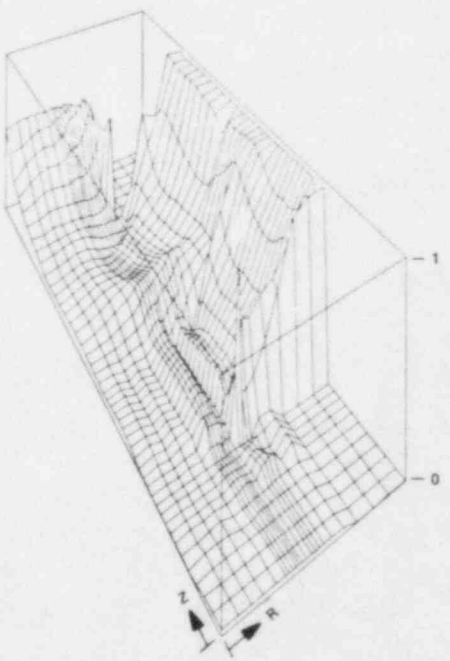

Fig. 20.
Liquid volume fraction distribution at 20 ms for the 200 $/s short-term expansion.

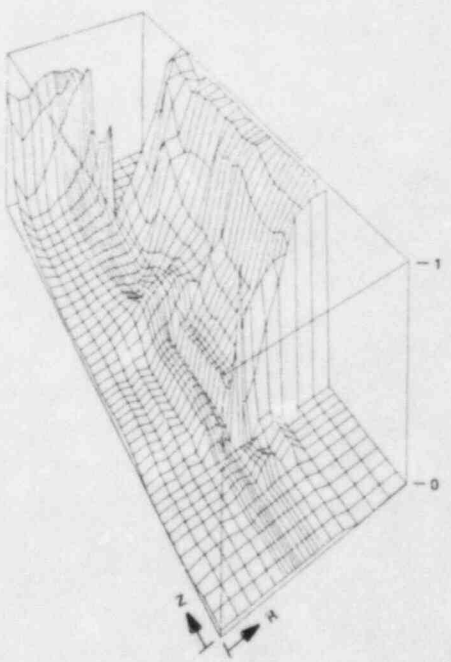

Fig. 21.
Liquid volume fraction distribution at 25 ms for the 200 $/s short-term expansion.

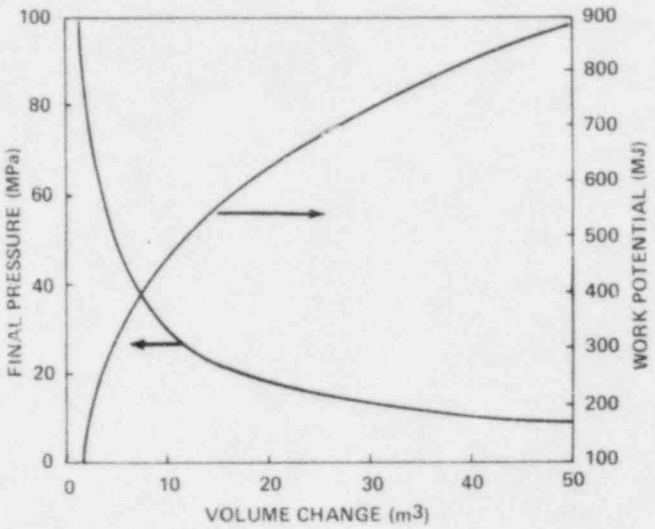

Fig. 22.
Isentropic expansion results for the 200 $/s disassembly.

it would be delayed well beyond the slug impact loading and its damage potential would be small because of the head-to-UIS mass ratio.

One additional check on internal consistency and on the degree to which nonadiabatic effects such as numerical energy mixing occurred in the calculations was made by comparing the calculated quasistatic pressure with the isentropic value for the change in volume of 14 m^3. This isentropic pressure is approximately 22.5 MPa. The average calculated pressure is 22 MPa. Thus, the calculated expansion agrees with the isentropic very well.

100 $/s adiabatic

The same procedure was used to generate the pressure loads in the UIS/CB/CSS enclosure for the 100-$/s case. The reduced severity of this accident can be seen from the initial average fuel temperature of only 4940 K or 77% T_{crit}. The characteristics of the expansion were similar to that for 200 $/s. The main difference is the lengthened expansion time. A complete set of results is provided in Figures 23 through 50. The isentropic expansion characteristics are given in Figure 51 for this case. The work potential expended during this stage of expansion (~10 m^3) was 140 MJ and the final pressure was approximately 9 MPa. The final SIMMER-II pressure was also approximately 9 MPa, again in excellent agreement.

Selected Variations

The effects of heat transfer to the residual in-core structures (subassembly walls and internal blankets) and among the liquids and particulates were evaluated. Using nominal SIMMER-II models for heat transfer, we find that the fuel rapidly cools and that the core pressures are reduced to about two-thirds of those for adiabatic expansion. The reduction could be greater if effective heat transfer were permitted to the UCS. The details of this analysis are given in the Compendium [1].

5. Summary

The large amounts of mechanical energy released during expansion within the UIS/CB/CSS enclosure are dissipated within or on this enclosure even if it is induced to fail. This released energy is effectively withheld from manifesting itself as kinetic energy in the sodium pool. The expansion of the core against the pool, if it occurs (enclosure must fail in a major way such as UIS column buckling), starts from a very degraded condition for which the work potential per unit volume change is much reduced. Thus, these structures produce a major mitigating effect on the real expansion.

The results are conservative because they are effectively isentropic. Heat transfer could further mitigate both the structure loads and the subsequent expansion work potential.

6. References

1. Compendium to NUREG/CR-3224, An Assessment of CRBR Core Disruptive Accident Energetics, Section 12, Nuclear Regulatory Commission report (March 1983).

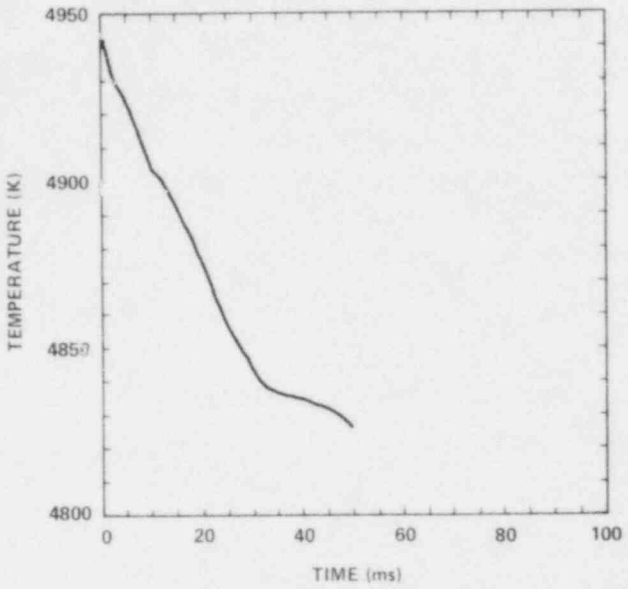

Fig. 23.
Average temperature of liquid fuel during the 100 $/s short-term expansion.

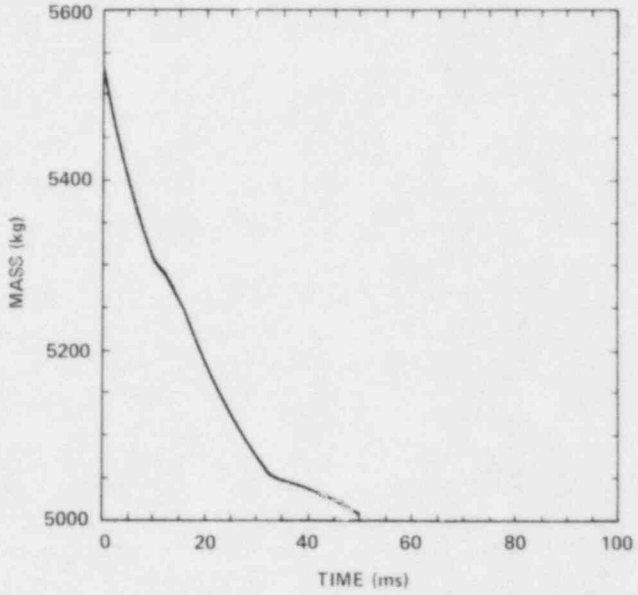

Fig. 24.
Mass of liquid fuel during the 100 $/s short-term expansion.

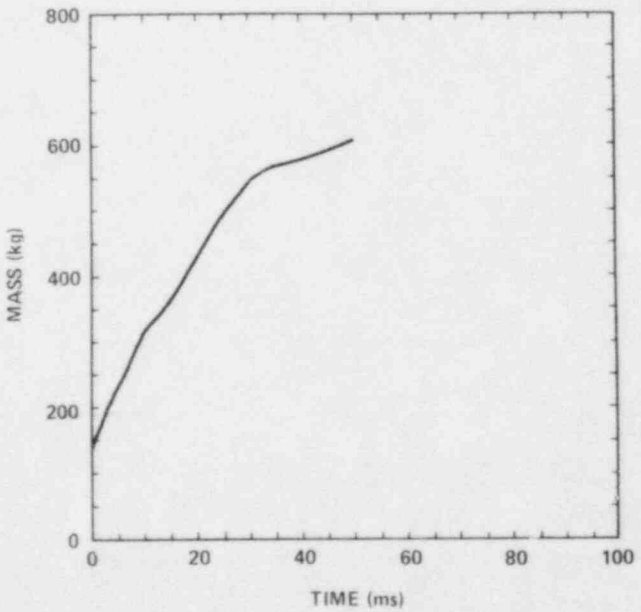

Fig. 25.
Mass of vapor fuel during the 100 $/s short-term expansion.

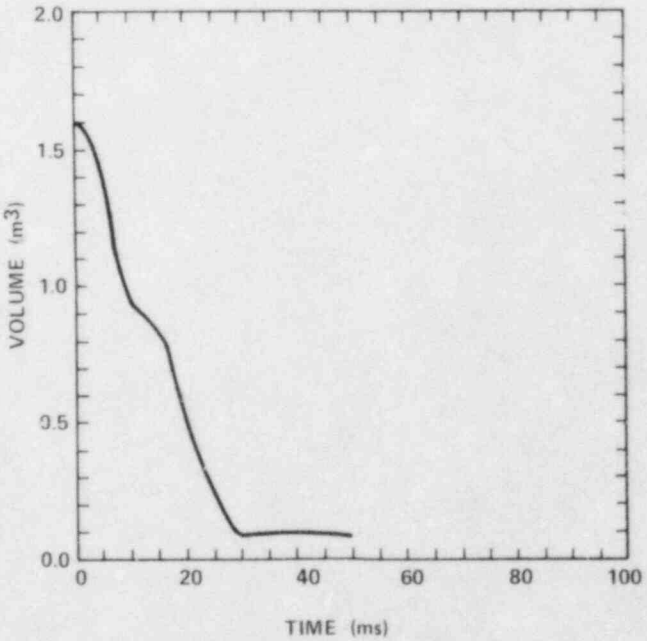

Fig. 26.
Collapse of the CB strain volume during the 100 $/s short-term expansion.

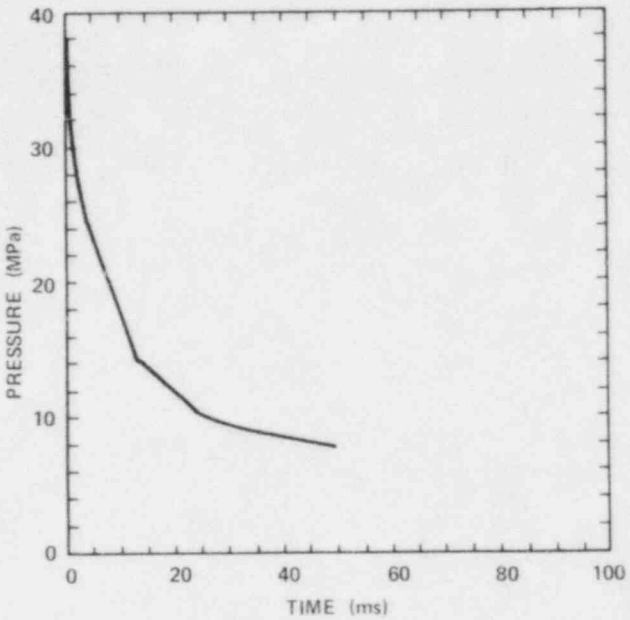

Fig. 27.
Peak core pressure during the 100 $/s short-term expansion.

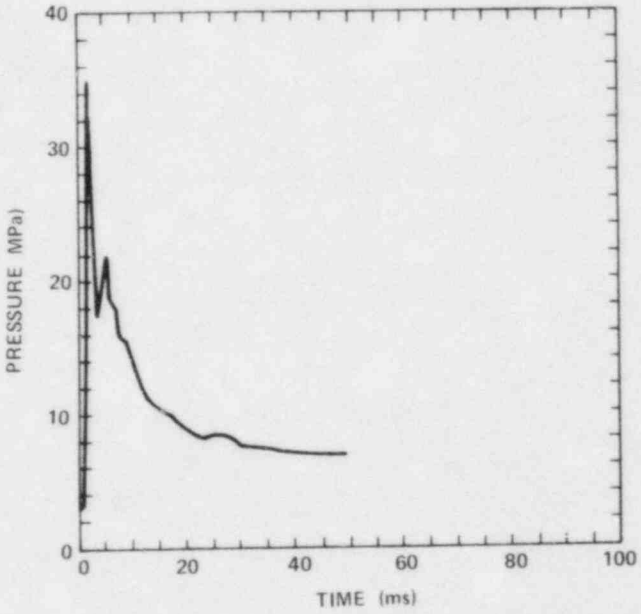

Fig. 28.
Average pressure at the core top boundary during the 100 $/s short-term expansion.

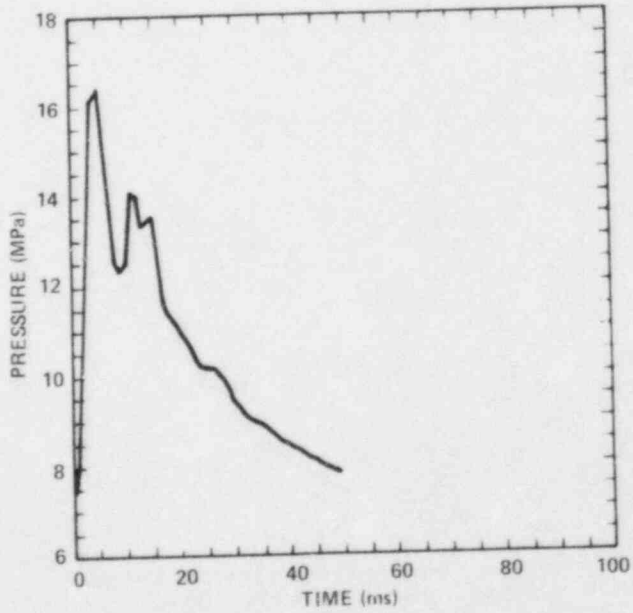

Fig. 29.
Average pressure at the core outer boundary during the 100 $/s short-term expansion.

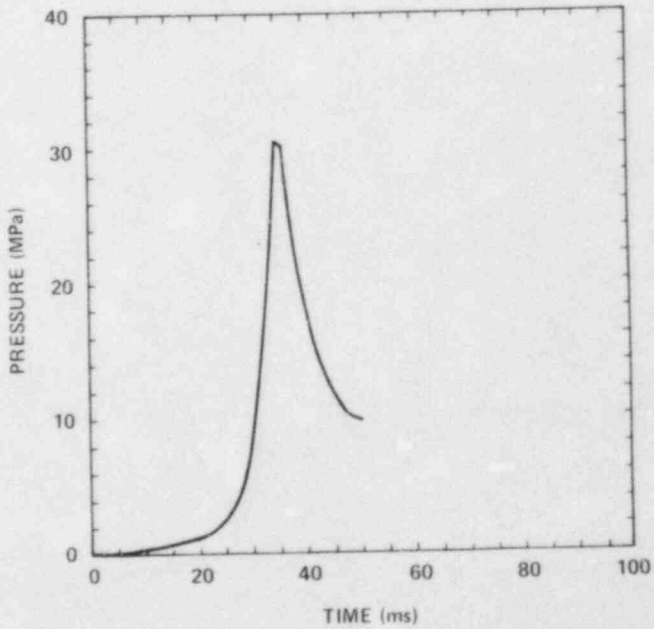

Fig. 30.
Pressure history at the UIS during the 100 $/s short-term expansion.

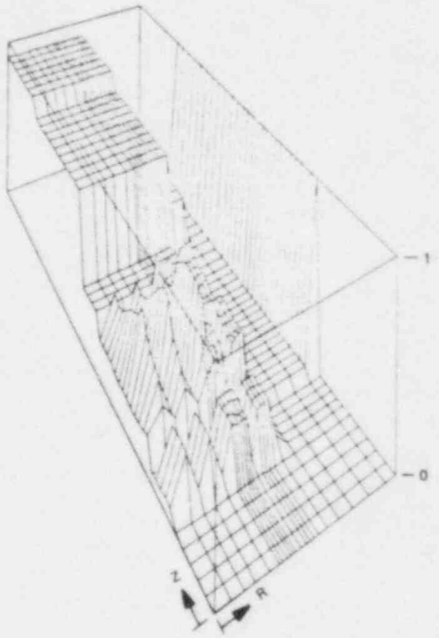

Fig. 31.
Vapor volume fraction distribution at 0 ms for the 100 $/s short-term expansion.

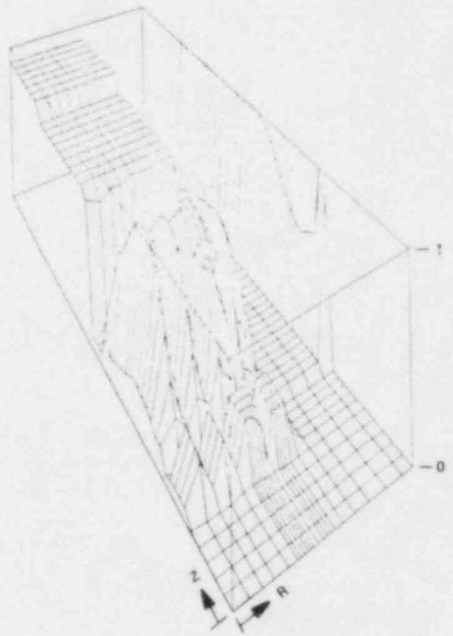

Fig. 32.
Vapor volume fraction distribution at 5 ms for the 100 $/s short-term expansion.

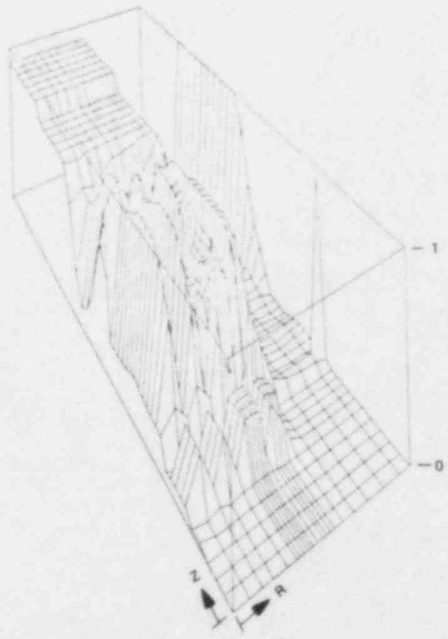

Fig. 33.
Vapor volume fraction distribution at 10 ms for the 100 $/s short-term expansion.

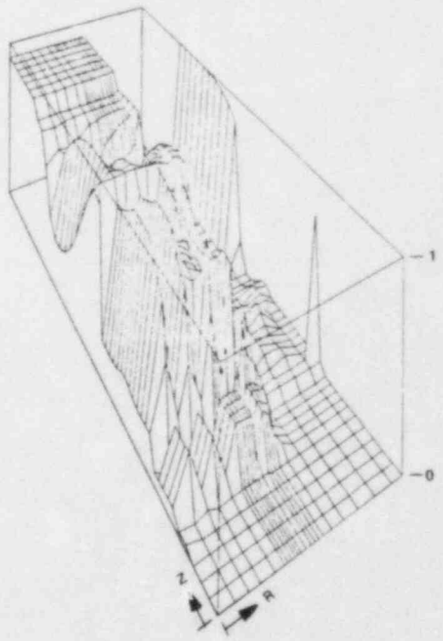

Fig. 34.
Vapor volume fraction distribution at 15 ms for the 100 $/s short-term expansion.

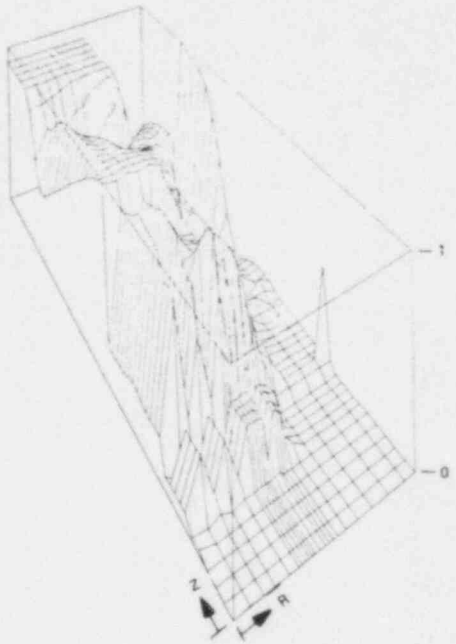

Fig. 35.
Vapor volume fraction distribution at 20 ms for the 100 $/s short-term expansion.

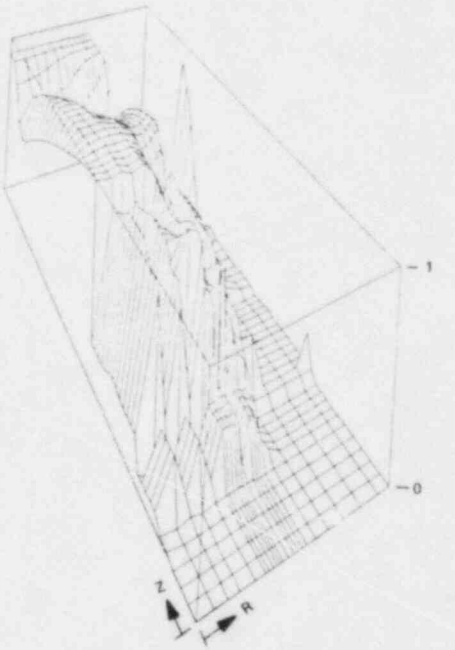

Fig. 36.
Vapor volume fraction distribution at 25 ms for the 100 $/s short-term expansion.

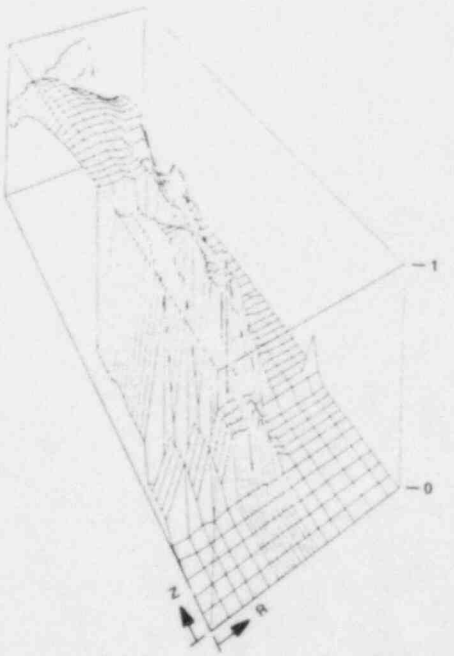

Fig. 37.
Vapor volume fraction distribution at 30 ms for the 100 $/s short-term expansion.

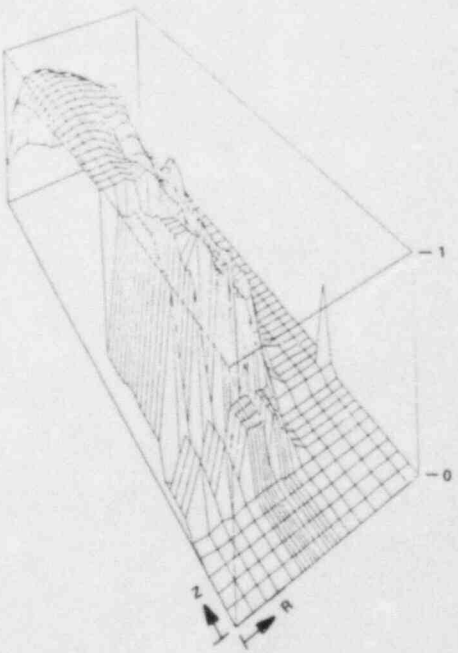

Fig. 38.
Vapor volume fraction distribution at 35 ms for the 100 $/s short-term expansion.

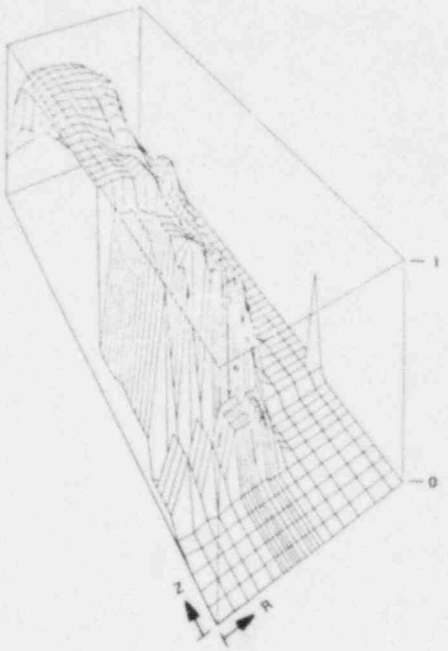

Fig. 39.
Vapor volume fraction distribution at 40 ms for the 100 $/s short-term expansion.

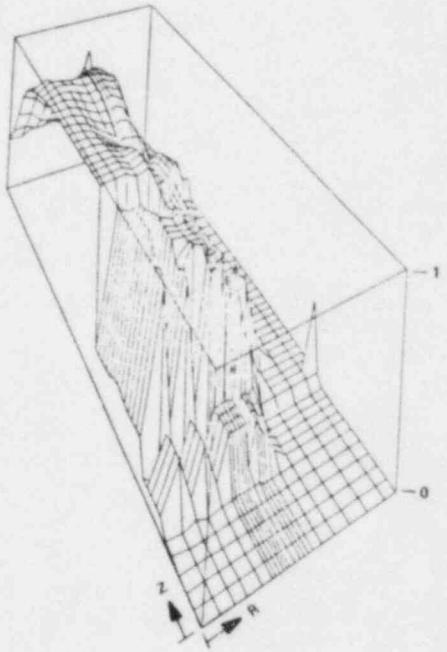

Fig. 40.
Vapor volume fraction distribution at 45 ms for the 100 $/s short-term expansion.

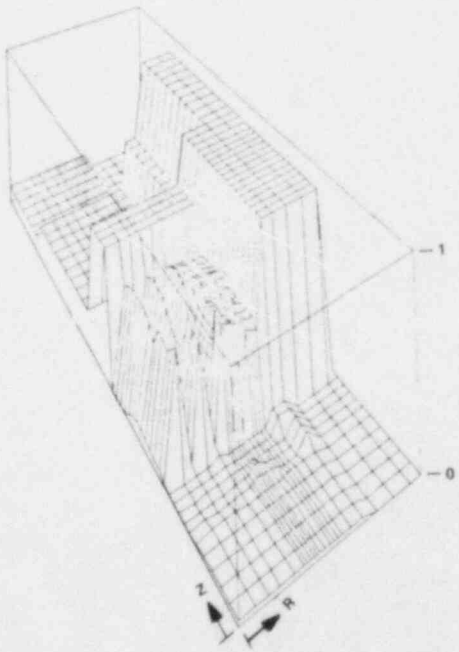

Fig. 41.
Liquid volume fraction distribution at 0 ms for the 100 $/s short-term expansion.

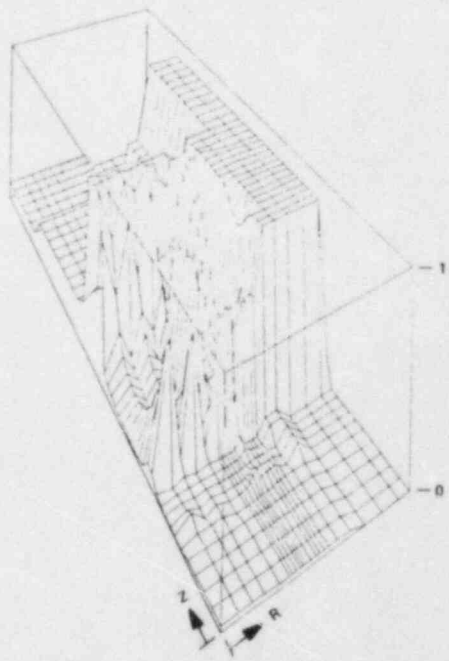

Fig. 42.
Liquid volume fraction distribution at 5 ms for the 100 $/s short-term expansion.

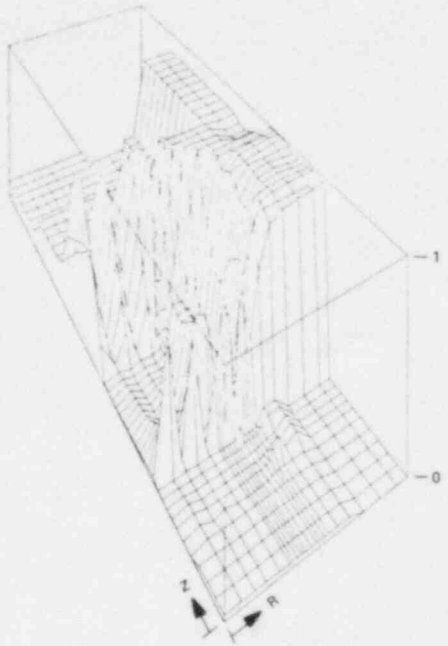

Fig. 43.
Liquid volume fraction distribution at 10 ms for the 100 $/s short-term expansion.

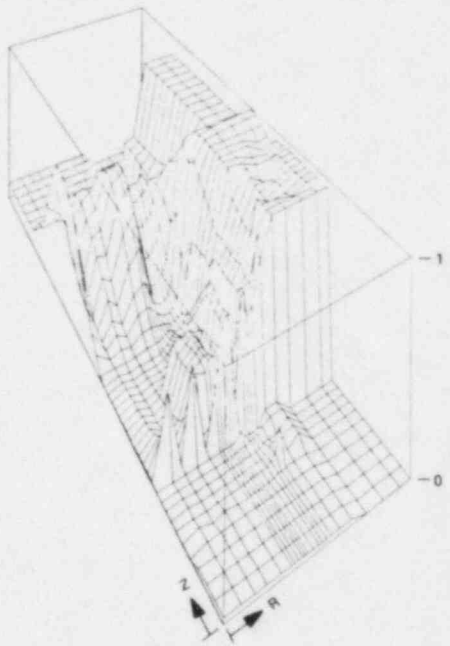

Fig. 44.
Liquid volume fraction distribution at 15 ms for the 100 $/s short-term expansion.

Fig. 45.
Liquid volume fraction distribution at 20 ms for the 100 $/s short-term expansion.

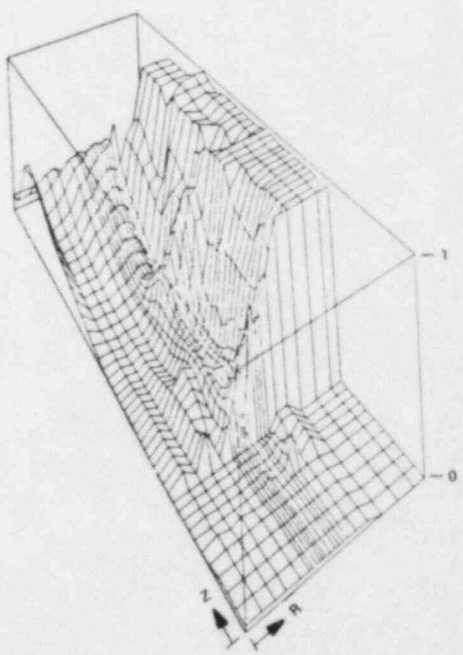

Fig. 46.
Liquid volume fraction distribution at 25 ms for the 100 $/s short-term expansion.

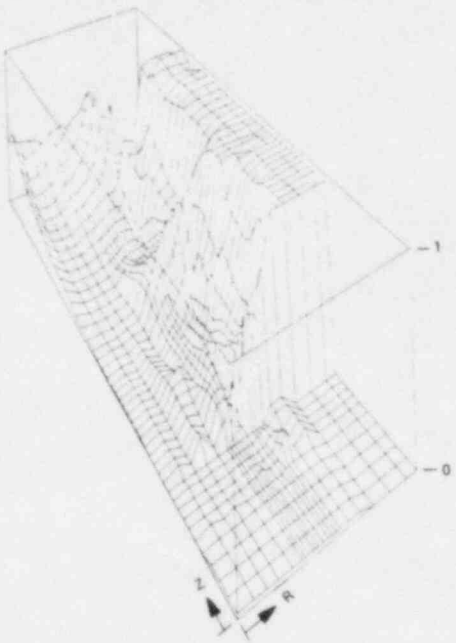

Fig. 47.
Liquid volume fraction distribution at 30 ms for the 100 $/s short-term expansion.

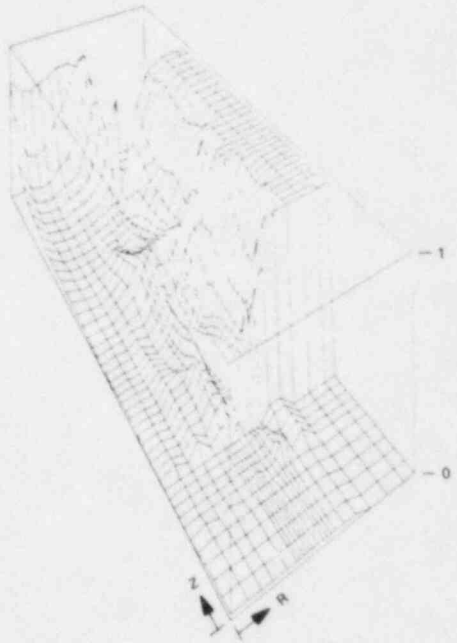

Fig. 48.
Liquid volume fraction distribution at 35 ms for the 100 $/s short-term expansion.

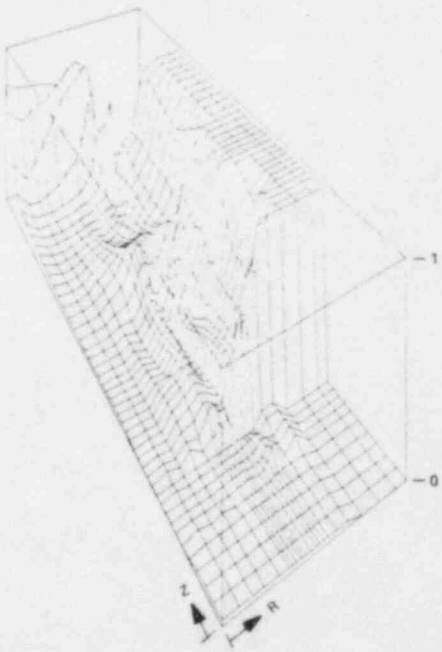

Fig. 49.
Liquid volume fraction distribution at 40 ms for the 100 $/s short-term expansion.

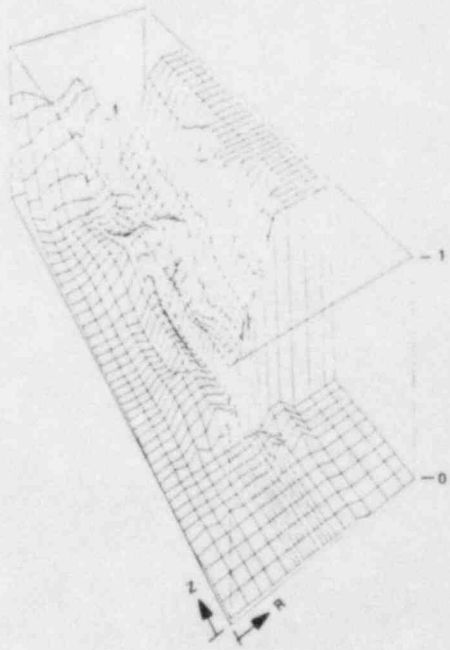

Fig. 50.
Liquid volume fraction distribution at 45 ms for the 100 $/s short-term expansion.

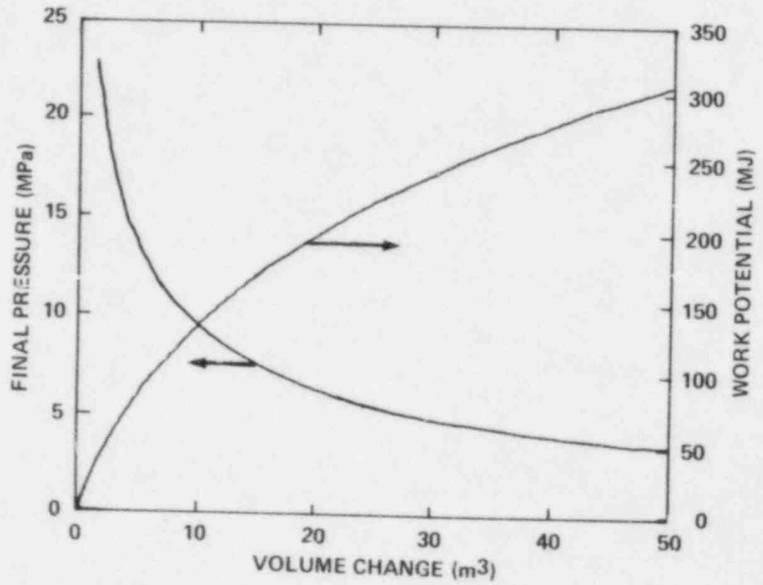

Fig. 51.
Isentropic expansion results for the 100 $/s disassembly.

APPENDIX B
UIS/CB/CSS STRUCTURAL ENVELOPE RESPONSE

1. Introduction

In this Appendix we evaluate the response of the CB and UIS to loads generated by the SIMMER-II computer code for the \$100/s and 200 \$/s energetics cases discussed in Section II.2.

The CB is a 304 SS cylinder with an inner radius of 1.93 m and a thickness of 0.05 m. Radial shielding for the core is positioned radially inward from the CB. Outside the CB are a 1.11-m-thick annulus filled with sodium and a 0.06-m-thick reactor vessel wall. Outside the vessel wall is a 0.19-m-gap and then a 0.025-m-thick guard vessel wall. Both the reactor vessel and guard vessel are 304 SS.

2. CB Analytical Model

To simulate the response of the CB during an HCDA, we used an axisymmetric finite-element model that includes the CB, sodium in the annulus, and the reactor vessel wall (Figure 1). The model was developed for the ABAQUS [1] computer code and all components, including sodium, were modeled with the CAX8 eight-node element. The CB and vessel wall were modeled with elastic-plastic material properties representing 304 SS at 672 K (750 F). An isotropic strain hardening rule with a Von Mises yield surface was used to simulate plastic behavior.

The sodium was modeled as an orthotropic material, incapable of carrying hoop or shear stress. At the CB-sodium and vessel-sodium interfaces, radial displacements of the sodium and steel boundaries were required to be equivalent, but the sodium was free to move vertically to simulate a frictionless boundary. Inertial effects from sodium above the plane of the model were included by lumping the equivalent mass of sodium above this plane at the sodium nodes on the upper plane of the model. This added mass was effective in the vertical direction only.

The model represents the radial dynamic response of the axisymmetric structure while the sodium elements are all in compression in the radial direction. This suffices to calculate the maximum radial deflection of the CB and vessel wall.

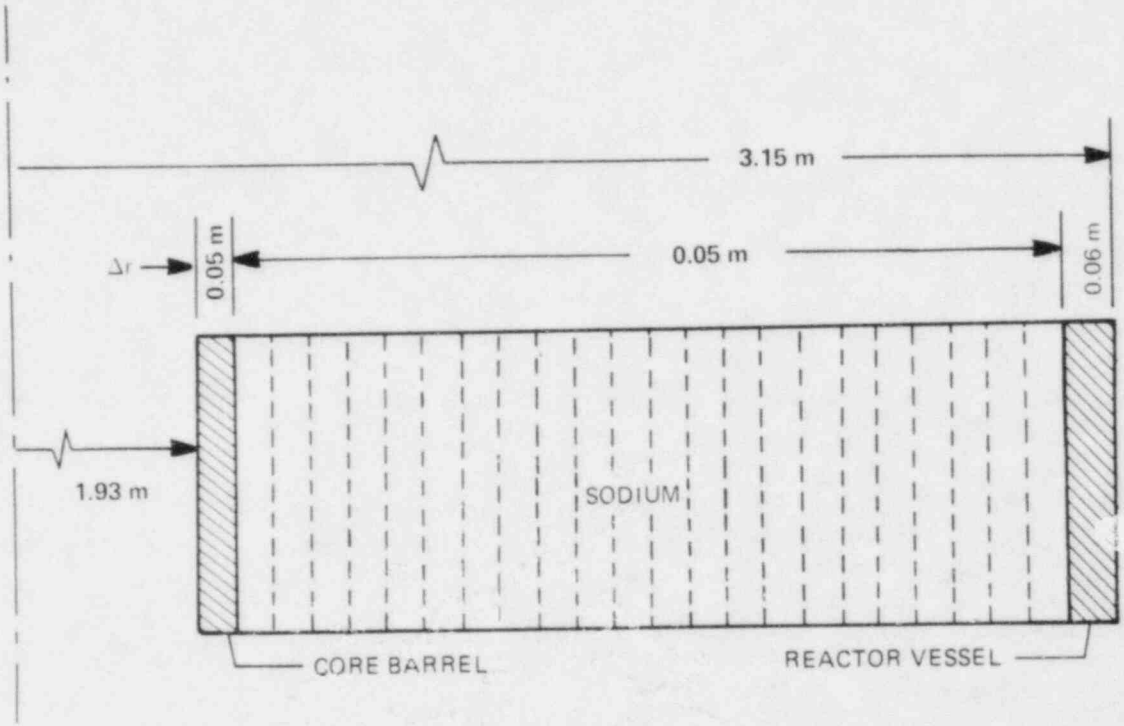

Fig. 1.
Model for core barrel and reactor vessel strain analysis.

3. Predicted CB Responses

Pressure transients at the core boundary generated with SIMMER-II were used to load the CB. The pressure at the core boundary was reduced by the ratio of the core diameter to the CB diameter before applying it to the model. The core boundary pressure transients for the 100-$/s and the 200-$/s cases, respectively, as shown in Figures 7 and 8 of Section II.2 were utilized.

Responses of the CB and vessel wall to these transients are shown in Figures 2 through 9 for displacement and hoop strain. For the 100-$/s case, the maximum strain predicted in the CB was 3%. This is well below strain levels that can be expected to fail the CB. A maximum CB hoop strain of 17% was predicted for the 200-$/s case. Reference 2 gives uniaxial ultimate strains of just over 20% for 304 SS between 644 K (700 F) and 811 K (1000 F). Strain rate effects were not important, with maximum strain rates predicted to be less than 10 s^{-1}. For structures in a biaxial state of stress, such as the CB, this value would be somewhat lower. Therefore, we predict that the CB is likely to fail for the 200-$/s case. The time of failure is difficult to determine but would probably occur between 15 and 20 ms. On the other hand, the vessel wall was predicted to strain approximately 10%. This prediction is high because when the wall has strained 6.5% it will contact the guard vessel wall, which is not included in the model. Therefore, we do not expect the vessel wall to fail.

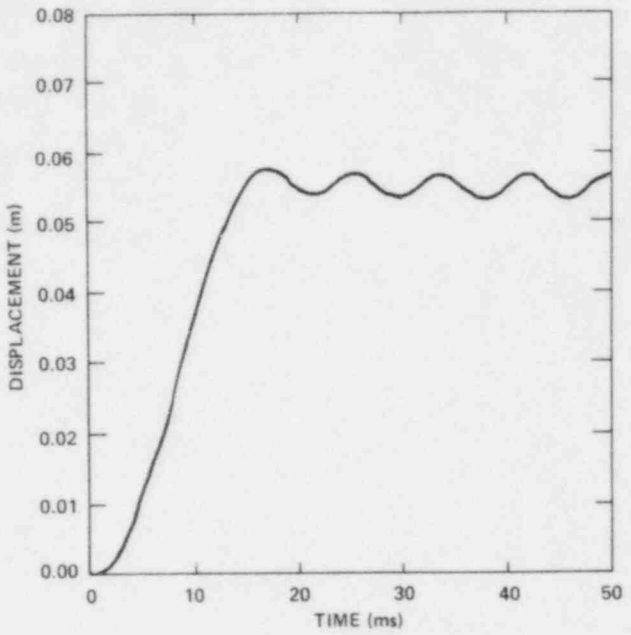

Fig. 2.
CB displacement during the 100 $/s short-term expansion.

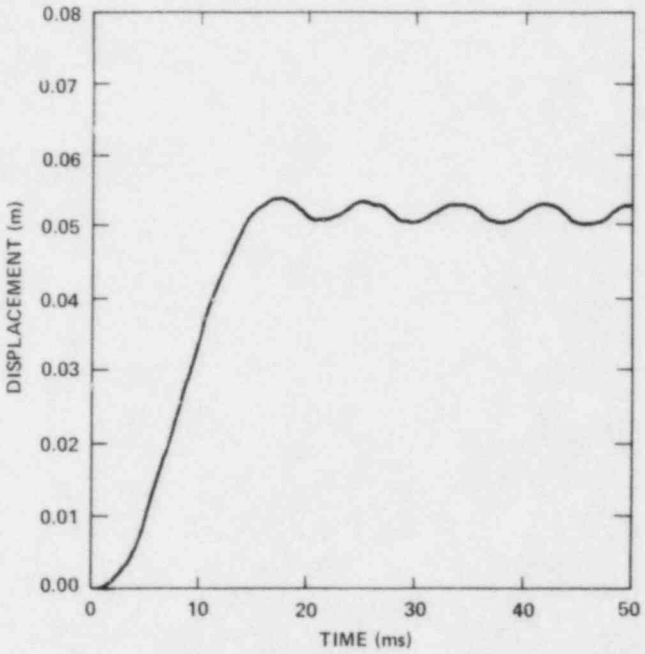

Fig. 3.
Reactor vessel wall displacement during the 100 $/s short-term expansion.

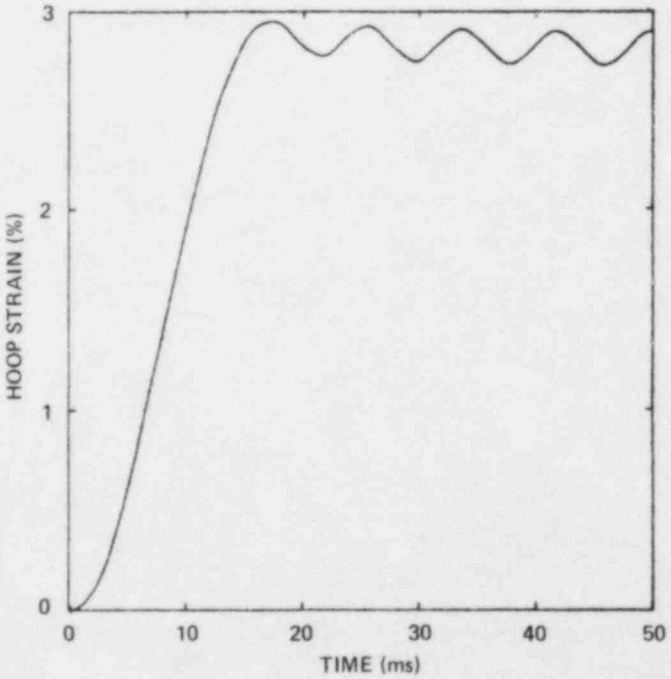

Fig. 4.
CB strain during the 100 $/s short-term expansion.

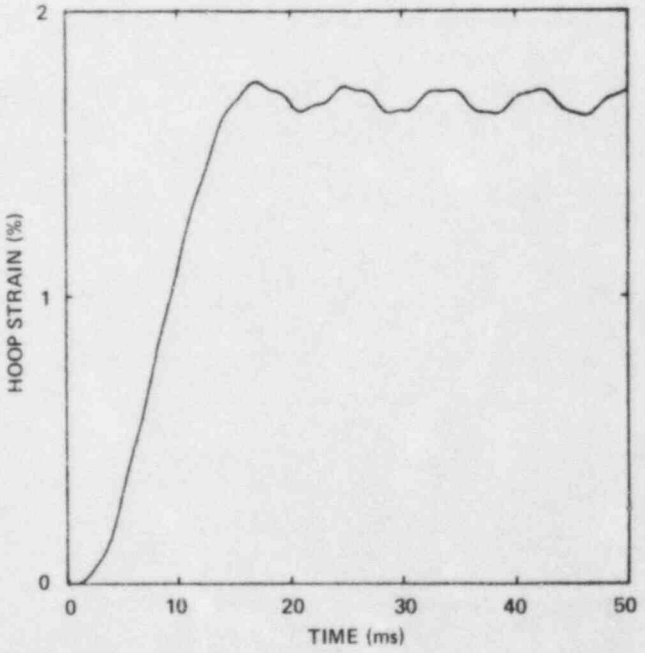

Fig. 5.
Reactor vessel wall strain during the 100 $/s short-term expansion

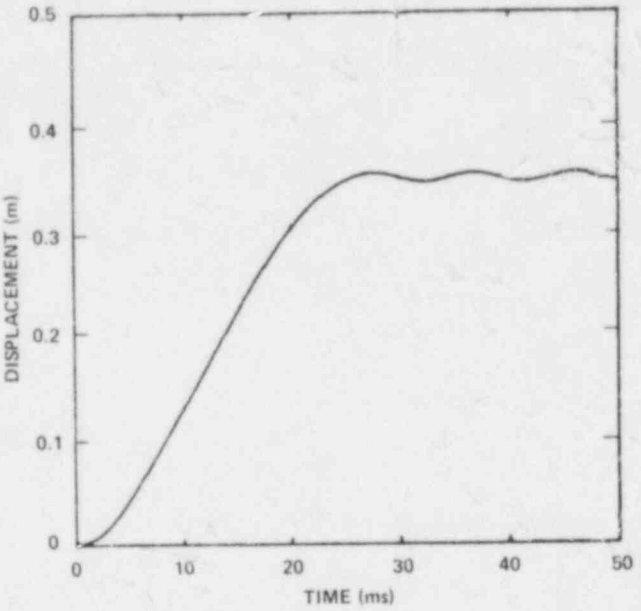

Fig. 6.
CB displacement during the 200 $/s short-term expansion.

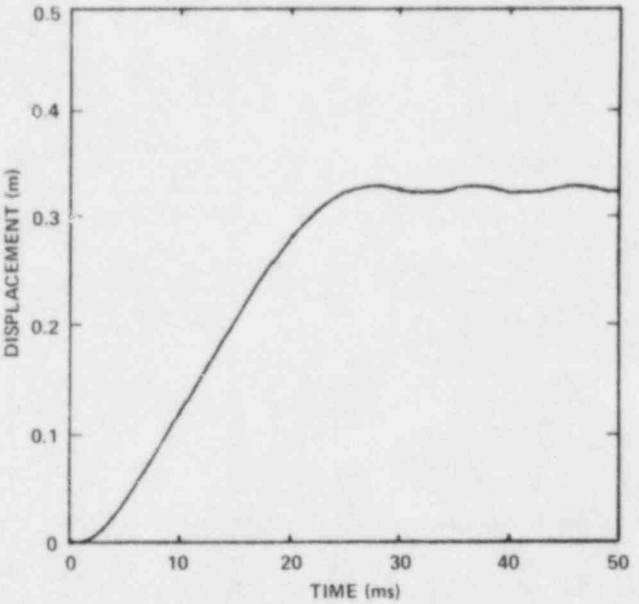

Fig. 7.
Reactor vessel wall displacement during the 200 $/s short-term expansion.

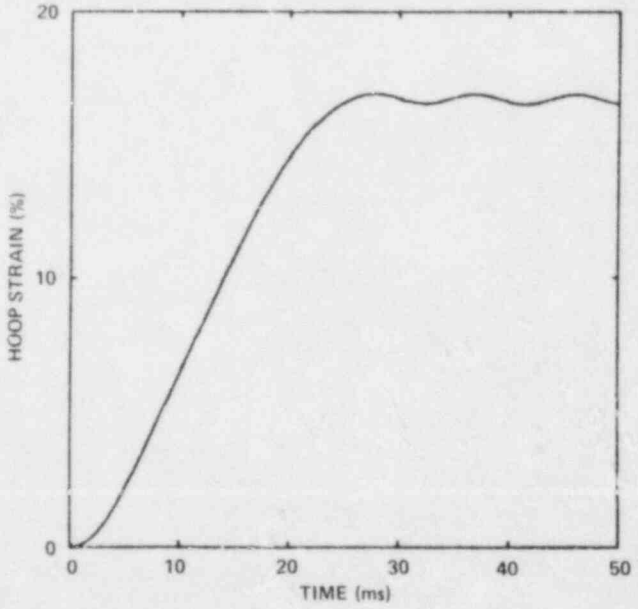

Fig. 8.
CP strain during the 200 $/s short-term expansion.

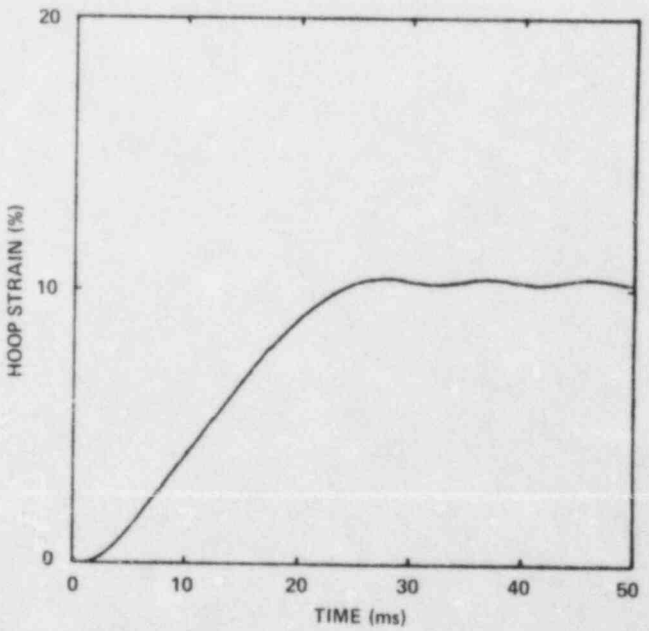

Fig. 9.
Reactor vessel wall strain during the 200 $/s short-term expansion.

To get an approximation of the energy absorbed by the CB as it strains, we use the expansion

$$\sigma = 163.3 + \frac{54.4}{0.03}\,\varepsilon \tag{1}$$

to represent stress (MPa) as a function of strain. Considering only the hoop component of strain, the strain energy (ΔE in MJ) absorbed is

$$\Delta E = \int_{\varepsilon} \int_{\text{volume}} \sigma \, dV \, d\varepsilon \tag{2}$$

or

$$\Delta E = V \int \sigma \, d\varepsilon \tag{3}$$

where V is the volume of material undergoing strain.

Substituting equation (1) into (3) gives

$$\Delta E = V\left[163.3\,\varepsilon + \frac{27.2}{0.03}\,\varepsilon^2\right] . \tag{4}$$

For a 1-m length of core barrel and a 10% strain, the energy absorbed is 16.1 MJ. The same calculation can be used for the vessel wall simply by changing the volume.

4. Benchmarking of the CB Model

To determine whether our model accurately predicts CB response, we have compared its predictions with scale-model test results [3]. Because our loads are significantly higher than those for the scale model tests and no pressures were recorded at the CB during the tests, we were constrained to compare the ratio of CB to vessel wall strain. Table 1 lists these ratios for our analyses and for the SM-3, SM-4, and SM-5 model tests. Final plastic strains are used for the test ratios. Note that the comparison is quite good and that it is very close compared to the experimental scatter between test SM-3 and tests SM-4 and SM-5.

TABLE 1
RATIO OF CB TO VESSEL WALL STRAIN

100 $/s	1.7
200 $/s	1.7
SM-3	1.7
SM-4	2.0
SM-5	2.0

The model also was tested against the coupled fiuid/structure interaction analysis [6] of REXCO for the CRBR CB under CDA loads. The pressure transient calculated by REXCO at the edge of the active core was used as the loading function for our model. The calculated strain transients for both methods are given in Figure 10. The agreement is very good through the first 15 ms indicating that the two methods produce similar radial kinetic energies. The maximum strain calculated by REXCO is 12.2% compared to 8.5% in our model. This agreement is generally within the REXCO to experiment comparisons of Reference 7.

5. Description of the UIS Models

The UIS is a very rigid steel structure suspended above the UCS. It weighs approximately 47600 kg and is held in place by four 316 SS cylindrical columns. The columns are approximately 5.3 m long with the upper end connected to the intermediate rotating plug of the vessel head through a jacking mechanism. For this study we assumed that all components of the UIS are rigid except for the columns.

Two simple models were developed with the ABAQUS computer code to simulate the UIS response during an energetic event. In both models the UIS was represented as one mass lump. In one model it was connected to the vessel head through a single truss element. This model was capable of simulating nonlinear material behavior but could not simulate column buckling. Material properties for the nonlinear truss were developed using data from Reference 3. For cases where column buckling is important, we used a second model where the column stiffness was represented by a spring that included buckling effects. The spring was based on the force deflection curve generated by the applicant using a more detailed finite-element model that included buckling [4]. This model with the nonlinear spring was capable

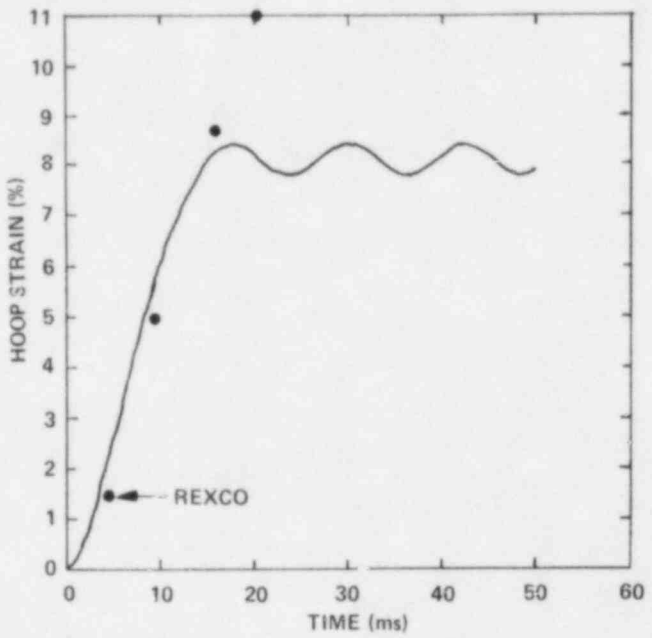

Fig. 10.
Comparison of calculated CB strain with that from REXCO.

of simulating UIS response as long as the displacement monotonically increased. For analyses where unloading occurred, the first model with the truss element had to be used. Both models gave very similar results in the regions of response where they both applied.

6. Predicted UIS Responses

The loads applied to the UIS models were based on the core boundary pressures predicted by SIMMER-II. There was a delay in time (approximately 20 ms for the 200-$/s case and 35 ms for the 100-$/s case) before the loads acted on the UIS. This delay was from the assumed crushing of the UCS. To develop a force from the pressures (Figures 7 and 8 of Section II.2), we assumed that the pressure was applied uniformly over 3.2 m^2 of the UIS (this corresponds to the full core area).

Figure 11 shows the UiS displacement response for the 100-$/s case. The UIS truss model was used for this calculation because some unloading did occur before the maximum displacement was reached. The UIS displaced a maximum of 0.15 m at 200 ms from the time it was initially loaded (235 ms from the start of the accident). This displacement is well below that required for column failure (> 0.25 m).

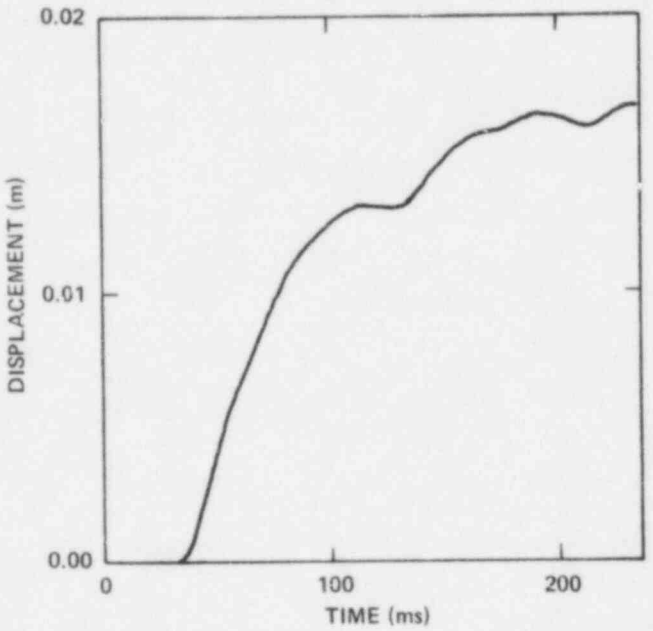

Fig. 11.
UIS displacement during the 100 $/s short-term expansion.

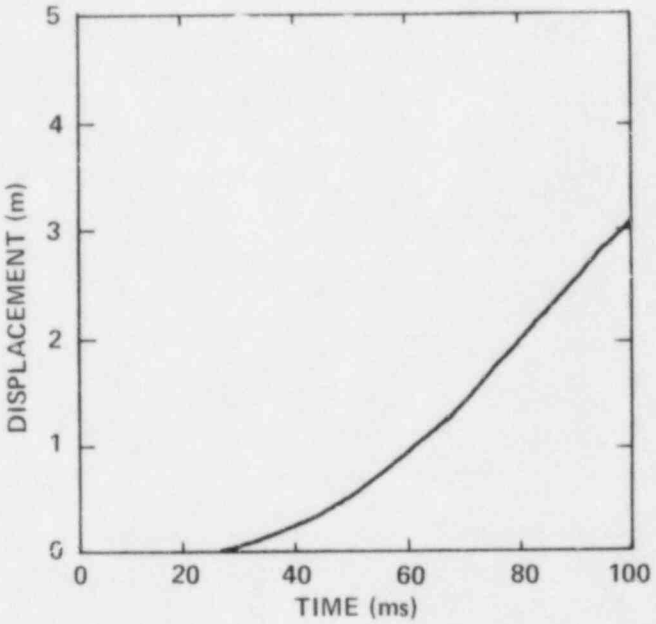

Fig. 12.
UIS displacement during the 200 $/s short-term expansion.

Displacement response of the UIS during the 200-$/s postdisassembly expansion is shown in Figure 12. The loads were sufficient in this accident to buckle the columns, so the second UIS model with the spring representing the UIS support columns was used. Displacement of the UIS was monotonically increasing and exceeded the 0.5 m displacement necessary for free discharge of the core to the sodium pool at approximately 30 ms after it was initially loaded. Therefore, the UCS would be dislodged from the core restraint structure at approximately 50 ms after the start of the postdisassembly expansion.

7. Benchmarking the UIS Models

The models have been benchmarked against scale-model test ACS2 [5], and conservative overpredictions of displacements were obtained. In test ACS2, a scale model of the UIS and its support columns was subjected to a pressure volume curve similar to that being used for the Applicant's base-case (661 MJ) scenario.

8. References

1. "ABAQUS User's Manual, Version 4," Hibbitt, Karlsson, Sorensen, Inc., Providence, RI (July 1982).

2. "Aerospace Structural Materials Handbook," Vol. 2, Mechanical Properties Data Center, DOD Materials Information Center, Battelle Columbus Laboratories, Columbus, Ohio (revised December 1980).

3. A. M. Christie, et al., "Structural Response of CRBRP Scale Models to a Simulated Hypothetical Core Disruptive Accident," Westinghouse report WARD-D-0218 (May 1978).

4. "Compendium to NUREG/CR-3224. An Assessment of CRBR Core Disruptive Accident Energetics," Section 6, Nuclear Regulatory Commission document (March 1983).

5. C. M. Romander, D. J. Cagliostio, H. E. Lindberg, and D. W. Ploeger, "Structural Response of 1/20 Scale Models of Above Core Structures to Increasingly Energetic Hypothetical Core Disruptive Accidents," SRI International Technical Report 7 (July 1979).

6. J. Marchaterre, T. Marciniak, J. Bratis, and H. Fauske, "Work Energy Characterization for Core-Disruptive Accidents," Proceedings of the International Mtg. on Fast Reactor Safety and Related Physics, Chicago, IL, October 5-8, 1976, CONF-761001.

7. C. M. Romander and D. J. Cagliostro, "Structural Response of 1/20-scale Models of the Clinch River Breeder Reactor to a Simulated Hypothetical Core Disruptive Accident," SRI International Technical Report 4 (October 1978).

APPENDIX C
LONG-TERM EXPANSION

1. Introduction

This Appendix provides the details of the core expansion against the sodium pool following failure of the UIS. It is through this mode that a mechanical threat is delivered to the reactor head. This analysis was performed for the 200-$/s transient only.

2. Geometric Model

The geometric and calculational model used for this vessel-scale analysis is shown in Figure 1. The core and part of the above core region (radial mesh 1 to 8 and axial mesh 1 to 8) were expanded to preserve the volume assumed in Appendix A for core barrel strain. A void region was introduced directly below the UIS (modeled as a jammed, no-flow region; radial mesh 1 to 9 and axial mesh 21 to 35) to account for the 0.5-m displacement of the UIS to permit venting into the pool. The cover gas volume was reduced to 15 m^3 to account for the previous voiding of sodium from the core and UCS and the displacement of the sodium from the plenum region under the UIS (it is assumed that the reactor vessel overflow piping is incapable of responding to this level change during the short times involved). The region below the active core was assumed to be nonparticipating and was not included within the problem boundaries. All boundaries in this assessment were assumed rigid.

3. Initial Conditions

The temperature and pressure throughout the core at the end of the short-term expansion were essentially uniform. This uniformity was preserved as an initial condition for the long-term expansion. The density distributions were transferred by averaging the density in the subregions shown on Figure 1 (called mesh sets) over the mesh used in Appendix A. This enabled the mesh structure to change while roughly maintaining the material arrangement. Total masses were conserved in this transformation. The cover gas was modeled as condensible sodium vapor. Thus, no gas compression mitigated the expansion through back pressure buildup. The expansion was forced to be adiabatic as in the short-term portion.

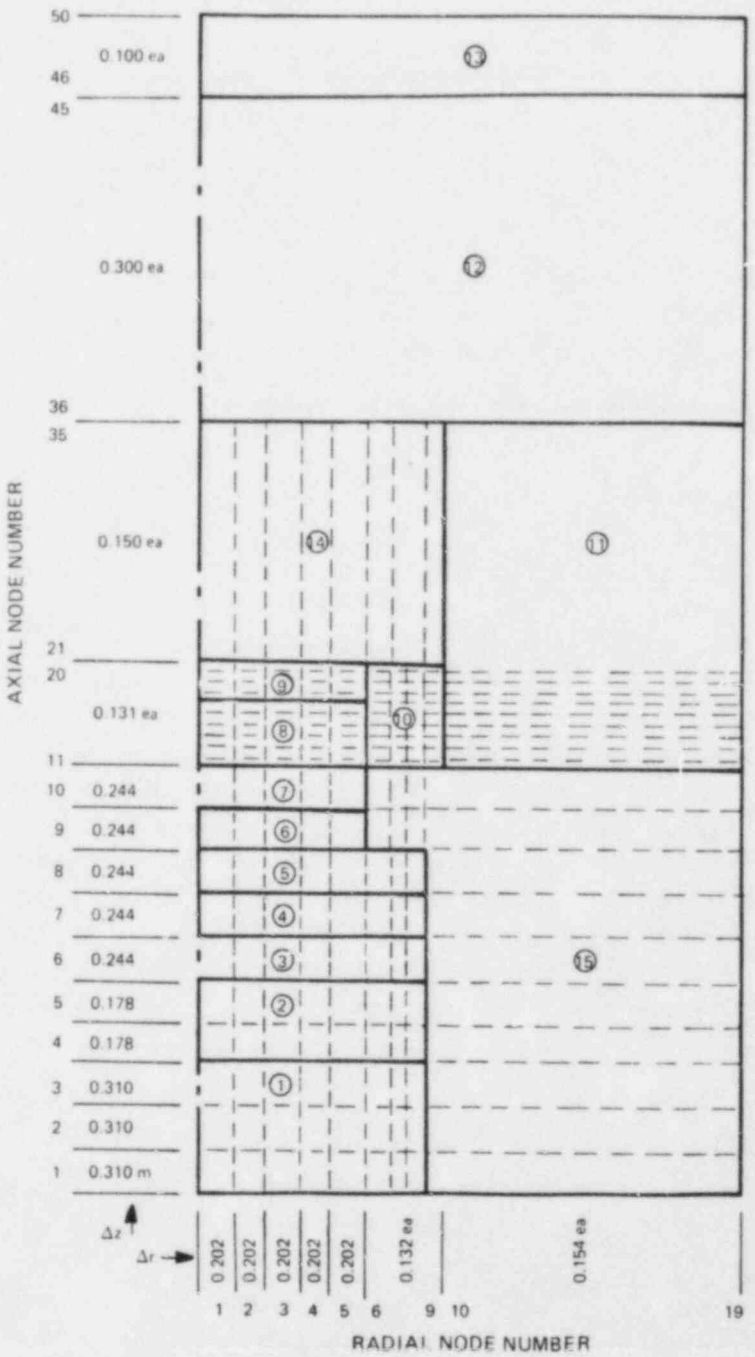

Fig. 1.
SIMMER-II geometric model for the long-term expansion analysis.

4. Results

The results for this part of the expansion are presented in the same format as those in Appendix A. The masses of liquid and vapor fuel continued to change as long as expansion to larger volume occurred. After expansion to the cover gas volume at about 80 ms, 42 percent of the fuel had vaporized as seen on Figures 2 and 3. The core pressure continued to fall as shown in Figure 4 until slug impact, at which time it leveled out at about 10 MPa. One important aspect of the transient expansion is the large pressure gradient between the source of pressure in the original core and UCS regions and the expansion bubble where work is done on the pool. When we compared the early pressure histories in Figures 4, 5, and 6 representing core, bottom of the UIS, and expansion bubble, respectively, we found that at 70 ms the pressures were 19 MPa, 8 MPa, and 7 MPa. Obviously, if the high pressures could act on the pool interface, considerably more work would be done on the pool. This is the source of the difference between the isentropic and adiabatic/dynamic expansion performed here. In an isentropic expansion, inertia is zero and the source material can be visualized as moving with the bubble interface. In reality, the high-density, two-phase fuel is far removed from the bubble interface (approximately 4 m), it has substantial inertia, it must turn a corner to get to the expansion interface, and it must continually accelerate to stay with the accelerating interface; thus, the pressure drop and the large reduction in delivered work potential. The work potential has not been dissipated or otherwise lost. The expansion simply has not developed its work potential in this highly dynamic situation.

The pool velocity is shown on Figure 7. Impact of the pool with the head was at ~77 ms. A small secondary expansion and impact occurred at ~95 ms. The impact pressures shown on Figure 8 should be simply related to the impact velocity and pool density for the sodium hammer situation in a rigid vessel. The simple fluid hammer formula gives a pressure of 63 MPa for the sodium properties used in SIMMER-II. The agreement is very good. Figure 9 shows the pressure at the top of the UIS as a result of the compression wave from slug impact propagating downward through the pool.

A more detailed view of the expansion is seen in Figures 10 through 14 for vapor volume fraction, Figures 15 through 19 for liquid volume fraction, Figures 20 through 25 for pressure, Figures 26 through 28 for radial velocity, and Figures 29 through 31 for axial velocity. On Figure 13 we can see some nonuniformity in the pool upper surface. This made the impact slightly incoherent but it is a second-order effect. Figure 19 gives a good view of the bubble at slug impact. The cover gas volume was so small that the bubble never reached the vessel wall. Figure 21 shows the pressure decrease from the original active core to the bottom of the UIS where the flow changed direction to enter the bubble radially. The initial fluid impact pressure is seen in Figure 24 and its propagation in Figure 25.

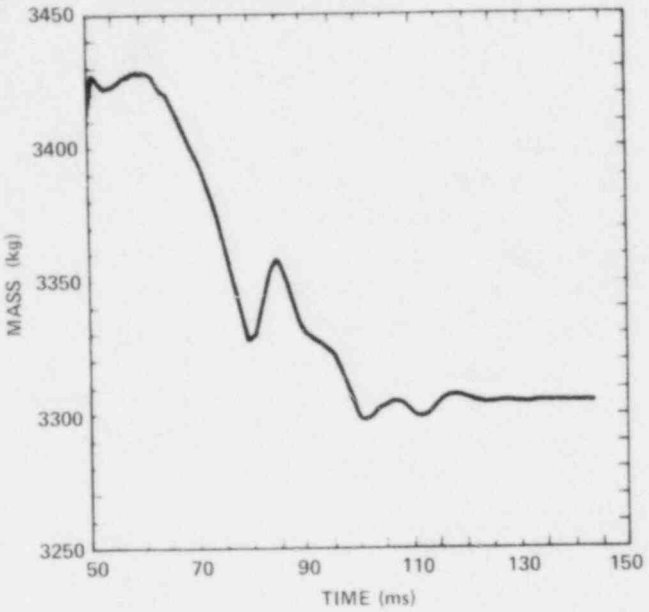

Fig. 2.
Mass of liquid fuel during the 200 $/s long-term expansion.

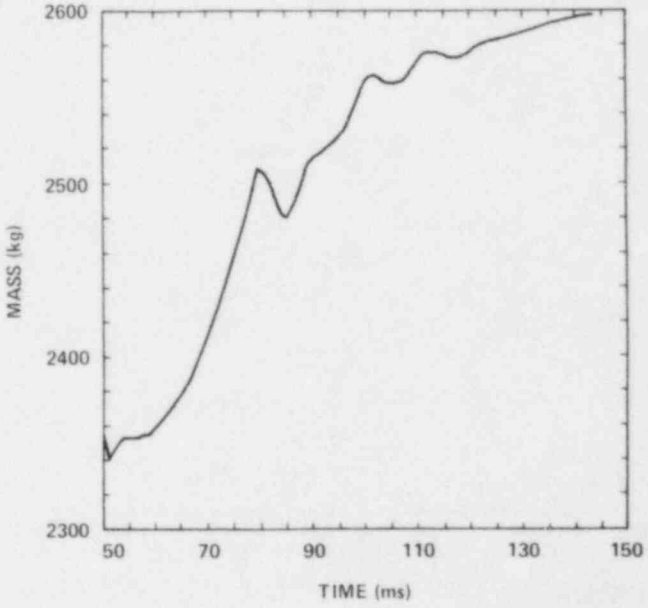

Fig. 3.
Mass of vapor during the 200 $/s long-term expansion.

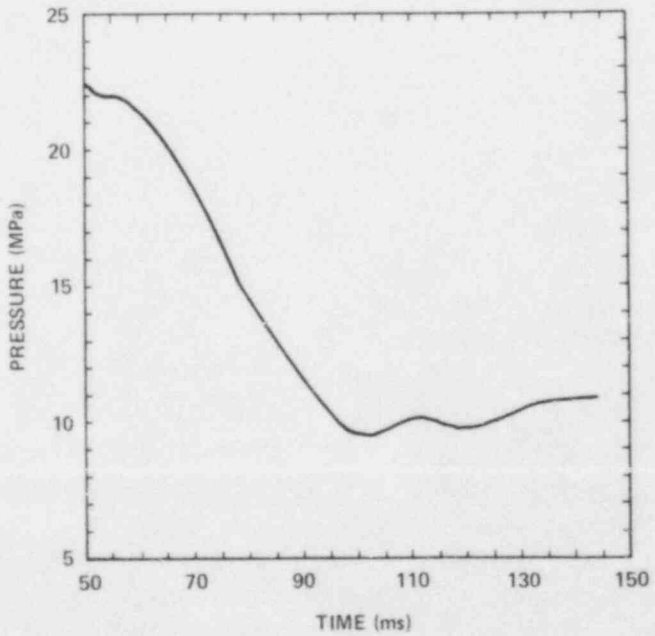

Fig. 4.
Core pressure during the 200 $/s long-term expansion.

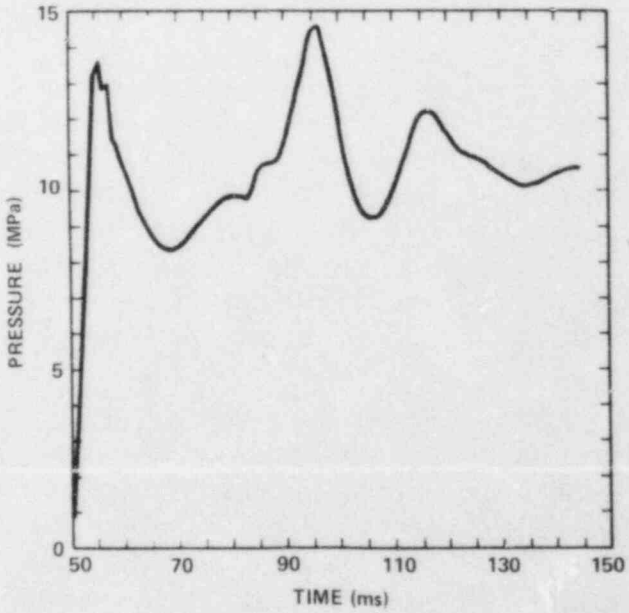

Fig. 5.
Pressure under the UIS during the 200 $/s long-term expansion.

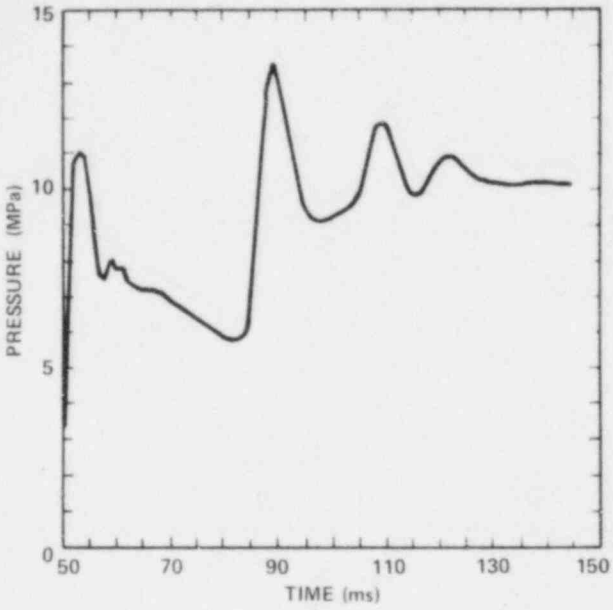

Fig. 6.
Expansion bubble pressure during the 200 $/s long-term expansion.

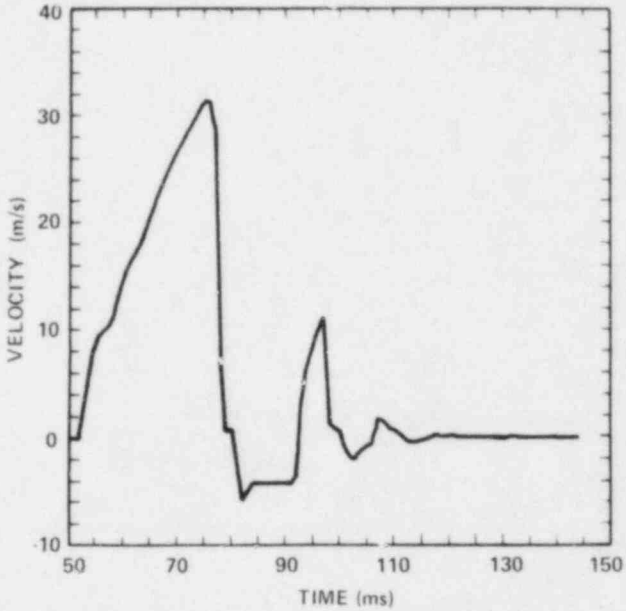

Fig. 7.
Sodium pool upper surface velocity during the 200 $/s long-term expansion.

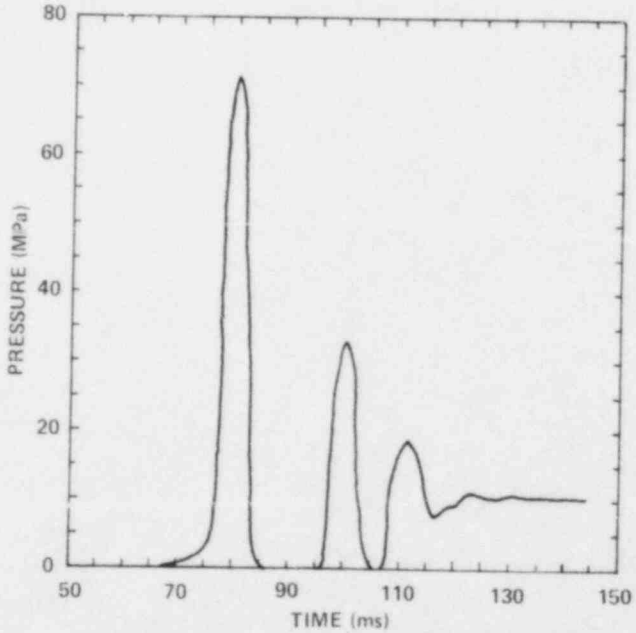

Fig. 8.
Average pressure at the reactor head during the 200 $/s long-term expansion.

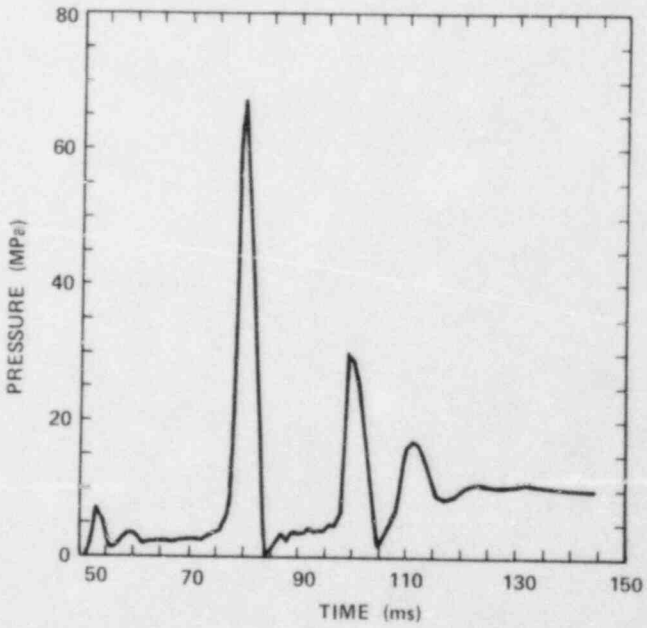

Fig. 9.
Average pressure at the top of the UIS during the 200 $/s long-term expansion.

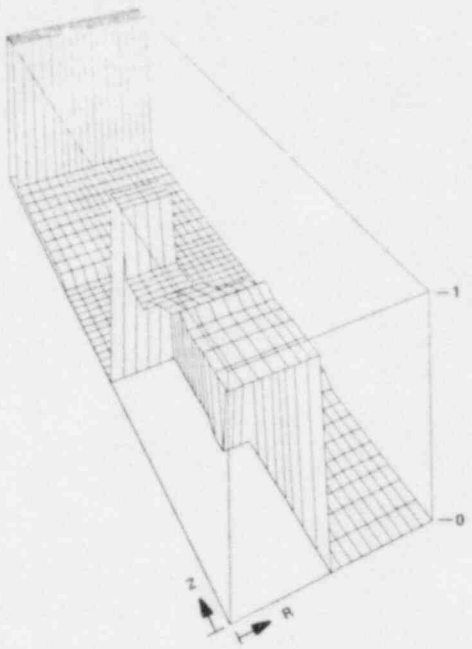

Fig. 10.
Vapor volume fraction distribution at 60 ms for the 200 $/s long-term expansion.

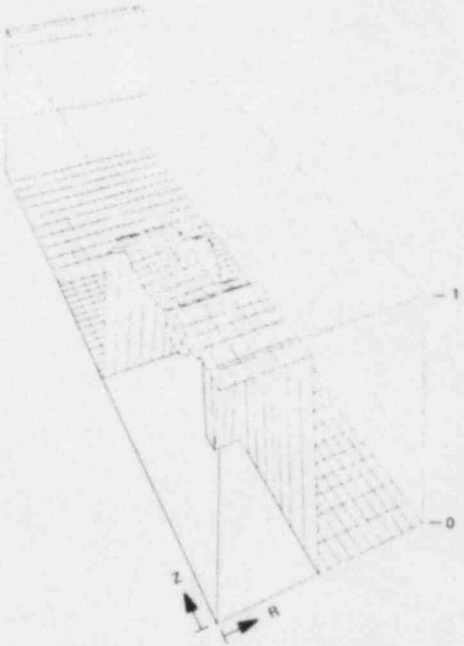

Fig. 11.
Vapor volume fraction distribution at 60 ms for the 200 $/s long-term expansion.

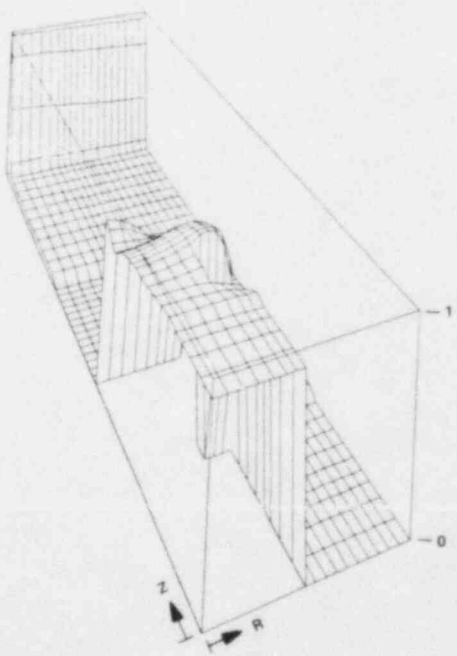

Fig. 12
Vapor volume fraction distribution at 70 ms for the 200 $/s long-term expansion.

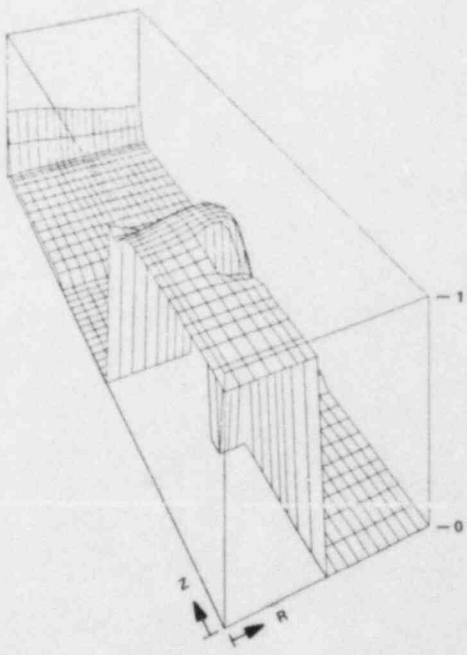

Fig. 13.
Vapor volume fraction distribution at 76 ms for the 200 $/s long-term expansion.

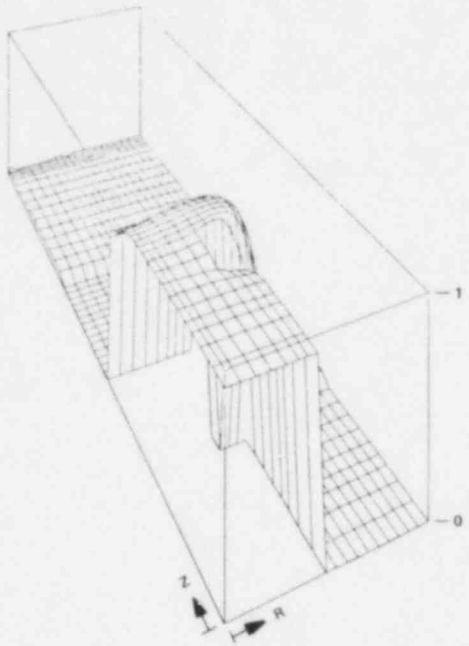

Fig. 14.
Vapor volume fraction distribution at 78 ms for the 200 $/s long-term expansion.

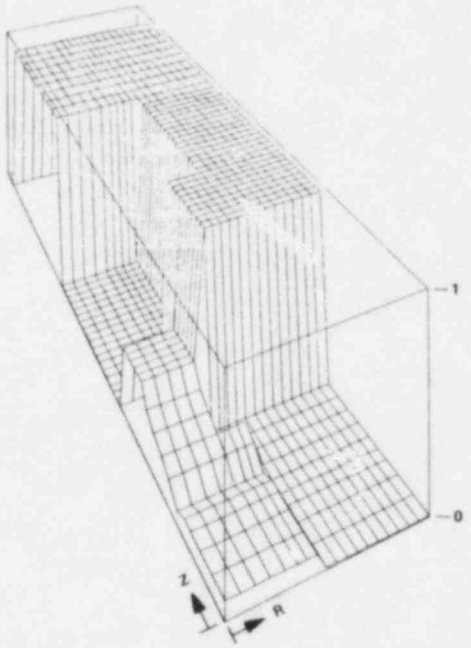

Fig. 15.
Liquid volume fraction distribution at 50 ms for the 200 $/s long-term expansion.

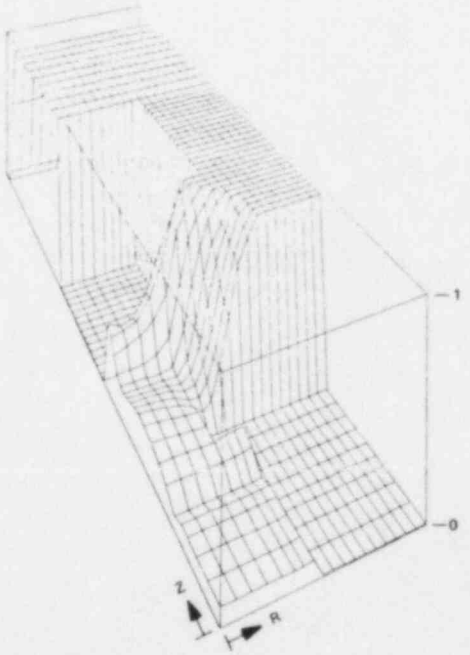

Fig. 16.
Liquid volume fraction distribution at 60 ms for the 200 $/s long-term expansion.

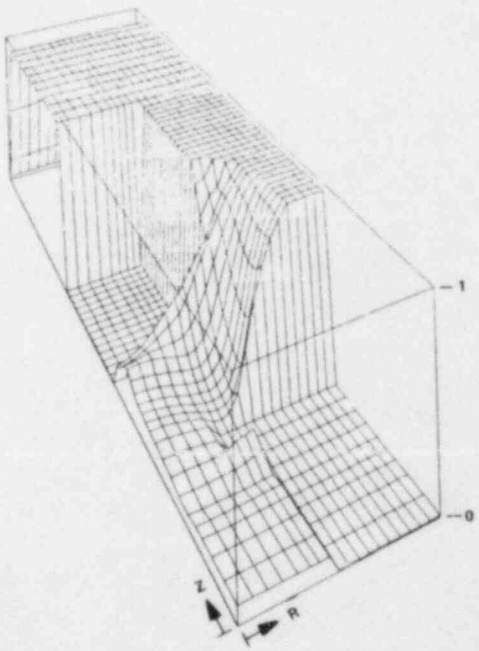

Fig. 17.
Liquid volume fraction distribution at 70 ms for the 200 $/s long-term expansion.

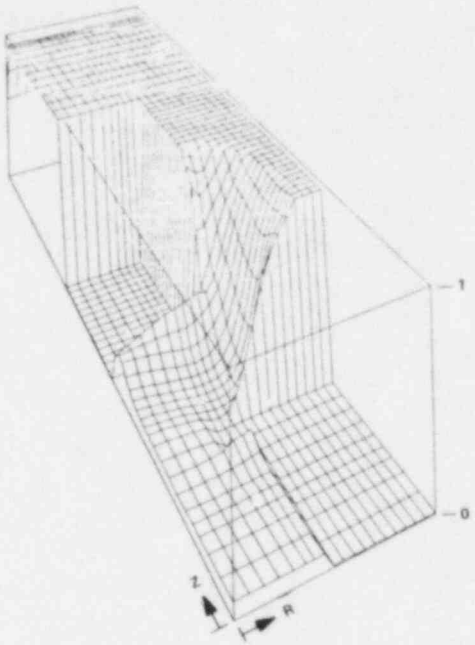

Fig. 18.
Liquid volume fraction distribution at 76 ms for the 200 $/s long-term expansion.

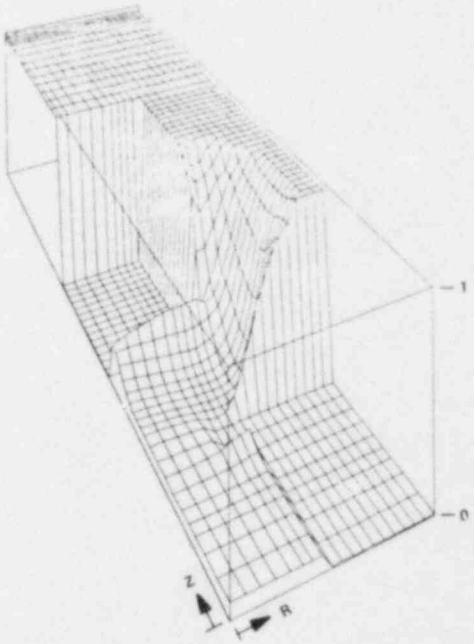

Fig. 19.
Liquid volume fraction distribution at 78 ms for the 200 $/s long-term expansion.

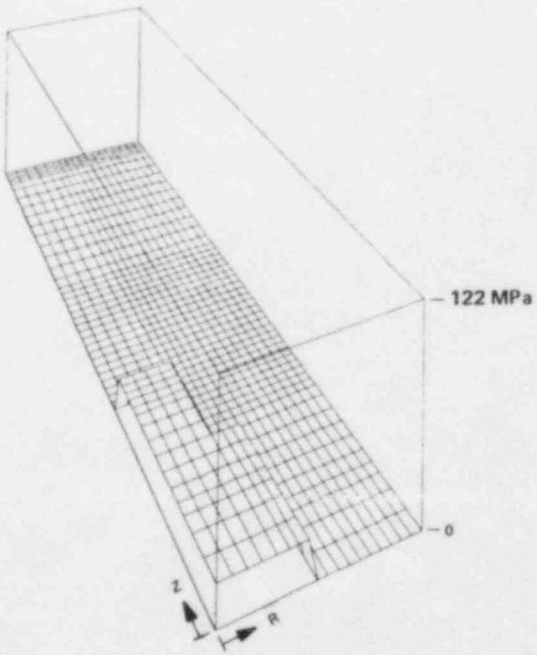

Fig. 20.
Pressure distribution at 50 ms for the 200 $/s long-term expansion.

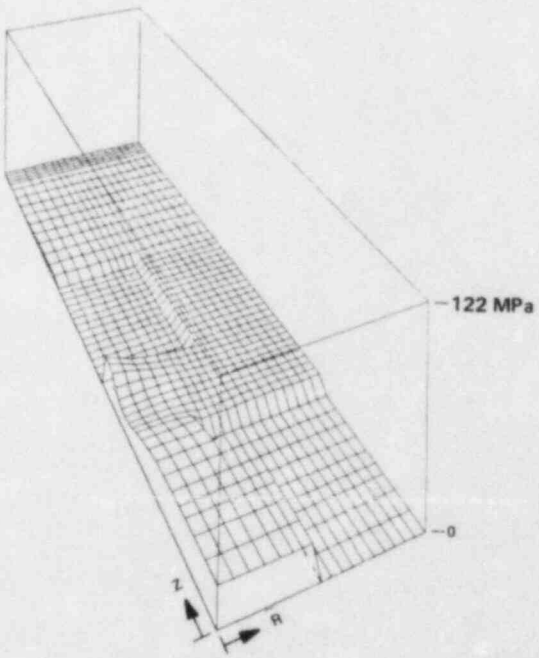

Fig. 21.
Pressure distribution at 60 ms for the 200 $/s long-term expansion.

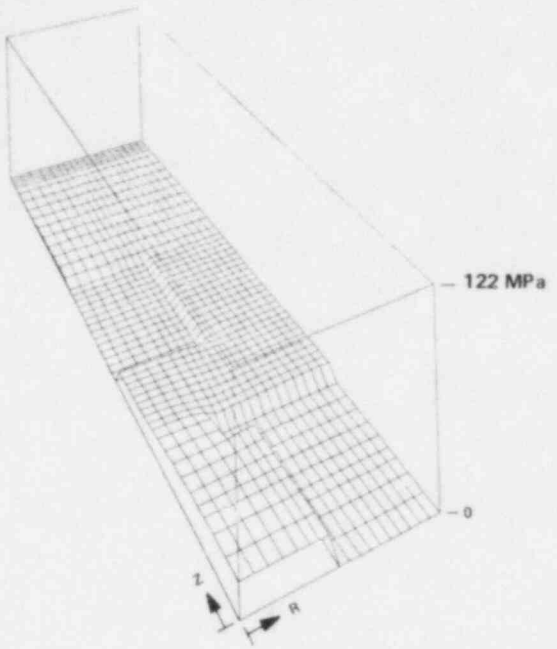

Fig. 22.
Pressure distribution at 70 ms for the 200 $/s long-term expansion.

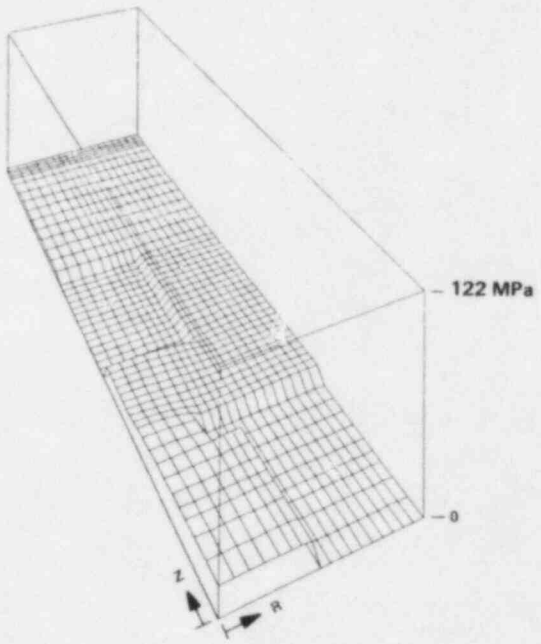

Fig. 23.
Pressure distribution at 76 ms for the 200 $/s long-term expansion.

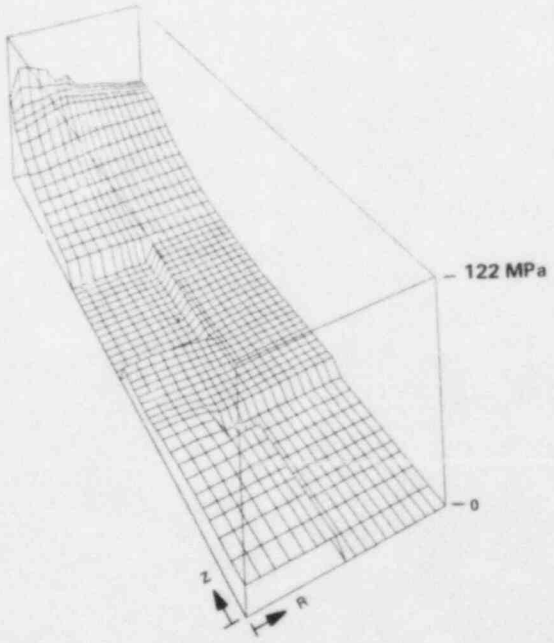

Fig. 24.
Pressure distribution at 78 ms for the 200 $/s long-term expansion.

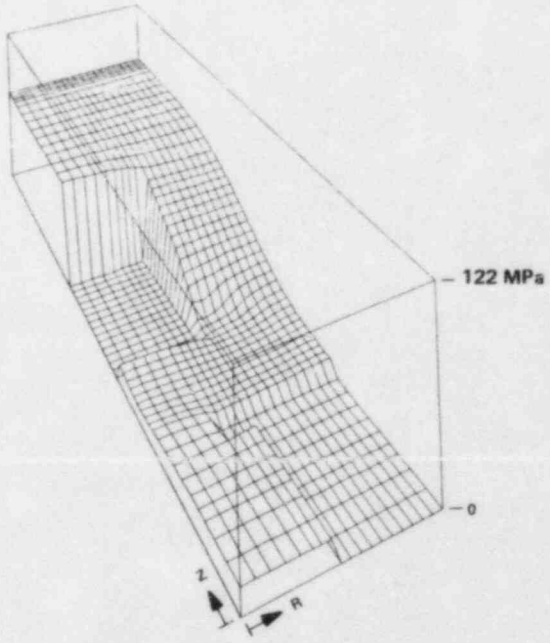

Fig. 25.
Pressure distribution at 80 ms for the 200 $/s long-term expansion.

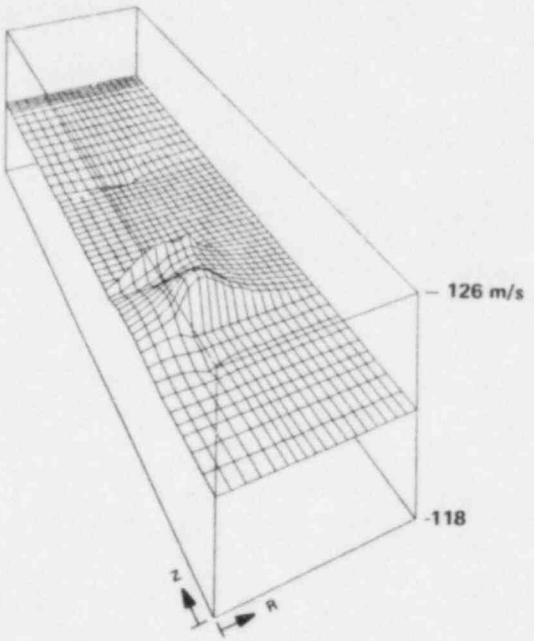

Fig. 26.
Liquid radial velocity distribution at 60 ms for the 200 $/s long-term expansion.

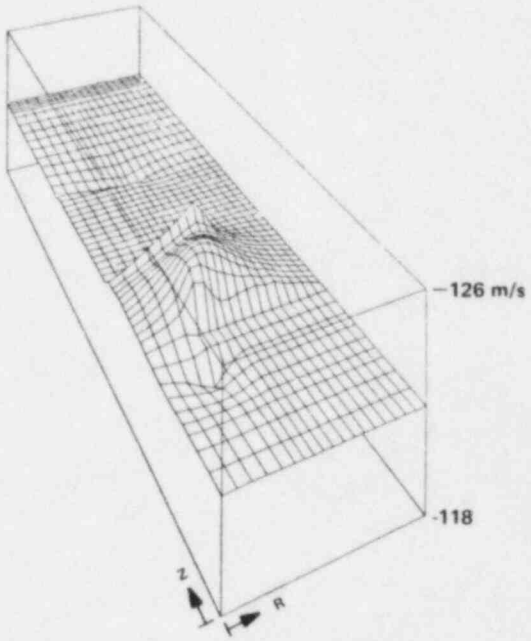

Fig. 27.
Liquid radial velocity distribution at 70 ms for the 200 $/s long-term expansion.

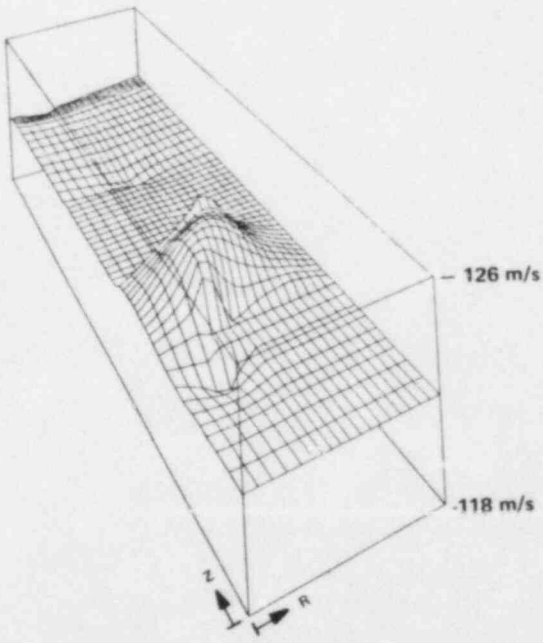

Fig. 28.
Liquid radial velocity distribution at 78 ms for the 200 $/s long-term expansion.

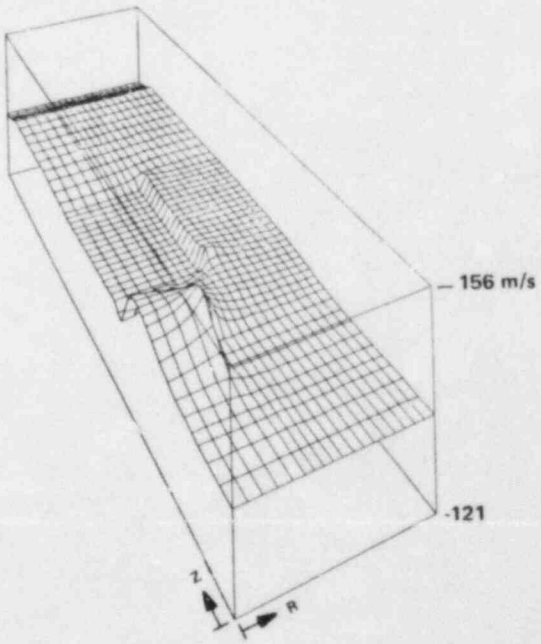

Fig. 29.
Liquid axial velocity distribution at 60 ms for the 200 $/s long-term expansion.

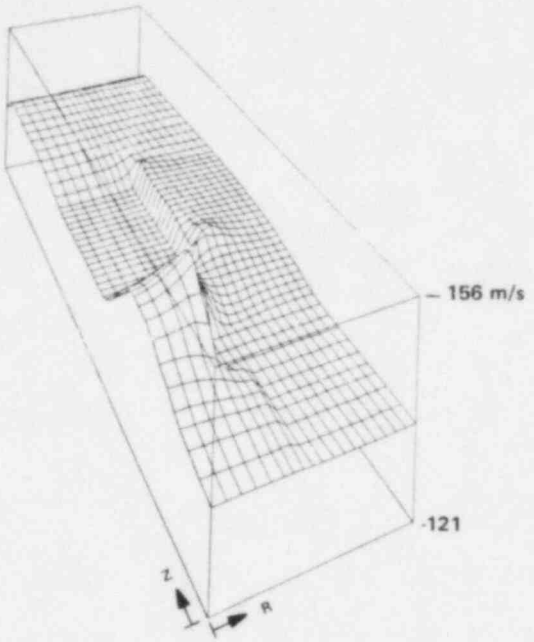

Fig. 30.
Liquid axial velocity distribution at 70 ms for the 200 $/s long-term expansion.

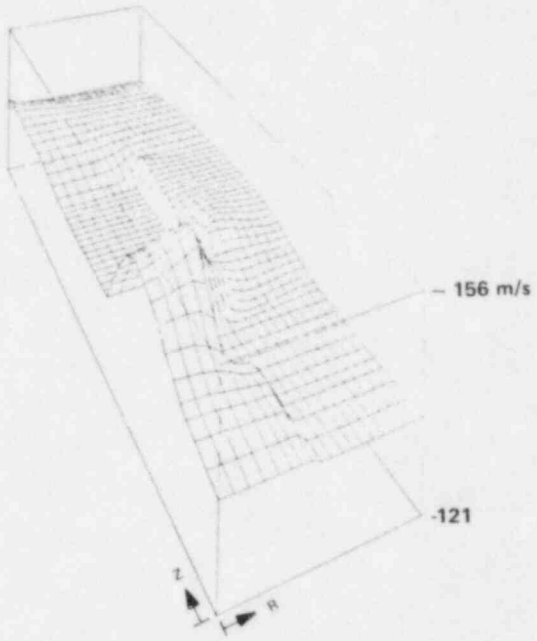

Fig. 31.
Liquid axial velocity distribution at 78 ms for the 200 $/s long term expansion.

The development of axial kinetic energy in the system and in the sodium pool alone is shown in Figures 32 and 33, respectively. The difference of about 20 MJ was associated with the high-velocity core material as it flowed to the expansion bubble. The damage potential to the head derives from the 80-MJ peak shown on Figure 33 for the sodium pool alone because the core material was uncoupled from the sodium pool. The radial kinetic energies are shown in Figures 34 and 35. Most of this kinetic energy, which also was uncoupled from the pool, was in the flow of core material from under the UIS to the expansion bubble. The maximum total system kinetic energy was 124 MJ.

Taking the starting point for the ideal isentropic expansion as the end of the short-term dynamic expansion, the isentropic work potential released during the long-term expansion to slug impact was 160 MJ. The dynamic reduction factor therefore is 2. If we compare the 80 MJ to that obtained from an ideal isentropic expansion to 29 m^3 (14 m^3 from the short-term and 15 m^3 from the long-term), a conversion efficiency of 11% results.

Heat transfer among the various materials within the core (steel, fuel, and internal blanket pellets) and expansion bubble (fuel, steel, and sodium) were assessed [7] using nominal SIMMER-II models. Two major effects were noted. First, the dynamic pressure drop between the core and expansion bubble was reduced because of sodium vapor generation in the bubble. Second, the pressure in the core and bubble was reduced as a result of heat transfer from the fuel in the core. The net effect was a factor-of-2 reduction in the IKE.

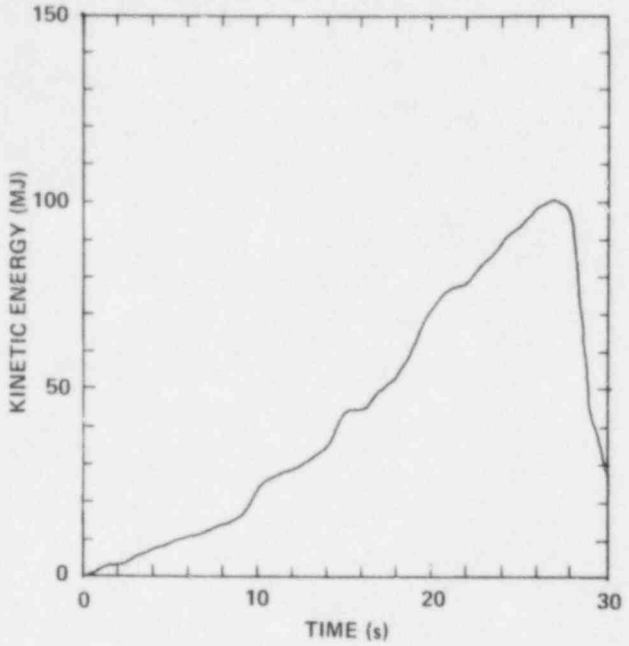

Fig. 32.
Axial kinetic energy of all materials during the 200 $/s long-term expansion.

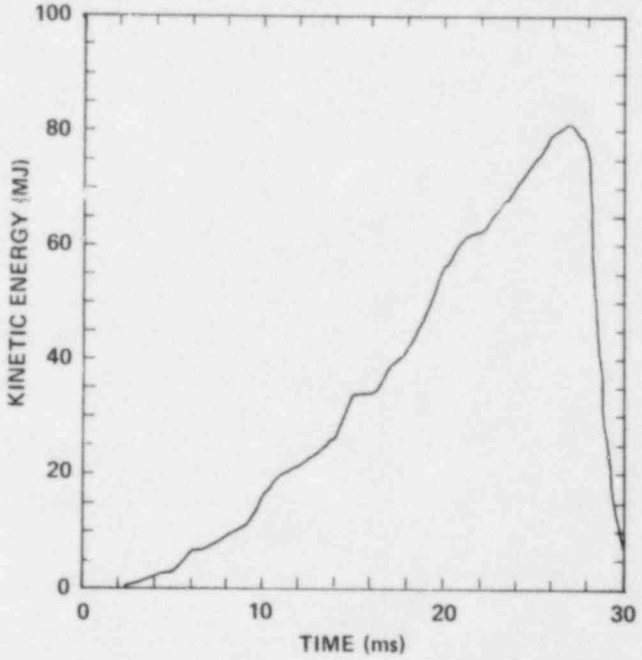

Fig. 33.
Axial kinetic energy in the sodium pool during the 200 $/s long-term expansion.

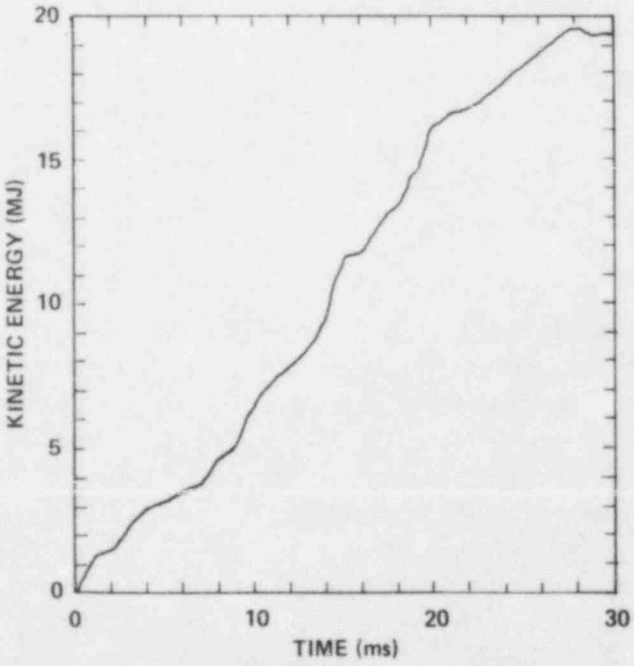

Fig. 34.
Radial kinetic energy of all materials during the 200 $/s long-term expansion.

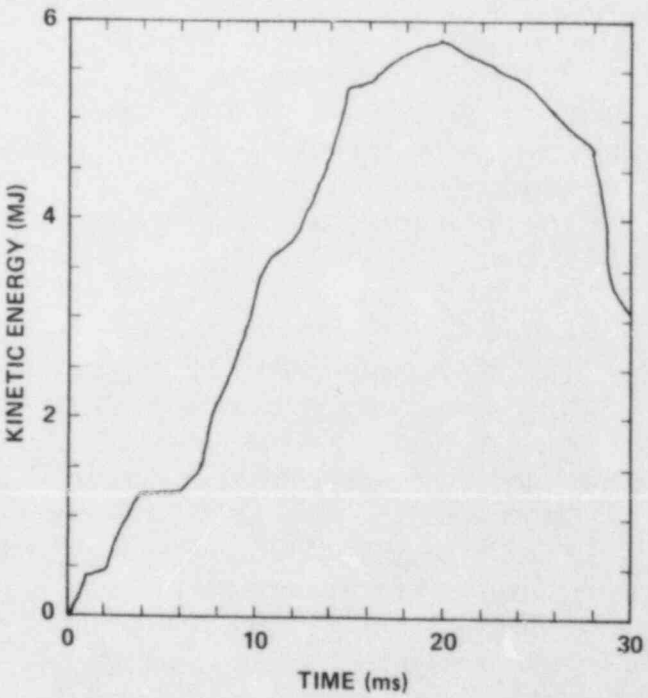

Fig. 35.
Radial kinetic energy in the sodium pool during the 200 $/s long-term expansion.

5. Validity of Results

The fluid dynamics in the long-term expansion are relatively simple and straightforward. SIMMER-II has been exercised [1-4] extensively on this type of problem and has been tested against data [5, 6] in this regime.

6. Summary

By including some fundamental aspects of the postdisassembly expansion, the effective generation of damage potential to the head (pool axial kinetic energy) is only 11% of thermodynamic maximum possible.

7. References

1. C. R. Bell, J. E. Boudreau, J. H. Scott, and L. L. Smith, "Advances in the Mechanistic Assessment of Post-Disassembly Energetics," Proc. of the International Meeting on Fast Reactor Safety Technology, Seattle, WA, August 1979.

2. C. R. Bell, and J. E. Boudreau, "SIMMER-I Accident Consequence Calculations," Trans. Am. Nucl. Soc. 27 (1977).

3. J. F. Jackson and M. Stevenson, "Nuclear Reactor Safety Quarterly Progress Report, April 1-June 10, 1978," Los Alamos National Laboratory report LA-7481-PR, NUREG/CR-0385 (October 1978).

4. J. F. Jackson and M. Stevenson, "Nuclear Reactor Safety Quarterly Progress Report, October 1-December 31, 1977," Los Alamos National Laboratory report LA-7195-PP (April 1978).

5. T. F. Bott and C. R. Bell, "SIMMER-II Analysis of SRI Postdisassembly Expansion Experiments," Los Alamos National Laboratory report LA-9452 MS (August 1982).

6. J. F. Jackson and M. Stevenson, "Nuclear Reactor Safety Quarterly Progress Report, October 1-December 31, 1979," Los Alamos National Laboratory report NUREG/CR-1516, LA-8299-PP (May 1980).

7. Compendium to NUREG/CR-3224, An Assessment of CRBR Core Disruptive Accident Energetics, Section 12, Nuclear Regulatory Commission document (March 1983).

II.3. REFERENCE INITIATING-PHASE BEHAVIOR

1. Objectives and Overview

The phenomenological sequence of the LOFA initiating phase has been well established both analytically and experimentally. Flow coast down occurs, typically with a time constant of ~8 s, and sodium boiling initiates at ~10 s at near nominal power level and 20% of full flow. This boiling process is unstable. It quickly leads to pressure buildup and liquid sodium expulsion out both ends of the coolant channel (subassembly). Following "coolant voiding" the cladding melts within a fraction of a second and the fuel soon after. Relocation of these molten/disrupted materials occurs under the influence of gravity and existing pressure gradients from fission gases, sodium vapor, any residual pump head, and the static liquid sodium head over the voided region. The timing of these subsequent processes depends upon the power level, which rises because of reactivity increases associated with the sodium voiding process. The power history, in turn, affects the core-wide sodium boiling inception and voiding pattern such that a highly coupled situation develops.

A sufficiently high sodium-void reactivity worth may produce a near prompt-critical condition well before complete core voiding. The resulting high overpower condition induces TOP-like phenomena (see Section III) in the unvoided subassemblies (cooled, strong cladding). This situation is known as the Loss-of-Flow driven Transient Overpower or LOF-d-TOP. The potential for such evolution was identified for the previous CRBR homogeneous core design as a major safety (energetics) concern [1, 2]. The mechanism is illustrated in Figure 1. It involves near-mid-plane failures and forceful (due to retained fission gases) molten fuel motion toward the failure location. A potentially autocatalytic character is possible. At this time neither the mechanisms of this LOF-d-TOP regime nor its energetic outcome can be predicted with confidence, hence, its occurrence is highly undesirable. The present, heterogeneous CRBR core design with its lower sodium-void reactivity worth is helpful in this regard.

The extent to which the LOF-d-TOP regime is avoided altogether may be conservatively assessed by analyses that accentuate the positive reactivity feedbacks (material relocation rates and worths chosen at the upper end of their uncertainty band) and minimize the negative ones (the magnitude of the axial thermal expansion of the fuel column and the value of the Doppler). However, such choices leading to a "fast" initiating-phase scenario also yield nearly simultaneous cladding melting and fuel disruption in the voided coolant

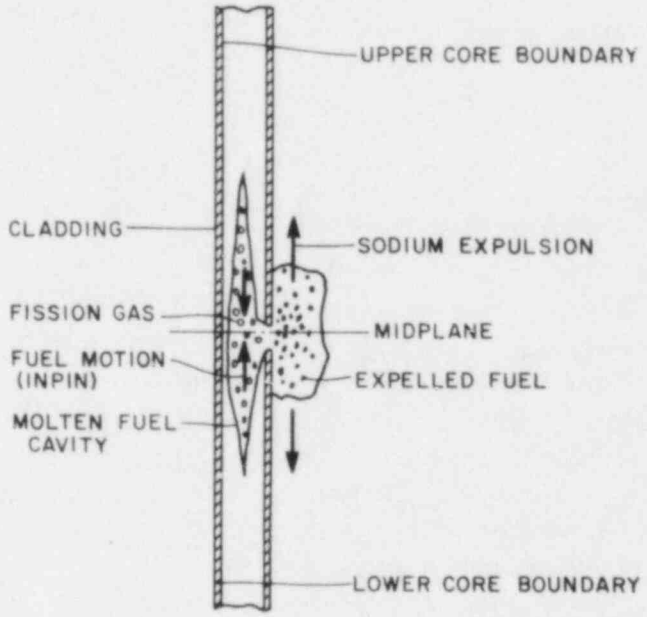

Fig. 1.
Illustration of the LOF-d-TOP mechanism.

channels and are, therefore, nonconservative with regard to steel blockage formation and hence recriticality potential during the postinitiation (disruption) stages of the accident sequence. This opposite extreme is explored by analyses that accentuate the negative feedbacks while minimizing the positive ones ("slow" scenario). Both of these extremes, as well as several in-between choices of parameters, were explored (using SAS3D calculations) for the EOC-4 core configuration. In addition, we considered the EOC-3 core (increased core-wide coherence due to replacement of the six highest power subassemblies by blankets) and the BOC-1 core (low sodium void reactivity and absence of fission gases in the fuel) to span the full range of behavior in the initiating phase. Representative results are presented in Section 6 and in more detail in Appendix BII.3.

The initiating-phase phenomena are modeled in great detail in the SAS computer code. This tool pioneered the field over a decade ago and, through a continuing research and development effort and a succession of new and improved versions, has helped define the state of the art in this area. However, as is common with large "systems" codes, the fidelity in portraying local behavior is limited. There are two aspects to these limitations. One results from viewing the whole subassembly (217 pins) response in terms of an average pin thereby neglecting multidimensional effects and associated intrasubassembly incoherencies. The other limitation is a consequence of representing the whole core as a relatively small number of these representative pins or "channels" in SAS terminology (many subassemblies

lumped into a single channel), and thus only approximately accounting for intersubassembly incoherencies. Our views on the nature and possible impact of these limitations are provided in the next few sections to put the accident analysis results of Section 6 in the proper perspective. All crucial ingredients in our SAS3D analyses also are presented and discussed in those sections.

The Applicant also has considered initiating-phase behavior in some detail. The SAS3D computer code was utilized in these evaluations. Results for various core configurations, parametric effects, and specific analyses conducted in response to our Questions #2 and #4 (Table 2 of Section II.1) were provided [3, 4]. Our initial review and evaluation of these results has been documented in References 5 and 6. Based on our own independent studies, we agree with the major conclusion of the Applicant concerning the absence of the LOF-d-TOP regime (for an important qualification in this matter, see Section II.4). On the issue of exit core blockage formation, our agreement with the Applicant is qualitative and tentative. It is qualitative because we predict a higher degree (although far from complete) of core exit plugging by relocated molten cladding and tentative because this agreement was obtained by fundamentally different approaches. According to the Applicant, irradiated fuel remains dispersive throughout the initiating phase; and plenum fission gas blowdown interferes sufficiently with the sodium vapor streaming to inhibit upward cladding relocation and plugging at the core exit (UAB area). In our view, the initial dispersiveness (upon disruption) of irradiated fuel will dissipate due to expansion pressure equilibration and de-entrainment. Thus, eventually the disrupted fuel will fall-back under gravity. On the role of plenum fission gas blowdown on cladding relocation, our analyses indicate that this effect, by itself, does not preclude net upward relocation. However, taken together with sodium vapor flow redistribution effects due to radial cladding melting incoherencies on a best-estimate basis, we arrive at this same general conclusion. Further discussion of these topics is given in the appropriate sections below.

2. Sodium Voiding

The sodium voiding process is important not only in providing the initial driving reactivity for power escalation but also in affecting the mechanism of the cladding relocation (see Section 3). The potential deviations from the simple, SAS, one-dimensional representation have been recognized for some time. However, progress in quantifying these so-called intrasubassembly boiling incoherencies has been slow. At this time the only analytical predictions available are based on a simplified homogeneous, equilibrium two-phase flow model (HEV-2D) applied to a two-dimensional (cylindrical symmetry assumed) bundle geometry [2]. The essence of the predicted trends is summarized in Figure 2.

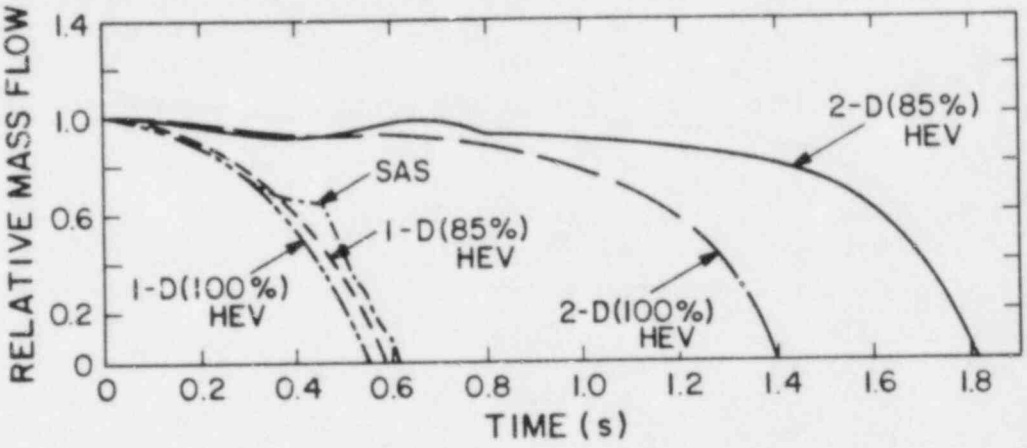

Fig. 2.
Comparison of analytical treatments for sodium boiling at 85% and 100% power (zero time is boiling inception).

First we note the good agreement in the inlet flow transient between the SAS and HEV-1D predictions (the HEV model applied in one dimensional geometry). Inlet flow reversal and macroscopic sodium voiding occurred within 0.6 s from boiling inception, and the boiling instability process seemed to have been overwhelmed by the heat input as indicated by the agreement between the two widely different two-phase flow models represented in these two calculations (annular flow in SAS, homogeneous flow in HEV). Allowance for two-dimensional effects contributed to flow stability, although again, flow reversal was obtained. A delay by ~1 s is noted between the one-dimensional and two-dimensional analyses. From a slightly different perspective, the two-dimensional results may be viewed as causing boiling initiation about 1 s too early. Indeed, the one-dimensional calculation indicated a delay for boiling inception (as compared to the two-dimensional case) by ~1 s, hence on an absolute time frame the results for rapid drop-off in inlet flow and reversal are nearly indistinguishable.

The recently run OPERA-15 test [7] also addressed this problem. A 15-pin triangular bundle was arranged to represent, by symmetry, a one-sixth segment of a 61-pin bundle and was subjected to a flow coastdown transient in the ANL OPERA facility. The technical community was invited [8] to submit pretest (blind) predictions to be published with the test results. The results [9] discussed above seemed pertinent to the test conditions and were therefore submitted [10] in response to this request. At this time the test results have been published [7]. It is our understanding

[11] that comparisons with all the pretest predictions submitted will follow shortly. The comparisons with our own results are shown in Figure 3. Satisfactory agreement is indicated. The time to flow reversal in OPERA-15 was 2.3 s vs the 1.8 s predicted by HEV-2D. However, there is some indication [11] that a slight bowing of the "outer" test assembly wall produced approximately a 10% additional bypass and this may be the reason for the somewhat longer delay observed experimentally.

Based on these results, we expect that the SAS one-dimensional predictions of the boiling flow excursion do not significantly suffer from neglecting the intrasubassembly boiling incoherencies. Further, based on extensive and well-documented calculations of in-pile tests, we expect that the voiding rates in the one-dimensional mode are accurately predicted. The main effect of the boiling incoherencies, then, is to induce a radial temperature distribution, which translates into radial cladding melting incoherencies; this, in turn, significantly affects cladding relocation phenomena as discussed in the next section.

3. Cladding Relocation

Flow reversal delays (two-dimensional boiling effects) translate to radial cladding melting incoherencies. We will discuss how such effects may be used to explain some apparent inconsistencies observed in in-pile test data. These data are summarized in Table 1.

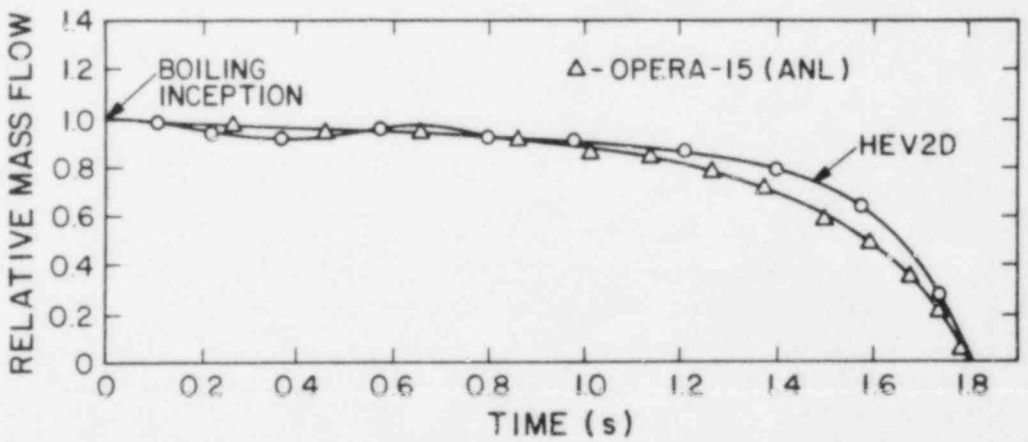

Fig. 3.
Comparison of predicted and experimental sodium boiling transients for the OPERA-15 test (data shifted by -0.5 s to synchronize boiling inception times).

TABLE 1
IN-PILE CLADDING RELOCATION DATA

• R-series	7-pin	mm-scale blockages
• R-8	7-pin 3-pressurized	no blockage
• P3A	37-pin	2-cm blockage
• P3	37-pin	10-cm blockage

Simulant material (woods-metal/air) experimental data have been correlated [2] in terms of the dimensionless gas velocity, J_g^*, as shown in Figure 4. These data indicate the following relocation regimes: (a) $J_g^* \sim 1$ cladding suspension and sloshing, (b) $J_g^* < 0.8$ cladding draining, and (c) $J_g^* > 1.5$ net and sustained upward relocation. A rough scale of relocation velocities may be estimated, again with J_g^* as the parameter, in terms of the transient film thickness data shown in Figure 5. The basic characteristics of the R- and P-series tests are compared to those estimated for the CRBR in Figure 6. The radial melting incoherence, $\tilde{A}$, is defined as the radial fraction of the pin bundle experiencing cladding melting simultaneously. It is interesting that in this respect the 7-pin bundle of the R-series is superior to the 37-pin P-series bundle in simulating the estimated (by HEV-2D) CRBR bundle incoherency. However, the available pressure drop, ΔP, in the R-series was below that present in the P-series and estimated (by SAS3D) for the CRBR for a LOFA. A similar trend is also noted for the magnitude of the chugging velocities, ΔV, and may be thus inferred for the associated pressure pulses.

The cladding relocation trends have been quantified [2] and are presented in the flow regime map of Figure 7. The quantity $\tilde{L}$ represents the axial melting incoherency and is defined analogously to $\tilde{A}$. The available pressure drop, ΔP, is expressed by the number, m, in terms of the number of the static sodium heads as shown. Any point on this map represents a particular incoherency state. The associated cladding relocation trend is determined by the value of the J_g^* trajectory passing through this point and the criteria established on the basis of the data of Figure 4. The points of departure and initial trajectories of the R- and P-series bundles are shown in this flow regime map. Due to the heat losses to the adjacent cold duct walls in the 7-pin R-series bundles, melting should progress rapidly downward rather than radially, that is, a more or less straight upward trajectory of melting incoherency states is indicated. The highly one-dimensional P-series bundles, however, should begin at $\tilde{A} \sim 1$. Now only a straight upward

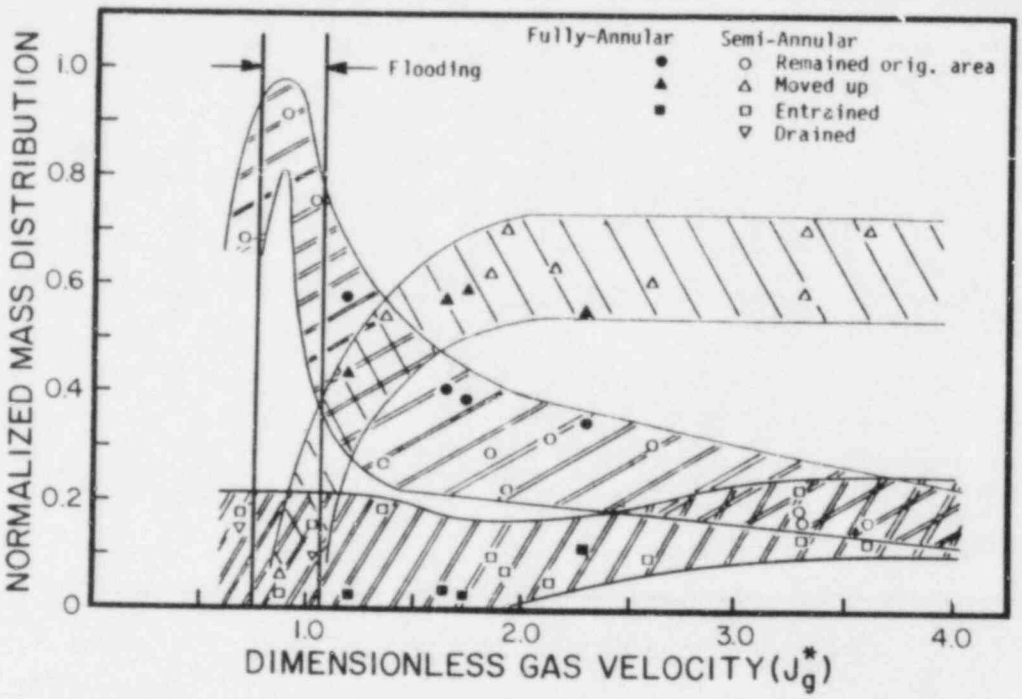

Fig. 4.
Correlation of wood-metal/air data to obtain cladding relocation tendencies.

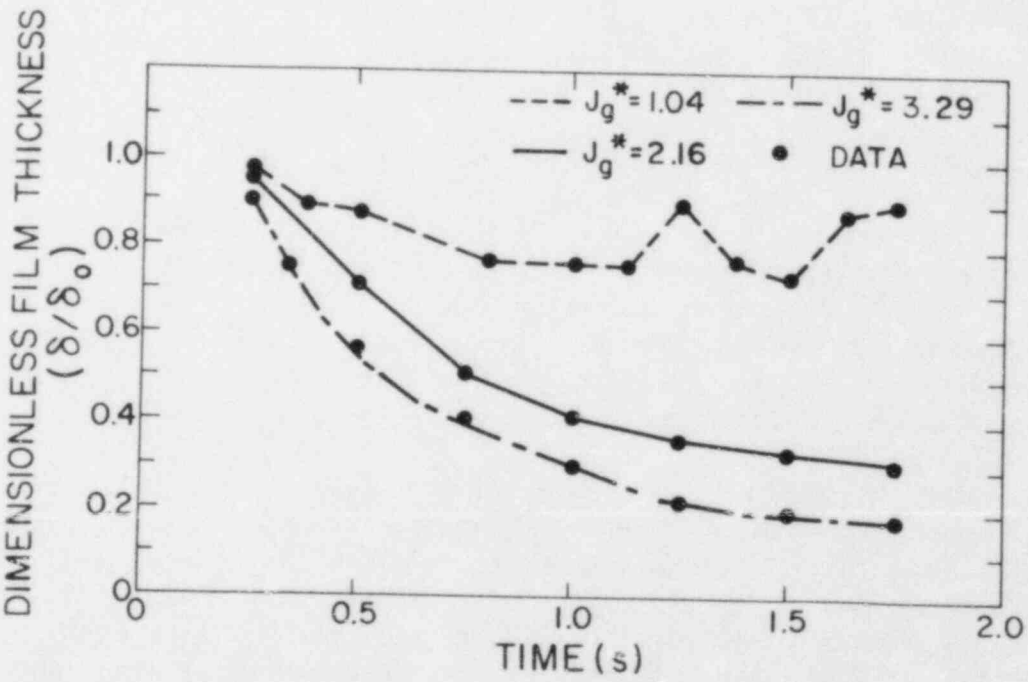

Fig. 5.
Woods-metal relocation transients for various air flow rates.

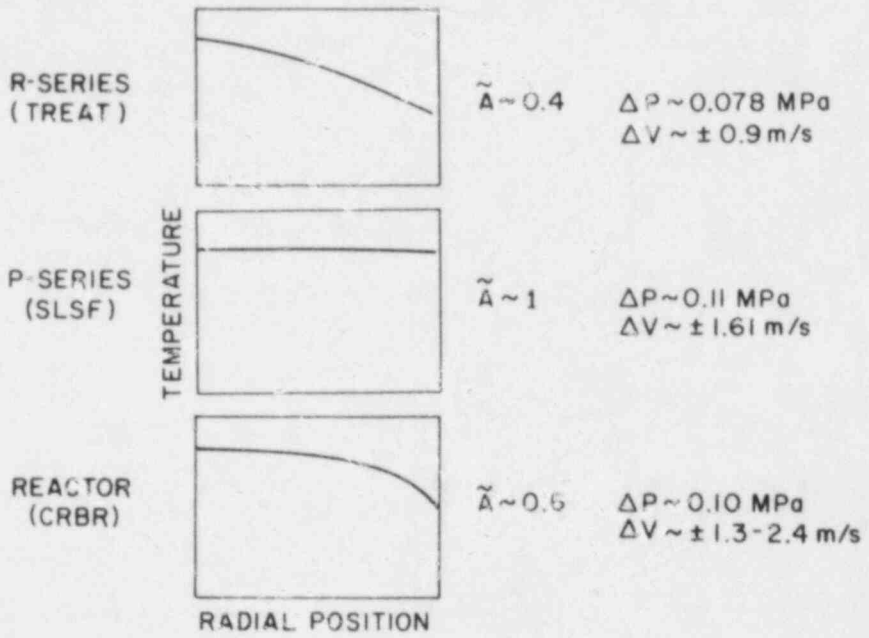

Fig. 6.
Comparison of in-pile test characteristics with those expected in typical CRBR S/As.

trajectory is possible. The R-series trajectory corresponds to marginal upward relocation ($J_g^* \sim 2.2 \times 0.7 \sim 1.54$) initially, and develops into clearly sloshing behavior along the indicated incoherency trajectory. Clearly, such marginal behavior could be easily reversed by the gas blowdown in R-8, as indeed the data show. The P-series tests, however, clearly meet the criteria for sustained upward relocation ($J_g^* \sim 2.5 \times 1.3 \sim 3.25$) as indeed occurred in the test. The estimated reactor trajectory also is shown. This process initially is characterized by $J_g^* \sim 1.7$, indicating a somewhat greater tendency for upward relocation than in the R-series. This tendency is maintained with time due to the sideways direction of the trajectory. Both the m-values and initial incoherency states indicate, however, that the P-series tests would greatly overestimate the upward cladding relocation and the extent of resulting blockage expected in the CRBR.

In addition, the effects of the plenum blowdown in redistributing the available pressure drop, and thus altering the m-value, need to be taken into account. The plenum fission gases are released near the top of the active core. Except for an initial small portion of the blowdown transient that is immaterial to cladding motion (since cladding melting follows cladding rupture typically by 0.6 s), this gas release cannot pressurize the coolant channel and reverse the pressure gradient. Rather it serves to concentrate the pressure gradient in the fission gas plenum and upper axial blanket regions in which it is flowing with a certain quantity of sodium vapor flow consistent with the overall pressure drop requirements. The effect is to reduce the

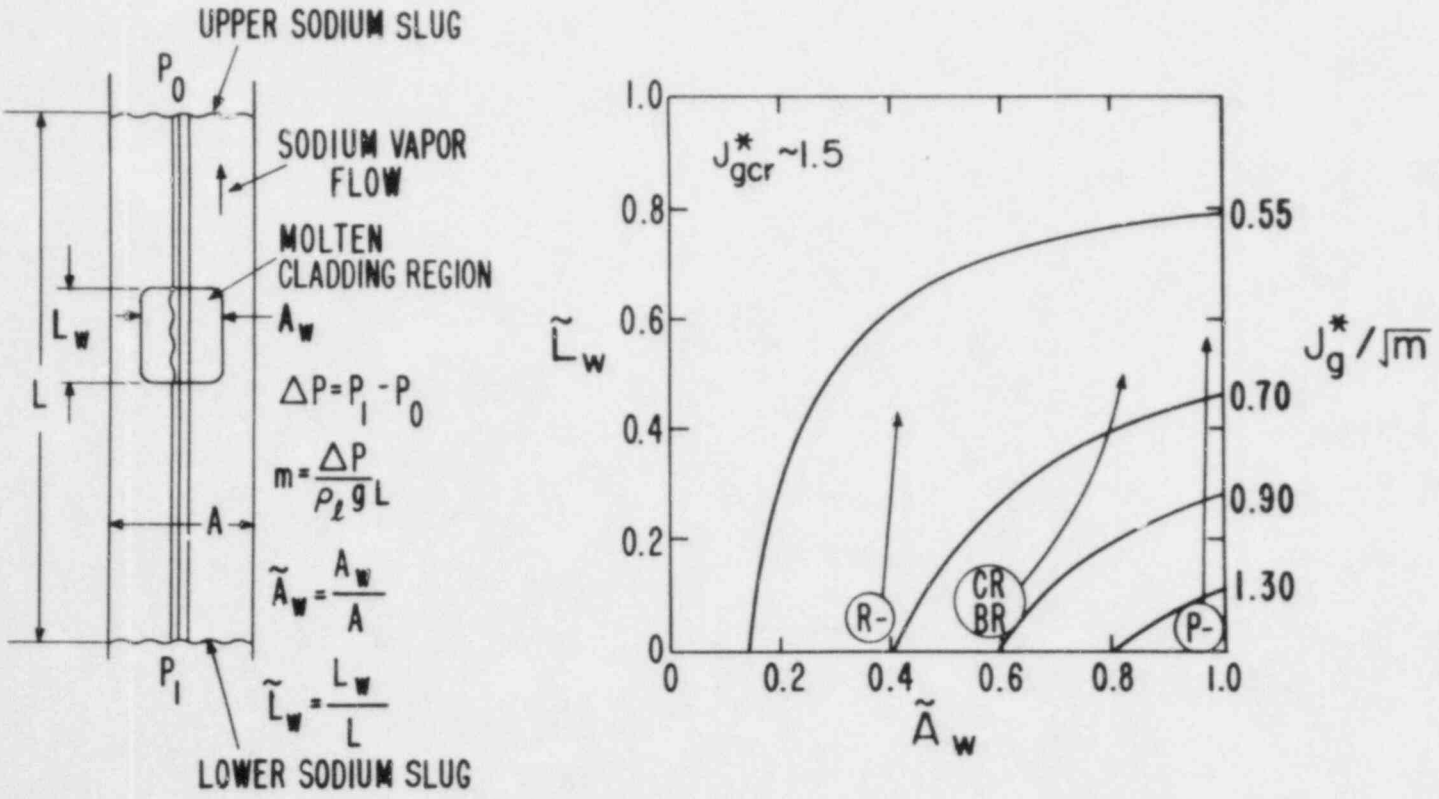

Fig. 7.
Cladding relocation trends for in-pile tests and for CRBR as melting of cladding progresses radially and axially.

sodium vapor flow or the effective m-value within the active core region as illustrated in Figure 8 and hence, to interfere with the cladding relocation process.

This pressure gradient redistribution process was modeled within the framework of the SAS3D code (see Section II.4). The effective m-values were calculated and used in conjunction with the flow regime maps to guide the SAS3D-calculated cladding relocation directions and rates. An example of the variation of the m-values calculated as a function of time (for the EOC-4 case) is shown in Figure 9. Following an initial rapid drop, the values of m increased as the plenum fission gases are depleted. For the example shown, at the time of cladding melting, we read $\sqrt{m} \sim 1.6$ from Figure 9, which, in combination with the beginning of the CRBR incoherency trajectory of Figure 7, yields $J_g^* \sim 1$. That is, a sloshing behavior is indicated with no net upward relocation. Therefore an absence of core exit blockages is predicted on the average. Furthermore, even for the "slow" cases, the power level will increase above nominal, thus reducing the time interval between cladding failure and cladding melting, and, with reference to Figure 9, even smaller values of $\sqrt{m}$ (and of J_g^*) will apply as these phenomena develop in subsequent groups of subassemblies (or SAS channels). Another effect of the increased power is to flatten the axial temperature distribution and thus promote axial cladding melting coherence (increase $\tilde{L}_w$). As may be seen from Figure 7, this effect will tend to further reduce the potential for upward relocation.

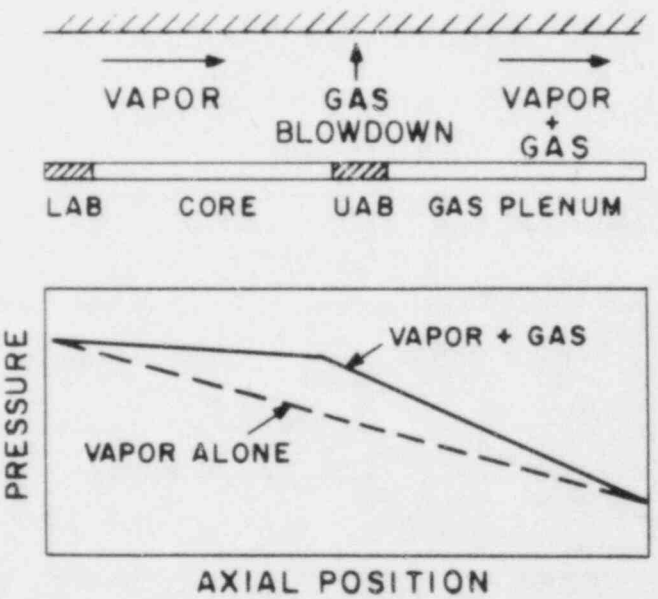

Fig. 8.
Effect of fission gas blowdown on the pressure gradients for cladding relocation.

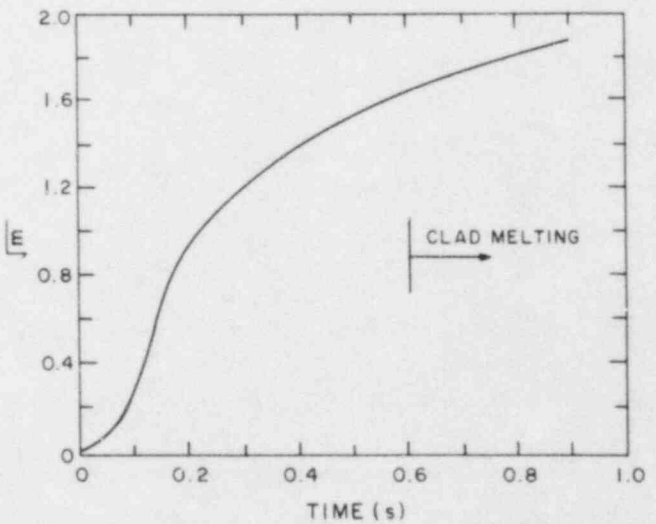

Fig. 9.
Effect of fission gas blowdown on the effective pressure gradient for caldding relocation during a SAS3D-calculated LOFA in CRBR.

A further pressure gradient redistribution effect that causes the decrease of the effective m-values develops during the formation of steel blockages in the upper axial blanket region. Consequenctly, well before complete blockages are formed, the J^*_g values decrease to the point where they cannot sustain continuing upward relocation.

Thus, on a best-estimate basis, we predict minimal net steel relocation and blockage formation during the initiating phase of core disruption. However, certain important qualifications need be mentioned: (a) the fission-gas plenum blowdown and its interference with cladding relocation are a function of the core burnup (the above estimates were given for conditions maximizing this interference and will reduce to zero for BOL conditions), (b) the radial cladding melting incoherence phenomena have not yet been adequately established (if these effects are neglected for the example case shown in Figure 9, a $J^*_g \sim 1.6 \times 1.3 \approx 2.1$ would result which is in the upward relocation regime), and (c) the effects of pressure pulsations due to liquid sodium "chugging" as it attempts unsuccessfully to re-enter the voided region were not taken into account in the above analyses.

To bound these uncertainties conservatively, we imposed moderate upward cladding relocation in all our SAS3D calculations. This was accomplished within the SAS3D framework as follows: (a) radial melting incoherencies were neglected, (b) a two-phase frictional multiplier of 12 was utilized, (c) the sodium vapor streaming was calculated on the basis of the quasistatic pressure differential across the core (neglecting the chugging effects) while taking into account the pressure drop redistribution from fission-gas plenum blowdown, and (d) relocation criteria consistent with the trends of Figure 4 were utilized. In this fashion upward cladding relocation velocities of ~ 0.70 m/s were obtained. These are considerably lower than the velocities predicted by the original SAS formulation (CLAZAS subroutine) but in view of the previous discussion still are adequately conservative with respect to the prediction of the extent of the core exit blockage.

4. Fuel Motion

Fuel disruption in voided subassemblies has been studied extensively over the past several years in the TREAT reactor. Experimental conditions have covered single and seven-pin bundles, normal and up to 20x nominal power, reduced and full-length fuel pins, and fresh and irradiated fuel. The neutron hodoscope was utilized to quantify the transient fuel motion. These measurements were augmented with temperature, pressure, and flow data to "reconstruct" the sequence of events in the experiments. More recently, the fundamentally oriented FD-series of experiments conducted in the ACRR facility at SNL produced direct visual information (high-speed movies) of the fuel disruption process under reasonably prototypic conditions.

Based on this cumulative experience, it is generally accepted now that the disruption of irradiated fuel under overpower conditions (from a few times nominal and up) is dispersive initially. The exact timing, rate, and extent of this dispersal process depend upon a number of complicated physical considerations and are subject to debate. These considerations include fission gas retention (within the fuel matrix) during steady-state irradiation, transient fission gas redistribution before fuel disruption, fission gas behavior subsequent to fuel disruption, fuel failure criteria, and mode of fuel disruption. They are crucial if the fuel dispersal process is viewed as a mechanism for the mitigation of highly overpowered, near prompt-critical conditions. This was the case, for example, in the Applicant's approach to the LOF-d-TOP concern for the previous CRBR homogeneous core application. The present heterogeneous core design substantially relaxes this concern and hence the need to base the safety case on such details. General and well-established trends will suffice in this case.

For fuel disruption at power levels of 5 to 10x nominal, typically expected for the CRBR conditions, the phenomenological SNL FD experiments provide some important insights.

(a) For the initial failures, at ~5x nominal power, experiment FD 2.6 showed that the disruption mode consisted of rapid liquid-state fuel swelling as fuel melting occurred. The expansion process was modeled quite well by assuming expansion of the gas in the liquid fuel to relieve the residual overpressure in the bubbles. The observed disruption in the radially unconstrained FD 2.6 geometry is more than sufficient to block the coolant channels. At that point, it is estimated that the trapped fission gas is still at high pressure (on the order of a few MPa). Therefore, strong fuel dispersal would be expected from gas trapped in the liquid fuel. Further, this mode of dispersal would be expected to dominate that from sodium vapor streaming in the coolant channels.

(b) For subsequent failures at higher power levels (5 to 10x nominal), especially in those channels where cladding motion occurs just before fuel disruption, the above described liquid fuel expansion is preceded by rapid radial dispersal of the outer, gas-bearing region of the fuel pin (experiments FD 4.3 and FD 2.8). It would appear that sodium vapor flow could provide some axial dispersal of this disrupted fuel. However, radial liquid-state swelling of the fuel blocks the coolant flow channel within 100 ms of the initial solid-state disruption. Thus, we can consider sodium-vapor flow-induced fuel dispersal during only the first 100 ms following initial disruption.

(c) There does not appear to be a fundamental change in the disruption mode at higher (9% vs. 4%) burnup. However, there is an enhanced likelihood of early, solid-state disruption of the outer gas-bearing fuel. At lower disruption powers, very nonenergetic disruption of the outer solid fuel was observed. Unlike the fine-scale (grain-size) solid-state disruption observed

at higher power levels, the lower-power disruption resulted in the ejection of large chunks of solid fuel into the coolant channel.

Fuel disruption in SAS3D analyses is calculated with the SLUMPY module. This is a parametric model and does not provide a fully mechanistic treatment of fuel disruption and dispersal. Thus, it has to be calibrated to reflect the general trends observed experimentally. The TREAT tests L6 and L7 were utilized for this purpose. The fuel-motion reactivity transients obtained with our final choice of parameters is compared with the experimental data and the results obtained by the Applicant (using a different set of parameters for each fit) in Figures 10 and 11.

Based on these comparisons we have made the following conclusions.

(a) Our fuel dispersal modeling (choice of parameters) may underestimate the early dispersal rates at high-power levels (L7) and may not yield the slight initial compaction effect observed at low-power levels (L6). The overall trends, however, are adequately depicted.

(b) The long-term fuel relative-worth increase depicted in our analytical results is the consequence of assuming fission gas de-entrainment and slumping of the previously dispersed fuel under gravity. This process cannot be evaluated on the basis of the L6 and L7 results.

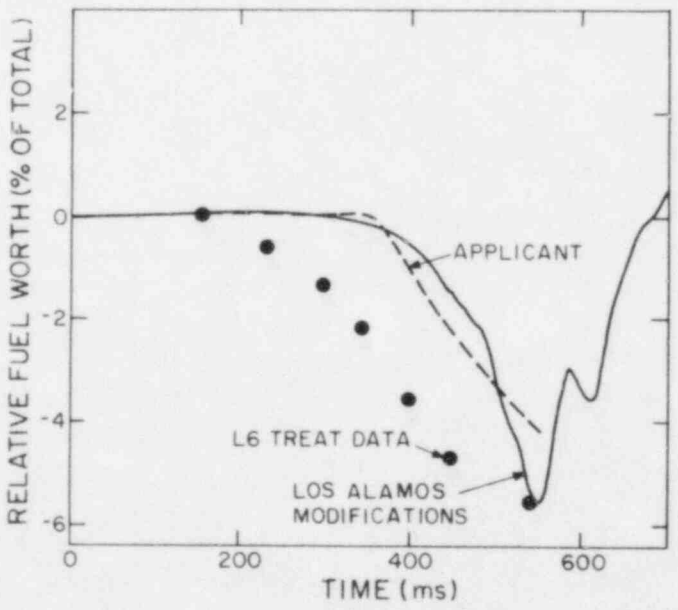

Fig. 10.
Comparison of fuel motion models (SAS3D/SLUMPY) with in-pile data (TREAT-L6).

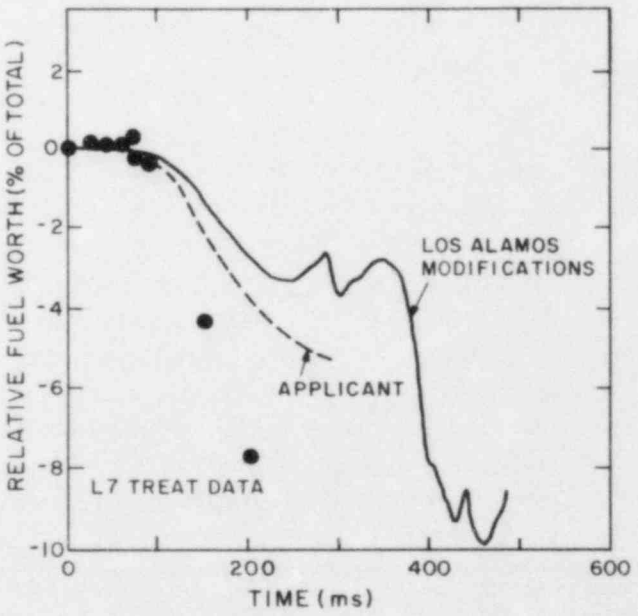

Fig. 11.
Comparison of fuel motion models (SAS3D/SLUMPY) with in-pile data (TREAT-L7).

5. Other Processes and Neutronic Feedbacks

We obtained from the Applicant the EOC-3 neutronic data and a re-evaluation of the sodium void reactivity and its uncertainty for the EOC-4 core configuration. Based on these data, we created reactivity-worth distributions, power distributions, and estimations of the Doppler feedback appropriate for SAS3D input from a fully independent set of calculations (our initial SAS3D calculations were conducted using the Applicant's input data). The calculational techniques, the results, and their contrast to those obtained by the Applicant are presented in Appendix A. It is in the nature of such elaborate calculations that some differences will be expected; however, because the initiating phase of the heterogeneous CRBR core is generally insensitive, no significant difference in overall accident evolution is noted (see Section 6).

Finally, the last significant neutronic feedback is due to axial thermal expansion of the fuel column. This feedback cannot be guaranteed because of possible cladding interference and, perhaps more importantly, because of the fuel expansion into existing voids (or gaps between the pellets). Therefore, it is common to treat this feedback parametrically. Typically, a 50% effectiveness (in reactivity feedback) of the expansion process is used as an arbitrary mid-range value. Limiting behaviors for "fast" and "slow" transients are explored by using effectiveness values of 0% and 100%, respectively. A similar parametric approach has been followed in our analyses.

6. Accident Analysis Aspects and Results

Our first effort was to delineate the boundary of the LOF-d-TOP regime. Several SAS3D calculations with deliberately fast scenario assumptions were conducted for this purpose. The combination of: (a) a sodium void worth at the upper 2 σ uncertainty limit of ~2 \$, (b) a 0% effective axial expansion, and (c) a near-neutral (nondispersive and noncompactive) fuel motion response, was found necessary to approach the LOF-d-TOP condition. Such a combination of parameters and physical processes is considered extremely unlikely, especially in view of the definitive experimental evidence that indicates a dispersive mode of fuel disruption at the high-power level developed during the approach to the LOF-d-TOP condition. Therefore, we conclude that LOF-d-TOP energetics in the heterogeneous CRBR core is physically unreasonable. In the remainder of this section we are concerned with establishing the nonenergetic aspects of the initiating phase, in particular the extent of core-exit cladding blockages, under more reasonable combinations of parameters. The only other energetics mechanism possible in the initiating phase is examined as a special problem in Section II.4.

The essential specifications for the three core configurations analyzed and the two parametric cases on the EOC-4 configuration are given in

Table 2. The main sequences of events are summarized in Figures 12 to 15 for the four cases, respectively. The reactivity and power histories and the mobile (molten) cladding and fuel patterns at the time of development of an overpower condition sufficient to produce fuel and steel vapor pressures are shown in Figures 16 to 19. The details of the accident sequences are given in Appendix B. Here, some of the main trends are identified.

All cases indicate substantial neutronic activity. The associated power transients reduce the time interval between cladding melting and fuel disruption, thus minimizing the extent of fuel/steel separation and core-exit blockage formation. This process is called "codisruption," and it is schematically illustrated in Figure 20. It is important in enhancing the termination potential by dispersal because of (a) greater axial path availability, (b) remeltable blockages, and (c) higher vapor (steel) pressures driving the dispersal process. Thus, even with pessimistic cladding relocation assumptions, codisruption is effective in limiting the duration of such relocation processes and hence a substantial fraction of the core exit paths remain unblocked.

The other general characteristic is that the advanced core-disruption states are approached in all four cases with (a) the absence of liquid sodium in the active core region; (b) a major fraction of cladding and fuel in the molten and intermixed state; and (c) considerable neutronic activity dominated by gravity-driven, oscillatory, fuel motions that lead to power bursts of 10x to 10^3x nominal power at the end of these calculations. Thus, the entry into the S/A-scale pool phase is clearly identified.

7. Summary

The occurrence of the LOF-d-TOP in the CRBR heterogeneous core is shown to be physically unreasonable (for a special qualification of this conclusion see Section II.4). In the absence of initiating-phase energetics, we have attempted to quantify the range of behavior concerning core-exit, cladding, blockage formation, and the core's characteristics at the entry to the S/A-scale pool phase. These results are pursued in Sections II.6 and II.5, respectively.

TABLE 2
SAS3D INPUT SELECTIONS

Parameter	Mid-Range EOC-4	Slow EOC-4	EOC-3	BOC-1
Doppler coefficient	As calculated in Appendix A	Adjusted to be 20% above WARD	As calculated in Appendix A	From GEFR-00523
Sodium void coefficient	As calculated in Appendix A	Adjusted to get $1.46 in driver S/As	As calculated in Appendix A	From GEFR-00523
Fraction of steady state fission gas available	0.51	1.05	1.05	1.05
Fraction of gas available instantaneously upon fuel motion	0.1176	0.1429	0.1429	0.1429
Fuel particle (drop) diameter	0.0002 m	-	-	-
Viscosity parameter	1000	10000	10000	10000
Extra upper segment acceleration	0	7.84 m/s^2	7.84 m/s^2	7.84 m/s^2
Axial expansion effective for reactivity feedback	50%	100%	50%	80%
Default for lower blockage	0.35 m	0.30 m	0.30 m	0.25 m
Default for upper blockage	1.30 m	1.40 m	1.40 m	1.30 m
Steel to fuel mass ratio in SLUMPY where cladding moves before fuel	0	0.001	0.001	0.001

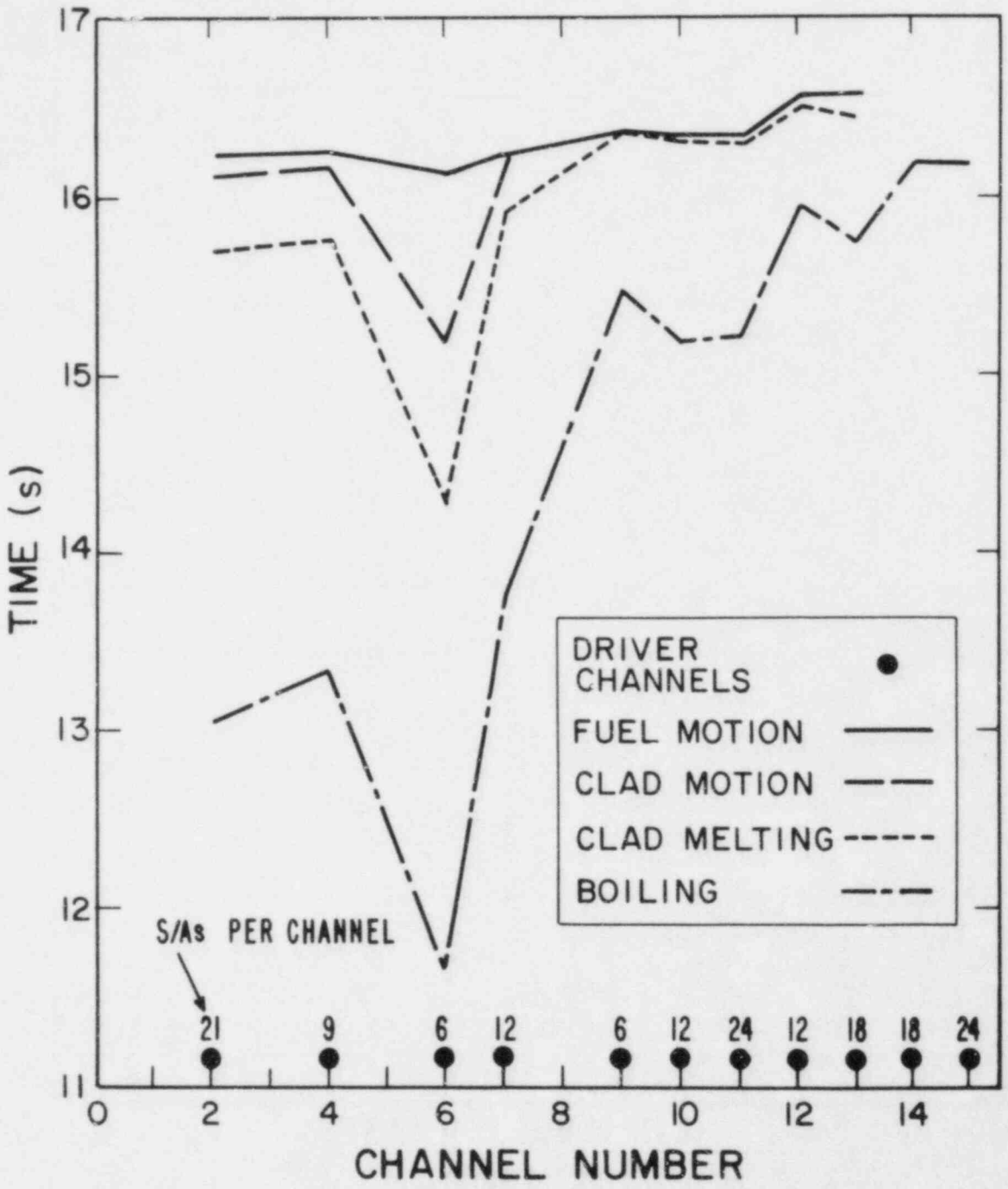

Fig. 12.
Core-wide voiding and disruption sequence for the mid-range EOC-4 LOFA.

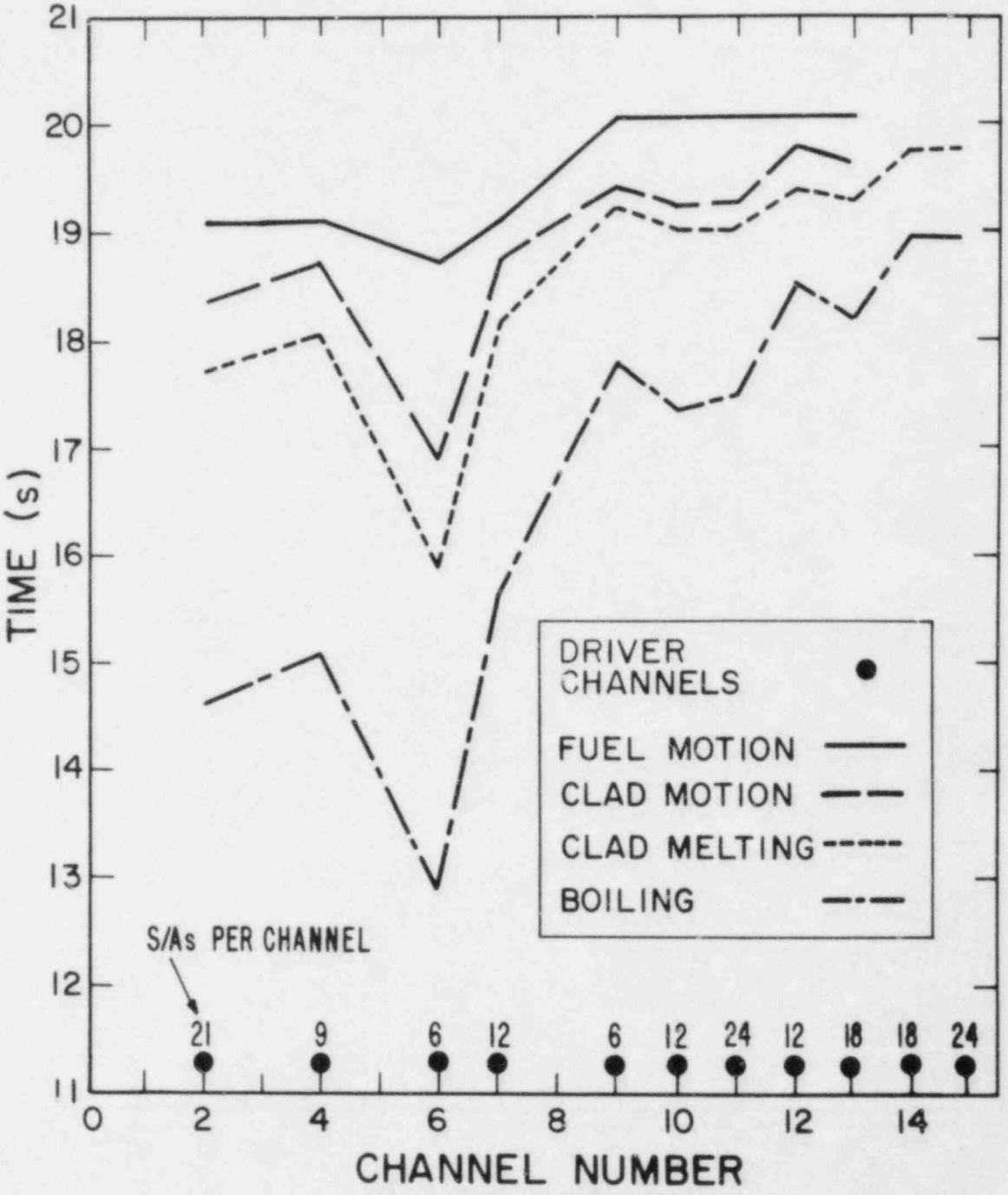

Fig. 13.
Core-wide voiding and disruption sequence for the slow EOC-4 LOFA.

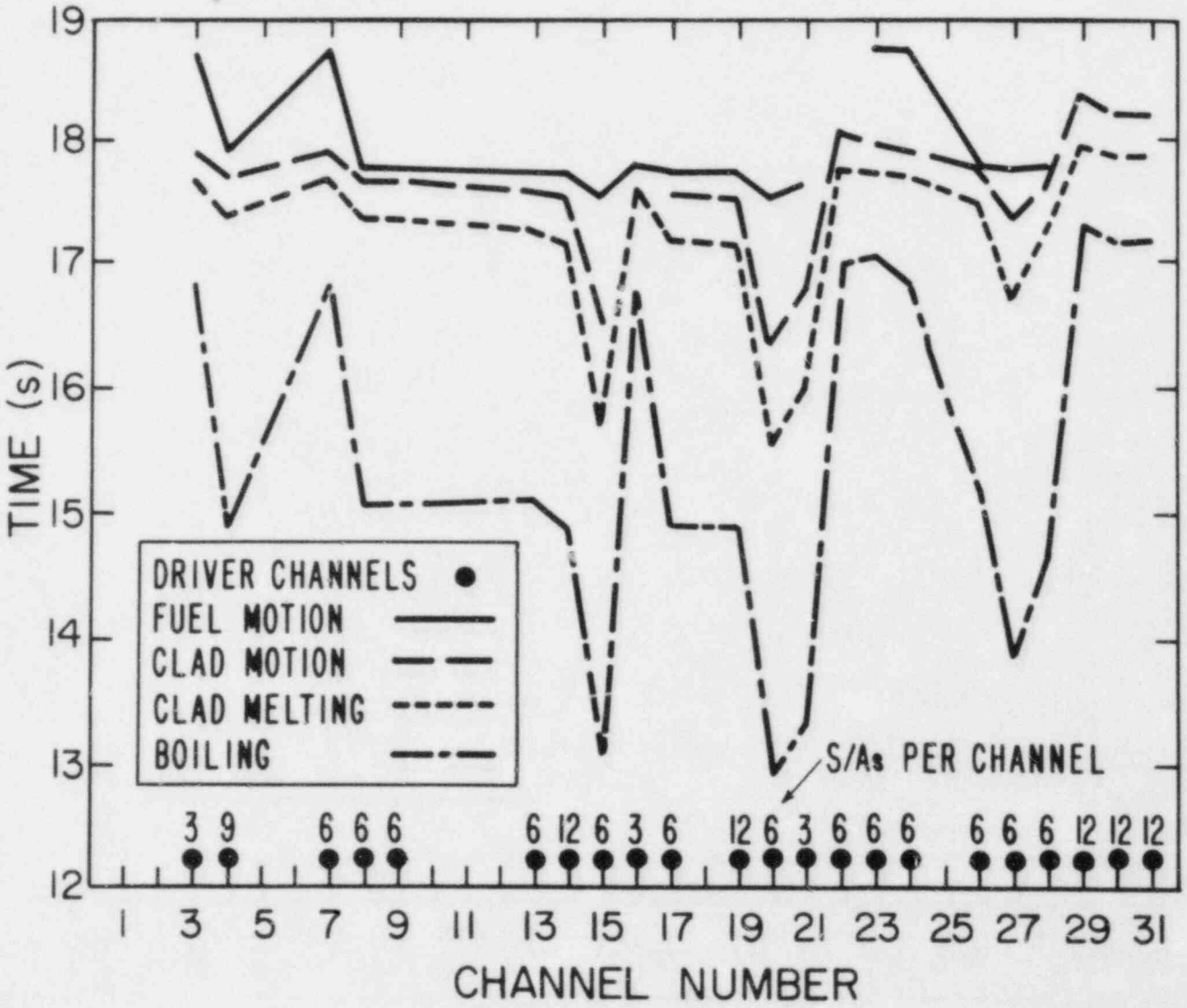

Fig. 14.
Core-wide voiding and disruption sequence for the EOC-3 LOFA.

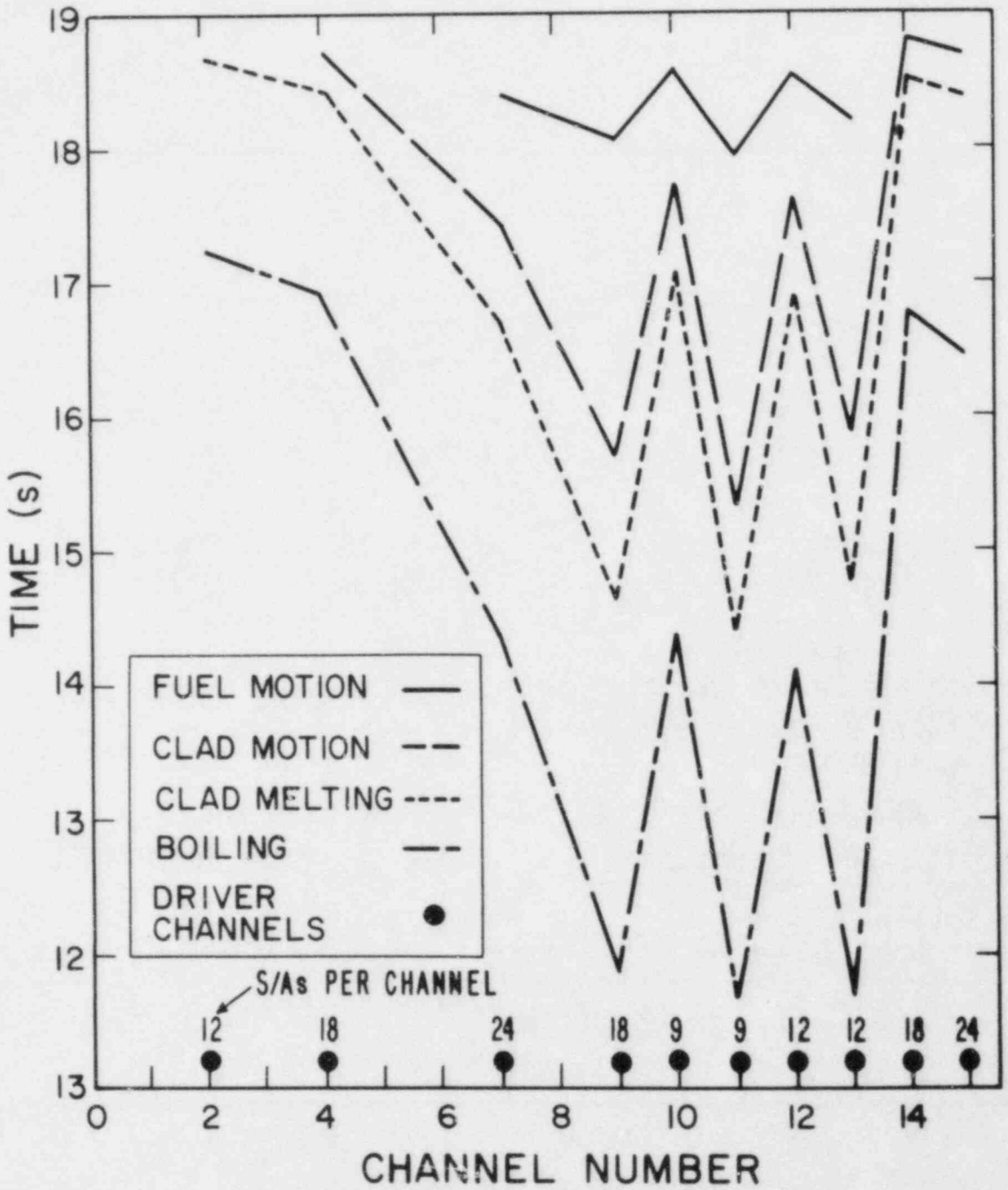

Fig. 15.
Core-wide voiding and disruption sequence for the BOC-1 LOFA.

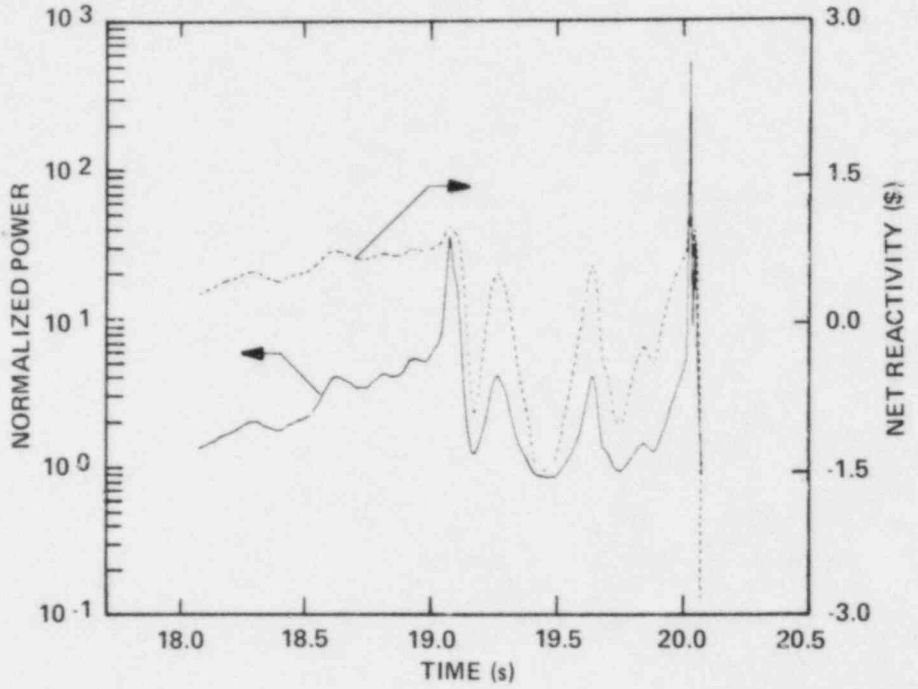

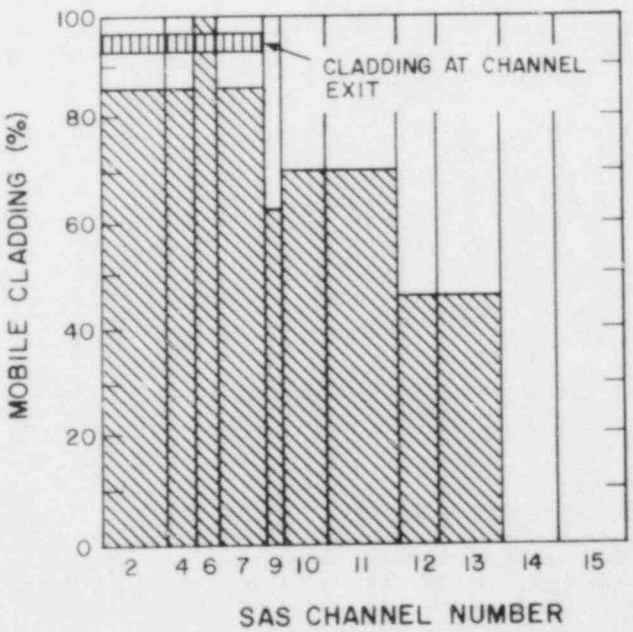

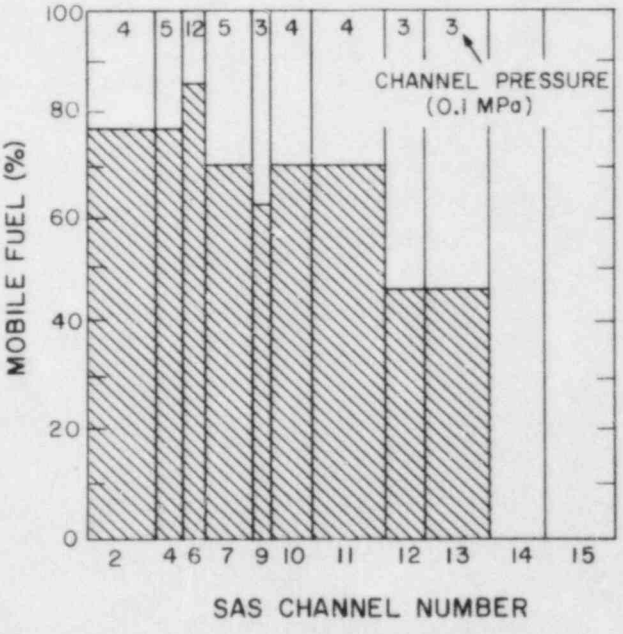

Fig. 16.
Summary results for the mid-range EOC-4 LOFA.

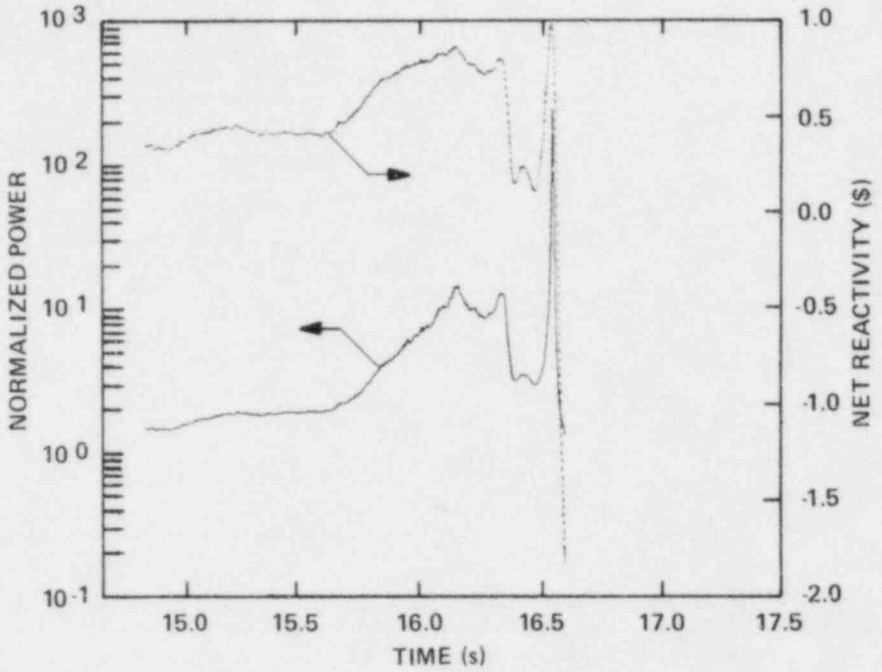

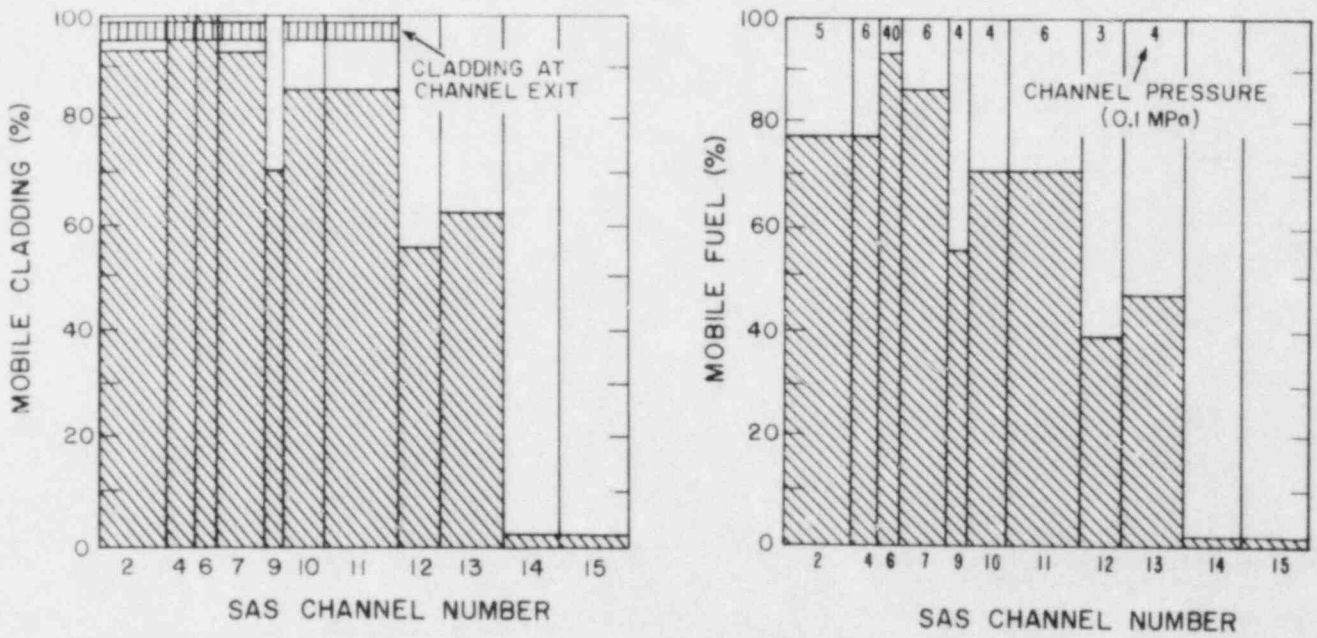

Fig. 17.
Summary results for the slow EOC-4 LOFA.

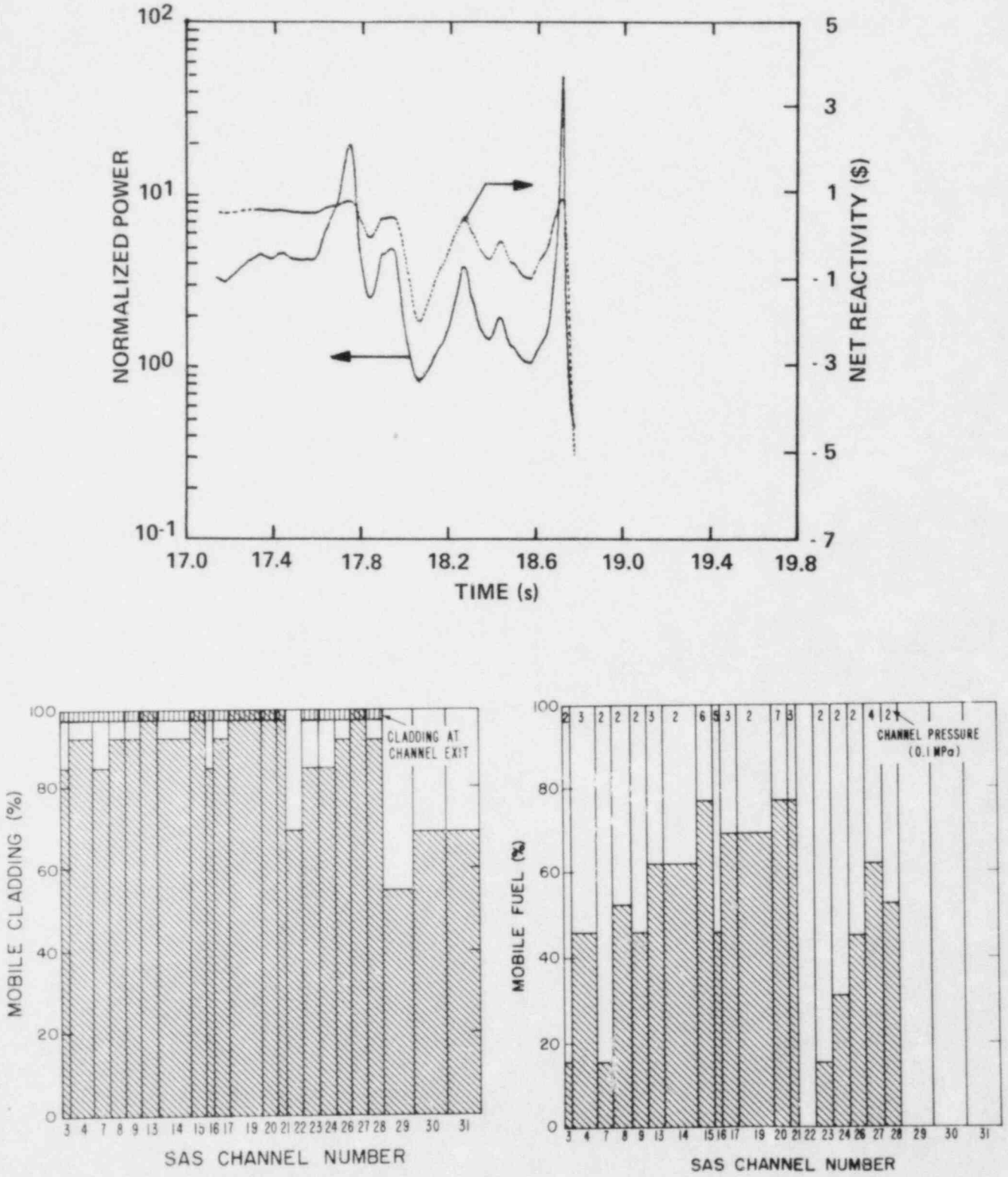

Fig. 18.
Summary results for the EOC-3 LOFA.

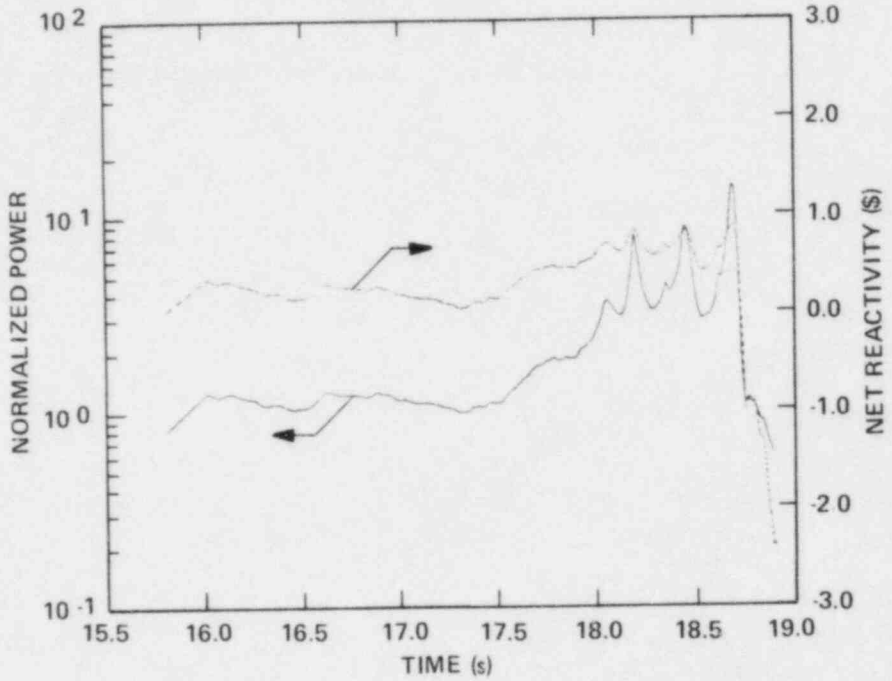

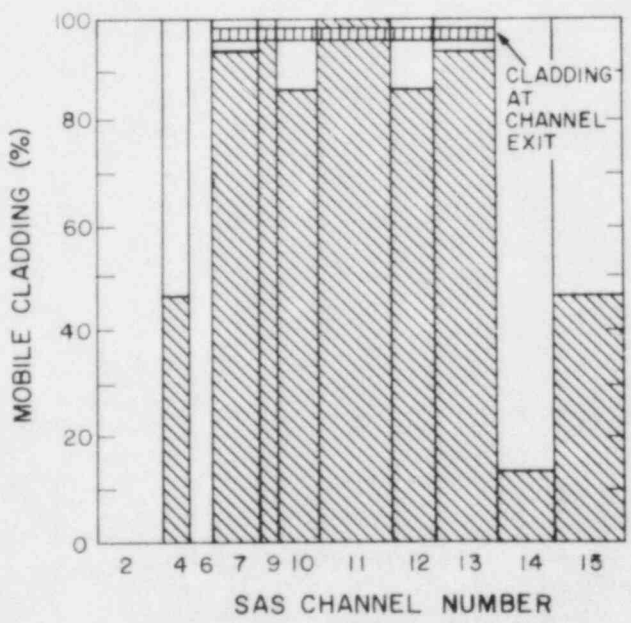

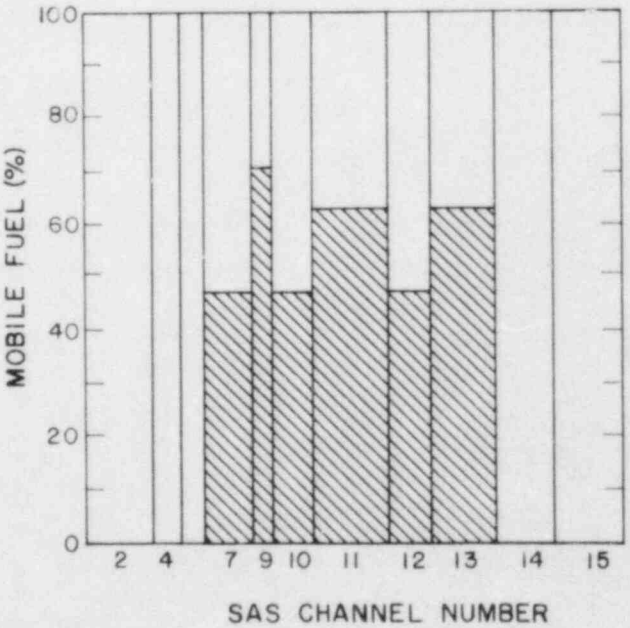

Fig. 19.
Summary results for the BOC-1 LOFA.

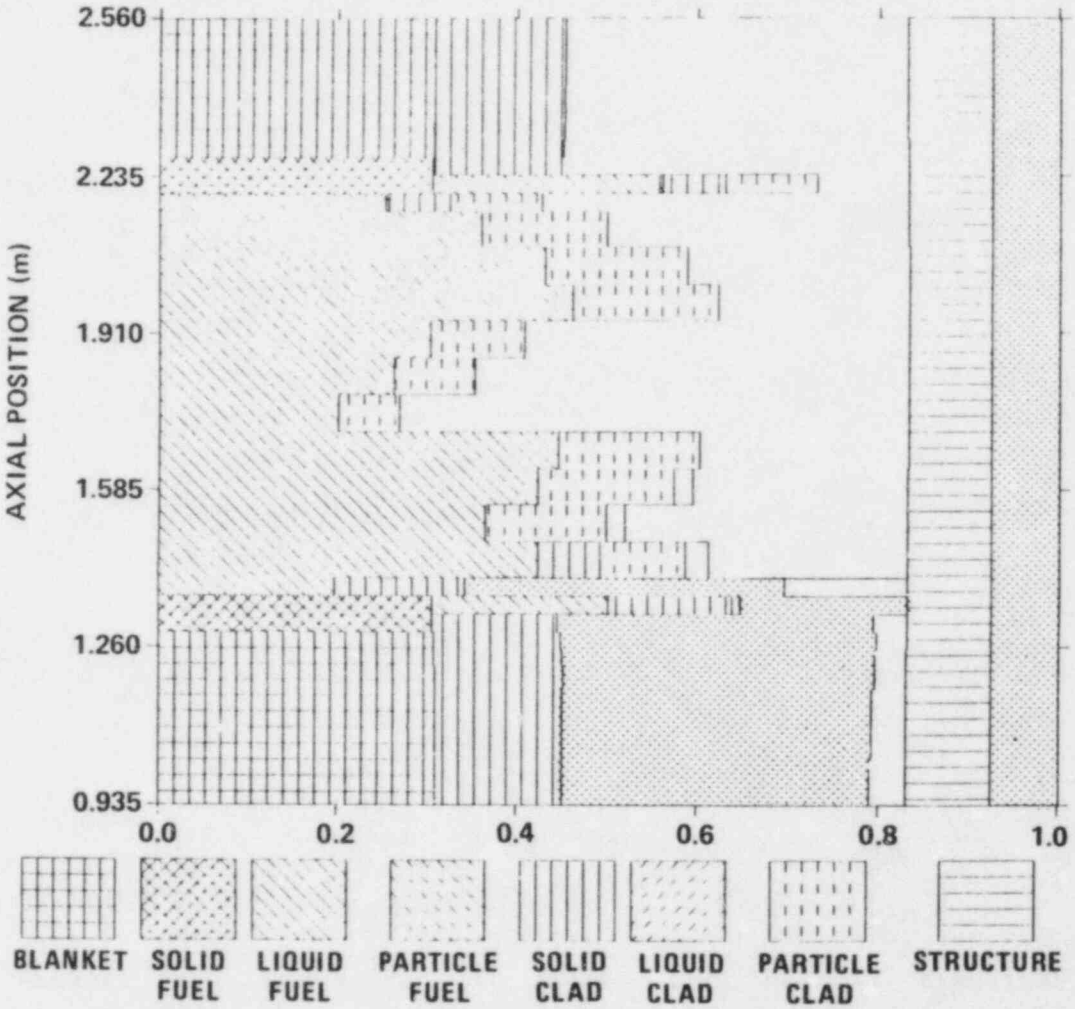

Fig. 20.
Illustration of a typical co-disruption situation (material volume fraction vs. axial position).

8. References

1. T. F. Meyer, L. Lois, J. L. Carter, and T. P. Speis, "An Analysis and Evaluation of the Clinch River Breeder Reactor Core Disruptive Accident Energetics," Nuclear Regulatory Commission report NUREG-0122 (March 1977).

2. T. G. Theofanous, "Multiphase Transients with Coolant and Core Materials in LMFBR Core Disruptive Accident Energetics Evaluations," Purdue University report NUREG/CR-0224 (July 1978).

3. S. K. Rhow, D. M. Switick, J. L. McElroy, and B. W. Joe, "An Assessment of HCDA Energetics in the CRBR Heterogeneous Reactor Core," General Electric Company report CRBRP-GEFR-00523 (December 1981).

4. "Compendium to NUREG/CR-3224, An Assessment of CRBR Core Disruption Accident Energetics," Section 6, Nuclear Regulatory Commission document (March 1983).

5. "Compendium to NUREG/CR-3224, An Assessment of CRBR Core Disruption Accident Energetics," Section 5, Nuclear Regulatory Commission document (March 1983).

6. "Compendium to NUREG/CR-3224, An Assessment of CRBR Core Disruption Accident Energetics," Section 7, Nuclear Regulatory Commission document (March 1983).

7.[a] T. J. Scale, B. W. Spencer, J. J. Santori, W. C. Jeans, and R. L. McDaniel, "Preliminary Data Report for OPERA 15-pin Experiment," Argonne National Laboratory report ANL/RAS 82-33 (October 1982).

8.[a] R. Avery, Cover Letter to Argonne National Laboratory report ANL/RAS 81-32, "Pretest Information Package for OPERA 15-pin Experiment" (December 15, 1981).

9. C. Miao and T. G. Theofanous, "Fast ICE Solution Procedure for Flows with Largely Invariant Compressibility," J. of Computational Physics 40, 254 (1981).

10. C. Miao and T. G. Theofanous, "Pretest Prediction of the OPERA 15-pin Experiment using HEV2D," Purdue University letter to B. Spencer, Argonne National Laboratory (March 27, 1982), (available at Purdue University).

11. P. W. Spencer, Argonne National Laboratory, Personal Communication to T. G. Theofanous (February 1983).

[a] Address requests for this document to F. X. Gavigan, Director, Office of Breeder Demonstration Projects (NE-50), U.S. Department of Energy, Washington, DC 20545, Telephone (301) 353-3134.

APPENDIX A

NEUTRONIC CHARACTERISTICS

1. Introduction

In the LOFA, sodium voiding provides an early positive feedback mechanism. The impact of the effect depends on the coherence of the sodium voiding and the magnitude of the sodium void reactivity. The positive reactivity effect is mitigated by the negative reactivity effects of Doppler and axial expansion.

The sodium-void reactivity effect is produced by the two large, competing components of leakage and nonleakage. The nonleakage component results from changes in the distribution of flux with energy (spectrum) caused by changes in macroscopic scattering cross sections as sodium is removed, and to a lesser extent by changes in neutron capture. The leakage component results directly from changes in the macroscopic scattering cross section with the removal of sodium. The nonleakage component is largest in the central portion of the core where both the real and adjoint fluxes are large. The leakage component is largest near the core-blanket interfaces where the real and adjoint flux gradients are large. Because of these characteristics, calculated sodium void reactivities are sensitive to calculational methods, to nuclear cross-section data, and to core composition. For example, typical results [1] for nonleakage component-dominated regions can vary 20% for calculations based on ENDF/III versus ENDF/IV cross-section data [2]. Results [1] for high-leakage component regions may differ as much as 30% when neutron transport corrections are included. Because the sodium void reactivity is highly dependent on the burn-up state of the reactor, the effect of uncertainties in the predicted isotopic compositions should be included along with other data and methods uncertainties.

The Doppler effect provides a negative reactivity feedback mechanism as temperature increases in fertile fuel. The effective Doppler feedback in a heterogeneous-core reactor is relatively small because the fertile material is concentrated in the blanket regions and does not heat as rapidly in a transient as the driver regions (lower specific power). The Doppler reactivity effect is important in the initiating phase, however, because it is a prompt effect, that is, there is no time delay due to heat transfer.

The Doppler effect is produced by the effective broadening of fission and capture resonances by the thermal motion of fertile isotopes. The

varying competition among fission, capture, and leakage reactions produces the effect as the fuel temperature changes. Because the affected resonances are mostly below 25 kev in energy, where the spectrum rapidly falls off in a typical LMFBR, the predicted Doppler effect is sensitive to the shape of the calculated spectrum.

Uncertainties in the predicted Doppler reactivities result from both data and method uncertainties. The effects of typical data uncertainties are smaller than for the sodium void effect because the partial cancellation of competing effects is not involved; however, experimental verification is less extensive. Method uncertainties involve the use of the calculated Doppler coefficients as well as their prediction. For example, because the Doppler effect is characterized as a "1/T" law for SAS3D, while theory predicts a mixture of $T^{-1/2}$ and $T^{-3/2}$ behavior, a temperature dependent bias is introduced. Exponents of -1.1 to -1.2 were calculated [3] for the homogeneous-core design of CRBR. As a second example, the Doppler effect will typically decrease 40% upon sodium voiding. This is treated as a local effect in SAS3D; that is, the Doppler reactivity for a given cell depends only upon the amount of sodium in that cell; however, the cell spectrum and thus the Doppler effect definitely are affected by the sodium in adjacent cells. This effect is expected to be larger in the heterogeneous-core reactors.

In the following section, our independently calculated results for sodium void reactivity, Doppler constant, and reactor power distribution are reported for the EOC-4 and EOC-3 cores of the CRBR. The EOC-4 results are compared with the values used in the GE accident analysis [4]. An evaluation of the differences is provided and sources of uncertainty are identified and evaluated.

2. Calculational Approach

The initiating-phase analysis [4] supplied for our review was developed by GE and was based on calculations performed with the SAS3D code [5]. Input to this code consists of basic geometry and thermal-hydraulics data defined by the CRBR design, parameters that control various phenomenological modeling assumptions, and parameters that describe the reactor's neutronic characteristics.

The SAS3D code can be used with neutronics parameters, such as reactivity worth distributions, input separately. This option was used by GE, based on neutronic parameters supplied by the Westinghouse Advanced Reactor Division (WARD). Alternatively, basic neutronics data, such as atom densities, can be supplied to SAS3D, which will then determine the required neutronics parameters by using the neutronics code, DIF3DS [6], as part of its initialization procedure. The later option was used for this work. WARD calculated the atom densities by synthesizing the results of Hex-Planar and R-Z burn-up calculations.

For the EOC-4 configuration, atom densities [7] were supplied to us for 997 core and blanket zones. WARD assumed one-third core symmetry with each subassembly divided into three separate axial regions in the core and two each in the axial blankets. Thermal-hydraulic data for modeling the reactor with 15 SAS3D channels, in which all data are averaged over all subassemblies comprising each channel, were supplied by GE. These data are used by the SAS3D models to define the reactor steady-state configuration and temperature. The following calculational steps were performed based on these data:

1. WARD atom densities were averaged for each channel and axial region and modified for input to SAS3D.

2. Los Alamos nuclear cross sections were collapsed and shielded.

3. The SAS3D steady-state calculation was performed without the fuel categorization option, thus avoiding the iteration between the SAS3D thermal expansion calculation and DIF3DS power distribution calculation.

4. Neutronics parameters required for SAS3D transient calculations were determined by DIF3DS perturbation calculations.

The WARD-supplied atom densities were averaged over groups of subassemblies representing the 15 channels defined in the GE SAS3D representation and two additional channels not present in the GE setup to represent the radial blanket. This approach resulted in considerable homogenization of spatial detail, that is, the 997 zones were condensed into 88 SAS3D regions.

The reference cross-section data [8] were the LIB-IV 50-group set of infinitely dilute cross sections and shielding factors. Shielded isotopic cross sections were separately calculated for each SAS3D region to account for background and temperature effects. The required background interpolation of shielding factors was performed by a multifunction cross-section code, XSPROC, which was recently developed to facilitate these types of calculations. Cross-section sets were constructed for each isotope over a range of temperatures; DIF3DS then performed the final temperature interpolations for each meshpoint. For calculating background cross sections, the 88 regions were further condensed to 15 regions. The 50-group set was collapsed to 18 groups by XSPROC based on a single weighting spectrum determined by performing a one-dimensional transport calculation in radial geometry using ONEDANT [9] and averaging the resulting fluxes over all space points.

The calculational approach used for the EOC-3 configuration was identical for that of the EOC-4 configuration as described above. The procedure used by WARD to determine atom densities also was identical; they synthesized the results of Hex-planar and R-Z burnup calculations. However, the SAS3D

data were set up for a 33-channel case to avoid averaging the azimuthal asymmetry in coolant flow rates. Atom densities were averaged over groups of subassemblies representing the 33 channels; the 997 WARD-defined zones were condensed onto 98 SAS3D regions.

3. Calculated Results

All neutronics parameters needed for the SAS3D initiating-phase calculation were generated for the EOC-3 and EOC-4 configurations of CRBR. Results for the EOC-4 case are summarized for the channel scheme used by GE in its transient SAS3D calculations. The subassembly-to-channel layout is shown in Figure 1. The reactivity changes resulting from the voiding of flowing sodium and the addition of cladding and fuel to each channel are shown in Table 1, along with the coolant-in and flowing-coolant-out Doppler constants. The power distribution and derivative quantities are shown in Table 2.

Because the uncertainty involved in performing burn-up calculations has not been addressed elsewhere up to this time, the magnitude of potential effects was estimated by two supplementary calculations. Isotopic composition uncertainties were not estimated a priori, but the impact of an assumed 10% uncertainty in the amount of bred plutonium was determined by varying arbitrarily the plutonium content of the internal blanket (with the total actinide content held constant). The impact of these variations upon the reactor power distribution is shown in Table 3, where a 10% increase in internal blanket Plutonium is assumed, and Table 4, where a 10% decrease is assumed.

The subassembly-to-channel layout used for the EOC-3 calculations is shown in Figure 2. The reactivity changes resulting from the voiding of flowing sodium and the addition of cladding and fuel to each channel are shown in Table 5, along with the coolant-in and flowing-coolant-out Doppler constants. The power distribution and derivative quantities are shown in Table 6.

4. Comparison with WARD/GE Results - EOC-4

The values for the power distribution and the reactivity changes supplied by WARD and used by GE for the transient SAS3D calculations are shown in Tables 7 and 8. These values were calculated with a three-dimensional first-order-perturbation calculation based on diffusion theory and using ENDF/III cross-section data.

A comparison of Tables 2 and 8 shows that our radial power distribution agrees well with the WARD values. The two main differences in our results

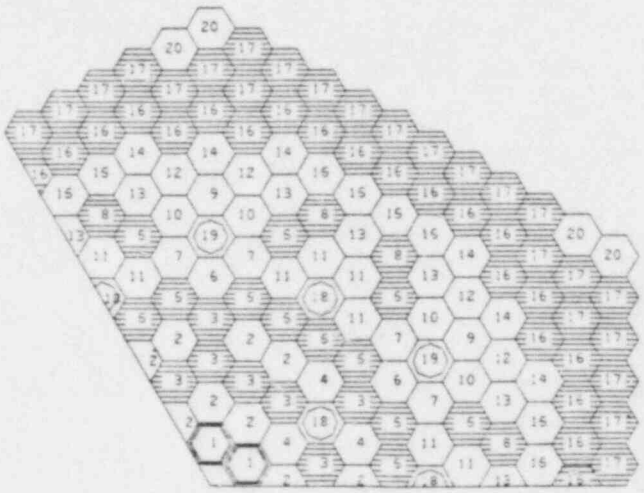

Fig. 1.
Subassembly assignments to SAS3D channels for the EOC-4 analysis.

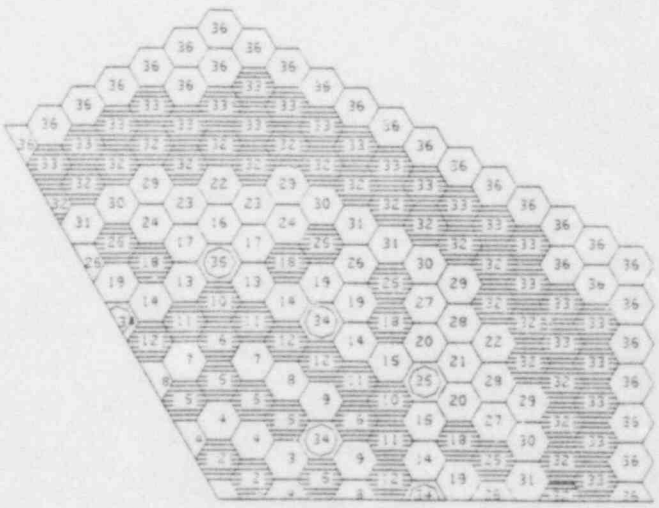

Fig. 2.
Subassembly assignments to SAS3D channels for the EOC-3 analysis.

TABLE 1
SAS3D CHANNEL CHARACTERISTICS at EOC-4

Doppler constants are multiplied by -10000.
Reactivities are in dollars, based on beta = 0.003311

Channel number	Channel type	Number of S/As	Coolant react.[b]	Clad react.	Fuel react.	Sodium-in Doppler	Sodium-out Doppler
1	blkt	7	0.13	-0.22	-1.11	3.06	2.72
2	driv	21	0.53	-1.27	18.71	2.73	2.13
3	blkt	21	0.42	-0.76	-3.62	10.68	9.05
4	driv	9	0.22	-0.53	7.92	1.26	1.00
5	blkt	36	0.69	-1.26	-5.31	17.62	14.03
6	driv	6	0.12	-0.34	6.65	0.90	0.65
7	driv	12	0.24	-0.66	11.26	1.71	1.22
8	blkt	12	0.15	-0.29	-1.23	4.15	3.16
9	driv	6	0.05	-0.21	4.85	0.71	0.48
10	driv	12	0.18	-0.54	10.26	1.52	1.05
11	driv	24	0.51	-1.30	20.44	3.23	2.35
12	driv	12	-0.01	-0.19	8.25	1.06	0.72
13	driv	18	0.18	-0.59	12.55	1.70	1.17
14	driv	18	-0.20	0.11	9.58	1.10	0.78
15	driv	24	-0.07	-0.17	12.32	1.53	1.09
16[a]	blkt	60	-0.28	0.32	3.92	6.72	5.55
17[a]	blkt	72	-0.14	0.18	1.47	2.34	2.15

total driver coolant reactivity	1.75
total driver clad reactivity	-5.70
total driver fuel reactivity	122.80
total internal blanket coolant reactivity	1.38
total internal blanket clad reactivity	-2.52
total internal blanket fuel reactivity	-11.27
total driver Doppler constant (no voiding)	17.46
total driver Doppler constant (Na voided)	12.64
total internal blanket Doppler constant (no voiding)	35.51
total internal blanket Doppler constant (Na voided)	28.96

[a] Channels 16 and 17 represent the radial blanket in the Los Alamos calculation. Channel 16 consists of blanket subassemblies adjacent driver subassemblies and Channel 17 consists of the remaining blanket subassemblies.

[b] Reactivity

TABLE 2
SAS3D CHANNEL CHARACTERISTICS at EOC-4

Channel number	Channel type	Number of S/As	Norm.[b] S/A power	Mass flux (kg/m²-s)	Average rod pow[c] (kW)	S/A pow/flow (J/g)	Norm. S/A pow/flow
1	blkt	7	0.56	3817	34.23	214.3	1.04
2	driv	21	1.32	4935	22.60	229.1	1.11
3	blkt	21	0.62	4345	37.95	208.7	1.01
4	driv	9	1.33	5056	22.67	224.3	1.09
5	blkt	36	0.64	4345	38.94	214.2	1.04
6	driv	6	1.48	5147	25.30	245.9	1.19
7	driv	12	1.34	5244	22.93	218.7	1.06
8	blkt	12	0.54	3817	32.85	205.6	1.00
9	driv	6	1.22	5244	20.92	199.5	0.97
10	driv	12	1.27	5244	21.69	206.9	1.00
11	driv	24	1.29	5433	22.08	203.3	0.98
12	driv	12	1.10	4914	18.78	191.2	0.93
13	driv	18	1.14	4962	19.44	196.0	0.95
14	driv	18	0.93	4312	15.92	184.6	0.89
15	driv	24	0.95	4331	16.17	186.8	0.90
16[a]	blkt	60	0.28	2578	17.18	159.3	0.77
17[a]	blkt	72	0.11	1445	6.71	111.0	0.54

[a] Channels 16 and 17 represent the radial blanket in the Los Alamos calculation. Channel 16 consists of blanket subassemblies adjacent driver subassemblies and Channel 17 consists of the remaining blanket subassemblies.

[b] Normalized

[c] Power

TABLE 3
SAS3D CHANNEL CHARACTERISTICS at EOC-4
(Increased Inner Blanket Plutonium)

Channel number	Channel type	Number of subs	Norm.[b] S/A power	Mass flux (kg/m^2-s)	Average[c] rod pow (kW)	S/A pow/flow (J/g)	Norm. sub pow/flow
1	blkt	7	0.61	3817	37.12	232.4	1.11
2	driv	21	1.34	4935	22.96	232.8	1.11
3	blkt	21	0.67	4345	40.63	223.4	1.07
4	driv	9	1.34	5056	22.94	227.0	1.09
5	blkt	36	0.67	4345	40.97	225.3	1.08
6	driv	6	1.47	5147	25.17	244.6	1.17
7	driv	12	1.32	5244	22.70	216.6	1.04
8	blkt	12	0.56	3817	33.96	212.6	1.02
9	driv	6	1.19	5244	20.47	195.2	0.93
10	driv	12	1.24	5244	21.30	203.2	0.97
11	driv	24	1.28	5433	21.89	201.6	0.96
12	driv	12	1.07	4914	18.32	186.5	0.89
13	driv	18	1.11	4962	19.06	192.2	0.92
14	driv	18	0.90	4312	15.50	179.8	0.86
15	driv	24	0.92	4331	15.81	182.6	0.87
16[a]	blkt	60	0.27	2578	16.71	154.8	0.74
17[a]	blkt	72	0.11	1445	6.51	107.7	0.52

[a] Channels 16 and 17 represent the radial blanket in the Los Alamos calculation. Channel 16 consists of blanket subassemblies adjacent driver subassemblies and Channel 17 consists of the remaining blanket subassemblies.

[b] Normalized

[c] Power

TABLE 4
SAS3D CHANNEL CHARACTERISTICS at EOC-4
(Decreased Inner Blanket Plutonium)

Channel number	Channel type	Number of S/As	Norm.[b] S/A power	Mass flux (kg/m²-s)	Average rod pow[c] (kW)	S/A pow/flow (J/g)	Norm. S/A pow/flow
1	blkt	7	0.52	3817	31.41	196.6	0.96
2	driv	21	1.30	4935	22.23	225.3	1.10
3	blkt	21	0.58	4345	35.29	194.1	0.95
4	driv	9	1.31	5056	22.38	221.4	1.08
5	blkt	36	0.61	4345	36.88	202.8	0.99
6	driv	6	1.49	5147	25.43	247.2	1.21
7	driv	12	1.36	5244	23.16	220.9	1.08
8	blkt	12	0.52	3817	31.68	198.3	0.97
9	driv	6	1.25	5244	21.37	203.9	1.00
10	driv	12	1.30	5244	22.08	210.6	1.03
11	driv	24	1.31	5433	22.25	204.9	1.00
12	driv	12	1.13	4914	19.25	195.9	0.96
13	driv	18	1.16	4962	19.82	199.8	0.98
14	driv	18	0.96	4312	16.34	189.6	0.93
15	driv	24	0.97	4331	16.54	191.0	0.94
16[a]	blkt	60	0.29	2578	17.67	163.8	0.80
17[a]	blkt	72	0.11	1445	6.91	114.3	0.56

[a] Channels 16 and 17 represent the radial blanket in the Los Alamos calculation. Channel 16 consists of blanket subassemblies adjacent driver subassemblies and Channel 17 consists of the remaining blanket subassemblies.

[b] Normalized

[c] Power

TABLE 5
SAS3D CHANNEL CHARACTERISTICS at EOC-3

Doppler constants are multiplied by -10000.
Reactivities are in dollars, based on beta = 0.003311

Channel number	Channel type	Number of S/As	Coolant react.[b]	Clad react.	Fuel react.	Sodium-in Doppler	Sodium-out Doppler
1	blkt	1	0.01	-0.02	-0.20	0.31	0.30
2	blkt	6	0.07	-0.14	-1.27	2.32	2.17
3	driv	3	0.05	-0.14	2.46	0.39	0.33
4	driv	9	0.14	-0.41	7.28	1.04	0.87
5	blkt	15	0.21	-0.42	-3.77	6.81	6.11
6	blkt	6	0.10	-0.17	-1.53	2.63	2.29
7	driv	6	0.11	-0.29	5.08	0.68	0.54
8	driv	6	0.11	-0.30	5.27	0.76	0.60
9	driv	6	0.11	-0.29	5.19	0.78	0.63
10	blkt	6	0.09	-0.17	-1.52	2.90	2.39
11	blkt	12	0.19	-0.35	-3.07	5.62	4.72
12	blkt	12	0.19	-0.37	-3.20	6.12	5.18
13	driv	6	0.09	-0.29	6.14	0.85	0.62
14	driv	12	0.21	-0.62	12.09	1.76	1.31
15	driv	6	0.10	-0.30	6.30	0.87	0.64
16	driv	3	0.02	-0.12	3.05	0.40	0.28
17	driv	6	0.07	-0.28	6.27	0.85	0.59
18	blkt	12	0.20	-0.40	-3.19	5.90	4.54
19	driv	12	0.19	-0.61	12.17	1.75	1.27
20	driv	6	0.08	-0.29	6.43	0.87	0.60
21	driv	3	0.02	-0.12	3.13	0.41	0.28
22	driv	6	-0.09	0.05	4.69	0.50	0.35
23	driv	6	-0.02	-0.11	5.39	0.63	0.43
24	driv	6	0.05	-0.22	5.39	0.65	0.45
25	blkt	12	0.16	-0.33	-2.67	4.92	3.74
26	driv	6	0.06	-0.23	5.50	0.70	0.48
27	driv	6	0.05	-0.22	5.52	0.67	0.46
28	driv	6	-0.02	-0.11	5.53	0.64	0.43
29	driv	12	-0.19	0.14	7.97	0.85	0.60
30	driv	12	-0.06	-0.07	8.03	0.92	0.65
31	driv	12	-0.05	-0.09	8.20	0.95	0.67
32[a]	blkt	60	-0.37	0.45	4.04	8.15	6.69
33[a]	blkt	72	-0.16	0.22	1.47	2.60	2.37

total driver coolant reactivity	1.03
total driver clad reactivity	-4.92
total driver fuel reactivity	137.09
total internal blanket coolant reactivity	1.21
total internal blanket clad reactivity	-2.37
total internal blanket fuel reactivity	-20.42
total driver Doppler constant (no voiding)	17.92
total driver Doppler constant (Na voided)	13.09
total internal blanket Doppler constant (no voiding)	37.51
total internal blanket Doppler constant (Na voided)	31.44

[a] Channels 32 and 33 represent the radial blanket. Channel 32 consists of blanket subassemblies that are adjacent to driver subassemblies and Channel 33 consists of the remaining blanket subassemblies.

[b] Reactivity

TABLE 6
SAS3D CHANNEL CHARACTERISTICS at EOC-3

Channel number	Channel type	Number of S/As	Norm.[b] S/A power	Mass flux (kg/m²-s)	Average rod pow[c] (kW)	S/A pow/flow (J/g)	Norm. S/A pow/flow
1	blkt	1	0.33	3852	19.92	123.6	0.62
2	blkt	6	0.37	3852	22.63	140.4	0.71
3	driv	3	1.31	5135	22.59	220.1	1.11
4	driv	9	1.29	4848	22.18	228.9	1.15
5	blkt	15	0.41	4383	25.14	137.1	0.69
6	blkt	6	0.40	4383	24.75	134.9	0.68
7	driv	6	1.31	5135	22.61	220.2	1.11
8	driv	6	1.34	5135	23.11	225.2	1.13
9	driv	6	1.34	5135	23.11	225.1	1.13
10	blkt	6	0.43	3396	26.62	187.3	0.94
11	blkt	12	0.44	4383	26.67	145.4	0.73
12	blkt	12	0.45	4383	27.57	150.3	0.75
13	driv	6	1.42	5518	24.51	222.1	1.12
14	driv	12	1.43	5518	24.62	223.2	1.12
15	driv	6	1.44	5135	24.83	241.9	1.21
16	driv	3	1.40	5518	24.12	218.7	1.10
17	driv	6	1.43	5518	24.62	223.2	1.12
18	blkt	12	0.49	4383	30.08	164.0	0.82
19	driv	12	1.43	5518	24.64	223.3	1.12
20	driv	6	1.45	5135	24.93	242.8	1.22
21	driv	3	1.42	5135	24.42	237.9	1.19
22	driv	6	1.16	4455	19.90	223.4	1.12
23	driv	6	1.28	5135	22.12	215.5	1.03
24	driv	6	1.32	5135	22.66	220.7	1.11
25	blkt	12	0.45	3852	27.33	169.5	0.85
26	driv	6	1.34	5135	23.01	224.1	1.13
27	driv	6	1.33	4848	22.92	236.5	1.19
28	driv	6	1.30	4848	22.39	231.0	1.16
29	driv	12	1.06	4342	18.22	210.0	1.05
30	driv	12	1.10	4342	18.93	218.2	1.10
31	driv	12	1.12	4455	19.20	215.6	1.03
32[a]	blkt	60	0.26	2392	16.01	159.9	0.80
33[a]	blkt	72	0.10	1396	6.19	106.1	0.53

[a] Channels 32 and 33 represent the radial blanket; Channel 32 consists of blanket subassemblies that are adjacent to driver subassemblies and Channel 33 consists of the remaining blanket subassemblies.

[b] Normalized

[c] Power

TABLE 7
WARD CALCULATION of
SAS3D CHANNEL CHARACTERISTICS at EOC-4

Doppler constants are multiplied by -10000.
Reactivities are in dollars, based on beta = 0.003403

Channel number	Channel type	Number of S/As	Coolant react.[a]	Clad react.	Fuel react.	Sodium-in Doppler	Sodium-out Doppler
1	blkt	7	0.10	-0.17	-1.16	3.55	3.27
2	driv	21	0.39	-0.98	16.73	3.82	3.23
3	blkt	21	0.33	-0.61	-3.86	12.24	10.64
4	driv	9	0.16	-0.41	7.11	1.78	1.53
5	blkt	36	0.56	-1.03	-5.86	20.37	16.43
6	driv	6	0.08	-0.27	6.05	1.24	0.93
7	driv	12	0.16	-0.51	10.20	2.29	1.74
8	blkt	12	0.13	-0.24	-1.46	4.84	3.70
9	driv	6	0.03	-0.16	4.43	0.92	0.67
10	driv	12	0.11	-0.42	9.35	2.00	1.46
11	driv	24	0.37	-1.03	18.69	4.45	3.47
12	driv	12	-0.04	-0.12	7.62	1.39	1.01
13	driv	18	.0.12	-0.47	11.61	2.30	1.69
14	driv	18	-0.20	0.15	8.96	1.51	1.14
15	driv	24	-0.08	-0.10	11.61	2.15	1.63

total driver coolant reactivity	1.10
total driver clad reactivity	-4.31
total driver fuel reactivity	112.35
total internal blanket coolant reactivity	1.11
total internal blanket clad reactivity	-2.05
total internal blanket fuel reactivity	-12.34
total driver Doppler constant (no voiding)	23.83
total driver Doppler constant (Na voided)	18.49
total internal blanket Doppler constant (no voiding)	41.00
total internal blanket Doppler constant (Na voided)	34.04

[a] Reactivity

TABLE 8
WARD CALCULATION of
SAS3D CHANNEL CHARACTERISTICS at EOC-4

Channel number	Channel type	Number of S/As	Norm.[a] S/A power	Mass flux (kg/m²-s)	Average[b] rod pow (kW)	S/A pow/flow (J/g)	Norm. S/A pow/flow
1	blkt	7	0.54	3817	32.50	203.4	1.00
2	driv	21	1.30	4935	21.89	221.9	1.09
3	blkt	21	0.61	4345	36.36	200.0	0.99
4	driv	9	1.31	5056	21.99	217.5	1.07
5	blkt	36	0.63	4345	37.54	206.5	1.02
6	driv	6	1.46	5147	24.59	239.0	1.18
7	driv	12	1.32	5244	22.16	211.4	1.04
8	blkt	12	0.54	3817	32.56	203.8	1.00
9	driv	6	1.22	5244	20.57	196.2	0.97
10	driv	12	1.26	5244	21.22	202.4	1.00
11	driv	24	1.29	5433	21.73	200.1	0.99
12	driv	12	1.12	4914	18.87	192.0	0.95
13	driv	18	1.16	4962	19.51	196.7	0.97
14	driv	18	0.96	4312	16.17	187.6	0.92
15	driv	24	0.98	4331	16.56	191.3	0.94

[a] Normalized

[b] Power

are a slight power shift (approximately 2%) toward the reactor center and higher relative power in blanket subassemblies. The central shift is not expected to be significant in the initiating phase because the leading driver channels keep the same sequence of power-to-flow ratios. The blanket power differences apparently are caused by differences in neutron capture energies used in the two calculations. These differences should not affect the initiating phase because the low specific power in the blankets retards the development of fuel disruption until late in the transient. A further difference in the two power distributions is the axial shape. A comparison for a typical channel is shown in Figure 3. The WARD curve has a truncated shape in the central portion, due to the three axial zone burn-up calculations used to determine the isotopic compositions. In our calculation, the isotopic densities were axially averaged, and thus do not have this characteristic. We chose to average the composition to provide consistency with the treatment for reactivity feedback from fuel motion in SAS3D. As a consequence of our more peaked distribution, fuel disruption will occur earlier relative to clad melting in the upper portion of the core.

Comparison of our results, Table 1, and WARD results, Table 7, shows significantly higher calculated sodium void reactivities in our case. The two calculations were similar in that both were first-order perturbation results based on three-dimensional diffusion theory. Several differences existed in cross-section group structure and weighting spectra determination, along with different fission product cross sections. Also, the WARD-supplied nuclear densities were averaged axially and over all subassemblies in each channel in our calculation. Finally, the WARD results were based on ENDF/III cross-section data, while our results were based on ENDF/IV cross-section data. This last difference is the most important contributor to the differences between these results; for example, comparison of critical experiments calculations for central sodium void coefficients shows ENDF/III results about 20% lower than ENDF/IV results.

5. Uncertainties

Uncertainties exist in the calculational methods and data, in the reactor configuration, and in the proper application of experimentally derived bias factors. Principal uncertainties in the calculational method for the determination of material reactivity worths are the use of first-order perturbation vs exact perturbation and the use of diffusion-theory calculated fluxes vs transport-theory based fluxes. First-order perturbation calculations tend to underestimate the positive nonleakage term and to overestimate the negative leakage term because both real and adjoint spectra harden and the spatial distribution flattens with sodium removal. A further approximation is made if the effect of sodium voiding upon other cross sections (primarily the increase in resonance self-shielding) is neglected, as it is in our calculation. Differences between transport and diffusion results become

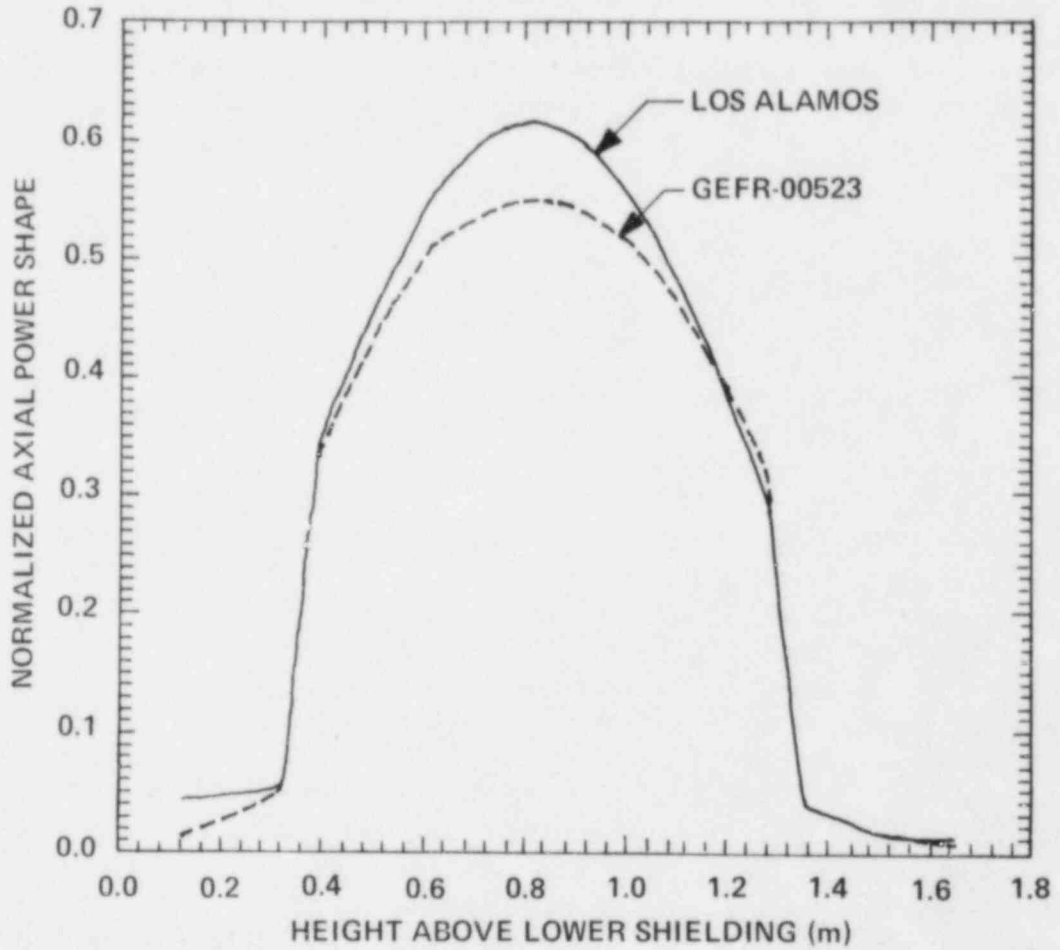

Fig. 3.
Comparison of calculated axial power distributions.

significant for regions near core-blanket or control rod interfaces. Reactivity changes may be either under- or overestimated with diffusion results. Cross-section data uncertainties stem from basic data and the methods used to determine resonance self-shielding and collapsing spectra. Calculational uncertainties of these types are difficult to estimate because the impacts are highly regional dependent. However, errors on the order of 10-20% have been quoted from use of first-order perturbation methods, errors on the order of 0 to 30% from use of diffusion theory, and as indicated previously, a 20% difference can result between calculations with ENDF/III and ENDF/IV cross sections.

Uncertainties in the reactor configuration result from two sources: errors in the reactor burn-up state and uncertainty in the global sodium content (due to previous voiding) when a given subassembly is voided. Errors in the reactor burn-up calculation stem from the use of diffusion theory and the use of approximate cross sections (which do not properly account for the effects of composition changes). Such errors affect the sodium void reactivity primarily because the Pu^{240} fission threshold occurs at a lower energy than that of U^{238} and the capture-to-fission ratio for Pu^{241} is not as steep with respect to neutron energy as that for Pu^{239}. A second effect occurs because the reactor power distribution is affected by Pu buildup in the internal blankets, which in turn affects the subassembly voiding sequence. The effect of uncertainty in the reactor sodium content is comparable to the use of a first-order-perturbation vs exact perturbation approaches in the void reactivity calculation (this effect cannot be incorporated into an accident code such as SAS3D without prior knowledge of the accident path). The magnitude of uncertainties in the blanket Pu content should be on the order of 10%.

Uncertainties in the calculational/experimental bias correction to the sodium void reactivities reflect the uncertainty in the comparability of physical, composition, and thermal characteristics of critical-assemblies vs power-reactors. The most important difference is the use of platelet geometry in the CRBR critical assembly mockup. Other differences include the absence of fission products and the lack of a temperature distribution in the critical assemblies. Comparison of calculational and experimental results for a number of critical assemblies shows that a significant bias factor is necessary to obtain general agreement for both leakage and nonleakage components. Such bias factors definitely reduce the variance in calculated/experimental ratios for critical assemblies. Some effects, such as streaming, however, are not comparable for platelet vs pin geometry. Thus, the use of bias factors determined for critical assemblies may not be justified for use in power reactors. Some have claimed, for example, that the overprediction of the non-leakage component, which is characteristic of the critical assembly sodium void calculation is almost entirely attributable to platelet streaming effects. In this case, the nonleakage bias factor should not be applied to power reactors.

6. Conclusions and Recommendations

Independent calculations of CRBR neutronics parameters have been made and compared to corresponding values generated by the Applicant for the CRBR initiating-phase analysis. The differences have been identified along with the sources of uncertainty. An independent quantitative uncertainty analysis has not been performed, however. The uncertainty analysis provided by the Applicant [10] in response to question #2 (Table 2; Section I) recommends an uncertainty for the Doppler effects of ±16% for driver S/As with a positive worth. We believe that these values adequately bound calculational, voiding sequence, temperature distribution, and fission product uncertainties. It has not been clearly established, however, that calculated-to-experimental bias factors for critical experiments should be applied to power-reactor calculated results. Thus, for EOC-4 the upper bound of total driver void worth reactivity is taken as 2.03$ based on our calculated value of 1.75$ plus 16% for uncertainty applied to all driver S/As. The lower bound is taken as 1.10$ based on a biased value minus 16% for uncertainty. In this assignment we have treated the bias factor as an additional uncertainty in the downward direction.

7. References

1.[a] C. L. Beck, M. J. Lineberry, D. N. Olsen, and H. F. McFarlane, "Sodium Voiding in LMFBR's: A Physics Assessment," Argonne National Laboratory report ZPR-TM-400 (1981).

2. Kalimullah, P. H. Kier, and H. H. Hummel, "Physics Calculations for the Clinch River Breeder Reactor," Argonne National Laboratory report ANL-77-27 (1977).

3. D. Garber, Ed., "Data Formats and Procedures for the ENDF Neutron Cross Section Library," Brookhaven National Laboratory report BNL 50274 (1976).

4. S. K. Rhow, D. M. Switick, J. L. McElroy, and B. S. Joe, "An Assessment of HCDA Energetics in the CRBRP Heterogeneous Reactor Core," General Electric Company report CRBRP-GEFR-00523 (December 1981).

5.[a] J. E. Cahalan and D. R. Ferguson, "A Preliminary User's Guide to Version 1.0 of the SAS3D LMFBR Accident Analysis Computer Code," Argonne National Laboratory (informal document included with code) (1977).

6. J. E. Cahalan, "D1F3DS: A Multidimensional, Multigroup Diffusion/Perturbation Theory Code," Argonne National Laboratory report ANL/RAS 79-1 (1977).

7. J. R. Longenecker, "Transmittal of Information," U.S. Dept. of Energy letter (HQ:S:82:006) to NRC-CRBRP Program Office, Docket No. 50-537 (February 1982).

8. R. B. Kidman and R. E. MacFarlane, "LIB-IV, A Library of Group Constants for Nuclear Reactor Calculations," Los Alamos National Laboratory report LA-6260-MS (1976).

9. R. D. O'Dell, F. W. Brinkley Jr., and D. R. Marr, "User's Manual for One-Dimensional, Diffusion-Accelerated, Neutral-Particle Transport," Los Alamos National Laboratory report LA-9184-M (February 1982).

10. "Compendium to NUREG/CR-3224, An Assessment of CRBR Core Disruptive Accident Energetics," Section 6, Nuclear Regulatory Commission document (March 1983).

[a] Address requests for this document to: F. X. Gavigan, Director, Office of Breeder Demonstration Projects (NE-50), U.S. Department of Energy, Washington, DC 20545, Telephone (301) 353-3134.

APPENDIX B
SAS3D ANALYSIS OF THE LOF INITIATING PHASE

1. Introduction

In this Appendix we describe the geometric models, assumptions, and results for four representative SAS3D [1] analyses. These particular cases were selected to investigate the general tendencies of the CRBR heterogeneous-core design to produce extensive core-wide steel blockages in the upper and lower axial blankets, extensive codisruption of fuel and cladding, sustained or cyclic neutronic activity, and significant ramp rates during the initial stages of disruption. The emphasis was on determining and quantifying those characteristics that are of greatest importance to the subsequent disruption-phase behavior particularly fuel dispersal or removal.

The four cases analyzed were BOC-1, EOC-3, EOC-4 (midrange), and EOC-4 (slow). The set spans the burnup range and also an uncertainty range for EOC-4. Many more cases could be performed to map the detailed response characteristics to uncertainties and initial condition variations. However, we could see from both the Applicant's analysis [2] and our own preliminary work that the response spectrum to uncertainties and variations is continuous, largely monotonic, and weakly coupled to the uncertainties and variations. Therefore, it is sufficient to consider only these representative cases that are formulated in a way to highlight and promote conservative conditions for the disruption phase.

2. BOC-1 Analysis

Geometric Model BOC-1

The fundamental idea in an SAS3D representation of the CRBR core is to lump groups of subassemblies into SAS channels each of which is modeled by a representative fuel pin and its associated structure. The starting point for the BOC-1 input was the GEFR-00523 [2] setup. The 15 channels used in this setup are shown in Figure 1. Within an individual channel the axial subassembly dimensions were taken from ANL/RAS 75-29 [3]. The coolant mesh is shown in Figure 2, while the heat-transfer mesh for the region of the fuel pin containing the fertile and fissile fuel is given in Figure 3. Pin radial dimensions and the surface areas for heat transfer were taken from GEFR-00523 [2].

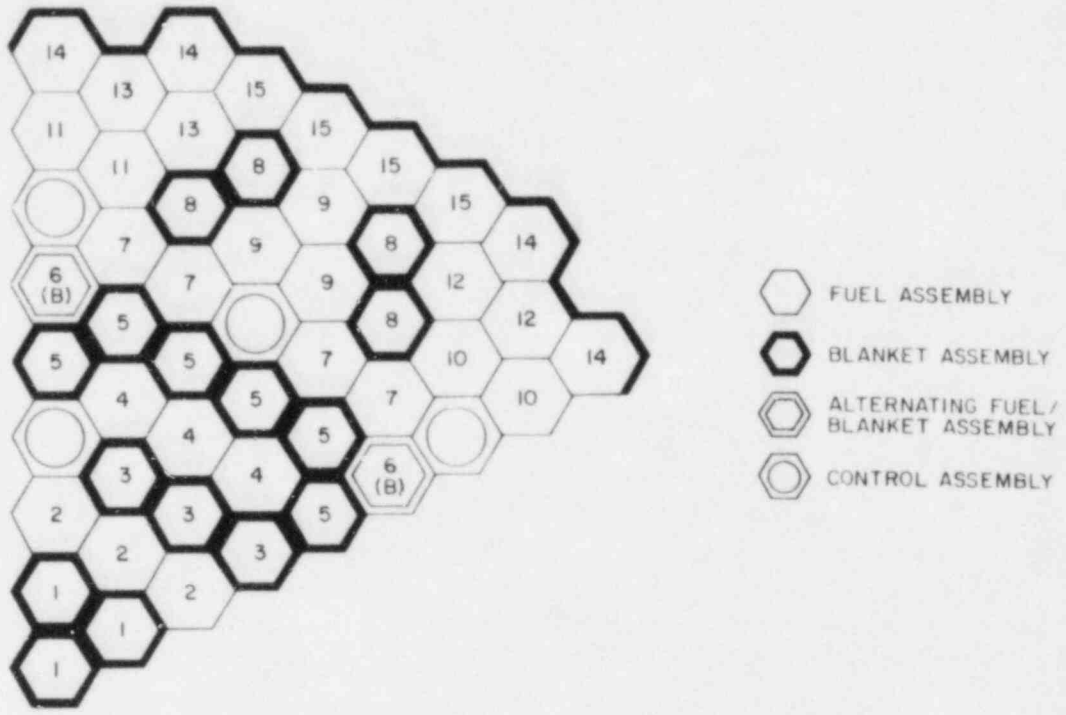

Fig. 1.
Subassembly assignments to SAS3D channels for the BOC-1 analysis.

Also of importance in the geometric modeling is the primary-loop model. A schematic of this model is given in Figure 4. The input values for this model were taken from GEFR-00523 [2]. Of particular interest is the size of the inlet plenum, which is a primary variable in determining the backpressure upon the core during voiding. The volume input was 535 m^3. This is approximately six times the actual CRBR plenum volume and is used so that sodium compressibility can represent the capacitance effects induced by the strain of the primary vessel wall and core support structure as pressure changes. A calculation for these effects is given in ANL/RAS 76-5 [4]. The actual curve for the pump head coastdown as a function of time was taken from ANL/RAS 75-29 as

$$\Delta p_{head} = \Delta p_o \exp(-0.358t + 0.012t^2 - 0.00014t^3)$$

where Δp_o corresponds to 1.1 MPa with the current input and t is the time in seconds from accident initiation.

Results BOC-1

Boiling initiated in Channel 11 at 11.66 s. Power stayed below nominal until cladding motion began at 15.31 s. Cladding motion reactivity is increased over that in GEFR-00523. This results from the earlier initiation of motion and the input and model changes (see Section II.3) which led to an

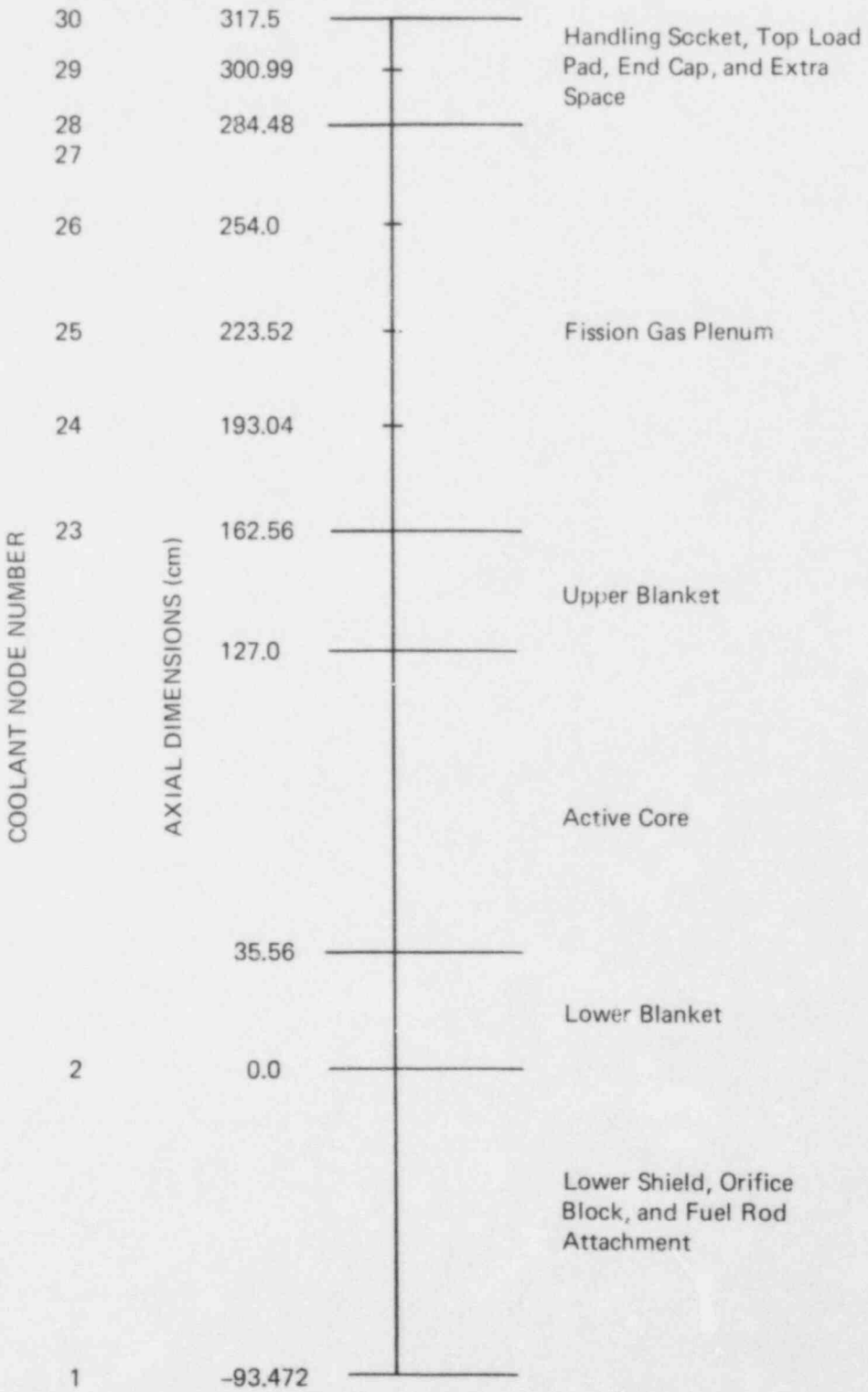

Fig. 2.
SAS3D coolant mesh used for representation of the CRBR core.

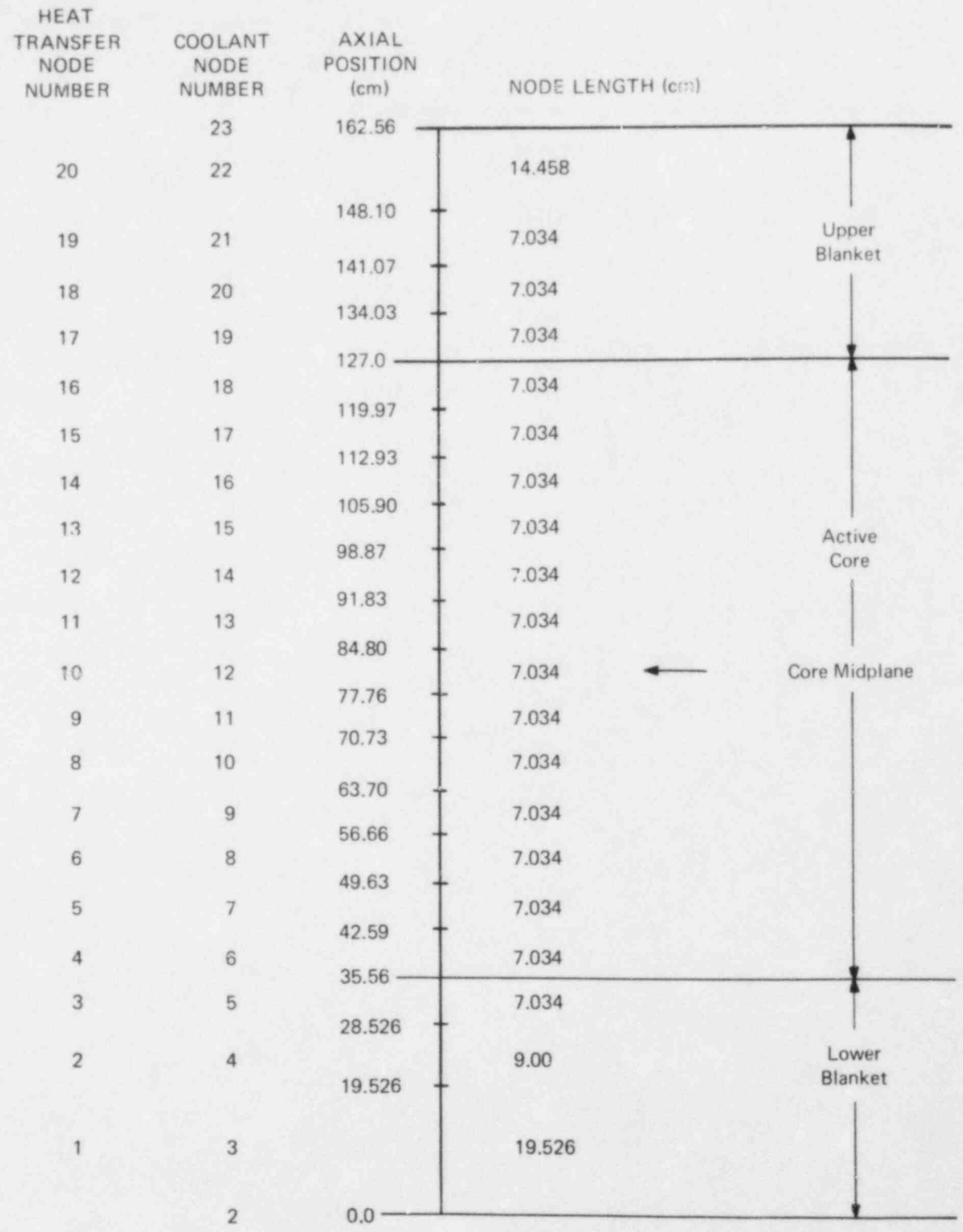

Fig. 3.
Heat-transfer mesh for the fueled portion of the CRBR pins.

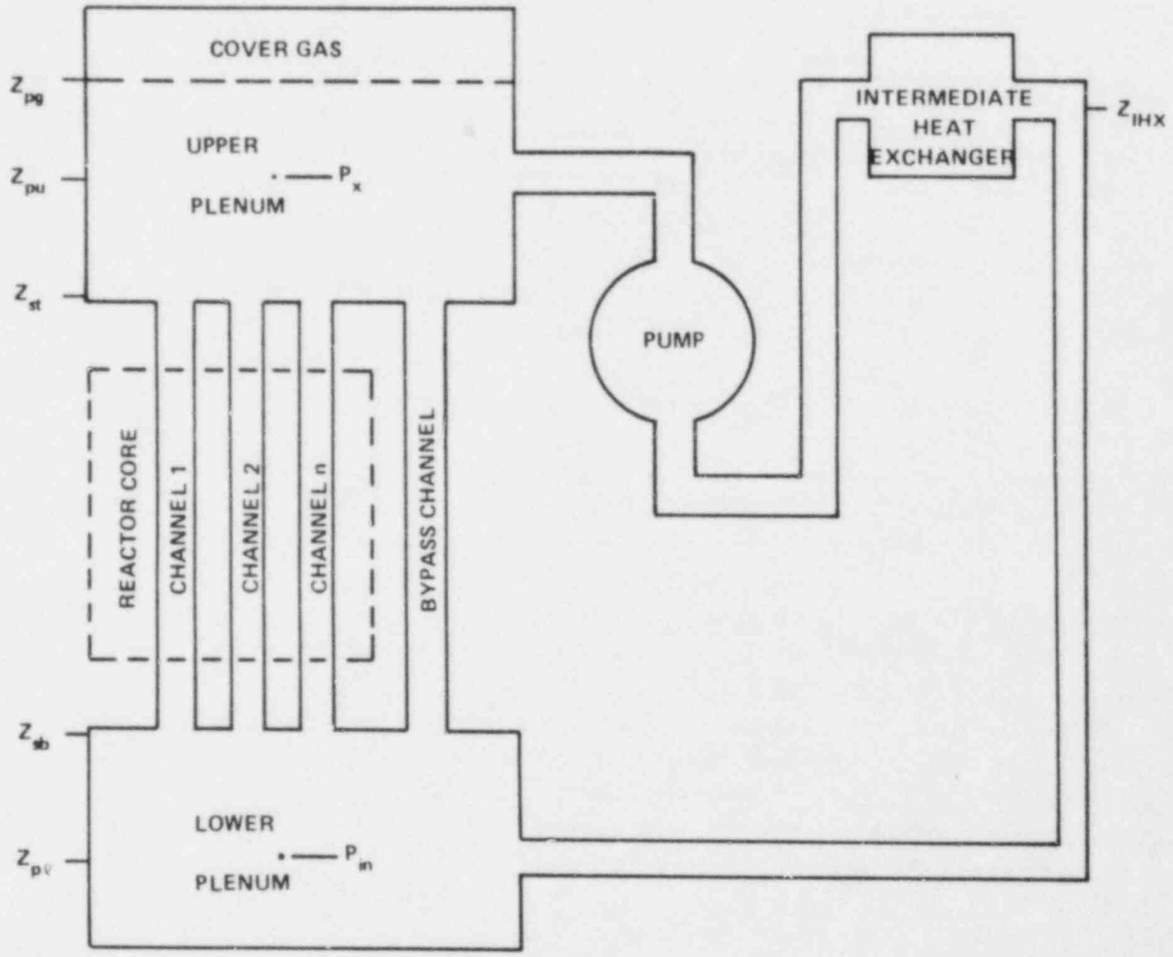

Fig. 4.
Primary loop schematic for the SAS3D LOFA analysis of CRBR.

accumulation of cladding at the core-blanket interface. Fuel motion began at 17.94 s when the power was 2.1 times nominal. A series of power pulses then resulted from fuel slumping. However, as a result of intersubassembly incoherence and the mitigating effects of entrained fission gas (a 30-day burnup was assumed), a prompt-critical burst did not develop before fuel vapor was produced in lead subassemblies, producing temporary neutronic shutdown.

Figure 5 gives the overall power and reactivity transients showing the influence of cladding relocation and fuel slumping in raising the power. Figure 6 shows the three power bursts when prompt critical was approached. Figures 7 and 8 give the individual reactivity components, illustrating the negligible influence of voiding reactivity on this transient. Cladding relocation produced the reactivity rise, while fuel motion controlled the power oscillations. Figures 9, 10, and 11 give a channel breakdown of coolant voiding reactivity, indicating the eventual complete voiding in all driver subassemblies. Figures 12 and 13 give a channel breakdown of cladding relocation reactivity, showing little cladding relocation in low-power channels thereby setting the stage for codisruption. Figures 14 and 15 give a channel breakdown of fuel motion reactivity showing that only Channels 9 and 11 develop appreciable positive reactivity, which tended to be offset by simultaneous dispersal in other channels.

Channel 11 is the highest power channel. The final calculated configuration of Channel 11 had cladding blockages above and below the core. A maximum fuel vapor pressure of about 0.4 MPa existed. Channel 12 is a typical medium-power channel. Its final configuration suggests an above core cladding blockage, although molten cladding was still 0.1 m from the lower core/blanket interface. Some codisruption was indicated. Channel 2 was the last channel to void. Partial cladding and fuel melting occurred at the termination of the calculation in Channel 2. Any further power burst might be expected to give rise to appreciable codisruption in this situation.

The final core state is summarized in Figure 19 of Section II.3.

3. EOC-4 Analysis

Geometric Model EOC-4

The only difference in the geometric model for the EOC-4 analysis relative to the BOC-1 was the channel arrangement. We used the channel arrangement of GEFR-00523 [2], which is shown in Figure 16.

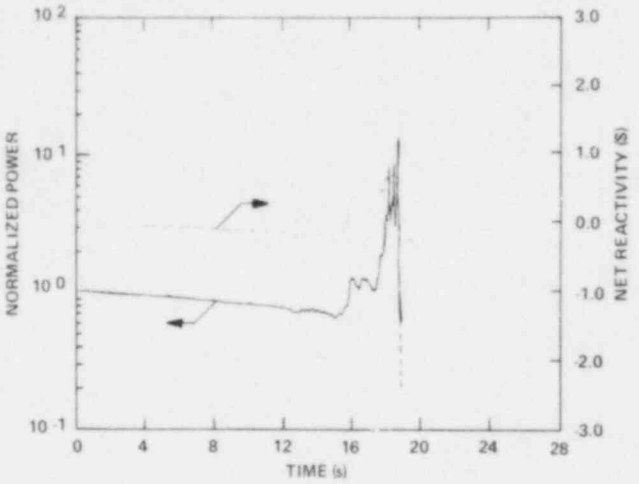

Fig. 5.
Overall power and reactivity transients for BOC-1.

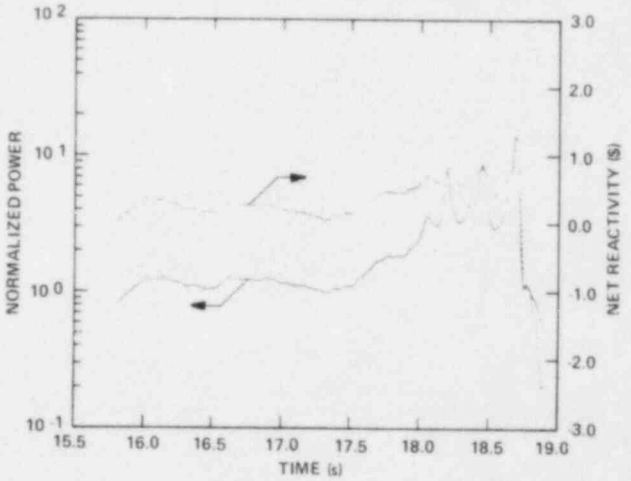

Fig. 6.
Overall power and reactivity transients during initial disruption for BOC-1.

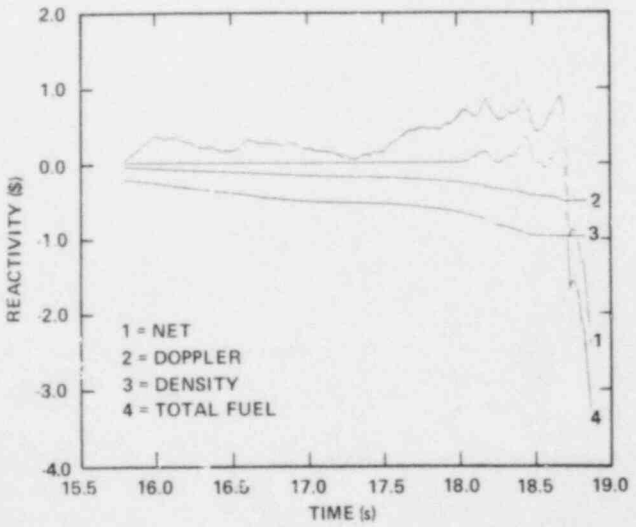

Fig. 7.
Overall component reactivity transients for BOC-1.

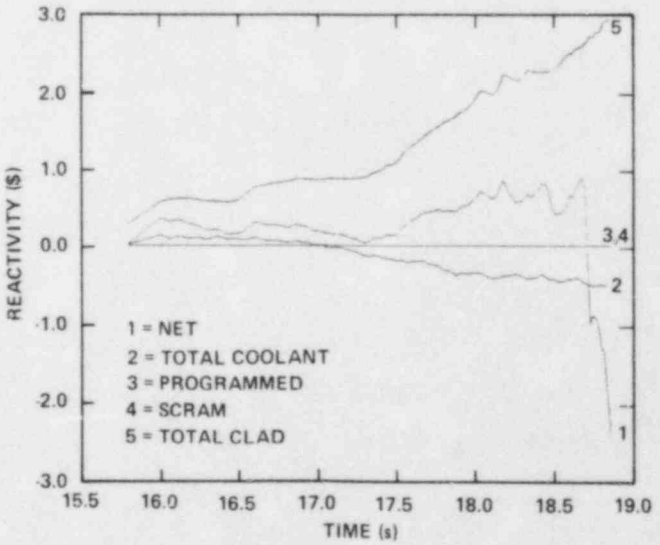

Fig. 8.
Overall component reactivities transients for BOC-1.

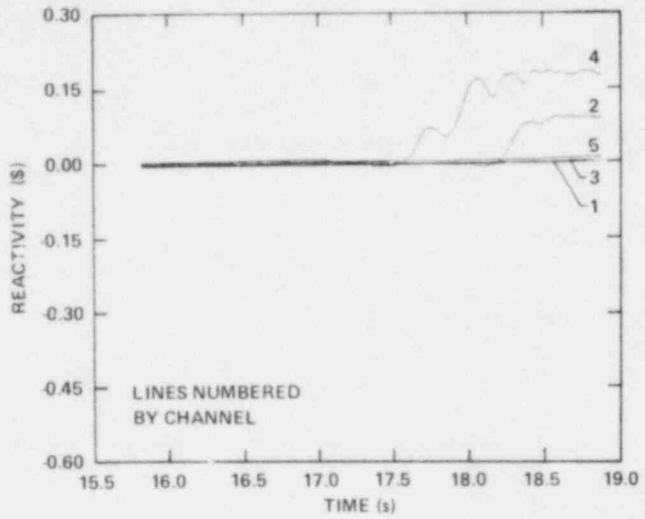

Fig. 9.
Coolant reactivity transients by channel for BOC-1.

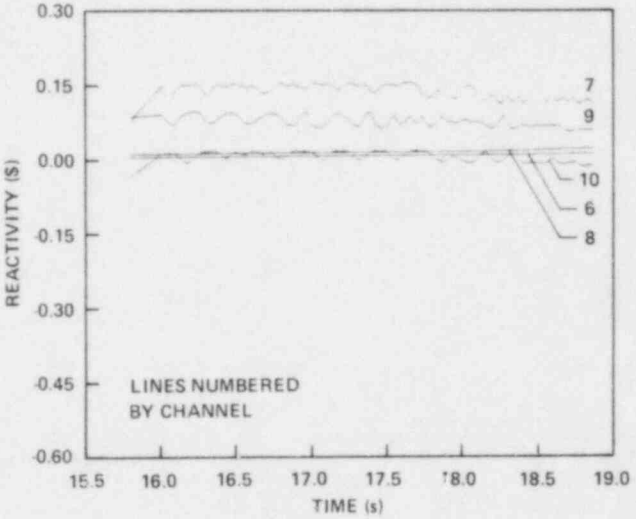

Fig. 10.
Coolant reactivity transients by channel for BOC-1.

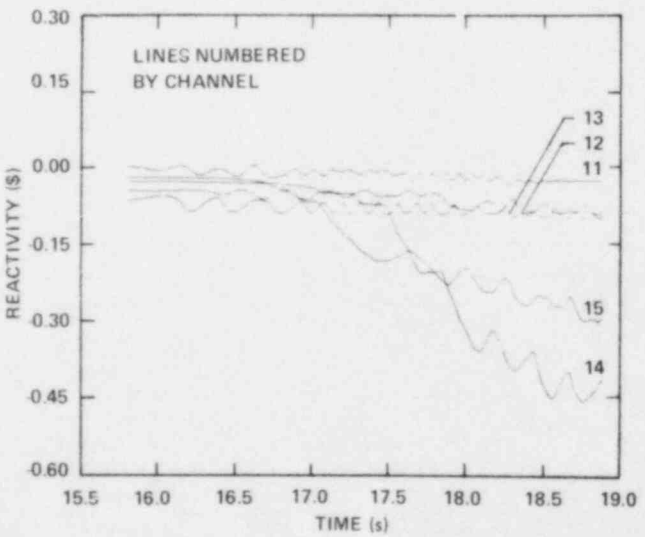

Fig. 11.
Coolant reactivity transients by channel for BOC-1.

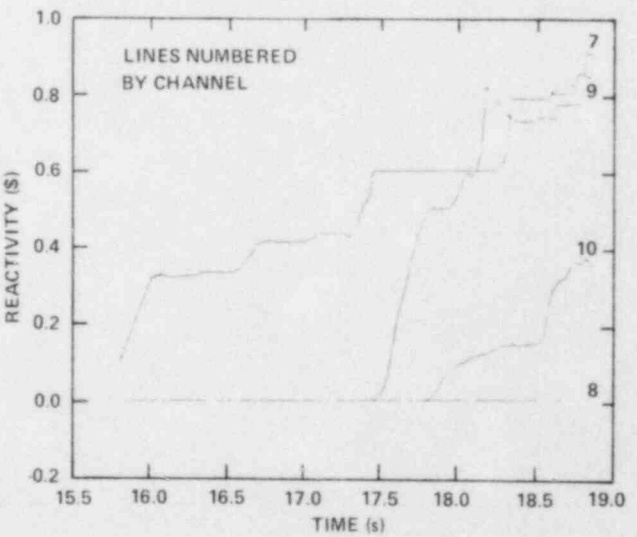

Fig. 12.
Cladding reactivity transients by channel for BOC-1.

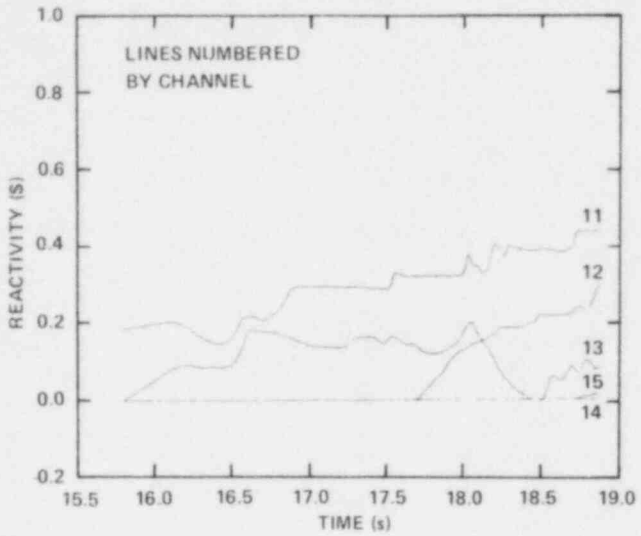

Fig. 13.
Cladding reactivity transients by channel for BOC-1.

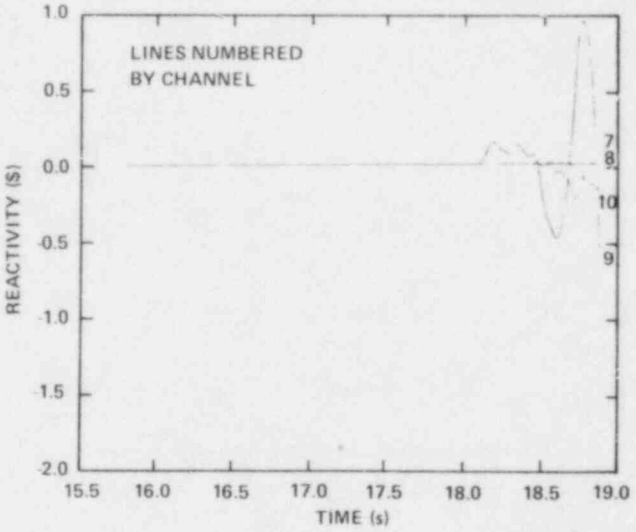

Fig. 14.
Fuel reactivity transients by channel for BOC-1.

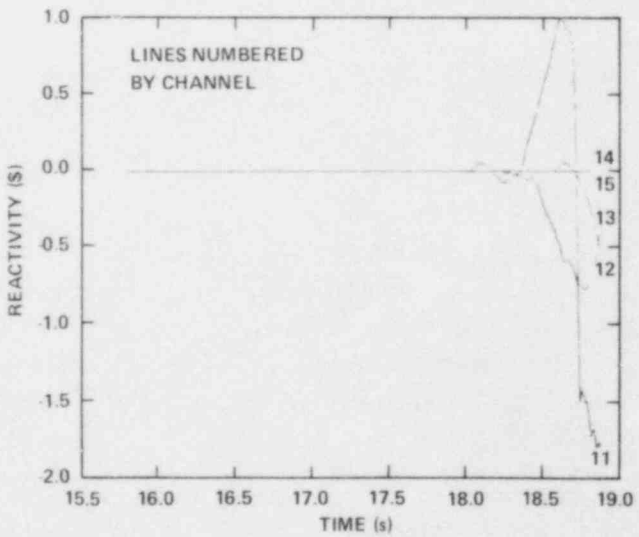

Fig. 15.
Fuel reactivity transients by channel for BOC-1.

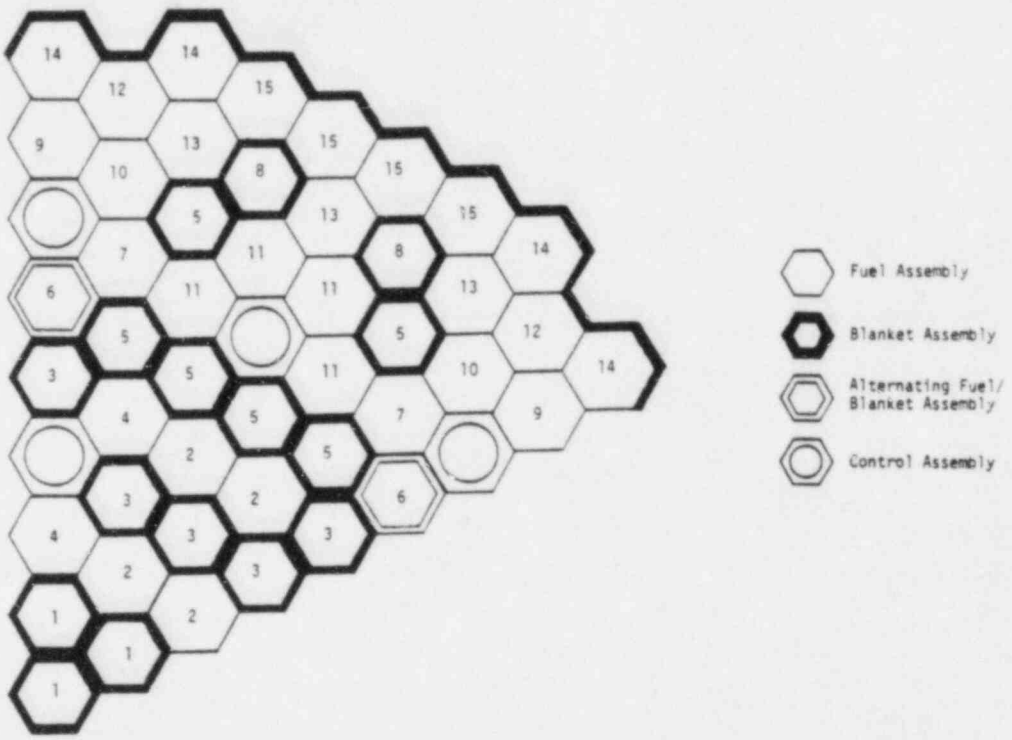

Fig. 16.
Subassembly assignments to SAS3D channels for the EOC-4 analysis.

Case Assumptions

Two cases were assessed for the EOC-4 state. The first is labeled mid-range because it was set up with mid-range assumptions for the primary uncertainties such as sodium void, Doppler, thermal expansion feedback, fission gas release behavior, and fuel viscosity. These assumptions are summarized in Table 2 of Section II.3. The second is labeled slow because it represents a slow, end-of-spectrum set of assumptions for Doppler, expansion feedback, and fission gas release characteristics along with a reduced value of void worth. The intent was to minimize, within reason, the net reactivity and therefore power escalation during early disruption. This case should tend to maximize the cladding blockage potential and minimize codisruption.

Results EOC-4 Mid-range

Boiling initiated first in Channel 6 at 11.66 s. The positive voiding reactivity led to a slow progressive power increase. The power was 1.84 times nominal by the time cladding motion started in Channel 6 at 15.18 s. This was about the time voiding began in a typical medium-power channel such as Channel 10. The rapidly increasing voiding reactivity following sodium flow reversal in the medium-power channels gave little time for cladding melting and relocation before fuel motion. Fuel motion initiated at 16.13 s with the reactor power at 10.49 times nominal. Initial fuel motion was mainly dispersive, reducing the power to below three times nominal by 16.5 s.

However, pressure equilibration did allow the SLUMPY upper pin segments to fall, producing a power burst reaching a peak power about 200 times nominal and marginally prompt critical. This burst led to codisruption in the medium-power subassemblies, and SAS termination with fuel vapor pressure produced in Channel 6.

Figure 17 gives the power and reactivity traces for the voiding and fuel-slumping-induced bursts of this transient. Figure 18 shows how closely the net reactivity followed the fuel motion reactivity after 16.1 s. Figure 19 shows that the voiding ramp rate before fuel motion was about 1.5$/s, and that most of the cladding relocation reactivity occured after fuel initiation of motion and also after the power burst (suggesting extensive codisruption). Figures 20, 21, and 22 give a channel breakdown of coolant voiding reactivity. They show that the internal blankets began to void at the end of the transient and that the low-power driver subassemblies voided late in the transient. Figures 23 and 24 give a channel breakdown of cladding relocation reactivity. Only the higher power S/As (Channels 2, 4, 6 and 7) had cladding relocation. Even here most of the cladding motion was driven by the dispersing fuel. Figures 25, 26 and 27 give a channel breakdown of fuel motion reactivity and indicate that fuel motions in several lead channels combined to produce the second burst.

The final configuration for the highest power channel, Channel 6, is given in Figures 28, 29, 30, and 31. The location of the S/As of Channel 6 in the core is shown in Figure 28. The distributions of all materials are shown in Figure 29 in terms of volume fractions. The fuel density and temperature distributions and the channel pressure distribution are shown in Figures 30 and 31, respectively. A tendency to form cladding blockages above and below the active core is indicated. Fuel is shown to have vaporized in the center of the core, with fuel slugs being pushed toward the cladding blockages. Figures 32, 33, 34, and 35 give the final configurational results in the same form for a typical medium-power channel, Channel 10. No motion of cladding independent from fuel was calculated, and the pressures observed were those from the entrained fission gas. Channel 14 was the last channel to void. At the termination of the calculation, the maximum fuel melt fraction was 0.46. The cladding temperature at the location of maximum fuel melt fraction was 1573 K. Fuel swelling and codisruption are expected in this situation as the LOFA progresses into the disruption phase.

Results EOC-4 Slow

With reduced void reactivity and increased negative reactivity feedback, voiding began at 12.91 s in Channel 6. The power was only 1.1 times nominal when cladding relocation started in Channel 6 at 16.87 s. Approximately 0.50$ of cladding reactivity was inserted by the time fuel motion started at 18.72 s, and the overall net reactivity at this time was 0.63$, which is similar to the EOC-4 cases in GEFR-00523 [2]. Only the four lead

channels (2, 4, 6, and 7) disrupted on the first burst. Gas de-entrainment and the resulting fuel slumping led to a second power burst, however. This second power burst did reach prompt critical, causing codisruption in medium-power subassemblies and generating fuel vapor pressures in Channel 6 at the termination of the SAS transient. The SIMMER-II case described in Section II.5 was started at 19.75 s, after voiding in all the driver subassemblies, but before the second burst.

Figures 36 and 37 give the power and reactivity transients for this case. The delay between the first and second bursts is evident. Figure 38 shows how dependent the net reactivity is on fuel motion. This dependency is illustrated further in Figure 39. While the cladding relocation reactivity was appreciable, the changes were slow enough that it did not affect significantly the instantaneous time derivative of the net reactivity. Figures 40, 41, and 42 give a channel breakdown of the voiding reactivity and illustrate how the lower power driver subassemblies voided during the quiescent period following the first burst. Figures 43, 44, and 45 give the cladding relocation reactivities as a function of time for each channel. The large increases in cladding reactivities were associated generally with the coupling of cladding to fuel motion and the downward motion of cladding into cold voided regions. For these situations, the quasi-steady-state limits on the upward pressure gradient were not active in restraining cladding motion. However, the model also did not guarantee cladding relocation velocities below 1 m/s until voiding of driver S/As was complete and the inlet plenum was depressurized. Figures 46, 47, and 48 give the channel breakdown of fuel reactivity versus time. Important initial dispersal reactivity was introduced by a sodium re-entry event, forcing fuel upward in Channel 2. Subsequent gas de-entrainment was an important contributor to the later power burst. The magnitude of the first power burst was controlled by Channel 6. Following some initial fuel dispersal in this channel, fission-gas release at the ends of the pins forced a limited degree of fuel compaction. This compaction was probably exaggerated by this version of SAS3D. However, the codisruption observed in this case was independent of this burst augmentation mechanism. All that was required to maintain neutronic activity was for fuel <u>not</u> to be monotonically dispersive. Indeed, it is reasonable that fuel puddling occur as gas de-entrains and vapor condenses.

Figures 49, 50, 51, and 52 give the final configuration results for Channel 6, the highest power channel. These results are similar to the mid-range case, with suggestions of an upper and lower cladding blockage restraining the vaporizing fuel. Figures 53, 54, 55, and 56 give results for a typical medium power channel, Channel 10. Codisruption was reduced relative to the mid-range case, but some steel was present with the fuel. More codisruption was observed in Channel 12, which voided about 0.8 s after Channel 10. This can be seen in Figures 57, 58, 59, and 60. Finally, the lowest power channel, Channel 14, experienced simultaneous cladding and fuel melting at the end of the calculated transient.

4. EOC-3 Analysis

Geometric Model EOC-3

The SAS3D channel geometry for the EOC-3 analysis was identical to the previous cases. The subassembly channel grouping was changed, however. Thirty-three channels were assigned, as illustrated in Figure 61. The driver subassemblies were grouped into channels within the orifice zones indicated in the PSAR [5]. Because the heterogeneous CRBR core only has one-third symmetry, more channels were required than might seem obvious for a core with a batch reloading scheme. The internal blankets also were separated by orifice zone and power. Although several blanket channels are not necessary to compute initiating-phase LOFA behavior, such a division was judged desirable to improve the accuracy of the neutronics calculations, as well as providing spatial detail for the TOP analysis in Section III.

Results EOC-3

Channel 20 had the highest power-to-flow ratio, and started to void at 12.91 s. However, all the initial subassemblies to void were in the outer fuel annulus region, and little positive voiding reactivity was obtained until about 15.85 s. At this point, sodium flow reversals began to occur in the inner subassemblies, which had higher void worths. The power was 1.3 times nominal at the start of cladding motion (16.37 s) and 4.2 times nominal at the start of fuel motion (17.53 s). This later power level was similar to that in the slow EOC-4 case. Indeed, some of the subsequent features indicated on the reactivity traces were similar in the two cases, which is not too surprising because of identical fuel motion modeling. Two bursts were observed. The peak power reached in the first burst was similar to the slow EOC-4 case and while appreciable cladding relocation reactivity was seen, the reactivity shape was dominated by fuel motion. The second burst did exhibit reduced energy because of the incoherence introduced by the detailed channel arrangement. Channel 20 did not develop subassembly wall melting during the SAS3D transient as did Channel 6 in the slow EOC-4 case because of the reduced radial power factor. However, in both cases appreciable codisruption occurred. Appreciable reduction in codisruption in the EOC-3 case would require both adjustments in the neutronics parameters (reduced void worth, etc.) and at least some further delay in fuel compaction following initial fuel dispersal.

Figures 62 and 63 give the power and reactivity profiles. Figures 64 and 65 give the reactivity components demonstrating again that the large cladding motion reactivity was easily compensated by that from fuel motion. Figures 66 through 71 give the channel-dependent voiding reactivities and show that all driver subassemblies had gone into sodium flow reversal by the time fuel motion was initiated in Channel 20. Figures 72 through 77 give the

channel-dependent cladding motion reactivities. In the EOC-3 case all channels except Channel 16 initiated cladding relocation. Figures 78 through 83 give the channel-dependent fuel motion reactivities. It was the lead subassemblies, Channels 15 and 20, that exhibited the largest gas de-entrainment and slumping, although there were many small contributions to the second burst from other channels, that started about 18.7 s.

Conditions at the end of the calculation for the lead channel, Channel 20, are given in Figures 84 through 87. This material configuration was similar to the previous cases. Conditions in a typical medium power channel, Channel 13 (Figures 88 through 91), were similar to those in Channel 10 of the slow EOC-4 case. Finally, the final conditions in the coldest driver subassembly, Channel 29, are shown in Figures 92 through 95. While cladding motion had started, cladding relocation velocities were very limited due to the inlet plenum pressure reduction following the completion of voiding in the driver subassemblies. Again, codisruption or the potential for codisruption occurred in the medium and low-power channels. A core-wide summary of the final state is given in Figure 18 of Section II.3.

5. Summary

The results of these SAS3D analyses indicate a general pattern in which negative neutronic feedback from initial fuel dispersal followed by gas de-entrainment and slumping is of insufficient magnitude to offset the neutronic effect of total removal of cladding (~5$). Therefore, cladding relocation over the entire core is not calculated. Typically, the high power-to-flow channels, which lead the voiding and disruption process as well as some medium-power channels, have calculated blockages in the upper axial blanket. These latter channels generally do not have solid blockages at the lower core interface however. The medium- and low-power channels typically have incomplete cladding separation before fuel disruption, thereby establishing a codisrupted state or the potential for such state in one third to one half of the core in all cases. Thus, the potential for some steel-vapor-assisted fuel dispersal or removal during the subsequent disruption phase is essentially universal.

Another characteristic of the calculated responses is the fuel motion domination of the net reactivity following initial fuel disruption and the resulting strong neutronic activity. This is not surprising in that the fuel worth is about 20 times that of the cladding. Thus, the fuel fluid dynamics over periods greater than 0.5 s and in S/A-scale geometry is important fundamentally. This is even more true for the slow situations, where the time interval of disruption is extended.

6. References

1.[a] J. E. Cahalan and D. R. Ferguson, "A Preliminary User's Guide to Version 1.0 of the SAS3D LMFBR Accident Analysis Computer Code," Argonne National Laboratory (informal document included with code) (1977).

2. S. K. Rhow, D. M. Switick, J. L. McElroy, and B. W. Joe, "An Assessment of HCDA Energetics in the CRBR Heterogeneous Reactor Core," General Electric Company report CRBRP-GEFR-00523 (December 1981).

3. W. R. Bohl, et al., "An Analysis of Transient Undercooling and Transient Overpower Accidents without Scram in the Clinch River Breeder Reactor," Argonne National Laboratory report ANL/RAS 75-29 (July 1975).

4.[a] F. E. Dunn et al., "The PRIMAR-2 Primary Loop Module for the SAS3A Code," Argonne National Laboratory report ANL/RAS 76-5 (March 1976).

5. "CRBRP Preliminary Safety Analysis Report, As Amended for the Heterogeneous Core Design," Clinch River Breeder Reactor Project document, Docket No. 50-537.

[a] Address requests for this document to: F. X. Gavigan, Director, Office of Breeder Demonstration Projects (NE-50), U.S. Department of Energy, Washington, DC 20545, Telephone (301) 353-3134.

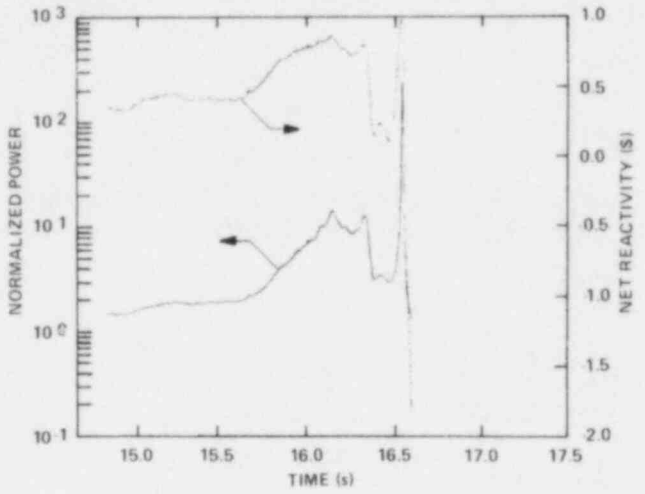

Fig. 17.
Overall power and reactivity transients during initial disruption for EOC-4 (mid-range).

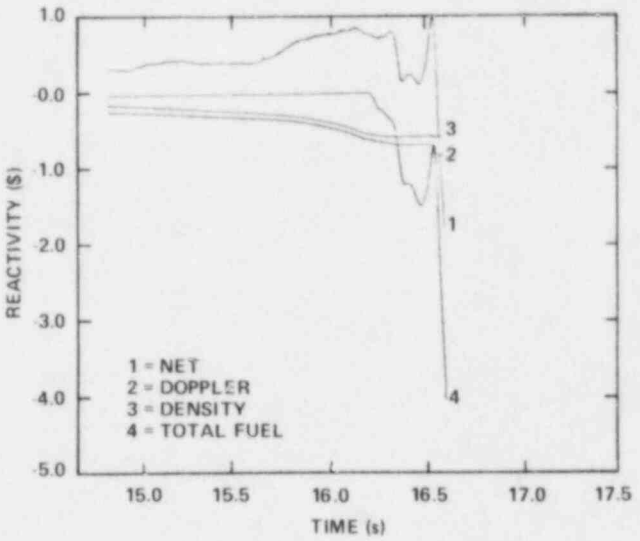

Fig. 18.
Overall component reactivity transients for EOC-4 (mid-range).

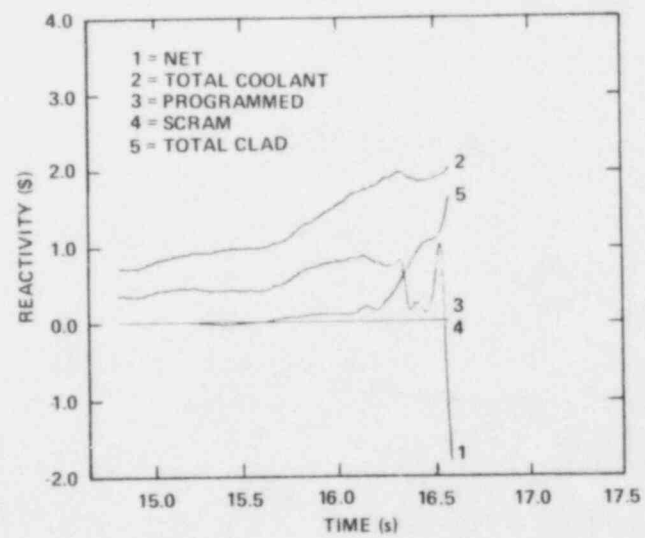

Fig. 19.
Overall component reactivity transients for EOC-4 (mid-range).

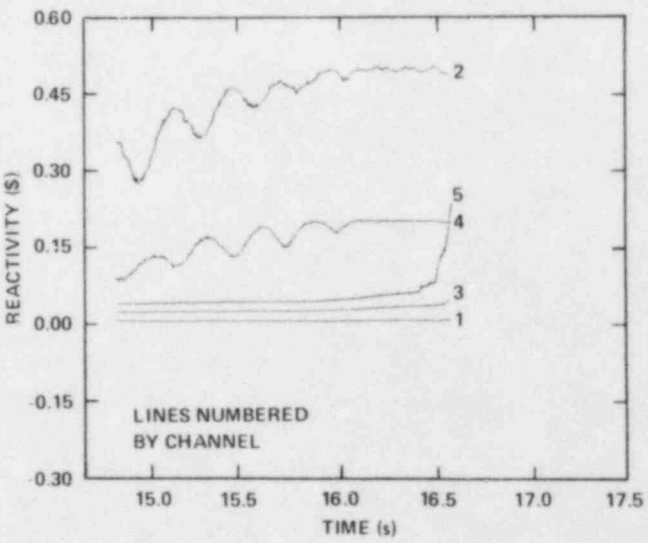

Fig. 20.
Coolant reactivity transients by channel for EOC-4 (mid-range).

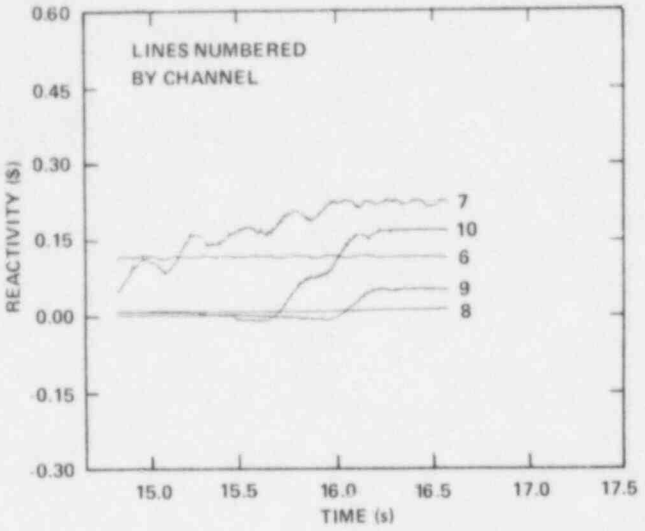

Fig. 21.
Coolant reactivity transients by channel for EOC-4 (mid-range).

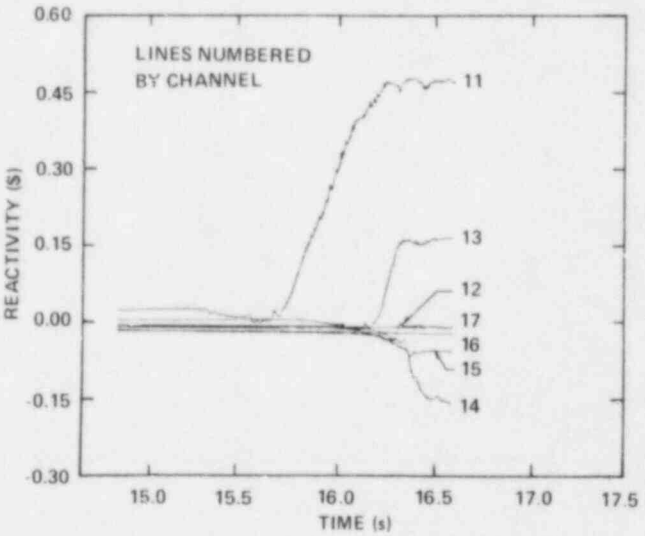

Fig. 22.
Coolant reactivity transients by channel for EOC-4 (mid-range).

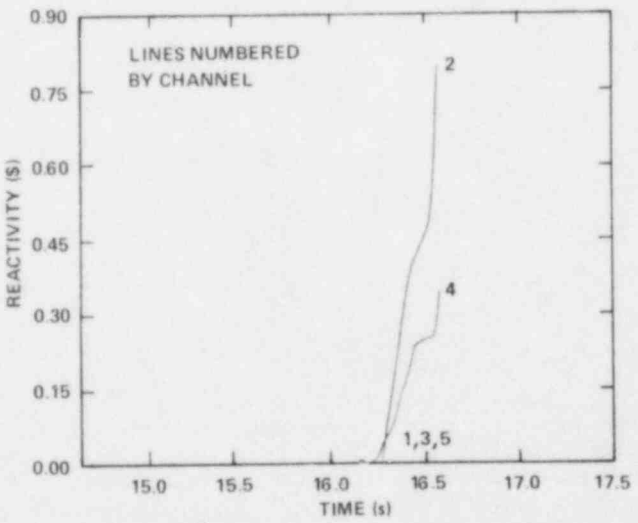

Fig. 23.
Cladding reactivity transients by channel for EOC-4 (mid-range).

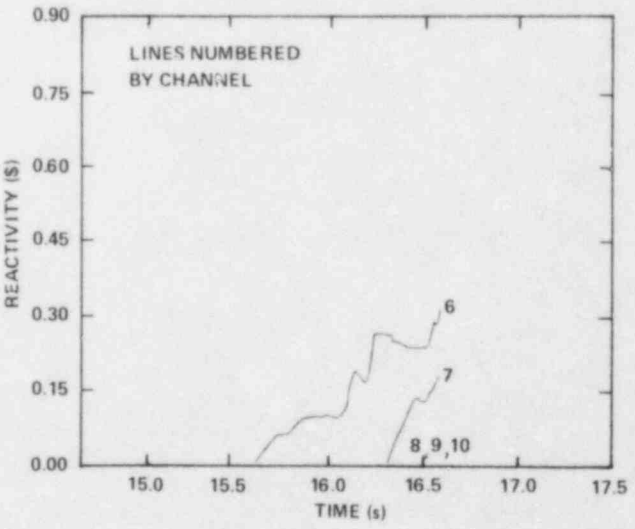

Fig. 24.
Cladding reactivity transients by channel for EOC-4 (mid-range).

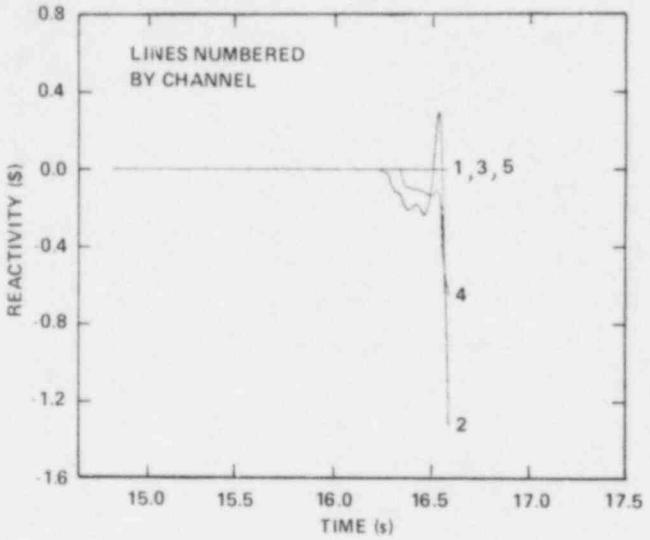

Fig. 25.
Fuel reactivity transients by channel for EOC-4 (mid-range).

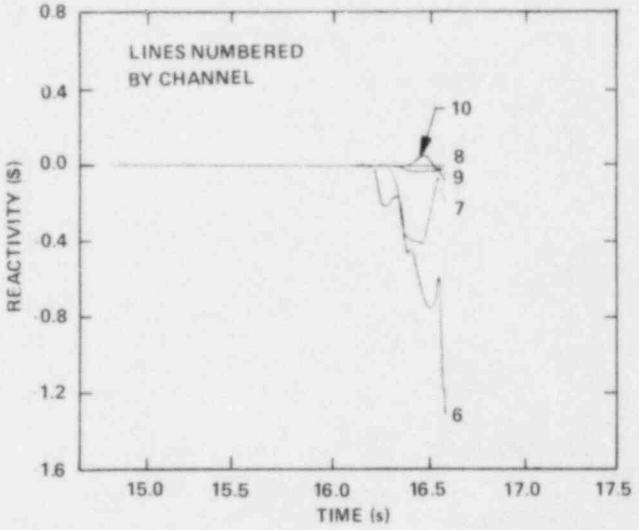

Fig. 26.
Fuel reactivity transients by channel for EOC-4 (mid-range).

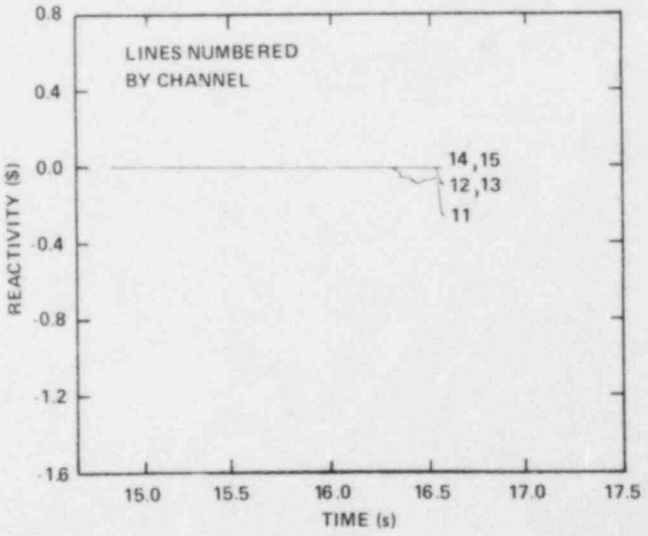

Fig. 27.
Fuel reactivity transients by channel for EOC-4 (mid-range).

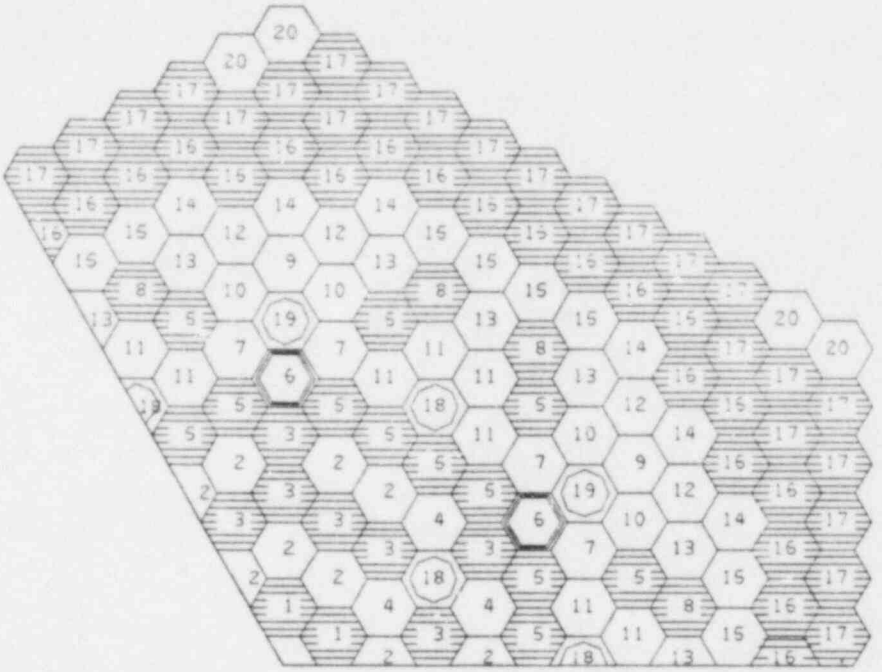

Fig. 28.
Location of channel 6 subassemblies for EOC-4 (mid-range).

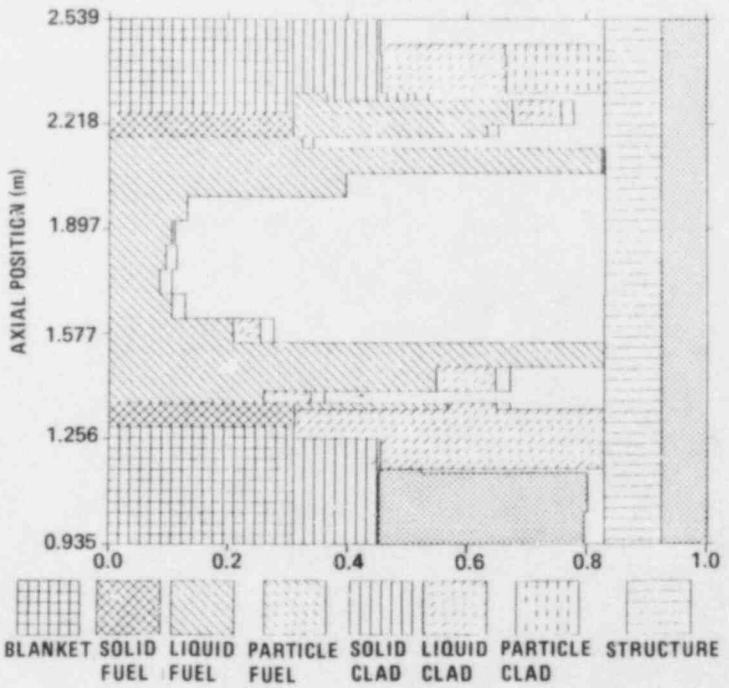

Fig. 29.
Final configuration of materials (volume fractions) in channel 6 for EOC-4 (mid-range).

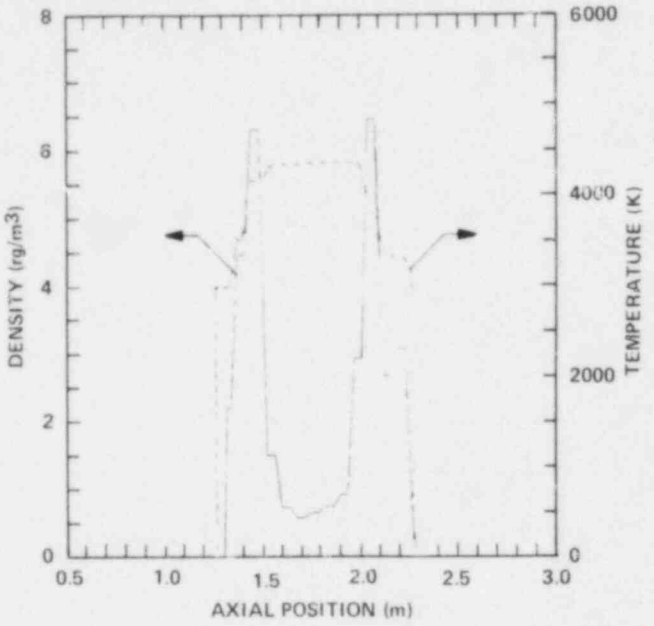

Fig. 30.
Final liquid fuel distribution and temperature in channel 6 for EOC-4 (mid-range).

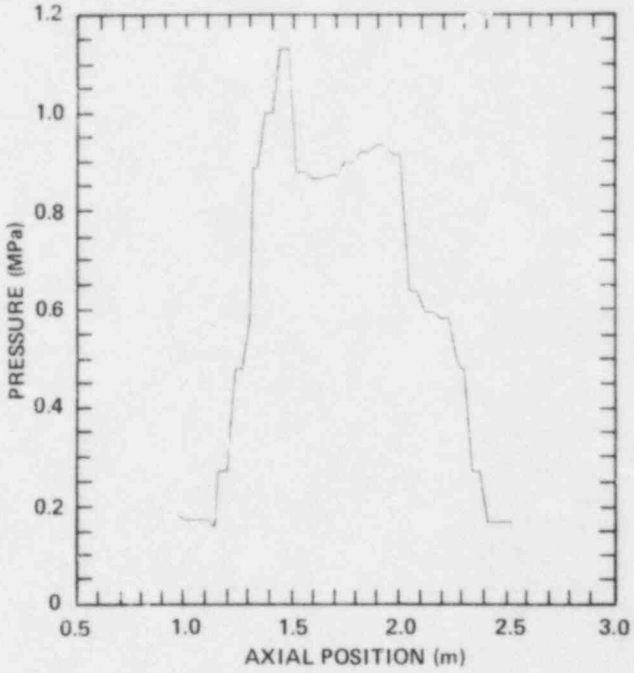

Fig. 31.
Final pressure in channel 6 for EOC-4 (mid-range).

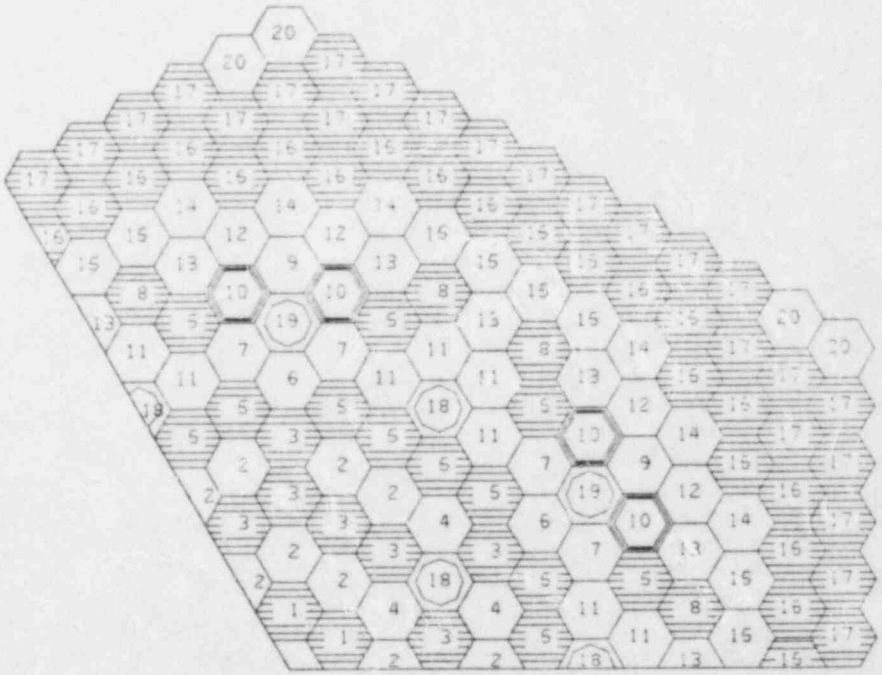

Fig. 32.
Location of channel 10 subassemblies for EOC-4 (mid-range).

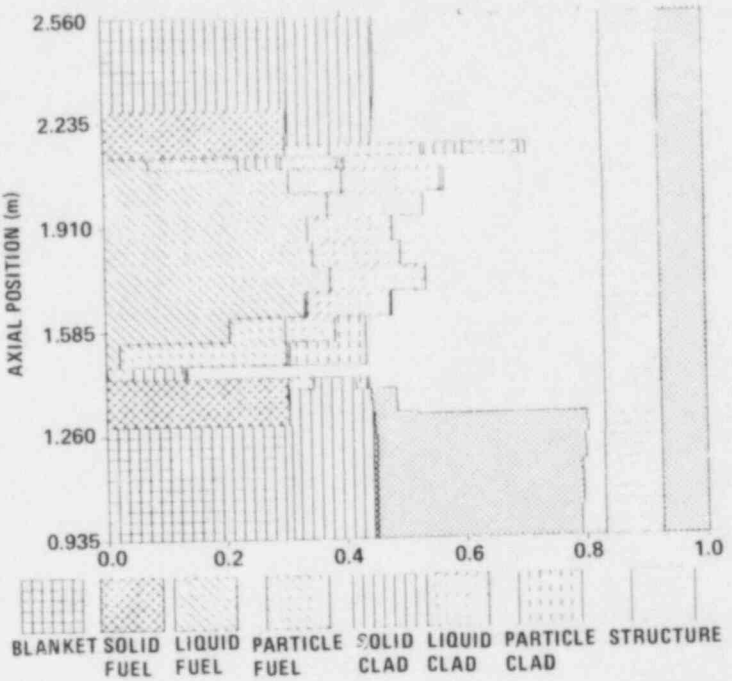

Fig. 33.
Final configuration of materials (volume fractions) in channel 10 for EOC-4 (mid-range).

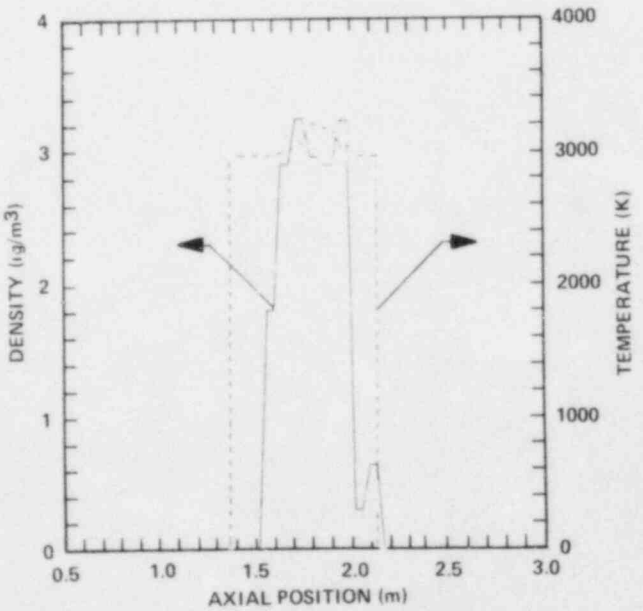

Fig. 34.
Final liquid fuel distribution and temperature in channel 10 for EOC-4 (mid-range).

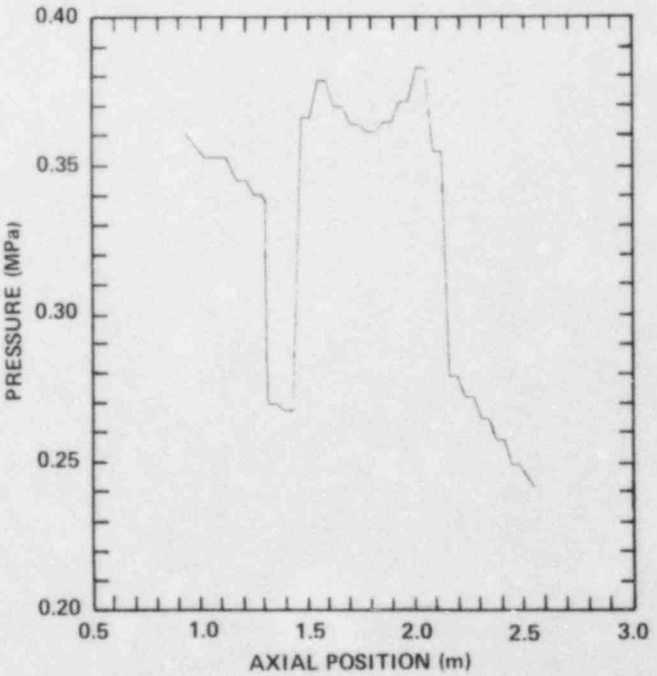

Fig. 35.
Final pressure in channel 10 for EOC-4 (mid-range).

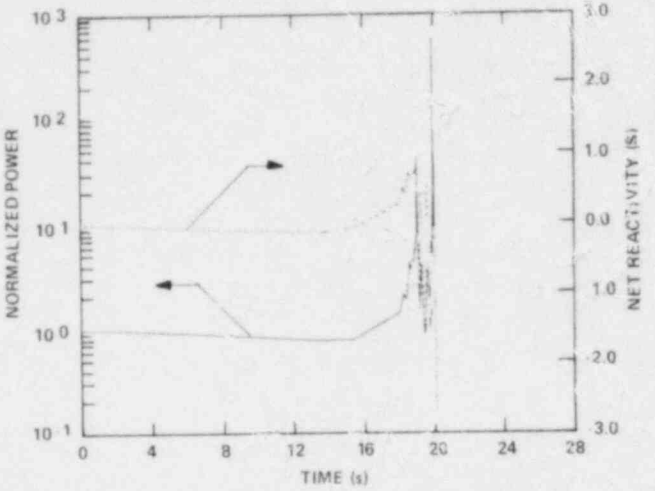

Fig. 36.
Overall power and reactivity transients for EOC-4 (slow).

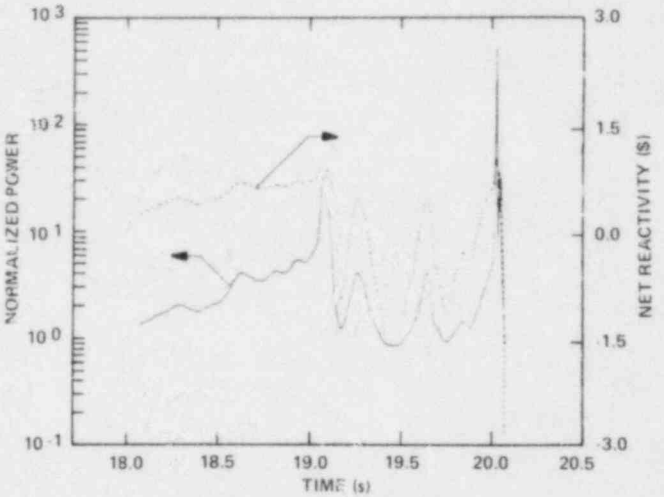

Fig. 37.
Overall power and reactivity transients during initial disruption for EOC-4 (slow).

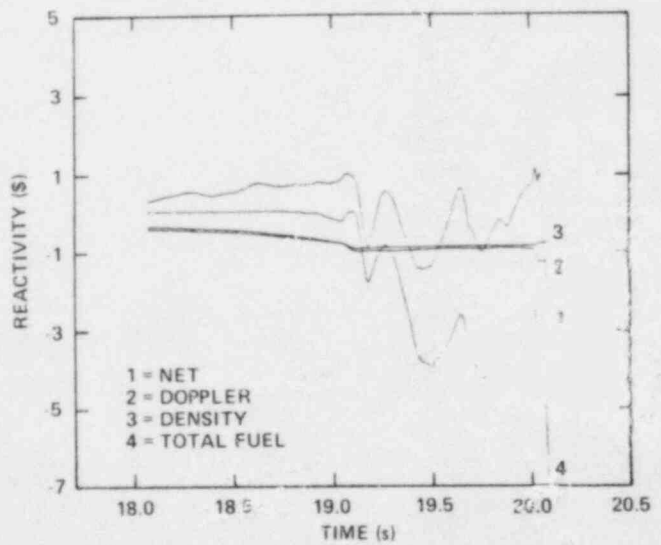

Fig. 38.
Overall component reactivity transients for EOC-4 (slow).

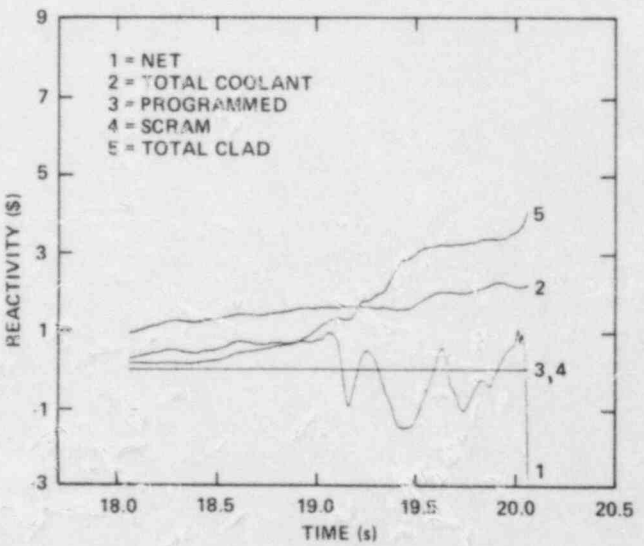

Fig. 39.
Overall component reactivity transients for EOC-4 (slow).

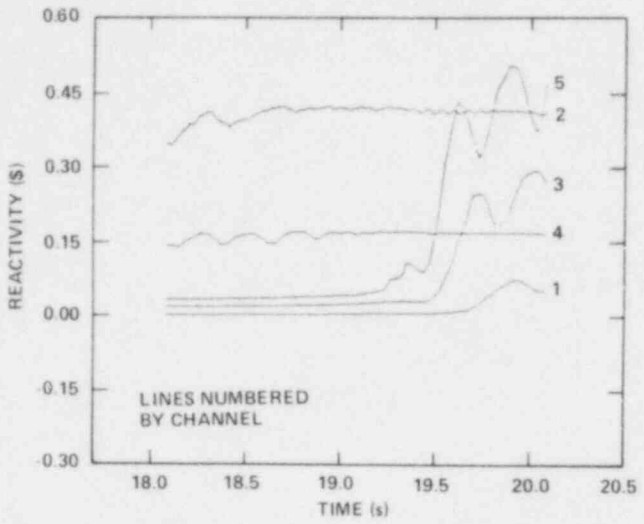

Fig. 40.
Coolant reactivity transients by channel for EOC-4 (slow).

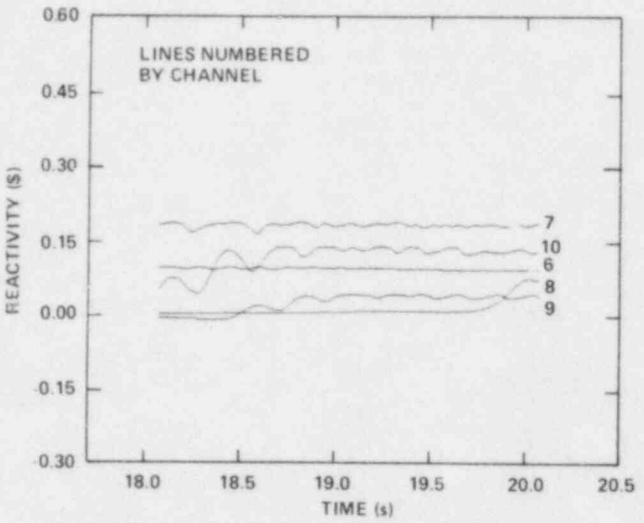

Fig. 41.
Coolant reactivity transients by channel for EOC-4 (slow).

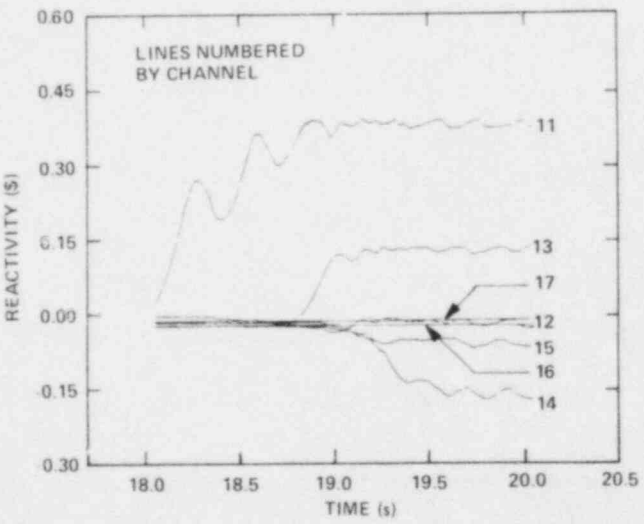

Fig. 42.
Coolant reactivity transients by channel for EOC-4 (slow).

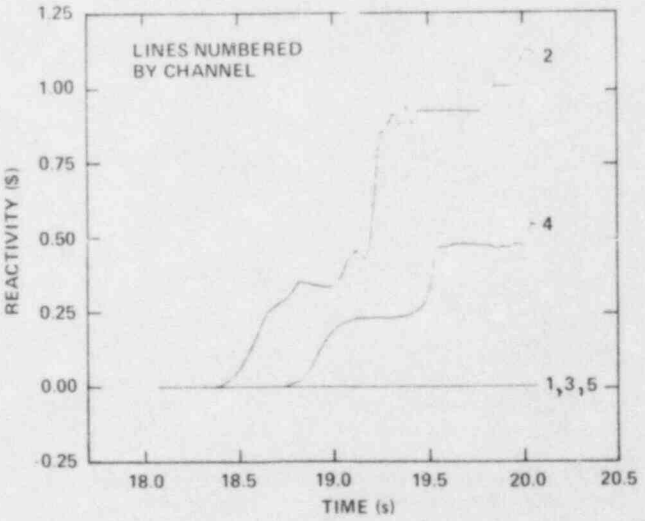

Fig. 43.
Cladding reactivity transients by channel for EOC-4 (slow).

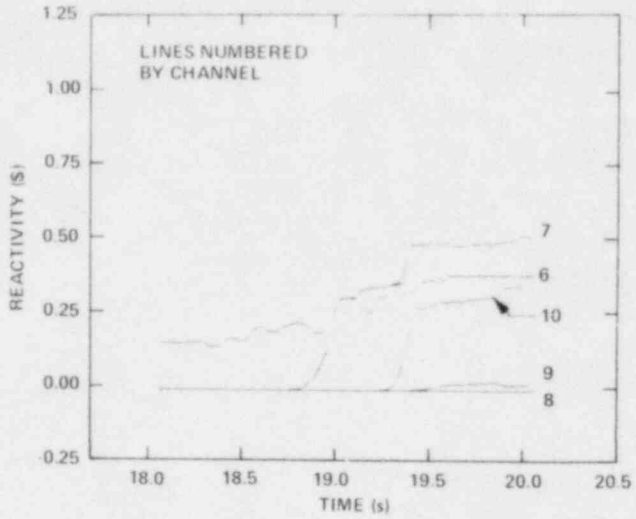

Fig. 44.
Cladding reactivity transients by channel for EOC-4 (slow).

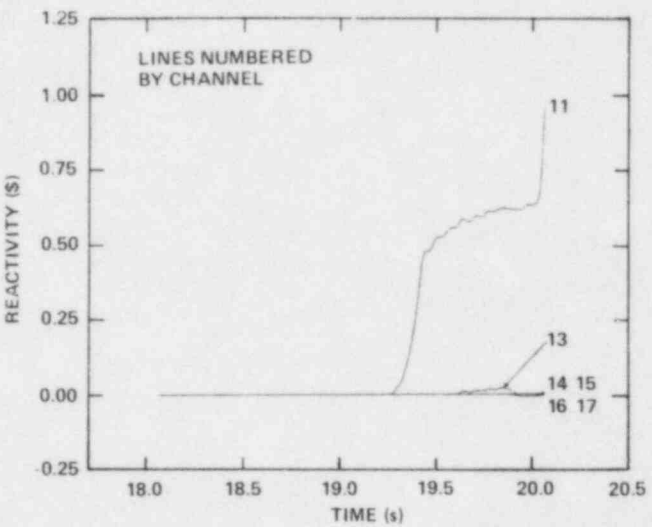

Fig. 45.
Cladding reactivity transients by channel for EOC-4 (slow).

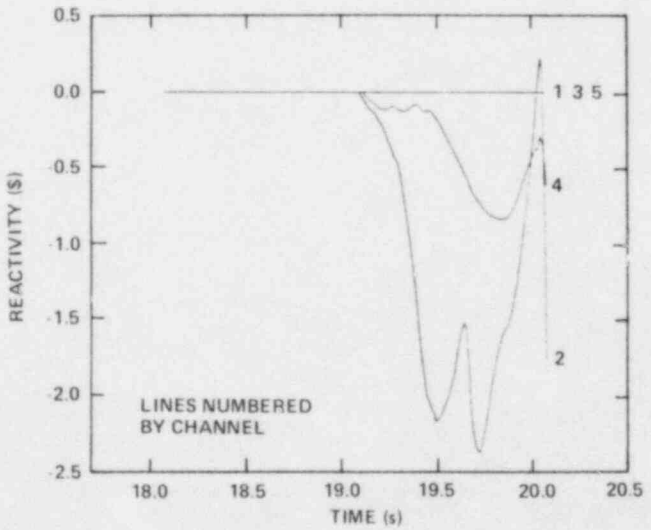

Fig. 46.
Fuel reactivity transients by channel for EOC-4 (slow).

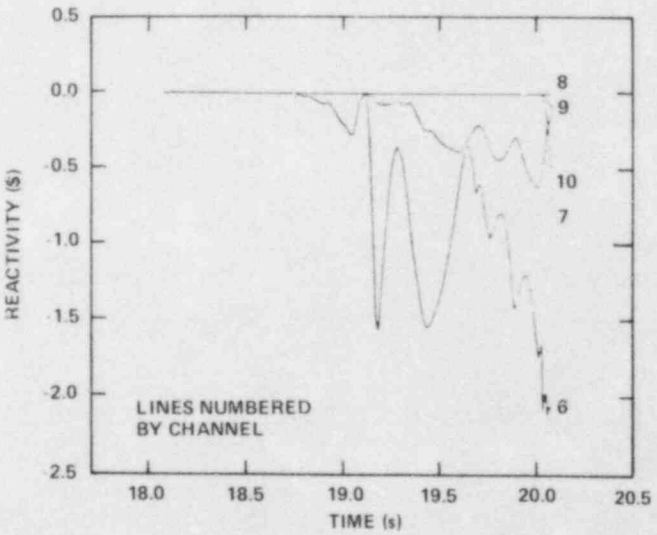

Fig. 47.
Fuel reactivity transients by channel for EOC-4 (slow).

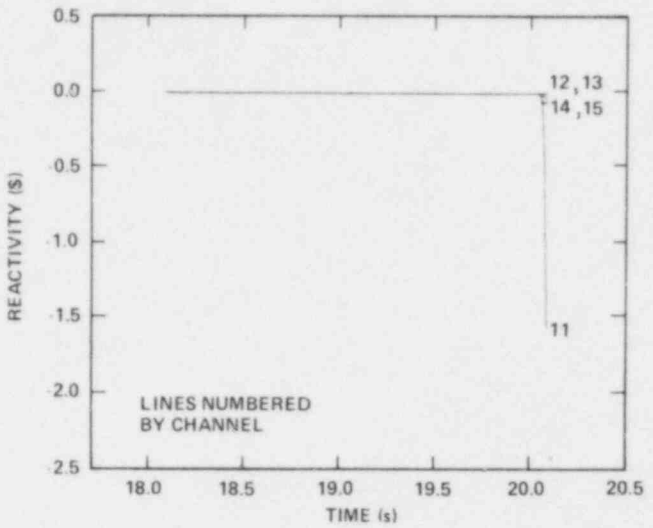

Fig. 48.
Fuel reactivity transients by channel for EOC-4 (slow).

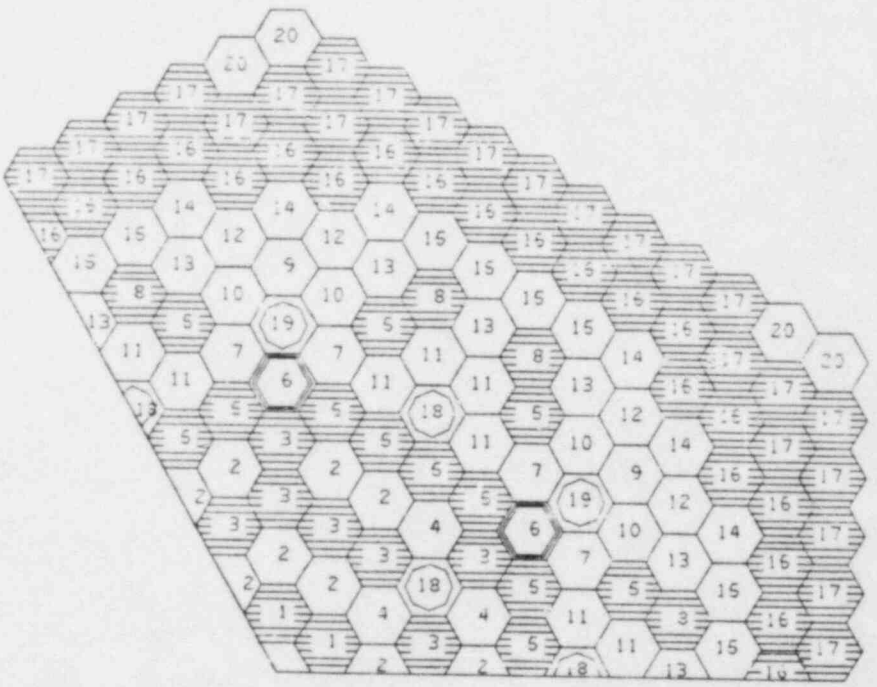

Fig. 49.
Location of channel 6 subassemblies for EOC-4 (slow).

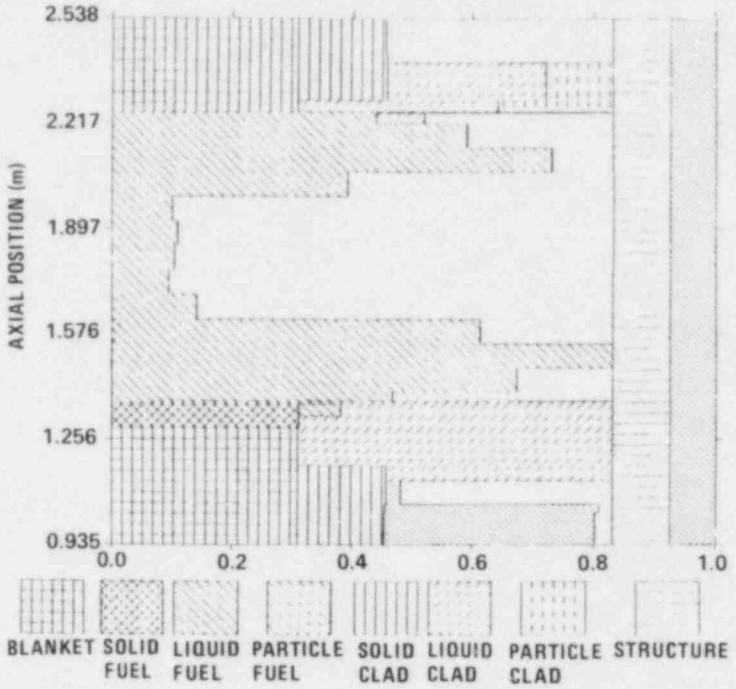

Fig. 50.
Final configuration of materials (volume fractions) in channel 6 for EOC-4 (slow).

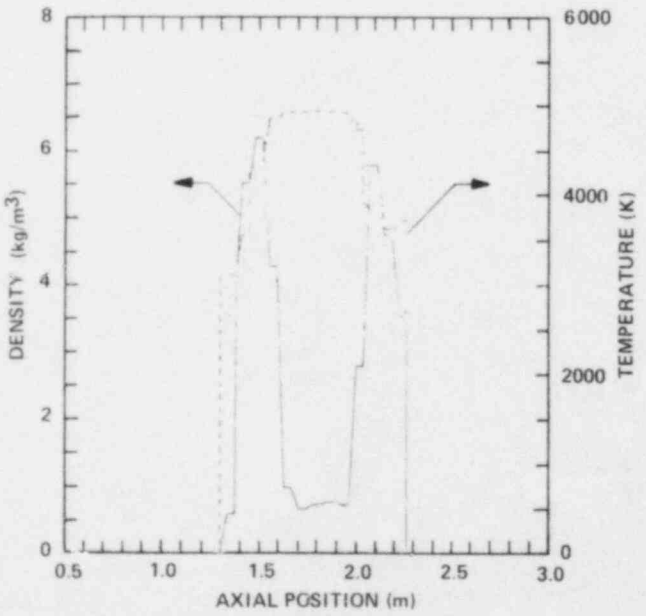

Fig. 51.
Final liquid fuel distribution and temperature in channel 6 for EOC-4 (slow).

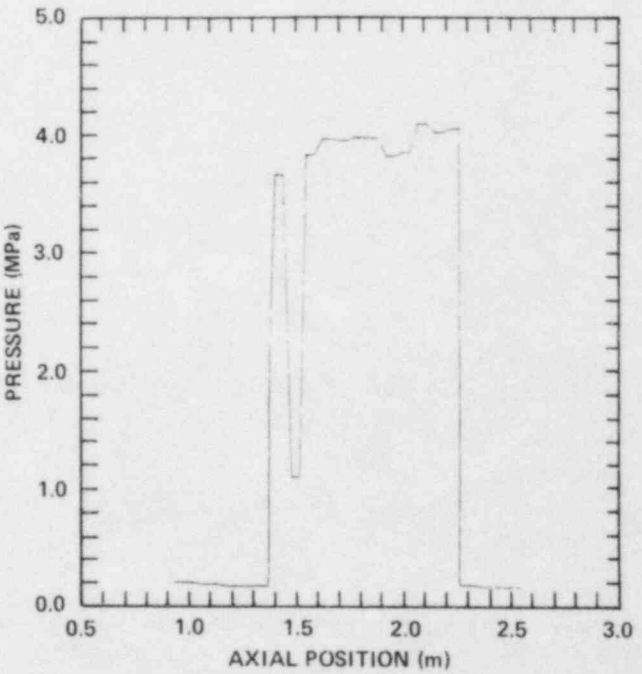

Fig. 52.
Final pressure in channel 6 for EOC-4 (slow).

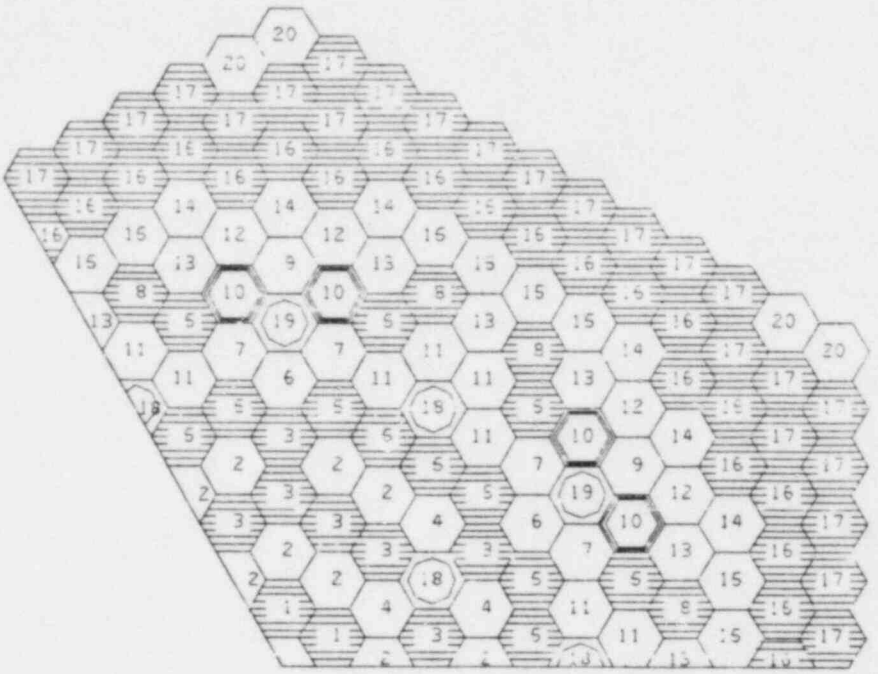

Fig. 53.
Location of channel 10 subassemblies for EOC-4 (slow).

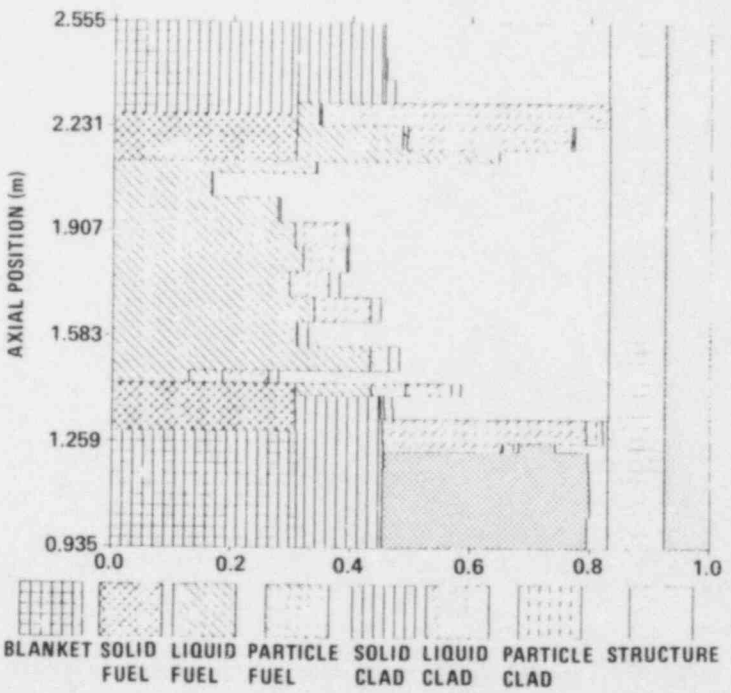

Fig. 54.
Final configuration of materials (volume fractions) in channel 10 for EOC-4 (slow).

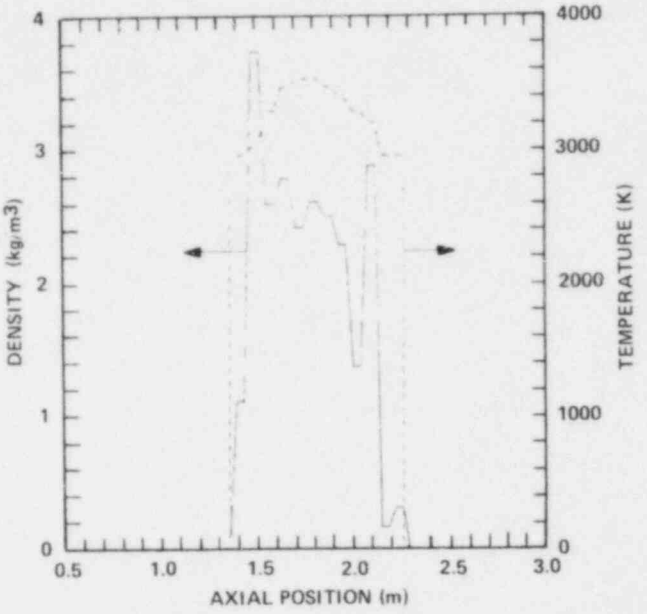

Fig. 55.
Final liquid fuel distribution and temperature in channel 10 for EOC-4 (slow).

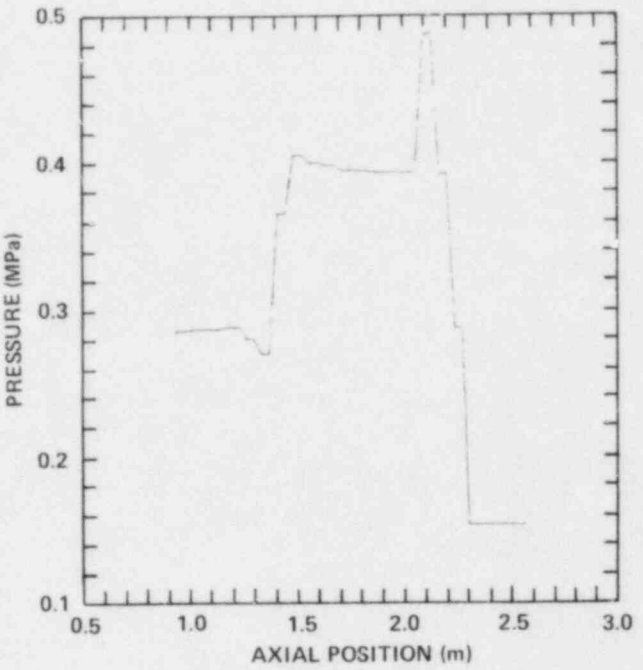

Fig. 56.
Final pressure in channel 10 for EOC-4 (slow).

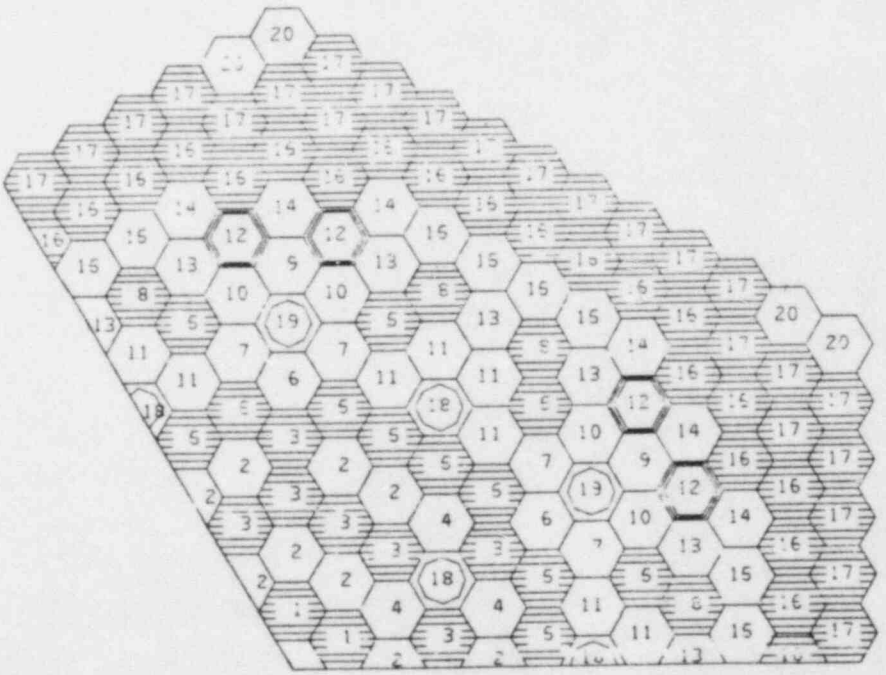

Fig. 57.
Location of channel 12 subassemblies for EOC-4 (slow).

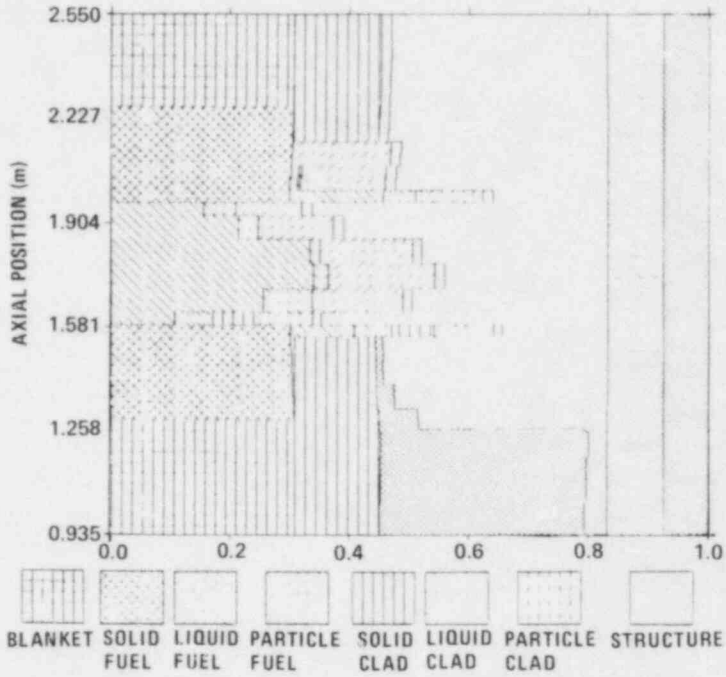

Fig. 58.
Final configuration of materials (volume fractions) in channel 12 for EOC-4 (slow).

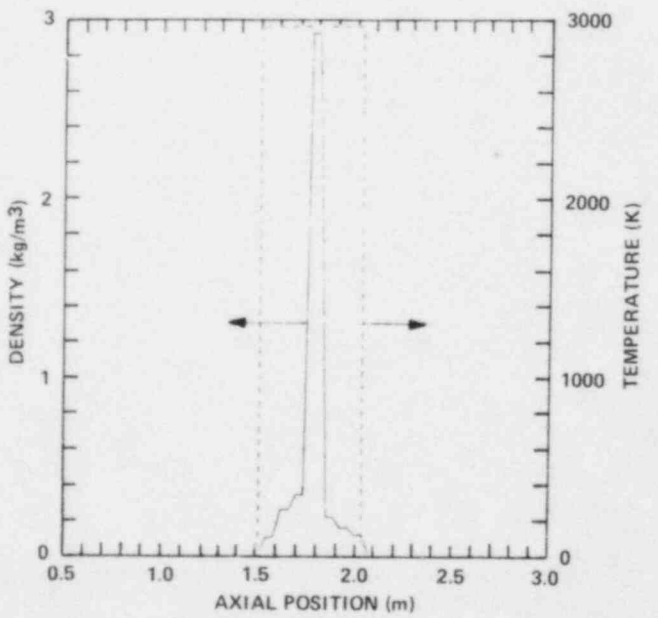

Fig. 59.
Final liquid fuel distribution and temperature in channel 12 for EOC-4 (slow).

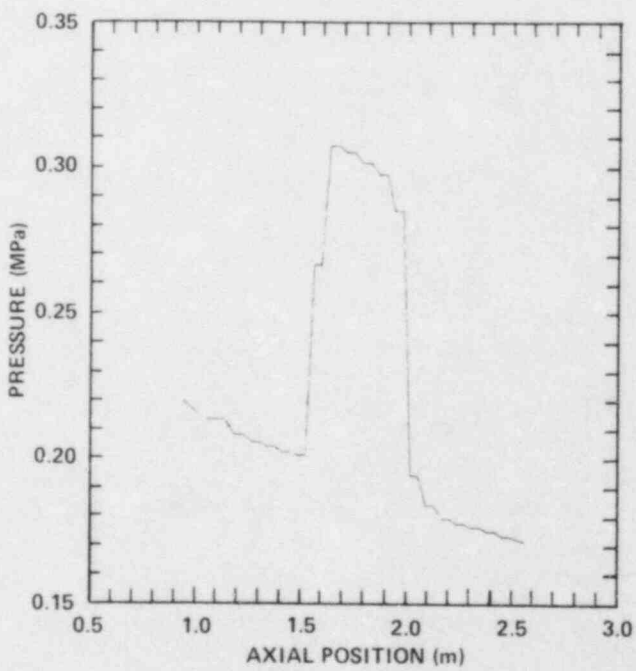

Fig. 60.
Final pressure in channel 12 for EOC-4 (slow).

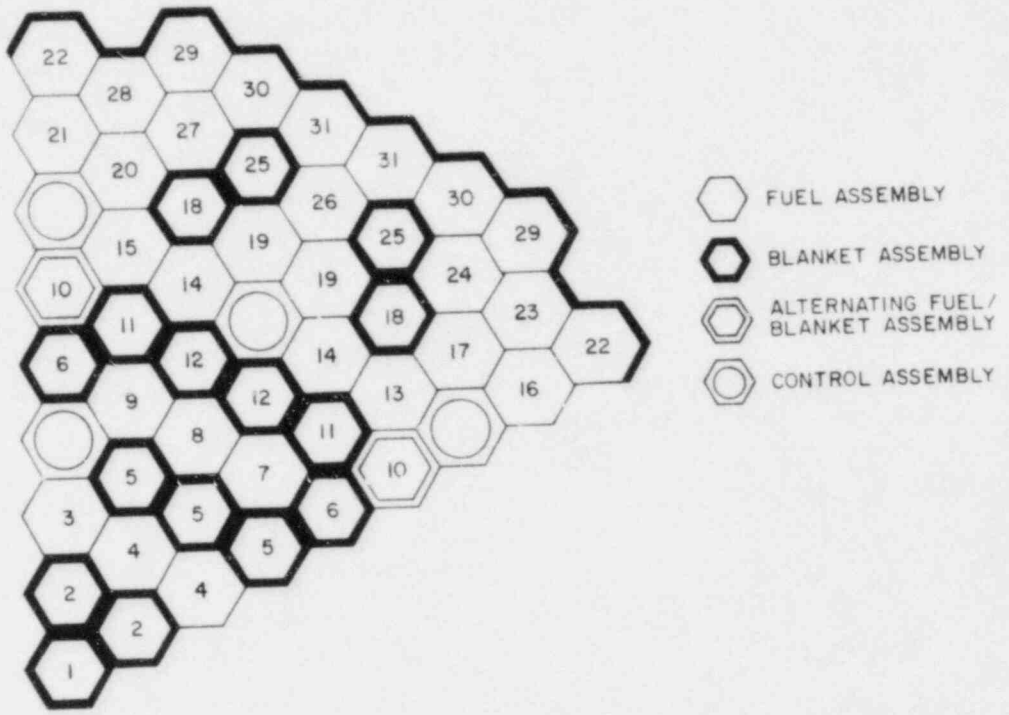

Fig. 61.
Subassembly assignments to SAS3D channels for the EOC-3 analysis.

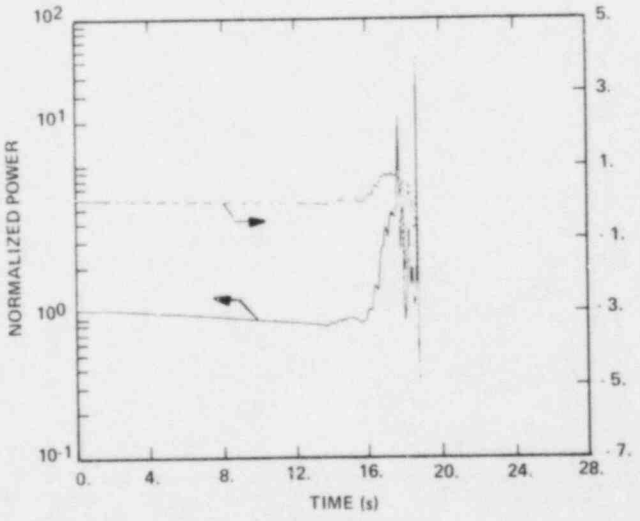

Fig. 62.
Overall power and reactivity transients for EOC-1.

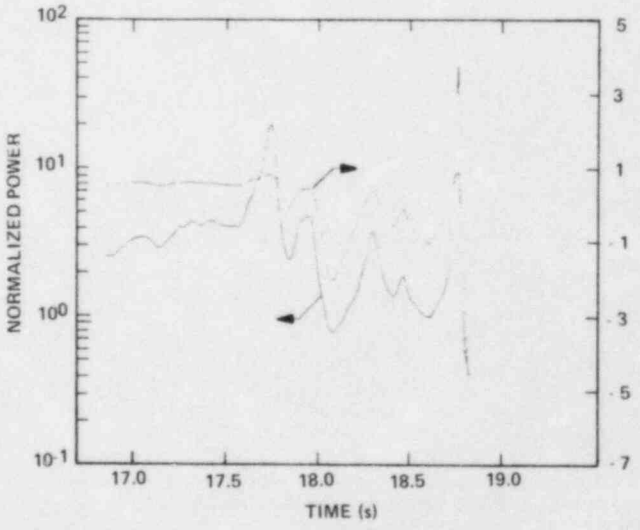

Fig. 63.
Overall power and reactivity transients during initial disruption for EOC-3.

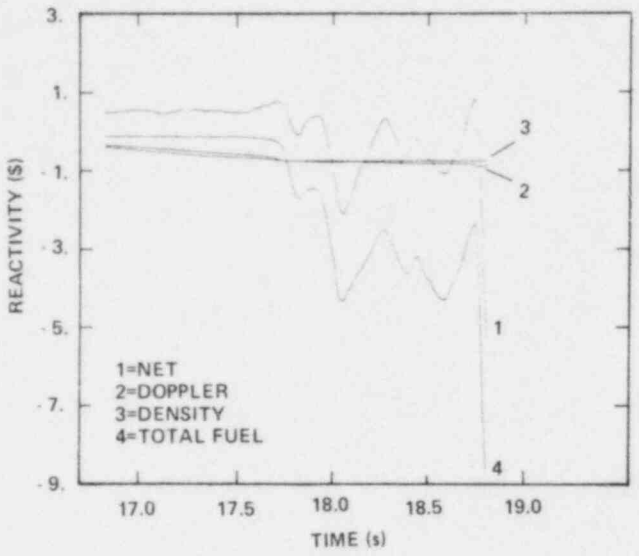

Fig. 64.
Overall component reactivity transients for EOC-3.

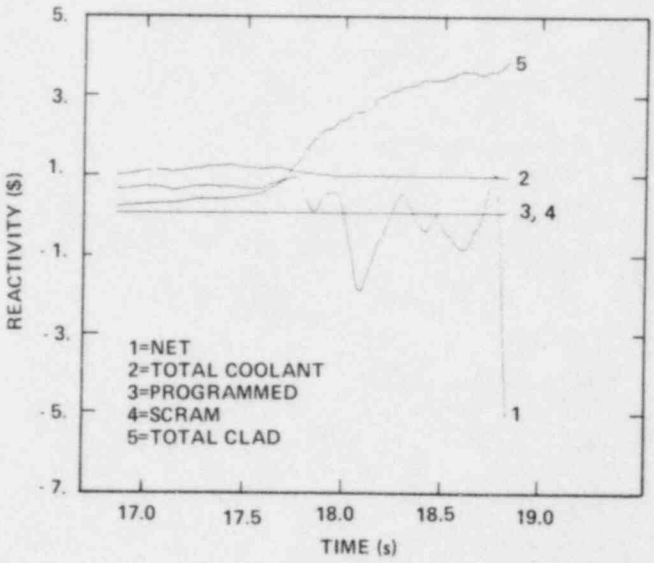

Fig. 65.
Overall component reactivity transients for EOC-3.

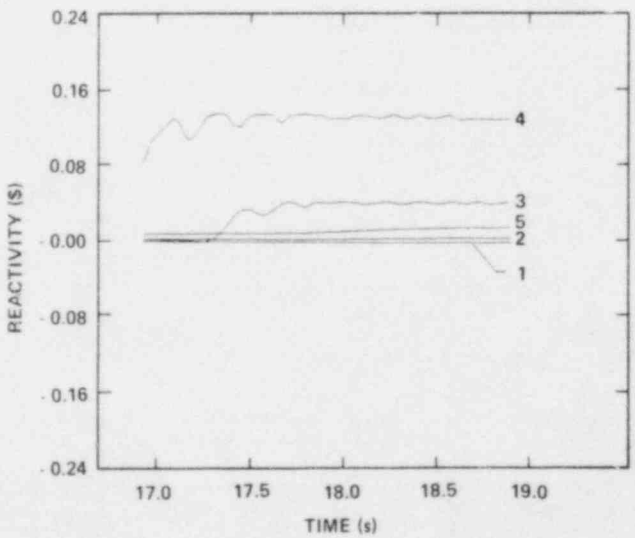

Fig. 66.
Coolant reactivity transients by channel for EOC-3.

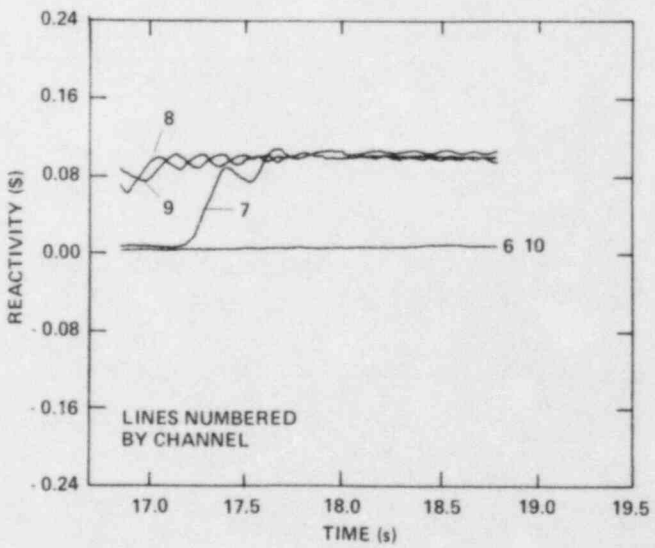

Fig. 67.
Coolant reactivity transients by channel for EOC-3.

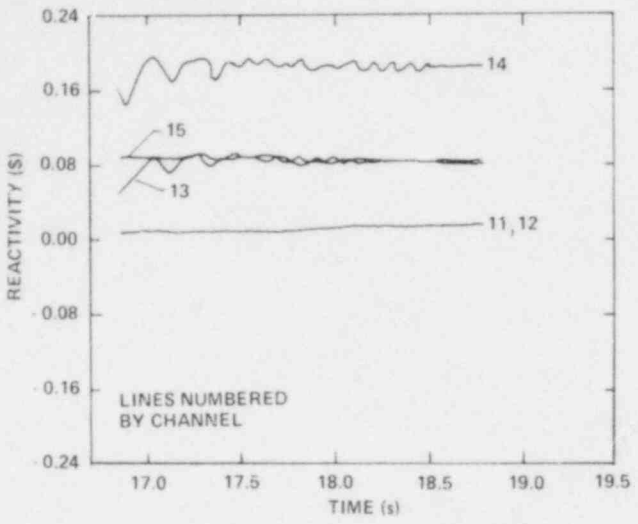

Fig. 68.
Coolant reactivity transients by channel for EOC-3.

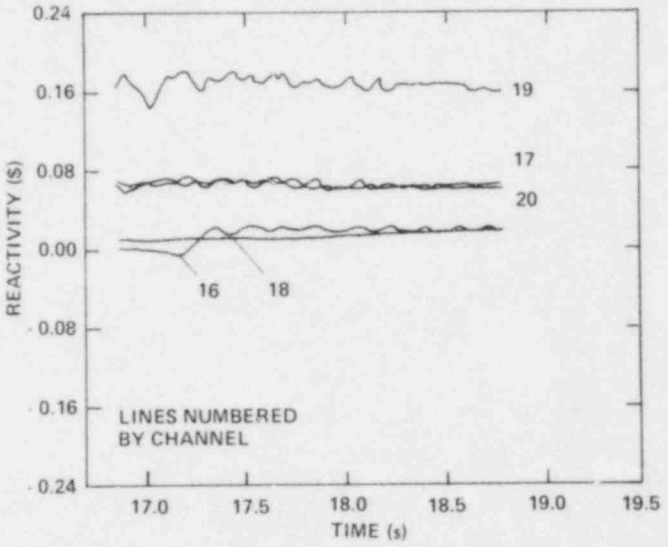

Fig. 69.
Coolant reactivity transients by channel for EOC-3.

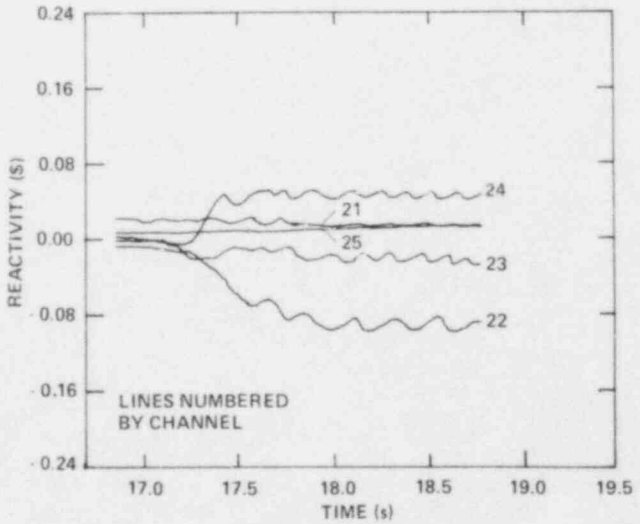

Fig. 70.
Coolant reactivity transients by channel for EOC-3.

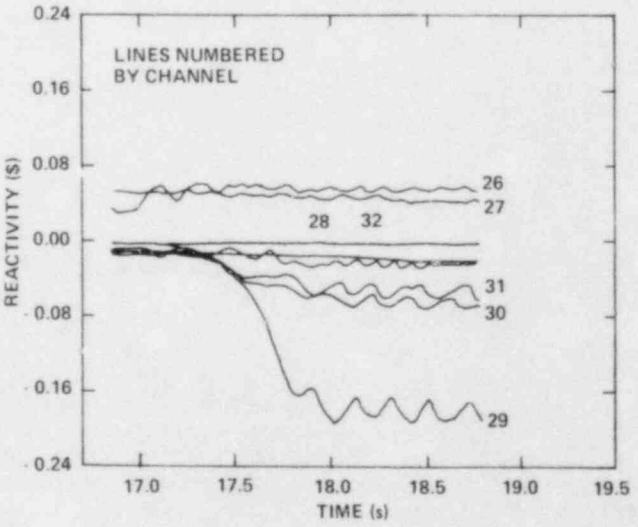

Fig. 71.
Coolant reactivity transients by channel for EOC-3.

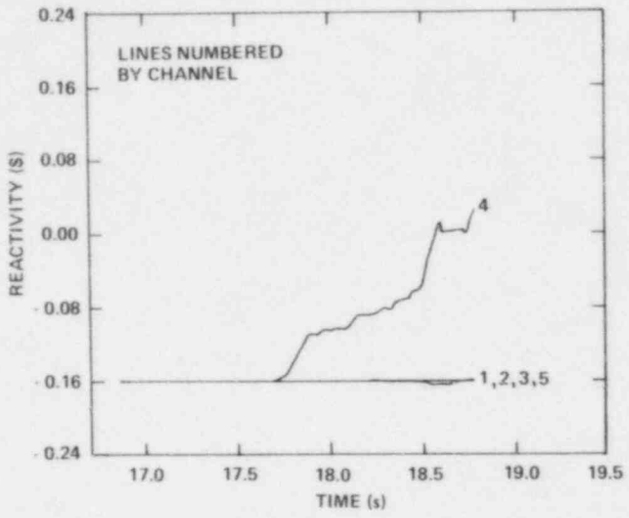

Fig. 72.
Cladding reactivity transients by channel for EOC-3.

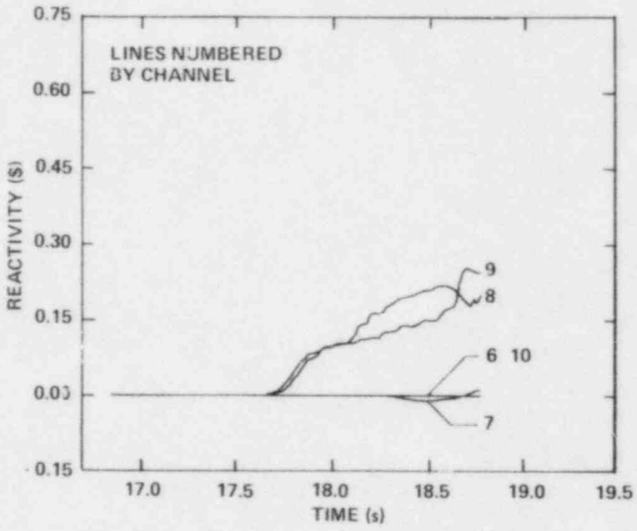

Fig. 73.
Cladding reactivity transients by channel for EOC-3.

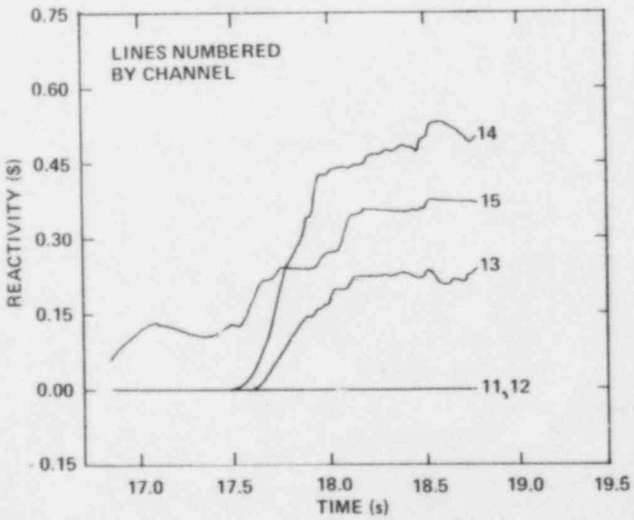

Fig. 74.
Cladding reactivity transients by channel for EOC-3.

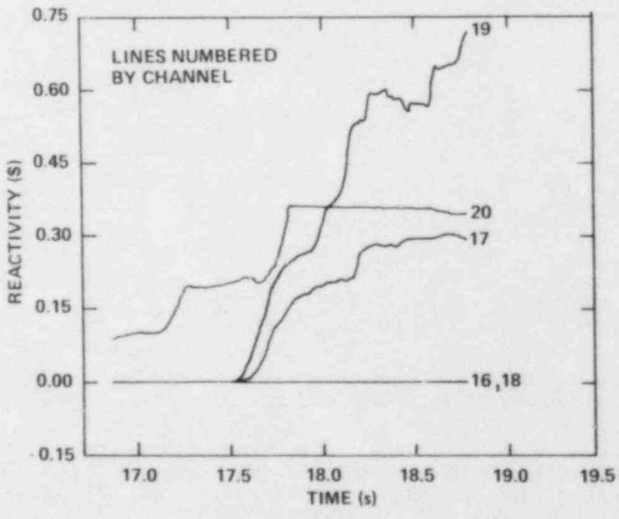

Fig. 75.
Cladding reactivity transients by channel for EOC-3.

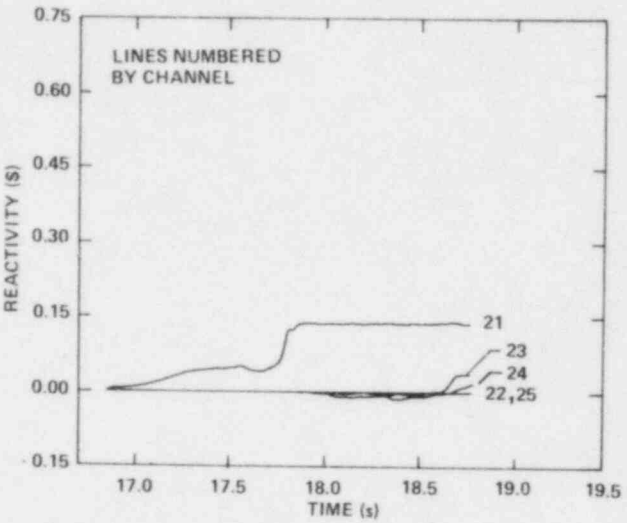

Fig. 76.
Cladding reactivity transients by channel for EOC-3.

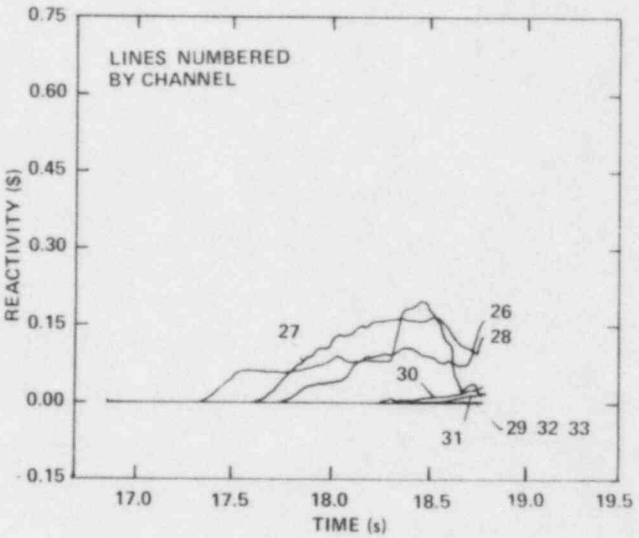

Fig. 77.
Cladding reactivity transients by channel for EOC-3.

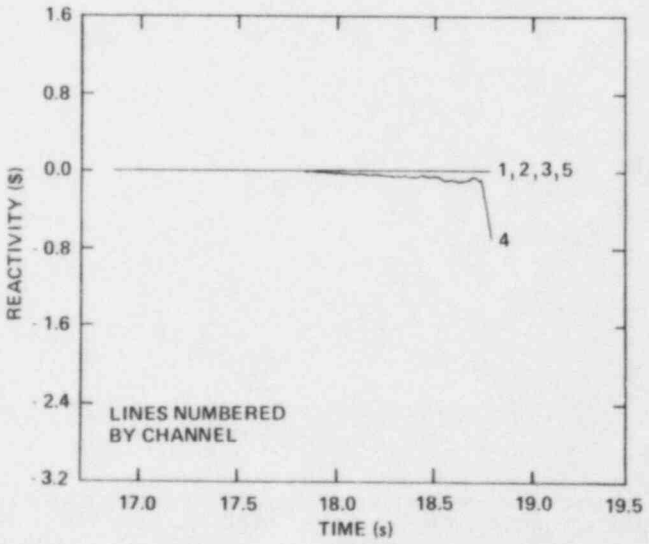

Fig. 78.
Fuel reactivity transients by channel for EOC-3.

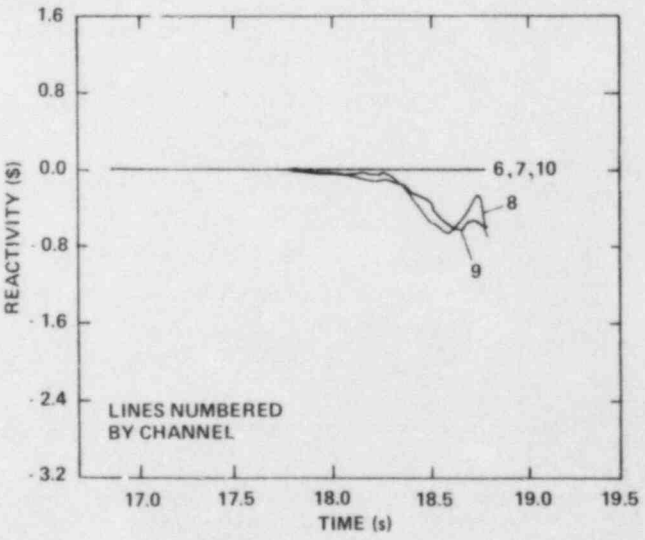

Fig. 79.
Fuel reactivity transients by channel for EOC-3.

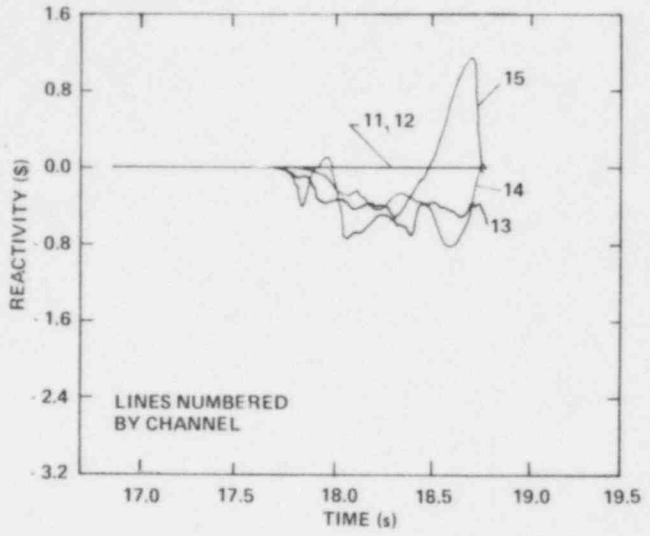

Fig. 80.
Fuel reactivity transients by channel for EOC-3.

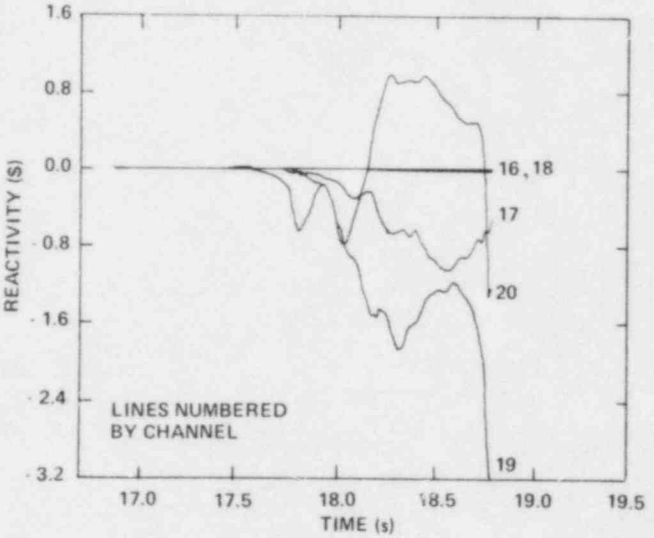

Fig. 81.
Fuel reactivity transients by channel for EOC-3.

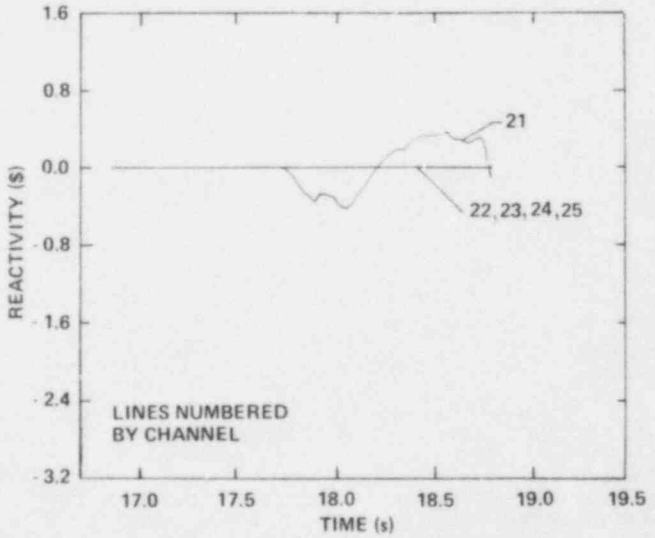

Fig. 82.
Fuel reactivity transients by channel for EOC-3.

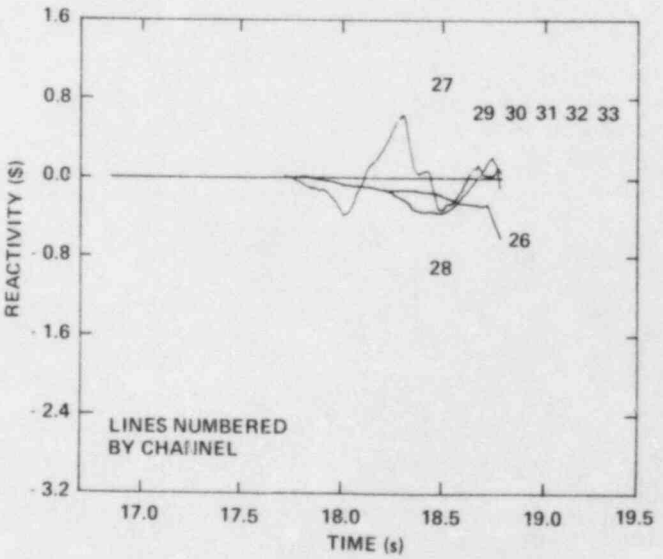

Fig. 83.
Fuel reactivity transients by channel for EOC-3.

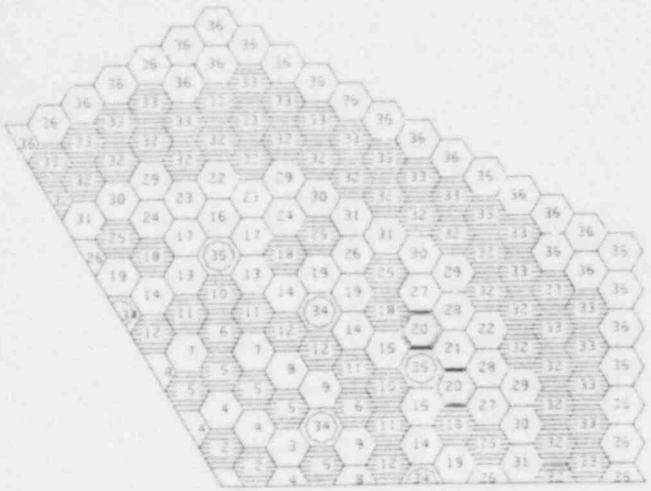

Fig. 84.
Location of channel 20 subassemblies for EOC-3.

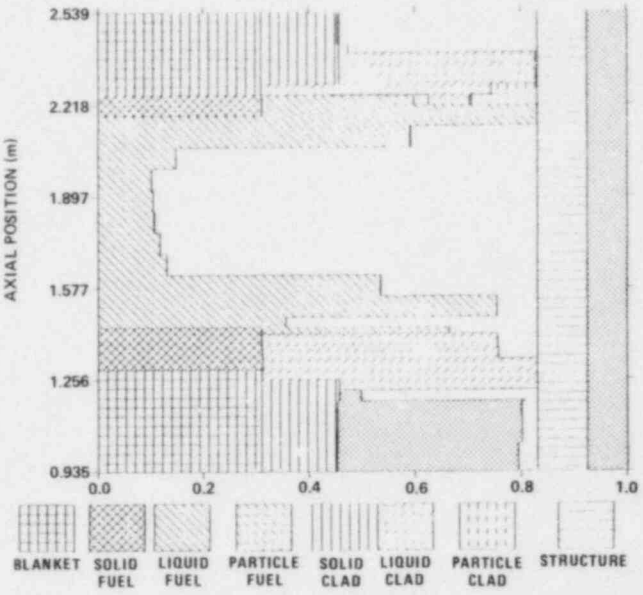

Fig. 85.
Final configuration of materials (volume fractions) in channel 20 for EOC-3.

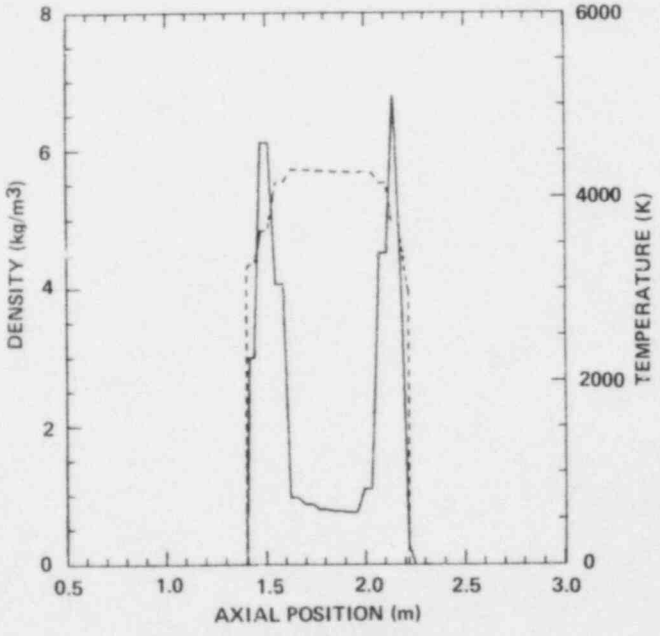

Fig. 86.
Final liquid fuel distribution and temperature in channel 20 for EOC-3.

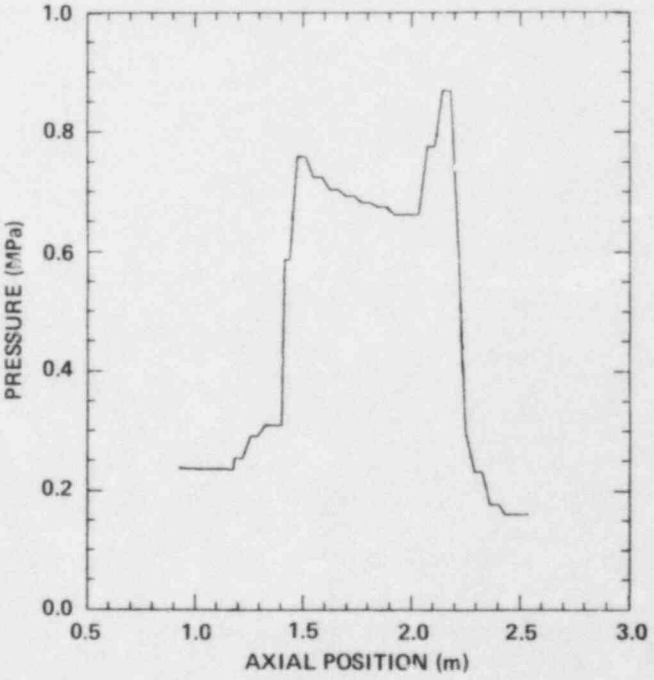

Fig. 87.
Final pressure in channel 20 for EOC-3.

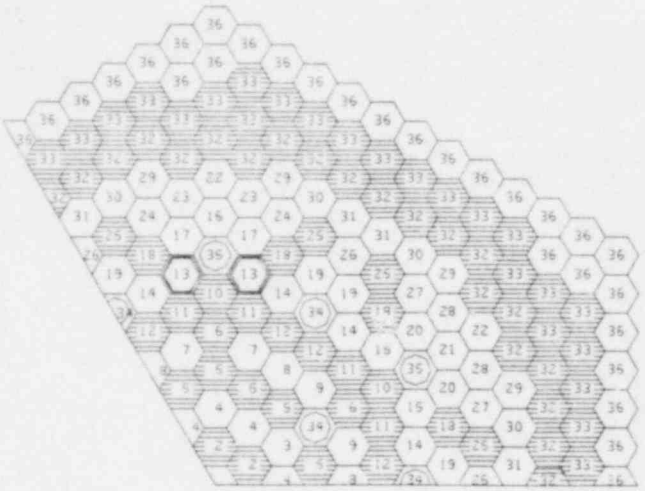

Fig. 88.
Location of channel 13 subassemblies for EOC-3.

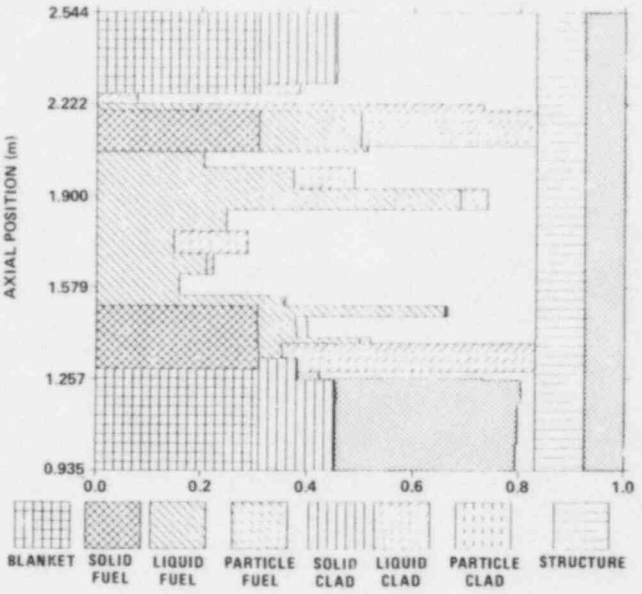

Fig. 89.
Final configuration of materials (volume fractions) in channel 13 for EOC-3.

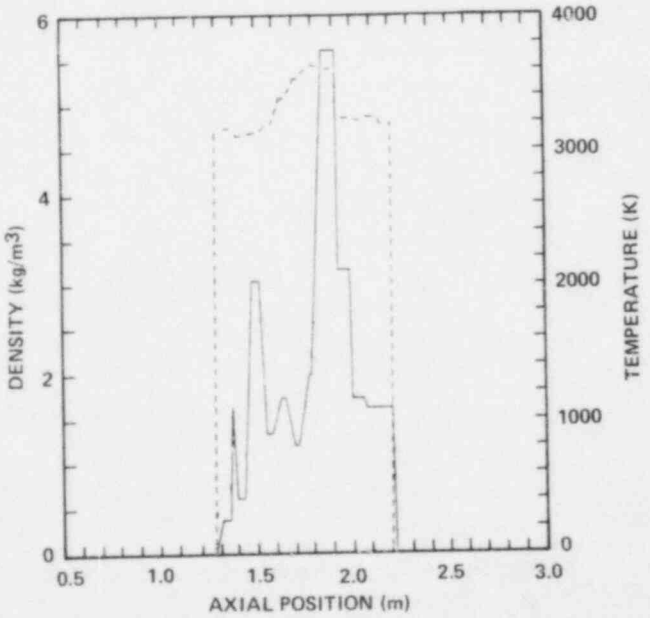

Fig. 90.
Final liquid fuel distribution and temperature in channel 20 for EOC-3.

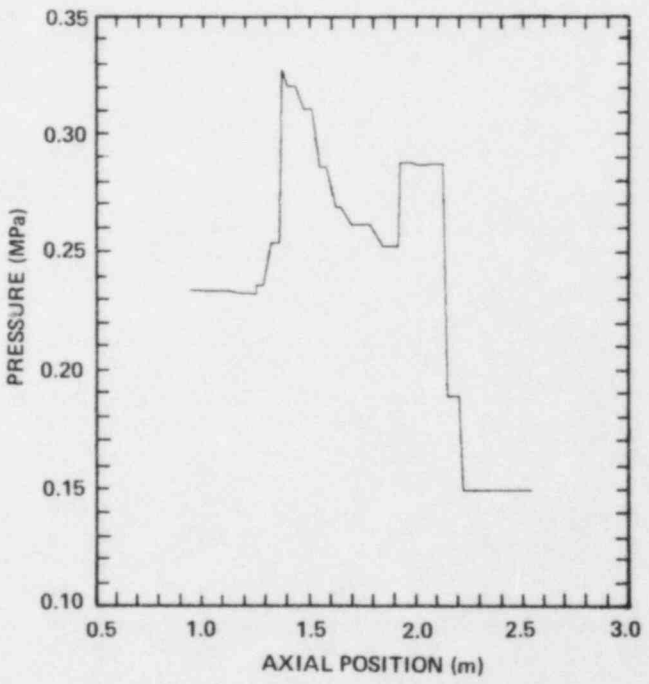

Fig. 91.
Final pressure in channel 20 for EOC-3.

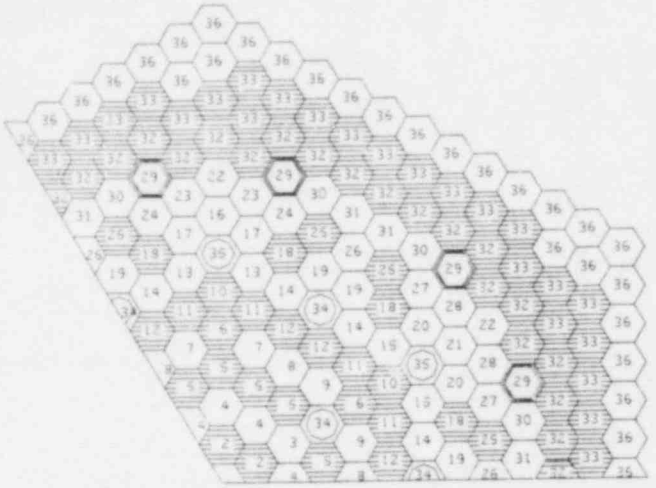

Fig. 92.
Location of channel 29 subassemblies for EOC-3.

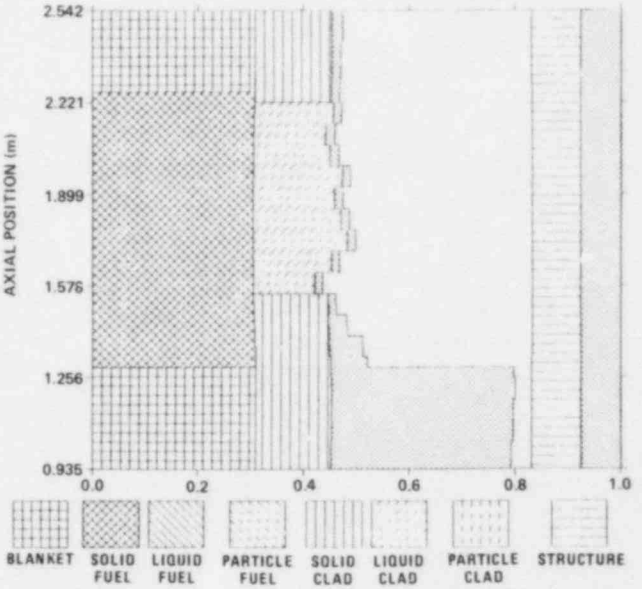

Fig. 93.
Final configuration of materials (volume fractions) in channel 29 for EOC-3.

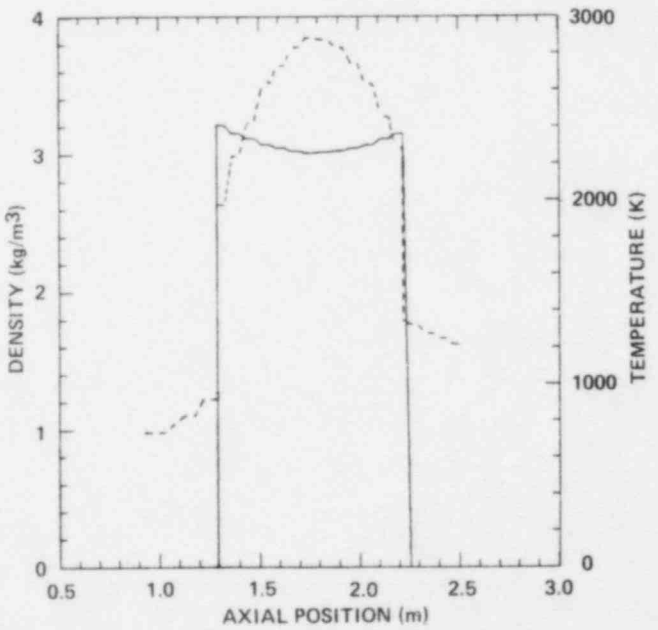

Fig. 94.
Final liquid fuel distribution and temperature in channel 29 for EOC-3.

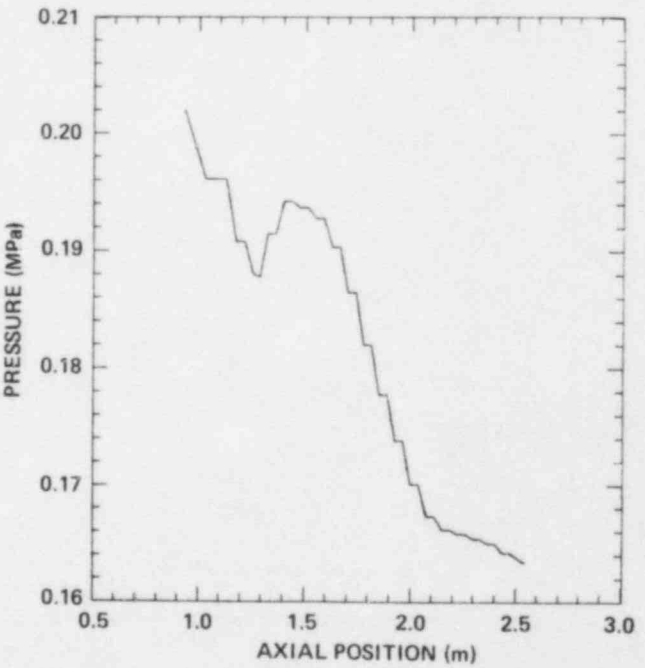

Fig. 95.
Final pressure in channel 29 for EOC-3.

II.4. PLENUM FISSION GAS COMPACTION

1. Objectives and Overview

A mechanism for rapid fuel compaction [1] during the initial phases of disruption is possible due to the high-pressure plenum fission gases that accumulate during irradiation. These pressures may build up to approximately 3 MPa during normal operation and to even higher levels during the accident. Following sodium voiding and cladding melting, fuel disruption occurs in the subassemblies with the highest power-to-flow ratio. Upon disruption, the fuel column, already under compression due to the plenum fission gases, becomes susceptible to axial compaction. The geometry is illustrated in Figure 1. The top portion of the severed cladding cannot withdraw upward due to the physical constraints at the subassembly exit. Rather, it forms a "gun barrel" through which the fission gas pressures may eject forcefully downwards the upper axial blanket pellets together with any nondisrupted portion of the fuel column. The resulting increases in reactivity and power accelerate the accident, causing an avalanche of additional fuel pin disruptions and compactions. The concern of a potentially autocatalytic behavior and high energetics is obvious.

Clearly, substantial blanket pellet/cladding mechanical interaction could strongly interfere and might even mitigate this compaction mechanism. However, there is no basis for claiming such behavior. Also, the rapid dissipation by blowdown of the plenum pressure before fuel disruption could help alleviate this concern. This mitigating mechanism may be evaluated analytically.

The Applicant considered this energetic mechanism in response [2] to our Question #3 (see Table 2 of Section I), and concluded that an energetic outcome would not be expected. This result was based on SAS3D analyses that indicated gas blowdown before fuel disruption. We do not agree with this assessment.

2. Key Parameters

The key parameters affecting such a sequence of events are summarized in Table 1. The initial plenum fission gas pressure is a function of the fuel burnup. However, due to the gas blowdown following cladding failure (typical time constants for associated pressure decay are estimated to be in the range of 0.5 to 1.5 s), only a fraction of this pressure would be available

for fuel compaction upon disruption of the fuel column. This delay between cladding failure and fuel motion is in turn affected by a number of parameters as listed in Table 1. Finally, the compaction potential would depend on the degree of friction between the intact upper portion of the cladding and the sliding pellets.

TABLE 1
KEY PARAMETERS FOR THE ASSESSMENT PLENUM FISSION GAS COMPACTION

- Stored Fission Gas Plenum Pressure
- Timing Between Clad Failures & Fuel Melting
  - Sodium Void Worths and Voiding Rates
  - Clad Failures and Relocation Rates
  - Relocation Trends of Disrupted Fuel
- Pellet/Cladding Friction

The variation of the plenum gas pressure with burnup is shown in Figure 2. We observe that reasonably high pressures dominate for nearly one-half of the fuel period. The mass of retained fission gases accumulated during irradiation also is shown in the same figure. We note that within the relative short exposure of 25-50 days the fuel is reasonably "gasee" such that dispersal (as indicated in TREAT experiments L6 and L7) rather than slumping would be expected upon disruption. We conclude that the end-of-cycle range of the spectrum is appropriate for this assessment and for consistency, dispersive fuel behavior will be assumed.

3. Analysis Methods

The SAS3D computer code was utilized in these evaluations. The incorporation of the plenum fission gas effects in the cladding relocation model is described in Section 3 of II.3. Here we will summarize the modeling and benchmarking of the blowdown model.

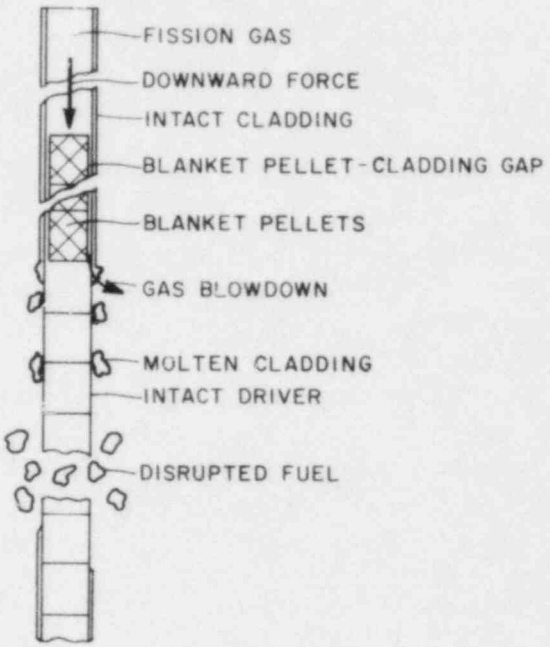

Fig. 1.
Schematic of the fission gas compaction process.

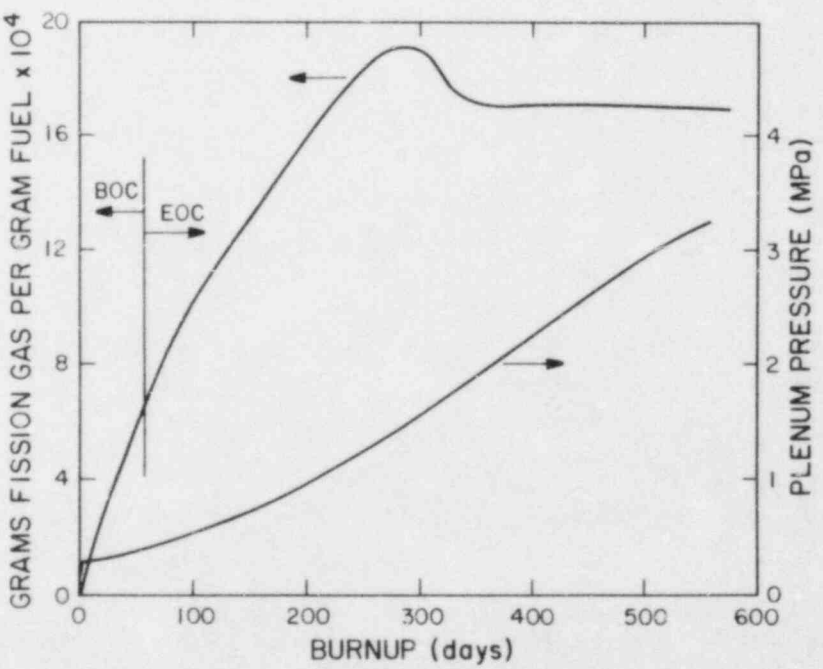

Fig. 2.
Fission gas characteristics during a burnup cycle.

Our experience with plenum fission gas effects is limited to the TREAT R-8 test [3]. It was run with prepressurized pins and it produced no upper cladding blockages. The blowdown occurred within ~1 s, which was well before fuel disruption. Hence, it did not provide any information on the compaction mechanism of concern here. However, the plena pressure transients were reported and, although the geometry is not exactly applicable to the problem at hand (inconel reflector and depleted UO_2 insulator pellets in the R8 vs blanket pellets in the CRBR), these results can be used as a convenient frame of reference for assessing gas blowdown.

The R8 geometry is shown in Figure 3. The reported diametral gap of 0.000254 m appears inconsistent with the indicated cladding failure location (top of active core) and the observed blowdown rates. Consequently, for best-estimate purposes we assumed the cladding failure occurred ~0.05 m below the top of the active fuel. This failure site was displayed by one pin in the post-test examination.

Because the flow was turbulent, the pressure drop was assumed to scale as $L/D^{1.25}$, where L is the flow length and D is the hydraulic diameter. The routine used to calculate depressurization was the SAS3D subroutine PIPFLO. Because PIPFLO cannot accommodate multiple flow areas, the effective length was determined by

$$L_{eff} = D_{fuel}^{1.25} \left[(L/D^{1.25})_{reflector} + (L/D^{1.25})_{insulator} + (L/D^{1.25})_{fuel} \right].$$

Table 2 gives the relevant quantities for this equation leading to an effective length of 0.1216 m.

This results in the comparison to the test data shown in Figure 4, if a friction factor, f, is defined by

$$f = 0.1264\ Re^{-0.25},$$

where Re is the Reynolds number. This friction factor is 1.6 times the standard Fanning friction factor. A plot of this friction factor relationship on a chart for tube flow is given in Figure 5.

Extrapolating to the reactor case results in the calculated depressurization time constants given in Figure 6. These were obtained under EOC LOF

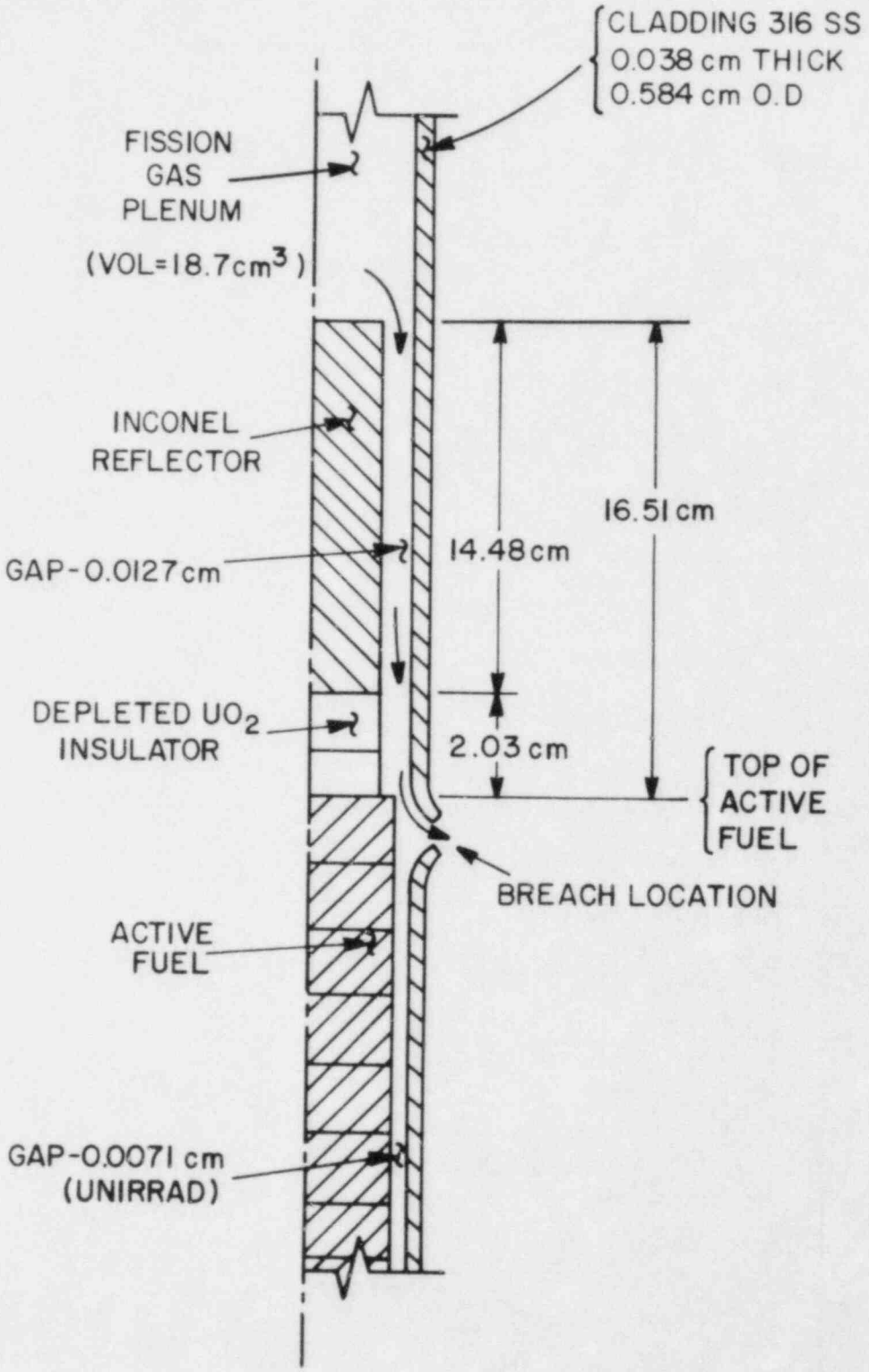

Fig. 3.
Model for TREAT test R8.

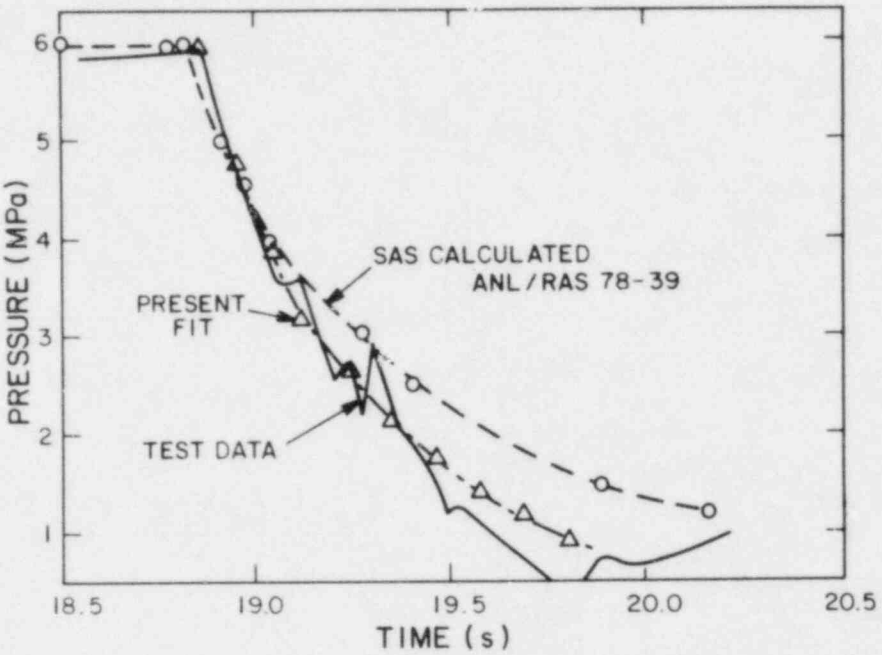

Fig. 4.
Fission gas blowdown during TREAT test R8.

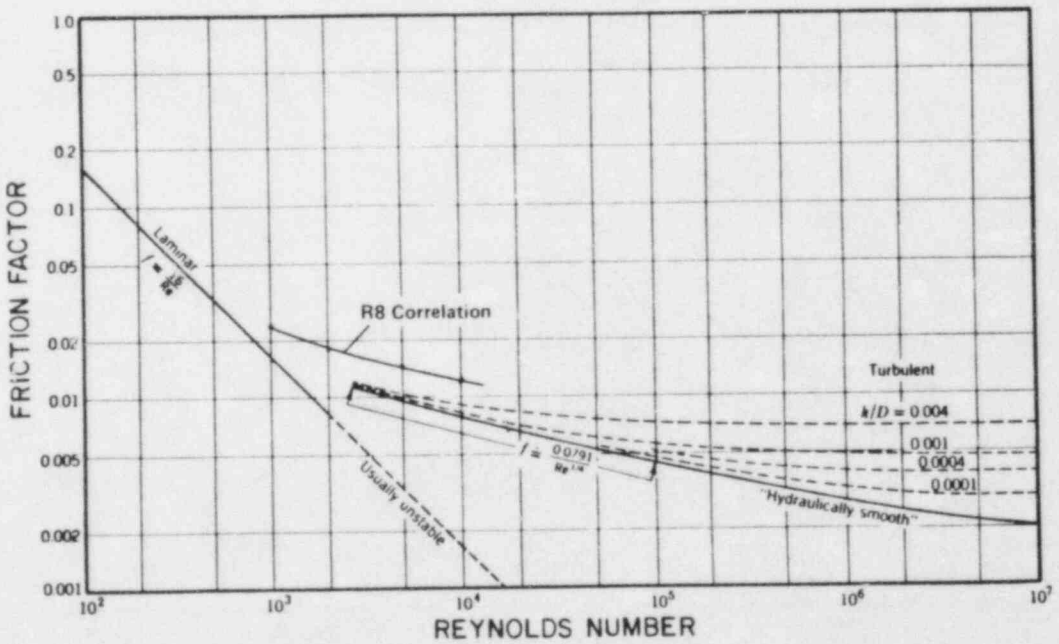

Fig. 5.
Effective friction factor for fission gas blowdown in TREAT test R8.

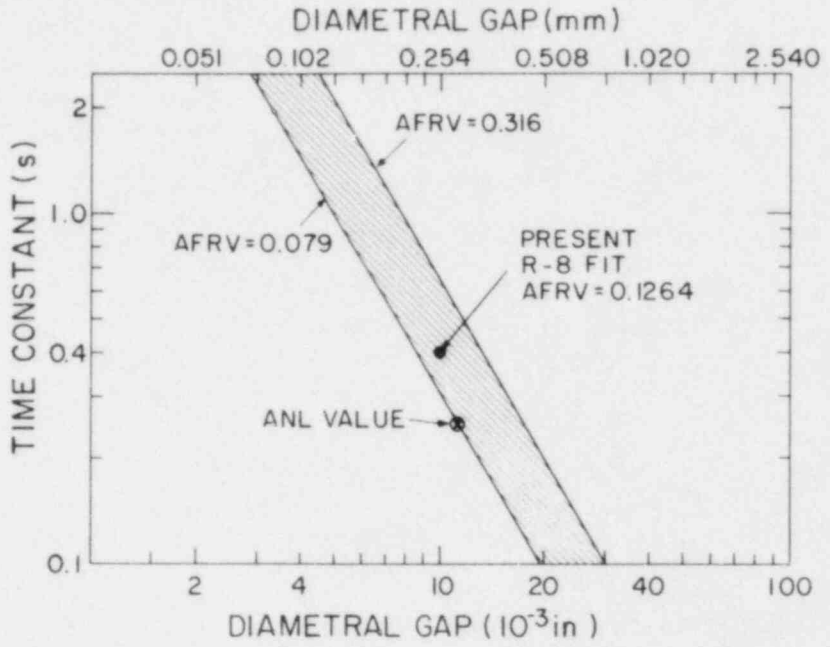

Fig. 6.
Fission gas blowdown time comstants for various assumptions.

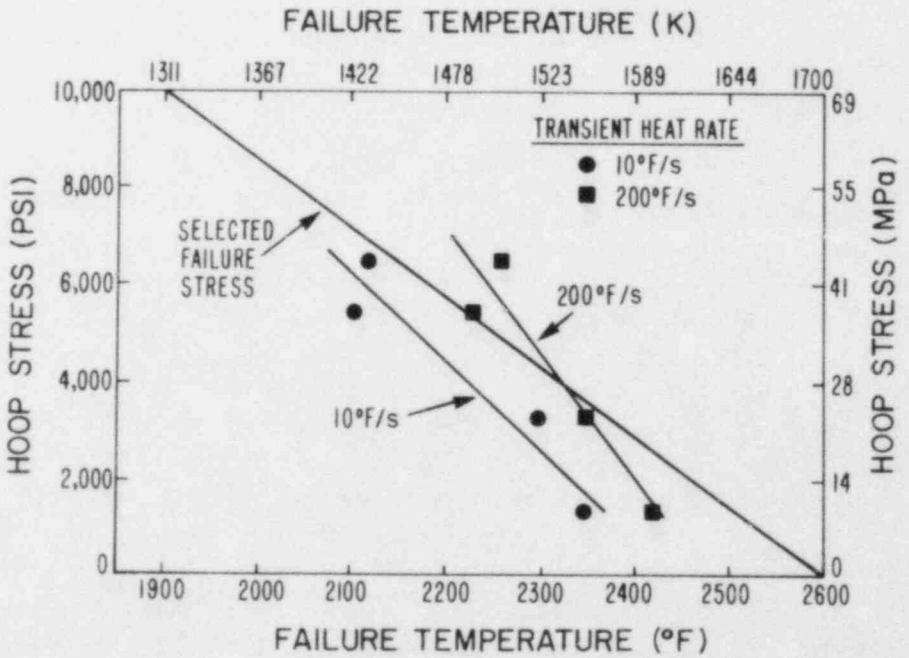

Fig. 7.
High temperature failure stress for the fission gas compaction analysis.

TABLE 2
QUANTITIES FOR DETERMINING THE EFFECTIVE LENGTH
FOR FITTING THE R8 TEST

Quantity	Length m (inches)	Hydraulic Diameter m (inches)	$L/D^{1.25}$
Reflector	0.145 (5.7)	$2.565\ (10^{-4})$ (0.0101)	1780
Insulator Pellets	0.0201 (0.792)	$2.438\ (10^{-4})$ (0.0096)	263
Fuel Column	0.0508 (2.0)	$1.295\ (10^{-4})$ (0.0051)	1467
Effective Values Used	0.122 (4.79)	$1.295\ (10^{-4})$ (0.0051)	3511

conditions assuming pin failure at the top of the active fuel. The best-estimate time constant is seen to be 0.4 s. Because the cold fabricated gap was used in the correlation to the R8 experiment, the best-estimate gap calculation did not take credit for thermal expansion in the reactor situation.

The cladding failure was calculated to occur when its circumferential stress at the top active-core node exceeded the failure stress. This failure stress was based on the unirradiated, 20% cold-worked 316 stainless steel data of Reference 4. The correlation used is given in Figure 7.

Upon fuel disruption (at ~50% radial melt fraction) the upper pin segments, including the axial blanket, were subjected to the fission-gas plenum pressure. The motion was calculated as if only limited by the pellet-column inertia, that is, neglecting friction with the cladding.

4. Accident Analysis Results

We have conducted extensive parametric evaluations using the SAS3D code. For the selection of early reactivity feedbacks that promote a slow transient (low power), sufficient time elapses between cladding failure and fuel disruption to assure complete plenum blowdown before loss of fuel column integrity and hence to assure negligible compaction potential. For a selection of stronger positive reactivity feedbacks, the accident proceeds rapidly and essentially undiminished plenum gas pressures are available for compaction. However, the reactivity before the initiation of such compactions is already near prompt critical and insufficient pellet acceleration time (and thus reactivity augmentation) is available to produce a large ramp rate before disassembly by fuel vapor pressures. That is, over the spectrum of the important reactivity feedbacks, an intermediate maximum in the accident severity occurs as schematically illustrated in Figure 8. Our effort has been to determine an upper limit for this intermediate maximum.

The results of such a bounding calculation are summarized in Figures 9 and 10. The details are given in Appendix A. This case is a restart of the mid-range EOC-4 initiating-phase calculation (see Table 2 of Section II.3), at the time of initial fuel disruption, but now taking into account the plenum fission-gas compaction effects.

The power burst shown in Figure 9 was characterized by a net reactivity ramp rate of ~ 50$/s. The core material configurations at the time of this power burst are schematically depicted by the bar charts of Figure 10. The sodium void map indicates that the core was about half voided and auto-catalytic fuel pin failures in sodium-filled channels, known as LOF-d-TOP, could occur. Also shown on this figure are remaining plenum gas pressures, together with radial melt fractions within the pins for each one of the 11 driver subassembly groups. From this figure the important core-wide incoherency effects in limiting the extent of the fuel compaction process can be visualized. As seen from the cladding melt fraction map (axial extent of melting), both ends of the core remain unblocked, providing escape paths for the high-pressure fuel/steel mixtures in the post-burst period. That is, accident termination is projected if the LOF-d-TOP is avoided.

5. Summary and Recommendations

Because of intrasubassembly incoherencies, we expect that only about one-half of the pins producing compaction in our calculations would in fact be able to do so. Consequently, the already modest level of energetics obtained as an upper bound, in reality, could be limited to values as low as 35 $/s, that is, barely qualifying as an energetic event. However, the potential for an LOF-d-TOP is troublesome and highly undesirable. We recommend, therefore, that a design fix be implemented to inhibit the precipitous

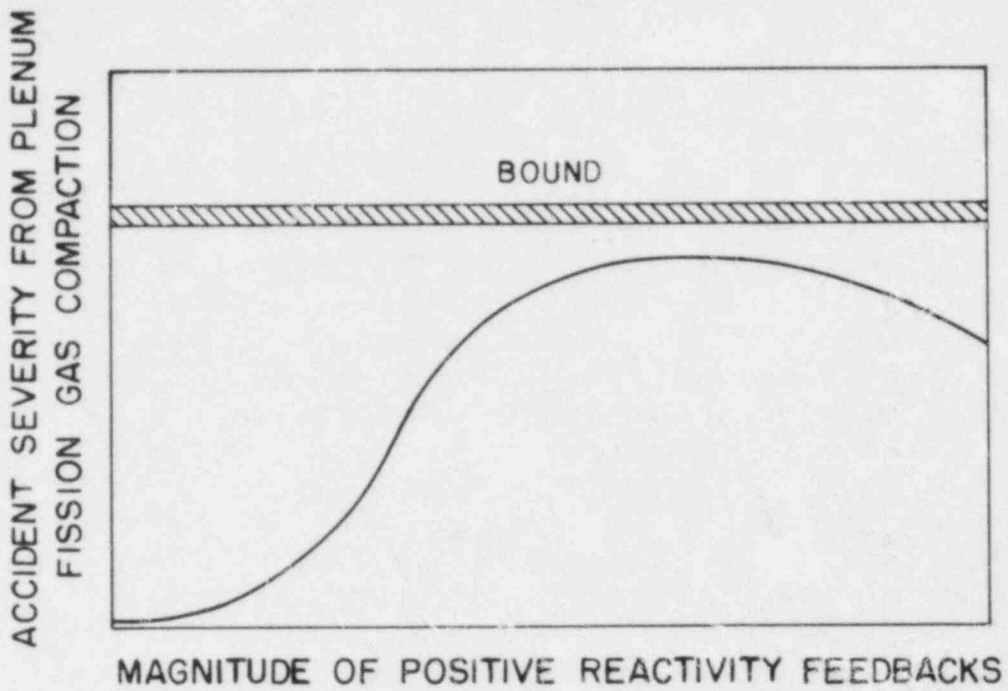

Fig. 8.
Schematic trend of accident severity with neutronic feedback assumptions.

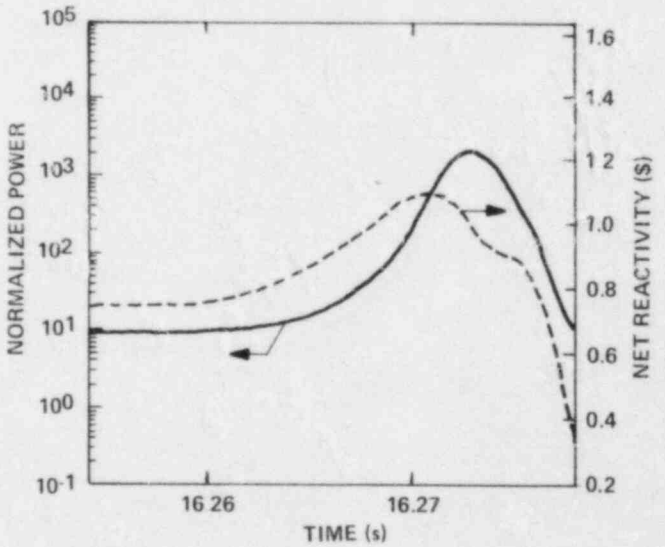

Fig. 9.
Expanded overall power and reactivity transient for fission gas compaction.

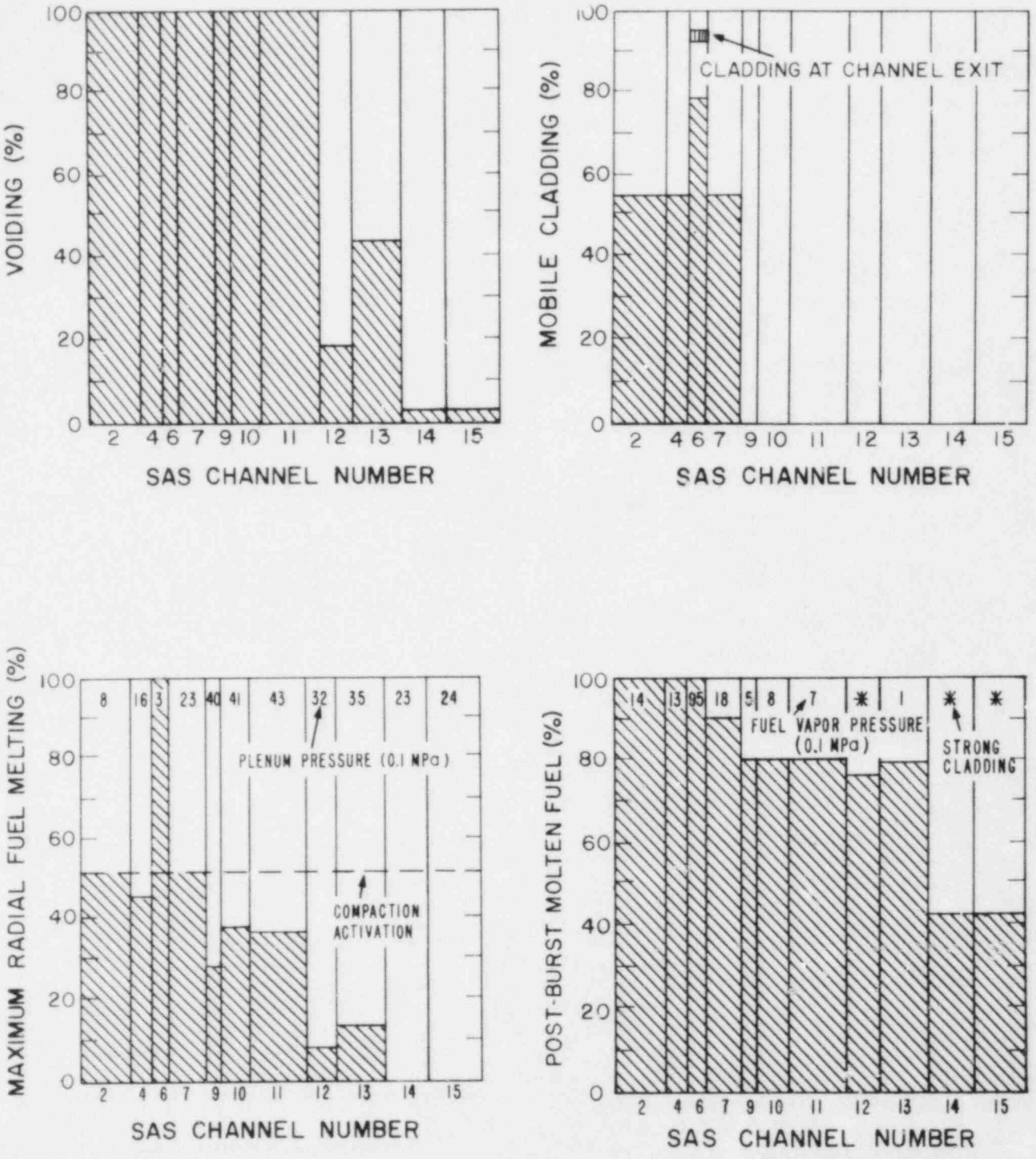

Fig. 10.
Summary of the core state at the compaction power burst.

manifestation of high gas pressures upon the fuel column as disruption occurs. No particular difficulties are envisioned in developing such a design change.

6. References

1. T. G. Theofanous, "Multiphase Transients with Coolant and Core Materials in LMFBR Core Disruptive Accident Energetics Evaluations," Purdue University report NUREG/CR-0224 (July 1978).

2. "Compendium to NUREG-CR-0224, An Assessment of CRBR Core Disruptive Accident Energetics," Section 6, Nuclear Regulatory Commission document (March 1983).

3. B. W. Spencer, F. J. Testa, N. A. Kramer, and C. H. Bowers, "Interim Report on TREAT Test R8, a Seven-pin Loss-of-flow Test with Pressurized Pins," Argonne National Laboratory report ANL/RAS 78-39 (September 1978).

4. C. W. Hunter and R. L. Fish, "Deformation and Failure of Fast Reactor Cladding During Simulated Loss-of-Flow Type Transients," Proceedings of the Fast Reactor Safety Meeting, Beverly Hills, CA, April 2-4, 1974, CONF-740401.

APPENDIX A
SAS3D ANALYSIS

1. Introduction

In this Appendix we present the SAS3D [1] analysis of a representative case with plenum fission-gas compaction of the fuel. The process itself is described in Section II.4. This case is identical to the mid-range case of Section II.3, Appendix B. A number of cases with other assumptions and conditions were explored during the review period preceding this independent assessment. It was found that the general behavior was not unique to a narrow band of assumptions or conditions except that it is most important in the latter part of the burnup cycle.

Because the SAS3D geometric model is identical to that of Section II.3, Appendix B, it will not be repeated here. A brief discussion of the treatment of plenum gas blowdown and of plenum gas acceleration of the fuel column is provided along with detailed results.

2. Unique Modeling

The unique modeling introduced for this analysis consists of (1) transient gas blowdown through the annular gap between upper axial blanket pellets and their cladding, (2) triggering of the blowdown process, (3) fuel column dynamics with plenum pressure as the upper boundary condition, and (4) triggering of the fuel column motions. The modeling of the blowdown and its benchmarking is discussed in Section II.4. The blowdown is triggered when the cladding of the uppermost core node reaches a high-temperature burst condition based on pin pressure and cladding temperature. The resistance to gas flow in the annulus of the active-core fuel column is assumed to be too large to permit significant blowdown for earlier, in-core cladding failures. The fuel column dynamics was analyzed by modifying the SAS3D upper-pin-segment model to utilize the plenum pressure to generate an acceleration term in addition to gravity. The column motion was triggered when the fuel column in the active core was disrupted locally (melt fraction criterion) and the cladding at the core/UAB interface was failed axially (axial stress was equal to the rupture stress).

3. Results EOC-4 Fission-Gas Compaction Case

As calculated with the best-estimate plenum fission gas release model described in Section II.4, the Channel 7 plenum pressure, when fuel motion initiates Channel 7, was about 2.5 MPa. In this mid-range case, Channel 7 was the second channel to initiate fuel motion. If the remaining plenum gas pressure was postulated to compact the fuel below it, a power burst should occur. Such a burst was calculated for the current case. The power and reactivity traces for this burst are shown in Figure 1. The burst starting at 16.26 s produced about 7 FPS. Figure 2 delineates the fuel motion reactivity and indicates a ramp rate of about 50 $/s near prompt critical. Figure 3 shows the negligible reactivity contributions of voiding and cladding motion on the burst. Figures 4, 5, and 6 give the channel details of the voiding reactivity during the power burst. Only Channel 13, which was in the process of flow reversal at elevated power, showed any real change during this time. Figures 7 and 8 show the influence of dispersal fuel pressures on cladding motion in the lead subassemblies. Figures 9, 10, and 11 give the channel-dependent fuel reactivities. Channels 2 and 4 developed some plenum fission gas induced compaction. Channels 12, 14, and 15 were predicted to enter TOP-type behavior (based on a melt fraction pin failure criterion of 50%) during the burst.

Figures 12, 13, 14, and 15 give the final conditions for the highest power channel, Channel 6. The presence of sodium is seen in the lower axial blanket. The moving cladding segments were prevented from entering this sodium by the SAS3D model. In turn, these cladding segments limited the degree of downward fuel motion. An interaction with liquid sodium also can be inferred from the final configuration shown in Channel 10 (Figures 16, 17, 18, and 19). Here codisruption occurred with both steel and fuel coexisting with liquid sodium. Finally, Figures 20 through 27 show the results in the unvoided channels. Because the SAS/FCI model of SAS3D was judged to be physically unrealistic, the analysis was not pursued directly. The concurrent failure of pins into the unvoided or recently voided channels was explored with SAS3D/EPIC [2]. As would be expected, the power burst was sufficiently large to cause coherent failure of all pins with a potential failure location bias toward the mid-plane. The internal fuel motion in the pins then dominated the subsequent reactivity leading to unacceptable results.

4. Summary

The results of this representative calculation indicate the potential for severe consequences if the pellets of the upper axial blanket are capable of free slip motion. These consequences are not the direct result of the compacting fuel (autocatalytic propagation by this mechanism does not occur because of the inertia of the pellet columns) but from the induced, coherent

LOF-d-TOP in the low-power channels. Thus, it appears prudent to eliminate or de-rate this mechanism by an appropriate means.

5. References

1.[a] J. E. Cahalan and D. R. Ferguson, "A Preliminary User's Guide to Version 1.0 of the SAS3D LMFBR Accident Analysis Computer Code," Argonne National Laboratory (informal document included with code) (1977).

2. P. A. Pizzica, P. L. Garner, and P. B. Abramson, "A User's Guide to EPIC, a Computer Program to Calculate the Motion of Fuel and Coolant Subsequent to Pin Failure in an LMFBR," Argonne National Laboratory report NUREG/CR-1504, ANL-80-47 (October 1979).

[a] Address requests for this document to: F. X. Gavigan, Director, Office of Breeder Demonstration Projects (NE-50), U.S. Department of Energy, Washington, DC 20545, Telephone (301) 353-3134.

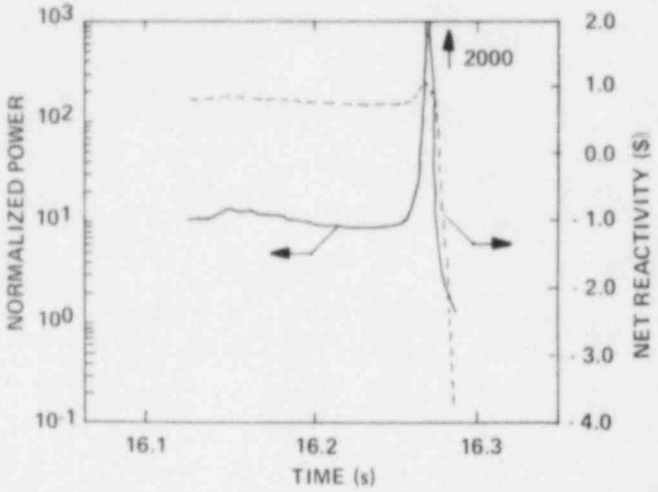

Fig. 1.
Overall power and reactivity transient.

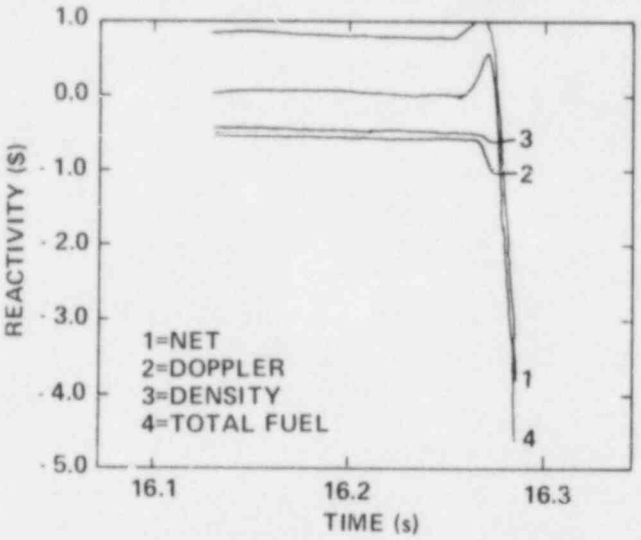

Fig. 2.
Overall component reactivity transients.

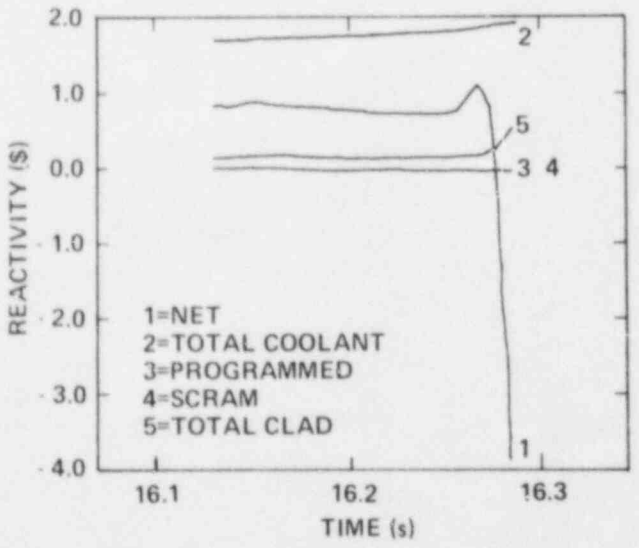

Fig. 3.
Overall component reactivity transients.

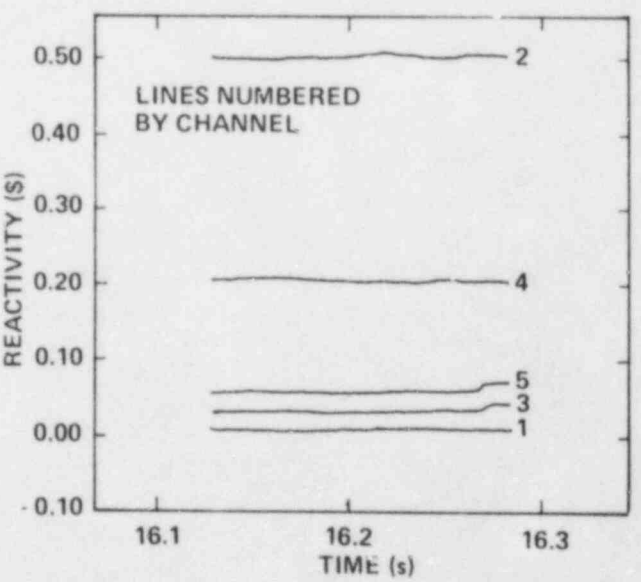

Fig. 4.
Coolant reactivity transients by channel.

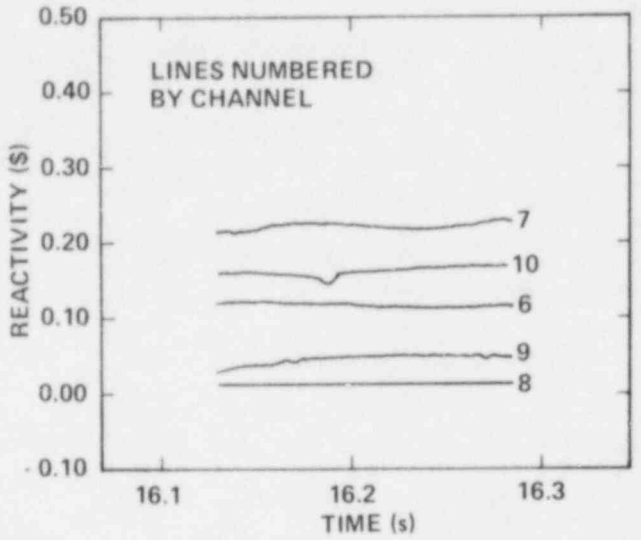

Fig. 5.
Coolant reactivity transients by channel.

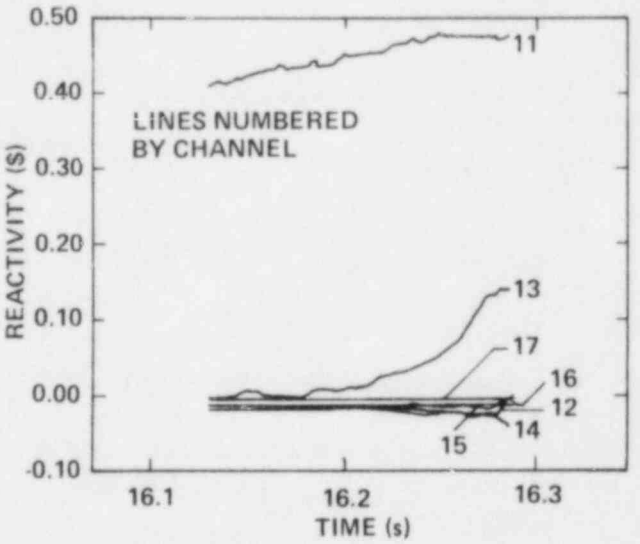

Fig. 6.
Coolant reactivity transients by channel.

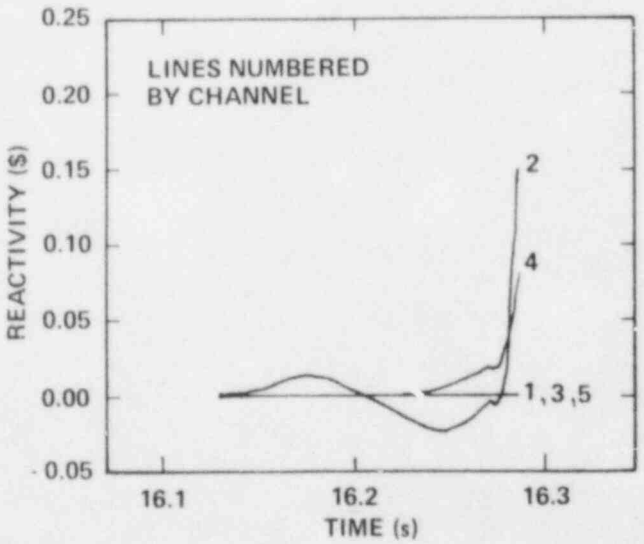

Fig. 7.
Cladding reactivity transients by channel.

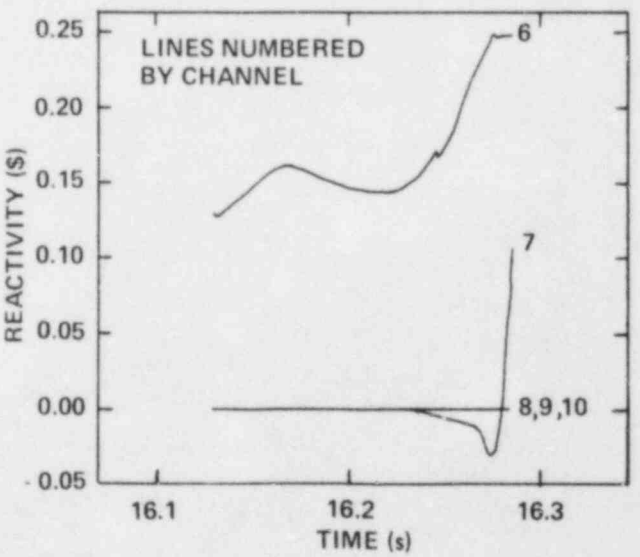

Fig. 8.
Cladding reactivity transients by channel.

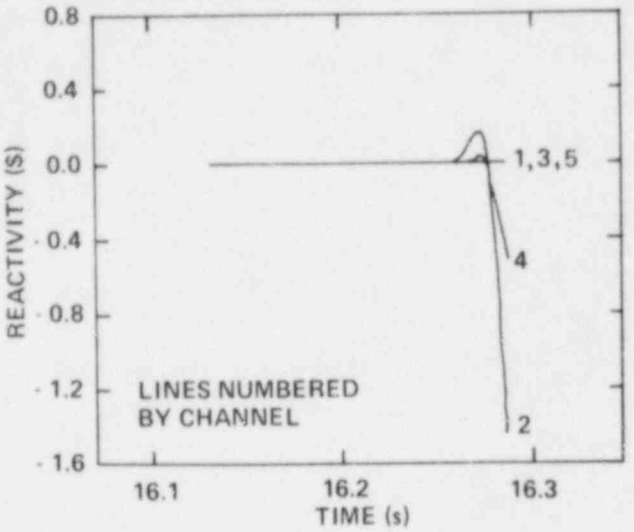

Fig. 9.
Fuel reactivity transients by channel.

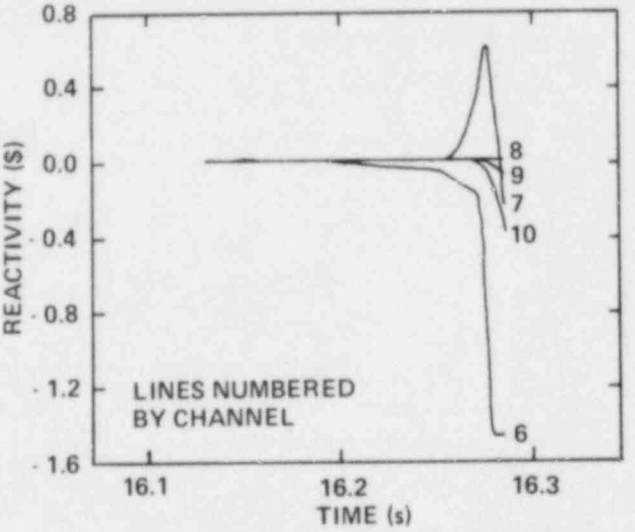

Fig. 10.
Fuel reactivity transients by channel.

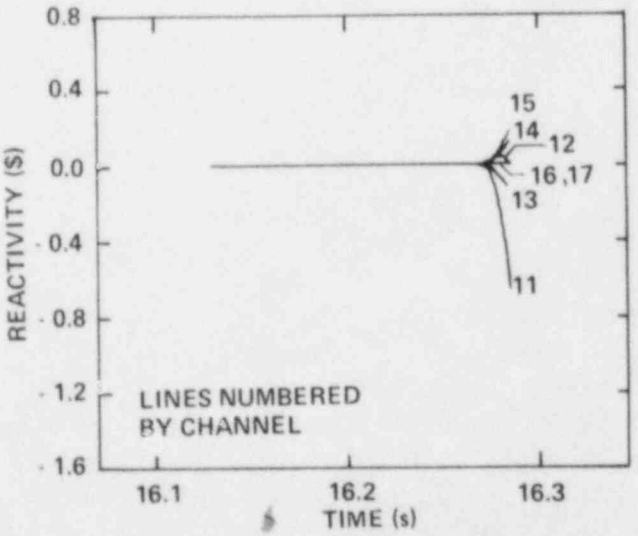

Fig. 11.
Fuel reactivity transients by channel.

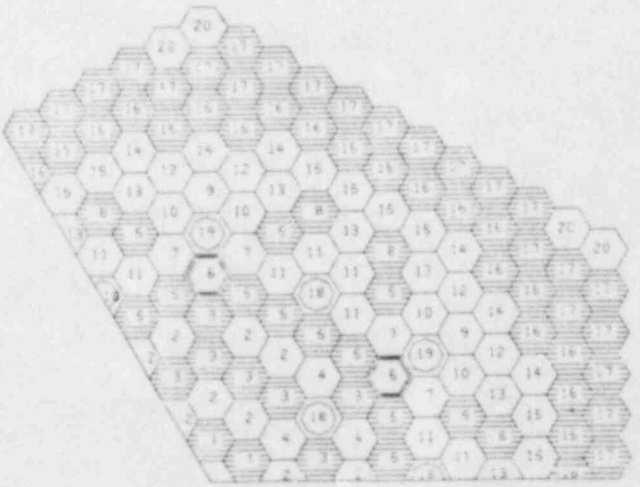

Fig. 12.
Location of channel 6 subassemblies.

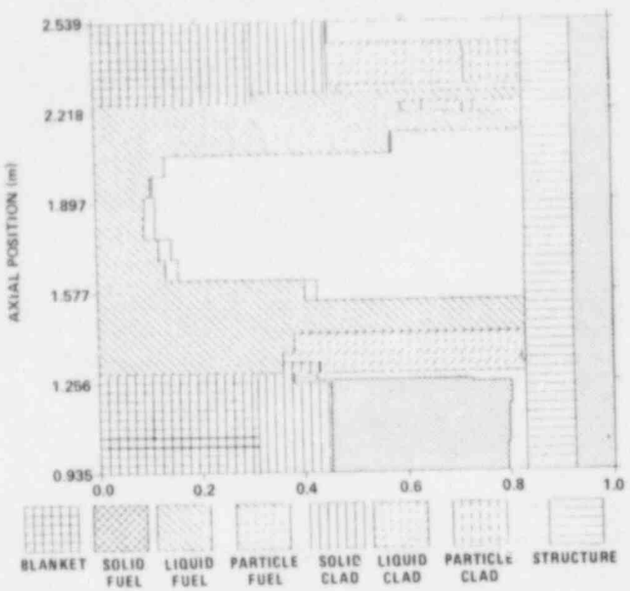

Fig. 13.
Final configuration of materials (volume fractions) in channel 6.

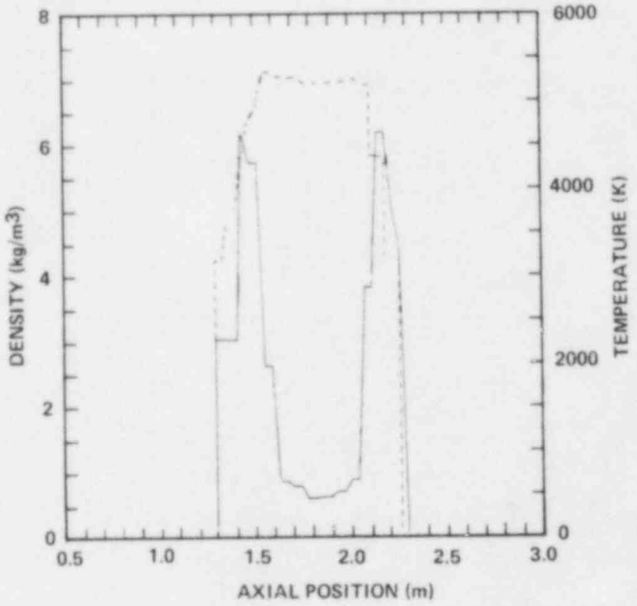

Fig. 14.
Final liquid fuel distribution and temperature in channel 6.

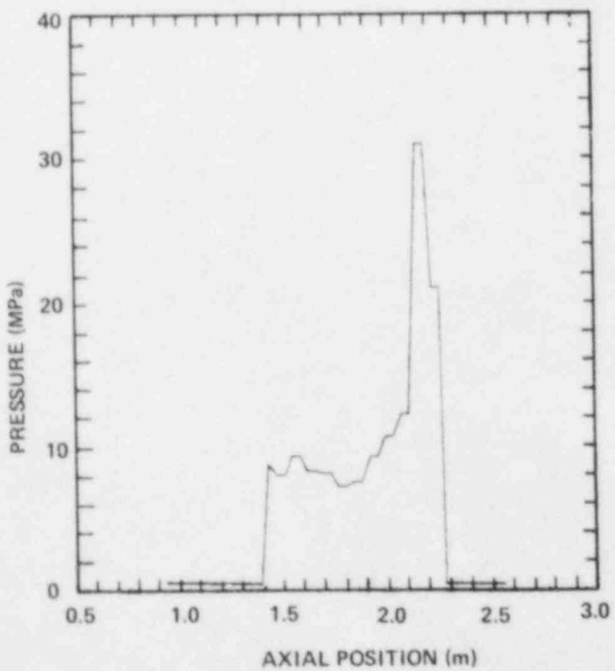

Fig. 15.
Final pressure in channel 6.

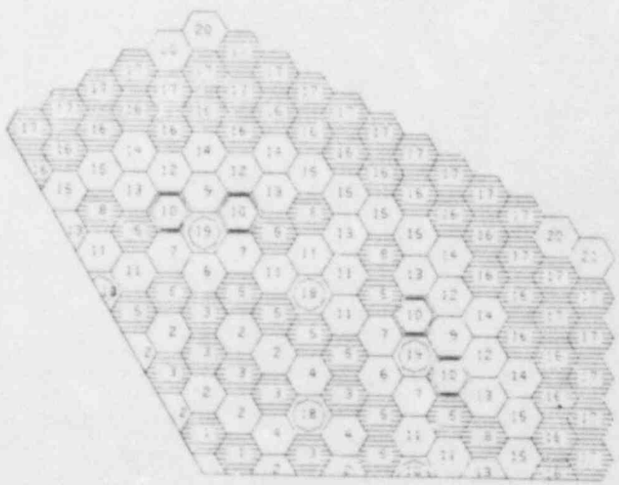

Fig. 16.
Location of channel 10 subassemblies.

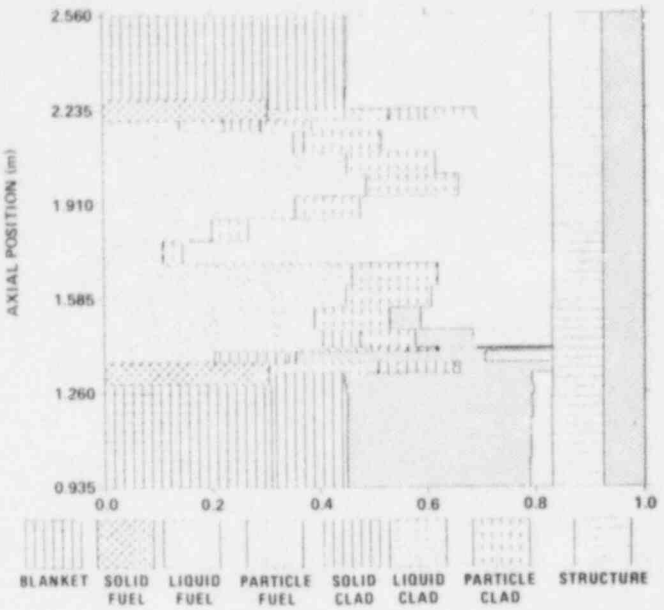

Fig. 17.
Final configuration of materials (volume fractions) in channel 10.

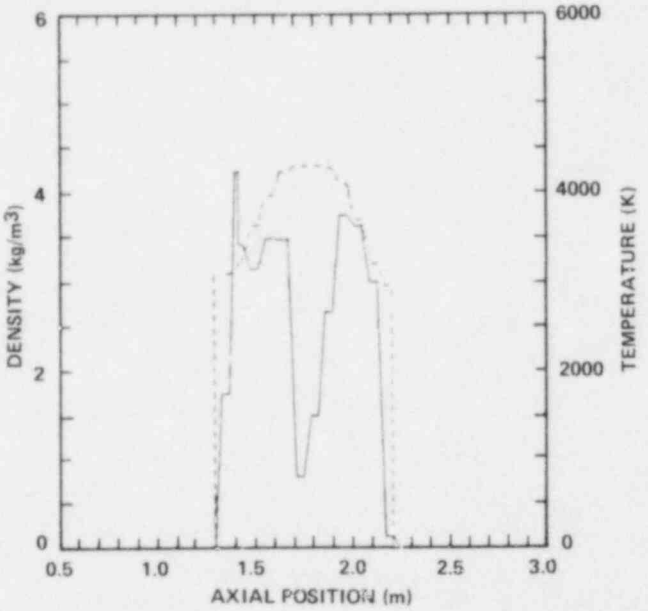

Fig. 18.
Final liquid fuel distribution and temperature in channel 10.

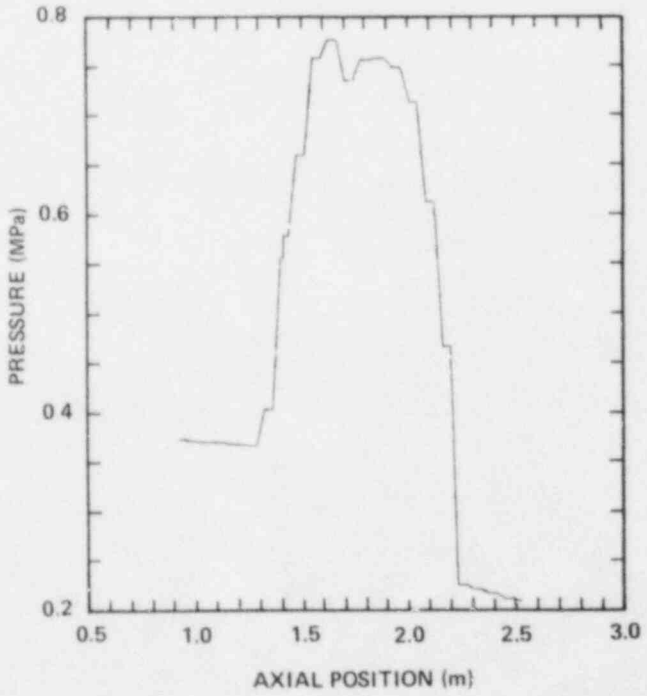

Fig. 19.
Final pressure in channel 10.

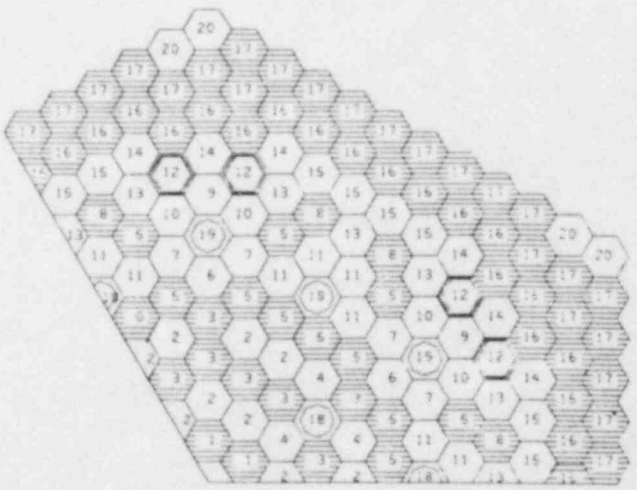

Fig. 20.
Location of channel 12 subassemblies.

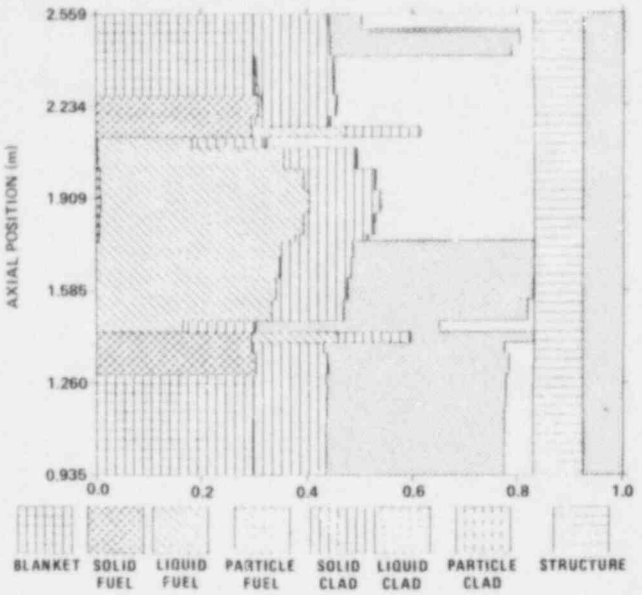

Fig. 21.
Final configuration of materials (volume fractions) in channel 12.

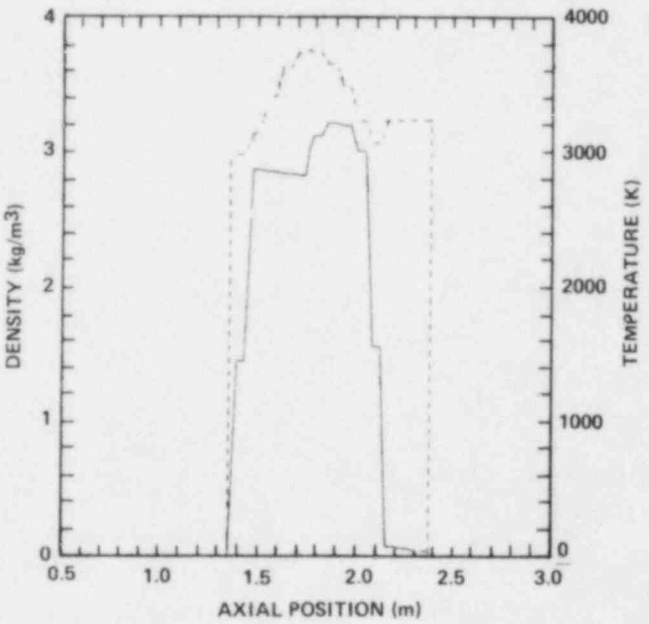

Fig. 22.
Final liquid fuel distribution and temperature in channel 12.

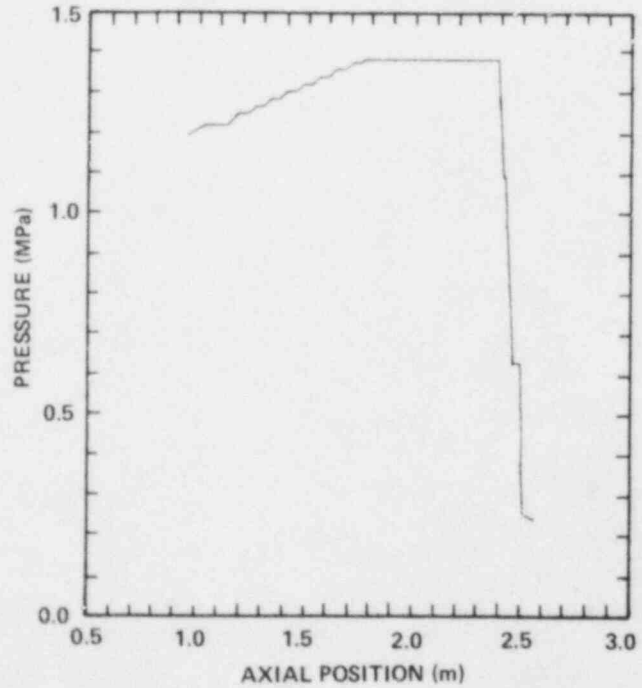

Fig. 23.
Final pressure in channel 12.

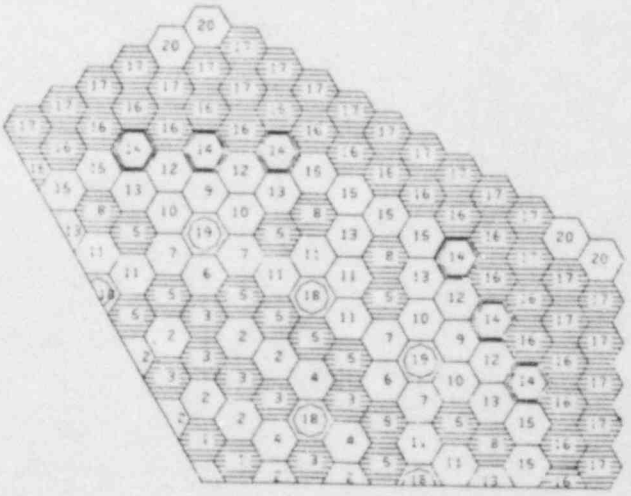

Fig. 24.
Location of channel 14 subassemblies.

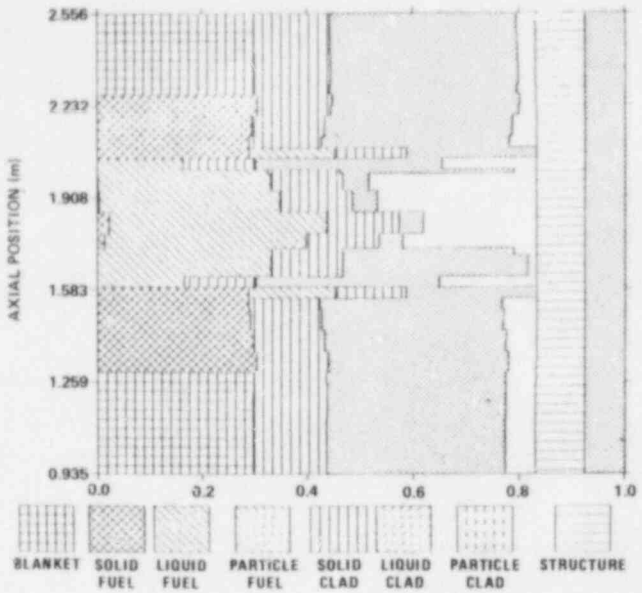

Fig. 25.
Final configuration of materials (volume fractions) in channel 14.

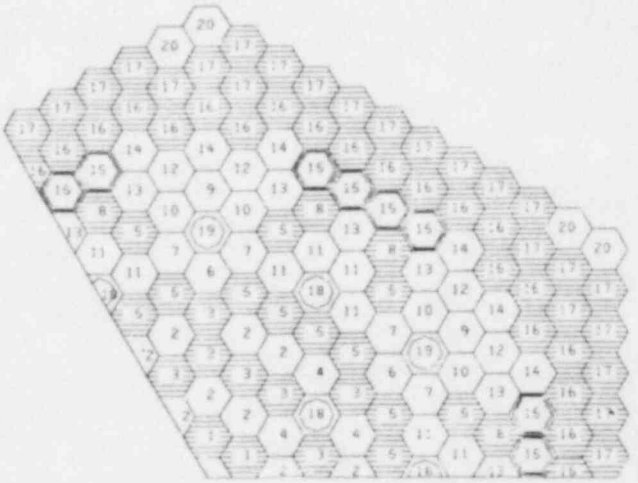

Fig. 26.
Location of channel 15 subassemblies.

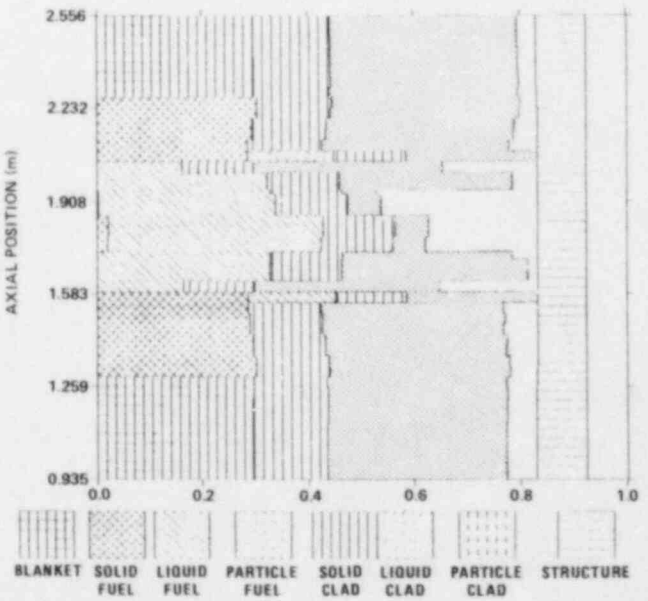

Fig. 27.
Final configuration of materials (volume fractions) in channel 15.

II.5. REFERENCE DISRUPTION-PHASE BEHAVIOR

1. Objectives and Overview

The mechanistic analysis of the LOFA beyond the initiating phase is a formidable task and one for which there are few precedences and limited experience. However, the nature of the neutronically active disruption phase is such that its treatment by simple, quasistatic approaches may be misleading, overly conservative (if conservative in this context even can be defined a priori), and necessarily speculative. An integral perspective on the complex, transient, coupled, nonlinear disruption process can be very valuable for guidance and orientation. Therefore, we have attempted such a whole-core, coupled (fluid dynamically and neutronically) transient analysis of a CRBR disruption sequence to establish a reference viewpoint for simpler scoping and bounding analyses.

The modeling approach and major assumptions are described in Appendix A. The calculated results are discussed in the following sections. We have found these limited results very useful in the overall assessment of the CRBR energetics potential and have made numerous links to other sections of this report.

2. Reference Disruption-Phase Analysis

The results of a reference whole-core disruption-phase calculation for EOC-4 are presented in this section. The model used for this analysis is described in Appendix A. The initial conditions were obtained directly from SAS3D for the "slow" EOC-4 case of Section II.3. The transformation of this voluminous detailed data also is discussed in Appendix A, along with the crucial modeling assumptions.

These types of analyses are very complex and are difficult to portray without the aid of a variety of graphics. We will attempt to highlight the progression of the disruption and in particular trace the movements of materials with time with these graphics aids. Because the material motions are strongly related to the neutronic behavior, we have overlaid the reactivity response on the global material inventory records.

The driver fuel configuration at time zero for SIMMER-II (19.75 s for SAS3D) is shown in Figure 1. Most of the core's outer channels have not disrupted at this time. The SAS3D results (see Section II.3) show a burst at

about 20 s or about 0.25 s on the SIMMER-II time scale. The reactivity history shown on Figure 2 also shows a burst at this time and is roughly the same magnitude as seen from the SIMMER-II power history in Figure 3. This provides some confidence that the overall behavior has been preserved through the transformation between codes.

The overall neutronic history shown on Figures 2, 3, and 4 for reactivity, power, and integrated energy, respectively, shows three distinct characteristics. During the first 1.5 s a repetitive cyclic pattern developed with a period of 0.4 s. This is consistent with the gravity-drainback time constant. We can see the connection between the neutronic and fluid behavior in Figure 5 showing the total driver fuel inventory in the bottom four nodes of the core. The reactivity responded each time this inventory increased, indicating slumping. The inventory was reduced following each power pulse as expected because of the upward ejection of fuel from the slumped region. During this period the temperature of the fuel was high and the heating and disruption of S/A walls was rapid. This is evident on Figure 6, which shows the driver fuel that entered the internal blankets. The time at which the curves depart from zero is when "gap flow" (between S/A walls) began indicating that driver walls were at the solidus energy state. As seen, all gaps were accessed within the first second. This is consistent with the greatly increased extent of disruption evidenced in Figure 7. From Figures 6 and 8 we can see that the internal blankets began to fail at about 1 s.

Another characteristic of the behavior during this early period was the tuning of the fluid-dynamic response on a core-wide extent. We can see the result of it in Figure 8 and the synchronization of the fluid responses before and after each power pulse in Figure 9. This tuning was first described on the basis of physical consideration in reference [1] and is important in recriticality estimates.

A change in character occurred after 1.5 s. The cyclic neutronic response terminated. The core now became capable of large radial motions as seen in Figure 10 from the radial interchange of fuel between the two regions of the annular pool (curves labeled D3→D7 and D8→D11; see Figure 2 of Appendix A for the region designations) and in Figure 11, which shows the breakdown of the internal blankets. The failing walls permitted fuel to fill the voided coolant volumes of the internal blankets. Because there was more of this volume in the central region of the core, a radial in-flow occurred to establish a new liquid level. The reactivity returned to supercritical as a result. The inward material motion can be seen by comparing Figures 12 and 13. The process was slow because the internal blanket stubs inhibited the inward flow (in-slosh).

By 3.5 s a full-core pool was established as seen in Figure 14 and a substantial out- and up-slosh of fuel occurred causing a deep subcritical

neutronic state. The fuel fell back subsequently as seen from the reactivity response in Figure 2 at 3.7 s. The subsequent in-slosh can be seen in Figure 10 as an interchange between regions labeled D3→D7 and D8→D11. The central region participated only weakly in this radial sloshing. The central region still contained much of its original blanket material (it hadn't homogenized or equilibrated) and had a reduced fuel temperature because of heat transfer to this colder blanket material. The general location of the fertile blanket material is shown in Figure 15. The curves give the inventory of blanket material in each blanket/driver region pair (again see Figure 2 of Appendix for region designations). The inventories in the central three regions all increased slightly with time until about 4 s. It is only after the final slosh at 4 s that appreciable additional blanket material appeared in the outermost region.

A further explanation for the weak participation of the central region in the sloshing process (and indeed an explanation for the weak sloshing behavior itself between 3 and 4 s) can be seen from the distribution of specific power in the core. A sequence of these distributions is shown in Figure 16. As more fuel slumping occurred in the outer regions and as internal blanket slumping occurred in the inner region (0-2 s), the peaking of the specific power in the outer slumped region became very dramatic (compare Figures 16a through 16c). As radial sloshing occurred in the 2 to 4-s time interval, the outer peaking still existed but was reduced by the out-sloshes that increased neutron leakage. This is very evident in Figure 16f, where we see a complete reversal of the peak location. However, as the pool reassembled, the outer peaking returned (as seen in Figure 16g). Its magnitude was greatly diminished at this time. Again, the reversal is seen in Figure 16h after another out-slosh. The important finding in this calculated behavior is that the sloshes are incoherent radially because of the outer power peaking, thereby preventing radially focused, coherent in-sloshes with their attendent large ramp rates.

There was a clear tendency for the sloshing to amplify in the time interval from 2.5 to 5 s as seen in both the reactivity and ramp rate histories shown in Figures 2 and 17, respectively. The ramp rates grew from the order of 10 \$/s up to about 40 \$/s before the critical state was lost because of fuel removal (see Figure 19). The growing height of the sloshes as seen in Figure 18 from 3.5 to 5 s also attests to the amplification.

The core inventory history given on Figure 19 provides major insight into the core behavior. The burst at 4 s caused approximately 500 kg of fuel to discharge from the core. This additional loss reduced the reactivity state by about 10 \$, thereby preventing the system from suffering a recriticality on the subsequent in-slosh. Because the internal blanket material had not homogenized, the system could not go recritical again. Fuel loss would continue, however, until core pressures decay. As seen in Figure 20, much of the removed fuel went into the lower axial blanket. The internal blanket

gap removal is not very efficient in this model because of the closed reservoirs that simulated the LAB gaps (see Appendix A). Also removal into radial blanket and reflector gaps was prevented by the modeling assumptions.

The potential for fuel removal to the radial blanket and reflector regions can be discerned by considering the availability of these gaps (when do the outermost driver walls reach their solidus energy) and the pressure for removal. The timing of radial gap availability can be seen from Figure 21 which shows the outer driver S/A wall temperature at several locations near the midplane. The solidus condition was met at about 2 s. Thus, these paths would be available for a major pa. of the transient and would therefore have had a major influence on the termination tendency (they would promote dispersal). The complete pressure history at the one-third elevation in the core for each driver region is shown in Figure 22. Each power pulse produced a pressure transient that was similar in character but of different magnitude depending on the incremental energy added (see Figure 4). The mean pressure level was about 0.5 to 0.6 MPa which was sufficient to remove a substantial quantity of fuel.

3. Summary

The reference disruption-phase calculation intentionally was selected as a conservative representation of a spectrum of initial conditions. In addition, the analysis itself was performed very conservatively by using a high effective component viscosity for fuel particles during fuel discharge, by neglecting radial blanket and control rod fuel removal paths, by derating internal blanket gap removal, by allowing a high quenching potential for the disrupted internal blanket material, and by defining initiating-phase blockages to be completely passive and indestructible. Even with all these conservative aspects, the analysis produced sufficient fuel removal to terminate the neutronic activity (~ 22% removed). The whole-core cylindrical pool was produced. Growing neutronic oscillations occurred, but the incoherent sloshing induced by outer region power peaking and the low void in the pool mitigated the ramps and the yields. A major aspect of the results was the role of internal blankets, even if completely disrupted, in suppressing the neutronic state and the amplification potential before homogenization. A more realistic analysis would have produced substantially more fuel removal and therefore shown even more support for termination by dispersal.

4. Reference

1. T. G. Theofanous, "Multiphase Transients with Coolant and Core Materials in LMFBR Core Disruptive Accident Energetics Evaluations," Purdue University report NUREG/CR-0224 (July 1978).

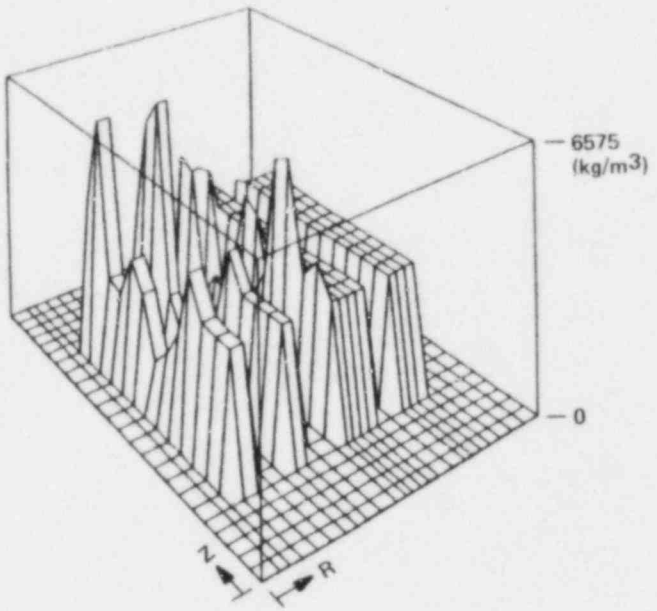

Fig. 1.
Driver fuel smear density distribution at 0 s.

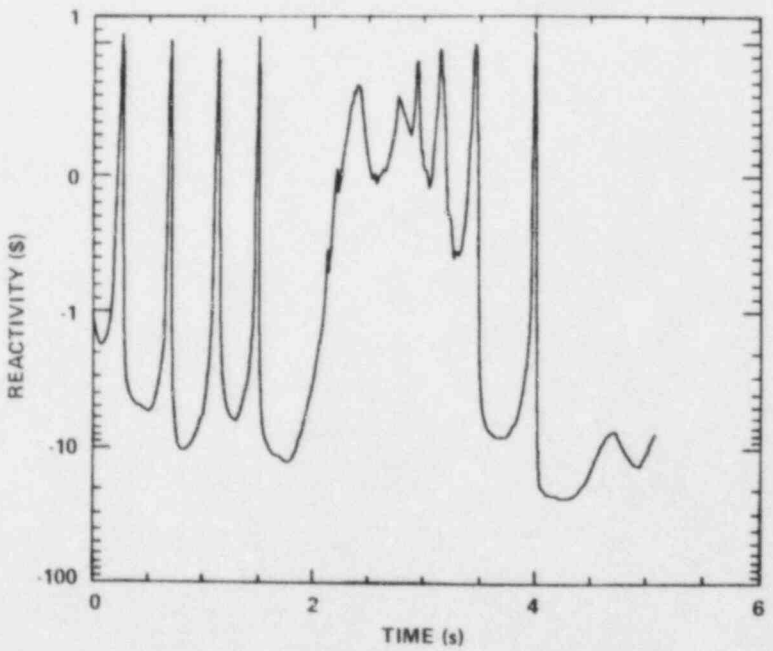

Fig. 2.
Disruption-phase reactivity transient.

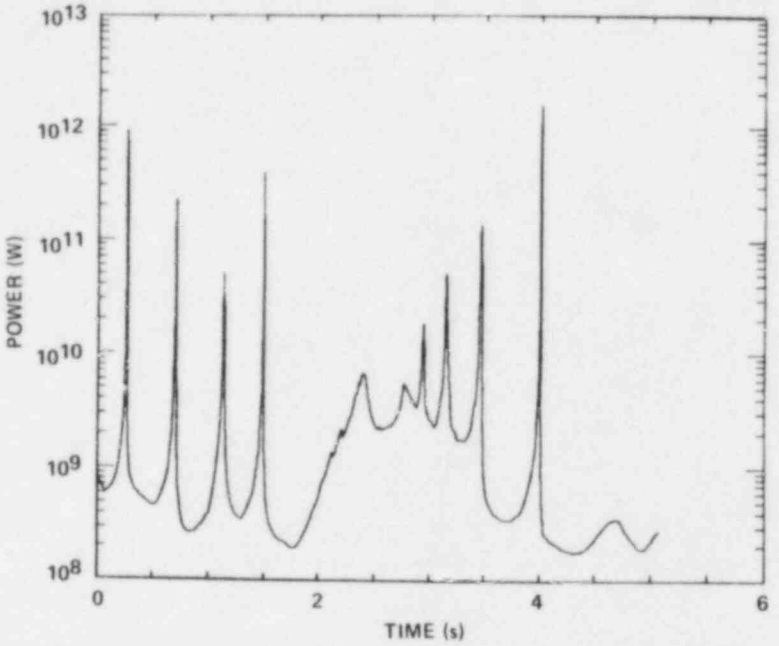

Fig. 3.
Disruption-phase power transient.

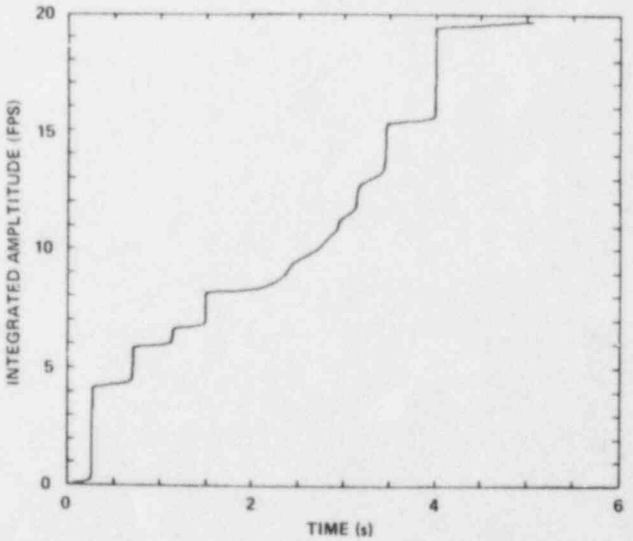

Fig. 4.
Disruption-phase ingetrated energy transient.

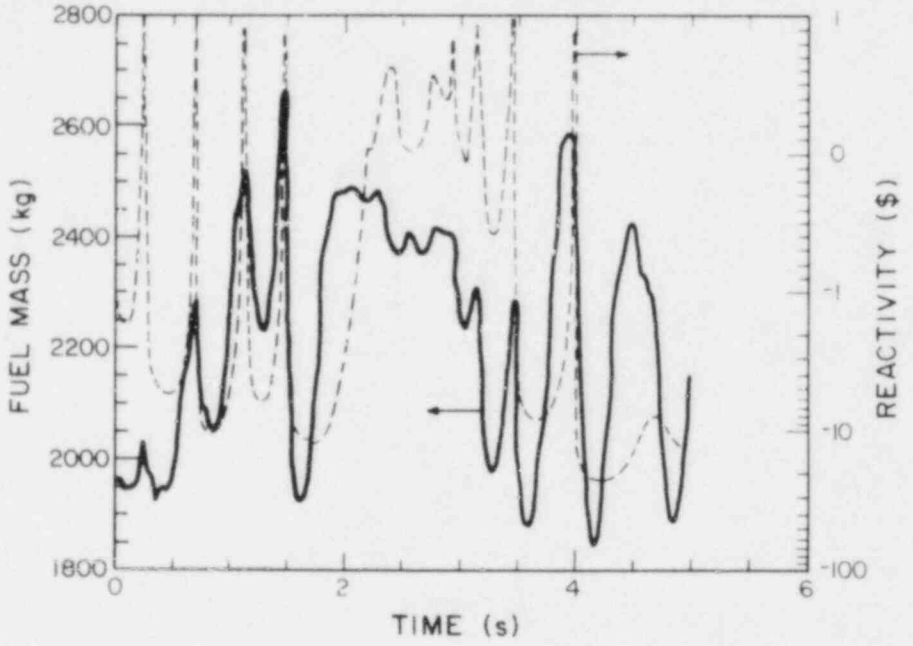

Fig. 5.
Driver fuel mass in the lower one-third of the core.

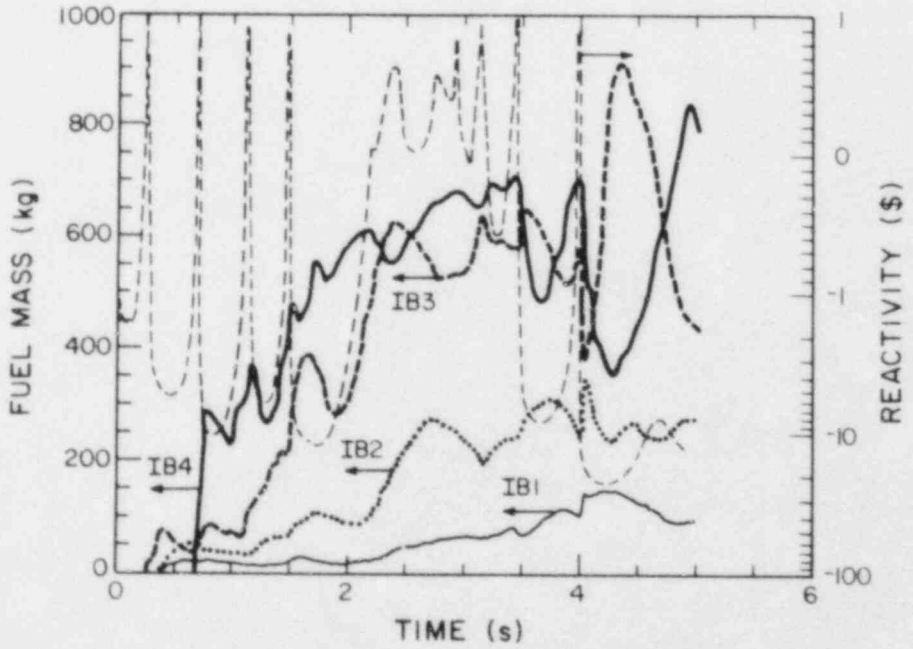

Fig. 6.
Total driver fuel mass in radial blanket region.

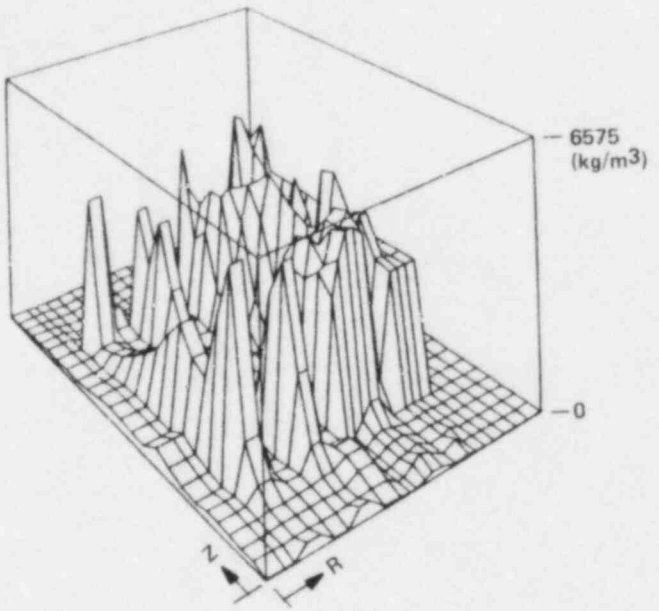

Fig. 7.
Driver fuel smear density distribution at 1.0 s.

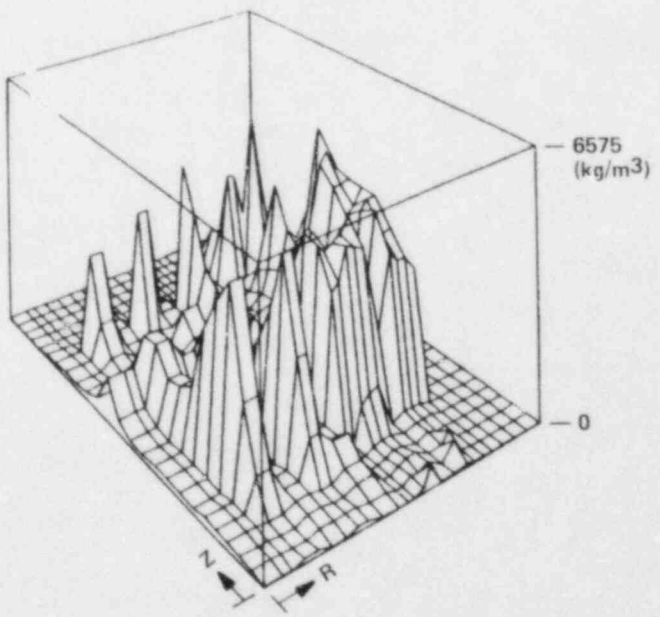

Fig. 8.
Driver fuel smear density distribution at 1.5 s.

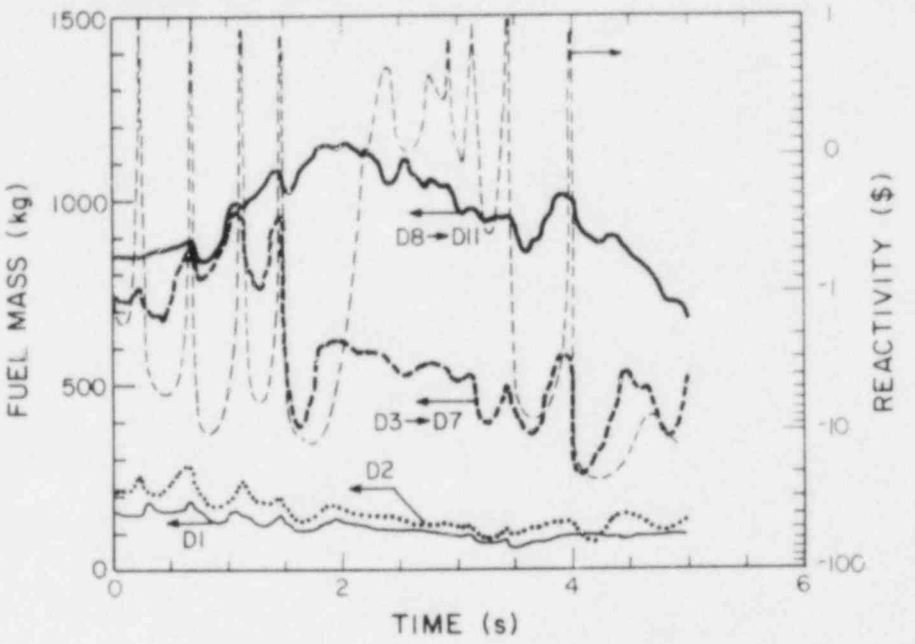

Fig. 9.
Driver fuel mass in the lower one-third of the radial driver regions.

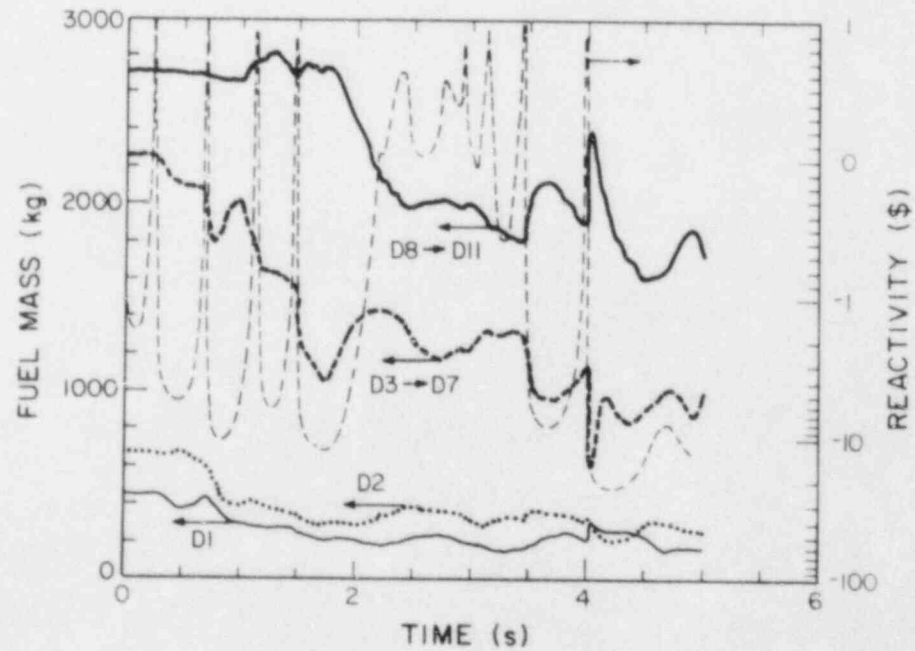

Fig. 10.
Total driver fuel in the radial driver regions.

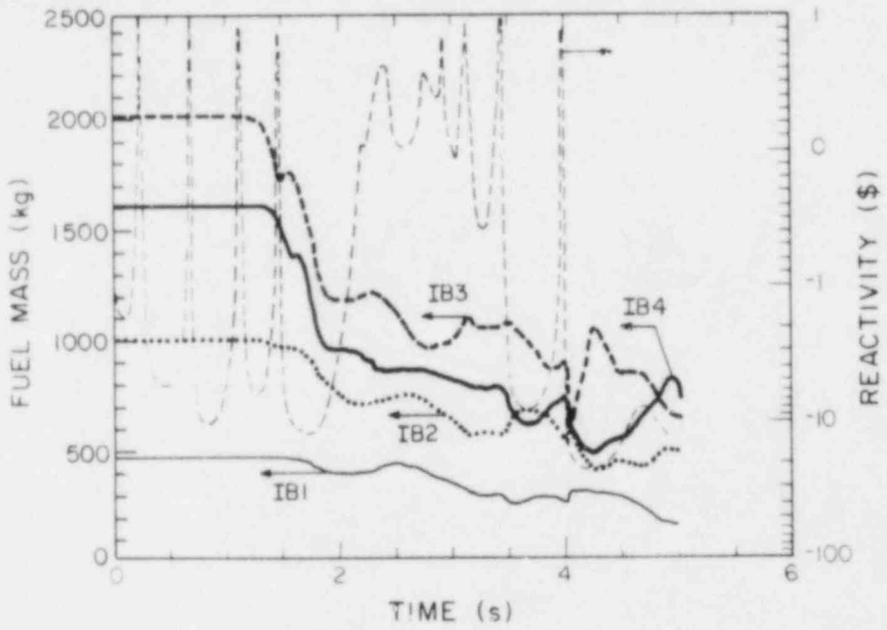

Fig. 11.
Total blanket fuel in the radial blanket regions.

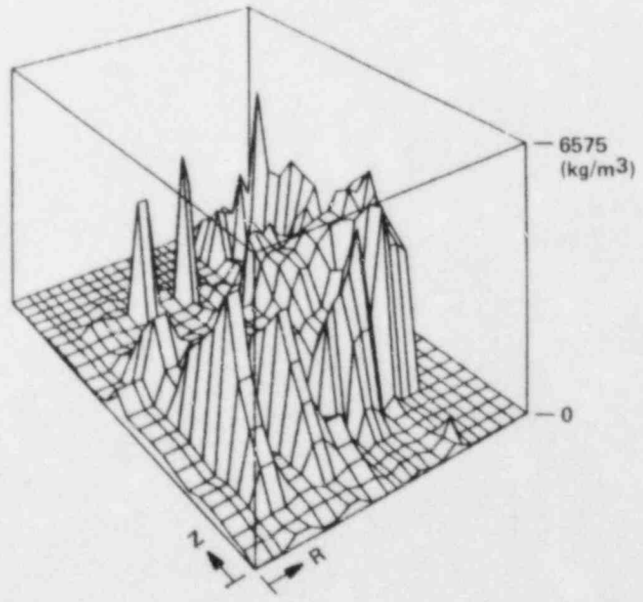

Fig. 12.
Driver fuel smear density distribution at 2.0 s.

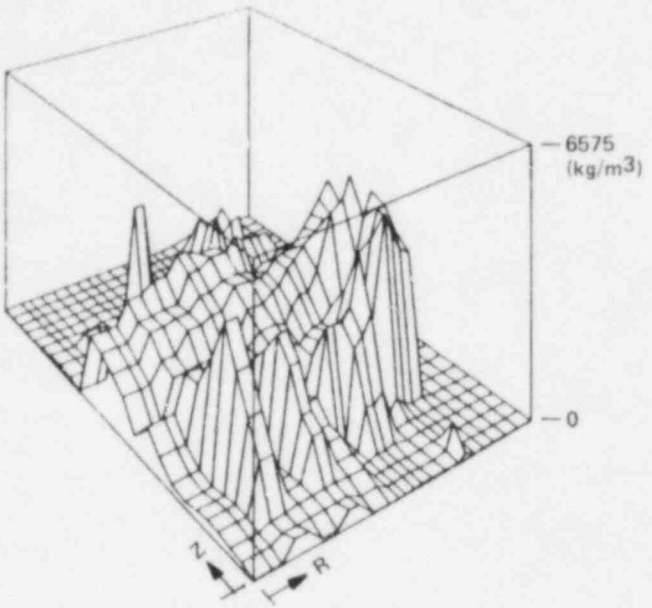

Fig. 13.
Driver fuel smear density distribution at 2.5 s.

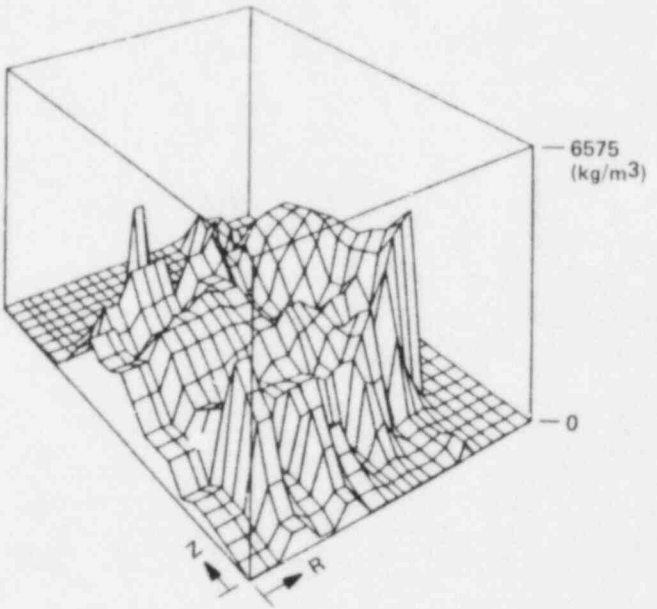

Fig. 14.
Driver fuel smear density distribution at 3.5 s.

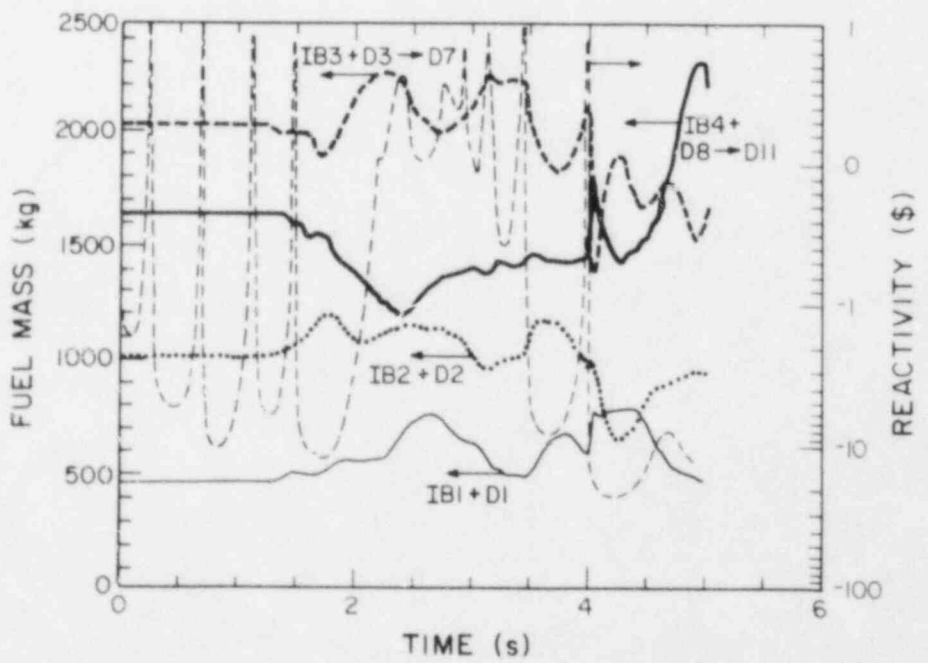

Fig. 15.
Total blanket fuel in combination radial regions.

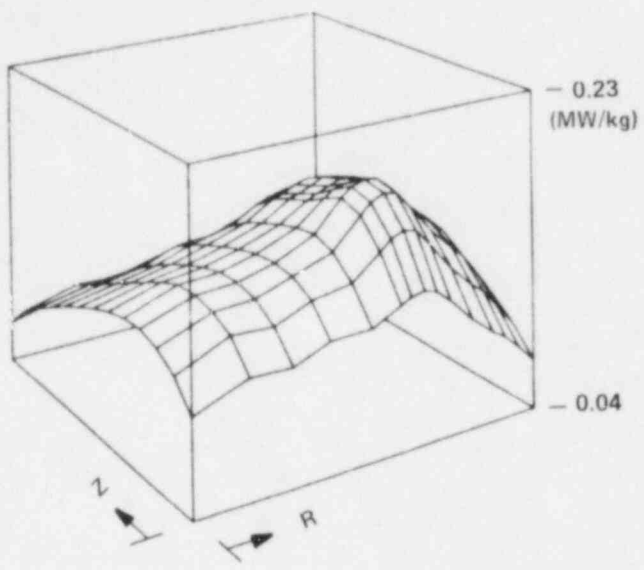

(a) Time = 0 s

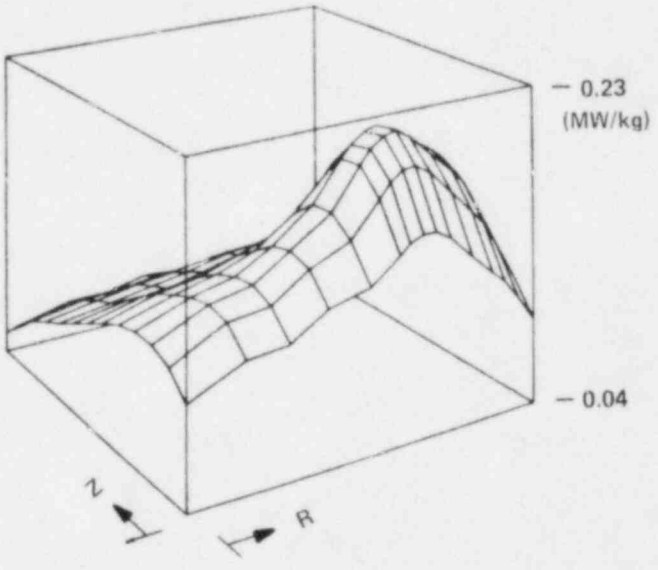

(b) Time = 1.5 s

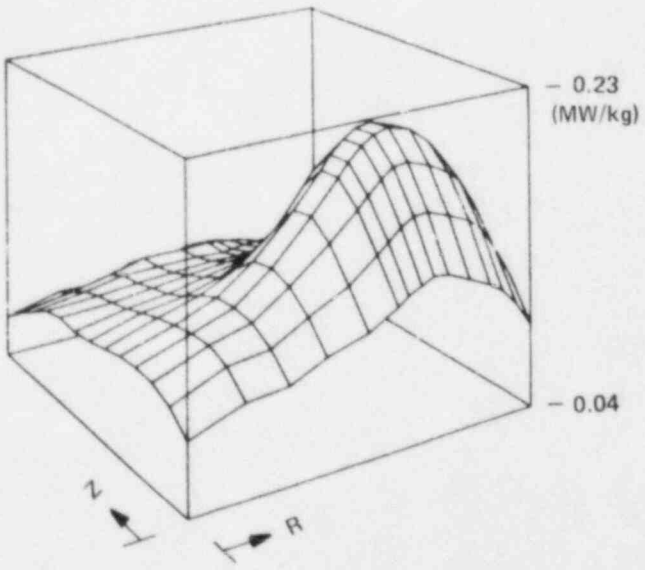

(c) Time = 2.0 s

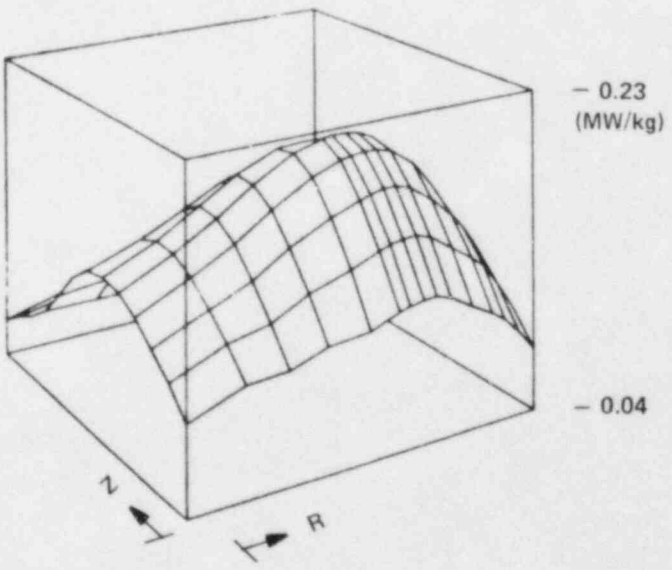

(d) Time = 2.5 s

Fig. 16.
Specific power distribution (shape only) in the active core.

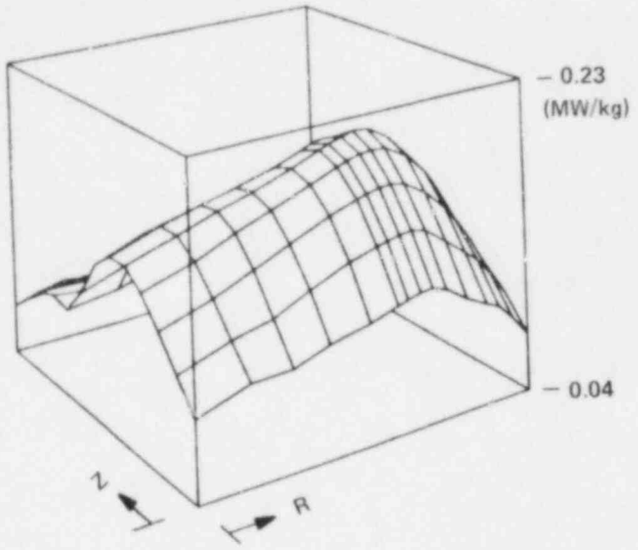

(e) Time = 3.0 s

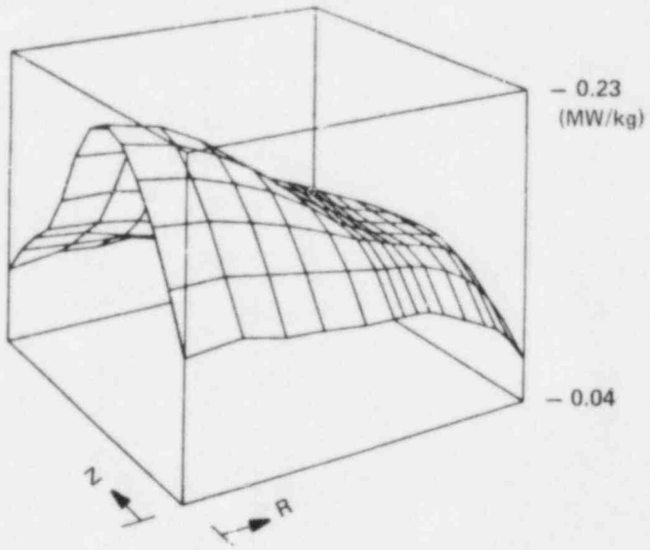

(f) Time = 3.7 s

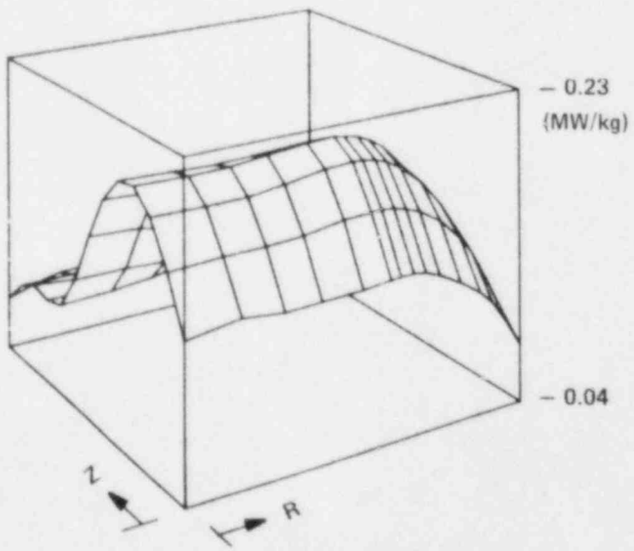

(g) Time = 4.0 s

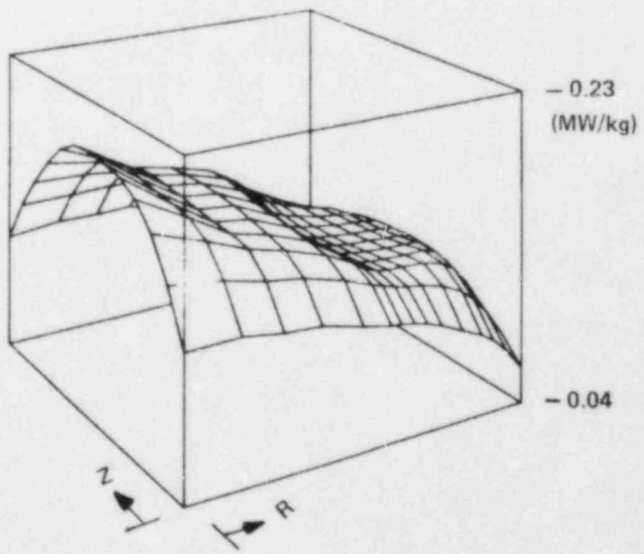

(h) Time = 4.2 s

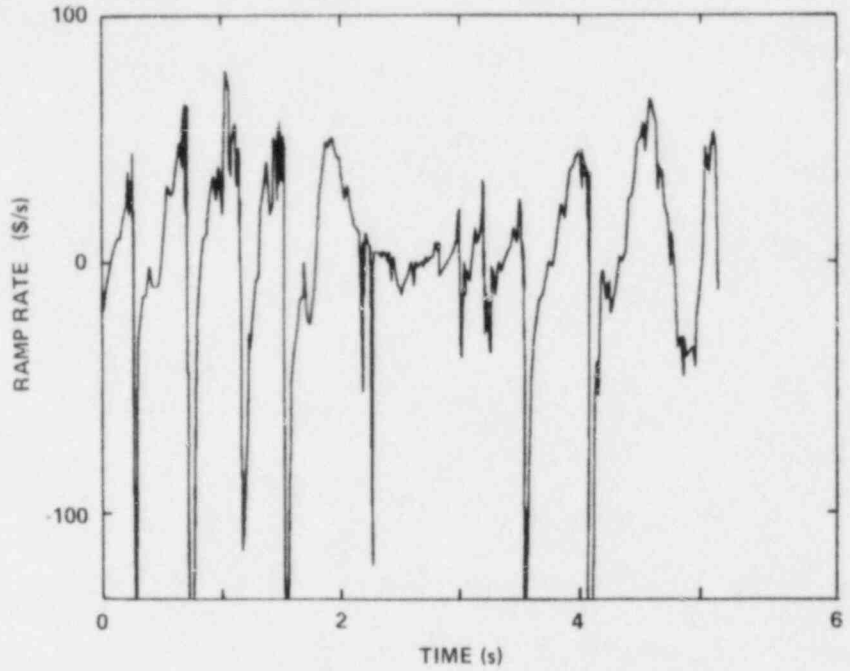

Fig. 17.
Disruption-phase ramp rate transient.

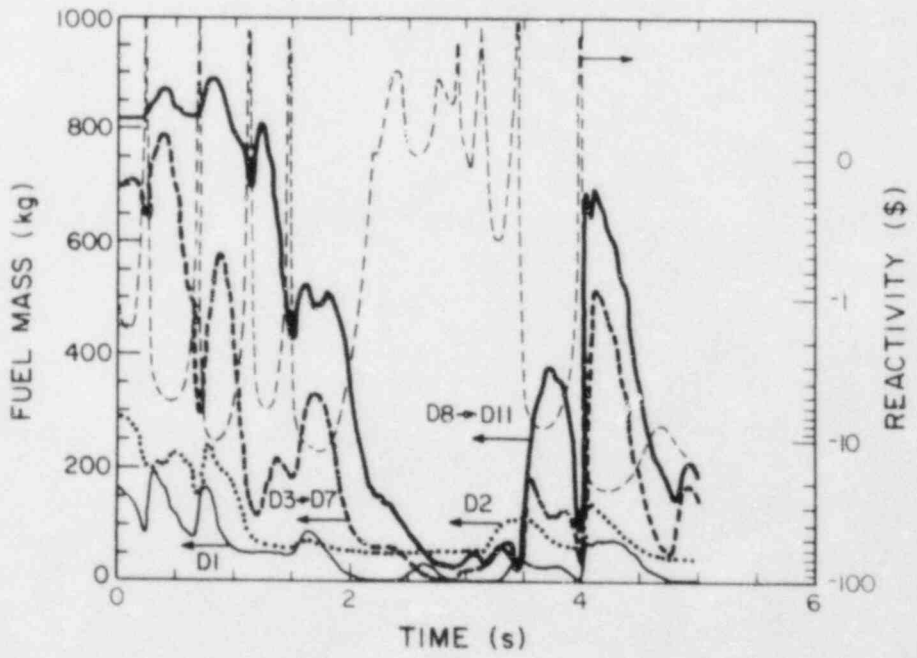

Fig. 18.
Driver fuel mass in the upper one-third in the radial driver regions.

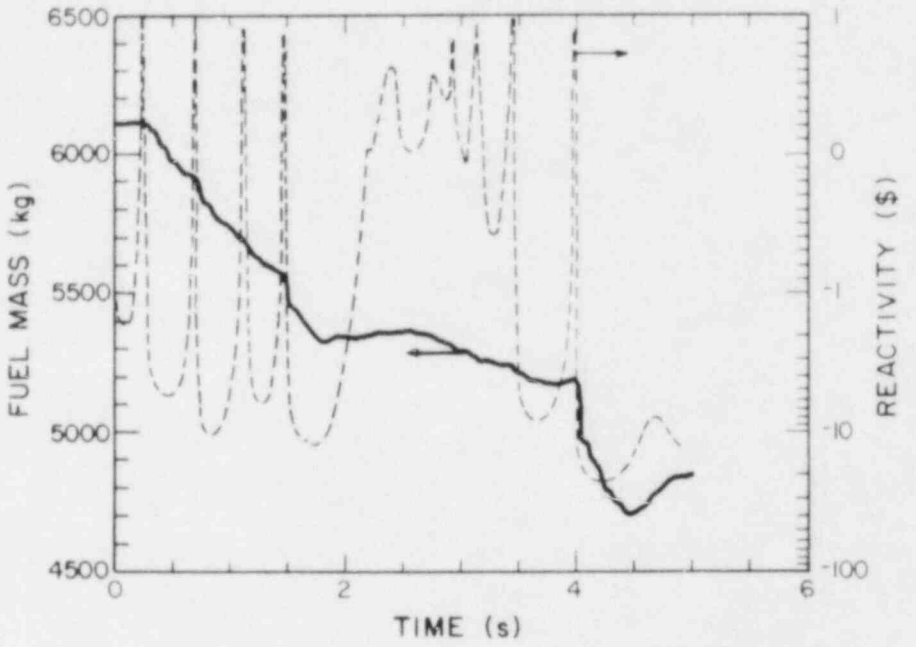

Fig. 19.
Total driver fuel mass in the active core.

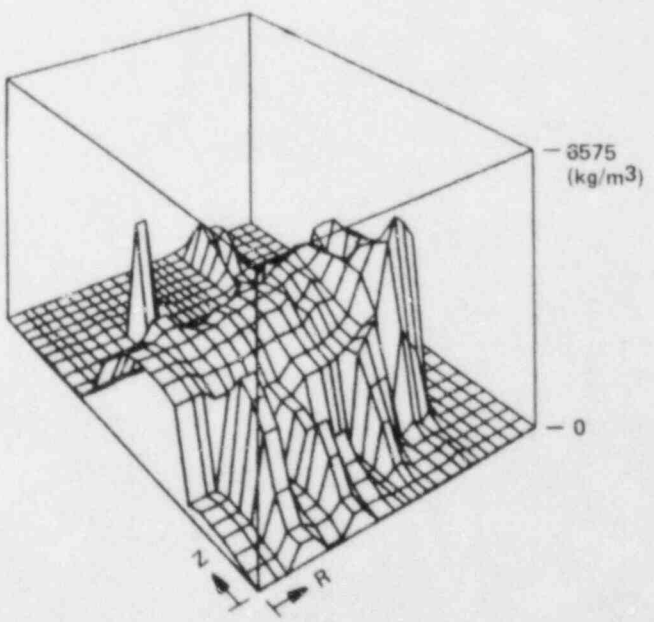

Fig. 20.
Driver fuel smear density distribution at 4.0 s.

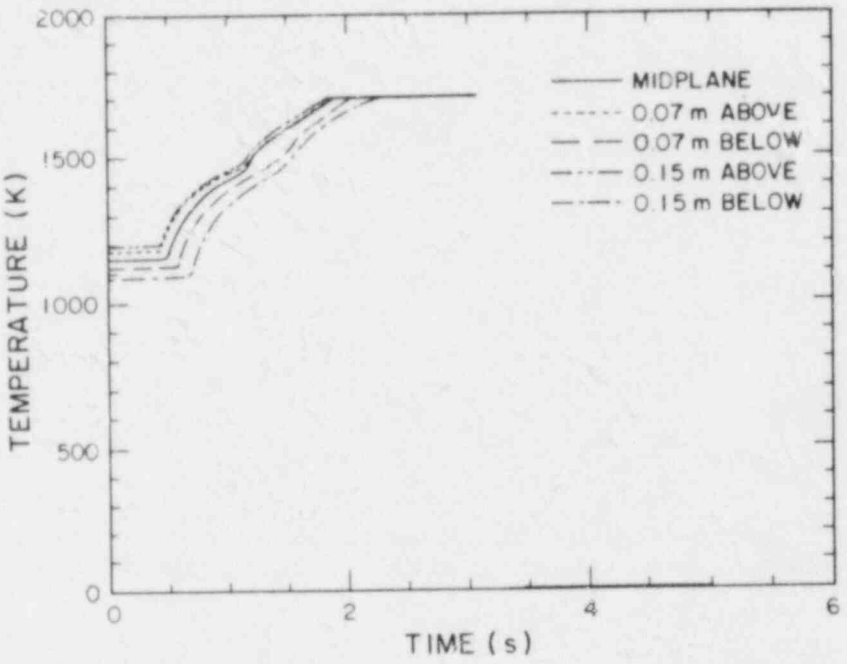

Fig. 21.
Outermost subassembly wall temperature at various elevations.

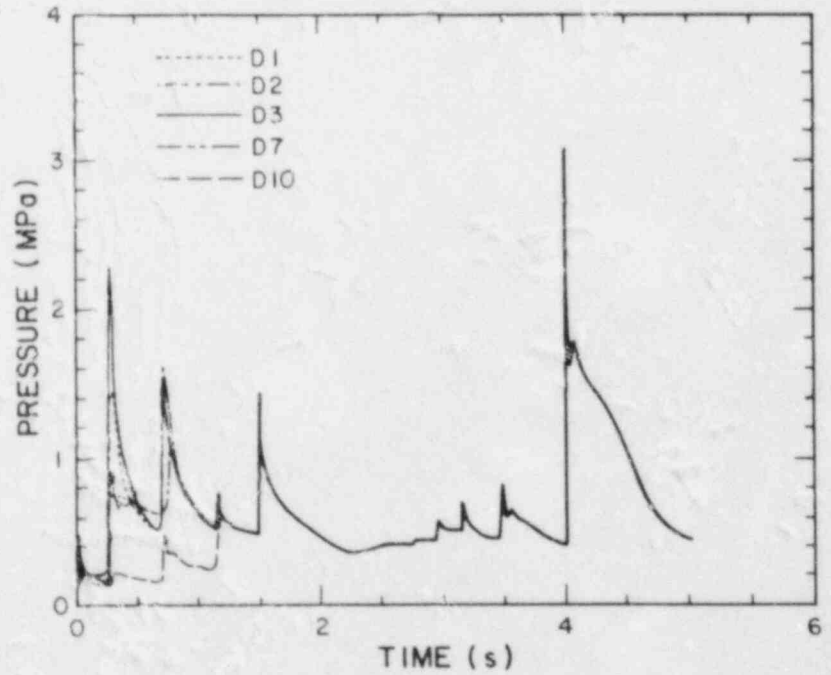

Fig. 22.
Midplane pressure transients in radial driver regions.

APPENDIX A
WHOLE-CORE DISRUPTION PHASE MODEL

1. Introduction

The capability to perform an integrated analysis of the disruption phase is relatively new and has not been utilized widely. It was previously attempted by Bohl [1] for the CRBR homogeneous core, by Luck [2] for the conceptual design study, and by Maschek [3] for SNR-300. Experience has been gained and many valuable insights obtained. This Appendix describes the application of this mechanistic capability to the heterogeneous core of CRBR to provide a reference viewpoint of the complex coupling between the fluid dynamics and neutronics and of the disruption progression in general.

2. Geometric Model

The purpose of an analysis of this type is to continue in a reasonably mechanistic manner the detailed treatment of the initiating-phase to a completely disrupted core state. This approach requires preservation of geometry in terms of SAS3D channel volumes and approximate radial locations. This was not achievable in practice because the SAS3D model grouped scattered subassemblies into channels while in SIMMER-II we had to transform that channel into an annulus. Axial geometry was preserved and expanded to include some of the sodium pool and UIS.

The case analyzed was the mild or slow EOC-4 LOFA. It was selected as a conservative attempt to envelop the disruption-phase energetics potential. Of particular importance in selecting an appropriate case is the blockage distribution (should be maximized), the expected lifetime of the internal blankets (radial power shape and blanket power), and the likelihood of early fuel removal to the radial blankets. The slow EOC-4 LOFA is expected to have rapid melt attack on internal blankets (minimum time to whole-core pool), delayed access to the radial blankets (delayed massive fuel removal), but not necessarily the maximum flow channel blockage extent (BOL is worse).

The SAS3D channel arrangement is shown in Figure 1 for the case of interest. The resulting SIMMER-II geometric model is shown in Figure 2 with correspondence between SAS3D channels and SIMMER-II rings given in Table 1.

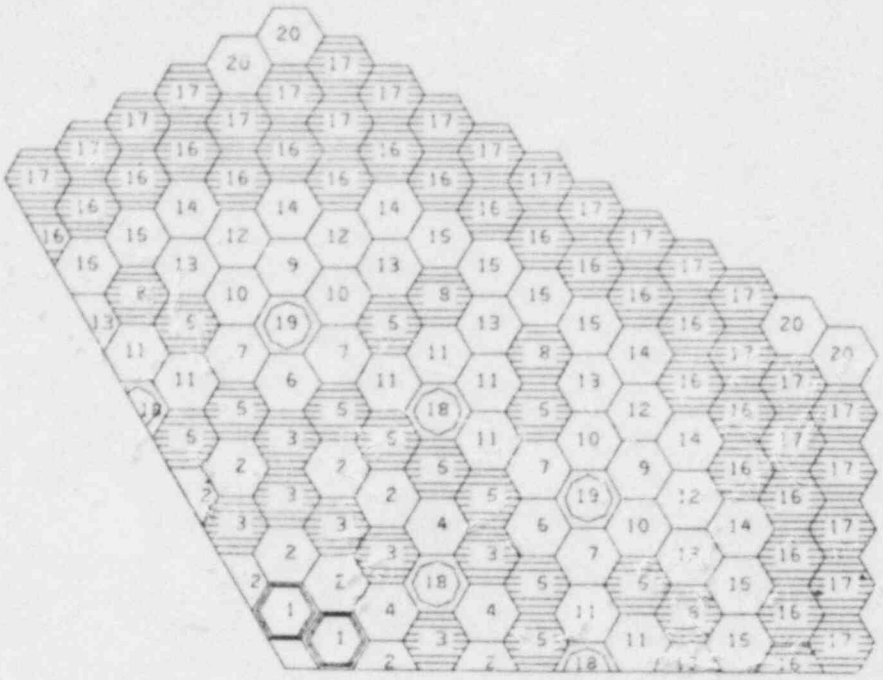

Fig. 1.
Subassembly assignment to SAS3D channels for the disruption-phase analysis.

The simulated inlet plenum provided a common and connected boundary condition at the inlets to the subassemblies. Thus, fluid-dynamic events that might occur in a particular channel had the opportunity to influence other channels or rings. The plenum obviously was too small compared to CRBR, but this size, coupled with an enhanced sodium compressibility, was chosen to give a reasonably prototypic dynamic response.

SIMMER-II does not have a primary-loop model so we inserted a length of inlet pipe in the geometric model to produce a proper static head on the inlet plenum. The loop flow had largely stopped at this time anyway.

The collector plenum above the core and the UIS simulation permitted sodium re-entry and a dynamic boundary condition in terms of inertia and thermal characteristics.

The internal blankets IB1, IB2, IB3, and IB4 (see Figure 2) were modeled as "gap" channels. This meant that the interiors of the internal blankets were fluid dynamically passive and the gaps were active. These gaps connected to the gaps in the axial blanket part of the internal blankets and into reservoirs in the lower reflectors of IB1, IB2, and IB3. These reservoirs were sized to correspond to the volumes of the lower axial blanket gaps of the neighboring drivers.

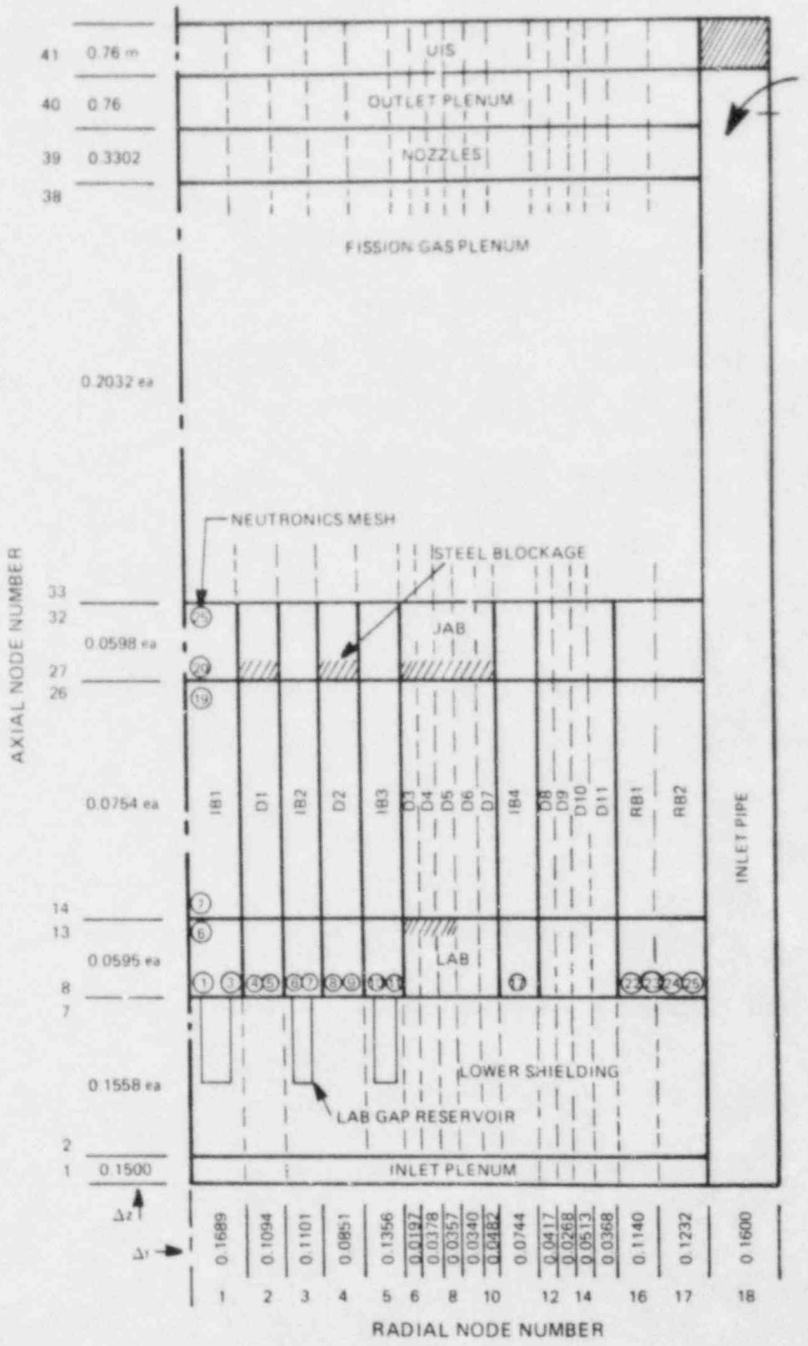

Fig. 2.
SIMMER-II geometric model for the disruption-phase analysis.

TABLE 1
CHANNEL-TO-RING CORRESPONDENCE

SIMMER-II Ring Number	SIMMER-II Ring Type	SAS3D Channel	Number of Subassemblies
1	internal blanket (IB)	1	7
2	driver (D)	2	12
3	internal blanket (IB)	3	18
4	driver (D)	4	18
5	internal blanket (IB)	5	36
6	driver (D)	6	6
7	driver (D)	7	12
8	driver (D)	11	12
9	driver (D)	11	12
10	driver (D)	10	18
11	internal blanket (IB)	5	30
12	driver (D)	13	18
13	driver (D)	12	12
14	driver (D)	15	24
15	driver (D)	14	18
16	radial blanket (RB)	16	60
17	radial blanket (RB)	17	72

3. Initial Conditions

The transformation from SAS3D was made at 19.75 s on the SAS3D time frame. It was selected because it is a quasistatic state as seen on Figure 3 and provided for overlap of the two methods, thereby permitting a check on the validity of the transformation. The thermal/physical state was transformed mechanistically with an interface code called SASSIM [3]. It bridges the various calculational meshes within SAS3D and between SAS3D and SIMMER-II. It also bridges the material property differences and modeling differences according to predefined prescriptions. Examples of these prescriptions are preservation of pressure, preservation of crucial geometry such as blockages, and elimination of artificial mixtures of liquid sodium and liquid fuel or steel.

The cladding blockage (assumed complete) extent was as follows: rings 2, 4, 6, 7, 8, 9, and 10 were blocked at the top, and rings 6 and 7 were blocked at the bottom. These blockages are shown on Figure 2.

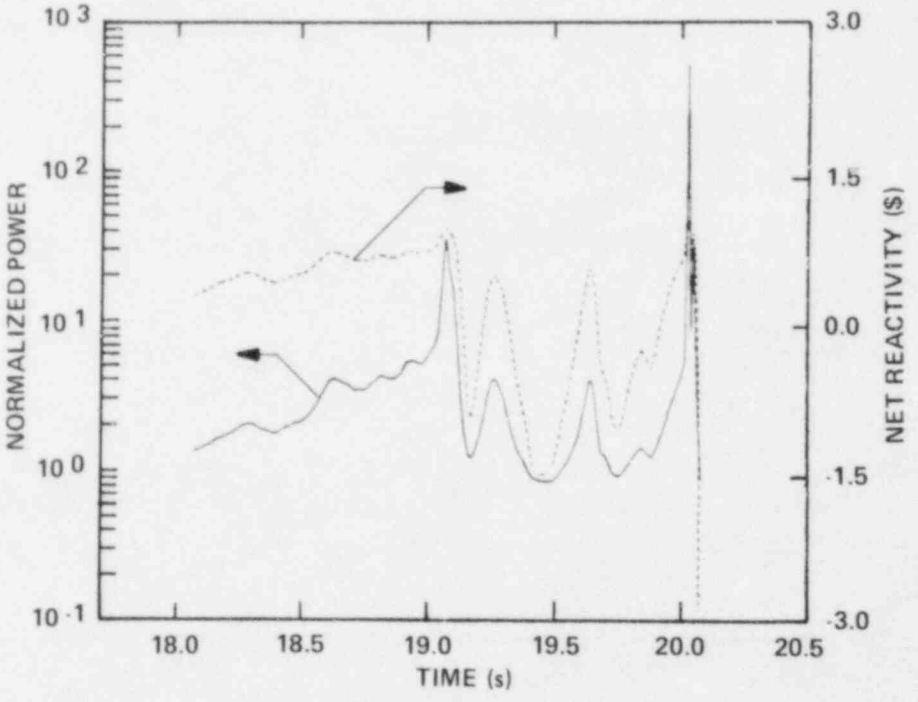

Fig. 3.
Reactor transient at conversion from SAS3D to SIMMER-II (19.75 s).

4. Modeling Assumptions

The neutronic approach was the same as used for other transient neutronics aspects of this assessment. Transport theory was used with 18 group cross sections. The neutronics mesh extended over the active core and surrounding blankets only. Some of the larger fluid-dynamic meshes were subdivided as shown on Figure 2.

The fluid-dynamics model assumptions were consistent with standard engineering correlations or the standard SIMMER-II models [4]. The specific important assumptions were: (1) the effective component viscosity for solid particles was 10 to be consistent with the discussion in Section II.6, (2) intact pin disruption was assumed to occur at a melt fraction of 50%, (3) subassembly walls were assumed to permit radial flow at the solidus energy, (4) gap flow initiated when the neighboring driver wall was at the solidus energy, (5) the Los Alamos fuel equation of state was used, (6) the maximum liquid dispersion size was 0.01-m diameter, (7) solid particle diameters were set at 0.001 m, and (8) thermal attack occurred on the interior of blanket subassemblies subsequent to complete wall melting in the gap channel.

5. References

1. W. R. Bohl, "Some Recriticality Studies with SIMMER-II," Proceedings of the Fast Reactor Safety Meeting, Seattle, WA, August 19-23, 1979.

2. L. B. Luck, et al., "An Evaluation of the Calculated Results of an Unprotected Transient Undercooling Accident in a Large, Heterogeneous-Core, Liquid-Metal-Cooled Fast Breeder Reactor," Los Alamos National Laboratory report NUREG/CR-3031, LA-9553-MS (December 1981).

3. W. Maschek, E. A. Fischer, and M. W. Asprey, "Transition Phase and Recriticality Analyses for a SNR-type Homogeneous Core with the SIMMER-II Code," Proceedings of the Fast Reactor Safety Meeting, Lyon, France, July 19-23, 1982.

4. L. L. Smith, "SIMMER-II: A Computer Program for LMFBR Disrupted Core Analysis," Los Alamos National Laboratory report NUREG/CR-0453, LA-7515-M (June 1980).

II.6. DISPERSAL BY EXTENDED FUEL MOTION

1. Objectives and Overview

In the previous section we saw that neutronic activity persisted throughout the progression of core-disruption states. However, we also saw a natural tendency of the system to resist development of large recriticalities. Both of these trends strongly favor "dispersal" rather than "disassembly" termination. In order to establish a common frame of reference as well as a conservative bias to the relative trend between these two termination modes, the manifestation of dispersal was deliberately minimized in the analysis in the previous section. Indeed, the insensitivity to obtaining large recriticalities translates into an insensitivity in timing margins for fuel removal, and the neutronic activity implies the persistence of "pumped-up" conditions and of driving forces for dispersal. In addition, dispersal path availability would increase with time (and level of core disruption) as more fuel, blanket, and control rod assembly walls melt and as old blockages remelt either by direct heating (fuel-containing blockages) or by melt attack (steel blockages). In this section we quantify these effects and estimate more realistically the tendency for the dispersal path as a function of the degree of core disruption.

The fundamental prerequisites for timely dispersal are the availability of fuel escape paths, the ability of core materials to move through these paths, and the existence of discharge pressure to provide the required rates. Each of these aspects is considered in the subsequent sections and generic fuel removal estimates are made.

Fuel escape paths may be found in the inter-pin (available at the beginning of the accident) and the inter-S/A-gap (becoming available as S/A walls melt) spaces as illustrated in Figure 1. In the latter category, blanket-to-blanket gaps would be particularly effective as their heating lags considerably behind the meltthrough of fuel assembly walls. In the heterogeneous CRBR core design with internal blankets, such effective gaps would be considerably more numerous than in the homogeneous design, thus providing a considerably enhanced potential for mild termination. This subject of initial escape path availability is addressed in the next section. However, the continuing availability over the time required for termination is equally important.

Steel (cladding or S/A wall) boundaries exist for both kinds of paths; hence, as a minimum, the escaping molten fuel (or fuel/steel mixture) would

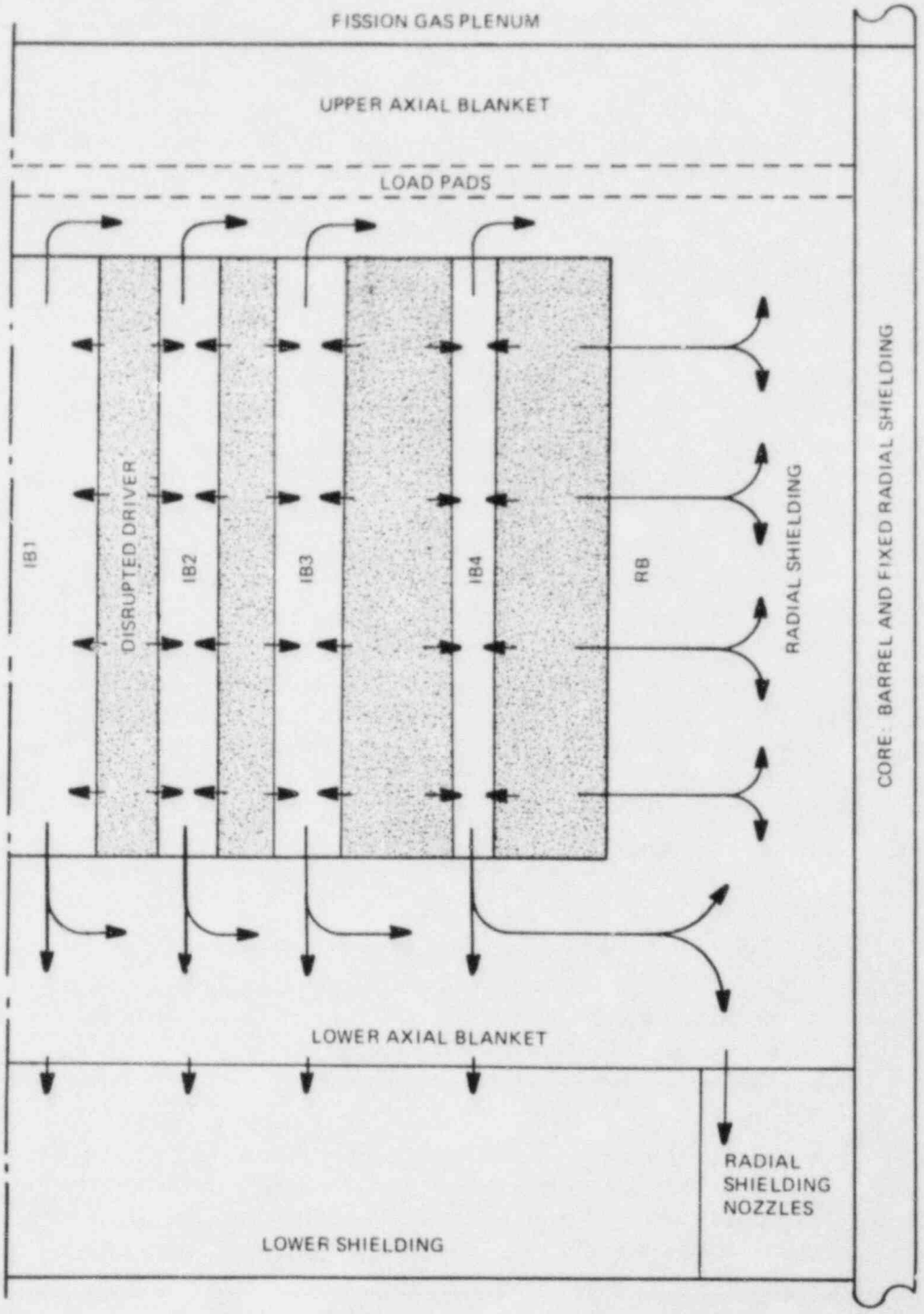

Fig. 1.
Intersubassembly gap fuel removal paths.

be subjected to approximately 1000 K lower temperatures (the difference between the fuel and steel melting points) at these boundaries. As a consequence of this strong cooling environment, the effectiveness of these paths in allowing the required fuel removal must be assessed against the potential for re-freezing and plugging during this dispersal process. Because of dimensional (characteristic hydraulic diameters: interpin approximately 3.5 mm and intersubassembly gaps approximately 11 mm) and geometric differences between the two path types, the propensity for plugging will differ. A generic characterization in this regard is attempted in Section 3 below. In Section 4, these results are integrated with a representative range of driving pressures, as deduced from Section II.5 to quantify the dispersal potential.

The Applicant's analyses considered this topic in substantial detail [1, 2] and concluded that dispersal ("meltout" in his terminology) would occur before disruption of the internal blankets (before the formation of a whole-core, cylindrical pool). Our evaluation of these analyses is documented in References 3 and 4. Our independent study differs from that of the Applicant not only in the use of considerably more sophisticated analysis tools, but also by our attempt to better quantify the forces available to drive the dispersal (Sections 4 and II.5). Our results indicate that internal blanket disruption could occur substantially sooner than expected by the Applicant. However, the fuel escape rates appear capable of keeping pace, especially with the creation of massive new escape paths into the radial blanket gaps just about simultaneously with entry into the whole-core pool phase. Thus, avoidance of the whole-core homogeneous pool is similarly (with the Applicant) concluded.

2. Fuel Escape Path Availability

In this section we summarize the fuel removal path characteristics, sizes, and general availability during the disruption sequence. The various reservoir sizes also are delineated.

The first available fuel removal paths are the normal flow channels from the active core into the upper and lower axial blankets. Their availability on a core-wide basis is determined primarily by the initiating-phase transient. Section II.3 reflects the SAS3D-predicted cladding blockages. Because the upward cladding relocation tendency is moderate to weak, upper cladding blockages will tend to be of the order of centimeters in thickness and perhaps initially incomplete. With the relatively short duration of the disruption phase, meltout of such blockages generally will not occur. In addition, the partial occlusion of channels by these blockages will act as a strong inhibitor to all discharges but those with superheated fuel at the leading edge. Therefore, it is appropriately conservative to consider such blockages effectively complete and sustained.

The flow channel volume in the axial blankets is relatively large, particularly when the freezing and plugging process effectively ablates the cladding and convects it to a downstream location as discussed in Appendix A. The resulting volume fraction for core materials is about 50%. Assuming a fuel steel mixture of nominal proportions, the two axial blanket could accommodate 70% of the core fuel.

The other path for early fuel removal is through the blanket-blanket or blanket-control S/A gaps within the core. We restrict this removal mode to only these gaps because the driver S/A walls will tend to deform against each other and against the internal blanket and control S/As as illustrated in Figure 2, because the drivers have higher pressure and temperature. These gaps, about 90 total (one side of a hex S/A), allow for axial removal to the upper and lower axial blanket gaps. The flow will generally initiate in the gap channel when the wall of the discharging S/A approaches its melting point. This can occur anywhere along the height of the core as thermal conditions dictate. Thus, channel access is virtually guaranteed.

In the reactor case (EOC-4), the gaps will be narrowed partially by radiation-induced swelling and will have increased effective heat capacity at the lower-core/lower-axial-blanket interface because of sodium in the gaps and within the lower part of the internal blankets. The in-core swelling is not a concern because the gaps can be accessed at virtually all axial elevations with

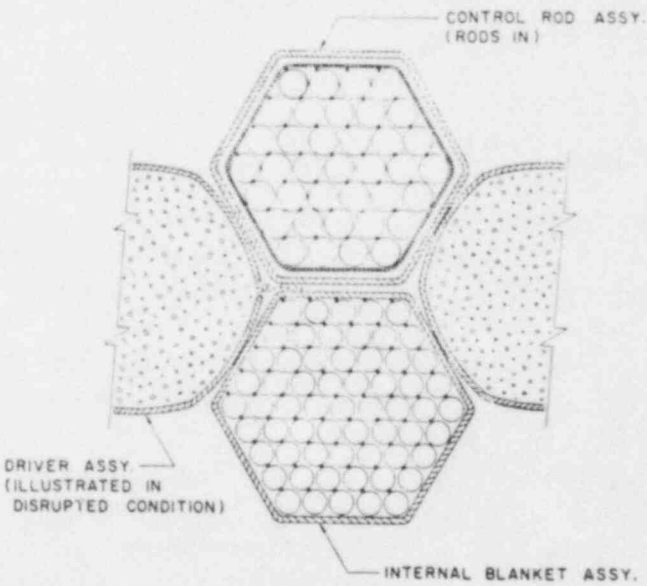

Fig. 2.
Intersubassembly gap fuel removal channels (courtesy of Argonne National Laboratory).

a minor time delay. Also, any in-core fuel occlusion will be remelted during each power burst. Therefore, the primary issue is the potential for occlusion at the exit of the gap channel where it discharges into the lower axial blanket gaps. As the neutronic activity continues during the early disruption phase, fuel in the lower active core is heated to disruption by melting. Any frozen fuel in an adjacent gap will be disrupted also by melting, because the neutron flux shifts toward the core bottom as a result of slumping recriticalities. Even frozen fuel in the top of the lower axial blanket will receive sufficient heat for melting. This can be seen from the strong flux shape changes for the slumping configurations of Section II.7 and from the reference disruption phase analysis of Section II.5. As a result, the gap channel will remain open for fuel removal.

For timely and substantial gap fuel removal, the reservoir for fuel deposition must be large and available. The volume fraction of gaps in the lower axial blanket is about 8% and the gap volume is 0.109 m^3. The mix of material will typically be in proportion to the nominal ratio in the core except for density changes at melting and except for previous cladding relocation. If we use a liquid-fuel to liquid-steel volume ratio of 1.36 and assume that this mixture will occupy the gaps, the lower axial blanket reservoir will hold a maximum of 600 kg or approximately 10% of the driver fuel.

The third major avenue for fuel removal is into the gaps of the radial blanket following failure of the peripheral driver S/A walls. This occurs late in the annular pool phase or at the beginning of the cylindrical pool phase. The flow channels are radially outward and contain changes in direction. The total outward flow area is about 0.3 m^2 which is an order of magnitude larger than the total internal blanket gap flow area. The volume in the gaps of the radial blanket for the active core height is 0.118 m^3 and it could hold about 600 kg of fuel (approximately 10%). A very large volume is available in the radial reflector region such that it can accommodate sufficient fuel for permanent subcriticality.

The rate of fuel expulsion is, of course, related to the magnitude of the net driving pressure, taking into account the presence of sodium in the gaps initially and the flow resistance across the load pads that control its escape. For example, based on simple steady-state flow approaches with a nominal total flow area at the load pad of about 0.06 m^2 and a hydraulic diameter based on load-pad clearances, 0.2-0.4 MPa of net driving pressure would be required to discharge 1 m^3 of sodium in 2 s. However, if the inventories of the lower and radial blanket gaps are of primary interest, then about 0.2 m^3 of sodium would need to be displaced in the same time interval, requiring perhaps 0.01 MPa of net driving pressure.

The final fuel removal paths are the control rod assemblies. They are cold relative to the disrupted core and are protected by residual sodium flow. However, some are located directly adjacent to peak power driver S/As.

Estimates have been made of the time to fail the control subassembly walls, but these are uncertain. We can be sure that they will not survive for very long if corner cracks develop and cause rapid voiding by small-scale fuel injection through the cracks. They represent a large shunt for core material transport, particularly downward. More than 10% of the core inventory can be accommodated downward without requiring fuel flow through the inlet orifices.

We can conclude, therefore, that because of the porosity represented by voided coolant channels, intersubassembly gaps, and withdrawn control rods, and because the volume necessary to accommodate approximately 40% of the core is small (approximately 0.5 m^3 if steel is included), reservoir capacity is not a problem. The available paths to access this capacity increase with disruption such that large-scale disruption with sustained high inventory in the core would be difficult to maintain.

3. Freezing and Plugging Behavior

The quantification of freezing in and plugging of fuel escape paths under reactor conditions has been controversial for most of the last decade. The fundamental difficulty arises because the fuel solidifies at a temperature of more than 1000 K higher than the steel melting point, such that substrate melting may occur during the fuel freezing process. Such melting is important because it may imply destruction of the insulating fuel crusts (these form because of the much lower fuel thermal conductivity as compared to that of the steel) and, hence, much higher heat losses and greater freezing and plugging potential. As far as predictability is concerned, this behavior transforms an otherwise straightforward heat-transfer calculation (conduction-controlled crust growth and plugging by channel occlusion) into an extremely complicated, interactive, fluid flow and heat-transfer problem including slurry formation, substrate entrainment and mixing, and crust stability. Further complications include variable fuel/steel inlet composition, variable compositions along the channel length from preferential deposition and/or entrainment, transient driving pressure, and complicated flow path geometries. It is our opinion, therefore, that the conduction model is oversimplified and, hence, inappropriate for such applications.

Having rejected this fundamentally-derived model, we must use prototypic material and geometry tests under carefully controlled conditions and a benchmarked generalized model to provide the basis for quantifying fuel removal. Such experimental basis is very limited at present, but work is continuing at several laboratories. Our approach was to conservatively predict fuel removal based on our generalized multiphase, multicomponent flow and heat transfer model that accounts for all the complications mentioned above and that automatically reduces to the conduction model when the appropriate conditions apply (one component flow with stable crusts). This

model is described in detail in Appendix A. It was benchmarked against the available prototypic-material experimental data, as discussed in the same Appendix. In this section we present and discuss the fuel removal and penetration trends predicted by this model for the reactor geometry and conditions.

- Pin Bundle Geometry

The geometric model used for one-dimensional benchmarking against the 7-pin thermite tests (Appendix A) was modified to represent a 217 pin, CRBR subassembly from the active core midplane to the top of the fission gas plenum. The thermite injector was replaced with the CRBR active core section. The same 0.05 m noding was used. This "real" geometry and "real" material mockup, together with our generalized freezing and plugging model, was used to investigate the fuel removal potential through CRBR pin bundles for a spectrum of conditions and discharge transients.

The first series of results, Figure 3, shows the effects of discharge pressure and initial fuel superheat. All these results assumed an isothermal, single-phase, fuel discharge driven by a constant pressure at the core midplane. An effective component viscosity of 200 times the liquid fuel value was used for the solid phase in a particulate slurry. The effect of superheat was small as expected because crust thickness did not dominate this process nor did the somewhat higher initial fuel energy. The early part of the penetration shown on Figure 3 is more inhibited by fuel superheat because it causes earlier cladding ablation and subsequent fuel particle formation. The significant point to note from these results is that nearly all of the fuel of the upper half of the core could be discharged quickly if pressures of 0.5 MPa were sustained for about 0.5 s.

Generally the figure of merit considered in assessing freezing and plugging models and data is fuel penetration distance. For recriticality potential we are more interested in the mass discharged. Obviously, penetration and removal are related directly in the S/A geometry. For these same cases we plotted the penetration distance vs pressure in Figure 4. A penetration of about 0.35 m corresponds to complete removal of one half the S/A contents (we consider one half upward and one half downward because the motivating neutronic activity roughly divides the fuel mass after each burst). There is a plateau in the penetration vs pressure response because of the tendency to freeze large steel occlusions in the "spring" region if the spring heat capacity is included as part of the wall. The spring does not have good contact with the cladding (line contact if any) and therefore should not be included as rapid-response heat capacity. The result of disregarding the spring is greater, more reliable, penetration into the low heat capacity, high flow area region above the blanket pellets. This can be seen for the "burst driven" results on Figure 4. In reality, the no-spring curve would be

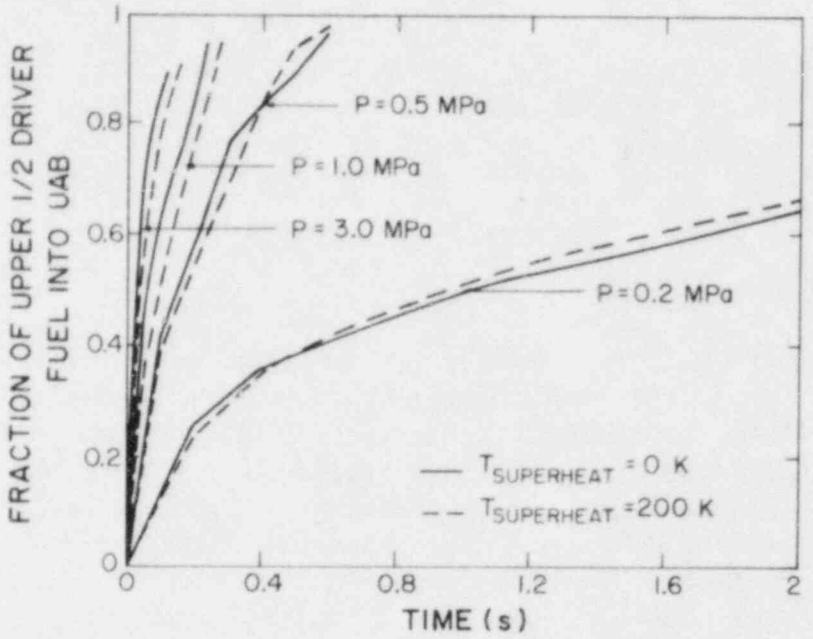

Fig. 3.
Fuel removal transients through pin bundles for various discharge pressures and temperatures.

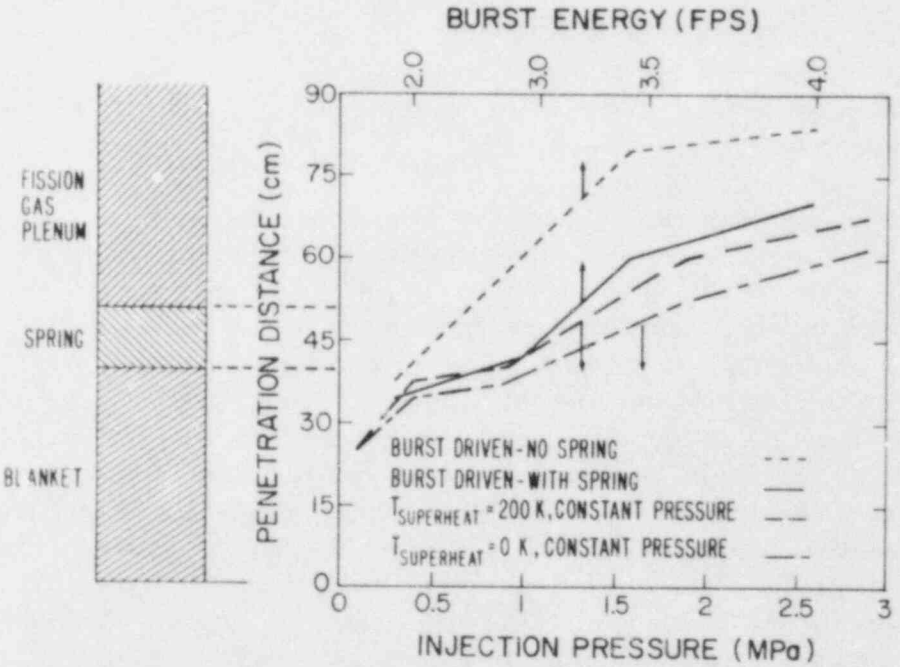

Fig. 4.
Fuel penetration distances in pin bundles for various assumptions and conditions.

off-scale if the hot material could flow inside the cladding in the fission gas region as it did in Spencer's 2.0-kg, hot wall test [5].

The second set of results shows the fuel removal potential for a discharge following a burst during the early subassembly disruption phase. The core material was assumed to be a mixture of cladding steel (codisruption) and fuel that was 50% solid and 50% liquid. The steel and fuel were thermally equilibrated at the fuel melting point. The discharge was driven by power bursts of different magnitudes with a representative CRBR axial power shape. Thus, small bursts produced low discharge pressures and had particulates at the leading edge. The cladding steel was assumed to be distributed physically on a scale for rapid heating by the fuel (in less than 0.2 s) and, therefore, was the pressurizing material. The correspondence between burst energy in full-power-seconds (FPS) and steel vapor pressure can be seen on Figure 4.

The results in terms of penetration distance are given on Figure 4. The "with spring" and "constant press" results agree well up to 1 MPa (3 FPS) and then diverge as the superheat effect becomes dominant at high burst energies. Figure 5 shows rapid and complete discharge in all cases.

The third set of results, shown on Figure 6, indicate the influence of the effective component viscosity for solid particles on fuel removal assuming no superheat and a constant pressure of 0.5 MPa. Even with a high assumed value of 2000 times that for liquid fuel, a high fraction of the fuel in the upper one half of the subassembly is removed. The rate is greatly reduced, however. This lengthened removal time is important if the lifetime of the discharge pressure is short compared to the required discharge interval.

- Subassembly Gap Geometry

A large set of calculations was performed with our model to determine the discharge characteristic of fuel and fuel/steel mixtures through gap channels under a variety of conditions. A detailed discussion of one particular calculation is given below to provide a view of the general problem. Then some additional results are provided to characterize the general fuel removal potential of the gaps.

The analyses have been oriented toward the fuel discharge through the gaps between internal blankets. These gaps are important as early removal paths. They can be visualized as channels connecting the active core to the reservoir space represented by the gaps in the lower axial blanket. As such, the discharge will not be short-term but will continue until occlusion, reservoir fill-up, or channel disruption by wall melt-through.

The calculational model represented a slab as shown in Figure 7. A plane of symmetry was placed at the middle of the gap. Typically the

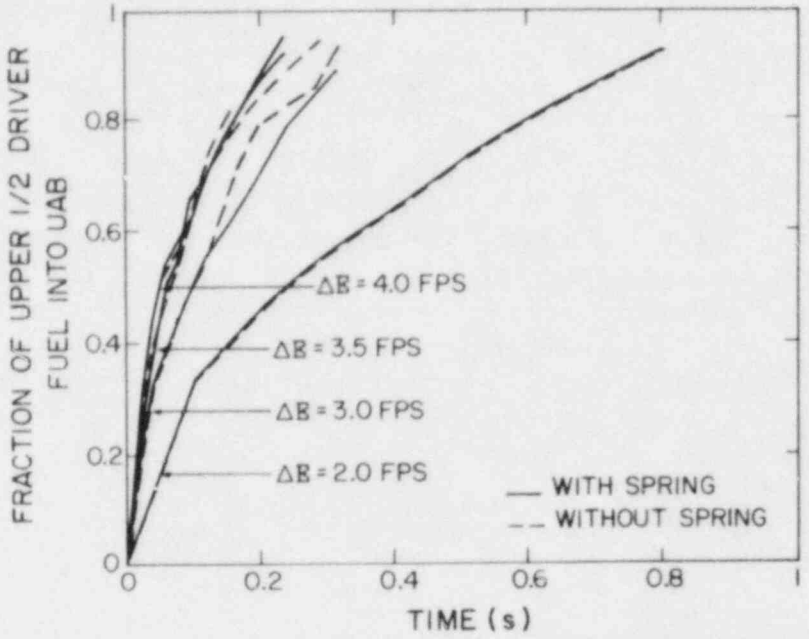

Fig. 5.
Fuel removal transients through pin bundles for various heating transients and channel assumptions.

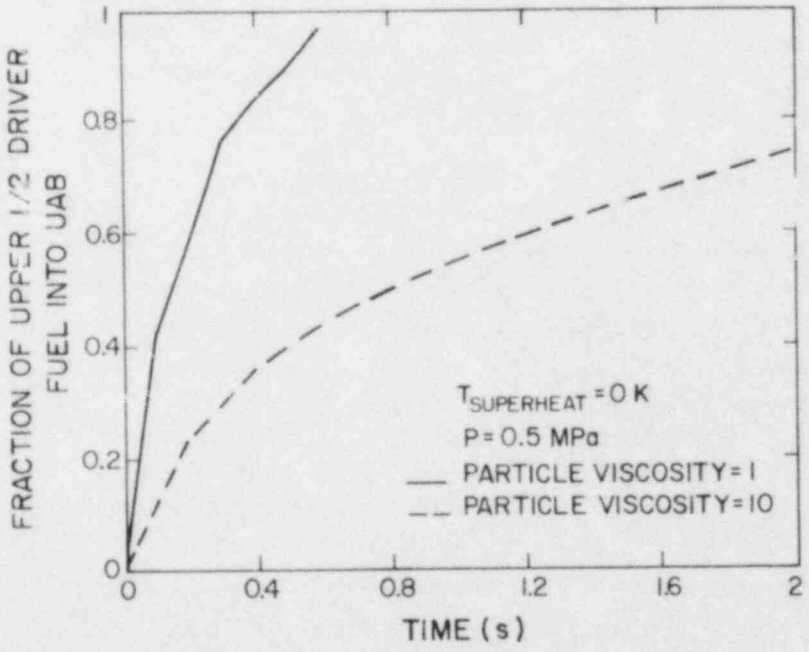

Fig. 6.
Effect of particulate viscosity on pin-bundle fuel removal transients.

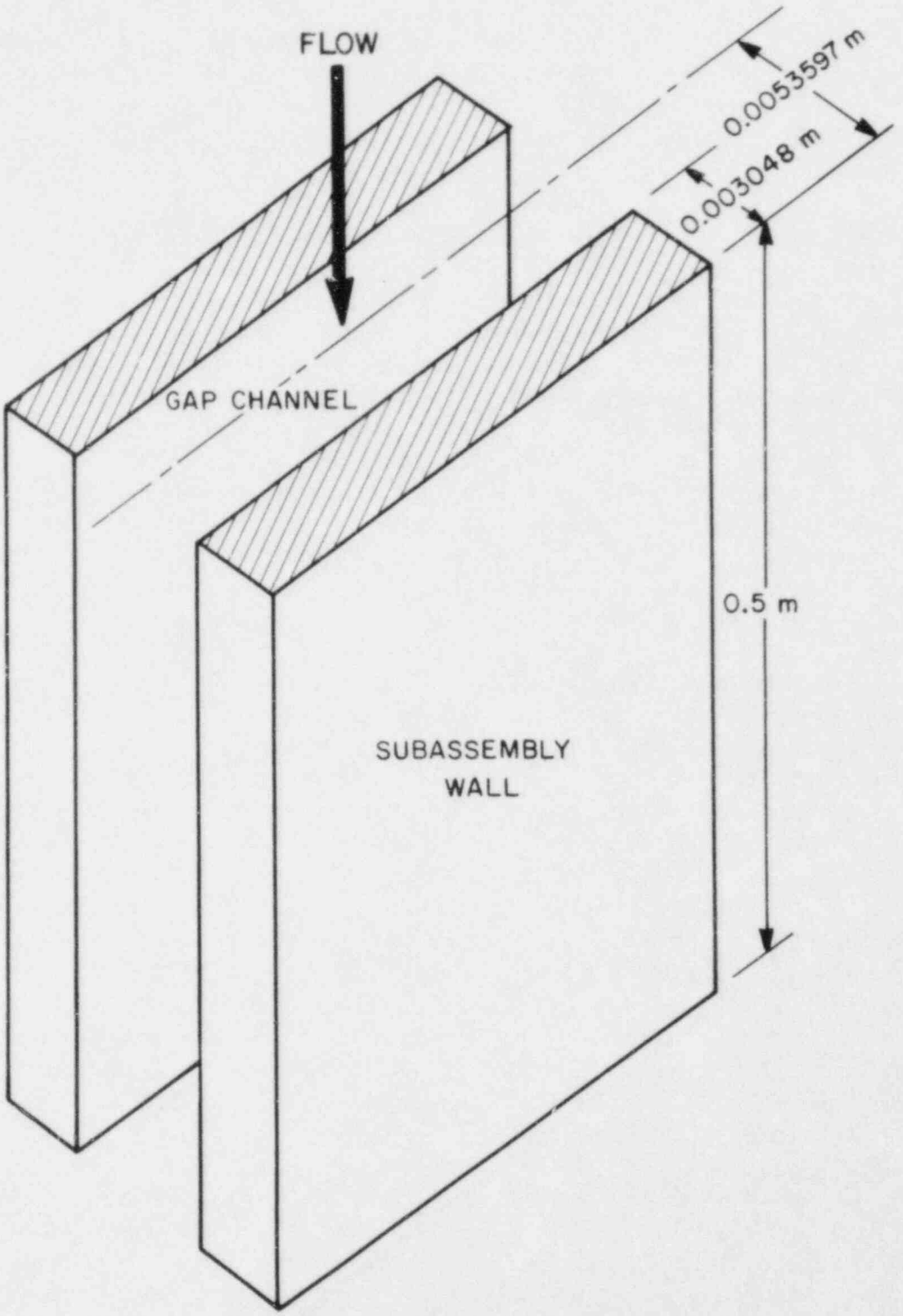

Fig. 7.
Gap channel geometry for fuel removal analysis.

channel length of interest (core mid-plane to lower axial blanket) is about 0.5 m. The gap lateral length was undefined in the two-dimensional slab geometry but was implied to be 1 m. Thus, for the calculational channel to represent one side of a hex subassembly, the calculated mass discharges were multiplied by the true hex-side dimension in meters.

We considered first a representative disruption-phase multicomponent discharge that was energy starved or had some upper internal blanket breakup to give a particle volume fraction of 35%. Also, we assumed that S/A wall melting had occurred to raise the steel content to 40% by volume. The remainder of the discharge was liquid fuel (25%). All materials were assumed to be at the fuel melting point which is typical for such slurries. The gap wall was assumed to have an axial temperature distribution running from 860 K at the exit to near the steel melting point at the inlet. These are conditions that could exist for an EOC-4 core where the sodium had voided from the internal blankets and further heatup had occurred by conduction from neighboring driver walls that were in physical contact. An injection pressure of 0.04 MPa was assumed. This pressure is of the order of the gravity head for a fuel/steel pool.

The results are portrayed visually on volume fraction plots. The solid materials are layered from right to left and the mobile materials (liquids and particles) from left to right. Figure 8 indicates the initial state. A 1-m channel was used to demonstrate the freezing and plugging potential. The reservoir at the end of the channel was of arbitrary size. Figures 8 through 14 show the evolution of the flow and channel characteristics. Figure 9 shows the fuel crust forming on the ablating wall. In this calculation the molten steel under the crust was assumed to entrain into the stream as it formed. This is a major uncertainty in calculations of this type. It is difficult to justify a completely stable crust and at the same time complete, instantaneous entrainment. The choice used here is conservative with respect to quenching the stream (forming more particles) but nonconservative from the standpoint of the continual opening of the channel by wall meltout. This situation has been considered at both extremes and the uncertainty is not a major influence because of the opposing effects.

Figure 10 shows the downstream steel blockage generated at the position where the fuel-particle/steel slurry has cooled by convective heat loss to the wall. The fuel crust did not grow at the downstream location because the liquid fuel was depleted by plate-out and bulk freezing (the particles from this mode are shown as indicated on Figure 9). Also seen is the particulate "blowby" generally seen in experiments. In the calculation, the steel was depleted by plateout, leaving only particles to convect downstream as a result of their earlier momentum and the influence of gravity. At 1 s a substantial occlusion formed and the steel/particle slurry accumulated on its upstream side. The crust did not grow rapidly in this case because the low liquid fuel volume fraction prevented full access of the liquid to the crust surface.

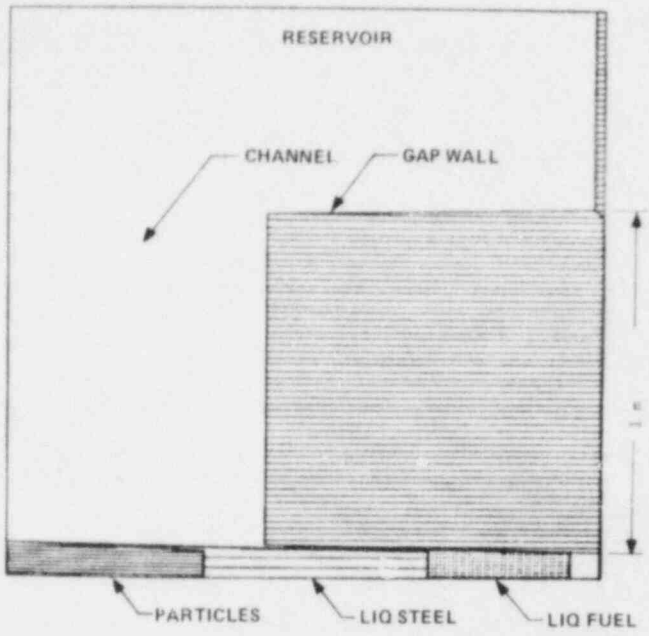

Fig. 8.
Calculated material configuration in a gap channel at 0 s.

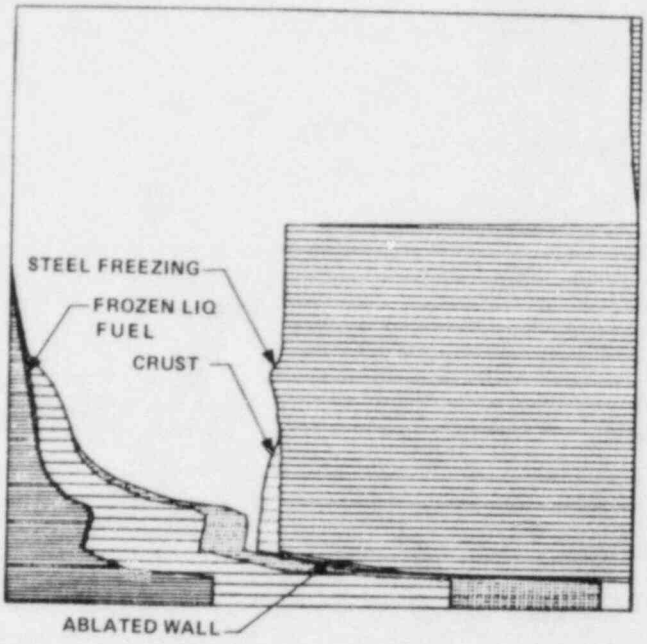

Fig. 9.
Calculated material configuration in a gap channel at 0.2 s.

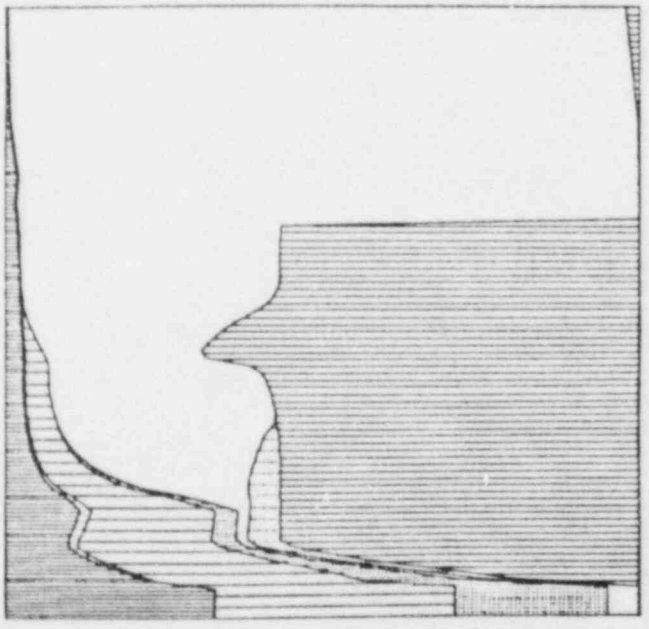

Fig. 10.
Calculated material configuration in a gap channel at 0.4 s.

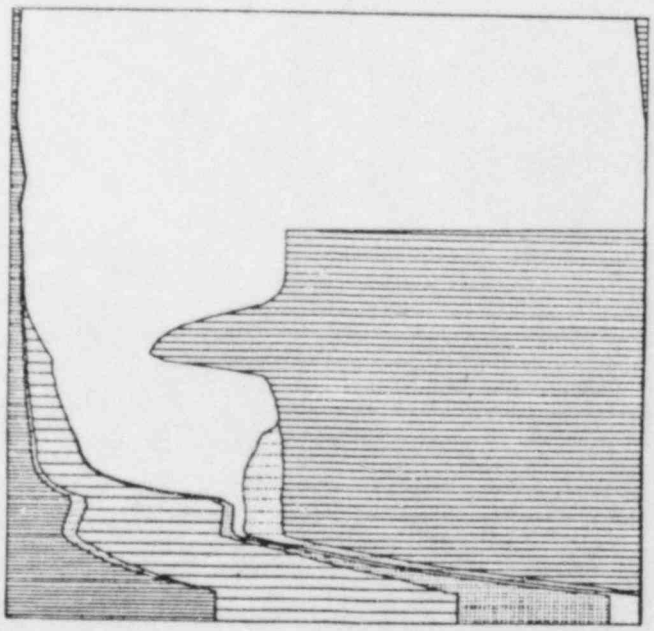

Fig. 11.
Calculated material configuration in a gap channel at 0.6 s.

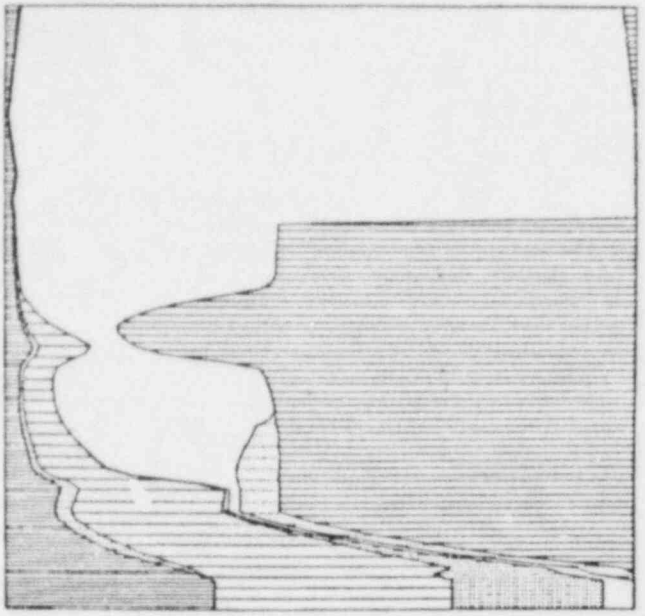

Fig. 12.
Calculated material configuration in a gap channel at 0.8 s.

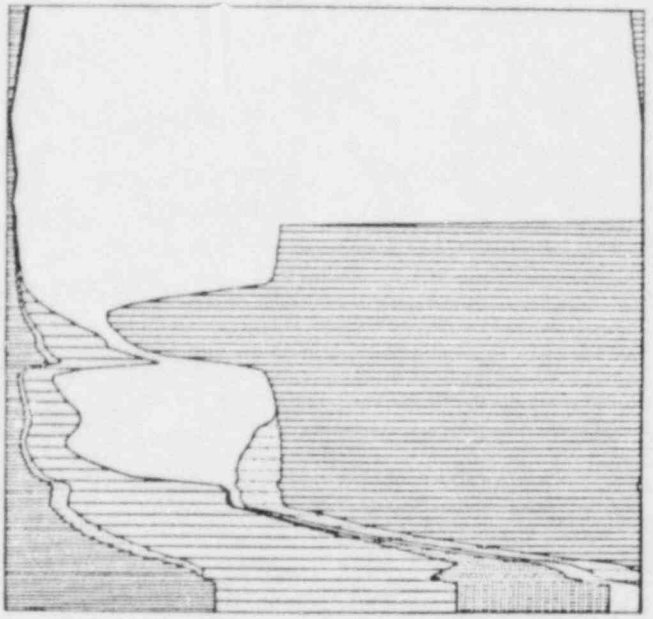

Fig. 13.
Calculated material configuration in a gap channel at 1.0 s.

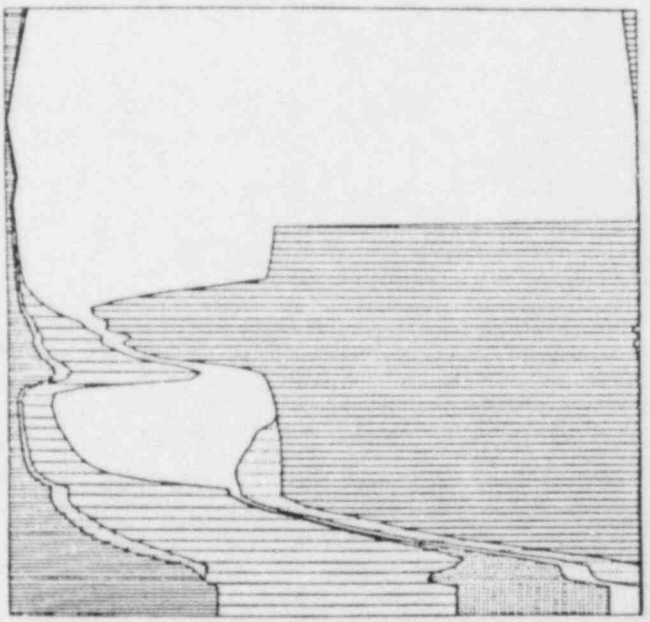

Fig. 14.
Calculated material configuration in a gap channel at 1.2 s.

In the longer time frame, the channel filled behind the blockage which occurred at a distance of about 0.7 m. Thus, in the reactor situation the occlusion would be well within the lower axial blanket and would permit radial flow into the neighboring gaps. Other calculations at higher driving pressures (0.1 to 0.2 MPa) completely ablated the channel with no plugging.

If we return to the internal blanket geometry with a channel 0.5 m long and calculate the fuel removal capability for different situations, we obtained the results on Figure 15. The areas under the curves represent the mass removed through the 0.5-m channel with a lateral extent equal to one side or flat of the hex subassembly. The injection in these cases was fuel only. The effect of superheat was to increase throughput initially because of delayed crust growth. The wall ablated and introduced large quantities of liquid steel into the stream that reduced the fuel throughput until it was transported out of the channel. Then the throughput increased rapidly because the ablating wall had been removed. Increased pressure produced higher throughput initially, more rapid wall ablation, and a quicker return to high flow. A typical fuel removal quantity for the superheat cases was approximately 15 kg/gap, occurring within approximately 1 s, even if the later flow re-establishment was neglected. Given the large number of gaps (see Section 2) an important fraction of the core inventory could be removed in this way.

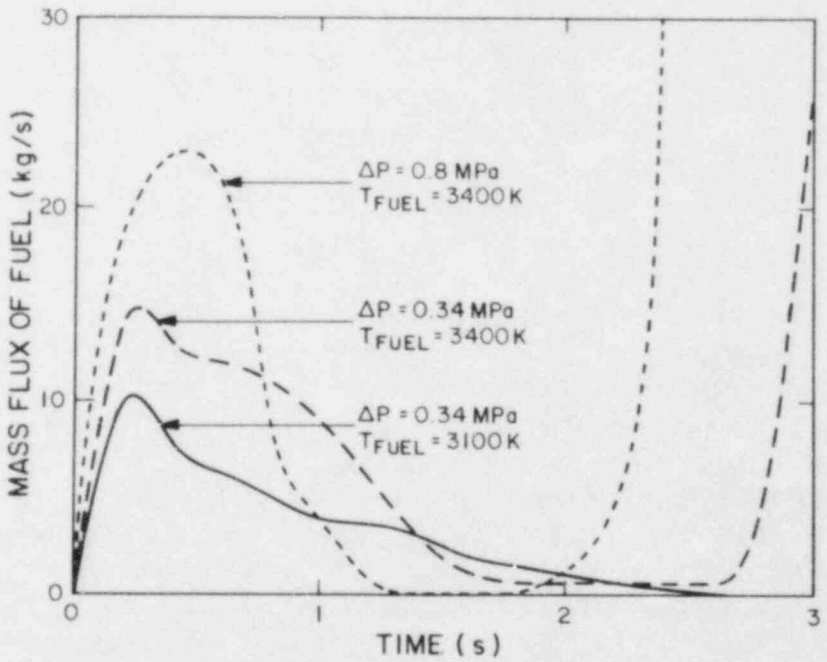

Fig. 15.
Gap channel fuel removal transients for various conditions.

4. Fuel Discharge Pressures

From the mechanics of freezing and plugging discussed in Appendix A, it is clear that high discharge pressures are desirable for assuring large quantities of fuel discharge from the core. Most estimates of fuel removal are made on a quasistatic basis for simplicity and clarity. To make estimates of whole-core fuel removal on this basis requires some insight into the general characteristics of the discharge pressures in heat-loss environments with transient neutronic heating.

We have seen from both the reference initiating-phase and reference disruption-phase analyses that the general environment for fuel removal is nonuniform, complex, and highly transient. The disruption begins with the core in an energy-poor state relative to the all-molten condition and at an average temperature incapable of producing a sustained pressure differential of 0.5 MPa. This pressure would generally assure massive fuel removal if paths were available and the time frame was a couple seconds. Thus, an absolute pressure of approximately 0.7 MPa is required. If fuel vapor must supply this pressure, a temperature of approximately 4200 K is necessary. However, if steel is available, its temperature need only be about 3600 K.

These temperatures are such that heat losses to any remaining structures would be very high (crusts would not be present). Thus, these states will tend to exist locally and temporarily only. Indeed, it is this local and temporary characteristic that causes the subsequent recriticalities. This implies that the loss of locally high temperature is a nonsustainable state if a potentially critical fuel inventory exists and fission gases are largely deentrained (fuel is not levitated by noncondensible gas). What we need to know is a typical pressure decay history of the pressure spikes associated with recriticalities. We would not expect this history to be linear because of the exponential relation between pressure and temperature.

To obtain a characterization of this pressure history, a number of subassembly-scale calculations were performed with various initial conditions, power pulses, and heat-loss assumptions. These calculations are described below.

The geometric model for the analysis was based on single subassembly dimensions as shown in Figure 16. The nominal subassembly wall was included at a temperature of 1240 K. This would be consistent with an early disruption-phase state. The calculations were performed with SIMMER-II in a nonneutronic mode. A programmed power pulse was used along with the power distribution shown in Figure 16. The calculational mesh also is shown.

The calculations were initiated from a slumped state that is consistent with an implied recriticality. All boundaries were closed. The pressure

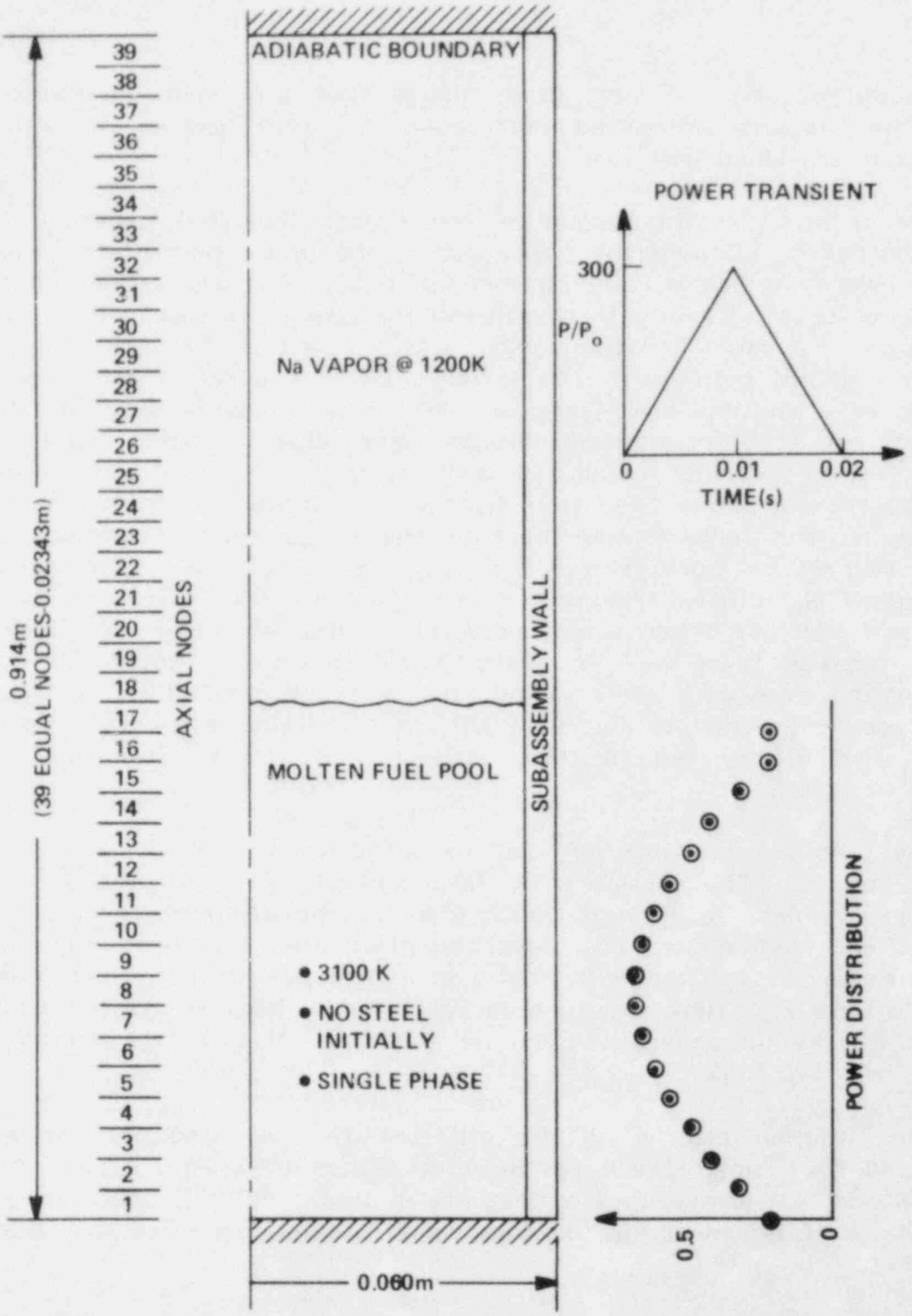

Fig. 16.
SIMMER-II geometric model for subassembly pool analysis.

decay could occur only from fluid mixing (hot into cold--this should be minimal in this one-dimensional representation), heat loss to the wall, and heat loss to entrained wall steel.

The results for this group of calculations indicated generally similar characteristics. Following the power burst, the upper part of the mass was driven upward, typically reaching the top in 0.1 s or less depending on the bubble pressures. Gravity then refluxed the upward displaced mass into the original pool region. For the various cases listed in Table 1, this reflux process is shown on Figures 17b through 25b. The reflux time interval is made up of a waiting time (time between initial dispersal and initiation of refluxing) and a reflux interval (time for upper slug spreading and fallback). In nearly all cases, the overall reassembly time was 0.5 to 0.6 s. Wall steel entrainment assumptions (wall melt fraction to initiate entrainment) had little influence on the fallback time because the initial crust formation delayed surface melting by more than 0.6 s. The cases with the small amount of entrained steel initially represented subassemblies that disrupted somewhat earlier and had just begun to entrain steel. These situations were much more dynamic because there was insufficient steel to cause quenching. Case 32 represented a case with 30% cladding steel from initiating-phase codisruption. These cases with steel exhibit very different characteristics on a time scale greater than 0.6 s, but in their early response they are similar to the others.

The pressure available for fuel discharge was that near the location of the peak power. The pressures at these locations for the various cases are shown on Figures 17a through 25a. Clearly, the discharge pressures were enhanced and sustained if small quantities of steel were present. The limiting situations were associated with fuel vapor pressure with no noncondensible gas as in Case 21. Here pressure decayed rapidly because of more expansion (no gas to take up volume). Even for this case, the average pressure (see Table 2) was 0.6 MPa.

The situation clearly will be different if a subassembly has massive distributed heat sinks (such as large quantities of unequilibrated particles and/or steel). If many subassemblies are in this condition, neutronic activity will continue if the need for fuel removal still exists (greater than a critical inventory).

Because low-pressure conditions cannot be sustained in a neutronically active system, fuel removal pressure sufficient for at least periodic removal is available. As seen in the previous section, the time for pin bundle penetration is a few tenths of a second if pressures are in the 0.5 to 1 MPa range. During early disruption, bursts of the necessary magnitude to produce 0.5 to 1 MPa of fuel vapor pressure are common for lead subassemblies (see Sections II.5 and II.7). Because codisruption occurs for the majority of situations,

TABLE 1
VARIATION MATRIX FOR SUBASSEMBLY-POOL PRESSURE TRANSIENT ANALYSIS

Case #	C02	C03	C04	C06	C13	C14	C21	C32	C33
Noding	1x39	1x39	1x39	1x39	4x39	4x39	1x39	1x39	1x39
Energy Input (FPS)	3	3	3	3	3	1.5	3	3	3
Initial Pool Void (%)	5	5	5	5	5	5	5	5	5
Cover Gas	NC	NC	NC	NC	NC	NC	C	NC	NC
Initial Steel (% Cladding)	0	0	0	0	0	0	0	0.30	0.02
Wall Heat Transfer	Yes	Yes	Yes	Yes	Yes	Yes	Yes	Yes	Yes
Steel Entrainment Melt Fraction (%)	100	0	100	0	70	70	0	0	0
Entrained Steel Effective Dispersion Size (m)	0.01	0.01	0.0001	0.0001	0.0001	0.0001	0.0001	0.0001	0.0001

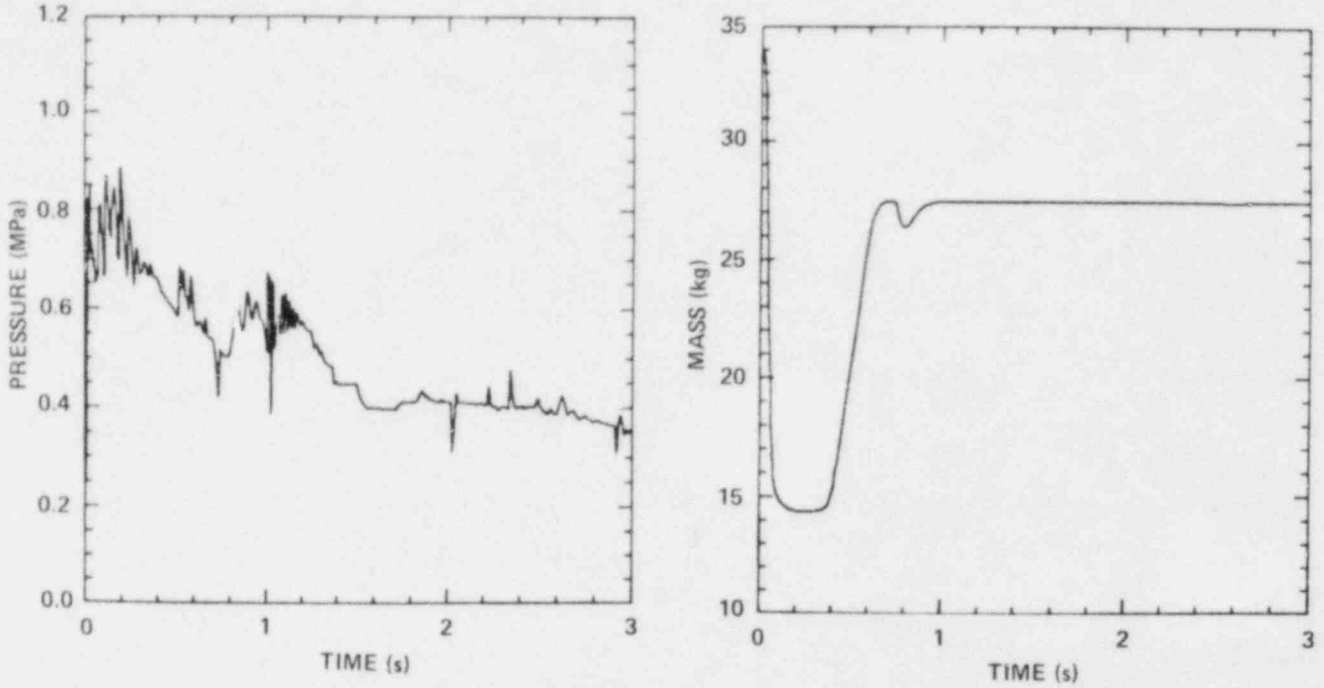

(a) Pool pressure. *(b) Pool mass.*

Fig. 17.
Transient pool behavior for case C02.

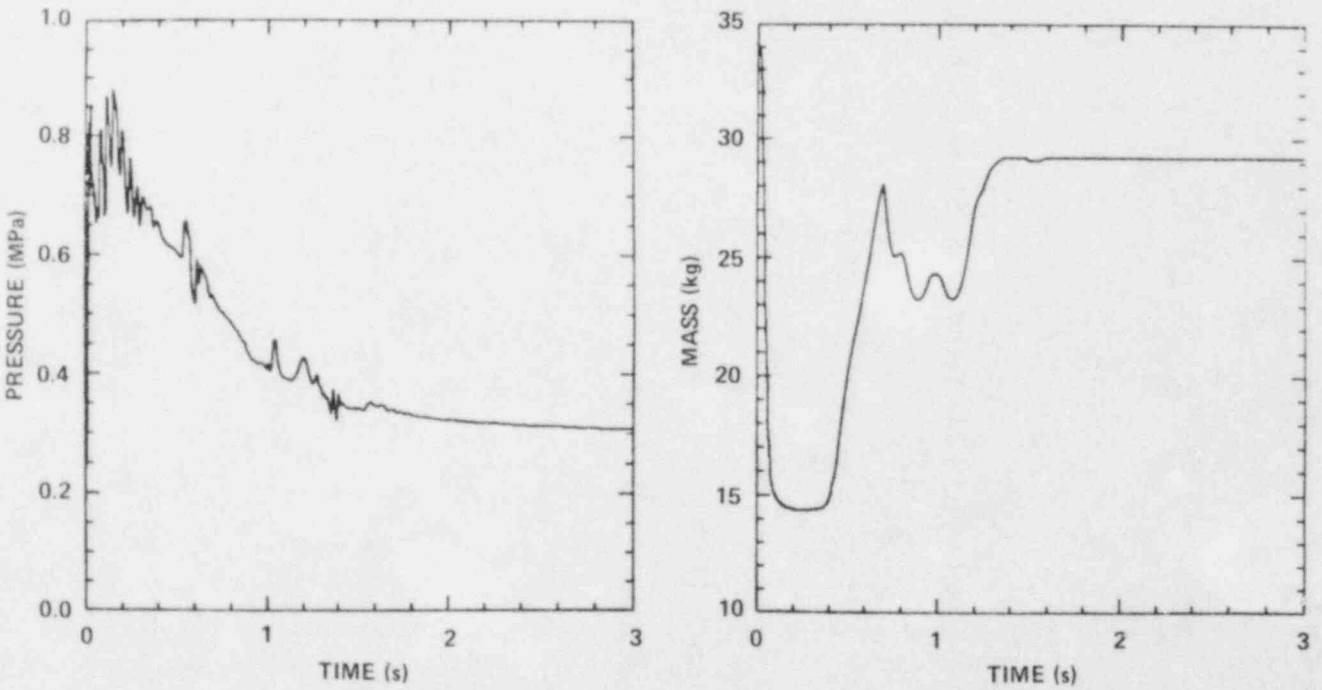

(a) Pool pressure. *(b) Pool mass.*

Fig. 18.
Transient pool behavior for case C03.

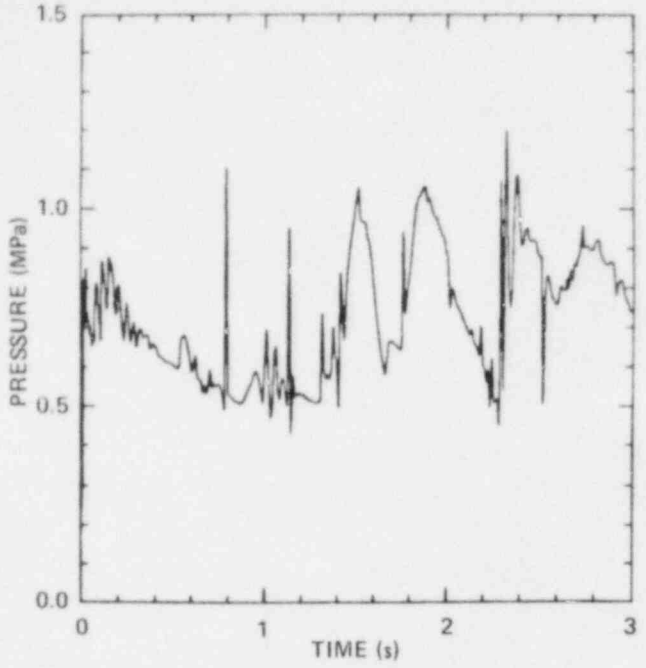

(a) Pool pressure.

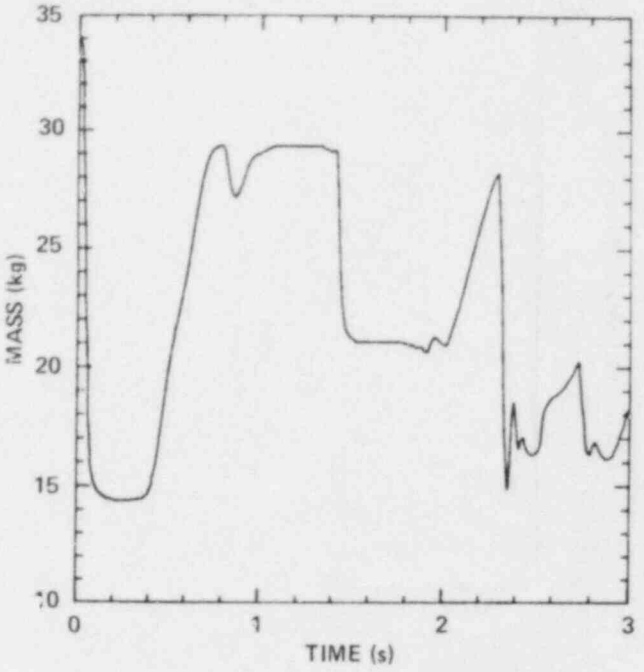

(b) Pool mass.

Fig. 19.
Transient pool behavior for case C04.

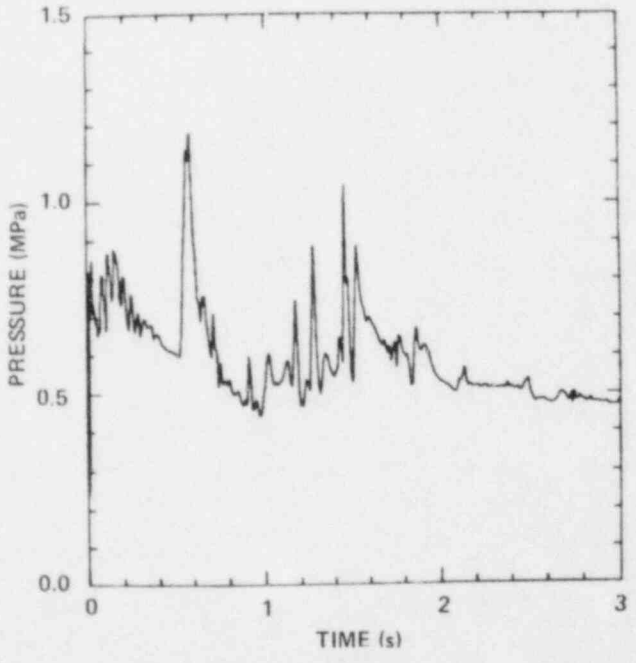

(a) Pool pressure.

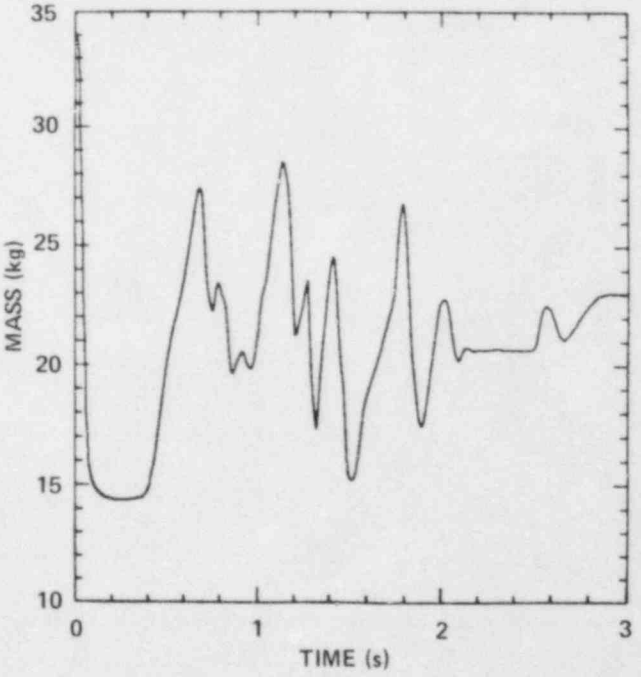

(b) Pool mass.

Fig. 20.
Transient pool behavior for case C06.

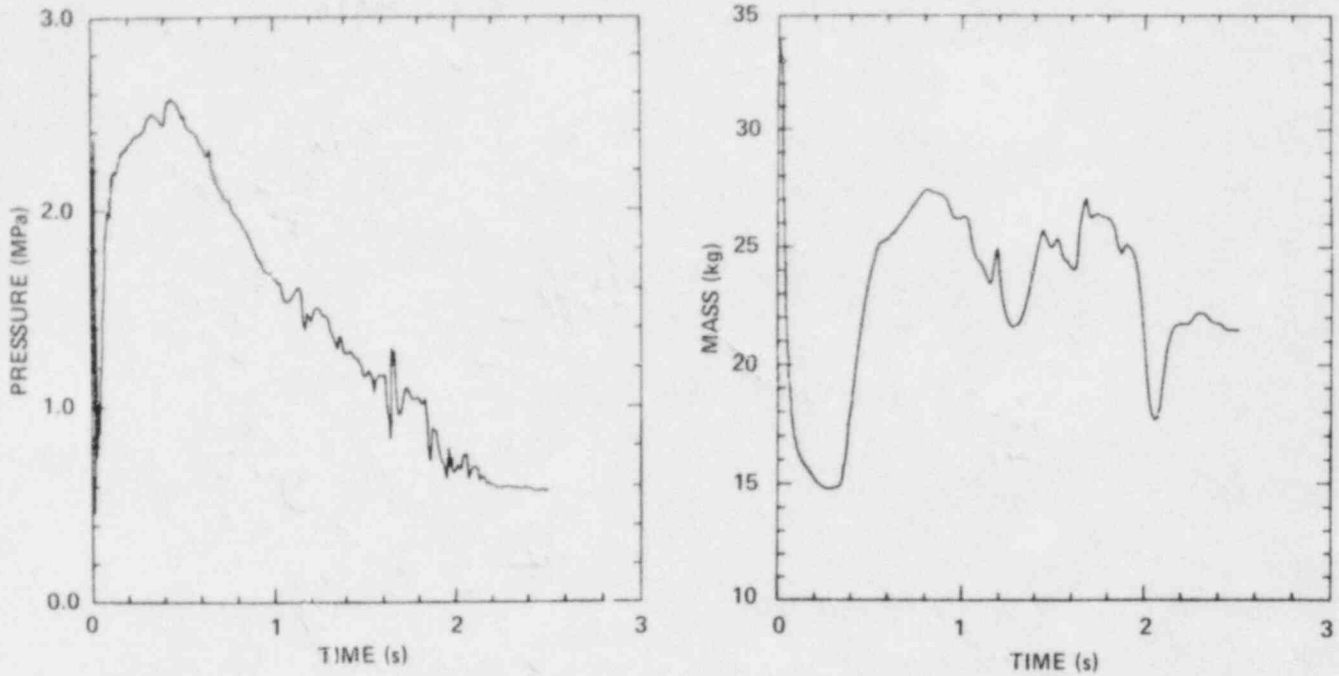

(a) Pool pressure. *(b) Pool mass.*

Fig. 21.
Transient pool behavior for case C13.

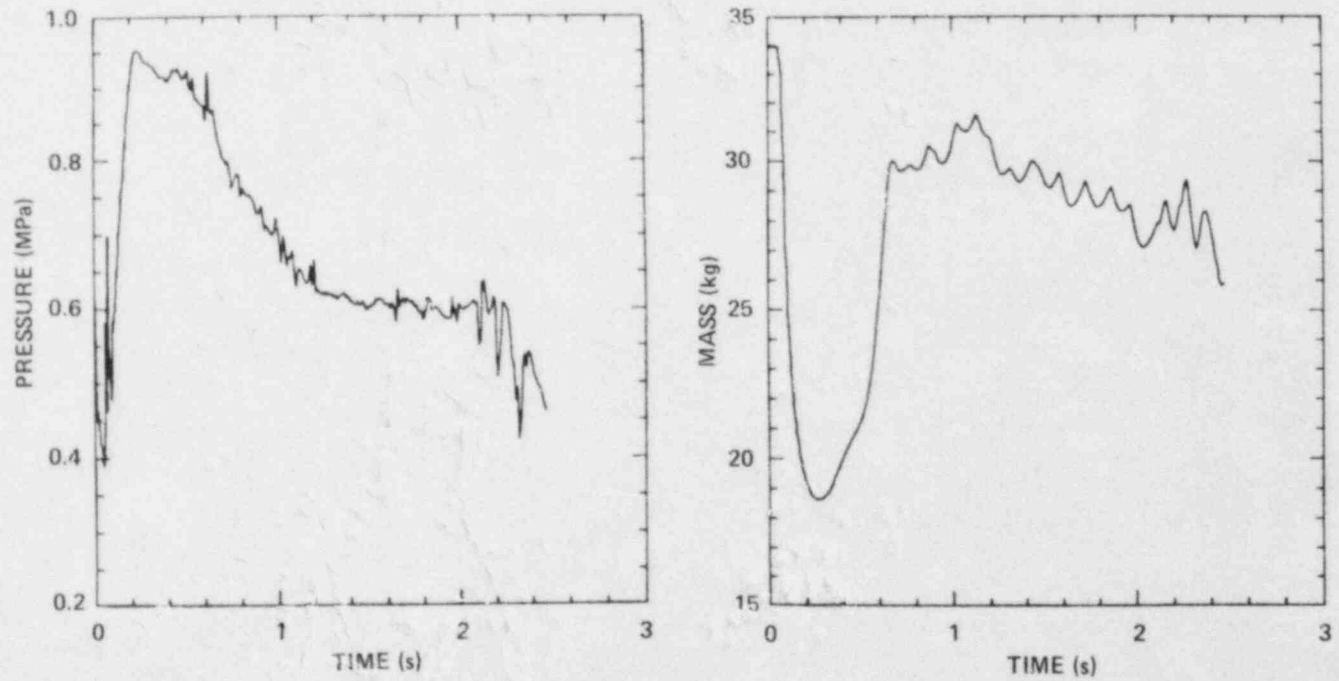

(a) Pool pressure. *(b) Pool mass.*

Fig. 22.
Transient pool behavior for case C14.

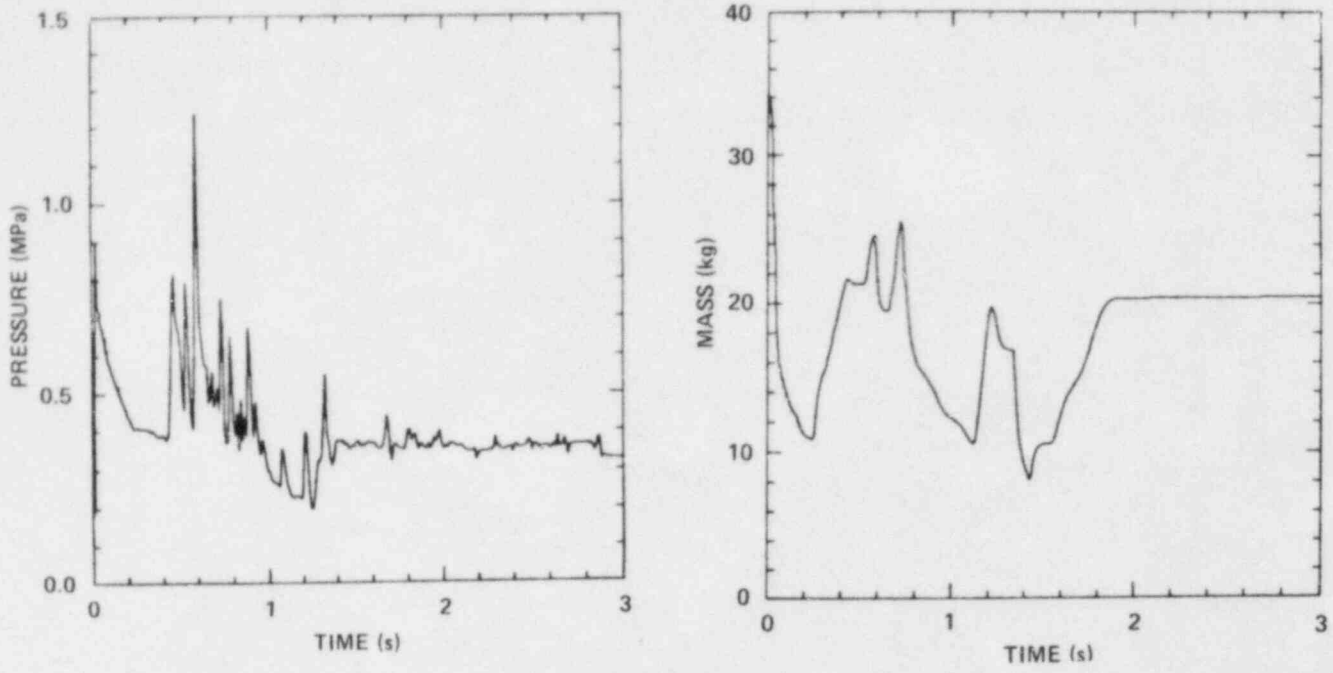

(a) Pool pressure. *(b) Pool mass.*

Fig. 23.
Transient pool behavior for case C21.

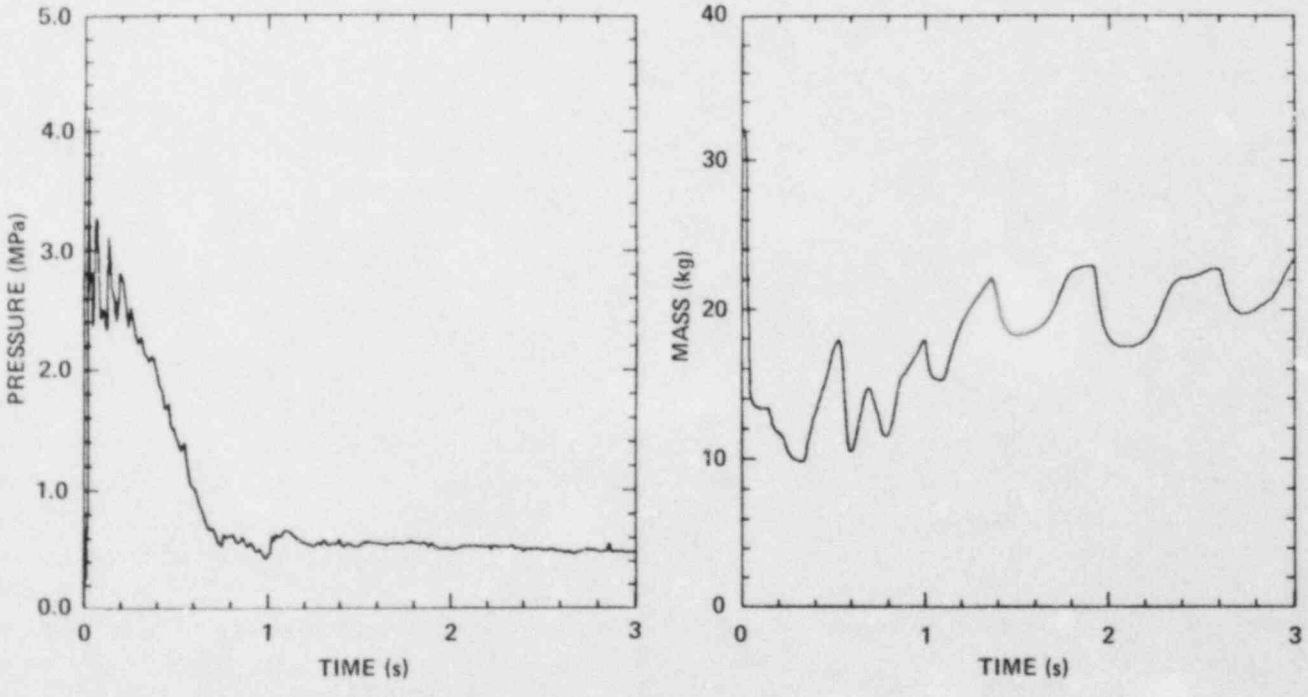

(a) Pool pressure. *(b) Pool mass.*

Fig. 24.
Transient pool behavior for case C32.

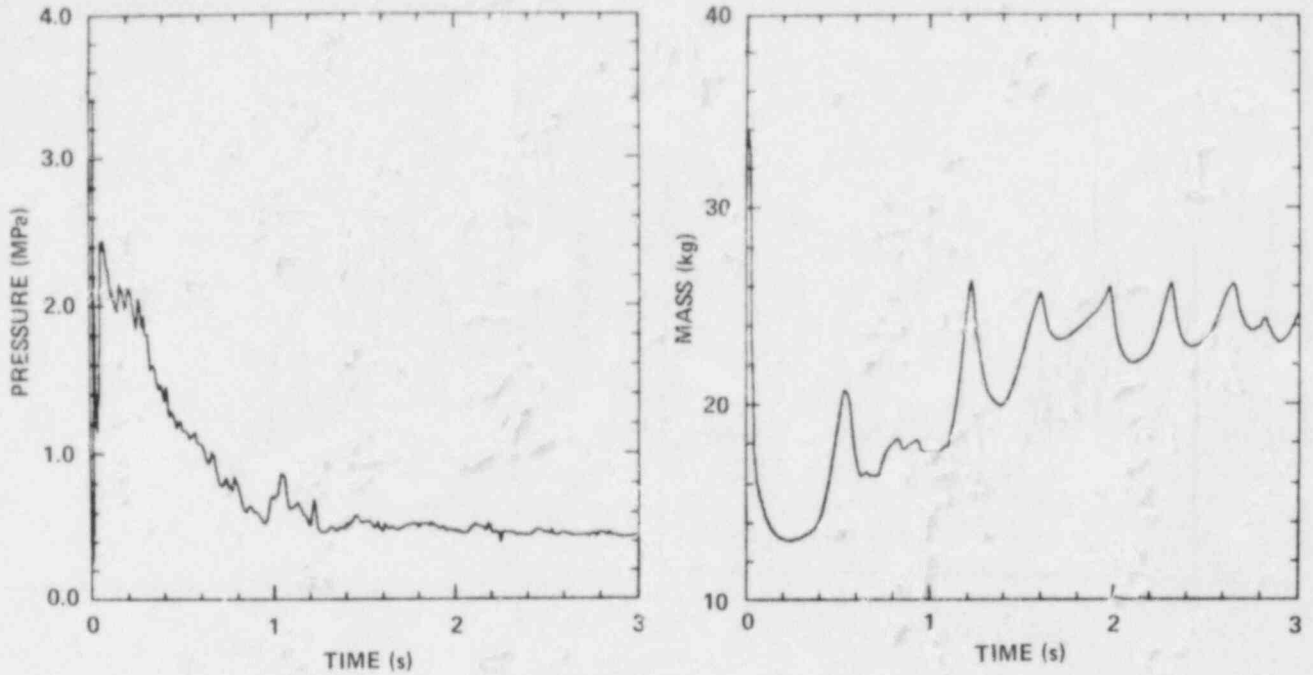

(a) Pool pressure. *(b) Pool mass.*

Fig. 25.
Transient pool behavior for case C33.

particularly in low-power subassemblies, steel vapor pressure enhancement will be commonplace.

Similarly, using the conservative estimate of 15 kg/gap over approximately 1 s (obtained for the range of pressures shown in Table 2) we can estimate that approximately 13% of the driver fuel would escape through the 90 gaps within the lifetime of the pressure pulse. It is important, however, to recognize that another pressure pulse will follow within a fraction of one second, remelting some of the frozen fuel in the gaps and thus allowing the removal process to continue.

5. Summary

Based on the fuel discharge characteristics predicted by our physically based, detailed, and benchmarked model, we have estimated the whole-core fuel dispersal potential as summarized in Table 3. The various paths are identified along with the times of availability (Section II.5). The rates of fuel removal for each path are maximums because all paths of a particular type are assumed to act simultaneously. To be conservative we should assume that the rates are only one-half of those listed to account for incoherence. There are special cases that require the rapid removal of sodium from the paths before or coincident with fuel discharge. These are the high-rate or high-area paths, radial blanket (RB) and radial reflector

TABLE 2
RESULTS FOR THE SUBASSEMBLY-POOL PRESSURE TRANSIENT ANALYSIS

Case #	Peak Press (MPa)	Fallback Time t_f(s)	Press (t_f) (MPa)	P_{avg} (MPa)
C02	0.8	0.6	0.6	0.7
C03	0.8	0.6	0.6	0.7
C04	0.8	0.6	0.6	0.7
C06	0.8	0.6	0.6	0.7
C13	2.5	0.5	2.5	2.5
C14	9.5	0.6	8.5	0.9
C21	0.8	0.5	0.4	0.6
C32	2.7	0.5 + boilup	0.6	1.6
C33	2.2	0.5 + boilup	0.6	1.4

TABLE 3
FUEL ESCAPE PATH AVAILABILITY AND CAPABILITY FOR EOC-4

Path	Characteristics	Access Time (s)	Removal Rate[a] (% of Inventory/sec at 0.5 MPa)	Capacity at Initiation of Homogeneous Pool Phase (~ 5 s) (%)
Upper Axial Blanket	Pin structure	0	6	12[b]
Lower Axial Blanket	Pin structure	0	12	25[c]
IB gaps to LAB gaps	Vertical Gaps/Horizontal Gaps	1-2	21[f]	10
IB gaps to UAB gaps	Vertical Gaps/Horizontal Gaps	1-2	21	1[g]
Gaps in RB	Horizontal Gaps/Vertical Gaps	2-4	200[h]	10
RB gaps to RR gaps	Horizontal Gaps/Vertical Gaps	2-4	200[h]	40
Control rods	Large diameter (0.1 m)	3-4	100[d]	10[e]

(a) Rates based on all available paths acting simultaneously.
(b) ½ SAs initially blocked plus 0.5 long-term removal effectiveness - based on Figure 6.
(c) Reduced penetrations assumed for colder walls of LAB (UAB x 0.5).
(d) Rate of removal if sodium previously removed below orifices.
(e) Assumes no upward removal or downward flow through inlet orifices.
(f) Based on Figure 15 with 90 gaps and no gap sodium impedance.
(g) Load pads block gaps plus a 0.5 factor for effective long-term removal.
(h) Assumes no gap sodium impedance.

(RR) gaps and control S/As. To be conservative and to be consistent with the only existing integral analysis [6] of fuel discharge into sodium-filled gaps with prototypic load pad resistance, we assumed rates one tenth as large as those listed in Table 3 for these three paths. The capacities listed in Table 3 are those conservatively associated with each path and are available before homogenization of the whole-core pool. The bottom-line estimate of likely dispersal before the energetics prone homogeneous-pool phase occurs was determined by applying the reduced rates over the time intervals for removal (5 s minus the path access time) for each path to obtain the removal per path (cannot exceed the available capacity associated with that path) and then summing over all paths. The results are presented in Table 4. The distribution of removal capability is such that neutronic termination can be achieved before the radial blanket and control S/A removal paths become available. However, the margin would not be large. The later removal through the large area paths provides large margin to assure a dispersal termination before the formation of the homogeneous pool.

6. References

1. S. K. Rhow, D. M. Switick, J. L. McElroy, and B. W. Joe, "An Assessment of HCDA Energetics in the CRBR Heterogeneous Reactor Core," General Electric Company report GEFR-00523 (December 1981).

2. "Compendium to NUREG/CR-3224, An Assessment of CRBR Core Disruptive Accident Energetics," Section 6, Nuclear Regulatory Commission document (March 1983).

3. "Compendium to NUREG/CR-3224, An Assessment of CRBR Core Disruptive Accident Energetics," Section 5, Nuclear Regulatory Commission document (March 1983).

4. "Compendium to NUREG/CR-3224, An Assessment of CRBR Core Disruptive Accident Energetics," Section 7, Nuclear Regulatory Commission document (March 1983).

5.[a] B. W. Spencer, G. T. Goldfuss, R. E. Henry, D. J. Quinn, and R. L. Roth, "Reactor Material Fuel Freezing Experiments Using Small-Bundle, CRBR-Type Pins," Argonne National Laboratory report ANL/RAS-79-11 (1979).

6. M. G. Stevenson, "Nuclear Reactor Safety Quarterly Progress Report, April 1-June 30, 1982," Los Alamos National Laboratory report NUREG/CR-2814, LA-9556-PR (November 1982).

[a] Address requests for this document to: F. X. Gavigan, Director, Office of Breeder Demonstration Projects (NE-50), U.S. Department of Energy, Washington, DC 20545, Telephone (301) 353-3134.

TABLE 4
ESTIMATE OF TOTAL FUEL REMOVAL
BEFORE THE HOMOGENEOUS POOL PHASE OCCURS

Path	Discharge Time (s)	Adjusted Rate (% inventory/s)	Maximum Removal (% of inventory)
UAB	5	3	12
LAB	5	6	25
IB/UAB	3	10	10
IB/LAB	3	10	1
RB	2	20	10
RB/RR	2	20	40
CONTROL	2	10	10
		Total	> 100

APPENDIX A
MODELING OF FREEZING AND PLUGGING

1. Introduction

Fuel dispersal was evaluated in Section II.6 with a transient flow model that accounts for freezing and plugging phenomena. This model is described in detail in this Appendix. The overall approach is to include in the formulation all flow and phase-change processes that are expected on physical grounds and to benchmark this model by comparison with prototypic material experimental data, and exact analytical results that are available for certain idealized, limit conditions. This benchmarking procedure also is included here.

2. Freezing and Plugging Model

The model is composed of a number of submodels for heat transfer, momentum transfer, mass transfer, configurations of solid structures and liquids, and equation of state all tied together by the conservation equations. The multiphase, multifield, numerical treatment is implemented within the basic SIMMER-II framework.

2.1. Configuration

Within a local region, solids are characterized primarily in terms of mass, surface area, intact geometry (for original structures) or supporting substrate (for frozen crusts), and temperature. The liquid components are characterized primarily by their masses and temperatures. All the liquid components in a local region are assumed to exist as discrete droplets moving with a common velocity. The droplet radius for each component is determined by the minimum of five constraints: (1) fluid-dynamic breakup based on a Weber number criterion, (2) the local hydraulic diameter, (3) the liquid mass available, (4) flashing breakup, and (5) droplet coalescence. The droplet radius and component mass determine the total surface area for each component in the local region. Because solids can break up below the liquidus energy (for example, fuel pellets or fuel crusts) and droplets can freeze within the liquid phase, solid particles are included in the liquid phase as spheres with specified radii. The vapor components are assumed to have a common temperature and velocity and a single set of thermophysical properties determined by the thermophysical properties and relative amount of each component in the mixture. Figure 1 depicts a typical local region.

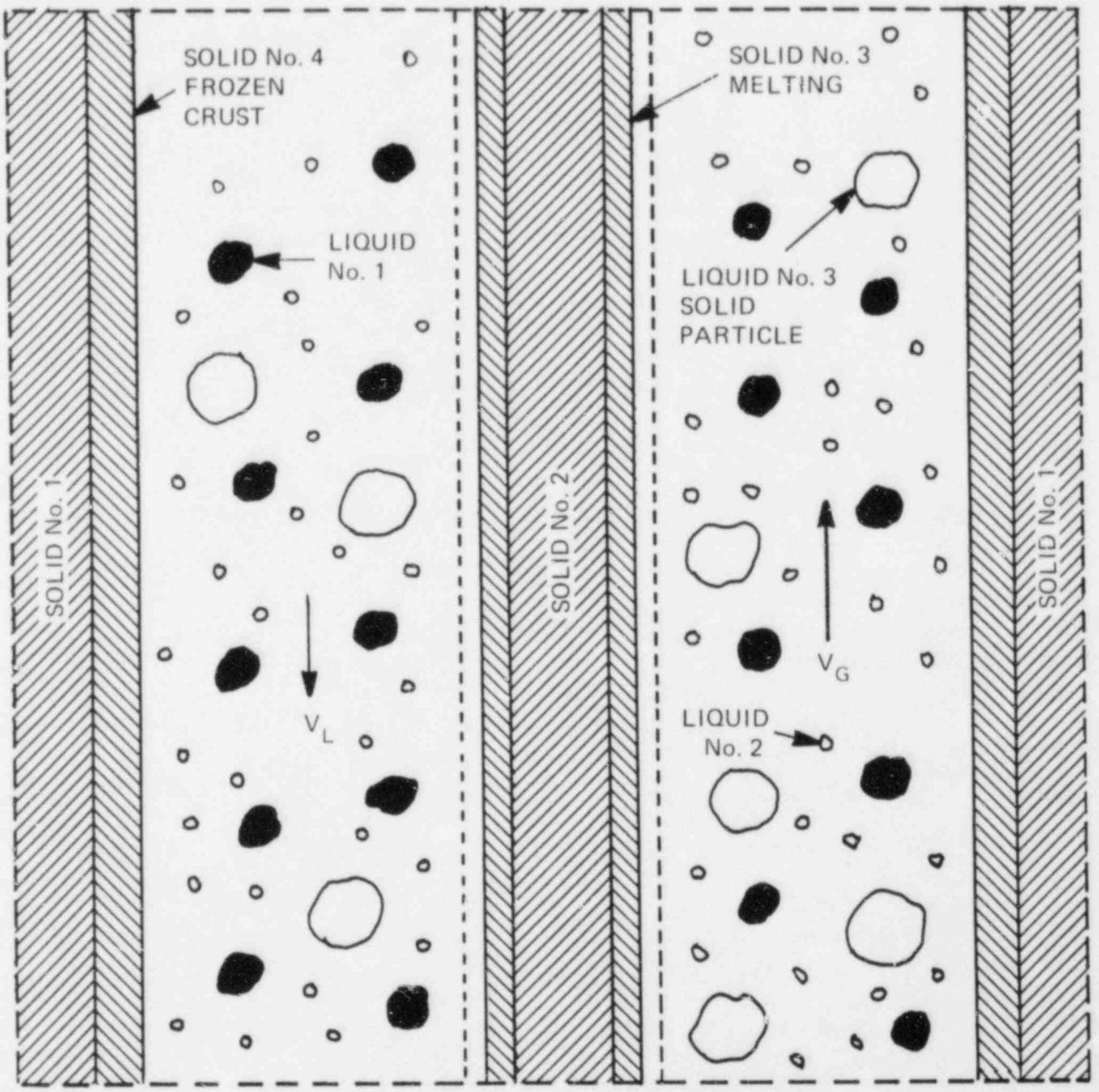

Fig. 1.
Schematic material configuration in a local region for the freezing and plugging model.

2.2. Conservation Equations

a. Mass Conservation

In the solid phase the mass-conservation equation for each component is (see nomenclature list in Table 1 at the end of this Appendix)

$$\frac{\partial \bar{\rho}_{Sm}}{\partial t} = -\Gamma_{Sm} \quad . \tag{1}$$

In the liquid phase each component is subject to

$$\frac{\partial \bar{\rho}_{Lm}}{\partial t} + \nabla \cdot (\bar{\rho}_{Lm} \vec{V}_L) = -\Gamma_{Lm} \quad , \tag{2}$$

while the conservation of mass for the gaseous components results in

$$\frac{\partial \bar{\rho}_{Gm}}{\partial t} + \nabla \cdot (\bar{\rho}_{Gm} \vec{V}_G) = -\Gamma_{Gm} \quad . \tag{3}$$

The mass-transfer terms Γ_{Sm}, Γ_{Lm}, and Γ_{Gm} can be positive or negative depending on the net mass transfer rates from all sources (freezing/melting, vaporization/condensation, etc). The mass transfer models are described in Section 2.3b.

b. Energy Conservation

In the solid phase, the energy-conservation equation for each component is

$$\frac{\partial \bar{\rho}_{Sm} e_{Sm}}{\partial t} = Q_{Sm} + \bar{\rho}_{Sm} NQ_{NSm} \quad , \tag{4}$$

where

$$Q_{Sm} = q_{HSm} + q_{\Gamma Sm} + q_{KSm} \quad . \tag{5}$$

In the liquid phase the energy-conservation equation for each component is

$$\frac{\partial \bar{\rho}_{Lm} e_{Lm}}{\partial t} + \nabla \cdot (\bar{\rho}_{Lm} e_{Lm} \vec{V}_L) = Q_{Lm} + \bar{\rho}_{Lm} NQ_{Lm} \quad , \tag{6}$$

where

$$Q_{Lm} = q_{HLm} + q_{\Gamma Lm} + q_{KLm} + q_{VLm} \quad . \tag{7}$$

Because each component in the gaseous phase is assumed to have the same temperature, the mixture is treated as a single component subject to the following energy-conservation equation:

$$\frac{\partial \bar{\rho}_G e_G}{\partial t} + \nabla \cdot (\bar{\rho}_G e_G \vec{V}_G) = - p \nabla \cdot (\alpha_G \vec{V}_G + \alpha_L \vec{V}_L)$$

$$+ Q_G + N \sum_m \bar{\rho}_{Gm} Q_{NGm} \quad , \tag{8}$$

where

$$Q_G = q_{HG} + q_{\Gamma G} + q_{KG} + q_{VG} \tag{9}$$

and the first term on the right of Equation (8) represents the pressure-volume work (expansion or compression) that is assigned entirely to the gaseous phase. The energy-transfer terms in Equations (5), (7), and (9) are described in Section 2.3a with the exception of the cell-to-cell viscous heating terms, q_{VLm} and q_{VG}.

c. Momentum Conservation

The solid phase is assumed to be an infinite momentum sink. Because each component in the liquid phase is assumed to have the same velocity, the mixture can be treated as a single component for conservation of momentum. Thus,

$$\frac{\partial \bar{\rho}_L \vec{V}_L}{\partial t} + \nabla \cdot (\bar{\rho}_L \vec{V}_L \vec{V}_L) = - \alpha_L \nabla p + \bar{\rho}_L \vec{g} + \Gamma_{GL} \vec{V}_G$$

$$- (\Gamma_{LS} + \Gamma_{LG}) \vec{V}_L + K_{GL} (\vec{V}_G - \vec{V}_L) - K_{LS} \vec{V}_L$$

$$+ \nabla \cdot (\overleftrightarrow{\bar{\pi}}_L \cdot \vec{V}_L) \quad . \tag{10}$$

The last term on the right side of Equation (10) describes the viscous drag between adjacent mesh cells. The gaseous phase can be described similarly with a single momentum equation because all the components have the same velocity,

$$\frac{\partial \bar{\rho}_G \vec{V}_G}{\partial t} + \nabla \cdot (\bar{\rho}_G \vec{V}_G \vec{V}_G) = - \alpha_G \nabla p + \bar{\rho}_G \vec{g} + \Gamma_{LG} \vec{V}_L - \Gamma_{GL} \vec{V}_G$$

$$+ K_{GL}(\vec{V}_L - \vec{V}_G) - K_{GS} \vec{V}_G + \nabla \cdot (\bar{\bar{\tau}}_G \cdot \vec{V}_G) \quad , \tag{11}$$

where, again, the last term on the right side of Equation (11) describes cell-to-cell viscous drag. The interphase drag terms, K_{LS}, K_{GS} and K_{GL} are described in Section 2.3c.

2.3. Transfer Process Models

a. Heat Transfer

Heat transfer can occur between solid components in contact with one another at a rate determined by

$$q_{HSmSk} = A_{Skm} \frac{h_{Sm} h_{Sk}}{h_{Sm} + h_{Sk}} (T_{Sk} - T_{Sm}) \quad , \tag{12}$$

where

$$h_{Sm} = h_{Smo} (\alpha_{Smo} / \alpha_{Sm}) \quad . \tag{13}$$

The initial heat-transfer coefficient, h_{Smo}, is specified by the user, and Equation (13) shows that the conductance of the solid, h_{Sm}, increases if the thickness of the solid (proportional to α_{Sm}) decreases.

Heat transfer can occur between liquid components and solid components exposed to the flow (with the exception of solid particles in the liquid). The liquid heat-transfer coefficient is given by the product of the pure liquid heat-transfer coefficient and a multiplier that accounts for multicomponent, multiphase effects. Thus,

$$q_{HLmSk} = A_{Sk} \frac{h_{LSm} h_{Sk}}{h_{LSm} + h_{Sk}} (T_{Lm} - T_{Sk}) \quad , \tag{14}$$

$$h_{LSm} = h_{LSmo} \left[\frac{\alpha_{Lm}}{\alpha_L} f(\alpha_G, \alpha_L, R) \right] , \tag{15}$$

where

$$h_{LSmo} = \frac{k_{Lm}}{D_h} \left[C_{HLm1} \left(\frac{\rho_{Lm} V_L D_h}{\mu_{Lm}} \right)^{C_{HLm2}} \left(\frac{\mu_{Lm} C_{pLm}}{k_{Lm}} \right)^{C_{HLm3}} + C_{HLm4} \right] \tag{16}$$

and

$$f(\alpha_G, \alpha_L, R) = \frac{\alpha_G \max(0, 2R-1) + \alpha_L \min(1, 2R)}{\alpha_G + \alpha_L} \quad . \tag{17}$$

The two-phase weighting factor, R, in Equation (17) can be varied from 0 to 1 to simulate flow regimes with increasing contact between the liquid and wall.

Heat transfer between liquid components is based on a droplet collision model similar to the droplet coalescence model used in the calculation of droplet radii. The total heat-transfer rate is the product of the collision frequency and the energy exchange per collision.

$$q_{HLmLk} = R_{mk} \frac{45}{8} \frac{1}{\frac{r_{pm}}{k_{Lm}} + \frac{r_{pk}}{k_{Lk}}} \frac{\alpha_{Lm} \alpha_{Lk}}{(1 - \alpha_S)} \frac{r_{pm}^2 + r_{pk}^2}{r_{pm}^3 r_{pk}^3}$$

$$\cdot (r_{pm} + r_{pk}) [\min(r_{pm}, r_{pk})]^2 (T_{Lk} - T_{Lm}) ; \tag{18}$$

or, if r_{pm} is very small, the maximum overall heat-transfer rate is governed by the maximum rate from the larger droplets.

$$(q_{HLmLk})_{max} = 15 \alpha_{Lk} \frac{k_{Lk}}{r_{pk}^2} (T_{Lk} - T_{Lm}) . \tag{19}$$

Heat transfer between the vapor and liquid or solid is assumed to occur only during phase transition. The heat-transfer coefficients are calculated from standard correlations with adjustable parameters similar to Equation (16). The model for vapor-structure surface area contains logic to preclude phase transition on the structure if α_G is less than $\alpha_{GS\Gamma}(1 - \alpha_S)$, where $\alpha_{GS\Gamma}$ is specified by the user. The determination of liquid-vapor surface area contains logic to switch from a droplet flow regime to a bubble flow regime representation when α_G is less than α_L; however, in such cases, the bubble radius is assumed equal to the droplet radius calculated for each component.

b. Mass Transfer

Mass is transferred between the liquid and solid phases by melting and freezing. Liquid component m will freeze on a solid when the interfacial temperature between the two phases is less than the freezing temperature of liquid component m and $(\alpha_{Lm}/\alpha_L)f$ is greater than 10 percent, where f is the two-phase weighting function defined by Equation (17). The interfacial temperature is determined by balancing the convection from all the liquid components with the conduction in the solid

$$(T_i)_{SkL} = \frac{h_{Sk}\, T_{Sk} + \sum_m h_{LSm}\, T_{Lm}}{h_{Sk} + \sum_m h_{LSm}} \quad , \tag{20}$$

where h_{Sk} is given by Equation (13) and h_{LSm} is given by Equation (15). If freezing occurs, the interfacial temperature is set equal to the freezing temperature in the heat-transfer calculations, and the imbalance in the heat fluxes from liquid convection for all components, p, and solid conduction determines the freezing rate

$$\Gamma_{LmSk} = \frac{h_{Sk}\,(T_{MELT,m} - T_{Sk}) + \sum_p h_{LSp}\,(T_{MELT,m} - T_{Lp})}{h_{FUS,m} + C_{vLm}\,(T_{Lm} - T_{MELT,m})} \quad . \tag{21}$$

In Equation (21), Γ_{LmSk} is the freezing rate of liquid component m on solid component k. However, before an appreciable amount of liquid has frozen, conduction in the solid phase is based on conduction in the solid substrate (Sk) on which the frozen crust forms. After a significant amount of crust has formed, h_{Sk} is replaced by a combined conductance for the

substrate and crust for determining the subsequent freezing rate from Equation (21). The sensible heat term in the denominator of Equation (21) appears because liquid component m must be desuperheated before it can freeze.

If the interfacial temperature from Equation (20) exceeds the solid components' melting temperature and none of the liquid components are predicted to freeze, then the interfacial temperature is set equal to $T_{MELT,k}$ and the melting rate becomes

$$\Gamma_{SkLj} = \frac{h_{Sk}(T_{MELT,k} - T_{Sk}) + \sum_{p} h_{LSp}\,(T_{MELT,k} - T_{Lp})}{h_{FUS,k} + C_{vSk}\,(T_{MELT,k} - T_{Sk})} \quad , \qquad (22)$$

where Sk and Lj must represent the same material. The sensible heat term in the denominator of Equation (22) appears because solid component k must be heated to the melting point before it will melt.

If the interfacial temperature exceeds the solid melting temperature, but a liquid component freezes, then the energy of the solid will increase beneath the freezing crust. Because the mechanical integrity of the solid becomes dubious above the solidus energy, a failure model has been incorporated to address this situation. The user sets the failure energy between the solidus and liquidus; and when the solid's energy exceeds this point, the solid is assumed to begin failing. Additional modeling flexibility is provided by allowing the user to specify the proportion that fails as liquid rather than as particles. Because the melted material and particles enter the liquid phase at the liquidus and solidus energies, respectively, while the solid remaining after failure initiation is assumed to be at the failure energy, energy conservation requires that the liquidus proportion exceed the fraction of the latent heat of fusion that defines the failure energy. Within the liquid phase, the components transfer heat to one another so that the particle volume fraction may increase or decrease as liquids freeze or particles melt, respectively.

Vaporization and condensation can occur at liquid-vapor and vapor-structure interfaces as previously mentioned. The simple vaporization/condensation model is similar to the interfacial freezing/melting model because it is based on setting the interfacial temperature equal to the saturation temperature and comparing the resulting heat fluxes into and out of the interface. A net heat flux into the interface results in vaporization, while

the converse results in condensation. Because the saturation temperature depends on the partial pressure of the vapor component, the vaporization/condensation model is more complicated than the freezing/melting model.

The mass fluxes associated with freezing/melting and vaporization/condensation also transport energy such that

$$q_{\Gamma Sm} = e_{SOL,m} \sum_{k} (\Gamma_{LkSm} - \Gamma_{SmLk}) \quad , \tag{23}$$

$$q_{\Gamma Lm} = e_{LIQ,m} \sum_{k} (\Gamma_{SkLm} - \Gamma_{LmSk} + \Gamma_{LkLm} - \Gamma_{LmLk} + \Gamma_{GkLm} - \Gamma_{LmGk}) \quad , \tag{24}$$

$$q_{\Gamma Lm} = e_{SOL,m} \sum_{k} (\Gamma_{SkLm} + \Gamma_{LkLm} - \Gamma_{LmLk}) \quad , \tag{25}$$

and

$$q_{\Gamma G} = \sum_{m} \left[e_{VAP,m} \sum_{k} (\Gamma_{LkGm} - \Gamma_{GmLk}) \right] \quad . \tag{26}$$

Equation (24) applies to liquids, and the Γ_{LkLm} terms apply to liquid-particle, freezing/melting transfer. Equation (25) applies to particles, and the Γ_{LmSk} term is absent because particles cannot go directly into the solid (structure) phase. Because sublimation is not modeled, no terms for gas phase transfer appear.

c. Momentum Transfer

Momentum transfer between the phases is caused by drag forces and mass exchange. The pressure drop caused by drag between the two-phase, gas-liquid mixture and the structure is given by the Martinelli correlation.

The friction factors and correlation exponent are given by the following correlations:

$$\nabla p_{2\phi} = \phi_L^2 \nabla p_L + \phi_G^2 \nabla p_G \quad , \tag{27}$$

where

$$\nabla p_L = -\frac{2f_L}{D_h}\,\rho_L\,|\vec{j}_L|\,\vec{j}_L \quad , \tag{28}$$

$$\nabla p_G = -\frac{2f_G}{D_h}\,\rho_G\,|\vec{j}_G|\,\vec{j}_G \quad , \tag{29}$$

and

$$\Phi_L^2 = \left[1 + (1/X^2)^{1/n}\right]^n$$

$$\Phi_G^2 = \left[1 + (X^2)^{1/n}\right]^n \quad , \tag{30}$$

with

$$X^2 \equiv \frac{\Phi_G^2}{\Phi_L^2} = \frac{f_L \rho_L |j_L|^2}{f_G \rho_G |j_G|^2} \quad . \tag{31}$$

The friction factors and correlation exponent are given by the correlations,

$$f_L = 16/Re_L, \qquad Re_L \leq 2000 \quad , \tag{32}$$

$$f_L = C_{fL1} Re_L^{C_{fL2}}, \qquad Re_L \geq 2000 \quad , \tag{33}$$

$$Re_L = \frac{\bar{\rho}_L D_h |j_L|}{\sum_m \alpha_{Lm} \mu_{Lm}} \quad . \tag{34}$$

$$f_G = 16/Re_G, \qquad Re_G \leq 2000 \quad , \tag{35}$$

$$f_G = C_{fG1} Re_G^{C_{fG2}}, \qquad Re_G \geq 2000 \quad , \tag{36}$$

$$Re_G = \frac{\bar{\rho}_G D_h |j_G|}{\alpha_G \mu_{G,mix}} \tag{37}$$

and

$$n = 4.0, \quad Re_G \geq 2000 \quad \text{and} \quad Re_L \geq 2000 \quad . \tag{38}$$

If the liquid and gas momentum equations are added and the acceleration, phase change, and body force (gravity) terms are neglected, the result is

$$(\alpha_L + \alpha_G) \nabla p_{2\phi} = - (K_{LS} \vec{V}_L + K_{GS} \vec{V}_G) \quad . \tag{39}$$

Substituting Equation (27) into Equation (39) yields

$$\alpha_L \phi_L^2 \nabla p_L + \alpha_G \phi_G^2 \nabla p_G = - (K_{LS} \vec{V}_L + K_{GS} \vec{V}_G) \quad . \tag{40}$$

This suggests the following general interphase coupling coefficients,

$$K_{LS} = \frac{\phi_L^2 \nabla p_L}{|V_L|} (\alpha_G + \alpha_L) \left[f(\alpha_G, \alpha_L, R) \right] \tag{41}$$

and

$$K_{GS} = \frac{\phi_G^2 \nabla p_G}{|V_G|} (\alpha_G + \alpha_L) \left[1 - f(\alpha_G, \alpha_L, R) \right] , \tag{42}$$

where the two-phase weighting factor, R, can be varied from 0 to 1 to simulate flow regimes with increasing contact between the liquid and wall.

A particle viscosity model has been developed to simulate the frictional effects of particles in the liquid phase. Because of the theoretical and practical complexity of modeling particle effects from first principles, the particle viscosity model is heuristic in nature. In addition to a user-specified value for the particle viscosity used in Equation (34), the model includes logic for determining when the particle radius exceeds the local hydraulic diameter or when the particle volume fraction exceeds a user-specified maximum packing fraction. In either case, the liquid-structure momentum coupling coefficient given by Equation (41) is increased by the multiplier,

$$K_{jam} = \begin{cases} 10^{10} \max\left[10^{-10}, \left(\min\left(1, \bar{\rho}_L g/|\nabla P|\right)\right)^5\right] & , 2r_p \geq D_h \\ \dfrac{\max\left[10^{-10}, \left(\min\left(1, \bar{\rho}_L g/|\nabla P|\right)\right)^5\right]}{\max\left[10^{-10}, \; 1 - \dfrac{\alpha_p/(1-\alpha_s)}{\alpha_{p,max}}\right]} & , 2r_p < D_h \end{cases} \tag{43}$$

The dimensionless pressure gradient term in Equation (43) rapidly decreases K_{jam} to unity as $|\nabla p|$ approaches $100\,\bar{\rho}_L g$, and it simulates the tendency of large pressure gradients to dislodge blockages.

The liquid-vapor momentum coupling coefficient is given by

$$K_{GL} = \frac{3\bar{\rho}_G}{2\alpha_G\left(\frac{\alpha_G}{1-\alpha_s}\right)^{\lambda-1}\left[\frac{\alpha_G}{1-\alpha_s} - \alpha_0\right]} \left(3\nu_G \sum_m \frac{\alpha_{Lm}}{r^2_{pm}} + \frac{C_d}{4}|V_{LG}| \sum_m \frac{\alpha_{Lm}}{r_{pm}} \right) \tag{44}$$

which is based on stokes flow over a sphere for low Reynolds numbers and form drag on spheres for high Reynolds numbers. α_o is the value of α_G at the transition between single-phase and two-phase flow, and the α_G dependence accounts for the increased momentum coupling in lower void fraction situations.

2.4. Equations of State

The system of equations consisting of the conservation equations from Section 2.2 and the constitutive equations from Section 2.3 is not closed. The system is closed with the addition of material equations of state.

The equation of state for material m is given by

$$e_{Sm} = C_{vSm}\, T_{Sm} \quad \text{when } T_{Sm} < T_{MELT,m} \quad , \tag{45}$$

$$e_{SOL,m} = C_{vSm}\, T_{MELT,m} \quad , \tag{46}$$

$$e_{LIQ,m} = e_{SOL,m} + h_{FUS,m} \quad . \tag{47}$$

$$e_{Lm} = e_{LIQ,m} + C_{vLm} (T_{Lm} - T_{MELT,m}) \qquad (48)$$

when $T_{Lm} \leq 2/3\ T_{CRIT,m}$,

$$e_{Lm} = e_{LIQ,m} + C'_{vLm}(T_{Lm} - 2/3\ T_{CRIT,m}) + a_{Lm} - 1/2\ h^{+}_{VAP,m} \qquad (49)$$

when $T_{Lm} \geq 2/3\ T_{CRIT,m}$,

$$e_{CON,m} = e_{LIQ,m} = C_{vLm} (T_{SAT,m} - T_{MELT,m}) \qquad (50)$$

when $T_{SAT,m} \leq 2/3\ T_{CRIT,m})$,

$$e_{CON,m} = e_{LIQ,m} + C'_{vLm}(T_{SAT,m} - 2/3\ T_{CRIT,m}) + a_{Lm} - 1/2\ h_{VAP,m} \qquad (51)$$

when $T_{SAT,m} \geq 2/3\ T_{CRIT,m}$,

$$e_{VAP,m} = e_{CON,m} + h_{VAP,m} - p\Delta V_m \ , \qquad (52)$$

$$e_{G,m} = e_{VAP,m} + C_{vGm} (T_G - T_{SAT,m}) \ , \qquad (53)$$

and

$$e_G = \sum_m e_{G,m}\ \bar{\rho}_{Gm} / \sum_m \bar{\rho}_{Gm} \ , \qquad (54)$$

where

$$p_{v,m} (T_{SAT,m}) = p^*_m\ e^{-T^*_m/T_{SAT,m}} \qquad (55)$$

is the assumed pressure-temperature saturation curve and

$$h_{VAP,m} = h^{*}_{VAP,m}\left(1 - \frac{T_{SAT,m}}{T_{CRIT,m}}\right)^{\varepsilon_m} \qquad (56)$$

when $T_{SAT,m} \leq T_{CRIT,m}$,

$$h_{VAP,m} = 0 \qquad \text{when } T_{SAT,m} \geq T_{CRIT,m} ,$$

$$h_{VAP,m} = h^{*}_{VAP,m}\left(1 - \frac{T_{Lm}}{T_{CRIT,m}}\right)^{\varepsilon_m} \qquad (57)$$

when $T_{Lm} < T_{CRIT,m}$,

$$h_{VAP,m} = 0, \qquad \text{when } T_{Lm} \geq T_{CRIT,m} ,$$

$$a_{Lm} = 1/2\, h_{VAP,m}\,(1/3)^{\varepsilon_m} + C_{vLm}\,(2/3\, T_{CRIT,m} - T_{MELT,m}) , \qquad (58)$$

$$C'_{VLm} = 3(e_{CRIT,m} - e_{LIQ,m} - a_{Lm})/T_{CRIT,m} , \qquad (59)$$

and

$$p\Delta V_m = \frac{T_{SAT,m}}{T^{*}_{m}}\, h_{VAP,m} \qquad (60)$$

All starred (*) quantities in Equations (45)-(60) are material correlation constants.

The pressure in two-phase cells is the sum of partial pressures of the gaseous components

$$p_{2\phi} = \sum_{m} \rho_{Gm} R_m T_G , \qquad (61)$$

where R_m, the gas constant, is dependent on the quantity $\rho_{Gm} T_G$.

For $\alpha_G < \alpha_o$, the cell is assumed to be single-phase liquid, and the pressure is given by

$$p_{1\phi} = \hat{\rho}_L + \hat{C}^2\left(\frac{\alpha_L - \alpha_{Lo}}{\alpha_L}\right)\bar{\rho}_L , \qquad (62)$$

where $$\hat{p}_L = \sum_m \hat{p}_{vm} \quad . \tag{63}$$

$$\hat{p}_{vm} = P_{v,m}(T_{Lm}) \quad . \tag{64}$$

and

$$1/\hat{C}^2 = \frac{\alpha_L}{\alpha_{Lo}} \sum_m \frac{\alpha_{Lm}}{C^2_{Lm}} \quad , \tag{65}$$

where α_{Lo} is equal to α_L at the transition point between single-phase and two-phase flow.

At the transition between single-phase and two-phase flow, the energy of each vapor component is set equal to $e_{VAP,m}(T_{Lm})$ and $\rho_{Gm} R_m T_G$ is set equal to $P_{v,m}(T_{Lm})$ to uniquely determine ρ_{Gm} and T_g.

For small amounts of individual components, the changes in these relationships are given in Appendix B of the SIMMER Manual [6].

3. Model Benchmarking

3.1. Pin Bundles

The freezing and plugging model described above has been applied [1] to a number of experiments involving a range of materials, conditions, and geometries. The general success was reasonable over this wide range. The most important data available currently for benchmarking the model in pin bundle geometry is that of Spencer [2]. In Reference 1, the model testing was performed in a two-dimensional manner. Because it is applied one-dimensionally for the CRBR assessment, it must be benchmarked accordingly.

The test apparatus shown in Figure 2 was represented completely as were the details of the test pins shown in Figure 3. The one-dimensional model homogenizes the seven pins and the duct wall while preserving the overall flow channel and local heat-transfer characteristics. The noding structure utilized a 0.05-m node length in the test section to be comparable to that generally used in the full-scale reactor analysis. The test selected was number 1, which represents the upper axial blanket conditions and the expected quantity of fuel.

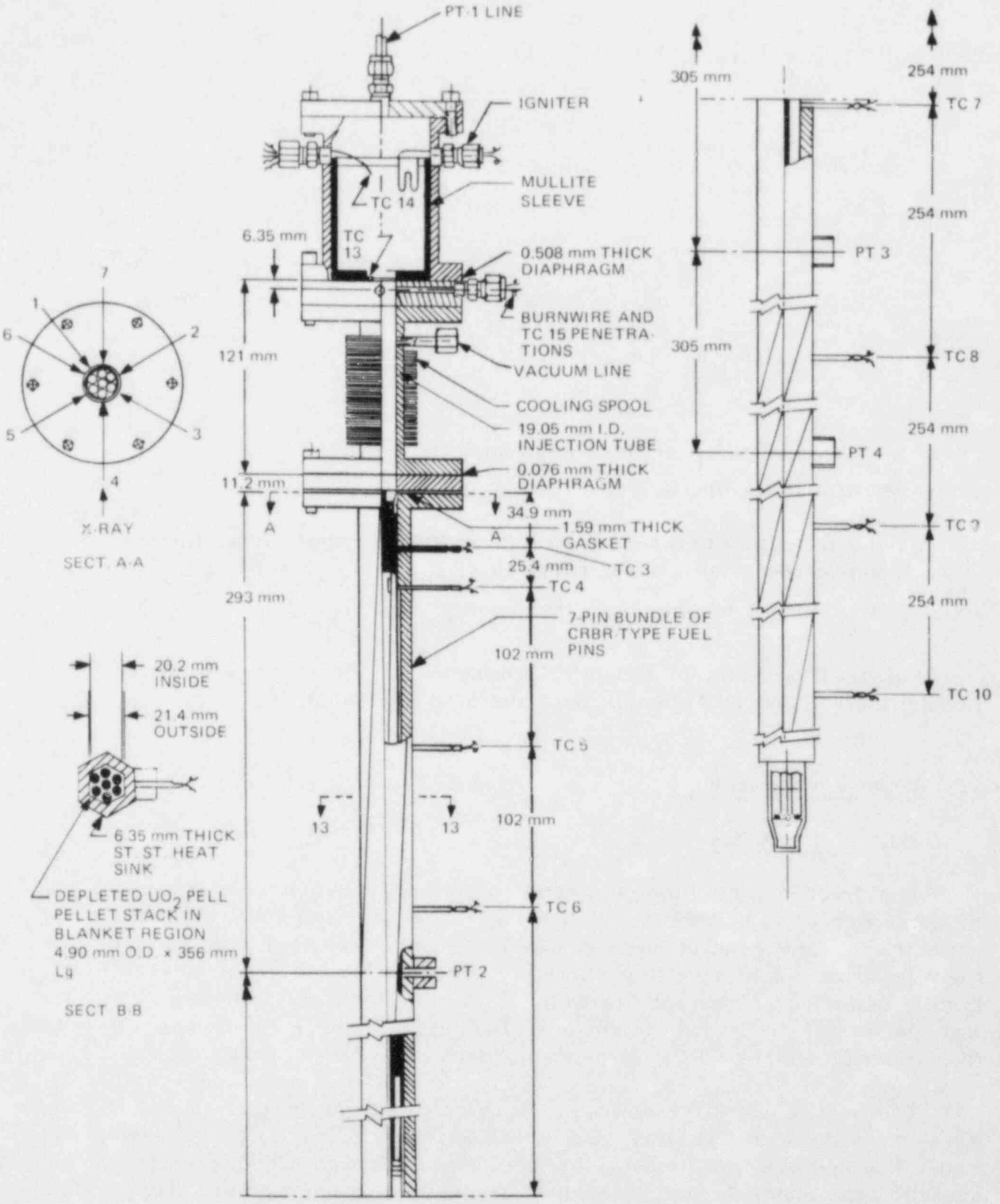

Fig. 2.
Experimental apparatus used for CRBR-series fuel freezing experiments (courtesy of Argonne National Laboratory).

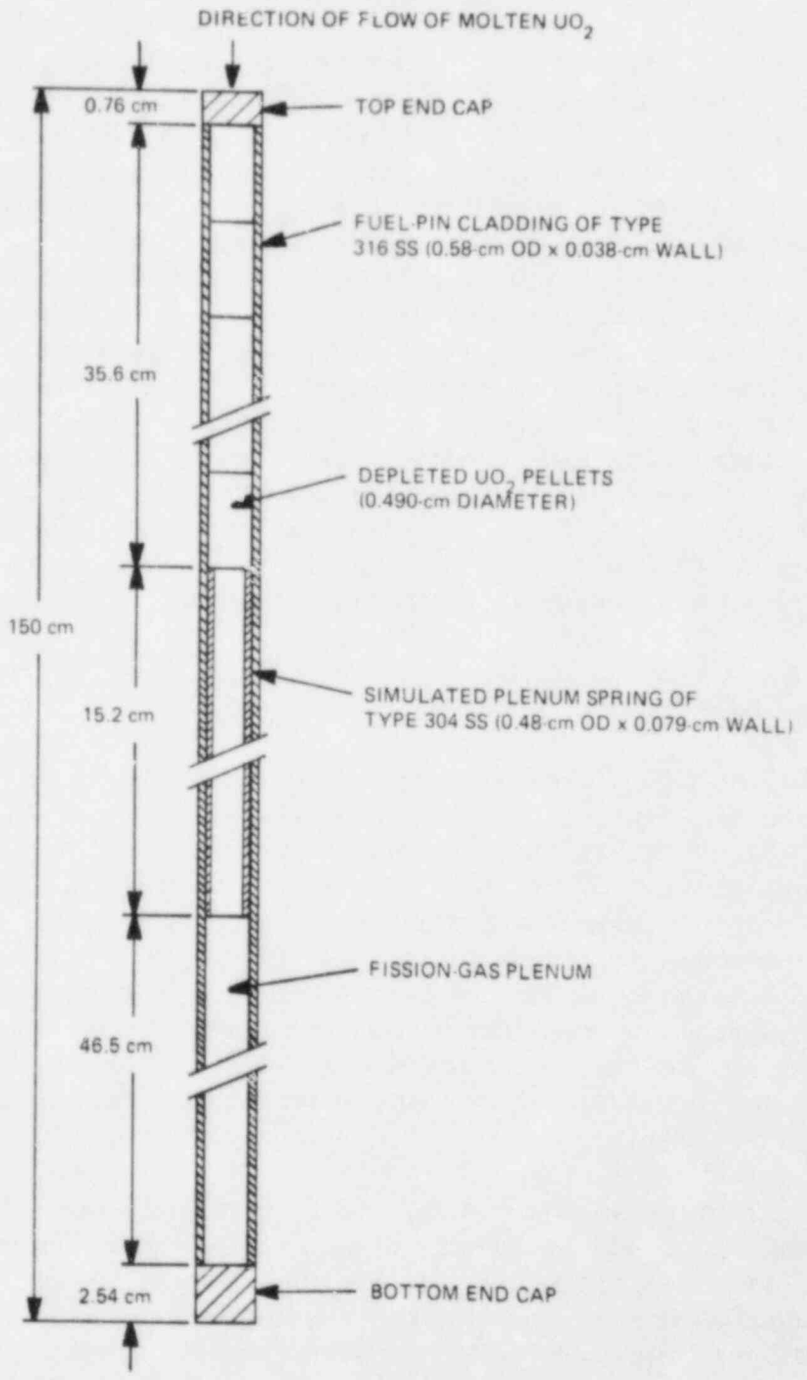

Fig. 3.
Configuration of CRBR-type pins used in fuel freezing tests (courtesy of Argonne National Laboratory).

Four calculations were performed to test different model assumptions. The main mass of fuel stopped in all cases between 0.30 and 0.35 m, which is the length of the blanket pellet region. Large steel blockages were formed in all cases downstream of the fuel. Some particulate fuel was blown downstream into the fission gas plenum region before the steel blockage formed. The general characteristics of the freezing and plugging process were the same as found previously with the two-dimensional modeling. As the fuel entered the test section, the cladding rapidly ablated and entrained into the flowing stream. The entrained steel cooled the fuel in a bulk freezing mode and produced a steel-fuel particle slurry. The bulk temperature of the slurry decreased as it flowed sluggishly downstream. The steel froze at the walls at a downstream location, generally at the simulated spring retainer location where the wall heat capacity is high. Even a partial occlusion by steel freezing acts as a blockage in that the particulate slurry has a very difficult time flowing through it. There is some support for using an effective particle viscosity of 10 instead of 1 because it permits less particulate material to proceed beyond the blockage in better agreement with the experiment.

3.2. Gap Channels

At the present time there are only a few experiments on fuel injections into gap channels. These are the GAP1 and 2 [3 and 4] experiments performed at ANL in 1978 and more recently GAP3 and 4 [5]. For our benchmarking objective, GAP3 and 4 are of interest because of their prototypicality and low injection pressures. The test results are somewhat surprising in that they produced short penetrations, 0.10 to 0.30 cm, in an environment that was expected to be controlled by conduction controlled freezing. Therefore, long penetration was expected. It is believed that the short penetrations were caused by the stratification of the molybdenum to the leading edge of the injection and perhaps some particulate fuel at the leading edge of the injection also.

We attempted to scope these experiments with the above model to seek guidance as well as possible benchmarking. The straightforward application of the model led to penetrations of greater than 0.30 cm. The model ultimately caused the flow to stop by the amplification of local fluid viscosity from bulk freezing of the fuel by the stratified molybdenum. Therefore, the timing and magnitude of this enhanced viscosity during the flow transient are of major importance. The terminal velocity of the gravity-driven flow in the laminar regime is

$$V = \frac{g \rho D_h^2}{32 \mu},$$

where g is the acceleration due to gravity,
ρ is the fluid density,
D_h is the channel hydraulic diameter,
μ is the fluid viscosity, and
V is the terminal velocity.

For normal liquid fuel this velocity becomes 47 m/s for a gap channel. Obviously, the viscosity must be enhanced greatly to cause flow stoppage. If the effect of particles in the stream is to increase the effective stream viscosity to the order of 2 instead of 0.005 Pa-s for liquid, the terminal velocity becomes 0.1 m/s. This suggested that with a specific particle viscosity of 10, a volume fraction of particles of greater than 20% is required to slow and stop the flow. To achieve this fraction of frozen material in the stream before significant penetration and velocity establishment, rapid heat transfer must occur to the walls or particles must pre-exist in the injected stream.

The nominal model with its convective heat-transfer treatment produces the material penetration and compositions shown in Figures 4 through 7 for liquid fuel, liquid molybdenum, fuel particles, and fuel crust, respectively, when applied to GAP3 with an assumed molybdenum stratification of 60% and no fuel superheat. Similar results were obtained for other stratification assumptions up to 100%. All values are in kilograms per cubic meter (smear density). At 0.1 s, the flow should have stopped to be consistent with the experiment; however, in the calculation the velocity was greater than 1 m/s. The particulate fraction, formed by molybdenum heat transfer to the wall and concurrent cooling and freezing of the liquid fuel in the stream was only about 10% at this time. The stream began to decelerate at this time. The heat rejection rate from the leading edge of the stream must be larger by at least a factor of 3 to get agreement with GAP3. If, however, the stream initially contained 5 percent by volume of particles, the average stream penetration velocity would be reduced to less than 0.5 m/s, thereby permitting a longer time for particle-generating heat transfer and rapid stream stoppage. GAP4 may not have had these particles because of the reduced waiting time. The predicted behavior using this model agreed well with this test.

Although a unique match to these experiments is not possible because the conditions in the leading edge of the discharge cannot be determined, the model does suggest plausible explanations for both results without major model adjustment.

The other benchmarking that has been performed for gap geometry is classical freezing of stable crusts on the wall to occlude the channel. Figure 8 shows the comparison of results from our model and from conduction theory. The agreement is excellent. A further check was made of the integrated fuel throughput until occlusion for a net driving pressure of

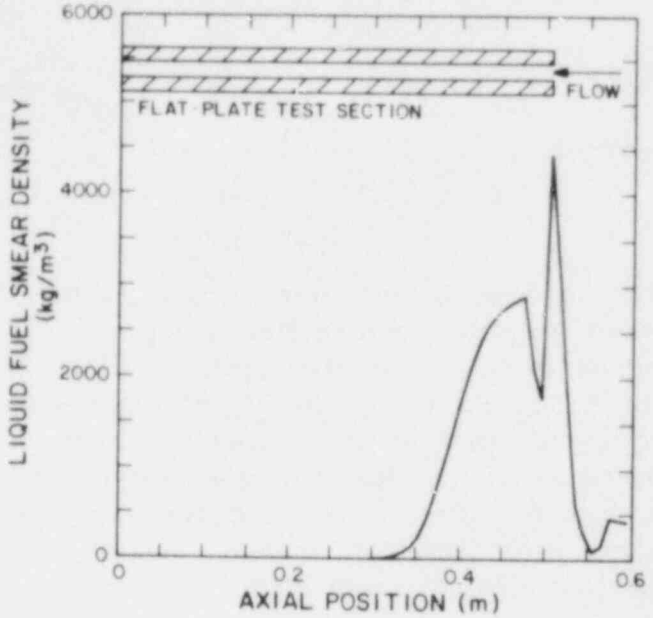

Fig. 4.
Liquid fuel smear density at 0.1 s from the SIMMER-II exploratory analysis of the ANL GAP3 test.

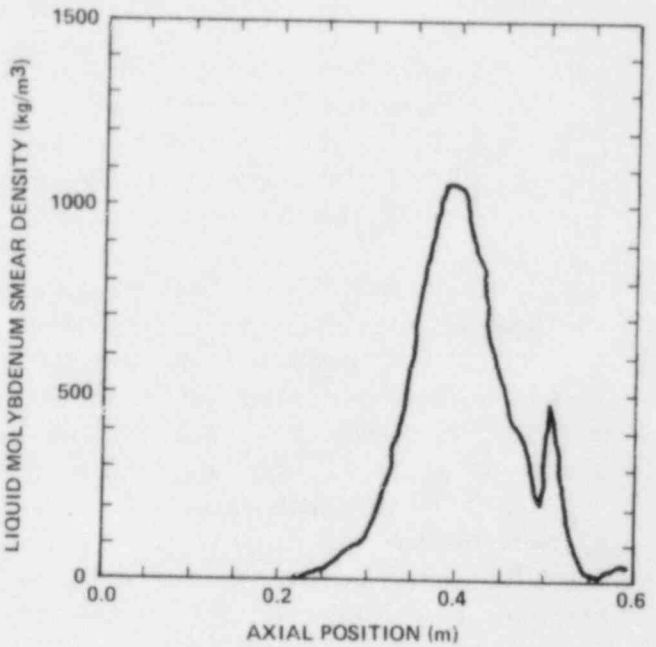

Fig. 5.
Liquid molybdenum smear density at 0.1 s from the SIMMER-II exploratory analysis fo the ANL GAP3 test.

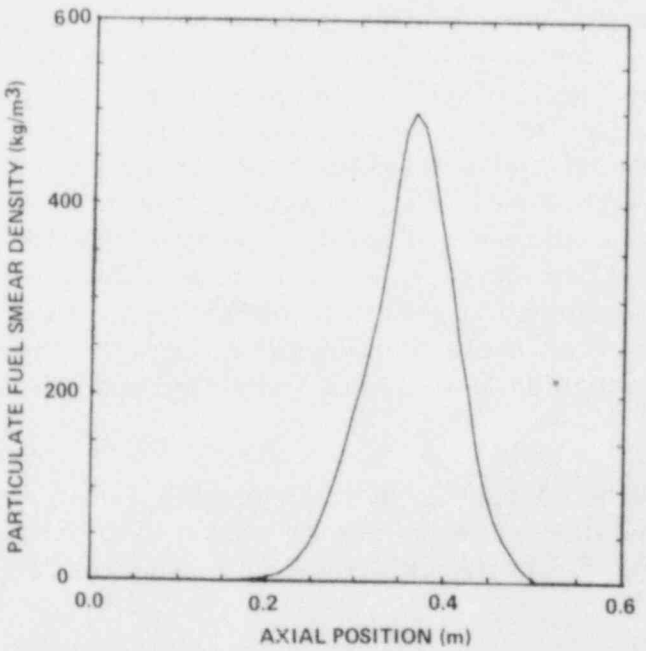

Fig. 6.
Fuel particulate smear density at 0.1 s from the SIMMER-II exploratory analysis of the ANL GAP3 test.

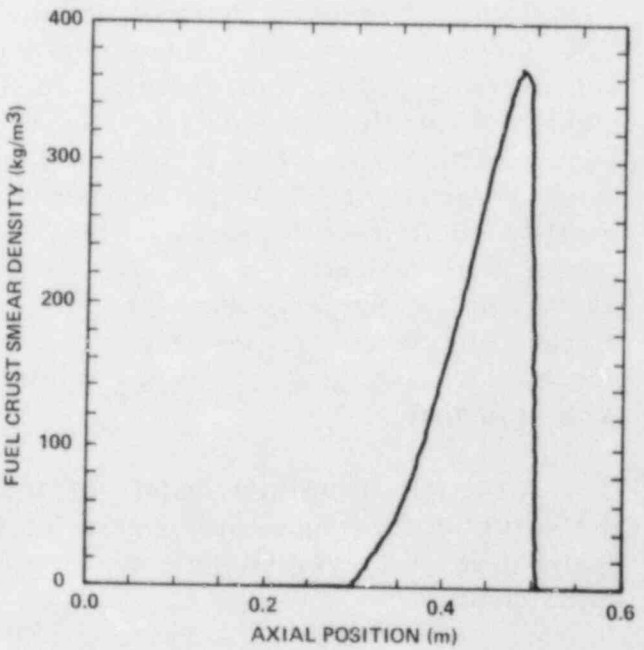

Fig. 7.
Fuel crust smear density at 0.1 s from the SIMMER-II exploratory analysis of the ANL GAP3 test.

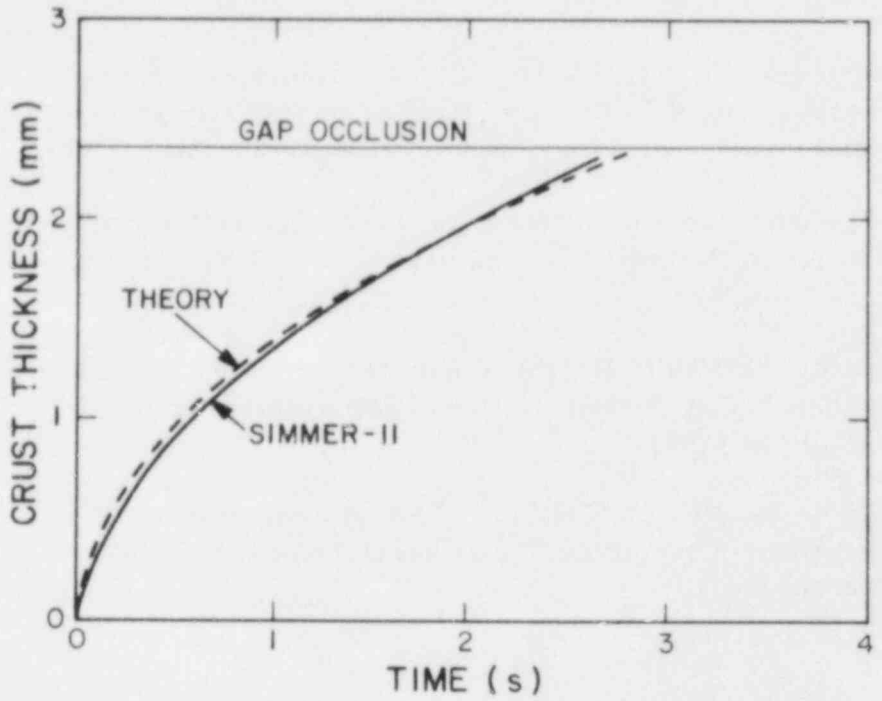

Fig. 8.
Comparison of the SIMMER-II treatment of conduction controlled fuel freezing with the known solution.

0.34 MPa. The calculated mass discharge as a function of time is shown on Figure 16 of Section II.6 as the solid curve. This result compared very well with that calculated [7] by Sandia National Laboratory with a specialized and more sophisticated freezing method that uses transient conduction in the wall and crust.

4. References

1. T. F. Bott and R. C. Smith, "An Examination and Test of the SIMMER-II Freezing and Melting Models," Los Alamos National Laboratory report LA-9618-MS (January 1983).

2.[a] B. W. Spencer, G. T. Goldfuss, R. E. Henry, D. J. Quinn, and R. L. Roth, "Reactor Material Fuel Freezing Experiments Using Small-Bundle, CRBR-Type Pins," Argonne National Laboratory report ANL/RAS-79-11 (1979).

3. B. W. Spencer, R. L. Roth, and G. T. Goldfuss, "Fuel Freezing Tests," Reactor Development Program Progress Report, Argonne National Laboratory report ANL-RDP-74 (August 1978).

4. B. W. Spencer, R. L. Roth, G. T. Goldfuss, and R. M. Hodges, "Fuel-Freezing Tests," Reactor Development Program Progress Report, Argonne National Laboratory report ANL/RDP-71 (May 1978).

5. B. W. Spencer, et al., "Results of Reactor-Material Fuel Dispersal Tests," Argonne National Laboratory report ANL/RAS 82-36 (December 1982).

6. L. L. Smith, "SIMMER-II: A Computer Program for LMFBR Disrupted Core Analysis," Los Alamos National Laboratory report NUREG/CR-0453, LA-7515-M (June 1980).

7. "Compendium to NUREG/CR-3224, An Assessment of CRBR Core Disruption Accident Energetics," Section 3, Nuclear Regulatory Commission report (March 1983).

[a] Address requests for this document to: F. X. Gavigan, Director, Office of Breeder Demonstration Projects (NE-50), U.S. Department of Energy, Washington, DC 20545, Telephone (301) 353-3134.

Nomenclature

α_{Sm}, α_S	Volume fraction of solid component m and total solid volume fraction ($\alpha_S = \sum_m \alpha_{Sm}$).
α_o	Value of α_G at the single-phase/two-phase transition.
$\alpha_{p,max}$	Maximum particle packing fraction in Equation (43).
Γ_{Sm}, Γ_{SL}, Γ_{SkLm}	Net mass transfer rate from solid component m, mass transfer rate from solid to liquid phase, and mass transfer rate from solid component k to liquid component m.
ρ_{Sm}, $\bar{\rho}_{Sm}$, ρ_S, $\bar{\rho}_S$	Microscopic and macroscopic densities of solid component m ($\bar{\rho}_{Sm} = \alpha_{Sm}\rho_{Sm}$) and microscopic and macroscopic densities of the total solid phase ($\bar{\rho}_S = \alpha_S\rho_S$ and $\bar{\rho}_S = \sum_m \bar{\rho}_{Sm}$).
ϕ_G^2, ϕ_L^2	Gas and liquid two-phase friction multipliers used in the Martinelli correlation, Section 2.3c.
μ_{Lm}, $\mu_{G,mix}$	Liquid component m and vapor mixture viscosities.
A_{Sk}, A_{Skm}	Surface area of solid component k exposed to the fluid and interfacial surface area between solid components k and m.
C_{pSm}, C_{vSm}	Specific heats of solid component m at constant pressure and constant volume.
C_{fLn}, C_{fGn}	Correlation parameter for the liquid-structure and vapor-structure friction factors, Equation (16).
C_{HLm1}, C_{HLm2}, C_{HLm3}, C_{HLm4}	Correlation parameters for the liquid m convective heat transfer coefficient.
D_h	Hydraulic diameter.
e	Specific energy.
f	Two-phase weighting function defined by Equation (17).
g	Acceleration of gravity.

h_{Sm}, h_{LSm}	Solid component m heat transfer conductance and liquid component m to structure heat transfer coefficient.
j_G, j_L	Gas, liquid superficial velocities $\left(j_G = \frac{\alpha_G}{1 - \alpha_S} \lvert \vec{V}_G \rvert\right)$
k_{Sm}	Solid component m thermal conductivity.
K_{LS}, K_{GL}, K_{GS}	Liquid-structure, gas-liquid and gas-structure momentum coupling coefficients.
n	Parameter used in Martinelli correlation.
N	Power generation amplitude function.
p, ∇ p	Pressure and pressure gradient.
q_{HLm}, q_{TLm}, q_{KLm}, q_{VLm}	Energy transfer rate to liquid component m from heat transfer, mass transfer, interfield drag, and viscous friction.
Q_{Lm}, Q_{NLm}	Net energy transfer rate to liquid component m and specific power generated in liquid component m.
R	Two-phase weighting factor used in Equation (17).
R_m	Gas "constant" for gas component m.
T	Temperature.
$\vec{V}_G$, $\vec{V}_L$	Gas and liquid velocities.
ΔV	Change in volume at vaporization
X^2	Martinelli parameter defined by Equation (31).
S, L, G	Solid, liquid, and gas.
Sm, Lm, Gm	Solid, liquid, and gas component m.
SOL, LIQ, CON, VAP, CRTI	solidus, liquidus, condensate, vapor, and critical energies.

II.7. RECRITICALITY BY EXTENDED FUEL MOTION

1. Objectives and Overview

According to the results of the previous two sections, mild termination by dispersal is far more likely than energetic termination (recriticality). However, recriticalities cannot be ruled out, in fact, they were calculated to occur, albeit only at relatively mild levels (Section II.5). Recognition of the limitations of current understanding and experience in this area, however, provides strong incentives for a better clarification of the potential severity of such events in CRBR. It is the purpose of this section to provide this clarification.

All three of the postinitiation, core-disruption states (see Figure 2 of Section II.1) are considered. Postulated recriticality events are specified as limiting conditions for the type of oscillatory material motions observed in the reference disruption-phase calculations of Section II.5. This oscillatory behavior is a consequence of the unstable character of subcritical states, as well as, of course, of the critical (and supercritical) ones. Under these conditions a limit-cycle behavior is possible only in the presence of adequate damping that was shown in Section II.5 to be present. However, the limits (or bounds) of behavior may be explored by removing the damping and/or considering ad hoc perturbations that "overdrive" the system. The extent of possible amplification can be explored accounting for uncertainties in modeling of damping effects or in the nature and magnitude of perturbations generated in the integral analysis. This is the approach adopted here.

Obviously, much judgement is required to define conditions that adequately explore the limits of behavior yet avoiding those that are physically unreasonable. The rationale for our choices will be given on a case-by-case basis. Certain general aspects, however, that may be helpful as background in this regard, are mentioned below.

In principle, fuel may be driven into a recriticality by pressure and/or gravity forces. We already saw one example of pressure-driven fuel motions (Section II.4) during the initiating phase. However, even with a flow limiter, these plenum fission gas pressures would dissipate within the S/A-pool stage, and would not affect recriticality considerations. Pressures from intense coolant boiling, that is, rapid fuel/coolant thermal interactions, remain the other possibility. However, if such interactions were to occur, they would follow immediately the codisruption of the pins and any associated forceful injection of the high-temperature fuel into the sodium-containing portions of

the coolant channels (upper and lower extremities of the subassemblies). Available experimental evidence with reasonably prototypic materials indicates the absence of any significant pressure generation events under such conditions. But even if such events were possible, core-wide incoherencies are substantial at the early core-disruption stages and would dictate local, isolated, occurrences; hence, these would be of limited significance for energetic recriticalities. At later times, coherence may develop. However, recriticality concerns for such times presuppose the existence of a "bottled-up" core. Hence, again, we see the impossibility of such fuel/coolant interactions at the immediate core boundary. Remelting of these blockages and destruction of the bottled-up state is possible, and likely. However, such remelting most likely will occur under power burst conditions, yielding a forceful discharge of materials rather than a fuel re-entry condition. Based on this reasoning, pressure-driven recriticalities are not considered further (we will discuss pressure-induced pool sloshing in Sections 3.3 and 5.3).

As we will see later in this section, the energetically significant recriticalities pertain to small fuel inventory depletions. Under such conditions the difference in whole-core compaction states between criticality and prompt criticality is about 0.01 m (approximately 1 $/cm fuel-worth gradient). That is, for an approach velocity corresponding to a 100 $/s recriticality (approximately 1 m/s), there would be only approximately 10 ms of significant power production (at and above nominal levels) before reaching "disassembly" conditions. Taken at an average power of 10x nominal, this predisassembly transient could deposit only 0.1 FPS (100 MJ), which is equivalent to a specific fuel energy deposition of approximately 10 J/g. With a fuel heat capacity of approximately 0.5 J/g-K this heating corresponds to approximately 20 K and a vapor pressure change of only 0.1 MPa (14.7 psia). It is easy to see, therefore, that the commonly held view that criticality can provide a recriticality-mitigating mechanism is true only in principle. In practice, the mechanism of predisassembly heatup is effective only for small magnitude recriticalities. For those that matter energetically, the compressed time interval severely limits any mitigating character.

A couple of corollary interpretations of this highly nonlinear damping mechanism also are possible. (a) Since the damping may be effective for low recriticalities, the higher nonlinear regime may not be physically relevant. (b) Any ad hoc choice of perturbations that drive the system outside the early well-damped regime must be carefully scrutinized and interpreted in terms of the likelihood of its occurrence. The evaluation of the recriticalities studied with regard to both of these topics will be made for each case considered.

The Applicant's treatment of the postinitiating-phase, core-disruption sequence has emphasized the dispersal phenomena [1, 2]. The issue of recriticality was qualitatively considered to conclude that: (a) mild

recriticality events in the S/A-pool stage are possible but of limited amplitude and do not amplify, and (b) the accident sequence will terminate benignly without the development of a large-scale confined pool. Our evaluations of these positions are documented in References 3 and 4.

Our assessment began with the consideration of certain idealized disassembly situations that help generate a perspective on certain crucial aspects of neutronic shutdown (Section 2). In particular, the effects of voids and the associated role of the equation of state were considered. Also, these simple test cases were used as a convenient basis for comparison between the Eulerian hydrodynamics approach of SIMMER-II and the Lagrangian methods of the VENUS-II code [5] that has been the standard tool in this area for the past decade. The hydrodynamic responses of pools with various sizes and material configurations to postulated perturbations are examined in Section 3. These hydrodynamic re-assembly conditions then are converted to recriticality severity estimates (Section 4) through the use of criticality estimates and the associated fuel-worth gradients. Finally, coupled neutronic/hydrodynamic calculations are presented (Section 5) to quantify the excursion yields and to order the recriticality events in terms of their respective severity and likelihood.

2. Neutronic Shutdown Mechanisms

At super-prompt-critical conditions the power doubles approximately every 0.01 ms. Hence, it can reach many thousands of times the nominal level within 1 or 2 ms. This intense heating is self-terminating by the combined action of Doppler (a negative reactivity feedback related to temperature rise which is a prompt effect) and of outward fuel motion, that is, disassembly. This latter effect is not prompt because such motions result only after fluid inertia is overcome. Although relatively small displacements are adequate for shutdown, the time scale imposed by the high power levels requires extremely high acceleration and consequently enormous pressures. Such pressures develop from heating either by thermal expansion or by the build-up of vapor pressures. However, because of the centrally peaked flux shape, the generation of such pressures also will be centrally peaked. Since for shutdown we are concerned with the global system expansion rather than a local one, pressure pulse propagation (and relief due to expansion) must be considered. Fluid compressibility is the important parameter in this regard. Indeed, it is well recognized that single-phase liquid (highly incompressible) disassemblies terminate very quickly and produce low yields even at extremely high ramp rates [6].

Single-phase liquid conditions also may develop during two-phase disassemblies. For example, with an initial liquid fuel density of 8000 kg/m^3, a 50%-void fuel-vapor system undergoing constant-volume heating will reach the liquid saturation line at a temperature of approximately 6250 K

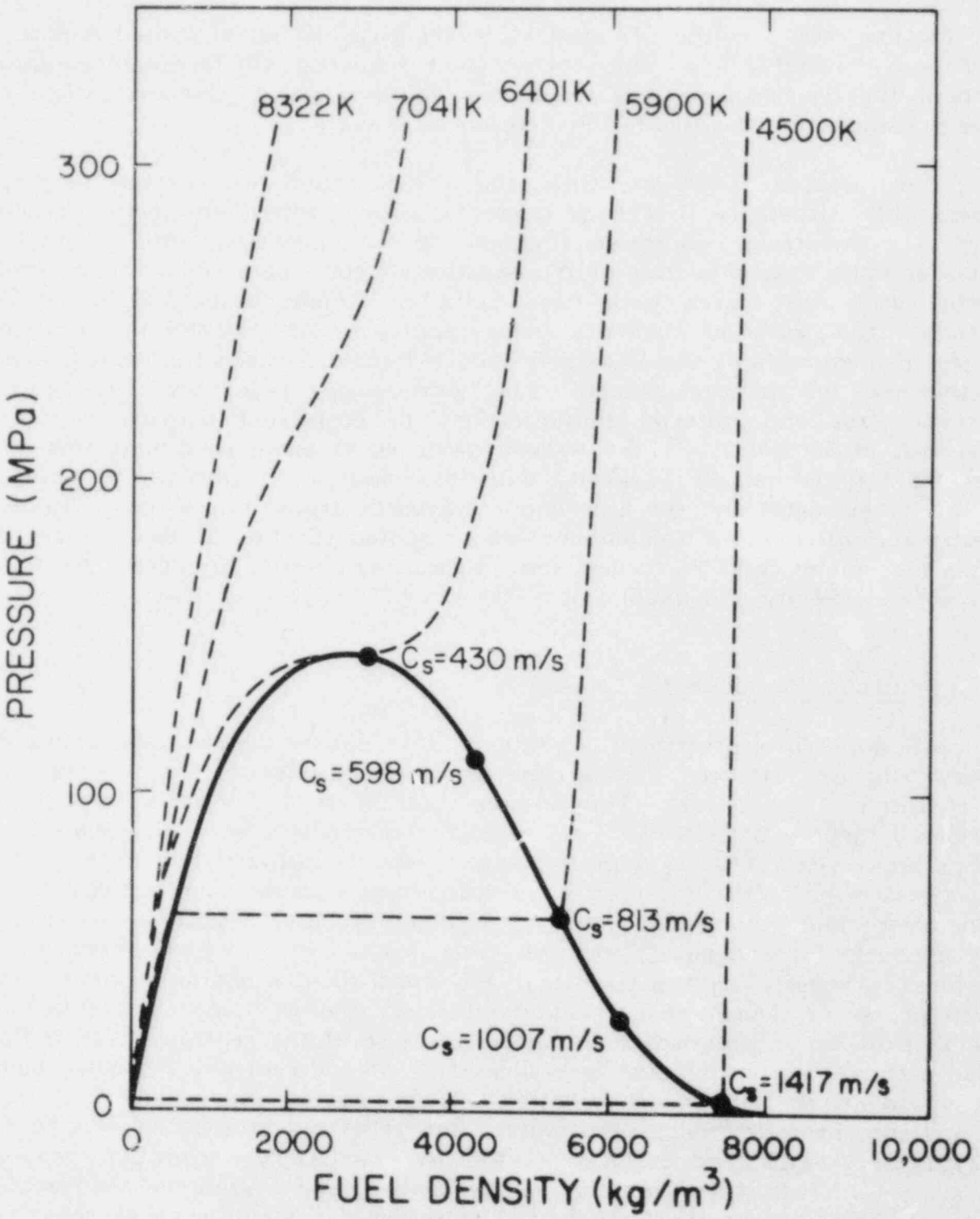

Fig. 1.
Los Alamos equation of state for fuel. C_s is the isentropic speed of sound.

(corresponding to approximately 120 MPa) as shown in Figure 1. However, at these elevated temperatures the liquid compressibility increases substantially, hence the "single-phase" condition may not be as effective in limiting the disassembly yield. A parametric evaluation of this effect was carried out using a simple one-dimensional, uniform void, SIMMER-II model (a special case of that described in Appendix A) equivalent to one CRBR subassembly including the full steel inventory. A fixed energy generation rate was imposed on this model. The time interval for disassembly was determined from the calculated fluid displacements and a given (fixed) fuel-worth distribution. The yield of this idealized disassembly was obtained from the product of this time interval and the fixed power level.

The results are summarized in Figure 2. Note that the single-phase effects dominate for cases with an initial void fraction up to approximately 15 to 20% which agrees with previous studies with a different code and model [7]. As the quantity of distributed steel decreases, the above limit range of initial void fractions would increase. The above cases imply a single-phase effect for a void-to-fuel volume ratio of approximately 0.5; hence in the absence of steel, single-phase disassembly-limiting effects should be observable up to void fractions of approximately 30%. A representative case from the range with a strong single-phase effect is compared with one from the asymptotic range in terms of calculated detailed responses in Appendix A. From these comparisons the important aspects of the hydrodynamic shutdown mechanism(s) may be visualized. The shutdown behavior for one such case is shown in Figure 3 in comparison with that calculated using VENUS-II. The agreement is excellent.

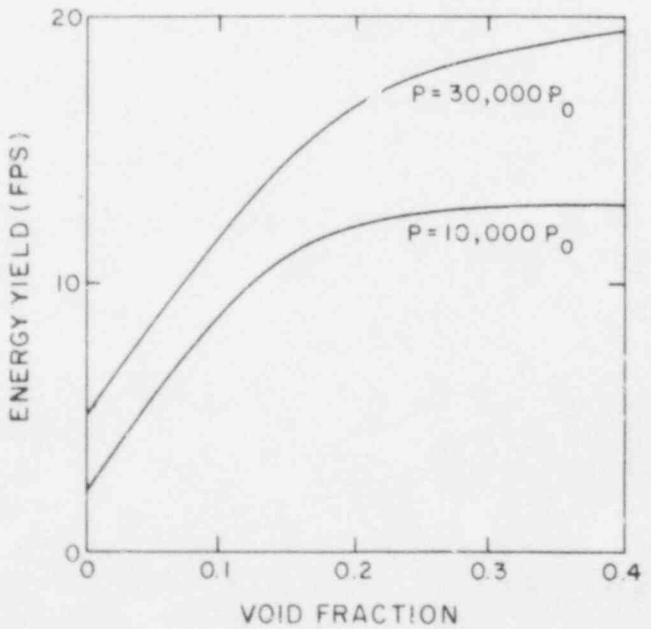

Fig. 2.
Disassembly thermal energy yield vs initial void fraction.

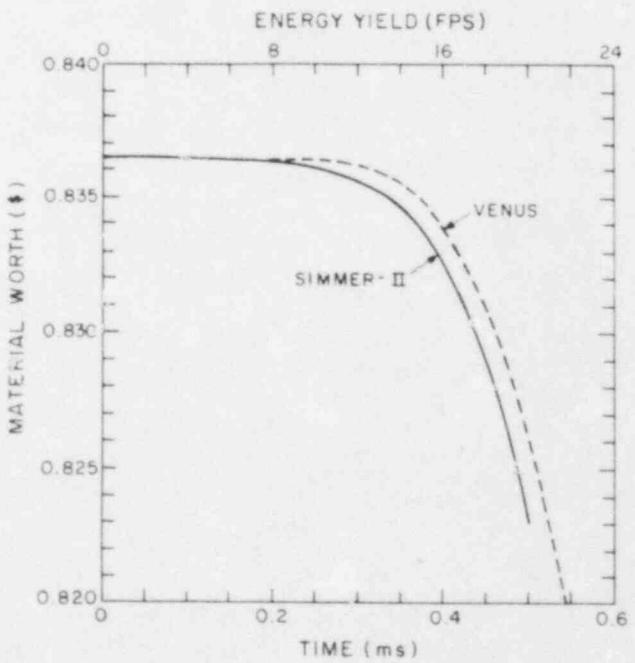

Fig. 3.
Comparison of SIMMER-II and VENUS disassembly transients.

3. Molten Pool Fluid Dynamics

3.1. Subassembly-Scale Pools

As discussed in Section II.5, this phase is dominated by oscillations in fuel mass (axial) distribution and by the associated power pulses. Although "tuning" and amplification did not occur to any significant extent in that one calculation, the possibility cannot be excluded altogether at this time. To quantitatively explore such possibilities, the basic fluid mechanical behavior of such oscillatory fuel motions within S/A-scale geometry (sealed at both ends) needs to be characterized.

The oscillations result from the unstable character of a S/A-scale pool dispersed into a subcritical configuration. The high heat loss environment due to the presence of solid (S/A walls) or melting steel (cooler by approximately 1000 K) and/or equilibration of vapor pressures in the sealed geometry are primarily responsible for this character. When the dispersive vapor pressures subside, downward relocation under the influence of gravity must occur. It is the character of this "collapse" of the dispersed state that we seek to establish.

First we consider the extreme case depicted in Figure 4. It represents a microscale of the classical Bethe-Tait recriticality regime; a power pulse has previously separated (due to the centrally peaked flux) the fuel column into two parts (between states t_1 and t_2 in the figure). The upper half approaches the lower half under free fall and as a coherent mass. If the velocity at prompt critical is j_{pc}, the rate of reassembly (and the reactivity ramp rate) would be proportional to j_{pc}. In addressing the situation more realistically, we need to consider what factors influence this simple reassembly expression.

Under free-fall conditions (constant acceleration, g), the velocity j_{pc} is related to the displacement to achieve prompt criticality, s_{pc}, by

$$j_{pc} \sim 1.4(gs_{pc})^{\frac{1}{2}} \quad .$$

As a result, the recriticalities from near-critical initial states should be more benign than those from highly subcritical ones. However, the fallback configuration at t_2, resembling the well-known experiment of turning a full glass of water over, will be highly unstable. It is well known that under these conditions liquid slug breakup occurs within a travel distance of approximately 1 slug length [8]. The breakup has the appearance of a large vapor (gas) bubble penetrating the slug. In a frame of reference fixed on the subassembly wall, the process has the appearance of the slug draining around a large central void space as shown in Figure 5. The relative velocity at fully developed flow conditions is given [9] by

Fig. 4.
Schematic representation of slug-type mild disassembly and reassembly.

Fig. 5.
Schematic representation of instability controlled reassembly.

$$u_\infty \sim 0.35(gD)^{\frac{1}{2}} \quad ,$$

where D is the subassembly hydraulic diameter. This relative velocity is defined with reference to the bubble nose and the undisturbed liquid slug and implies a substantial liquid slug holdup as compared to that estimated in the undisturbed, free-fall regime. If the local (area average) void fraction over the draining portion is α and the local liquid velocity over the same portion is u, the reassembly rate, now represented by the superficial velocity at time t, is given by

$$j_{pc} = (1 - \alpha)u(t) \quad .$$

A conservative estimate of this reassembly rate may be obtained assuming steady-state, fully developed flow. Then by continuity we obtain

$$j_{pc} \sim u_\infty \sim 0.35(gD)^{\frac{1}{2}} \quad ,$$

which, for a subassembly diameter of approximately 0.1 m yields $j_{pc} \sim 0.35$ m/s.

As another but somewhat artificial limit, we may think of the upper slug breaking up due to instabilities during initial upward acceleration, but reversing direction just in time to avoid reagglomeration at the top of the S/A

(hypothesizing the presence of a noncondensible gas at the top). For a more-or-less uniform dispersion, an average void fraction of $\alpha \sim 65\%$ would result for the upper half of the material (see volume ratios of Figure 4). The reassembly rates obtained from such conditions would be given by

$$j_{pc} \sim 1.4(1 - \alpha)(gs_{pc})^{\frac{1}{2}} \quad .$$

In the limit of a highly diluted system $s_{pc} \sim 0.60$ m, $j_{pc} \sim 1.14$ m/s. We can see that this "rainback" process is considerably more forceful than the "drainback" considered previously. However, at this limit the differential worth would be considerably smaller than the typical upper range of approximately 1 \$/cm (on a whole-core basis); hence, the reactivity insertion from this considerably higher reassembly rate would be mitigated substantially (see Section 4 below). As another example, for a rainback of approximately 0.30 m, where the 1 \$/cm value may be applicable, a reassembly rate of approximately 0.82 m/s is estimated.

Subassembly-scale pool fluid-dynamic behavior was also explored with SIMMER-II calculations, including the thermal aspects of the problem (vapor production and condensation) in Appendix C of Section II.6. These calculations utilized somewhat coarse noding for resolving the details of the fluid dynamics. However, the results indicate substantial agreement with the positions formulated above, and in particular they show no evidence of substantially altered behavior in the presence of heat transfer effects.

3.2. Annular Pool

The fluid-dynamic response of the annular pool to power perturbations (neutronic slosh) was examined. Significant differences with the S/A-scale pools examined above arise due to the strongly two-dimensional character of the flow field. Indeed, based on the power peaking, as shown in Figure 6, the fuel vapor bubble (torroidal) would grow from a position less than one pool width from the free surface ($L/D < 1$). The available upward displacement space, Z, corresponds to roughly two slug lengths ($Z/L \sim 2$). Some experience with such geometries is available from experiments in Mark-III pressure suppression containments. They indicate that preferential upward bubble growth as opposed to growth in the radial direction will occur, leading to breakthrough (of the liquid slug) and bubble venting before a net displacement of 1 to 2 slug lengths. Unfortunately, these experimental data are limited in detail and are not openly available. Specific aspects of interest to our problem include: (a) the quantitative aspects of the breakthrough phenomenon, (b) the flow regime aspects of the arrest and reversal of upward-moving liquid masses following breakthrough, and (c) the existence of any secondary breakup flow regimes. Our approach is based on a combination of SIMMER-II modeling and phenomenological simulant-material experiments.

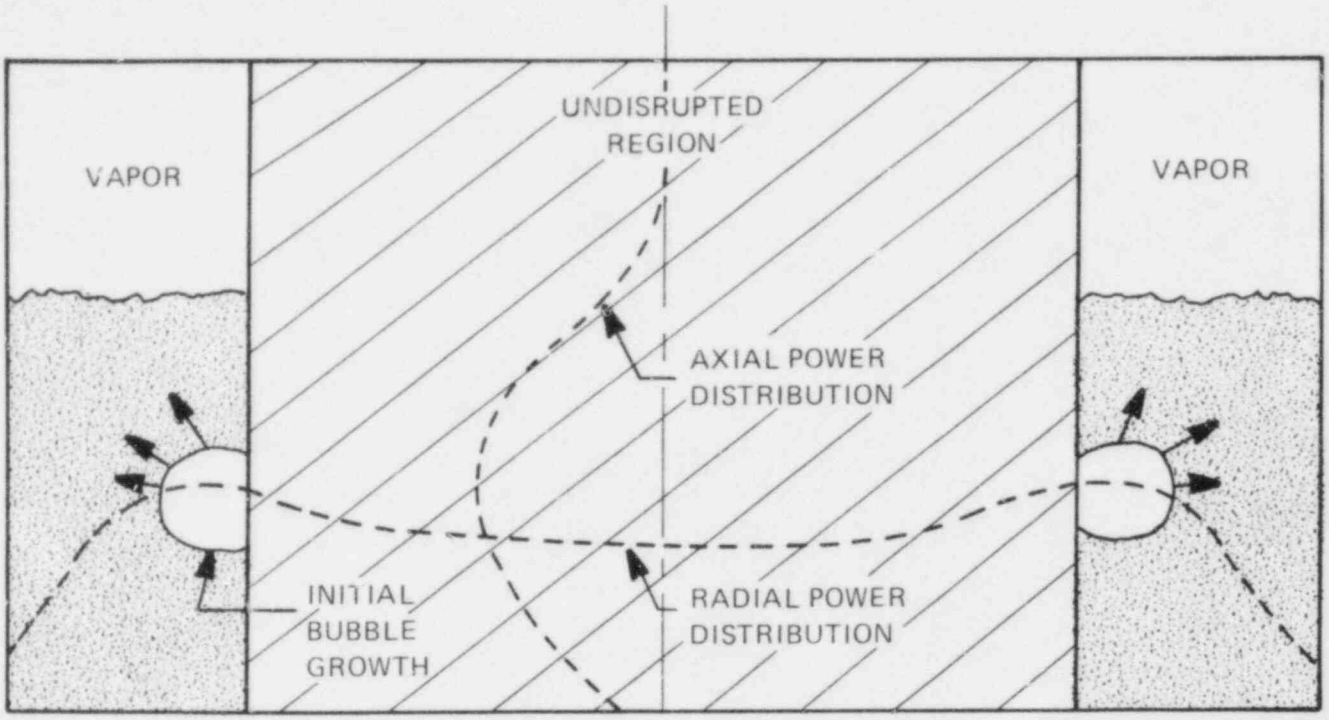

Fig. 6.
Schematic representation of annular pool mild disassembly.

The experiments were conducted in the Omega facility (Purdue) that was modified by the addition of a central cylinder to form an annular pool (OD ~ 1 m, ID ~ 0.30 m, L ~ 0.60 m). With these dimensions, and a pool height of 0.20 m, the whole CRBR annular pool was modeled at full scale, except that the radius of curvature of the annulus was half the actual. The water pool was driven by nitrogen gas with the pressure chosen to match the expected acceleration of the fuel pool. The experimental results confirmed the breakthrough trends expected. The SIMMER-II calculations appear to provide an adequate representation of the global fluid dynamics (see Appendix B). However, the calculations could not portray the fine-scale breakup and intense mixing conditions that were observed experimentally following breakthrough. Such phenomena would tend to impede liquid fallback, hence their neglect should provide a conservative estimate of reassembly rates.

The CRBR annular pool response to triangular power pulses, at amplitudes of 100X and 300X nominal power and a half-width of 10 ms, was modeled with a SIMMER-II model as described in Appendix B. The power levels chosen represent mild prompt-critical conditions typical of this stage of an LOFA. The overall behavior was similar to that observed in the calculation of the Omega experiments. A schematic representation of the flow evolution is given in Figure 7. The important aspect of the bubble breakthrough phenomenon is the distribution of the rising portion of the liquid along the outer wall of the pool, and hence, the lenghtening of the reassembly time interval. Driven by its momentum, acquired during the

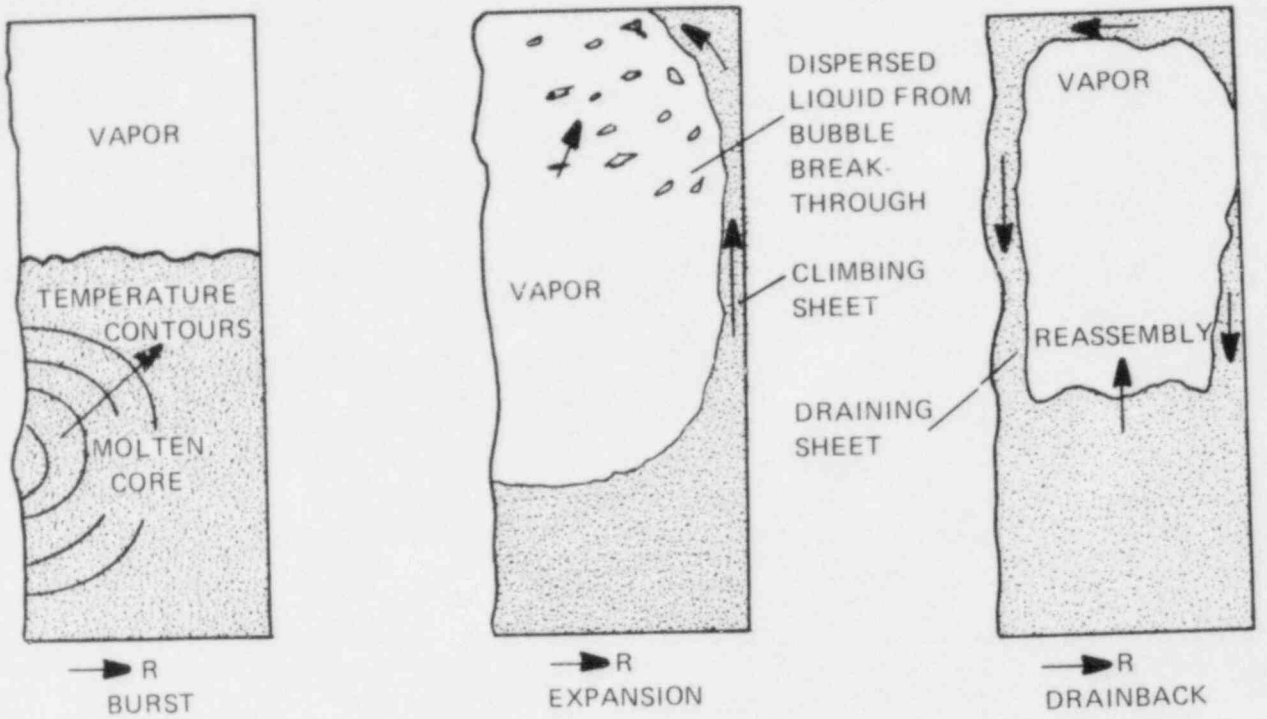

Fig. 7.
Schematic representation of annular pool mild disassembly and reassembly.

bubble growth phase, this wall jet would continue to rise while decelerating under gravity, would impact the upper boundary, would turn around at the upper boundary, and would jet downward along the inner wall of the annulus. At a certain time the outer wall jet also will reverse motion and accelerate downward under gravity. Typically, this reversal would occur near the end of the whole process, hence it is not likely to contribute greatly to the reassembly rate produced by the inner and more forceful jet. The quantitative aspects of these processes are depicted and discussed in Appendix B. The overall result from a total of seven simulations was a reassembly rate of approximately 0.25 to 0.35 m/s; which, interestingly enough, is quite close to that obtained for S/A-scale pools.

A substantially higher degree of breakup than portrayed by the coherent jet structures in the SIMMER-II results was evident in the experiments. Unfortunately, due to time constraints, this aspect could not be quantified experimentally. It is clear, however, that during the jet deflection process, as well as during the subsequent flow, hydrodynamic instabilities would tend to produce a spray-type rainback rather than a jet-type drainback. Furthermore, substantial momentum dissipation would occur during the deflection process in the core (in the present calculations perfectly elastic collision was assumed) along a rough upper wall composed of exposed pin stubs, ends of S/A walls, and crusts of solidified material. Both of these processes would further reduce the rate of reassembly, hence the rates cited above are deemed to be conservative. At the other extreme of complete breakup, we

use an average void fraction of $\alpha \sim 65\%$ and free-fall velocities. Hence, as in the S/A-scale pool case, we obtain reassembly rates in the 0.80 to 1.10 m/s range depending on the applicable free-fall distances. As emphasized previously, however, this kind of situation is highly artificial, especially for the annular pool in which the material becomes distributed on its way up due to bubble breakthrough and no mechanisms can be identified for total reaglomeration prior to fallback.

3.3. Whole-Core Pool

The aspect that sets this case apart from the previous two considered is the possibility of significant radial motions aggravated by radial convergence of inward flows. This topic, together with its recriticality implications, was first discussed by Bohl [10]. Additional studies were conducted early in the CBBR review process [11]. The basic idea is schematically illustrated in Figure 8. The generally symmetric geometry and equally symmetric neutron flux distribution produce bubble growth and fuel mass separation that is radially and axially symmetric following a mild recriticality event (the assumed perturbation). Bubble breakthrough occurs and generates an outward peaked mass distribution, which would tend to drain under gravity to fill the void generated by the venting vapor bubble. This inward slosh is augmented by radial convergence to produce a mass accumulation in the area of peak flux, hence a high ramp rate. Our objective was to study the physical behavior and quantify these radial slosh phenomena. Our approach was similar to that used for the annular pool and consisted of SIMMER-II calculations augmented by simulant material experiments.

The Omega facility (without the central structure present in the annular pool studies) was utilized to benchmark the SIMMER-II sloshing model as in the previous case. In this case also, the expansion phase was successfully modeled. Details may be found in Appendix C.

For the CRBR case, two different perturbations were examined, each provoking a somewhat different radial sloshing mode. Coupled neutronic/hydrodynamic computations were performed for these two cases with SIMMER-II. The neutronic feedback was suppressed in subsequent calculations to allow the in-slosh to proceed well beyond initial criticality so that the characteristics of more extensive in-sloshes could be observed. The methods employed are summarized, together with the detailed results, in Appendix C. In both cases, the in-sloshes observed were of constant rate equivalent to increasing the mass in the central one-fourth of the core at the rate of approximately 2500 kg/s and 6200 kg/s for the neutronic and pressure-driven sloshes, respectively.

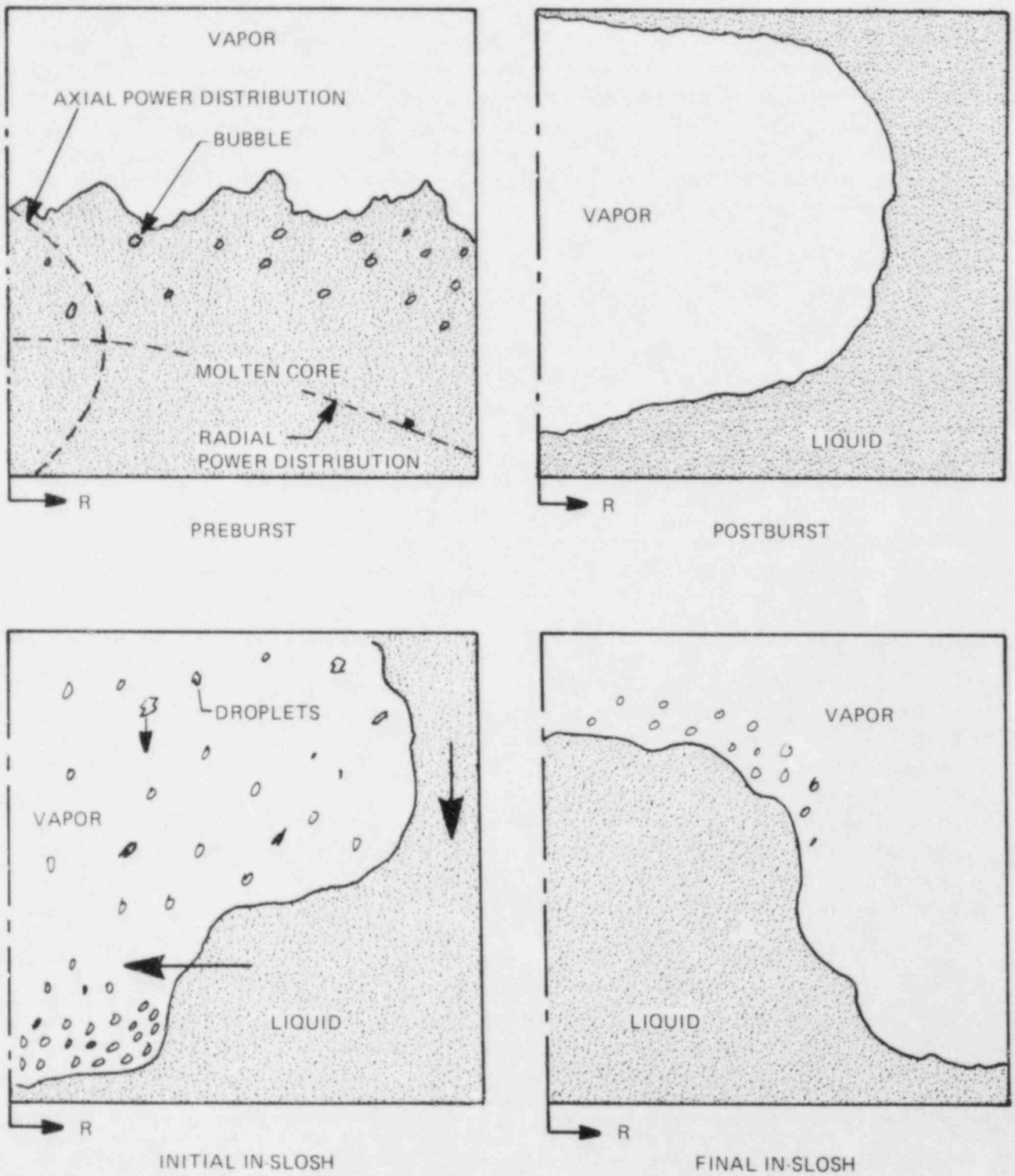

Fig. 8.
Schematic representation of whole-core pool mild disassembly and reassembly (sloshing).

4. Recriticality CRBR Neutronics

The fluid-mechanic reassembly rates developed in the previous section may be converted to reactivity ramp rates by the use of differential fuel reactivity worth values at the critical condition. The results obtained are sensitive to the fuel material configuration, particularly to the existence of low void or liquid-only regions. Our approach, therefore, was to span a broad range of possible configurations in terms of the simple three-step procedure employed here, rather than carry out a few of the considerably more involved, complex, neutronic/hydrodynamic recriticality calculations. In this fashion we can develop a better understanding of the important trends, and thus be able to more intelligently seek out the significant recriticality regimes.

Four whole-core recriticality configurations were selected for analysis for the S/A-scale pool and annular pool. These configurations are illustrated in Figure 9. Configuration "0" represents a uniform, core-wide compaction to investigate reference two-phase disassembly behavior. The other three configurations (2, 3, and 5 shown in Figures 9b, 9c, and 9d, respectively) represent partial slumps for various radial degrees of disruption with puddling at the bottom. A series of k_{eff} calculations was performed for each configuration as fuel was compacted and removed to achieve criticality. Similarly, a series of k_{eff} calculations was performed for the homogenized whole-core pool to simulate, in an idealized form, the in-slosh configuration, as shown in Figure 10. The neutronic treatment in these calculations is identical to that presented in Appendix C. The results are summarized below.

The vertical slumping configurations 2 and 5 gave results that were essentially the same. An examination of the power shapes as a function of the degree of slumping in conjunction with the associated puddle depths, as shown in Figure 11, revealed a new and interesting "disassembly" phenomenon. This phenomenon is due to the existence of conditions for which the peak power position is above the top of the liquid puddle. A disassembly from this condition would involve the rapid single-phase response to rapid heating discussed in Section II.7.2, except that, assuming that downwards movement is prevented due to blockages, this would represent a reactivity "boost" rather than a shutdown mechanism. The range of puddle depths over which this boost mode exists is shown in Figure 12. Puddle depths in excess of approximately 0.10 m at prompt critical would be required to avoid this mechanism. Combining this result with that of Figure 13, which shows the criticality threshold, we conclude that such puddle depths are possible only after removal of approximately 15-20% of the fuel inventory. As we have seen in Section II.6, such a situation is indeed likely. Conversely, for puddle depths greater than approximately 0.10 m, the single-phase shutdown mechanism would be strong and would significantly limit the energy release. The total reactivity and the differential reactivity are shown in

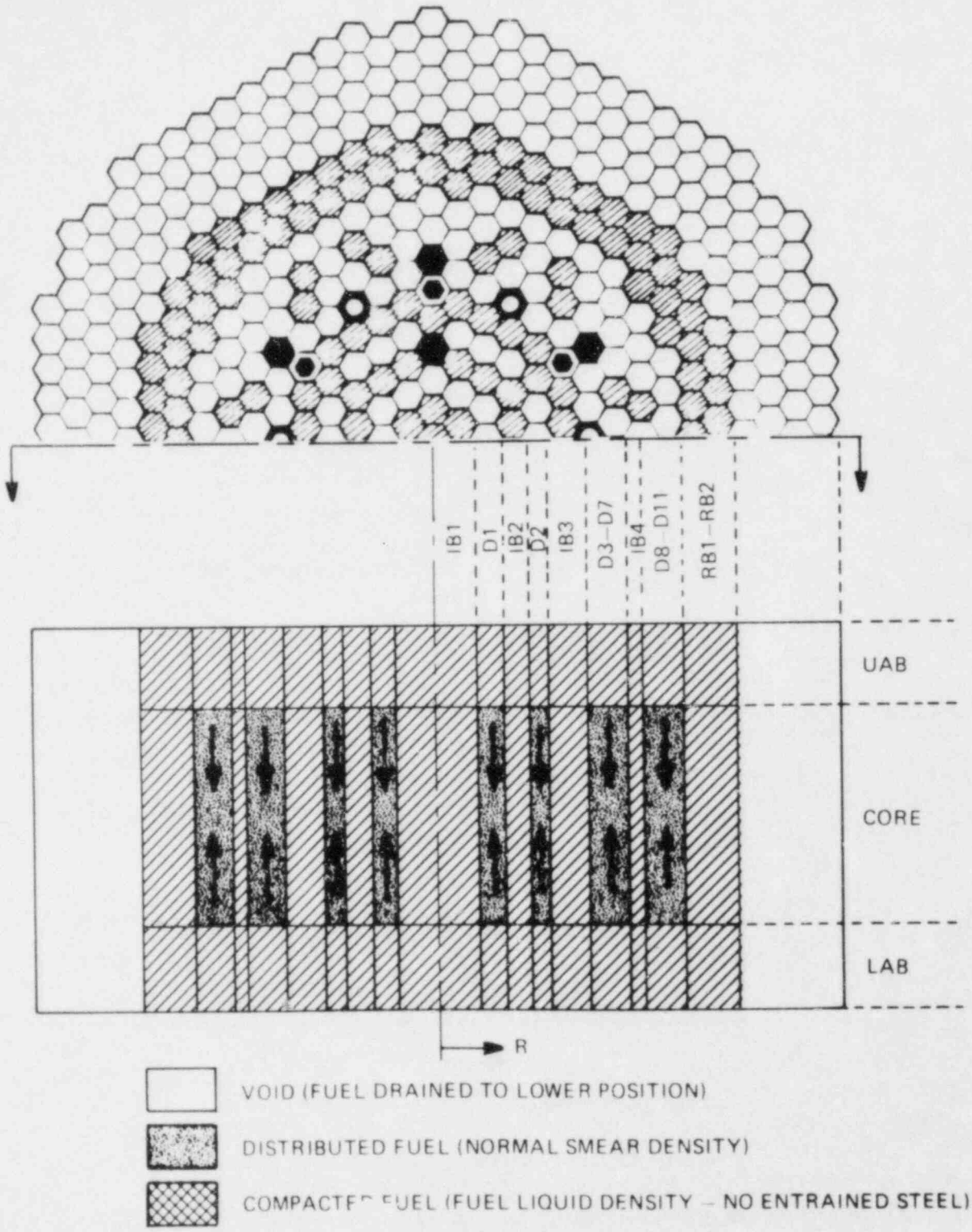

(a) Configuration 0.

Fig. 9.
Core configurations for subassembly pool and annular pool neutronics analysis.

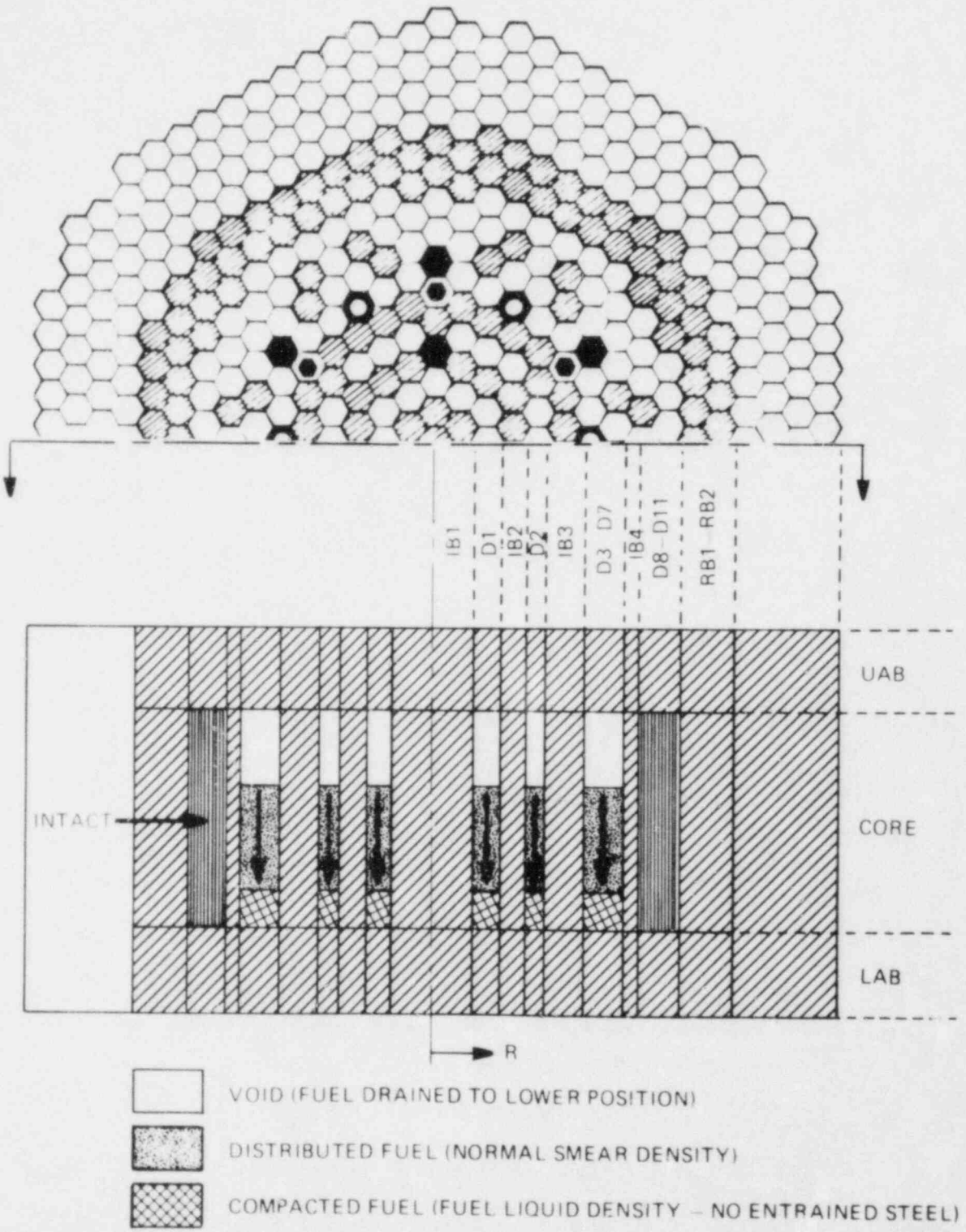

(b) Configuration 2.

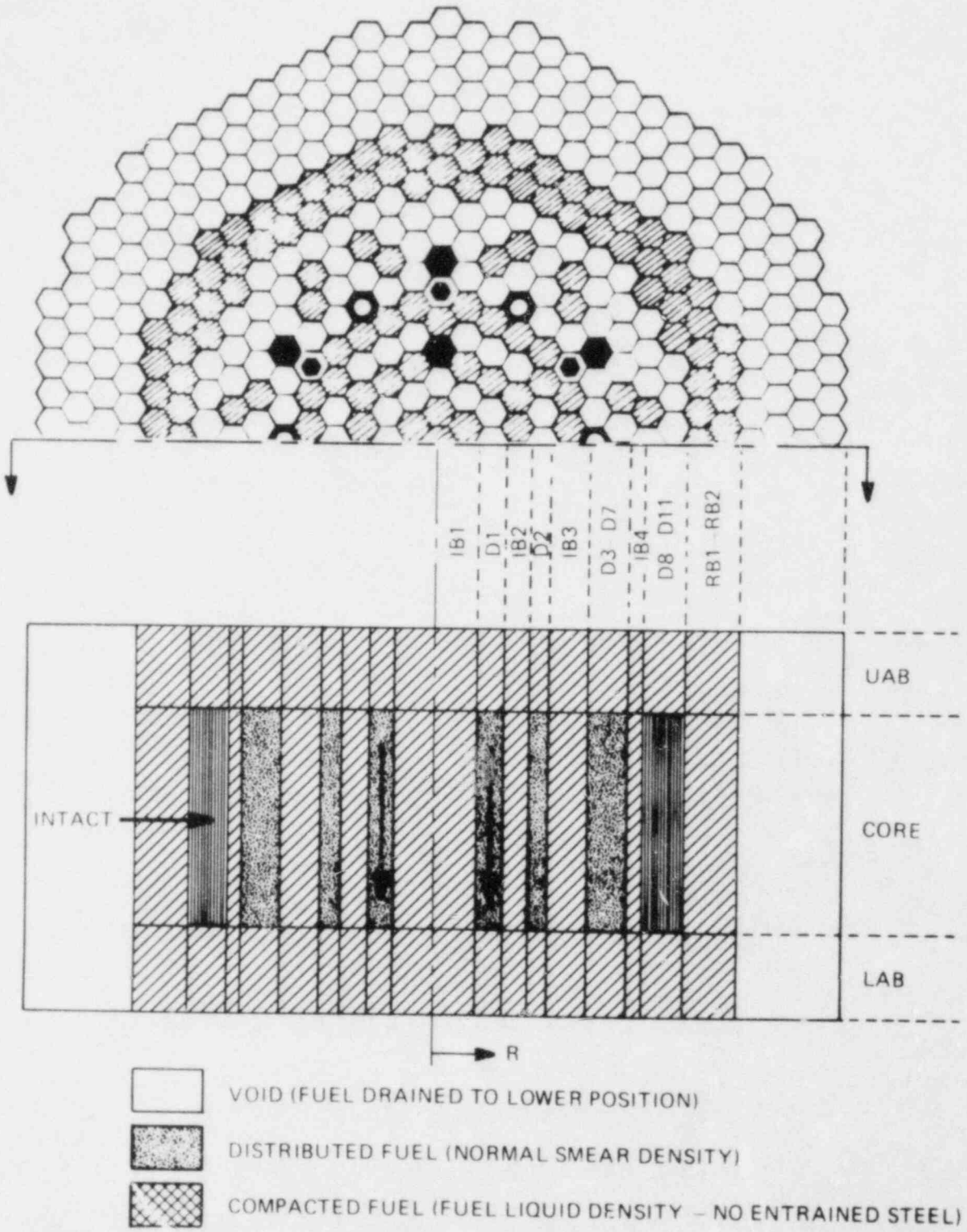

(c) Configuration 3.

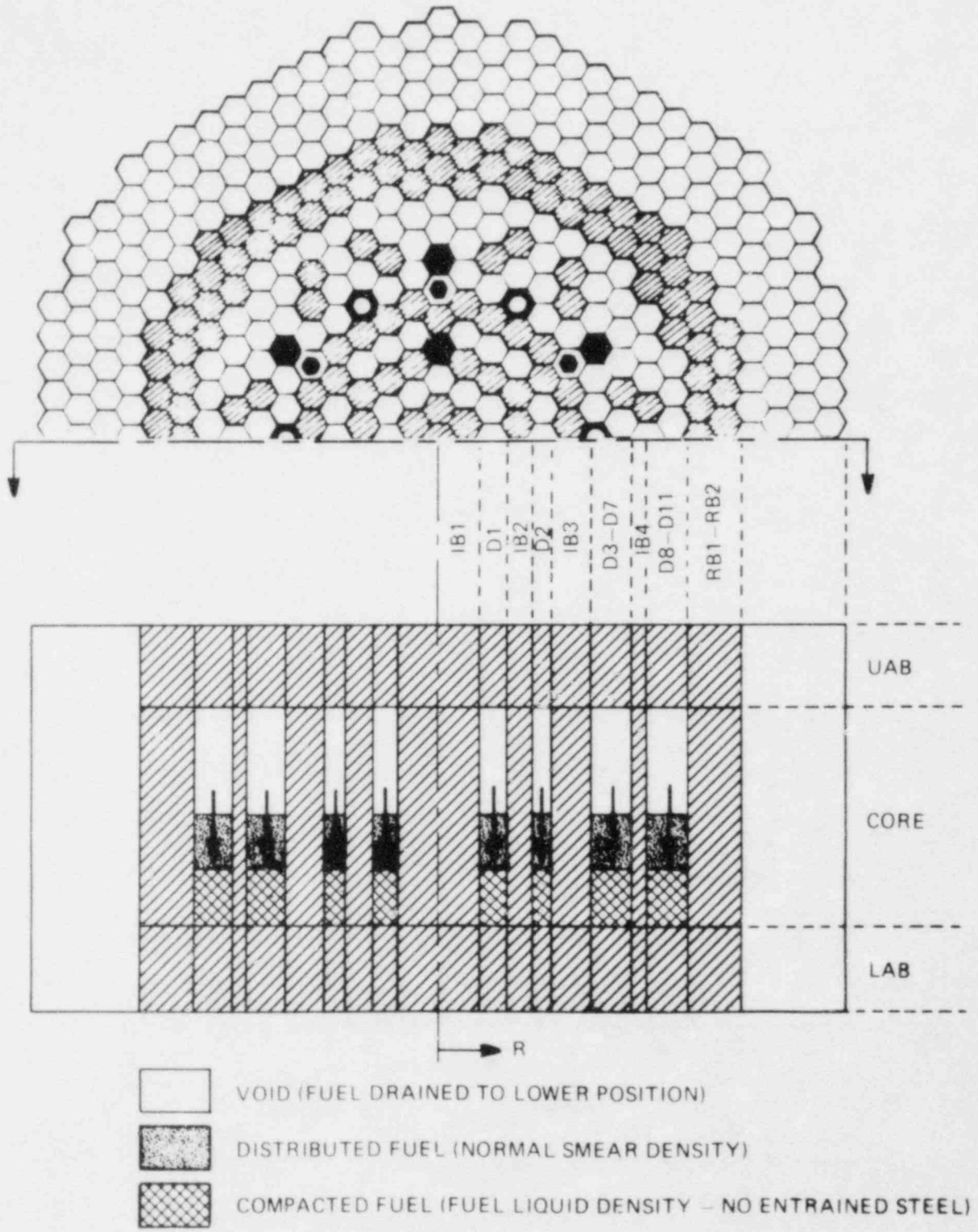

(d) Configuration 5.

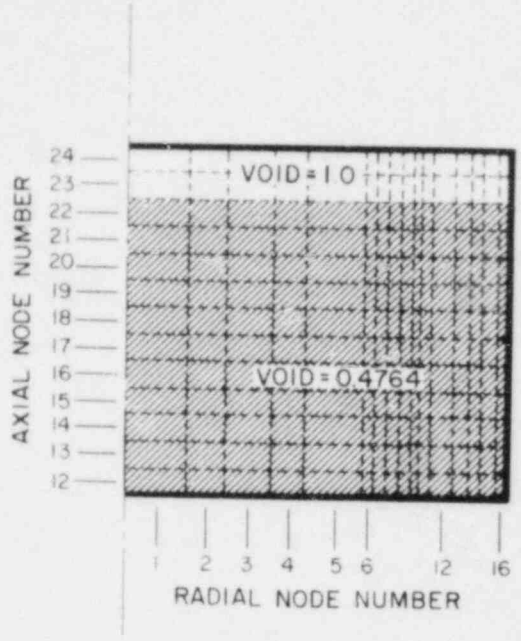

(a) Initial state.

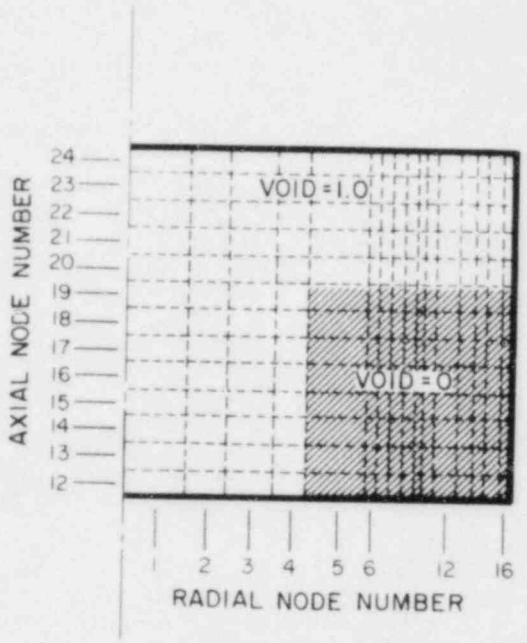

(b) Out-slosh.

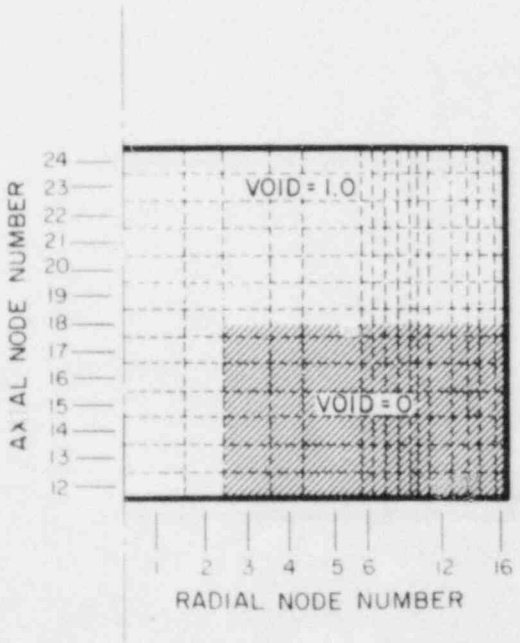

(c) Initial in-slosh.

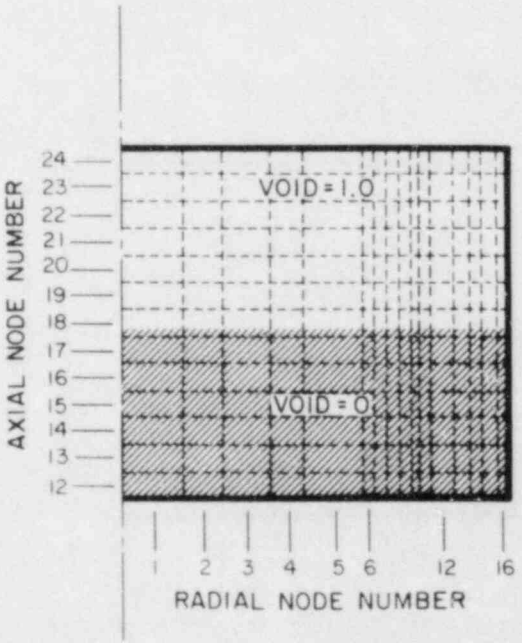

(d) Partial in-slosh.

Fig. 10.
Core configurations for whole-core pool neutronics analysis.

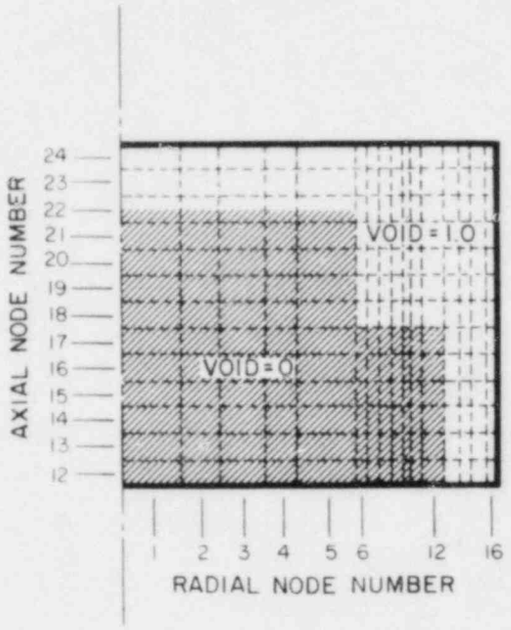

(e) Massive in-slosh.

Figure 14. Note that the differential worth was maximized at a pool height of approximately 0.20 m; however, the value is within ±40% from the 1 $/cm value utilized previously. The results for configuration 3 were similar in character but quantitatively different due to the considerably smaller quantity of fuel involved. Thus, the differential worths also were considerably smaller, approximately 0.25 ± 0.1 $/cm, and the boost could occur for puddle depths up to approximately 0.20 m. However, a dispersal of only 1-2% of the core inventory would be necessary to dispel such a concern. Such small quantities of fuel loss are virtually guaranteed even in the short time period appropriate for considering configuration 3-type recriticalities (early S/A-disruption phase. Finally, the homogeneous compaction mode represented by configuration 0 was characterized also by a differential worth of approximately 1 $/cm ± 40% but did not exhibit any of the threshold-type behavior of the puddled configurations.

The results for pool in-slosh states indicated low differential worth of approximately 0.6 ¢/kg through the inward translation until the fluid contacted the pool axis. Beyond this point further radial inward motion resulted, by continuity, in a central upward bulging of the pool that produced a differential worth of approximately 5 ¢/kg.

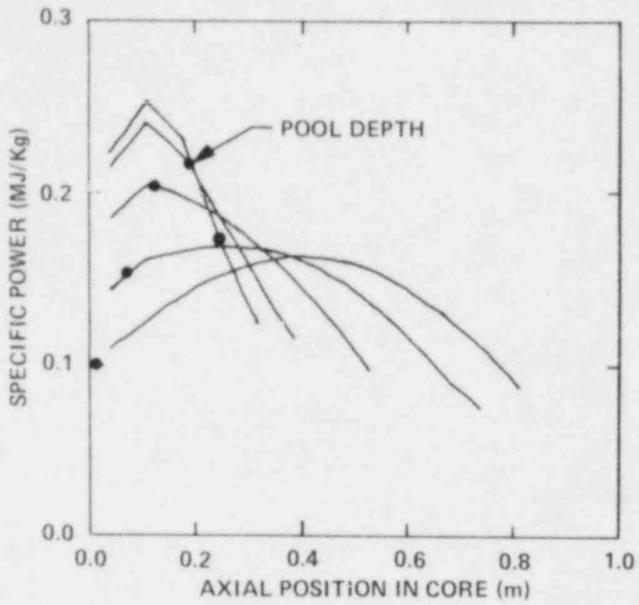

Fig. 11.
Specific power distribution changes with whole-core fuel puddling.

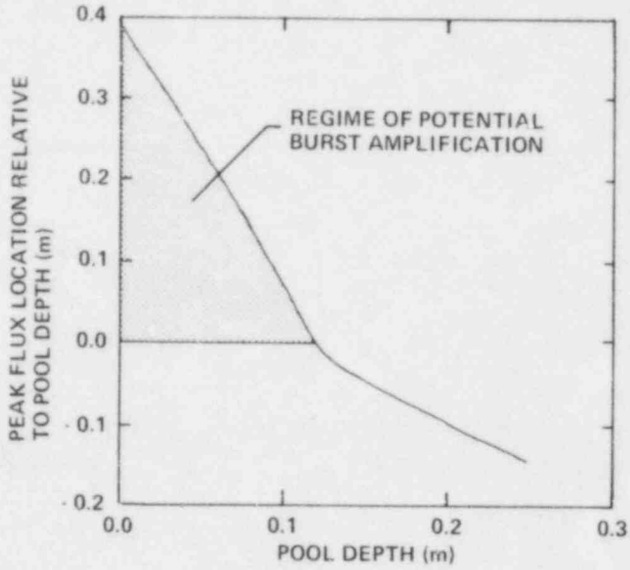

Fig. 12.
Regime of potential disassembly boost during whole-core puddling.

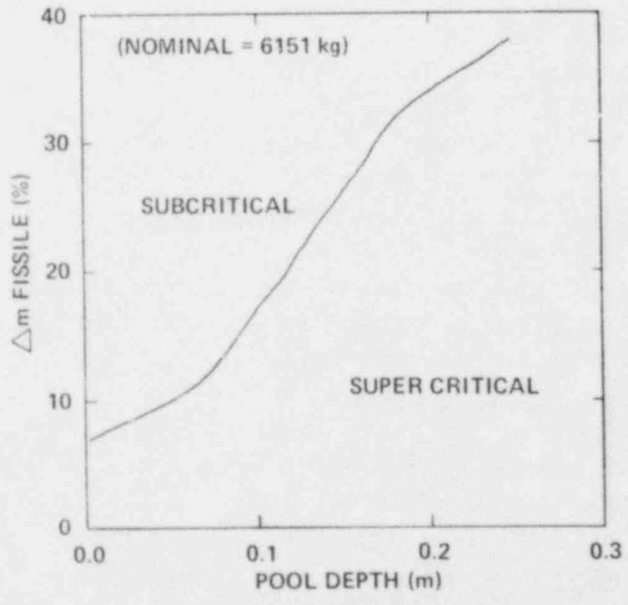

Fig. 13.
Criticality threshold for whole-core puddled configurations.

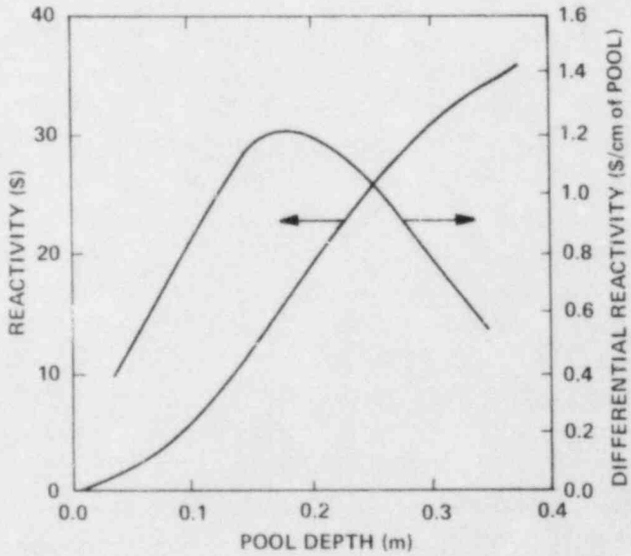

Fig. 14.
Reactivity effects of whole-core puddling.

5. Bounding CRBR Recriticality Yields

The purpose of this section is to combine the fluid-mechanics results of Section 3 with the differential worths determined in Section 4 to obtain ramp rates and to evaluate the corresponding disassembly transients (to be presented here) in order to scope the ranges of recriticality energy yields and respective likelihoods.

A SIMMER-II disassembly model similar to that utilized in the calculations of Appendix A was utilized to establish the excursion yield as a function of the reactivity ramp rate for the range of configurations examined in the previous section. The modeling details are provided in Appendix D and the results of these parametric studies are summarized in Figure 15. The 100- and 200-$/s two-phase disassembly (configuration 0) yields, which were examined in Section II.2 with reference to structural accommodation, provide a reference for judging the magnitude of the various effects as they are considered below.

Disassembly calculations for configurations 2 and 3 were performed with fuel inventories that imply the existence of the boost regime. A substantial augmentation of energetic behavior was clearly evident. However, the configuration-5 inventory lies at the other side of the boost threshold; hence, benign behavior even for extremely high ramp rates resulted.

Another interesting view of these results may be obtained by cross-plotting yields as a function of the fuel inventory reduction for a given ramp rate. This was done for the 100-$/s case and is shown in Figure 16. Indeed, it appears that although a fuel removal by approximately 40% is required for permanent subcriticality, for any removal more than approximately 20% (corresponding to the inventory loss for which the peak in flux coincides with the puddle depth at the critical condition), significant energetic behavior from puddle-type recriticalities (S/A-scale and annular pools) may be ruled out. Furthermore, the significant portion of the boost regime seems to exist only for a narrow inventory depletion "window." The physical reason for this behavior may be explained in terms of the relative puddle height and peak flux position, an example of which is shown in Figure 11. In order for the boost mode to occur, a certain minimum puddle height appears necessary because: (a) the single-phase region must extend well into the high flux region if it is to be heated and expanded before the inception of disassembly motions in the two-phase region, and (b) the puddle depth must be of adequate size if thermal expansion (which is a fractional effect) is to produce a substantial, reactivity-augmenting, net displacement into the higher worth region. However, it is a consequence of this requirement that the resulting boost is self-limiting because such rapid displacements will quickly extend beyond the peak fuel worth position, thus transforming into a shutdown mechanism.

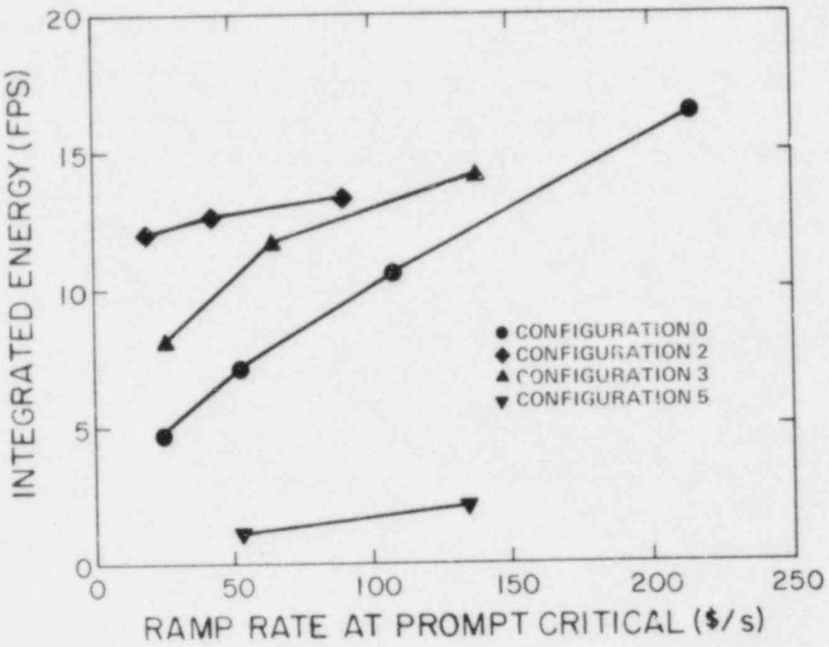

Fig. 15.
Whole-core disassembly energy yields vs. ramp rate and configuration.

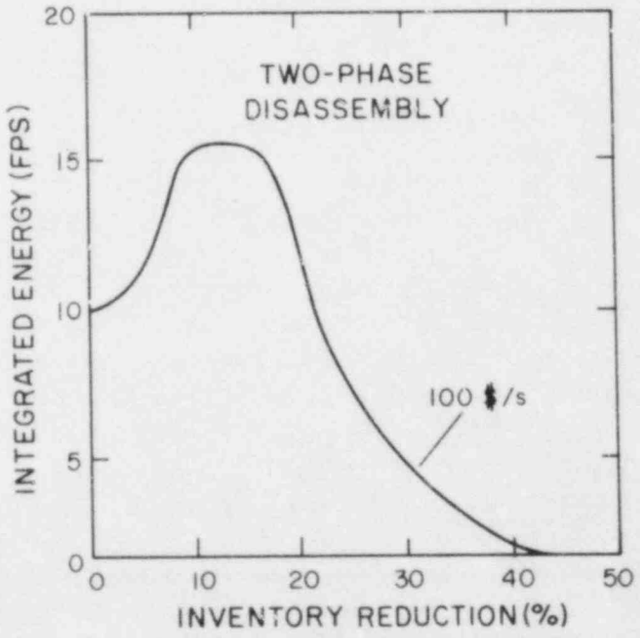

Fig. 16.
Schematic representation of the potential boost regime vs. fuel inventory reduction.

Additional important trends may be discerned from Figure 15. The magnitude of the single-phase boost (taken as the difference in yield from the homogeneous two-phase case, configuration 0, at the same ramp rate) increases with the fraction of the core involved in the recriticality as expected. The saturation in the magnitude of this boost with ramp rate also is expected because the sharp disassembly part of the transient begins at a particular displacement of the puddle (just beyond the flux peak). Once the yield level for this displacement is reached, further yield increases are inhibited. This characteristic indicates that for puddling-type recriticalities an "effectively asymptotic" behavior exists. This is particularly so if the puddling reactivity insertion rates in excess of approximately 80 \$/s are totally unreasonable on physical grounds as discussed below.

As a final step we relate the above concepts and trends to the CRBR core disruption sequence. The goal is to more closely explore the likelihood/severity relationship for energetic recriticalities. That is, for purposes of this discussion we will examine all three stages of the core-disruption sequence, regardless of the likelihood for achieving such states. Thus, the whole treatment here must be viewed in the perspective of the potential for mild termination provided in Sections II.5 and II.6.

5.1. S/A-Scale Pool Recriticalities and Yields

In view of the relatively short time, 1-2 s, required to disrupt the S/A walls (see Section II.5) compared to the period of the gravity-driven power oscillations (approximately 0.4 s), only a small number of recriticalities are possible within the S/A-scale pool stage. As a consequence, the degree of neutronic tuning is limited. The first mode of recriticality would be due to the slumping of the first-to-disrupt high-power channels, that is, configuration 3. The 1-2% inventory loss required to avoid the boost mode translates to approximately a 10% loss on a local basis (configuration 3 represents approximately 20% of the core). This represents a substantial fuel removal and would appear problematical in view of the flow path availability, plugging potential, and timing requirements. Because of the possibility of some steel blockages at the core exit in these lead disruption channels, it would appear that the boost mode would be avoided due to insufficient fuel loss (see Figure 16). Furthermore, the incoherence would still be substantial, and the negative feedback from continuously disrupting lower power channels also would help avoid the boost mode.

At near full inventory, the rainback reassembly rate of 0.82 m/s and a rough differential worth of approximately 1 \$/cm should apply. The resulting 82 \$/s on a whole-core basis implies a reactivity insertion rate of approximately 15 \$/s for this smaller slumping region, that is, an energetically negligible event. However, if substantial fuel removal were postulated, the 1.14 m/s reassembly velocity might be more appropriate. At this limit a

differential worth of approximately 0.5 $/cm would apply resulting in a (local) reactivity insertion rate of approximately 10 $/s. The drainback regime is considered more probable and would yield approximately 7 $/s. Even if the fuel inventory is reduced to within the boost window, significant boosting to threatening levels could not occur under such low initial driving ramp rates.

Subsequent disruptions will gradually lead into configuration 2 and eventually to configuration 5. We have seen already that these two configurations have quite similar neutronic characteristics, that is, a potential boost regime at approximately 10-20% inventory reduction and an approximate differential worth of 1 $/cm. Around the boost regime, a value of approximately 0.8 $/cm would be more appropriate. At higher fuel inventories a still lower value in the range 0.4-0.6 $/cm would apply. For inventory losses greater than 20%, the reactivity worth may be as high as 1.2 $/cm; however this regime yields negligible energetics. Finally, from Figure 14 we deduce an "average" differential fuel reactivity worth of approximately 1 $/cm. This value would be applicable to a system of uniformly distributed voids undergoing a uniform reassembly. Configuration 2 represents recriticalities from only the three inner driver regions, which include roughly one half of the core subassemblies. Hence, the above differential worth values must be modified by a factor of approximately one half when applied to this case.

For configuration 2 the boost regime corresponds to a local loss of approximately 20-40% of the fuel. Considering the results of Section II.6 and associated uncertainties, it is highly doubtful that the boost mode can be avoided at this stage if a strong puddling-type recriticality occurs. We will consider the various possibilities.

For a rainback reassembly rate of 0.82 m/s and fuel inventory in the boost regime (approximately 0.8 $/cm), we estimate that a totally coherent recriticality would yield approximately 38 $/s. Considering the short time available for neutronic tuning, a value of approximately 20 $/s might be more appropriate. At a higher inventory the reactivity worths would be approximately 0.5 $/cm, hence ramp rates in the range of 10 $/s result. For drainback conditions, a velocity of approximately 0.35 m/s would apply, producing, for a totally coherent recriticality, only 18 $/s. All cases represent similarly small recriticalities; and, as may be seen in Figure 15, even with the boost the yield would be well below the vessel head failure limit (~ 16 FPS).

Finally, for configuration 5 the boost regime would be represented by a 10-20% local (same as total for this case) fuel inventory loss. As seen in Section II.6, the additional time margins at this stage of disruption virtually guarantee losses greater than this range; hence the single-phase shutdown, rather than the boost regime, should prevail (negligible energetics). Furthermore, the disruption of the outer walls of the outermost driver S/As

would open new fuel escape paths into the radial blankets so that the energetically significant lifetime of this phase (assuming that it exists) would be short. Even if we ignore these energetics-mitigating reasons and we postulate the inability to remove 20% of the fuel inventory along with coherent reassembly, no large energetic events are envisioned. The results of configuration 2 (previous paragraph) apply except multiplied by a factor of 2X to account for the quantity of fuel involved. Assuming total coherence, values of approximately 76 \$/s, 36 \$/s, and 20 \$/s for rainback, drainback, and high-inventory rainback, result. Taking into account the short time available for tuning (typically a few cycles before walls melt), a reasonable upper limit ramp is judged to be approximately 40 \$/s referred to configuration 0 (see Section II.5). For these kinds of recriticalities a two-phase disassembly would yield insignificant vessel head damage. However, even with a boost we do not see a clear (see Figure 15) challenge to the reactor vessel head structure.

5.2. Annular Pool Recriticalities and Yields

The annular pool also would be short-lived; however, a substantial degree of coherence is expected here. With an average differential worth of approximately 1 \$/cm, reactivity insertions of approximately 35 \$/s and approximately 110 \$/s are estimated for drainback and rainback reassemblies, respectively. As seen in Figure 15 for two-phase disassemblies (also see Figure 14 of Section II.2), such recriticalities do not approach the vessel head capability. Due to significant radial power profiles and pressure relief zones (voided internal blankets and radial blankets), the one-dimensional boost mode discussed previously does not apply here.

5.3. Whole-Core Pool Recriticalities and Yields

The upper limit differential worths of approximately 5 ¢/kg for radial pool in-sloshes developed in Section 4 can be combined with the estimated reassembly rates of 2500 kg/s and 6200 kg/s for the neutronic and pressurization sloshes, respectively (Section 3.3) to yield ramps of approximately 125 \$/s and 310 \$/s. Compared to the recriticalities examined previously, these represent relatively high ramp rates. However, the original SIMMER-II calculations that lead to this particular concern [10] did not take into account single-phase liquid expansion. This deficiency was corrected in the present investigations.

The inclusion of the single-phase effects reflect a combination of boost and rapid shutdown as in the puddling-type reassemblies. However, here again, the boost regime seems to be associated with a narrow range of unique circumstances, and the shutdown regime prevails more universally. The two

idealized cases examined yielded the equivalent (based on driver fuel only) of approximately 10 FPS (for the 125 $/s case) and approximately 5 FPS (for the 310 $/s case). Thus, the neutronic slosh gives rise to a yield equivalent of a classical two-phase disassembly, while the pressurization slosh produces negligible energetics. If plotted on Figure 15 it would lie on the extension of the similarly benign configuration-5 curve. The pressurization slosh suppressed nearly all boiling and yielded an essentially single-phase reassembly. It is such single-phase behavior that leads to very high ramp rates; however, it is also responsible for early neutronic shutdown. Additional results on these two calculations may be found in Appendix C.

From these results it appears that the highly visible "whole-core pool concerns" of the past 2 to 3 years have been reduced and their yields are not beyond accommodation. In addition, the extraordinary circumstances assumed in the two calculations that lead to this conclusion need to be mentioned: (a) pressurization events at the boundary due to fuel/coolant interactions are speculative and (b) pool homogenization as assumed in these calculations requires time to develop (as shown in Section II.5); hence additional margins exist for fuel removal beyond the time of disruption of the internal blankets making the existence of this state very questionable.

6. Another View of Severe Recriticality Amplification

The boost mode of disassembly was discovered during the course of this work as a consequence of including the single-phase (liquid) equation of state in SIMMER-II. The aim of these studies was to explore the amplification potential of recriticalities along the lines of our Question #6 to the Applicant (see Table 2 of Section II.1). By the time our investigations into the single-phase boost phenomena were complete we were ready, based upon the understanding developed from this work, to re-evaluate our approach concerning amplification. The results of this reevaluation are presented in this section.

The reevaluation indicates that results presented in the previous section for amplification by axial motions (S/A-scale pools and annular pools) are extremely conservative. In our opinion the development presented in this section adequately addresses the problem of S/A-scale and annular-pool recriticality energetics. The presentation in the previous sections is intended as an introductory exercise; however, there may be readers who will interpret those previous results as complementary to the one given here.

As discussed above, the whole subject of energetic recriticalities arises from the unstable character of both a subcritical and a critical (and a supercritical) disrupting core. The concern is that power oscillations could amplify into the highly energetic regime. Indeed, the results of the previous two

sections showed that such amplification would not imply the violation of physical reality as far as the nature of the forces and phenomena involved are concerned. Yet these results, particularly those that exhibit the boost phenomenon, are the artifact of very specialized initial conditions. These initial conditions (configurations 0, 2, 3, and 5) are not only highly idealized, but they are generally inappropriate for the neutronically active situations which have the highest likelihood.

The key idea is that under a power perturbation the system will separate at the peak flux position (mass centroid). In a core-wide, one-dimensional sense such an event will separate the fuel mass into two equal parts. The lower portion already being in a state of rest will remain at rest until and unless boilup or venting occurs. The upper portion as we saw in Sections 3.1 and 3.2, will distribute itself more or less over the available space and will reassemble. Due to the increased overall separation between the two fuel masses, criticality will occur only after some puddling of the dispersed upper fuel mass has taken place thereby adding to the lower puddle that already exists. But this is precisely the condition for the peak power (flux) location to move toward and even within the puddle, thus narrowing strongly the boost regime. If a small fraction of the core puddles, the power peak may be at a higher position (controlled by the rest of the core) making a limited boost possible (with a small puddling ramp rate, however). If a large fraction of the upper half of the core puddles coherently, then the flux peak would move into the puddle as criticality is approached and results similar to those for configuration 5 would apply. If boilup occurs in the lower puddle because of pressure reduction in the upper S/As, the puddling ramp would be reduced thereby making the boost impotent.

The above reasoning cannot be applied to the whole-core pool because its two-dimensional character can allow axial-to-radial slosh conversion. However, as we have seen, other limitations apply in that case.

7. Summary

Even for postulated severe rates of reassembly, S/A-scale pools and annular pool recriticalities will show no severe amplification and should be considered energetically benign. The basis for this conclusion is that under conditions physically consistent with power perturbations (neutronically driven material motions), recriticality shutdown generally would be enhanced by the single-phase effect. A single-phase boost phenomenon with significant potential for energetic behavior is physically possible; however, such events can occur only under very specialized initial conditions. The homogeneous whole-core pool yields are the most important from the standpoint of potentially damaging energetics. Several recriticality events were considered with varying degrees of extraordinarily contrived conditions. In no case, however, was the structural boundary of the primary system significantly threatened.

8. References

1. S. K. Rhow, D. M. Switick, J. L. McElroy, and B. W. Joe, "An Assessment of HCDA Energetics in the CRBR Heterogeneous Reactor Core," General Electric Company report CRBRP-GEFR-00523 (December 1981).

2. Compendium to NUREG/CR-3224, "An Assessment of CRBR Core Disruptive Accident Energetics," Section 6, Nuclear Regulatory Commission document (March 1983).

3. Compendium to NUREG/CR-3224, "An Assessment of CRBR Core Disruptive Accident Energetics," Section 5, Nuclear Regulatory Commission document (March 1983).

4. Compendium to NUREG/CR-3224, "An Assessment of CRBR Core Disruptive Accident Energetics," Section 7, Nuclear Regulatory Commission document (March 1983).

5. J. F. Jackson and R. E. Nicholson, "VENUS-II: An LMFBR Disassembly Program," Argonne National Laboratory report ANL-7951 (1972).

6. W. R. Stratton, L. B. Engle, and D. M. Peterson, "Energy Release from Meltdown Accidents," ANS Transactions 17, 362 (1973).

7. W. R. Stratton, Los Alamos National Laboratory letter to T. G. Theofanous, Purdue University, "PAD Code Results for CRBR Disassemblies" (October 27, 1976), (available at Purdue University).

8.[a] F. J. Moody, "Prediction of Fluid Free Surface Motions Under the Influence of Body Force Acceleration and External Pressures," General Electric Company report NEDO-10212 (November 1970).

9. G. Wallis, One Dimensional Two Phase Flow (McGraw Hill 1969).

10. W. R. Bohl, "Some Recriticality Studies with SIMMER-II," Proceedings of the Fast Reactor Safety Meeting, Seattle, Washington, August 19-23, 1979.

11. Michael G. Stevenson, "Nuclear Reactor Safety Quarterly Progress Report April 1-June 30, 1982," NUREG/CR-2814, LA-9556-PR (November 1982).

[a] Address requests for this document to: F. X. Gavigan, Director, Office of Breeder Demonstration Projects (NE-50), U.S. Department of Energy, Washington, DC 20545, Telephone (301) 353-3134.

APPENDIX A
NEUTRONIC SHUTDOWN MECHANISMS

1. Introduction

In this Appendix we explore in detail the range of fluid dynamic/ thermodynamic phenomena that generate the necessary fluid motions for neutronic shutdown. A series of simple, one-dimensional calculations were performed for high heating rates (typical of high ramp rate, prompt critical excursions) and for a range of initial void fractions from zero to 40 percent. The model used is discussed along with the analysis approach. The results of the series of calculations are given with two particular cases discussed in sufficient detail to indicate clearly the operative phenomena.

2. Calculational Model and Analysis Approach

The calculations were performed in one dimension to provide maximum visibility to the operative mechanisms and to permit a simple figure-of-merit for neutronic shutdown to be applied for case-to-case comparisons. The model used for the SIMMER-II [1] calculations is shown in Figure 1. A single S/A is represented with one radial node and 39 equal axial nodes. The boundaries are assumed open and at a pressure of 0.1 MPa. The material represented was that normally present in the core (fuel, cladding, wire wrap, and S/A wall) but at an initial state of 3100 K for the all-liquid mixture. This mixture had the volume fraction ratio of 0.377:0.314:0.309 for fuel:steel:void. The corresponding smear densities were 3290 kg/m^3 and 1860 kg/m^3 for fuel and steel, respectively. As the void changed in the following calculations to simulate compaction of the core, the fuel:steel ratio was held constant.

A power distribution from channel 7 of the EOC-4, SAS3D analysis (Section II.3) was used, along with consistent fuel and steel specific reactivity (Δ k/kg) worth distributions. These distributions were slightly skewed toward the bottom of the S/A because of the control rod induced flux depression in the upper core. A simple integration of the change in reactivity was performed over the S/A as the materials moved. When a total reactivity change of -1.0¢ (based on the nominal densities above) was observed, we pronounced neutronic shutdown. This is equivalent to a change of approximately -1.6$ for the whole-core and is sufficient to decrease the reactivity to below critical.

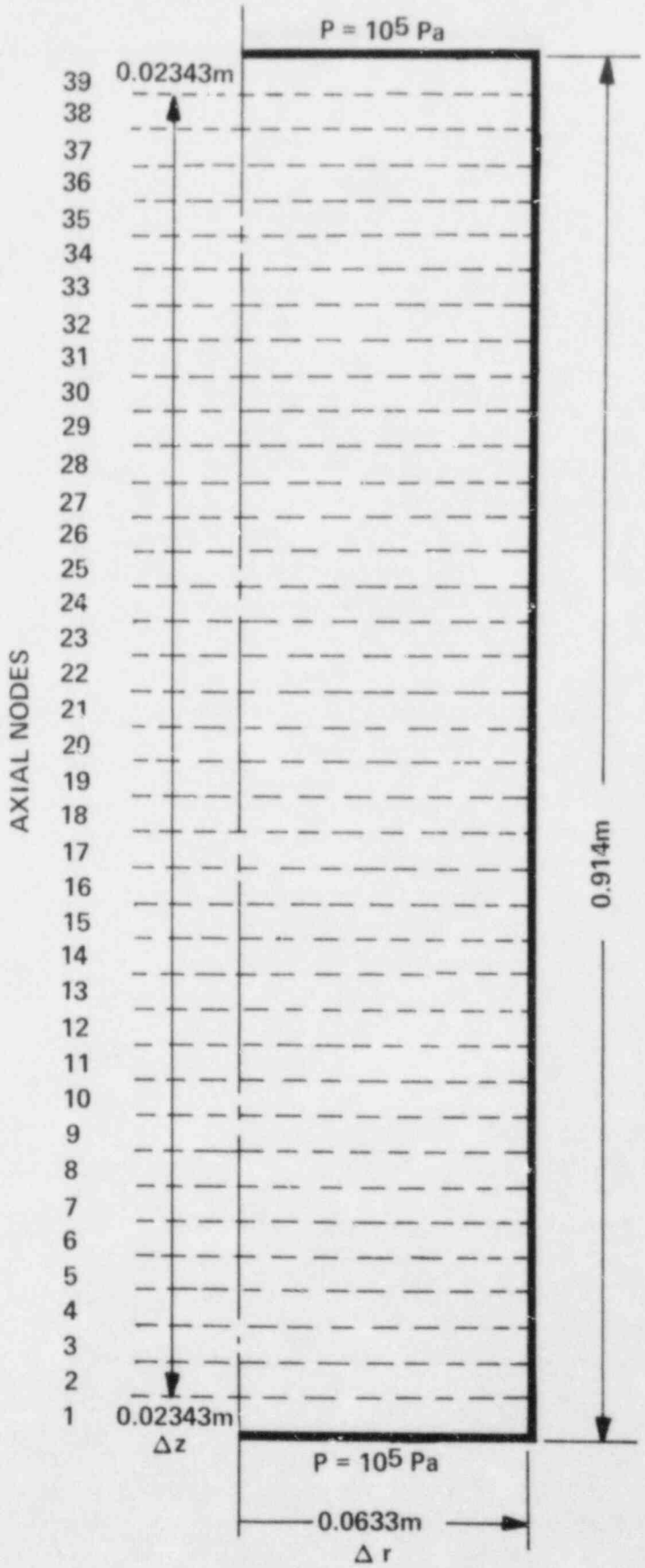

Fig. 1.
SIMMER-II model for 1-D disassembly analysis.

The energy yields for the various cases was very simply obtained because of the manner in which the analyses were performed. The power was not calculated from the point-kinetics equations normally applied in disassembly analyses. This coupled procedure would produce highly transient power histories thereby, adding to the difficulty of discerning the operable fluid dynamics during neutronic shutdown. Therefore, we chose to apply constant powers of different magnitudes that are representative of severe disassembly events. Then by obtaining the time to shutdown as defined by the required reactivity change of 1.0¢, the yield became the power times this shutdown time. In the following section we use power in terms of multiples of nominal full power and excursion energy yield in terms of full-power-seconds (FPS).

3. Analysis Results

Our objective in this series of calculations was to determine clearly the influence of initial void on the disassembly energy yields for different excursion severities that were varied through the power level applied. For a calibration against whole-core disassemblies driven by specific ramp rates, we turn to Section II.2, where 100 $/s and 200 $/s produced peak powers of 10000 and 27000 times nominal, respectively. Therefore, we chose a power range of 10000 to 30000 for this investigation. We chose a void range from 0 to 0.4, which spans the situations of interest in the LOFA sequence.

The matrix of cases analyzed is shown in Table 1 and the energy yields are tabulated in Table 2. It is clear that a wide range of yields are calculated as the initial void varies. This trend can be visualized better on Figure 2 of Section II.7. A saturation effect occured at a void of about 0.2 for the range of power levels, indicating a yield-mitigating effect for initial voids below 0.2. If we relate this to the fuel volume fraction, we find this void threshold at a volume fraction ratio of 0.45:0.2 (fuel:void) or approximately 2:1. In a fuel rich region, mitigation would occur up to about 30% void.

We proceed now to consider the phenomena that led to the trends calculated. We will do this by following the progression of the transient in detail for cases 31b and 33b (these represent conditions on each side of the threshold). An overall perspective for case 31b is obtained by observing the evolution of several key output variables such as material worth, fuel temperature, mid-plane pressure, and mid-plane void fraction shown in Figures 2 through 5 respectively. The time interval for shutdown activity is from 0.4 to 0.6 ms from Figure 2. The key to the rapid shutdown (fuel axial motion) can be seen on Figures 4 and 5. The single-phase condition was reached at about 0.3 ms, at which time the temperature was only about 4700 K. For the equation of state [2] used in this analysis, the liquid fuel density change was about 20% (see Figure 6). With an initial fuel volume

TABLE 1
MATRIX OF CASES FOR THE
1-D DISASSEMBLY INVESTIGATION
(Case numbers)

Void	0	0.1	0.2	0.3	0.4
Power					
10000	30a	31a	32a	33a	34a
20000	30b	31b	32b	33b	34b
30000	30c	31c	32c	33c	34c

TABLE 2
ENERGY YIELDS FOR THE 1-D DISASSEMBLY
INVESTIGATION (FPS)

Void	0	0.1	0.2	0.3	0.4
Power					
10000	2.4	8.7	12.2	13.0	13.0
20000	4.0	10.4	14.6	16.4	16.5
30000	5.1	11.5	16.8	18.6	19.5

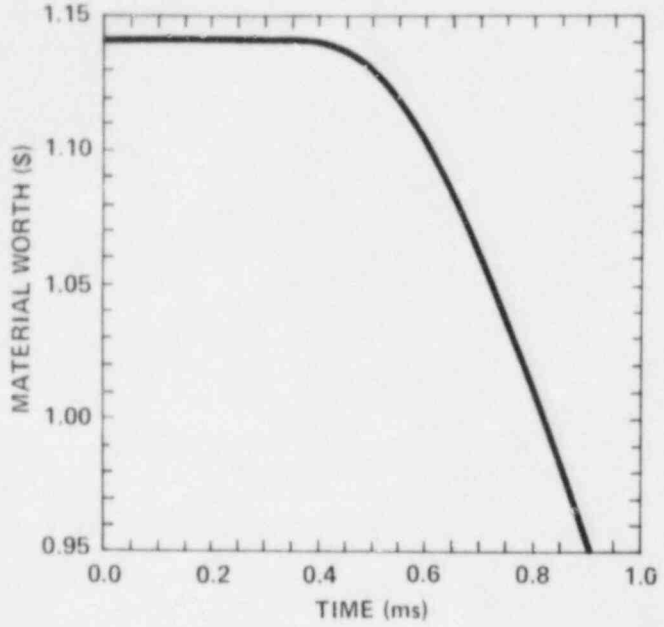

Fig. 2.
Material worth transient for case 31b.

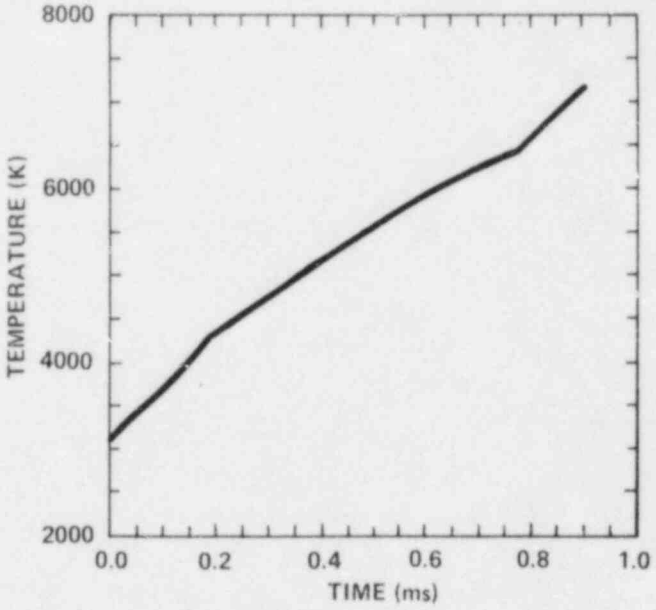

Fig. 3.
Fuel temperature transient for case 31b.

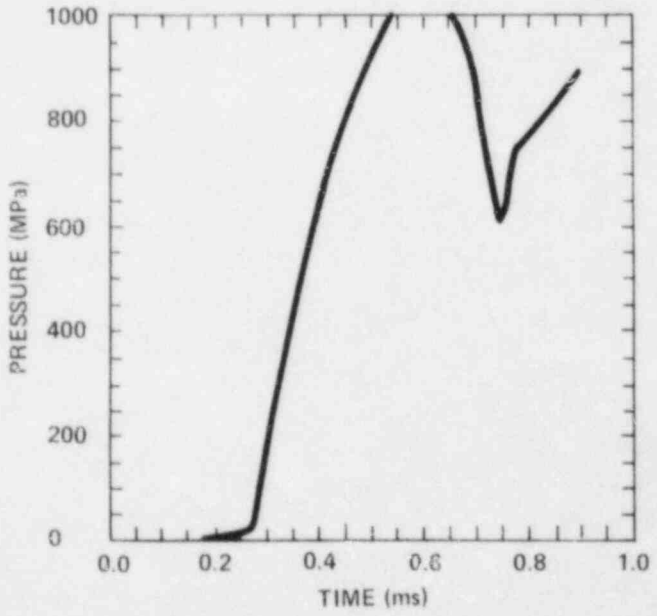

Fig. 4.
Midplane pressure transient for case 31b.

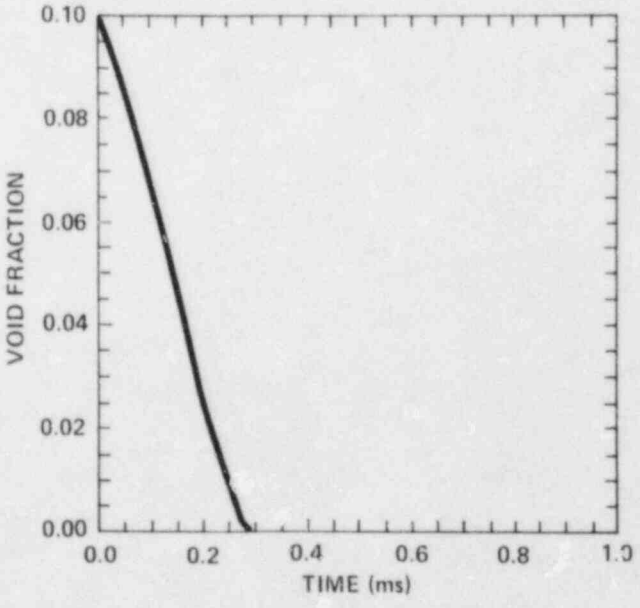

Fig. 5.
Midplain void fraction transient for case 31b.

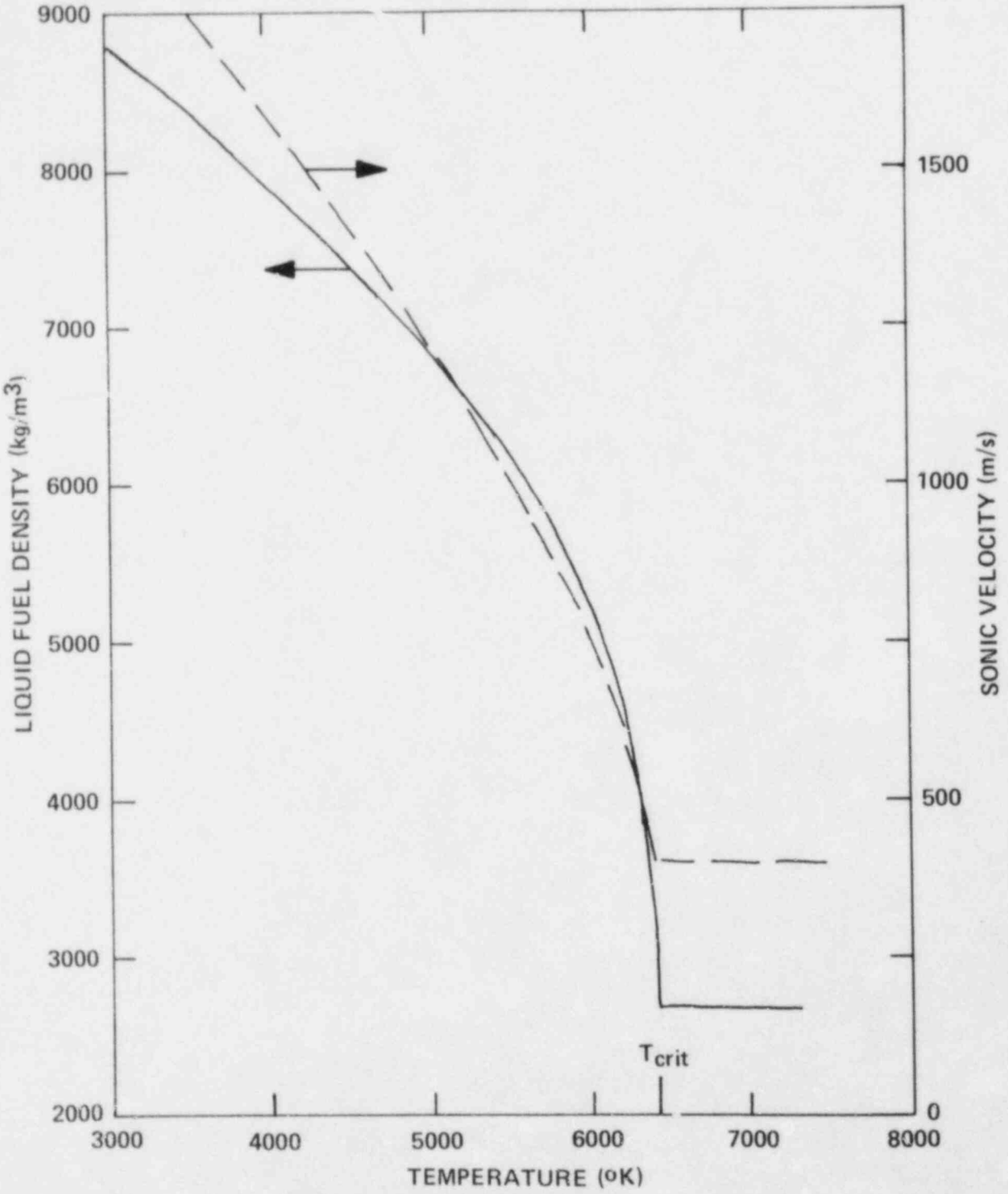

Fig. 6.
Dependence of liquid fuel density and sonic velocity on temperature.

fraction of about 50% for this case, we should see a void change of 0.2 x 0.5 or 10% and we do in Figure 5. At 4700 K the sonic velocity of the fuel remained high, approximately 1300 m/s, and should have caused large pressure increases as the liquid continued to expand with further heating. The pressure response is shown in Figure 4 (the flat top is a built-in limit of the plotting routine) and it is indeed high (greater than 1000 MPa). The pressure reduction at 0.7 ms resulted from the decompression waves returning from the open boundaries. The neutronic shutdown was achieved before this occured thereby making the results independent of this decompression process. Thus, we see the manifestations of the classical single-phase liquid disassembly.

The progression of the disassembly process in time and space is shown in Figures 7 through 11. The nonsymmetry in all of these plots is the result of the skewed axial power profile mentioned previously. The temperature distribution is shown in Figure 7. It simply elevated with time because the liquid specific heat changes only slightly with temperature over this range. Shutdown was completed at about 0.5 ms with a peak temperature of about 5500 K. At the midplane location (0.46 on the horizontal axis), the sonic velocity decreased to about 900 m/s at this shutdown temperature. The axial progression of the single-phase region is seen in Figure 8. The entire S/A is single phase at the time of shutdown. The pressure propagation is shown in Figure 9. The rarefaction wave can be seen moving inward from the lower boundary in Figures 9b through 9d. Its speed is about 1000 m/s as it should be. The velocities induced in the materials are shown in Figure 10. Velocities of about 50 m/s were generated rapidly. The local density changes are seen in Figure 11. The initial uniform density was 4470 kg/m^3. We can see the material being displaced from the central region to the ends and even out of the lower boundary.

A very different situation results for case 33b. We can see the key differences by comparing the time histories for material worth, fuel temperature, midplane pressure, and midplane void fraction for this case (Figures 12 through 15, respectively) with corresponding ones for case 31b (Figures 2 through 5). The reduction in reactivity occurred much later (approximately 0.8 ms compared to 0.5 ms for case 31b), thereby allowing 6 FPS (an additional temperature rise of approximately 1000 K) of additional energy to be added to the material. As seen in Figure 13, the critical temperature of 6400 K is reached. The change in slope before 0.8 ms results from the increased heat capacity of the liquid fuel as the critical point is approached. The initial void at the midplane was not closed by the expanding liquid until 0.65 ms as compared to about 0.25 ms for case 31b. Furthermore, the establishment of the single-phase state did not generate pressures that are nearly as high (see Figure 14). This resulted from the reduced sonic velocity (increased compressibility) in the critical point regime. Typical values are 400 m/s for sonic velocity or a factor of about 2-2.5 below that for case 31b. Thus, the compressibility is 4-6 times greater. For this

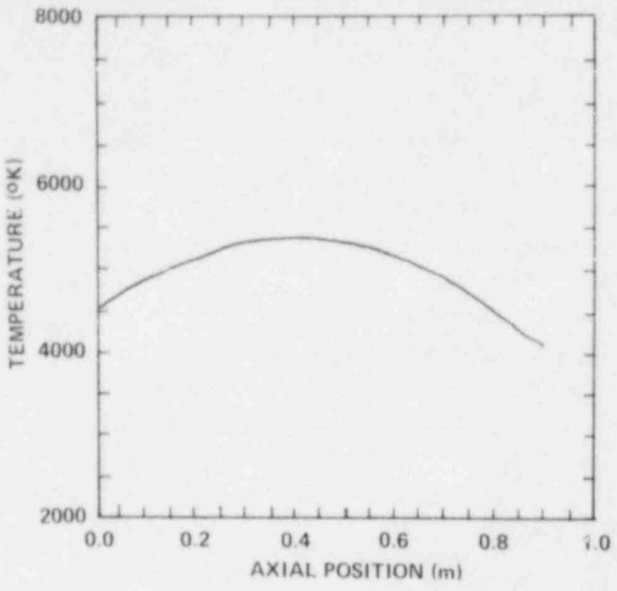

(a) Time = 0.45 s.

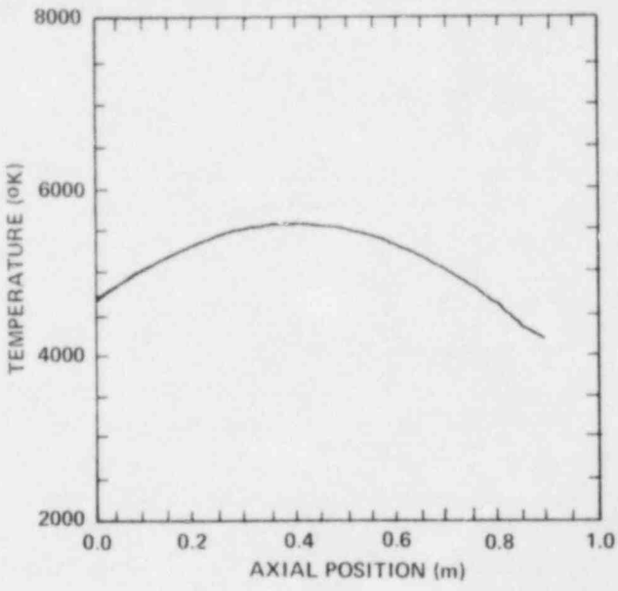

(b) Time = 0.50 s.

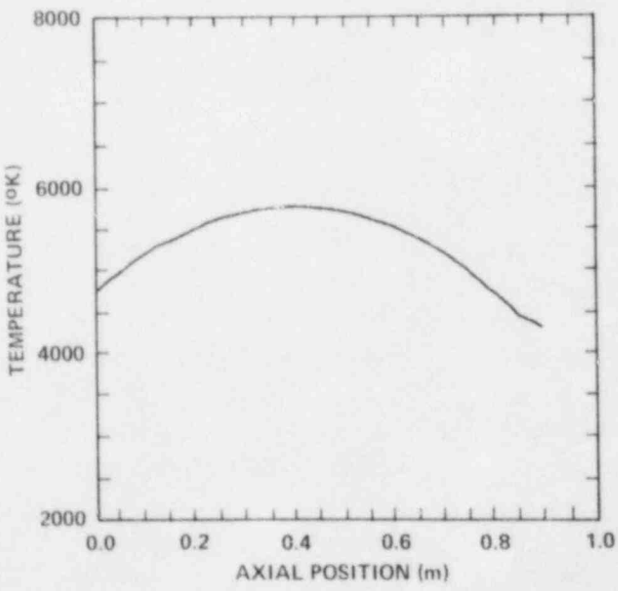

(c) Time = 0.55s

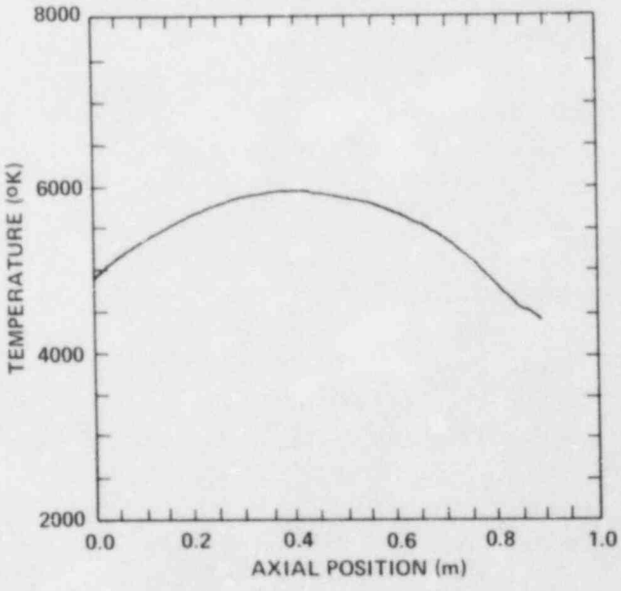

(d) Time = 0.60 s.

Fig. 7.
Fuel temperature distribution vs. time for case 31b.

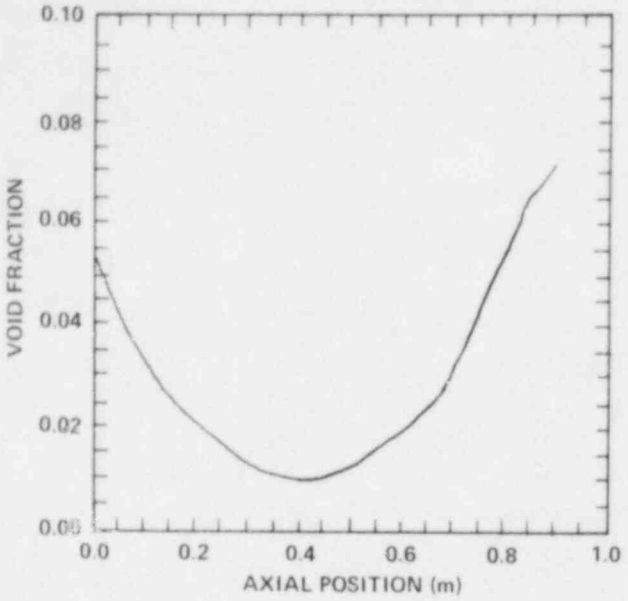

(a) Time = 0.25 s.

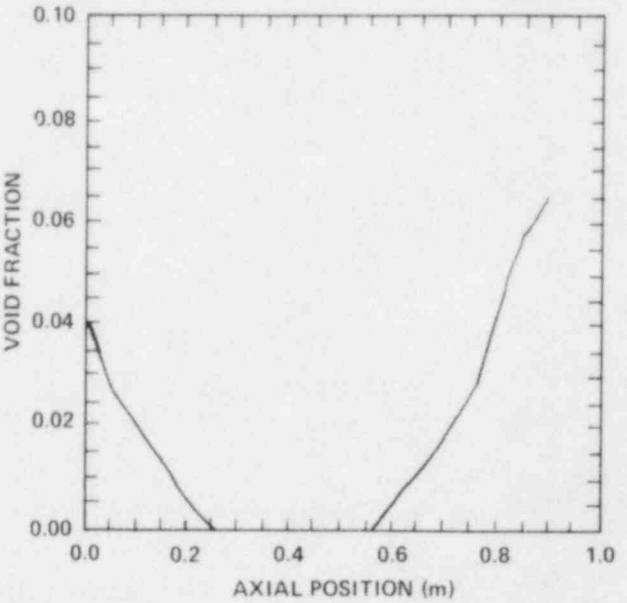

(b) Time = 0.30 s.

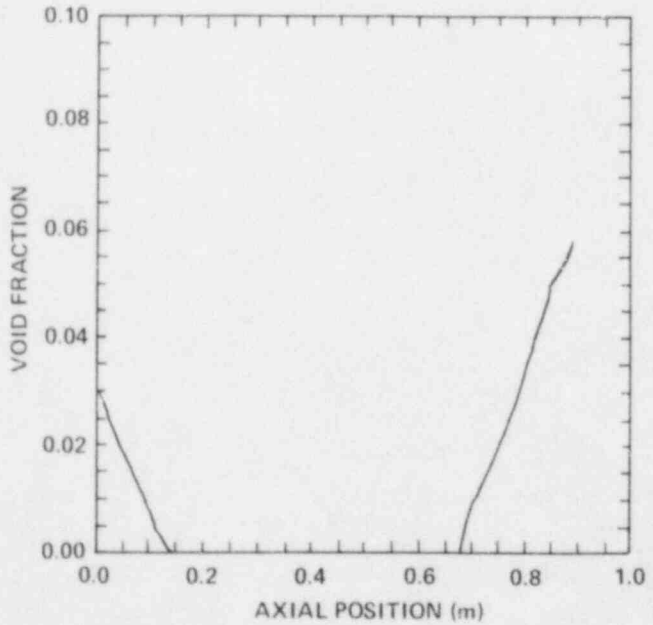

(c) Time = 0.35 s.

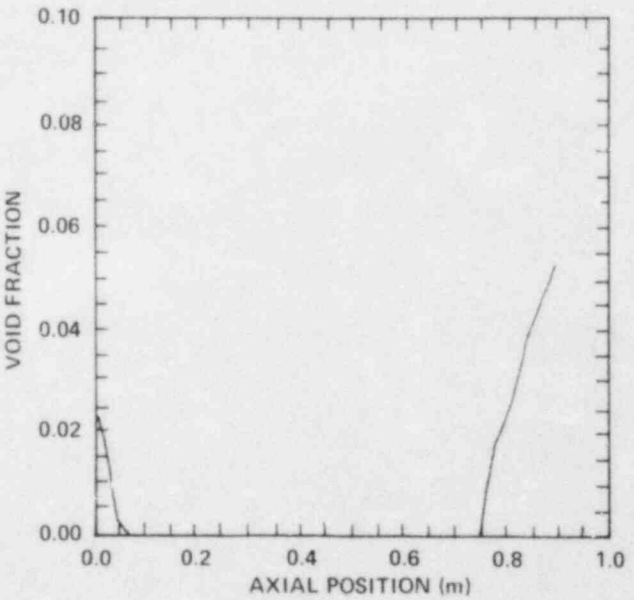

(d) Time = 0.40 s.

Fig. 8.
Void fraction distribution vs. time for case 31b.

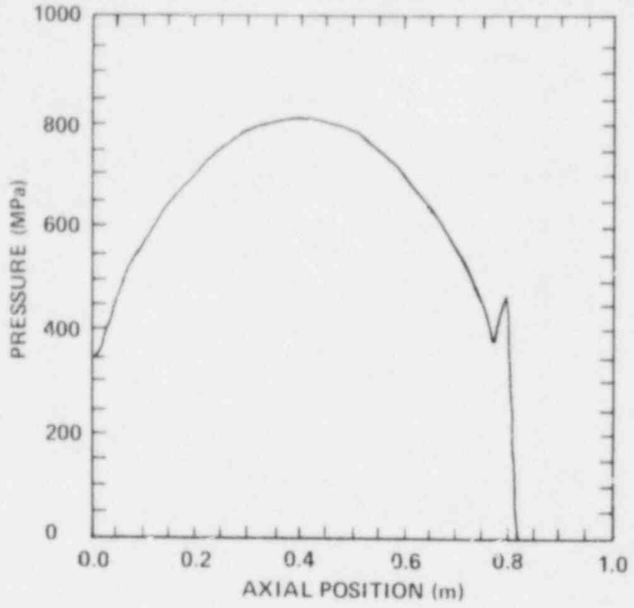

(a) Time = 0.45 s.

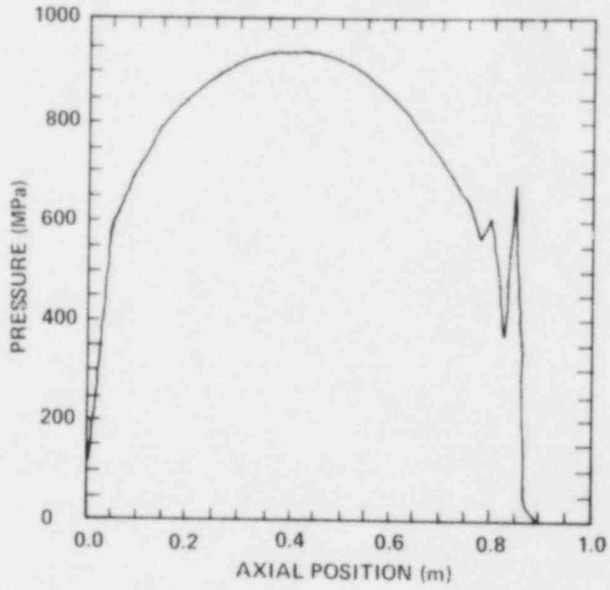

(b) Time = 0.50 s.

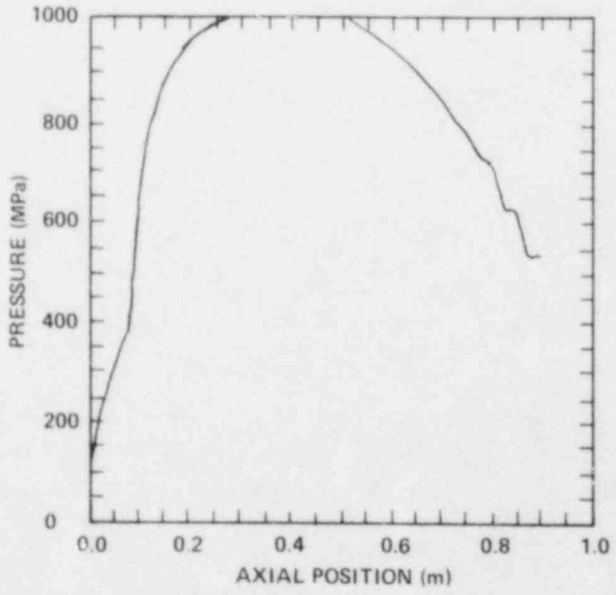

(c) Time = 0.55 s.

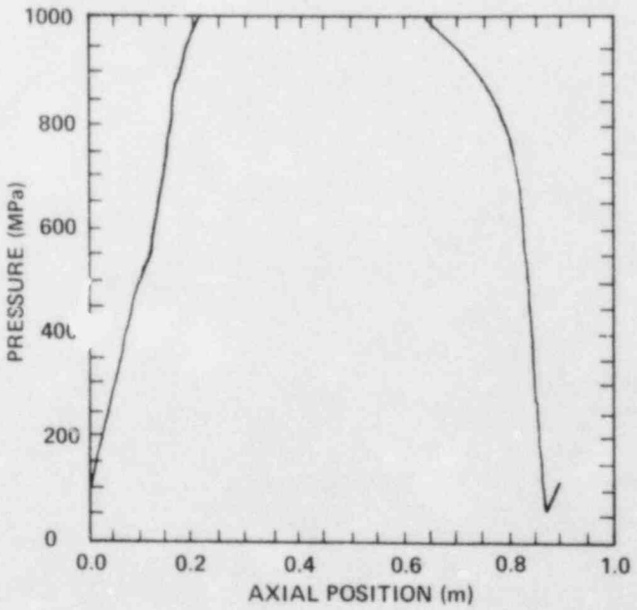

(d) Time = 0.60 s.

Fig. 9.
Pressure distribution vs. time for case 31b.

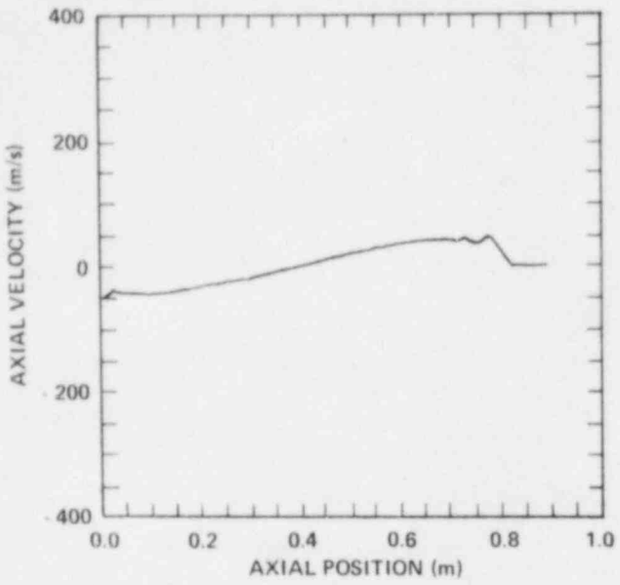

(a) Time = 0.45 s.

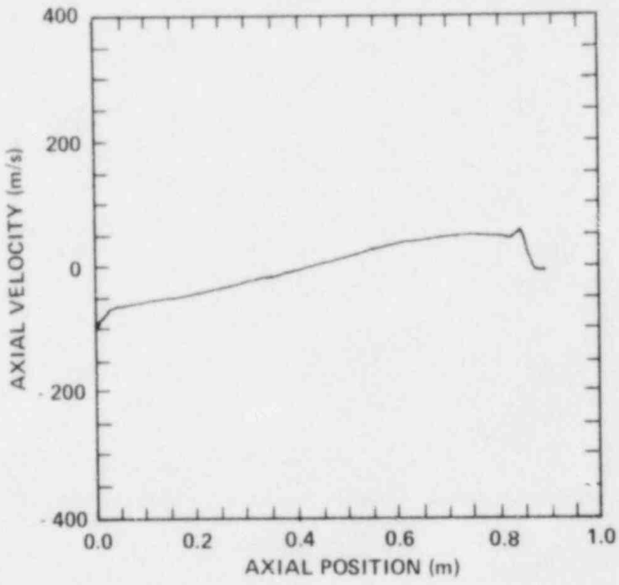

(b) Time = 0.50 s.

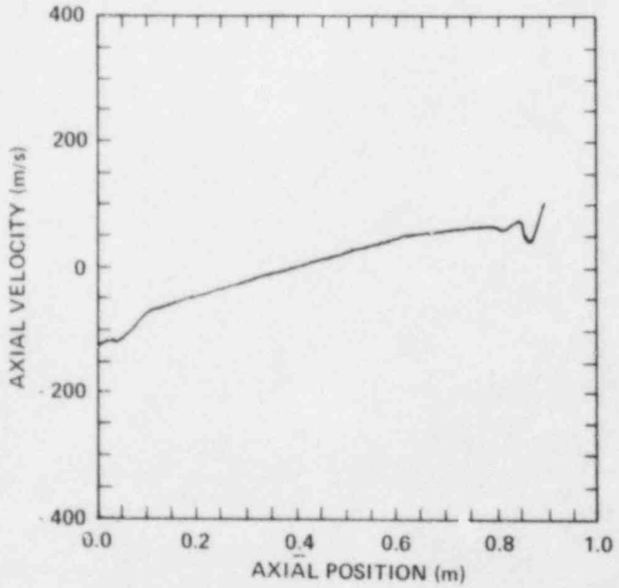

(c) Time = 0.55 s.

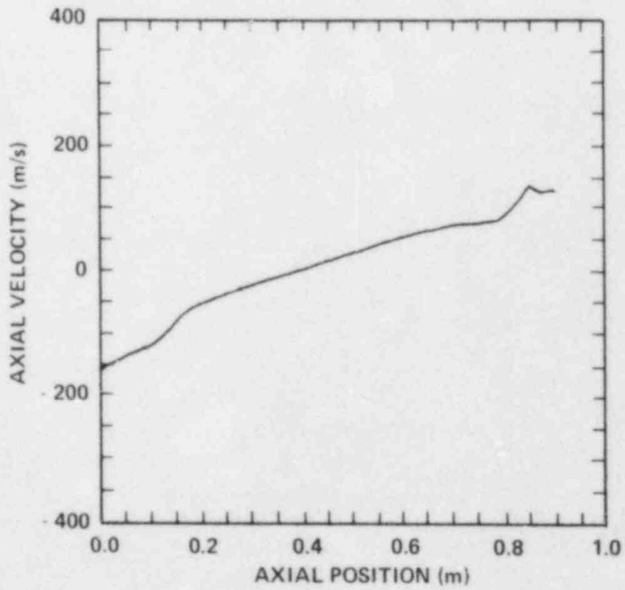

(d) Time = 0.60 s.

Fig. 10.
Axial velocity distribution vs time for case 31b.

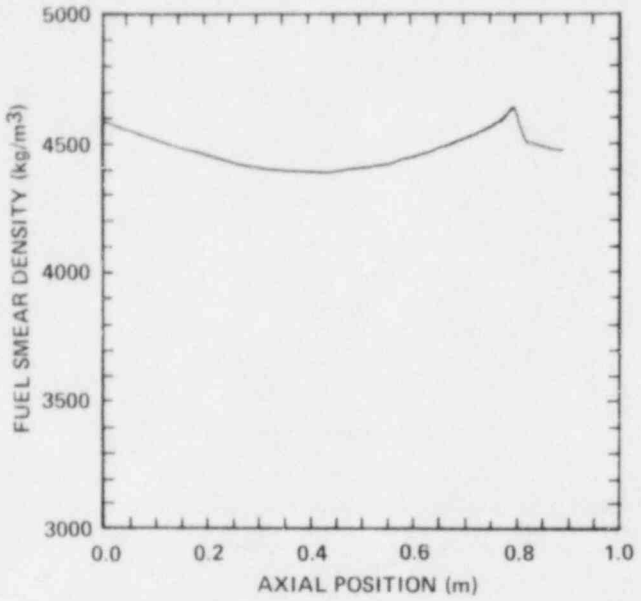

(a) Time = 0.45 s.

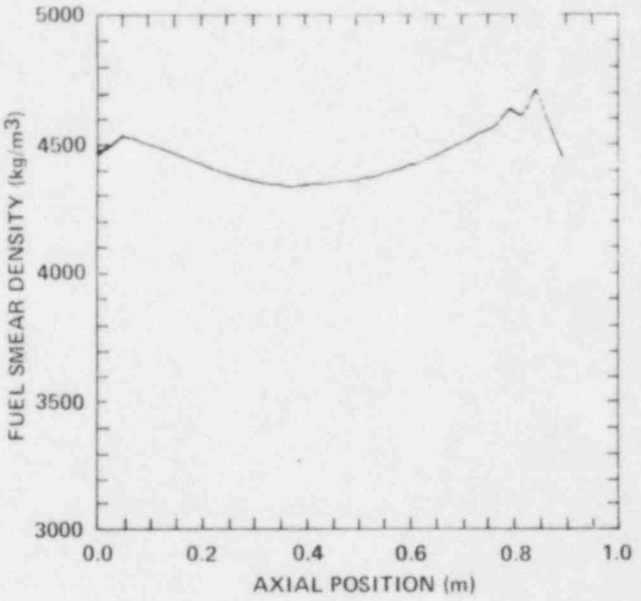

(b) Time = 0.50 s.

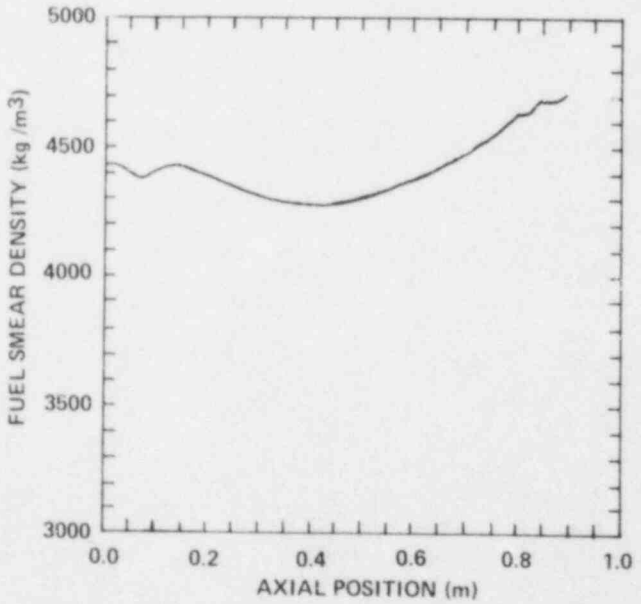

(c) Time = 0.55 s.

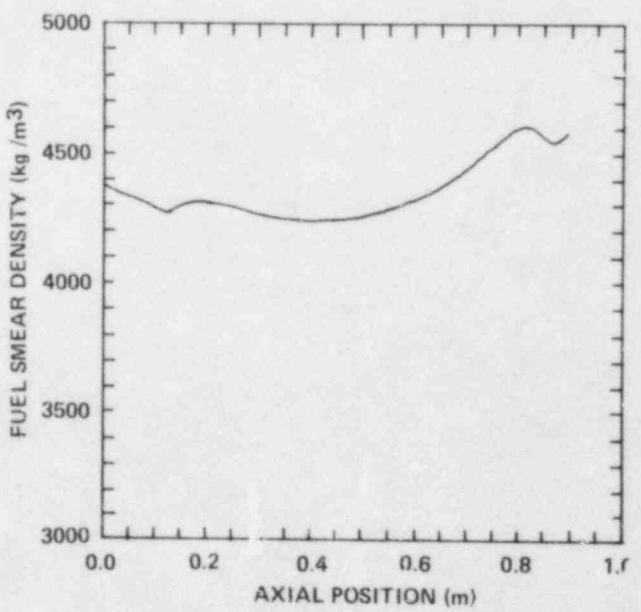

(d) Time = 0.60 s.

Fig. 11.
Fuel smear density distribution vs. time for case 31b.

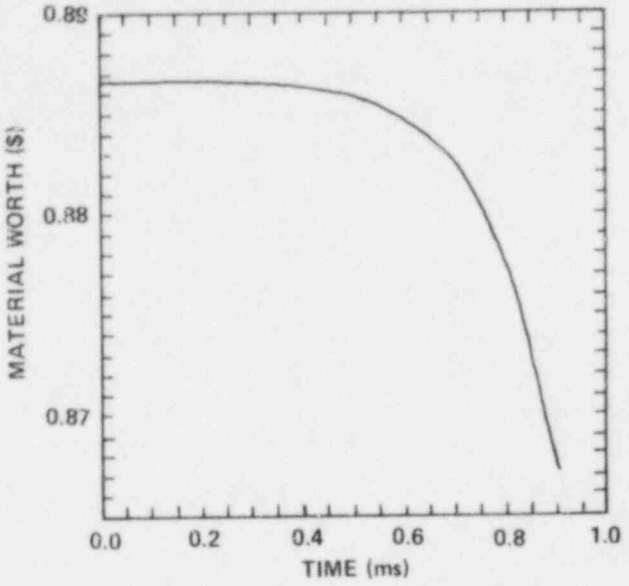

Fig. 12.
Material worth transient for case 33b.

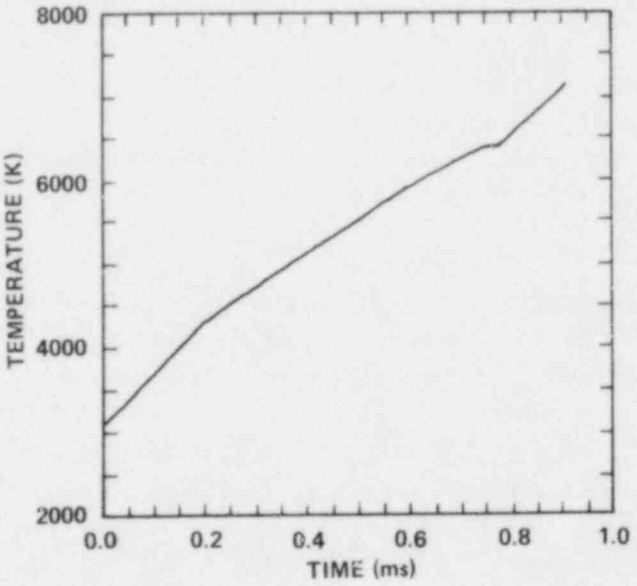

Fig. 13.
Fuel temperature transient for case 33b.

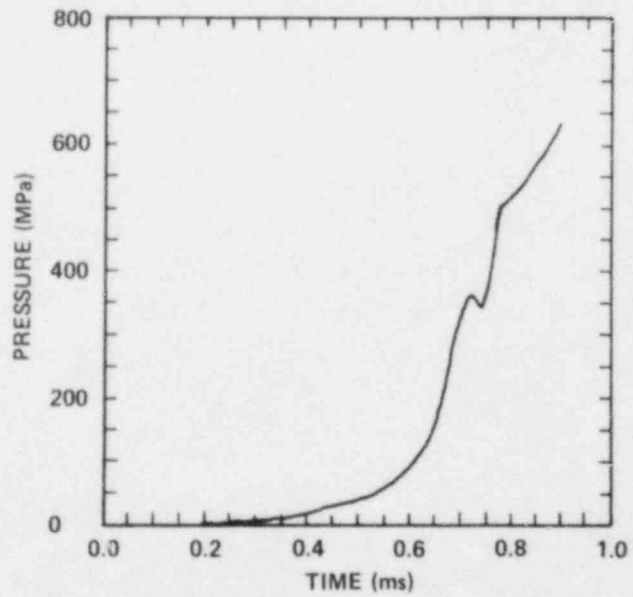

Fig. 14.
Midplane pressure transient for case 33b.

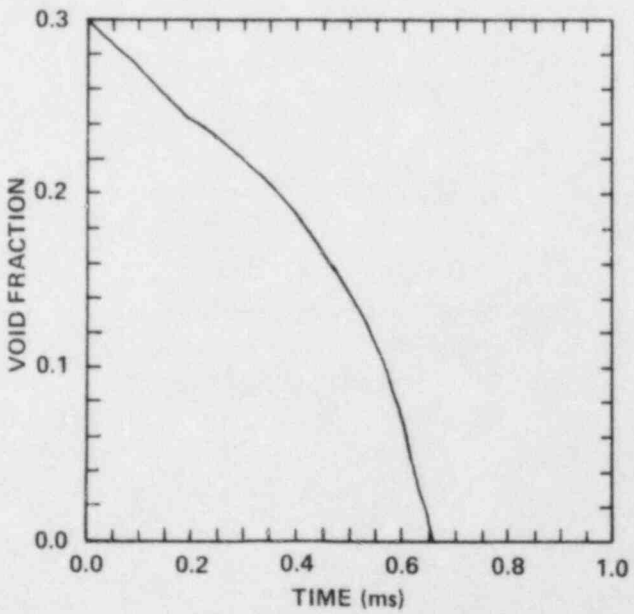

Fig. 15.
Midplane void fraction transient for case 33b.

case the initial fuel volume fraction was about 0.4. Therefore, the fuel had to expand by 75% to fill the void corresponding to a density of about 5000 kg/m^3. From Figure 6 we can see that this does not occur until the critical point is approached.

The progression of the disassembly in space and time provides additional insight into the mechanics of disassembly for this case. The temperature distributions, Figure 16, are similar to case 31b except they proceed to a higher level. The progression of void closure shown on Figure 17 is delayed as expected because of the higher initial value. Also, it is important to note that at the time of shutdown the single-phase region had not progressed to the ends of the S/A. This means that the shutdown fluid dynamics was not dominated by the acoustic characteristics of the single-phase region over the entire S/A as in case 31b with the associated generation of large boundary discharges. In this high-void case, the fuel moved locally from the midplane region to the end regions where local void or accommodation space remained. This is seen in Figures 18 through 20 in which the evolution of the distributions of pressure, velocity, and fuel smear density are shown. The large pressure gradients are only at the edges of the single-phase regime. They could not effectively propagate into the two-phase regime.

For still larger initial voids (such as 40%), the behavior was very similar because the additional energy required to close one third more void was small (see Figure 6). Indeed, this is in agreement with the results in Table 2. This void-to-fuel ratio is about as high as can exist in the core and still produce criticality. Therefore, we need not investigate higher void situations.

4. Summary

These results show that single-phase behavior is to be expected in all realistic disassembly events that are sufficiently severe to be a threat to the vessel head structure (as defined in Section II.2). However, the mitigating effect is substantial only for fuel-to-void volume fraction ratios greater than 2:1 or for typical void fractions of less than 20% for the nominal mixture of fuel and steel.

5. References

1. L. L. Smith, "SIMMER-II: A Computer Program for LMFBR Disrupted Core Analysis," Los Alamos National Laboratory report NUREG/CR-0453, LA-7515-M (June 1980).

2. "SESAME'83: Report on the Los Alamos Equation-of-State Library," Los Alamos National Laboratory report LALP-83-4 (February 1983).

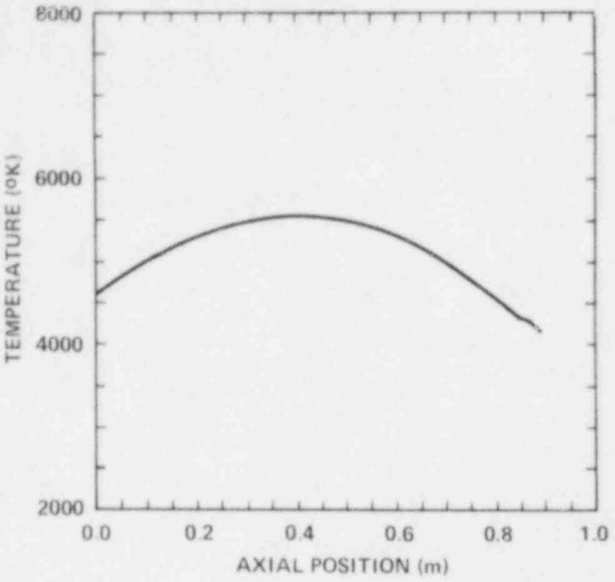

(a) Time = 0.50 s.

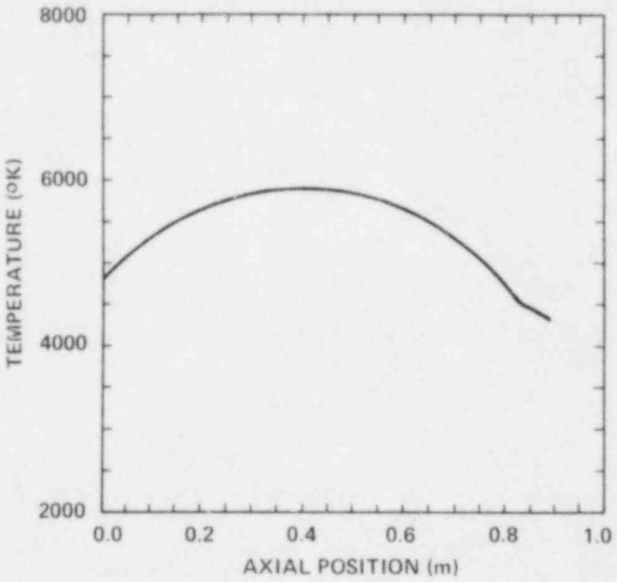

(b) Time = 0.60 s.

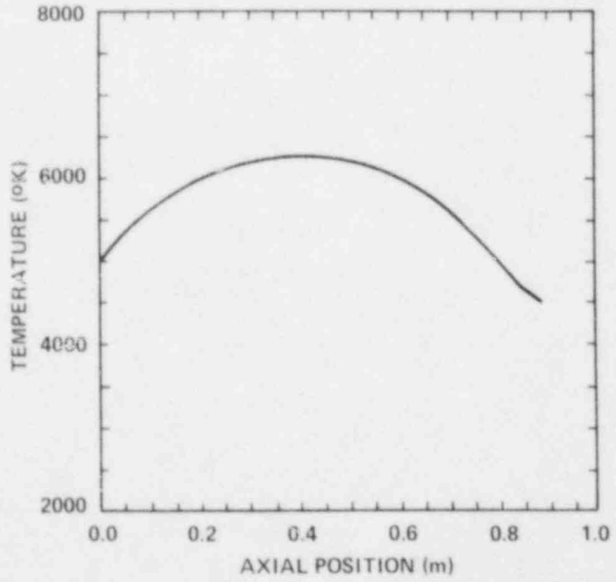

(c) Time = 0.70 s.

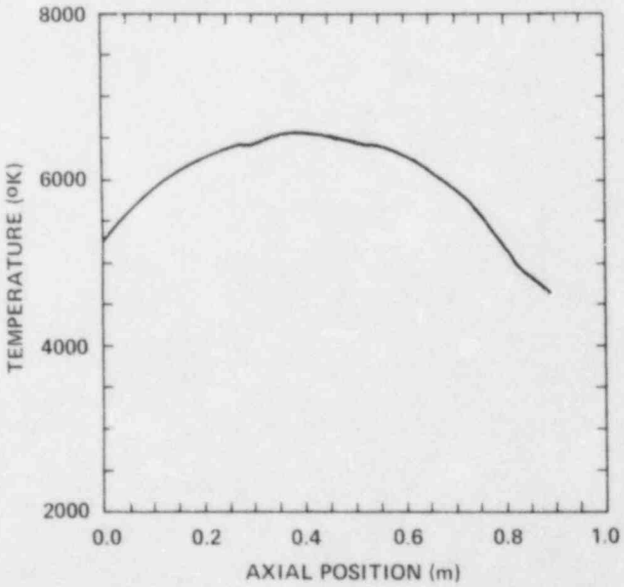

(d) Time = 0.80s.

Fig. 16.
Fuel temperature distribution vs. time for case 33b.

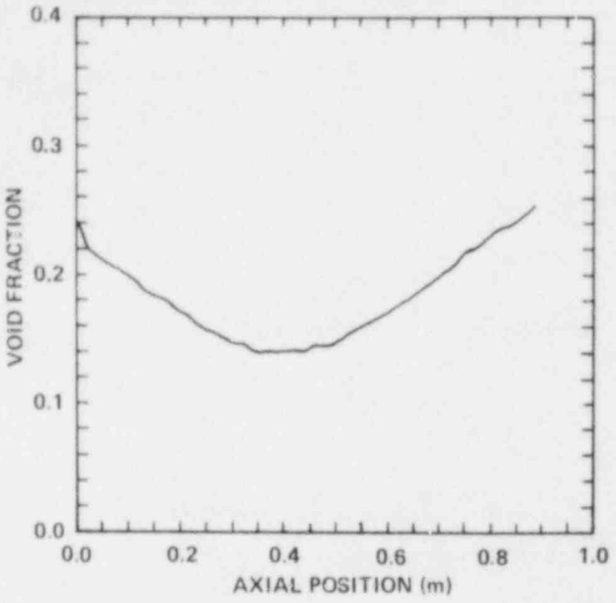

(a) Time = 0.50 s.

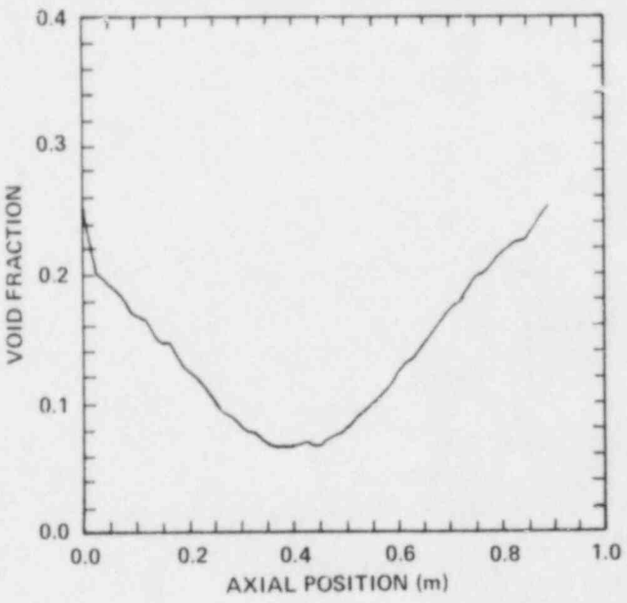

(b) Time = 0.60 s.

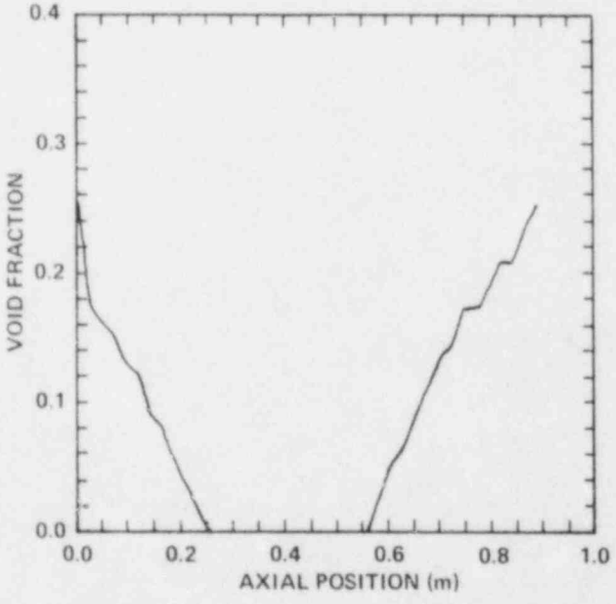

(c) Time = 0.70 s.

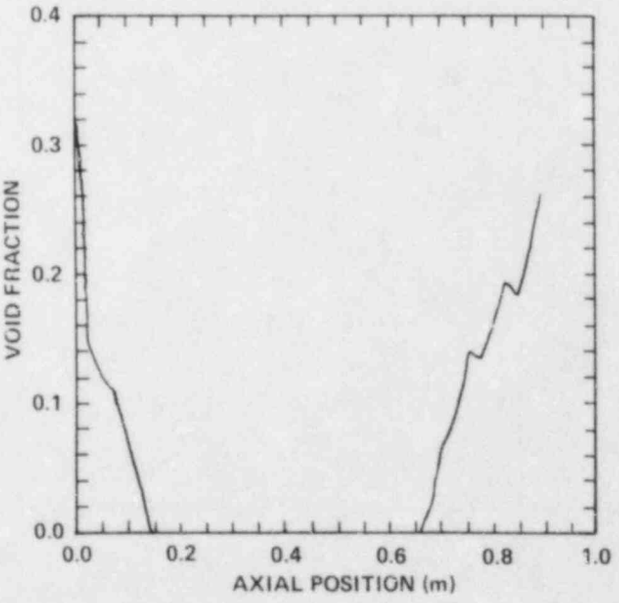

(d) Time = 0.80 s.

Fig. 17.
Void fraction distribution vs. time for case 33b.

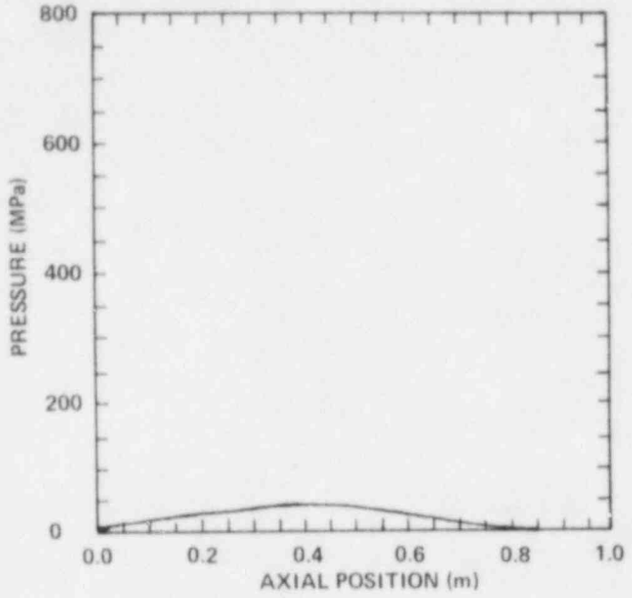

(a) Time = 0.50s.

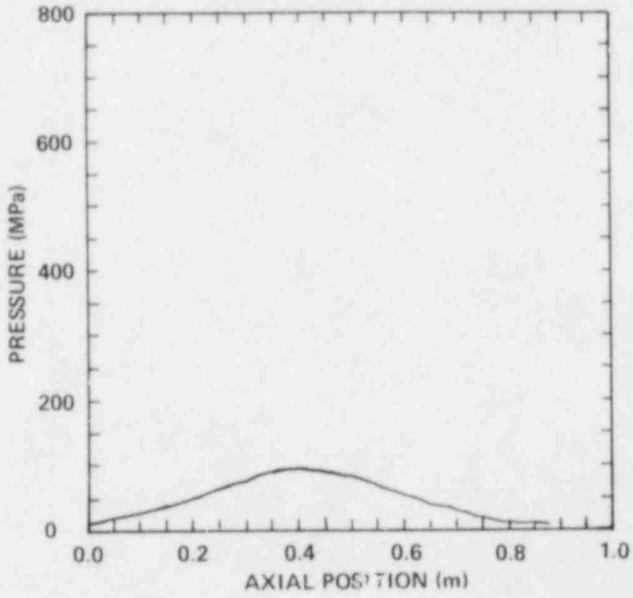

(b) Time = 0.60 s.

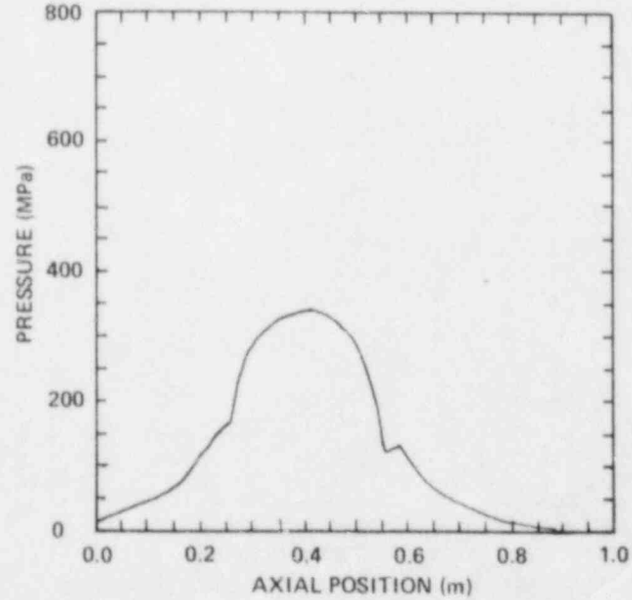

(c) Time = 0.70 s.

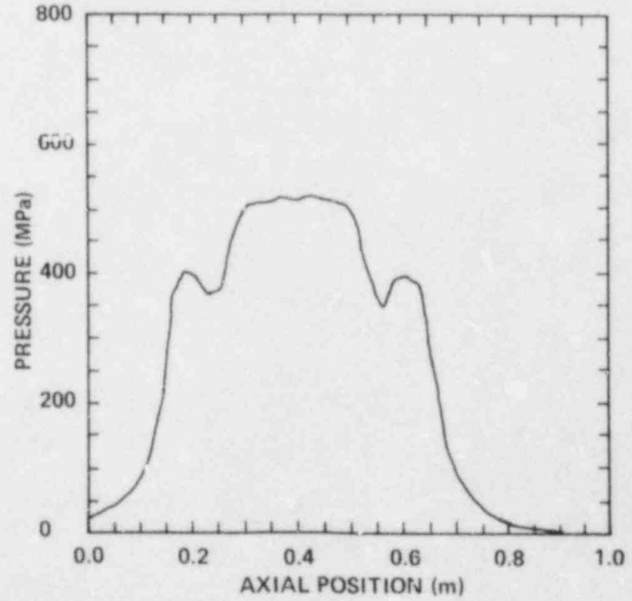

(d) Time = 0.80s.

Fig. 18.
Pressure distribution vs time for case 33b.

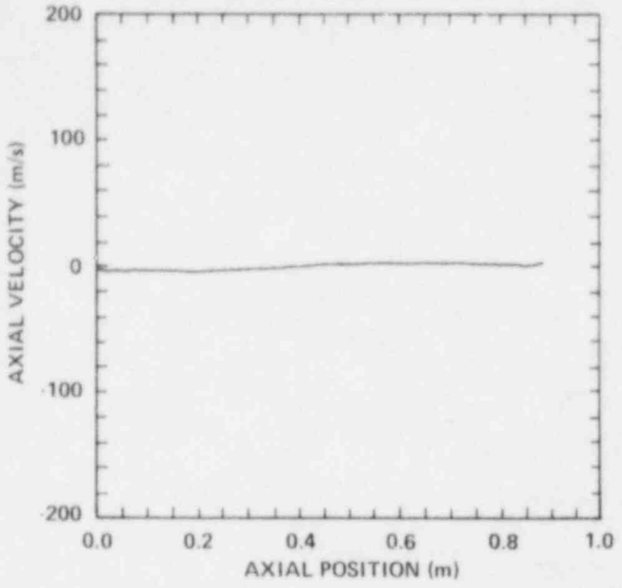

(a) Time = 0.50 s.

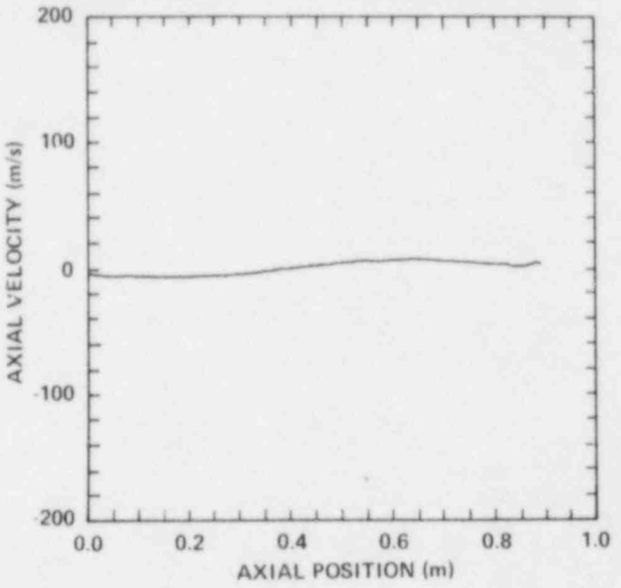

(b) Time = 0.60 s.

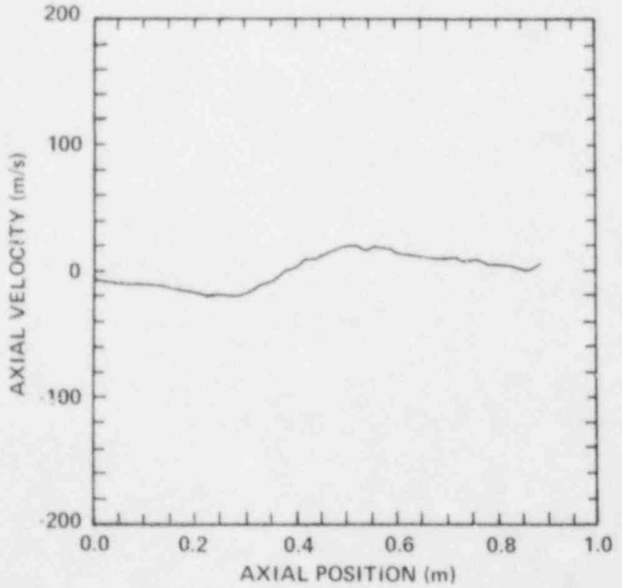

(c) Time = 0.70 s.

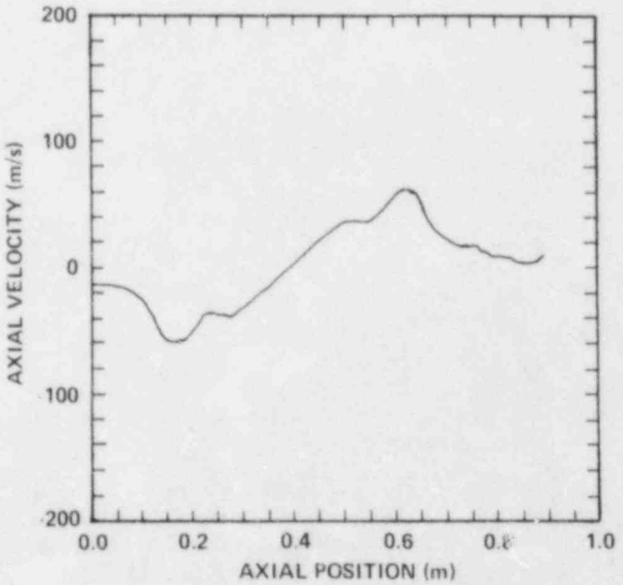

(d) Time = 0.80s.

Fig. 19.
Axial velocity distribution vs. time for case 33b.

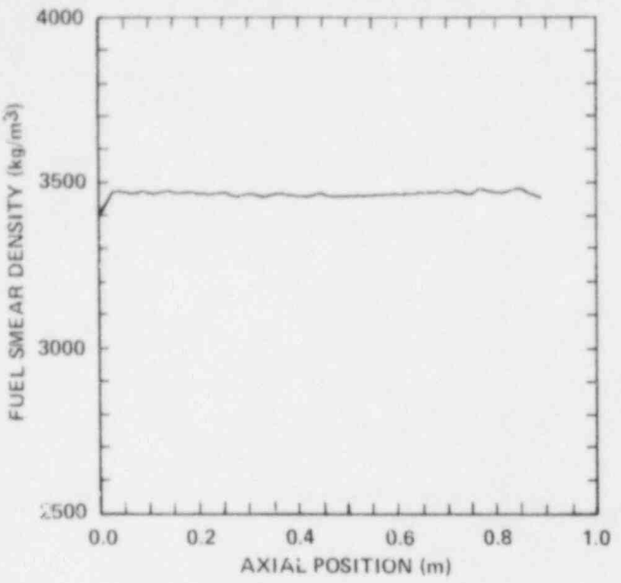

(a) Time = 0.50 s.

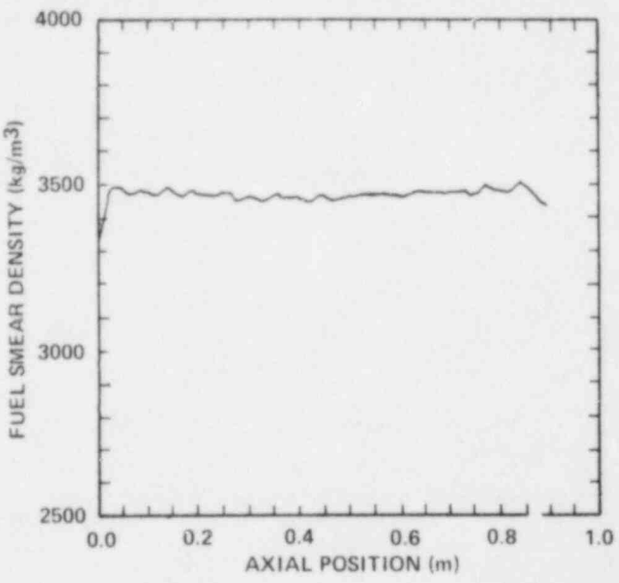

(b) Time = 0.60 s.

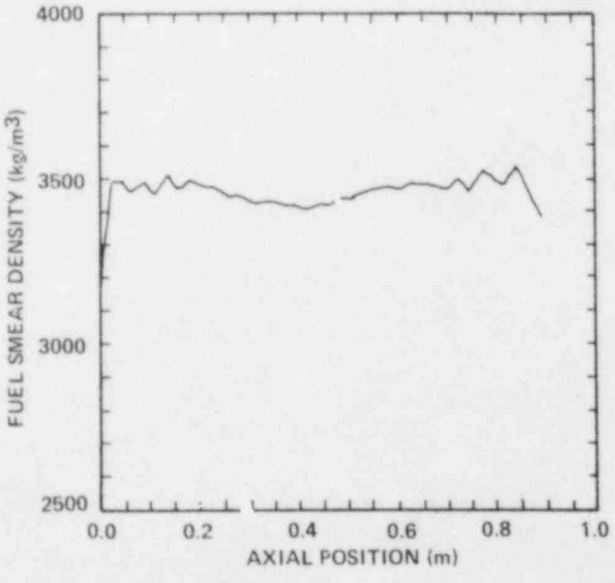

(c) Time = 0.70 s.

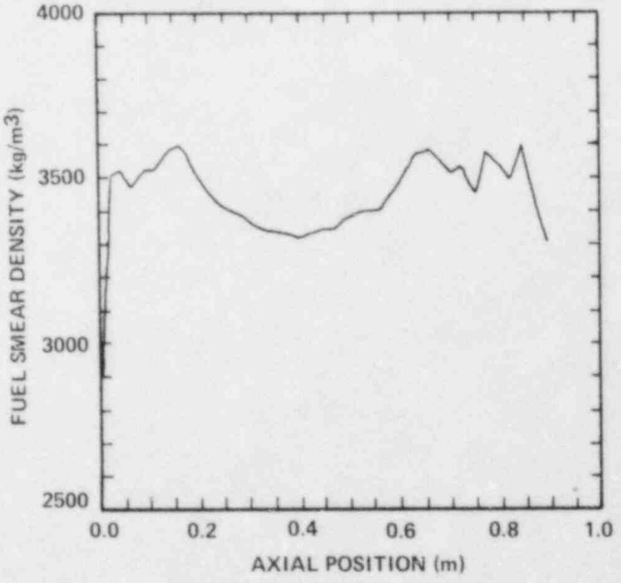

(d) Time = 0.80 s.

Fig. 20.
Fuel smear density distribution vs. time for case 33b.

APPENDIX B
ANNULAR POOL FLUID DYNAMICS

1. Introduction

In this Appendix an assessment is made of the characteristics of the fluid motion in the annular pool geometry. Based on the reassembly or puddling rates, ramp rate estimates are made for a variety of situations and modeling assumptions. These are not coupled neutronic/fluid dynamic analyses but rather fluid-dynamic calculations with assumed initial conditions and simulated initial recriticalities. The material is presented in four sections: analysis model and assumptions, analysis results, experimental benchmarking, and a summary.

2. Analysis Model and Assumptions

The transient fluid-dynamic behavior of the annular pool was investigated using SIMMER-II [1] with a simplified pool geometry. Because a neutronic analysis was not performed, portions of the reactor outside the annular pool were not represented. The calculational model is shown in Figure 1. The fluid dynamic region (radial mesh 3 through 12 and axial mesh 1 through 20) represented the driver subassemblies between the third internal blanket ring and the radial blanket (132 subassemblies). The boundaries were assumed blocked. The annular pool was assumed to consist of about 85% of the driver fuel and all of the wall steel in these subassemblies. All cladding steel was assumed removed.

The starting configuration assumed that the molten core materials were slumped into the bottom half of this annular core region. An initial temperature of 3100 K was assigned to both fuel and steel. The pool was perturbed with an assumed power transient with a triangular shape and a half width of 0.01 s. The assumed power distribution is shown in Figure 2. It was biased toward the inner edge because of the fuel in the inner driver regions. This radial distribution is in reasonable agreement with that calculated for similar configurations in Section II.7.

3. Analysis Results

A number of calculations of these annular-pool transients have been performed to assess variations in initial configuration, perturbation strength,

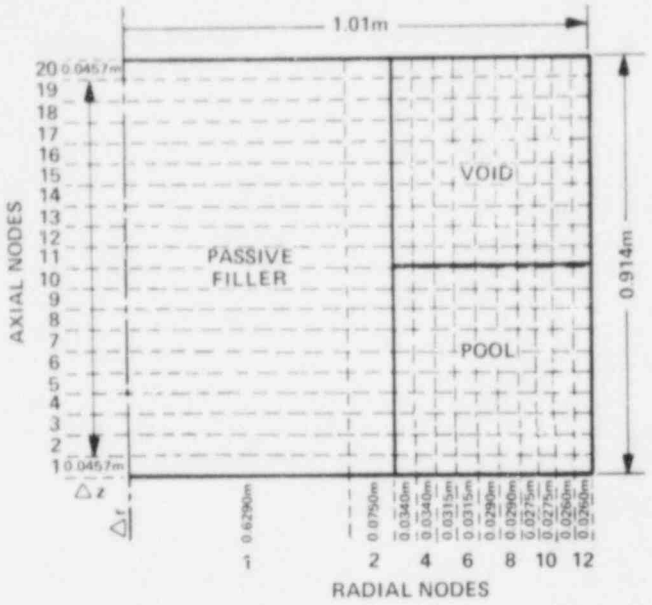

Fig. 1.
SIMMER-II geometric model for annular-pool analysis.

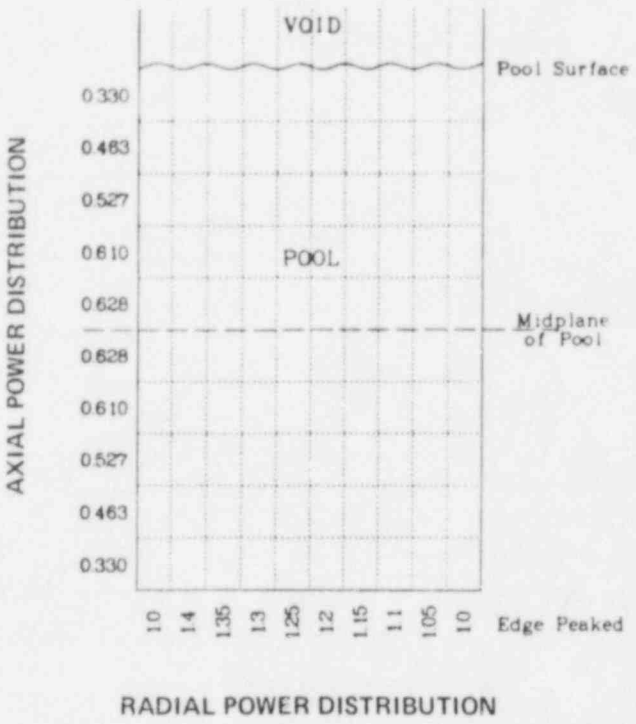

Fig. 2.
Power distribution for initiating annular pool transients.

and model assumptions. One case will be discussed in detail and the results of the other cases will be tabulated only.

The case chosen for detailed discussion is representative of all the other but had greater numerical resolution because the calculational node sizes in both directions were reduced to one-half of those shown on Figure 1 (four times as many nodes). The applied power transient had a peak of 300 times nominal full power, thereby adding about three FPS or about 700 K to the pool. Heat transfer between the fuel and steel in the pool occurred moderately fast and was characteristic (roughly) of a dispersion with a characteristic size of about 0.001-m diameter. The results indicate a thermal equilibration time of about 0.05 s for the mixture following the preferential heating of the fuel. The liquid/vapor momentum coupling was characterized by a dispersion size of 0.01-m diameter and a multidroplet augmentation parameter of 2.5. This parameter is the exponent on the void fraction which appears in the denominator of the interfield momentum coupling function (see Reference 1). As the void fraction decreases the overall coupling increases dramatically.

An overall perspective on the predicted fluid dynamics is given in a sequence of contour plots, Figure 3, for the pool liquid. The "L's" and "V's" indicate regions of liquid and vapor, respectively. Figure 3a shows the initial liquid pool. At 0.020 s all the energy from the assumed power pulse was in the pool but little motion is seen in Figure 3b. Small pockets of vapor

(a) Time = 0 s.

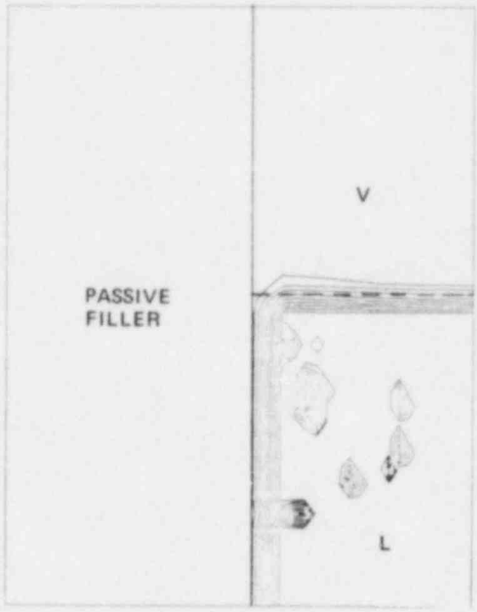

(b) Time = 20 ms.

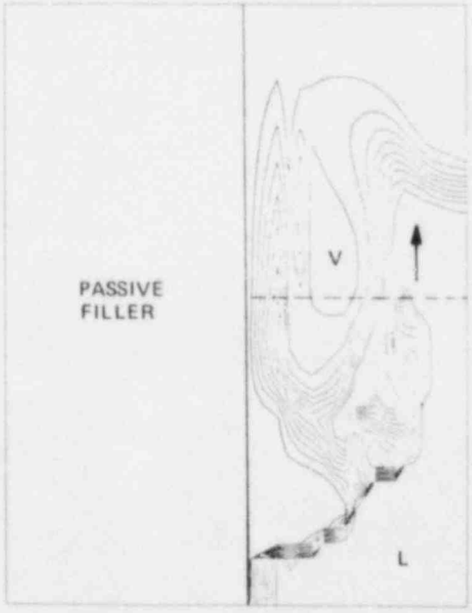

(c) Time = 40 ms.

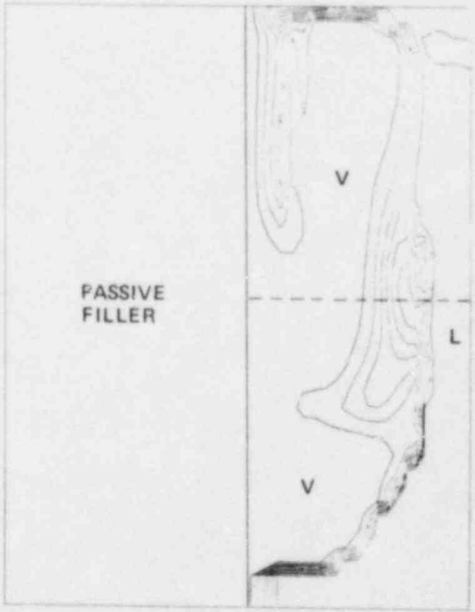

(d) Time = 60 ms.

Fig. 3.
Typical fluid-dynamic transient from power burst initiation (case C12).

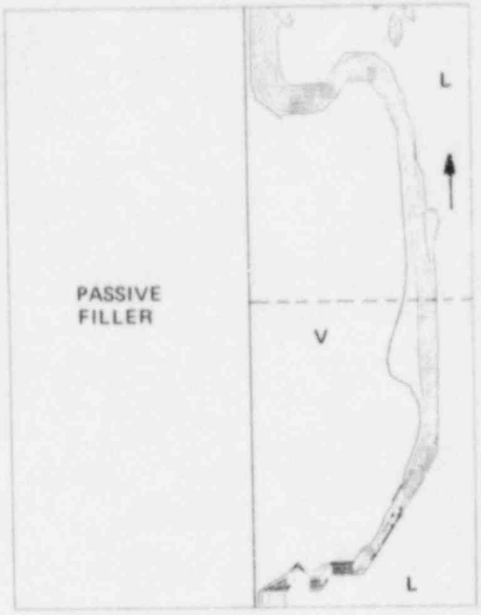

(e) Time = 80 ms.

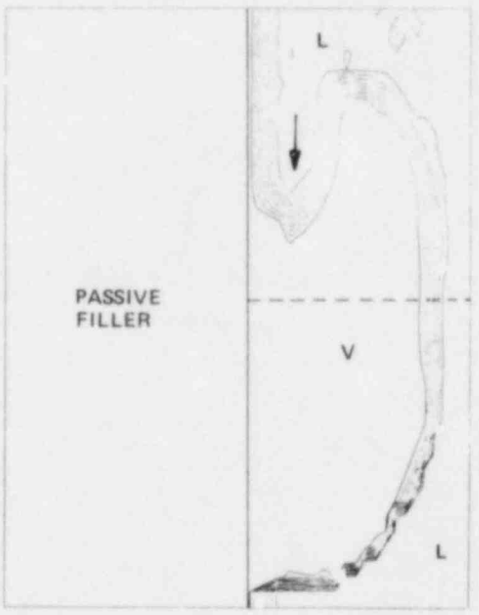

(f) Time = 100 ms.

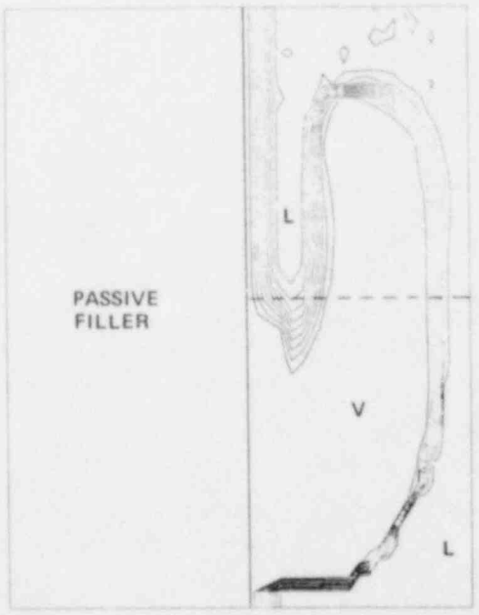

(g) Time = 120 ms.

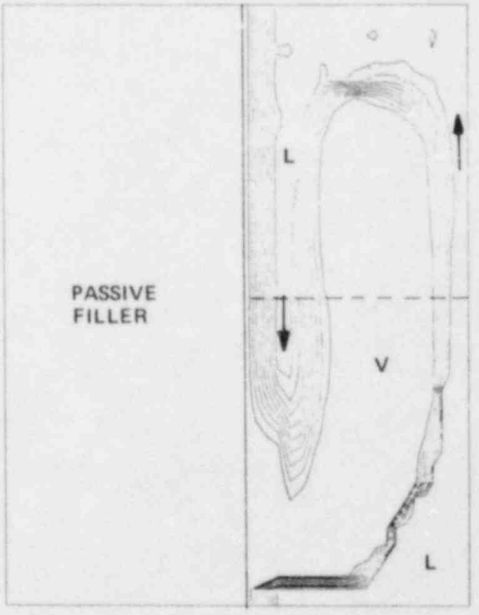

(h) Time = 140 ms.

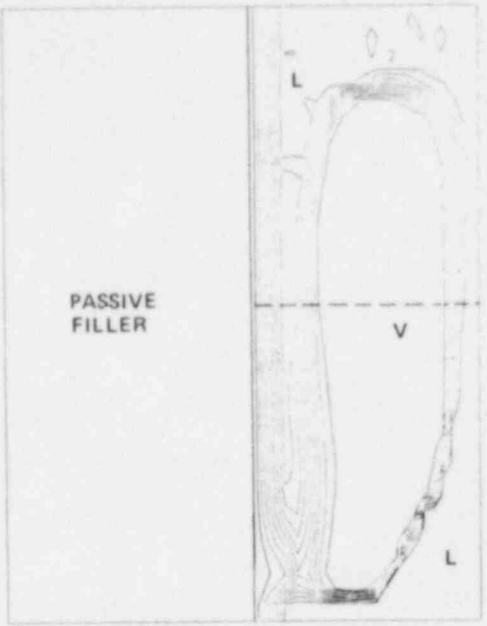

(i) Time = 160 ms.

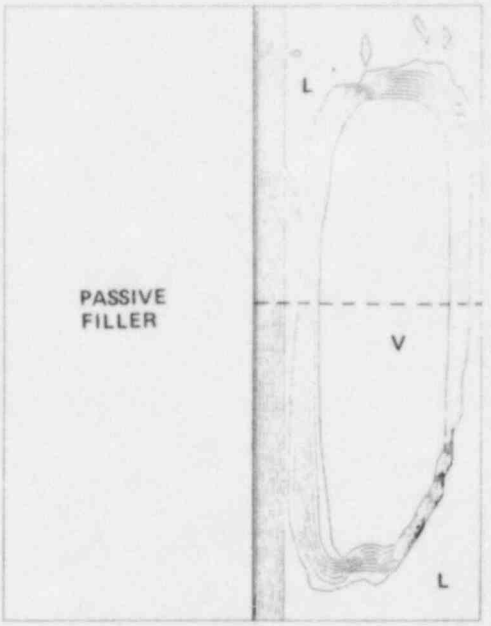

(j) Time = 180 ms.

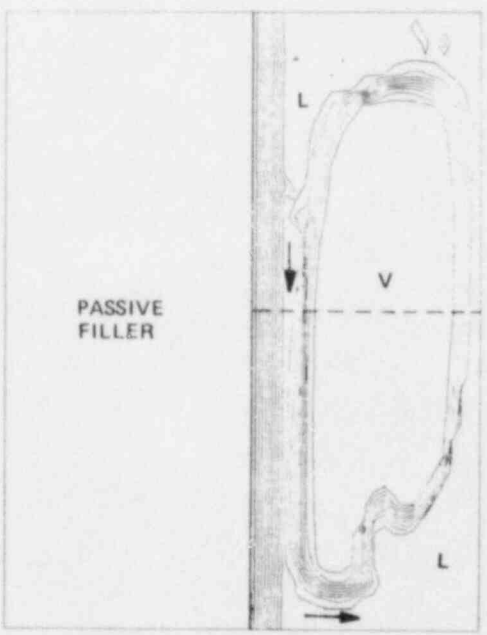

(k) Time = 200 ms.

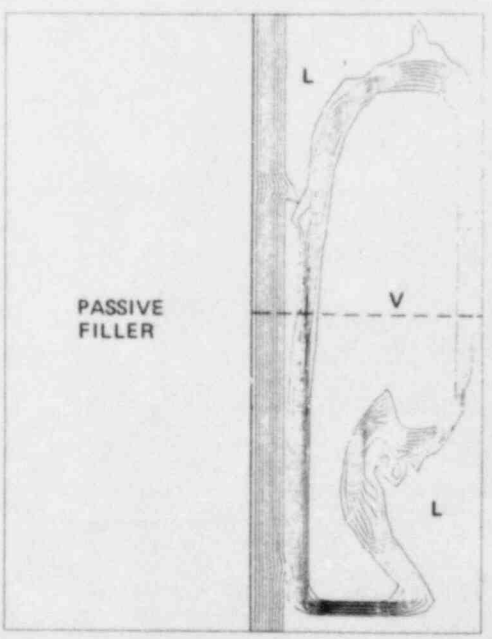

(l) Time = 240 ms.

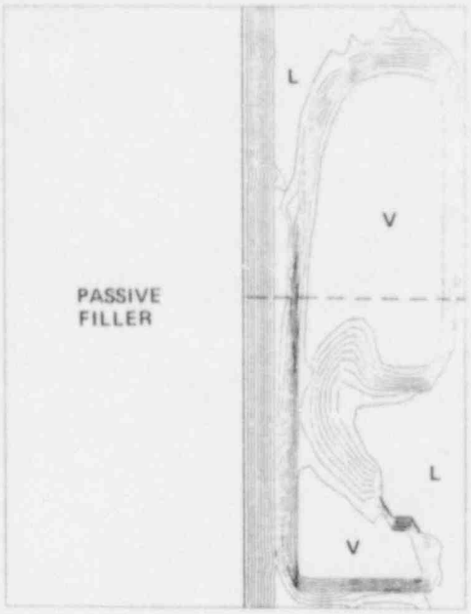

(m) Time = 280 ms.

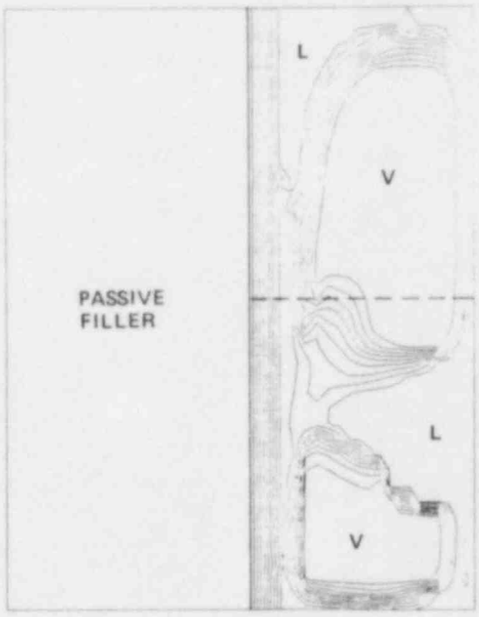

(n) Time = 320 ms.

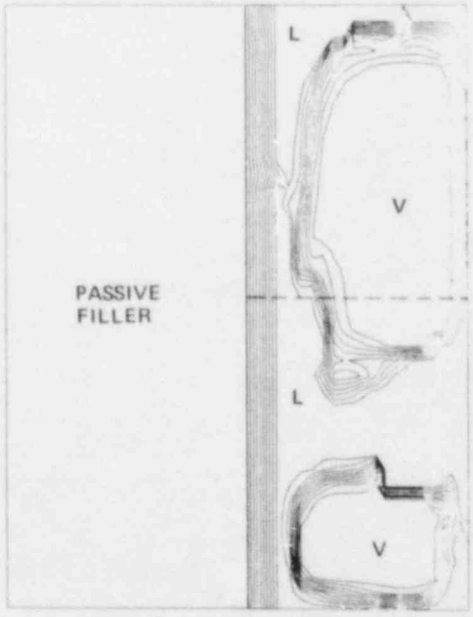

(o) Time = 360 ms.

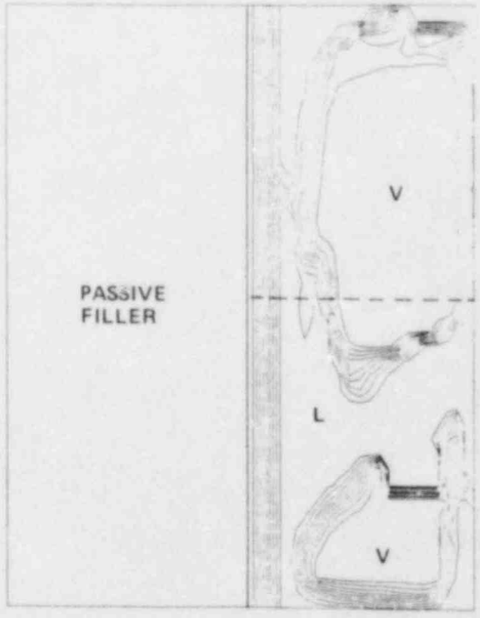

(p) Time = 400 ms.

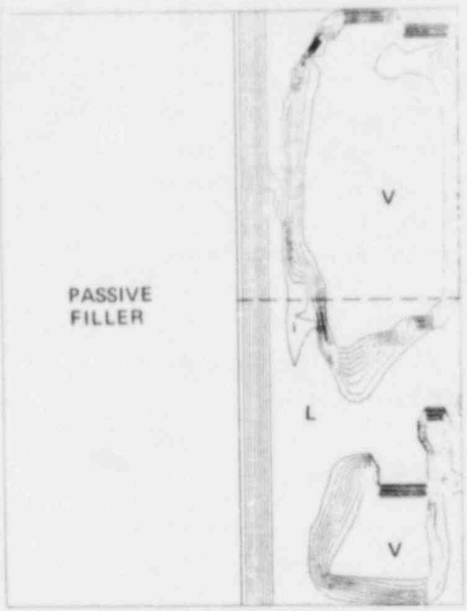

(q) Time = 440 ms.

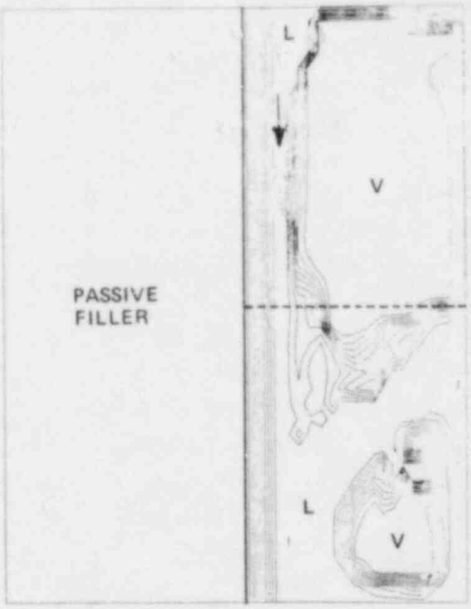

(r) Time = 480 ms.

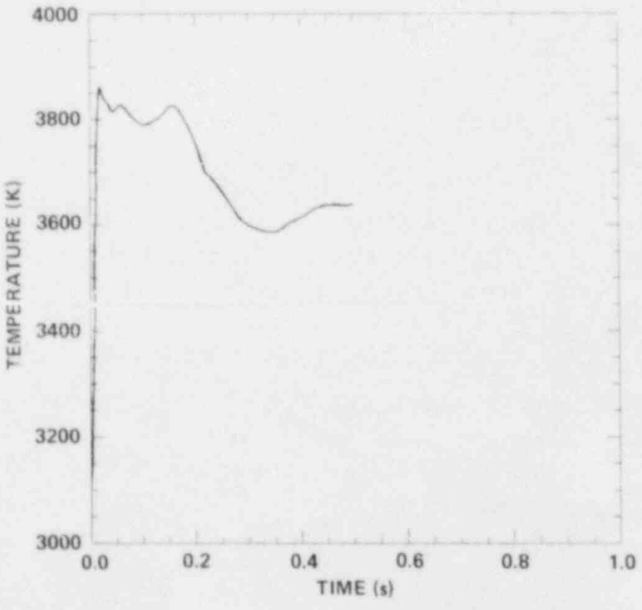

Fig. 4.
Peak fuel temperature during the annular pool transient (case C12).

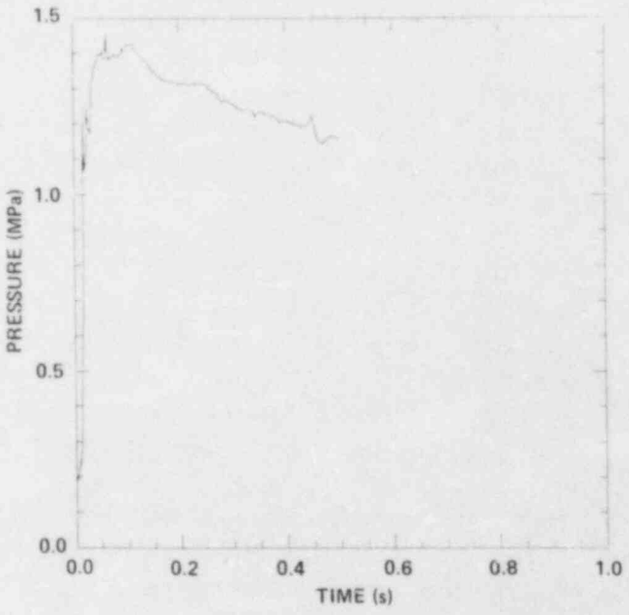

Fig. 5.
Midpool pressure during the annular pool transient (case C12).

are shown. These resulted from locally amplified heat transfer between the fuel and steel. As a vapor region formed the liquid fuel was calculated to flash, break up into a smaller dispersion, and create more area and less resistance to heat transfer. The scattered pattern was the result of local pressure nonuniformities. These scattered bubbles merged in Figure 3c as the effects of the power profile began to dominate the fluid dynamics.

The rapid heating of the fuel can be seen in Figure 4. The fuel vapor pressure associated with the maximum fuel temperature was about 0.2 MPa. Figure 5 indicates that a pressure much higher than this is generated rapidly. The steel that heated to about 3800 K produced a vapor pressure of nearly 1.5 MPa, however, and was the pressure source that perturbed the pool.

The expansion region broke the pool surface at about 0.04 s as seen in Figure 3c, but the imparted momentum at that time caused most of the material that was smeared in the breakthrough process to proceed to the top of the region as shown in Figure 3d. Significant upward momentum was imparted to the entire upper half of the pool before breakthrough. This liquid continued to move as a climbing film along the outer wall, to circulate around the top of the annulus, and to flow downward along the inner surface as shown in Figures 3e through 3i. At 0.16 s the original pool had been distributed completely around the periphery of the annulus. Reassembly of the pool from this point was highly incoherent because the outer film was moving upward while the inner one produced a mass reflux into the pool region. The subsequent pool reassembly is shown in Figures 3j through 3l. A vortex was generated in the pool as the film entered the pool and entrapped a large vapor bubble at 0.32 s.

The severity of a secondary recriticality from this mild initial event can be quantified approximately from the mass reflux into the pool (and associated puddling rate) and the differential worths for an annular-pool configuration. A secondary event can occur only for conditions that constitute a neutronically critical system. This depends on the inventory of fuel in the system. Even for an inventory of 100%, criticality will not occur until the fuel is concentrated locally or uniformly redispersed to nearly its nominal distribution. The configuration at 0.2 s (Figure 3k) is highly subcritical. A transient neutronics calculation was performed to scope these neutronic states. Criticality was approached when about two-thirds of the total mass was in the lower pool region.

The fuel inventory in the lower half of the annulus (corresponding to the original pool) is shown in Figure 6 as a function of time. Because the instantaneous slopes (reflux rates) are not uniquely related to differential reactivity at a critical state due to inventory considerations, an arbitrary selection of maximum slope and maximum differential worth is inappropriately conservative and assumes a level of detailed resolution incompatible with our

approach. Therefore, an average slope or reflux rate was used as well as an average differential worth. The average mass reflux rate was approximately 3400 kg/s. This produced an equivalent puddling rate of approximately 0.27 m/s. Using an average differential worth from Figure 7 of approximately 1.0 $/cm, we obtained a ramp rate of 27 $/s.

Other cases that were calculated are tabulated in Table 1. The reassembly transients are shown on Figures 8 through 13 and the results are tabulated in Table 2. The results indicated that mild initiators did not cause the large circulation around the top of the annulus but instead produced a sheet along the outer radius that simply drained back by gravity. Variation of the vapor-liquid momentum coupling had a small effect as seen by comparing cases C02 with C10 and C06 with C08. The initial pool configuration appeared to have the largest effect in the direction of larger ramps (compare cases C02 and C14). The partially two-phase situation permited a more rapid radial bubble growth initially and therefore lifted the upper half of the pool mass more coherently. The reflux then also was more coherent. The increased calculational resolution added more incoherence to the process by resolving the film flows better (compare cases C02 and C12).

4. Experimental Benchmarking

Because the pool states have a greater potential for larger ramps, it is important to provide an experimental calibration of our ability to assess the pool transients. To this end a timely set of experiments has been performed in the existing OMEGA facility [2] at Purdue University. This facility is designed for postdisassembly expansion experiment in one-seventh CRBR vessel scale. Its application to the active core provides approximately full annulus scale and full axial scale. Therefore, it is ideal for this benchmarking.

The experiments performed to date with a gas source at the annulus inner radius for the pool perturbation source indicated gross upward and outward movements of the upper half pool initialiy. Breakthrough occurred with substantial dispersal of liquid. Pressure transducers at the top plate provided an indication of initial liquid contact time and a rough estimate of mass flux.

SIMMER-II analysis of this experiment produced fluid-dynamic characteristics that were in general agreement with the data. The time that material reached the top plate agreed well with the data as did the initial bubble growth patterns and breakthrough time. The bulk material motions were reasonable but the dispersiveness was difficult to compare and would not be expected to be in agreement because the SIMMER-II modeling of these processes lacks the detailed physics. However, if the reflux rate to the puddled regions is controlled more by the bulk or gross motion than by the

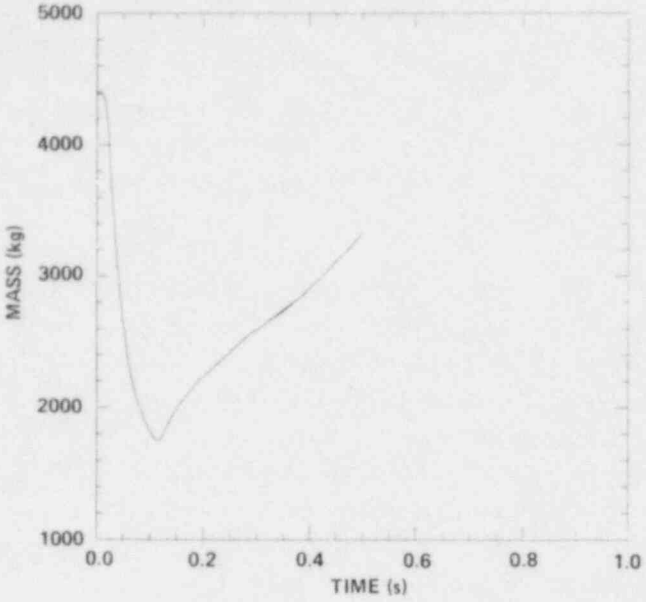

Fig. 6.
Mass of fuel in the original pool region vs time (case C12).

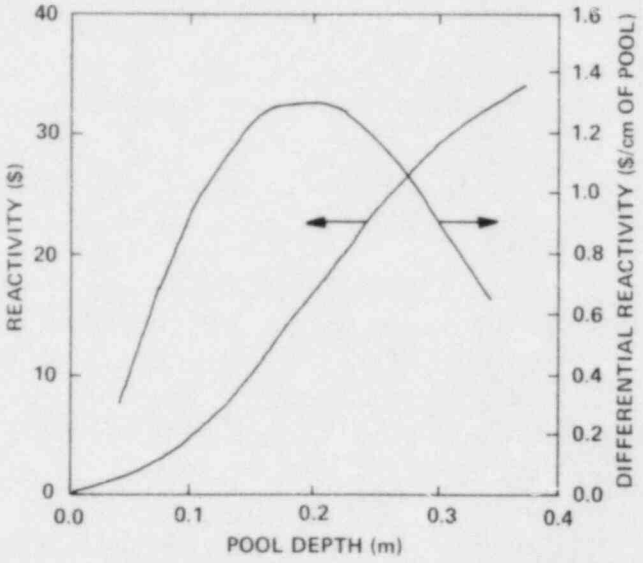

Fig. 7.
Annular pool reactivity characteristics.

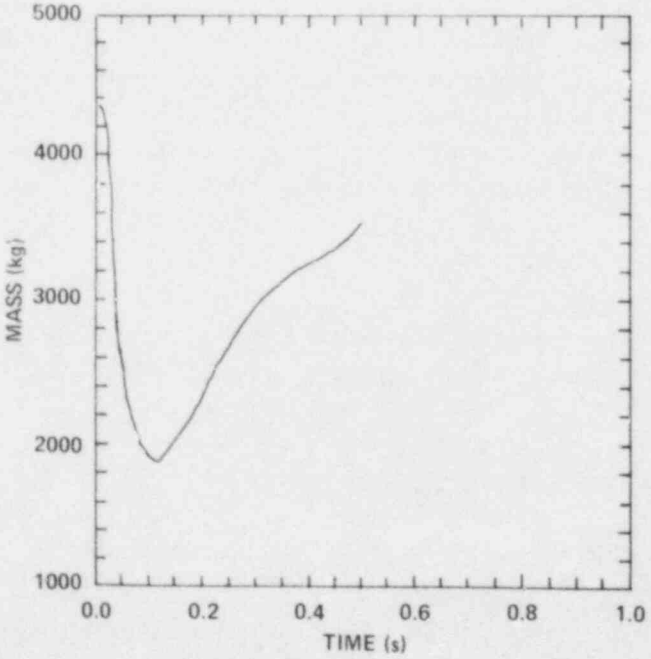

Fig. 8.
Pool inventory transient for case C02.

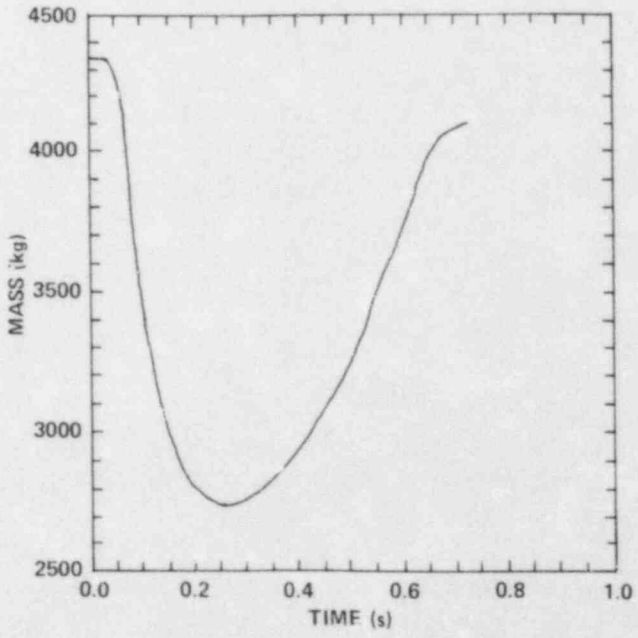

Fig. 9.
Pool inventory transient for case C04.

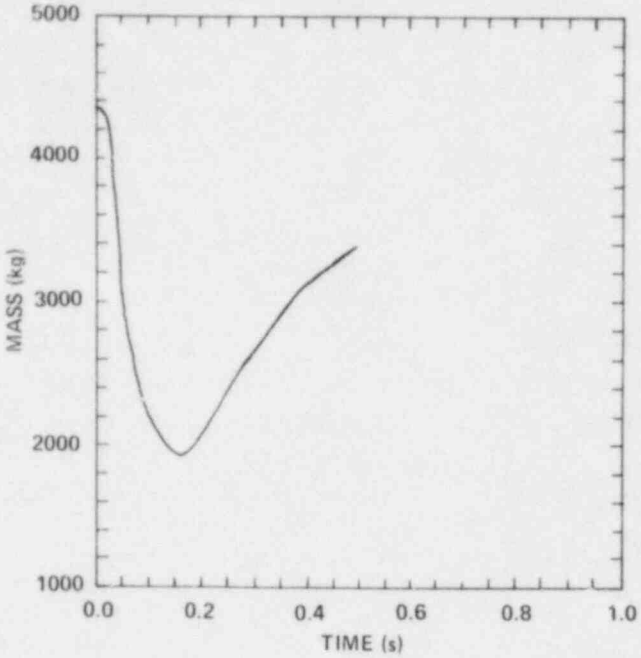

Fig. 10.
Pool inventory transient for case C06.

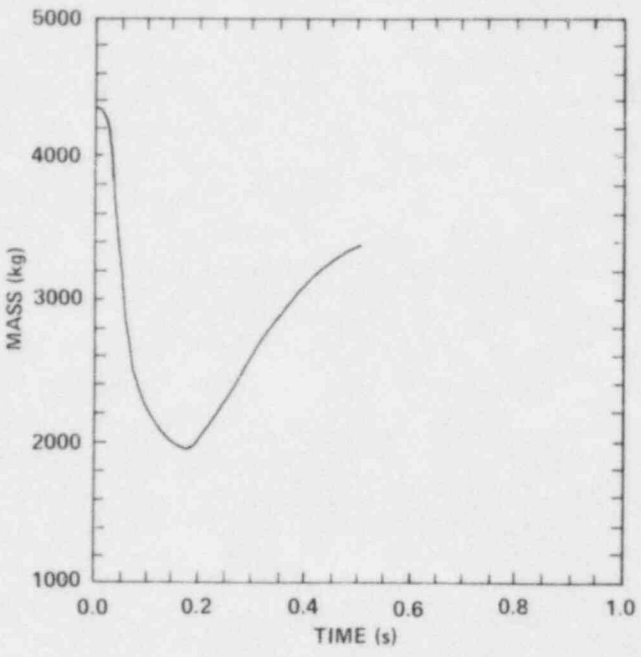

Fig. 11.
Pool inventory transient for case C08.

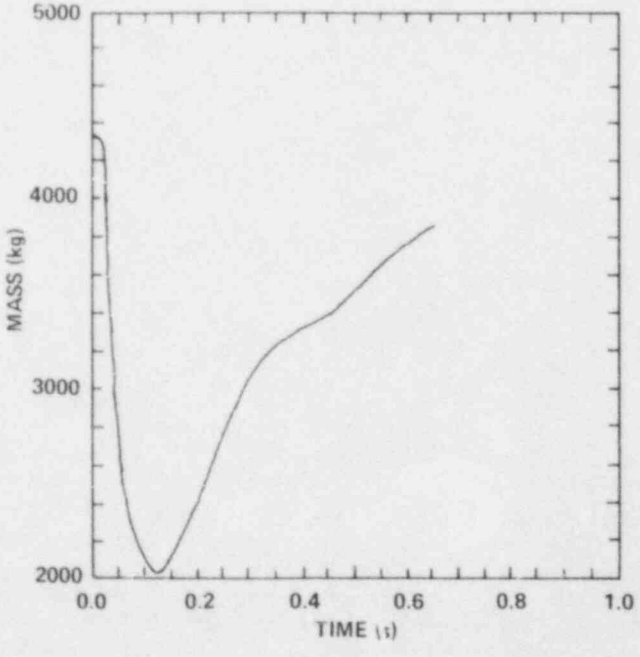

Fig. 12.
Pool inventory transient for case C10.

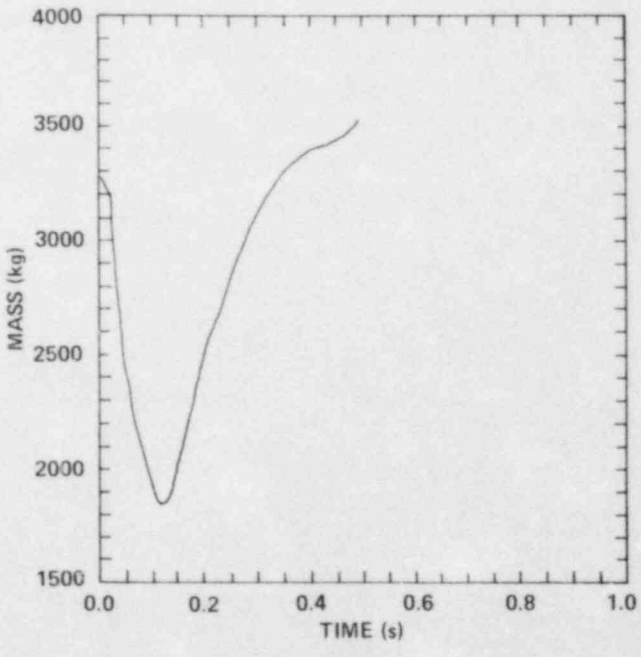

Fig. 13.
Pool inventory transient for case C14.

dispersal, the SIMMER-II analyses should be adequate for providing estimates. In fact, they should provide conservative results because massive dispersiveness would only impede the reflux to the pool.

5. Summary

The analysis of annular-pool fluid dynamics following an assumed mild recriticality indicates a tendency for this geometry to produce ramp rates less than that for coherent rainback. This mitigation comes from the spreading of the upper half of the pool into a film or sheet-type flow that reduces the reflux rate. Benchmarking experiments provided the basis for assigning credibility and adequacy to these analyses.

6. References

1. L. L. Smith, "SIMMER-II: A Computer Program for LMFBR Disrupted Core Analysis," Los Alamos National Laboratory report NUREG/CR-0453, LA-7515-M (June 1980).

2. J. J. Simpson, M. Saito, and T. G. Theofanous, "The Termination Phase of Core Disruptive Accidents in LMFBRS," Purdue University report PNE-81-151 (June 1981).

TABLE 1
ANNULAR POOL ANALYSIS MATRIX

Case	Peak Power (xP_0)	Momentum Coupling: Void Exponent	Momentum Coupling: Dispersion Radius (m)	Noding	Fuel-Steel Heat-Transfer Multiplier	Initial Pool Configuration
C02	300	2.5	0.005	10 x 20	100	Full Puddled
C04	100	2.5	0.005	10 x 20	100	Full Puddled
C06	300	2.5	0.001	10 x 20	0	Full Puddled
C08	300	2.5	0.005	10 x 20	0	Full Puddled
C10	300	6.0	0.005	10 x 20	100	Full Puddled
C12	300	2.5	0.005	20 x 40	100	Full Puddled
C14	300	2.5	0.005	10 x 20	100	Half Puddled & Half Distributed

TABLE 2
ANNULAR-POOL ANALYSIS RESULTS

Case	Reflux Rate (kg/s)	Puddling Rate (m/s)	Ramp Rate ($/s)
C02	4460	0.35	35
C04	3076	0.24	24
C06	4470	0.35	35
C08	4590	0.36	36
C10	3570	0.28	28
C12	3400	0.27	27
C14	5545	0.42	42

APPENDIX C
WHOLE-CORE TRANSIENT-POOL RECRITICALITY

1. Introduction

In this Appendix an assessment is presented of the coupled fluid-dynamic/neutronic, transient response of a postulated, homogeneous cylindrical pool. The material is in four sections: analysis model and assumptions, analysis results, experimental benchmarking, and a summary.

2. Analysis Model and Assumptions

The analysis of the cylindrical pool behavior was performed with the SIMMER-II code [2]. The calculational model for the CRBR active core and surrounding regions was adapted from that used for a previous inter-subassembly-gap, fuel-removal investigation [1]. The calculational mesh is shown on Figure 1. The regions within the mesh represented local regions in the reactor where geometry or thermal-physical conditions did not differ initially. They were used for specifying the local conditions and physical characteristics to the code. The modeling characteristics of these regions are listed in Table 1.

The specific characteristics of all regions surrounding the active core, regions 20 through 67, are unimportant in this assessment except that they contain the true material smear densities to provide proper neutronic boundary conditions for the active core. They were treated as nonflow regions, thereby producing a sealed pool configuration.

The active core, regions 1 through 16, was treated as a completely homogenized pool. The fuel and subassembly wall steel of internal blanket and driver subassemblies were mixed at the fuel liquidus temperature of 3100 K. This mixture was assigned to the core region with an assumed uniform void except for the two top node rows, which were assumed totally voided. Because the homogenization produced a large positive reactivity effect and some slumping was assumed, the full inventory of core materials could not be utilized in conjunction with the specification of a neutronically critical system.

Adjustments were made in the inventory to provide the initial critical state. The resulting initial pool void fraction was 48% and the fuel inventory was approximately 75% of nominal. This implies a prior fuel loss of 25%. The

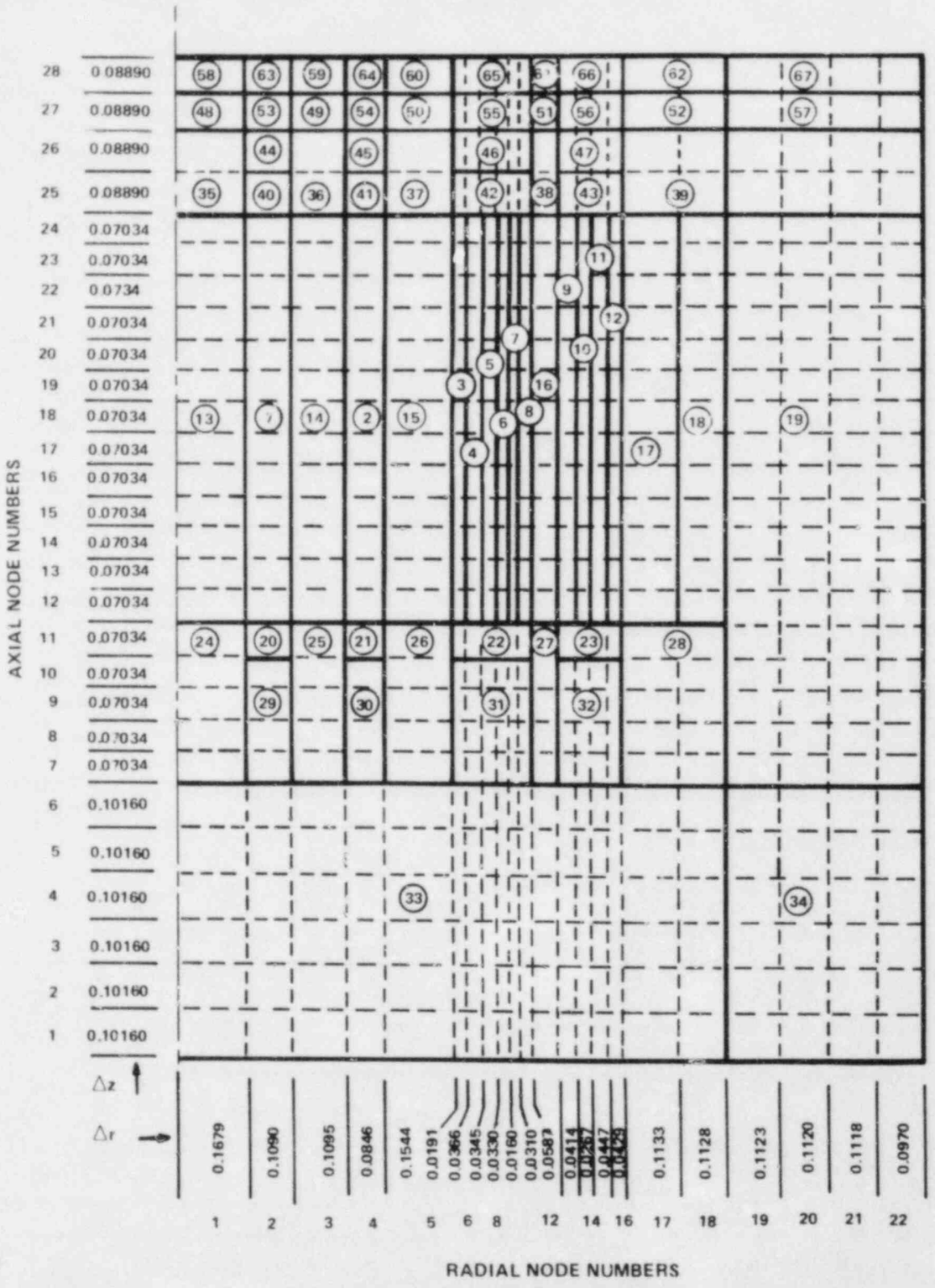

Fig. 1.
SIMMER-II geometric model for whole-core pool analysis.

TABLE 1
REGION CHARACTERISTICS IN THE SIMMER-II
WHOLE-CORE MODEL FOR ANALYZING
CYLINDRICAL POOL BEHAVIOR

Region Number	Reactor Region	Modeling Characteristics
1 through 12	Active core	Homogenized pool
13 through 16	Internal blanket (IB)	Homogenized pool
17 and 18	Radial blanket (RB)	Interconnected gaps - closed
19	Radial reflector (RR)	Interconnected gaps - closed
20 through 23	Lower axial blanket-driver	Complete blockage
24 through 27	Lower axial blanket-IB	Interconnected gaps - closed
28	Lower axial blanket-RB	Interconnected gaps - closed
29 through 32	Lower axial blanket-driver	Interconnected gaps - closed
33	Lower shield	Interconnected gaps - closed
34	Radial reflector nozzles	No structure
35 through 38	Upper axial blanket-IB	Interconnected gaps - closed
39	Upper axial blanket-RB	Interconnected gaps - closed
40 through 43	Upper axial blanket-driver	Complete blockage
44 through 47	Upper axial blanket-driver	Interconnected gaps - closed
48 through 51	Upper axial blanket -IB load pad	Interconnected gaps - closed
52	Upper axial blanket -RB load pad	Interconnected gaps - closed
53 through 56	Upper axial blanket -driver load pad	Interconnected gaps - closed
57	Radial reflector load pad	Interconnected gaps - closed
58 through 61	Upper axial blanket-IB	Interconnected gaps - closed
62	Upper axial blanket-RB	Interconnected gaps - closed
63 through 66	Upper axial blanket-driver	Interconnected gaps - closed
67	Radial reflector	Interconnected gaps - closed

cladding steel, assumed to have been removed, was placed in the axial blankets equally. The removed fuel was assumed to be neutronically inert and therefore was assumed to be physically removed beyond the axial and/or radial blankets.

The neutronics treatment was 18-group, space-time, transport theory. The isotopic mixtures and distributions used in this assessment were obtained from Westinghouse (see Appendix A of Section II.3) for the EOC-4 core state. The neutronics calculational mesh overlaid the fluid-dynamic mesh from node 7 to node 28 axially and node 1 to node 18 radially. The larger radial fluid-dynamic mesh cells were subdivided for the neutronic analysis. The aspects of the SIMMER-II modeling that are of primary importance in this assessment are the interfacial smearing of material, void collapse, and the liquid-vapor momentum coupling.

The interfacial smearing in SIMMER-II is a known result of the donner-cell differencing of the Eulerian fluid-dynamics equations. Its true extent is proportional to mesh-cell size and, in a two-phase system, to liquid-vapor momentum coupling. If interfacial interactions dominate the physical problem of interest, considerable care must be exercised in the analysis because of this smearing. The primary interfacial physics of concern in this analysis are fluid-dynamic breakup and dispersion by instability mechanisms. If a large portion of the fluid is highly dispersed during the initial out-slosh, the reassembly rates and resulting yield characteristics can change significantly. This was discussed in detail in Appendix B for the annular pool. The adequacy of the SIMMER-II treatment or, more appropriately, simulation of this process is addressed below in the benchmarking section.

Void collapse in this assessment is associated with condensation because of the assumption that fuel and steel vapors only are present in the pool initially. As the pool compressed by the perturbing pressure source, the vapors in the pool compressed and supersaturated, thus producing a condensation potential. If the vapors condensed on a time scale that was smaller than the sloshing interval, the spring-back characteristics of a two-phase, compressed system would be mitigated. It would then occur only as a result of reboilup, which could be suppressed by a slightly increased over pressure in the core that is the natural result of the initial pressure perturbance. Thus, rapid void collapse would result in an essentially single-phase slosh-in.

In SIMMER-II, condensation is treated as a heat-transfer-limited process at the liquid-vapor interfaces. The local saturation temperature is computed from the vapor density and temperature (vapor may be superheated). This saturation temperature exists at the condensing interface and is the thermal "force" to drive the condensation energy into the liquid. This condensation is calculated only at the liquid interface of the condensing specie in a multicomponent situation such as the fuel-steel pool. In the absence of local

noncondensibles, this model is straightforward and adequate with the primary uncertainty being the interfacial or condensing area. The areas are computed in SIMMER-II based on the local liquid dispersion size from fluid-dynamic breakup, flashing, or input constraint and on the local liquid volume fractions. For this assessment the time scale available for condensation was a few tenths of a second and therefore the uncertainties in the detailed modeling were not a factor in the overall results.

The modeling of liquid-vapor momentum coupling is important primarily in determining the effectiveness of the initial pressure perturbation in creating the coherent out-slosh. SIMMER-II treats this coupling as an effective drag resulting from the relative velocity between the liquid and vapor, each of which is treated with its own momentum equation. The effective drag depends on the local dispersion of the material and void fraction. This coupling has been tested [3, 4, 5] over a wide range of conditions and flow regimes and was found to be very reasonable for predicting overall fluid motions. For this application we postulated initial pressure perturbations that assured the out-slosh. Therefore, these details were not of major importance.

3. Analysis Results

Two cases are presented that represent two regimes of initial pool perturbations, mild recriticality and local sodium interaction. The results are presented in terms of the reactivity and power histories, sequences of liquid fraction plots, and integral mass redistribution plots.

3.1. Recriticality Sloshing

This case was initiated by gravity slumping of the pool leading to a prompt-critical burst yielding approximately 5 FPS. This resulted in a rapid out-slosh that dropped the reactivity to a highly negative value as shown on Figure 2. The associated power transient and energy yield is shown on Figures 3 and 4, respectively. The subsequent pool motion is shown on the sequence of fuel smear density plots in Figure 5. The classical postdisassembly distribution is seen in Figure 5b. The material discharged to the top drained back as seen in Figures 5c and 5d. The material at the outer wall began draining at 0.8 s. The initial void was eliminated in most of the core mass. During this period the material at the outer periphery drained downward and turned inward at the bottom. At approximately 1.0 s, criticality was reached at a ramp rate of approximately 120 \$/s. By suppressing the reactivity state at about 0.99 s, the fluid motion was observed beyond 1.0 s. This is shown in Figures 5h and 5i. The main mass of material continued to move inward at a nearly constant rate as seen on Figure 6. This figure gives the inventory of fuel in a central cylinder

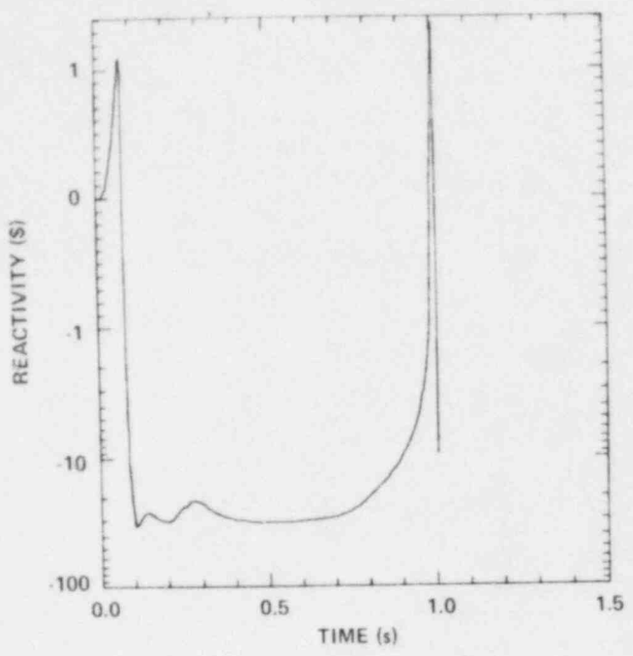

Fig. 2.
Reactivity transient for recriticality induced sloshing.

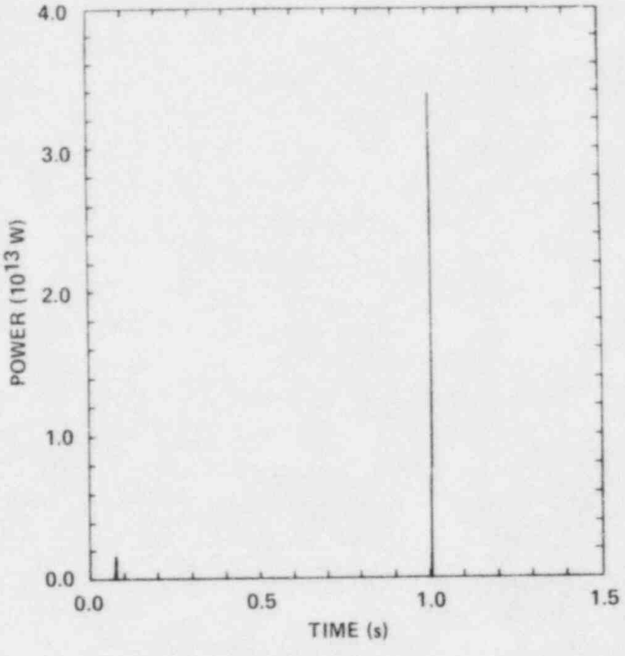

Fig. 3.
Power transient for recriticality induced sloshing.

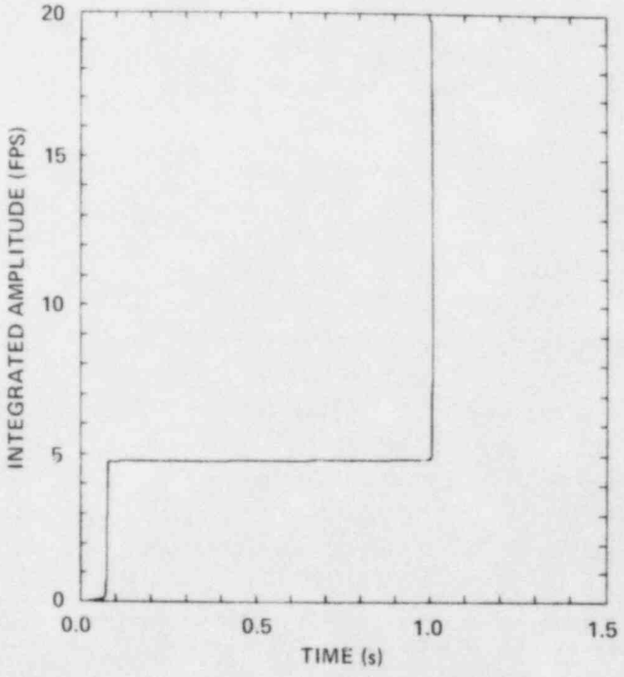

Fig. 4.
Energy yield transient for recriticality induced sloshing.

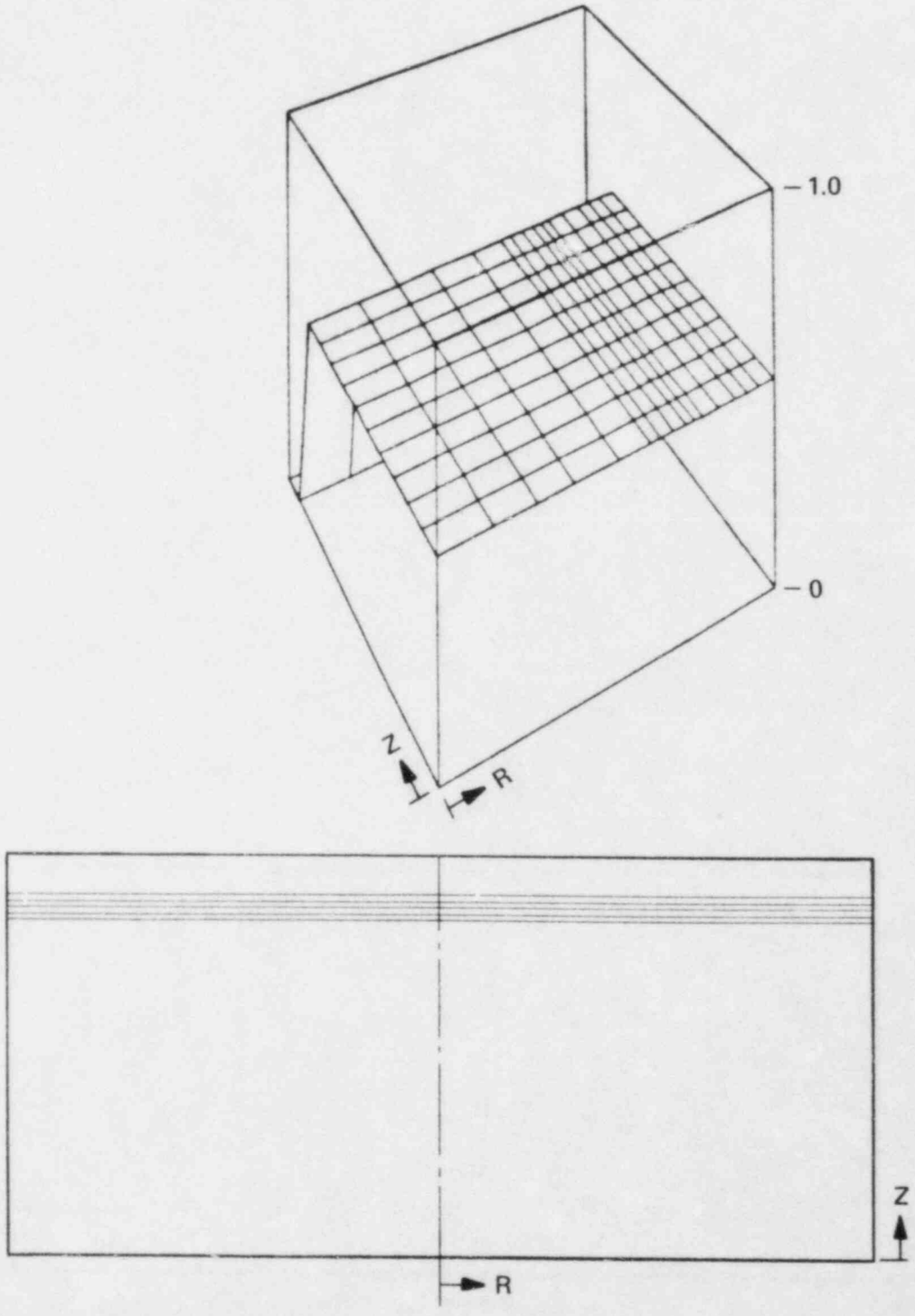

(a) Time = 0 s.

Fig. 5.
Fluid-dynamic transient for recriticality induced sloshing.

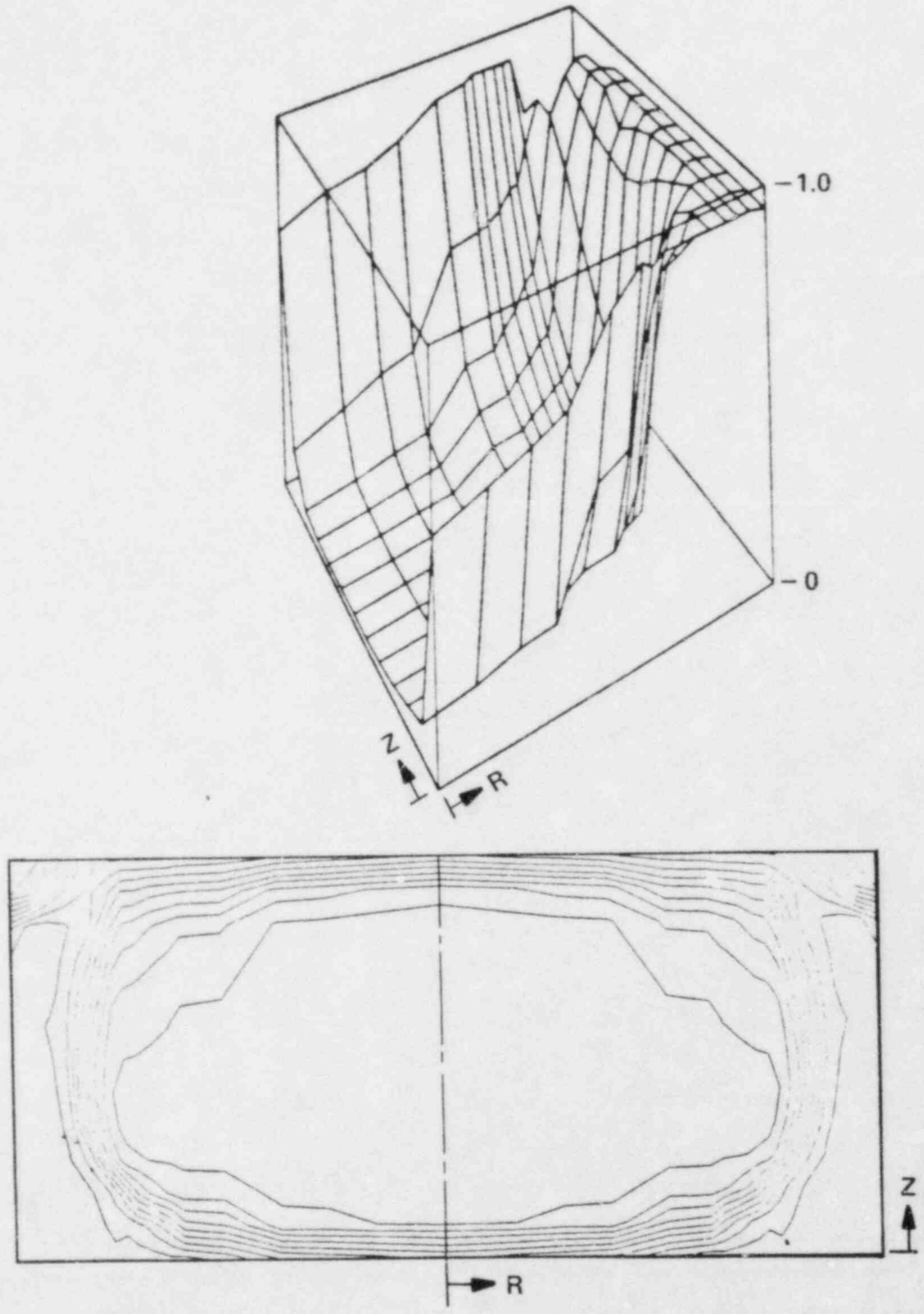

(b) Time = 1.1 s.

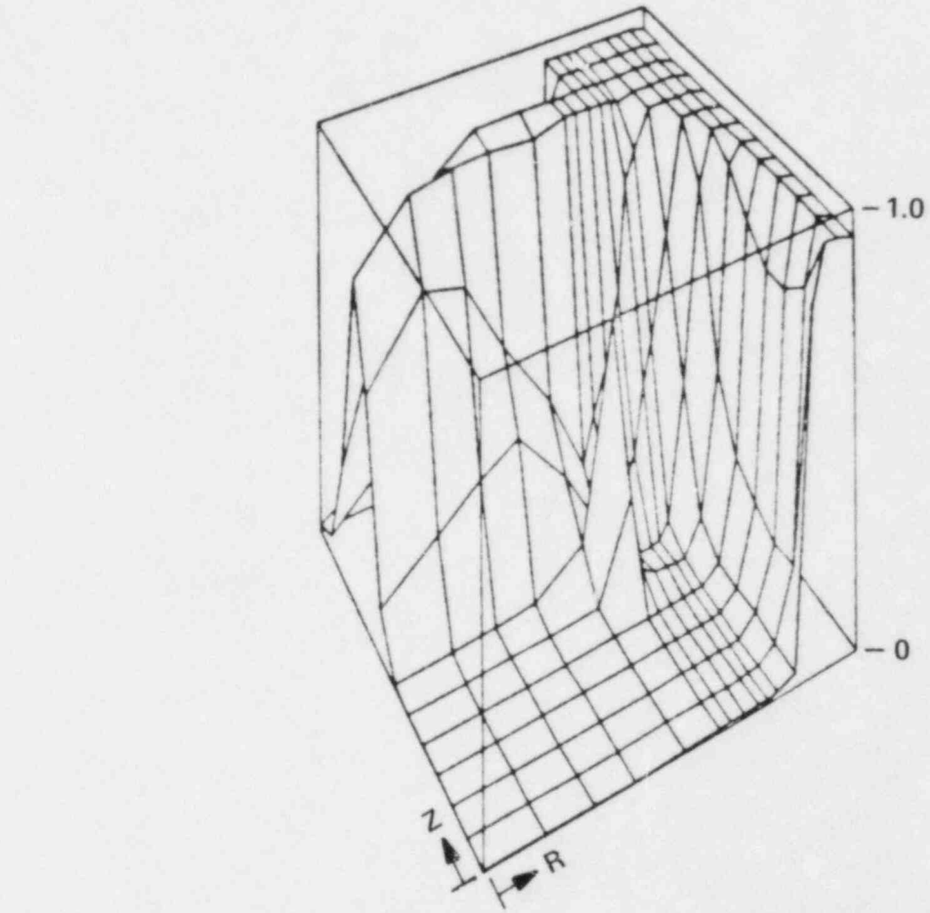

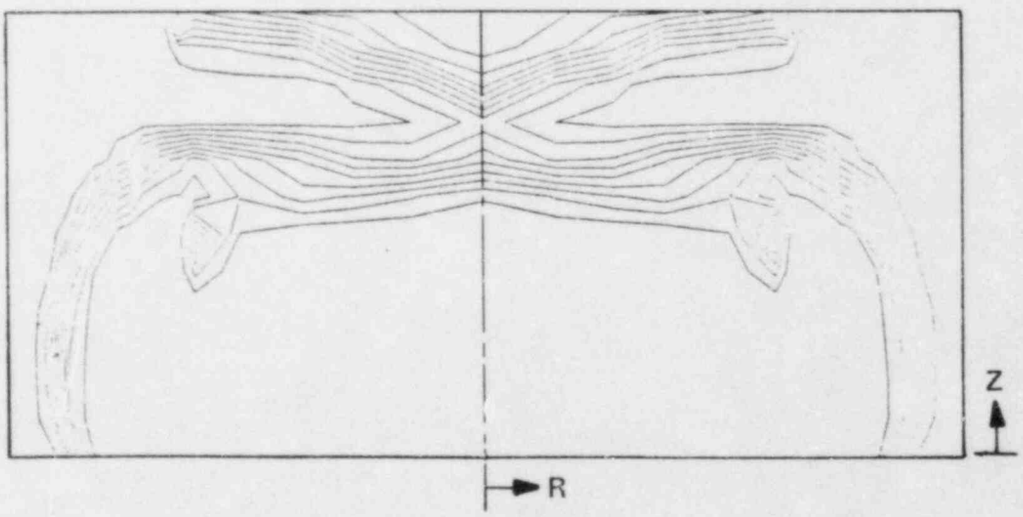

(c) Time = 0.2 s.

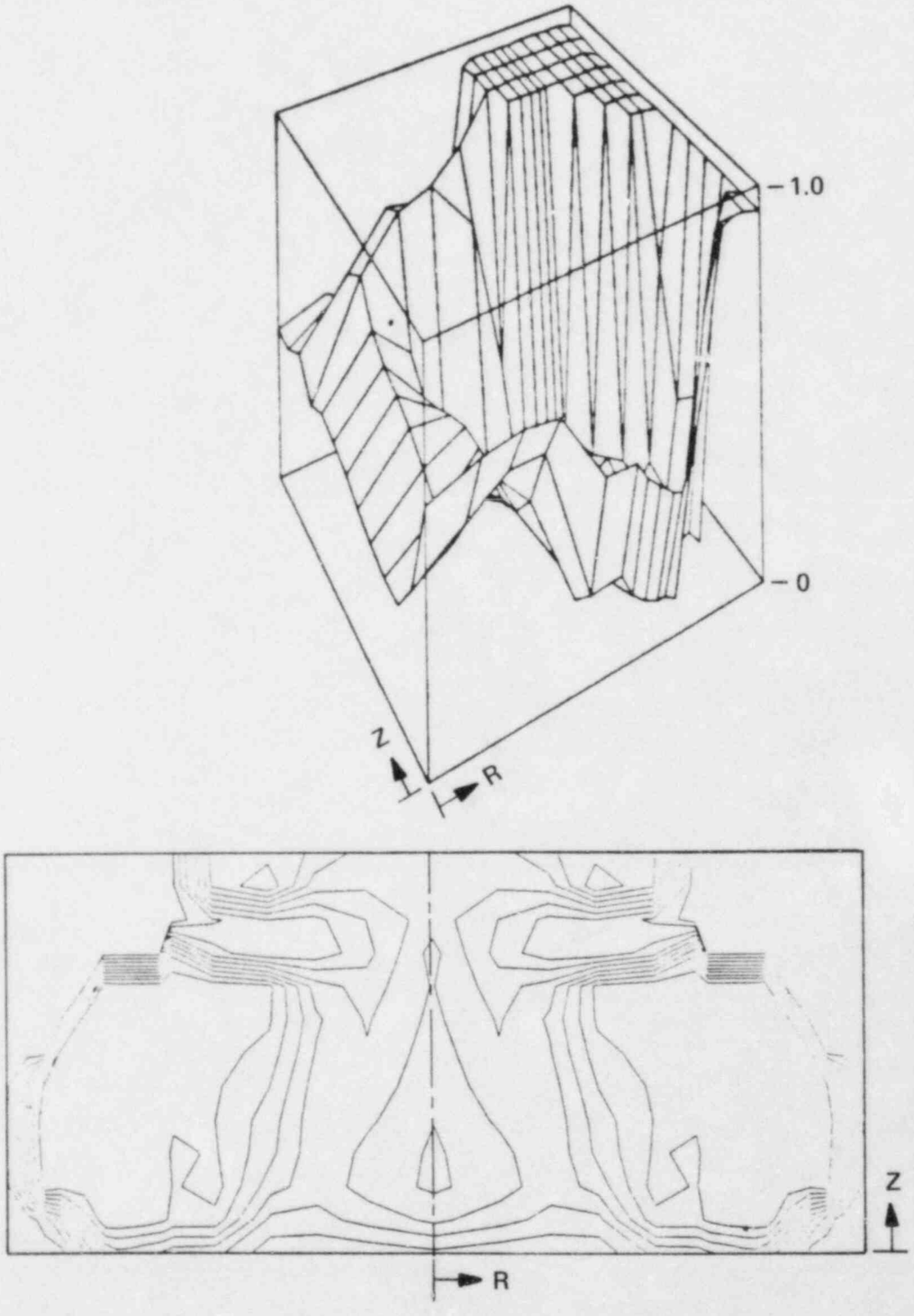

(d) Time = 0.4 s.

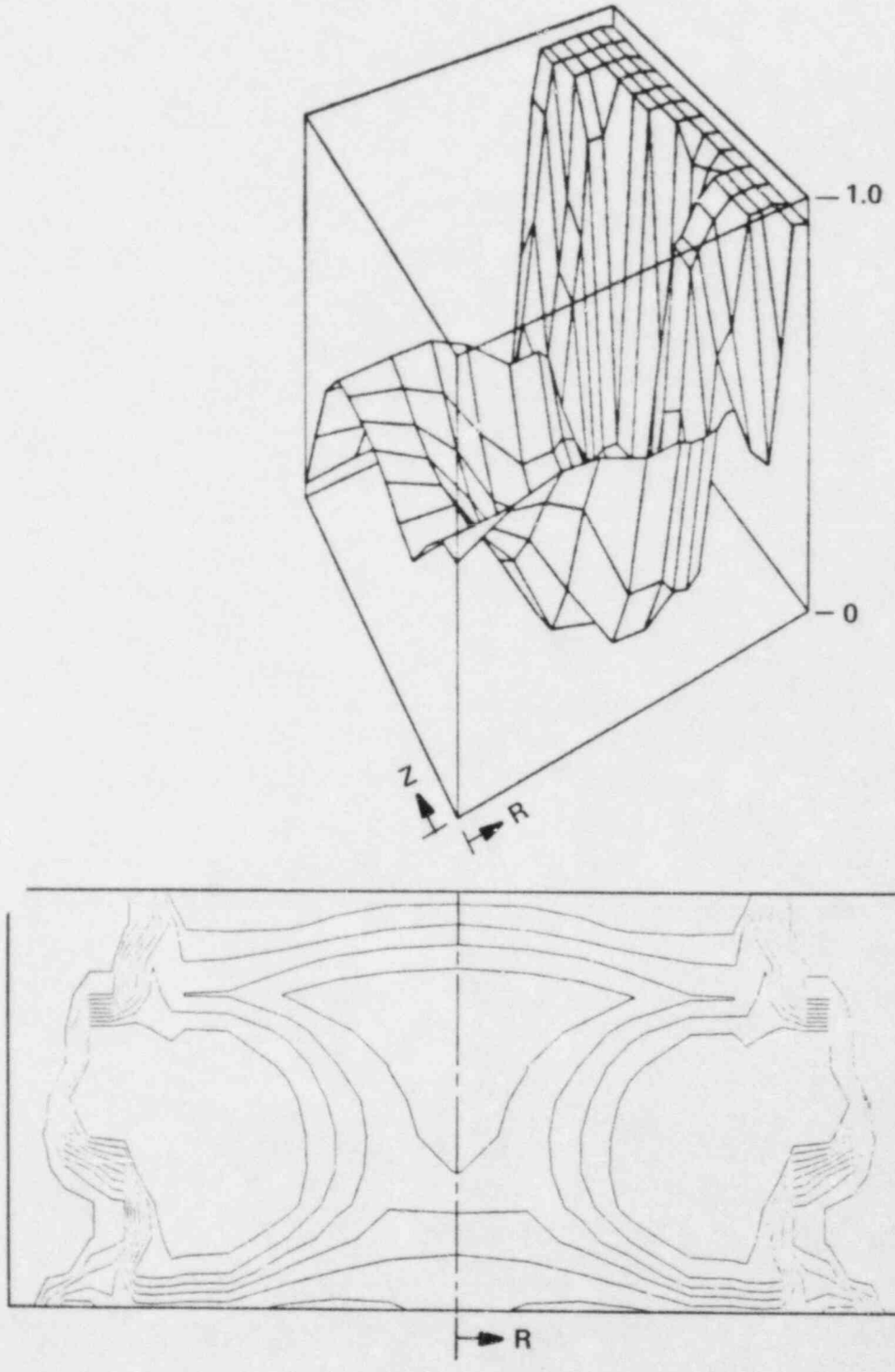

(e) Time = 0.6 s.

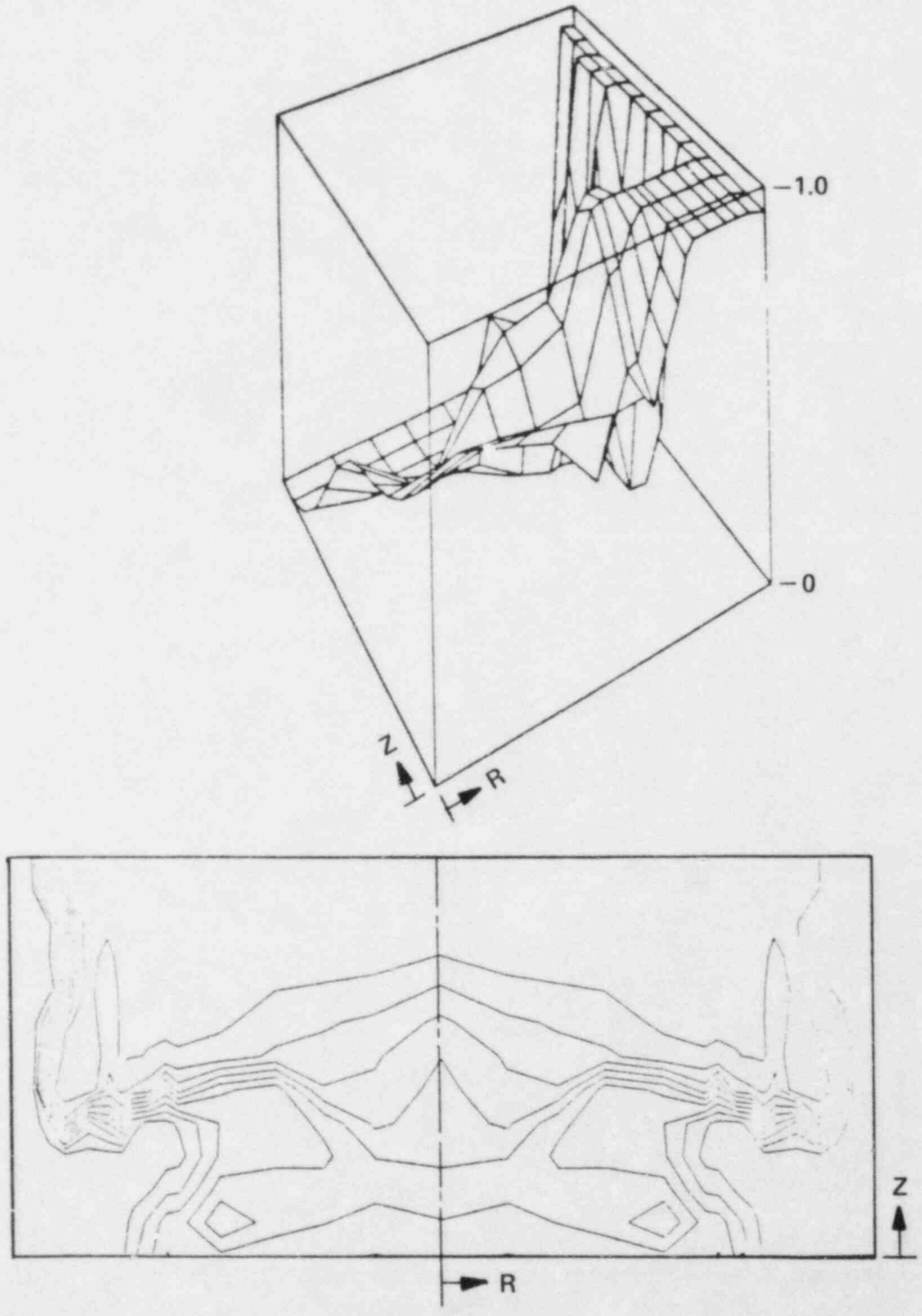

(f) Time = 0.8 s.

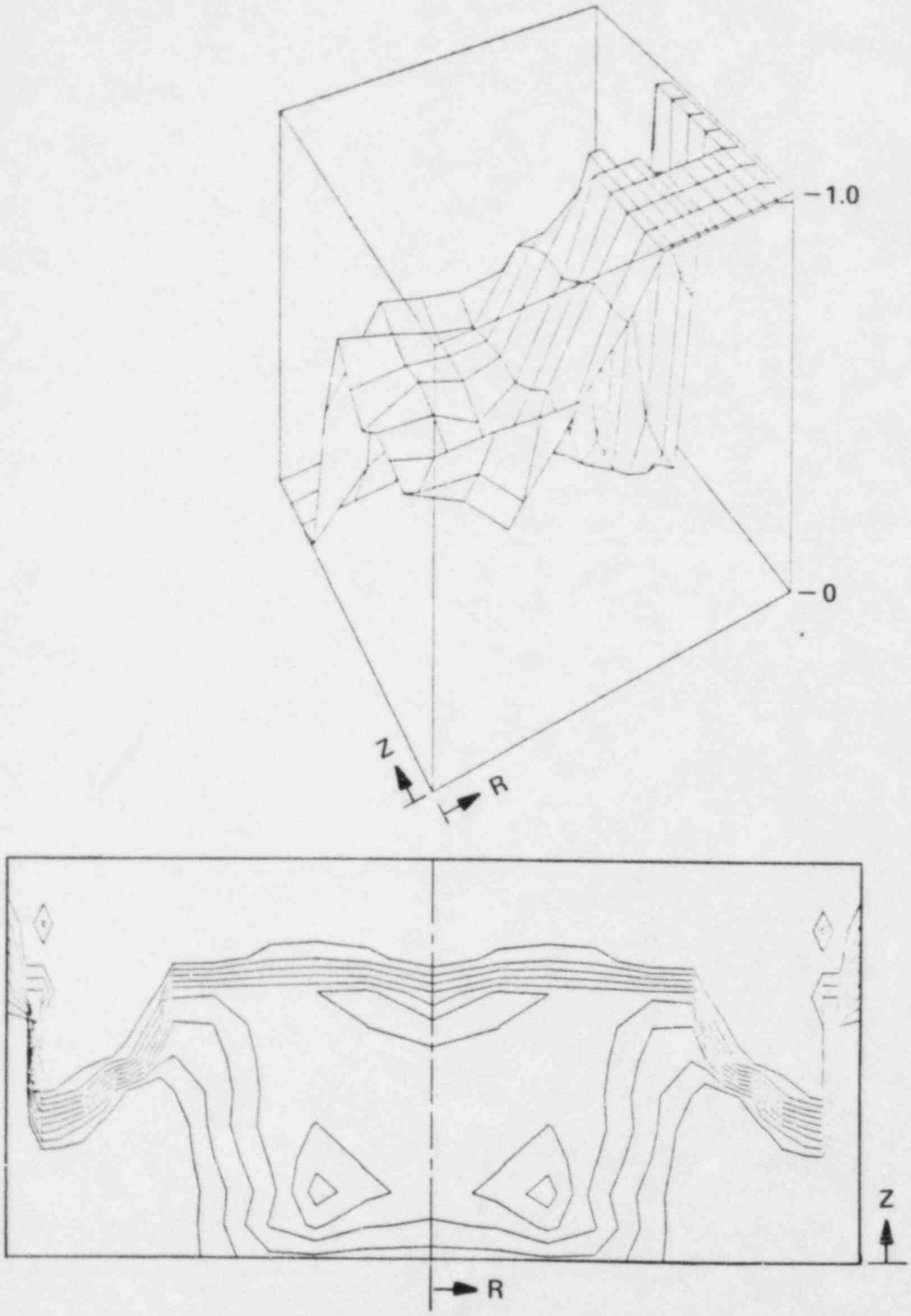

(g) Time = 1.0 s.

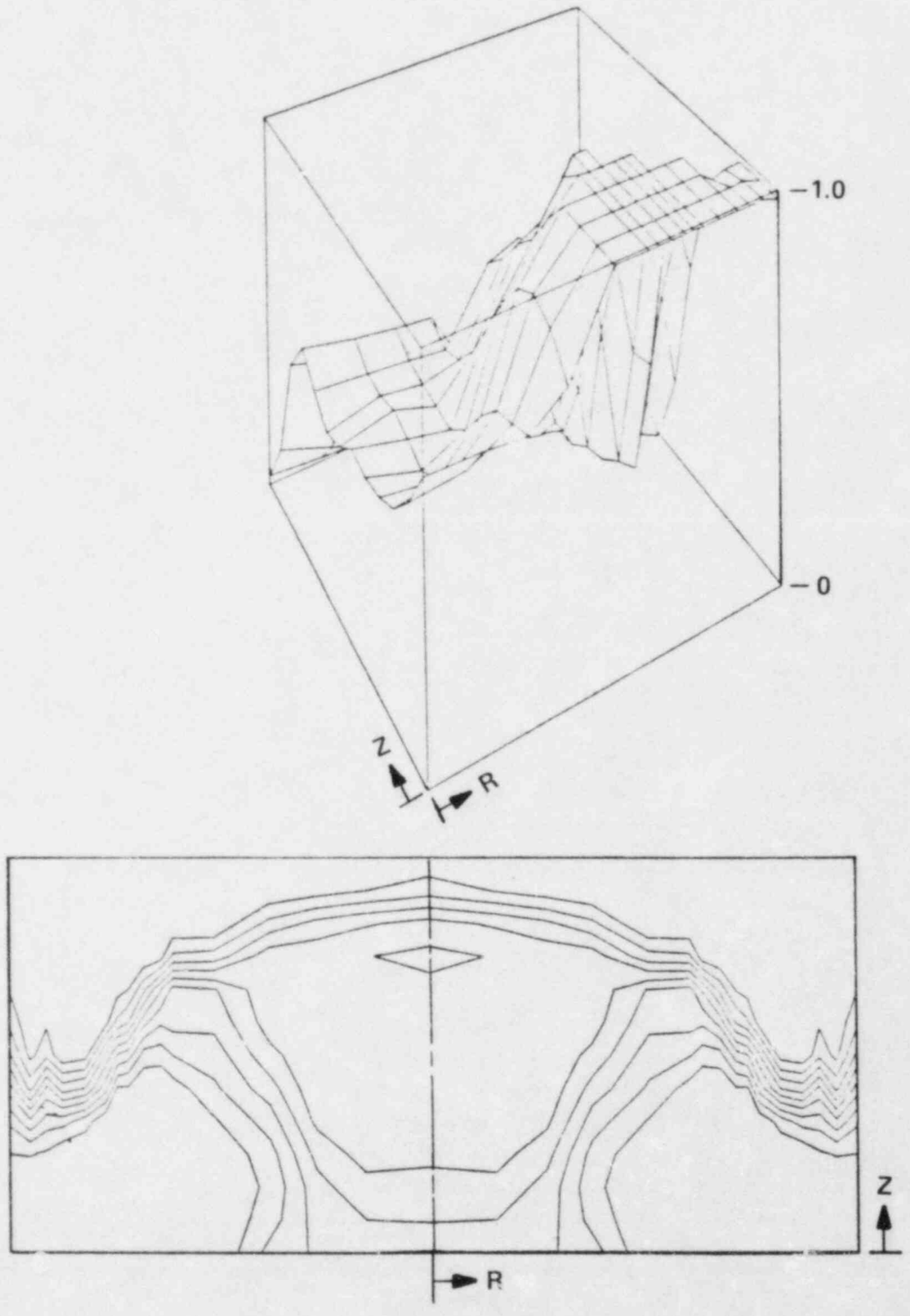

(h) Time = 1.1 s.

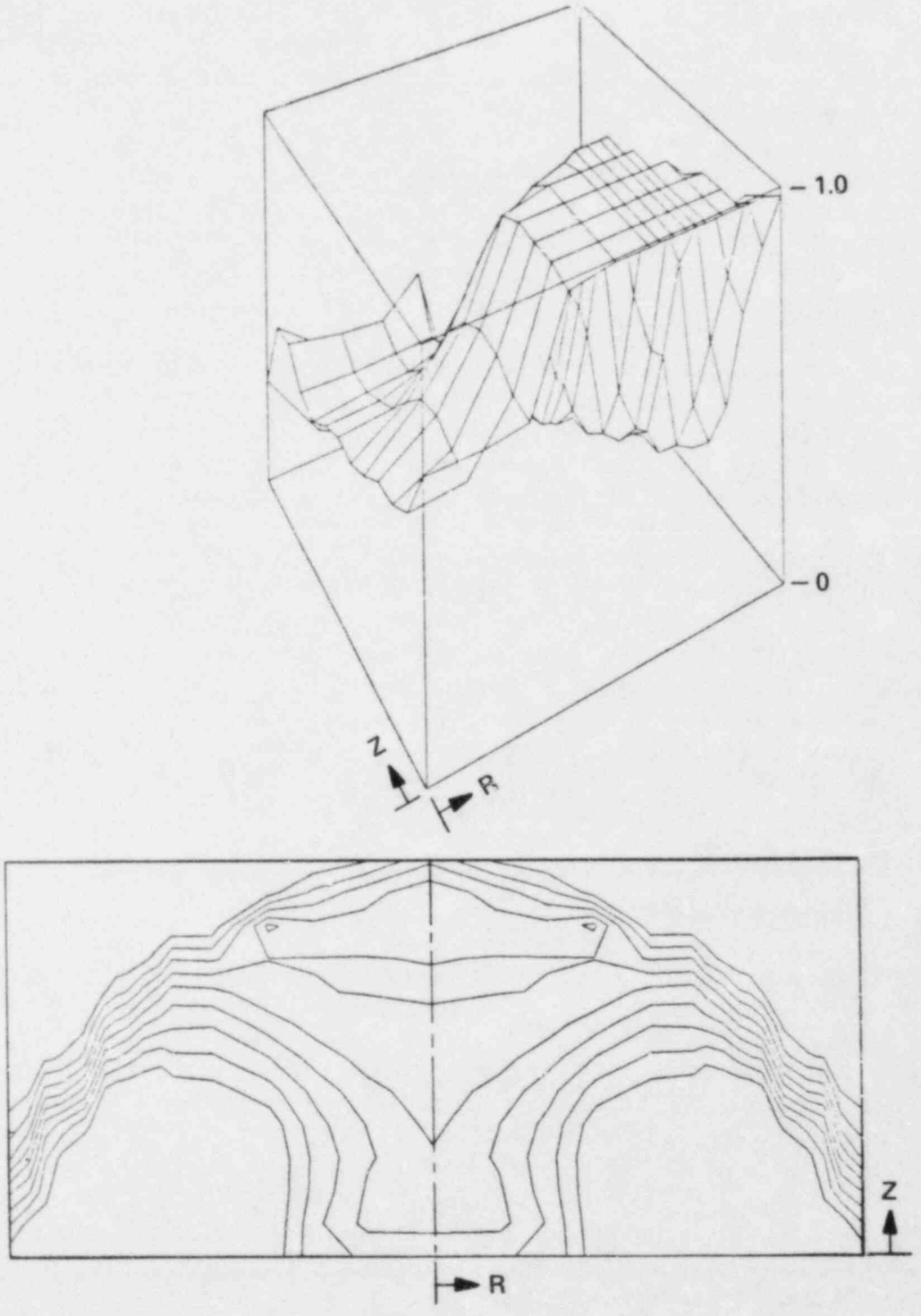

(i) Time = 1.2 s.

(radial nodes 1 through 5) having the full core height. This constant mass in-flux (approximately 2500 kg/s) to the center of the reactor suggests an increasing ramp rate as the in-slosh proceeds because of the increased differential worth that develops as the mass accumulates in the central region. This effect does not become pronounced, however, until material begins to peak in the central region (see Section II.7).

The two-phase mass in the central region of Figure 5i remained two-phase and was displaced upward by the in-slosh instead of collapsing. The fuel temperature in this region was higher than that at the outer periphery. Thus, a vapor flux was generated that maintained the dispersed state in this region.

Figures 7 and 8 show the fuel inventory and the average void fraction in the central region over a height of approximately one-third of the core (axial nodes 12 through 16). The average void in this region is important from the standpoint of energy yield for a given ramp. We saw in Appendix A that a void in the range of 20% or less will moderate the yield and its dependence on ramp rate. The recriticality at about 1.0 s had an average void in this region of about 30% and did generate a relatively large yield of about 15 FPS. The mass of the pool included the internal blankets in this case instead of the driver fuel alone that was used for the disassembly results in Appendix A and Section II.7. Thus, the equivalent energy deposition per unit mass is very similar to the 100-$/s case discussed in Section II.7 (configuration 0) for the high void situation. The important trend to note is that larger ramps require central compaction and associated reduced void. Thus, the yield is strongly moderated. This was very evident in the result of the sodium-induced sloshing case discussed next.

3.2. Sodium-Induced Sloshing

This case was initiated by assuming that 250 g of liquid sodium interacted at the bottom of the pool at its axis. The neutronic transient is shown on Figures 9 through 11. The reactivity ramp changed very rapidly from 0.40 to 0.45 s. Plots of the fuel distribution in Figure 12 show the sloshing behavior and the reassembly at the center. The resulting ramp rate was approximately 300 $/s. The integrated amplitude or energy yield was only 8 FPS.

The mass influx into the central cylinder is essentially constant (from Figure 13). Comparison of Figures 9 and 13 implies the rapid change in differential fuel worth as this central region filled.

Figure 14 shows the reason for the small energy yield for this large ramp, that is, low void fraction. This result is also consistent with those of Appendix A and Section II.7.

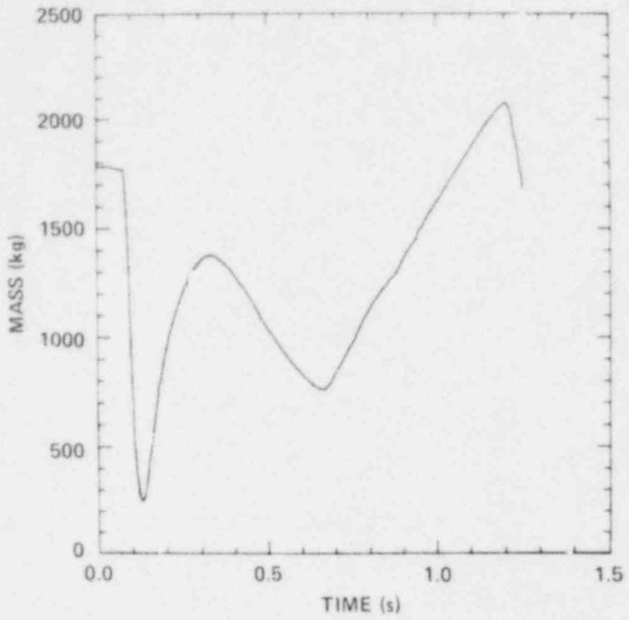

Fig. 6.
Fuel inventory transient in the central core region (radial nodes 1 through 5) for recriticality induced sloshing.

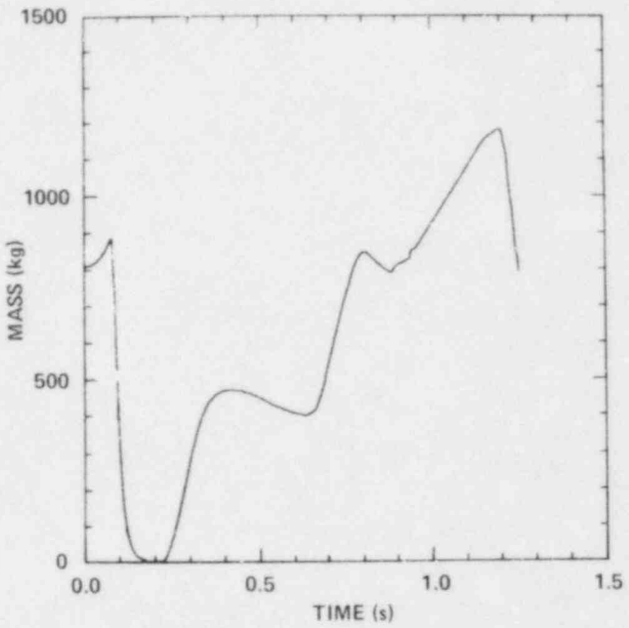

Fig. 7.
Fuel inventory transient in the lower central core region (axial nodes 12 through 16) for recriticality induced sloshing.

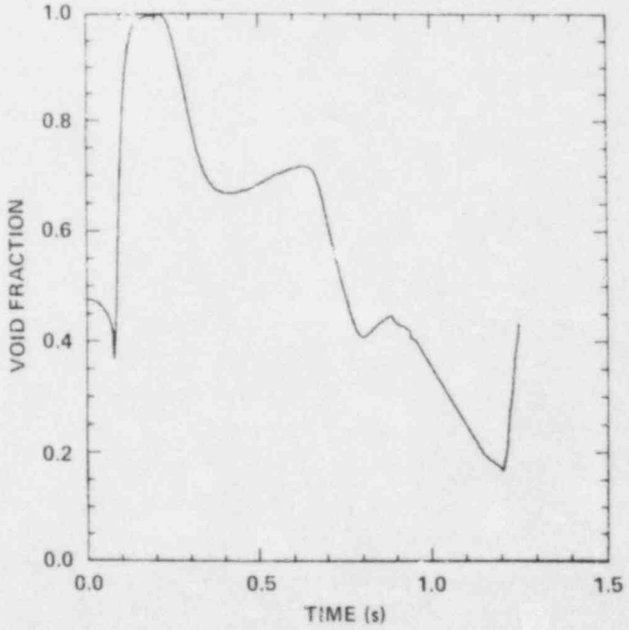

Fig. 8.
Void fraction transient in the lower central core region for recriticality induced sloshing.

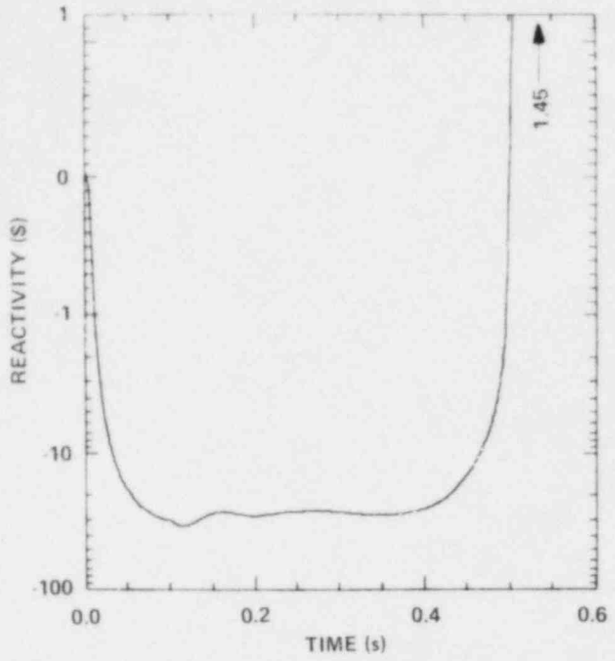

Fig. 9.
Reactivity transient for sodium induced sloshing.

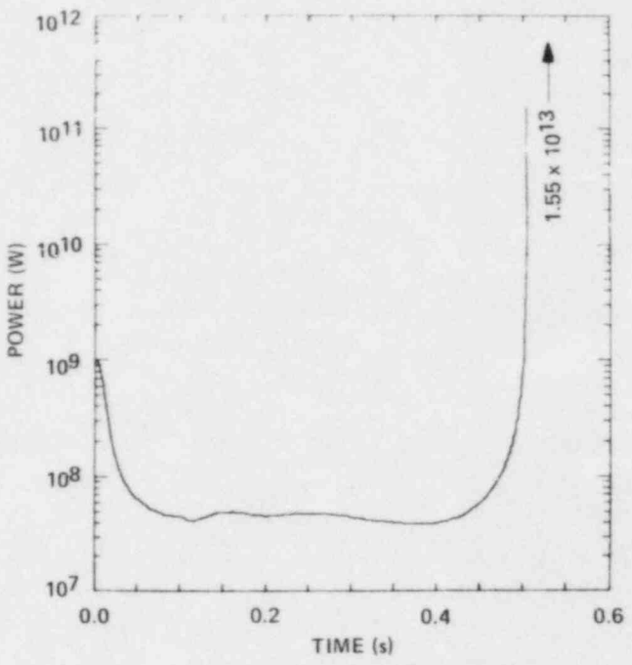

Fig. 10.
Power transient for sodium induced sloshing.

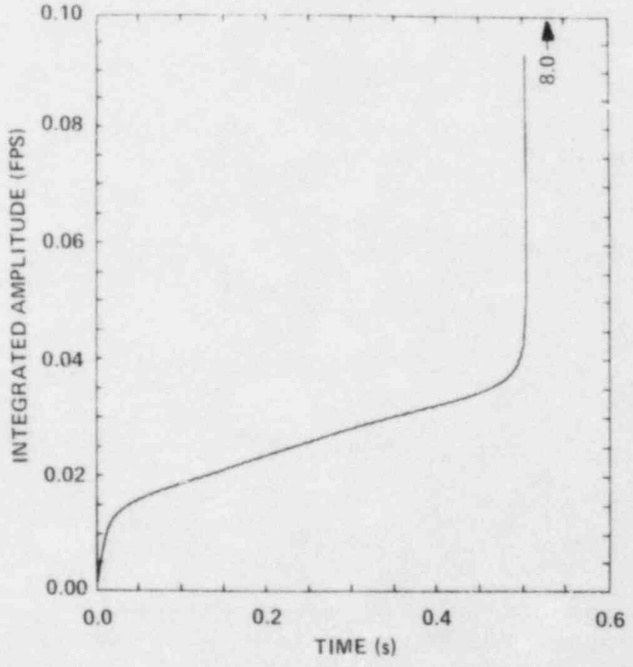

Fig. 11.
Energy yield transient for sodium induced sloshing.

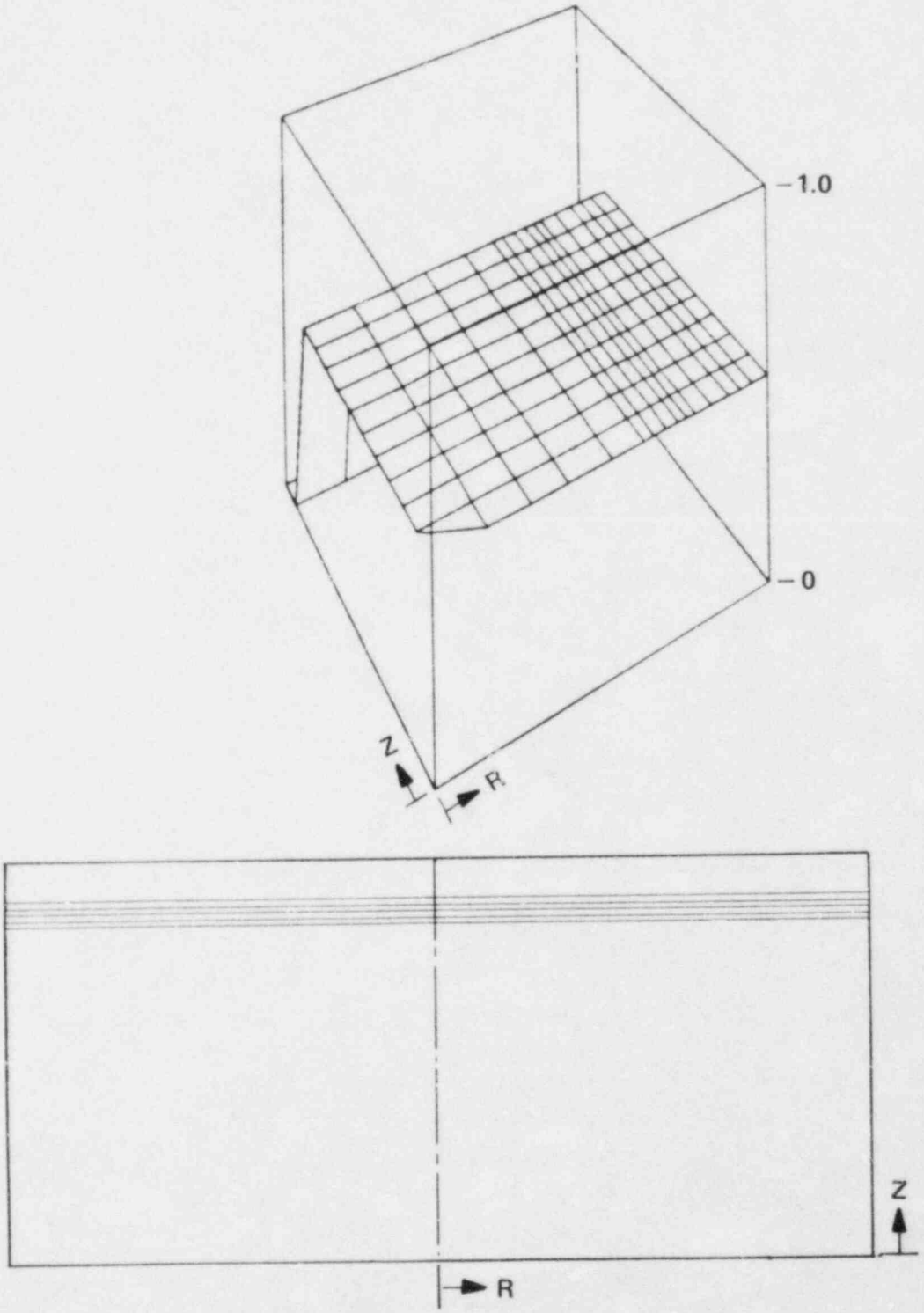

(a) Time = 0 s.

Fig. 12.
Fluid-dynamic transient for sodium induced sloshing.

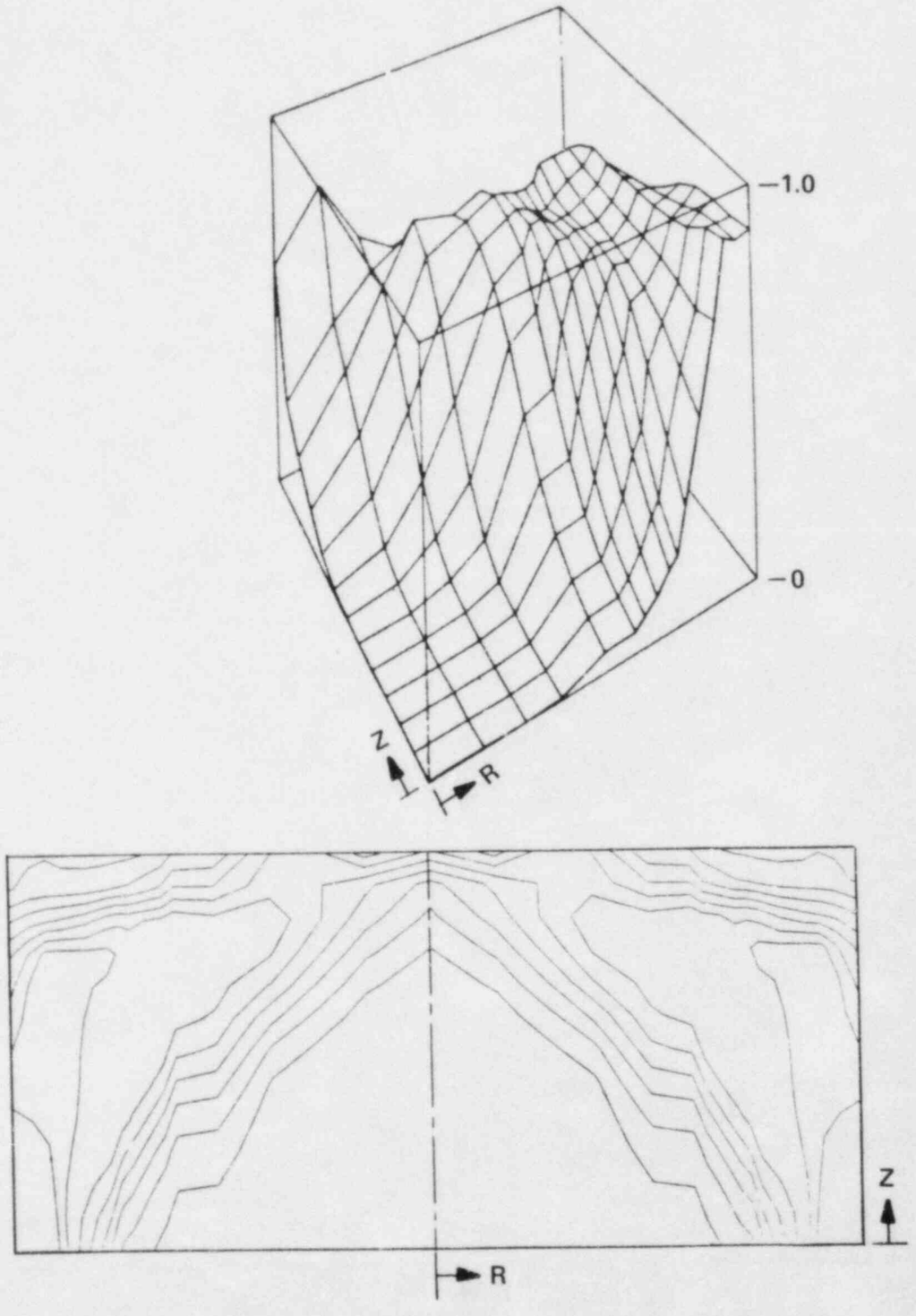

(b) Time = 0.05 s.

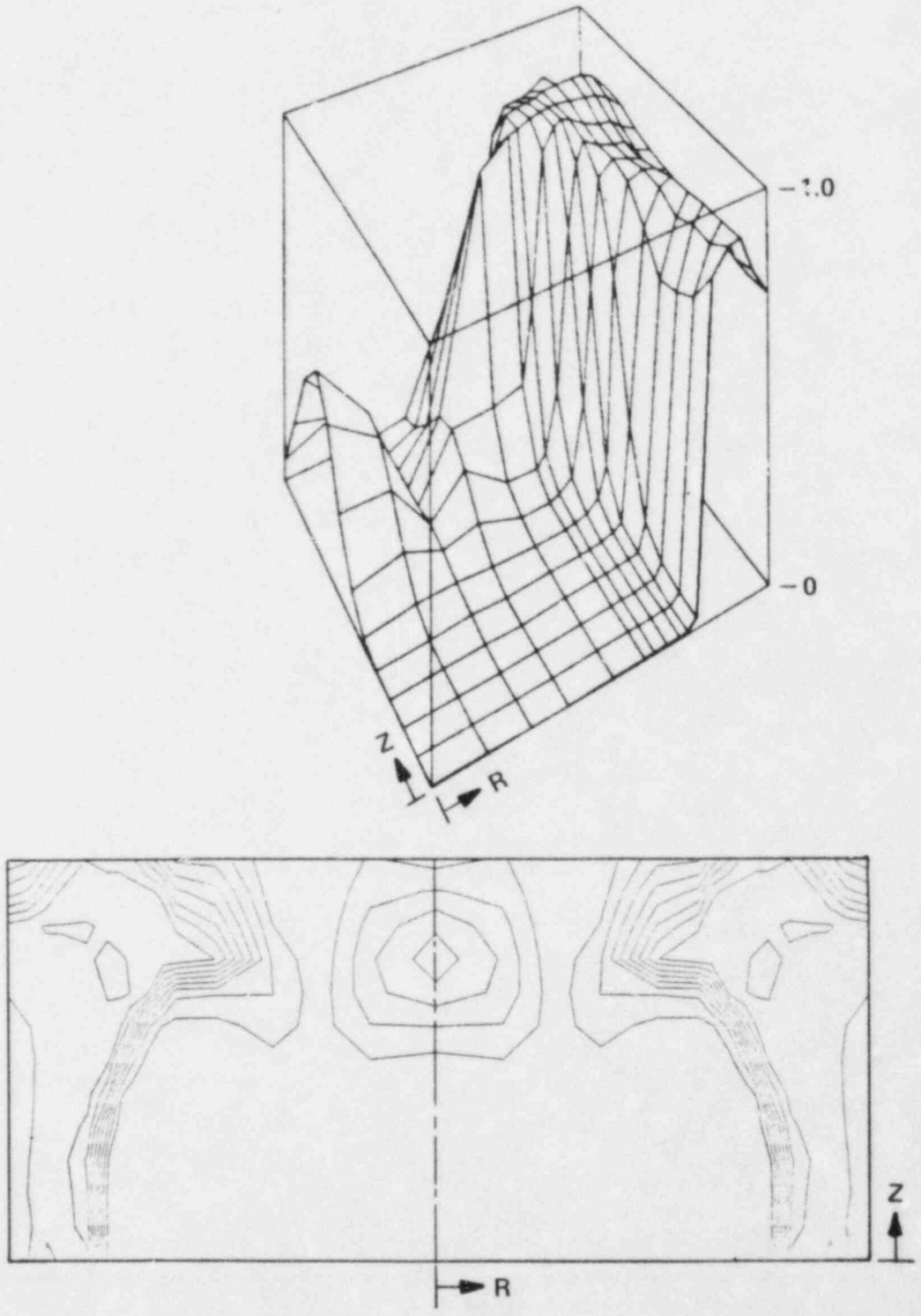

(c) Time = 0.10 s.

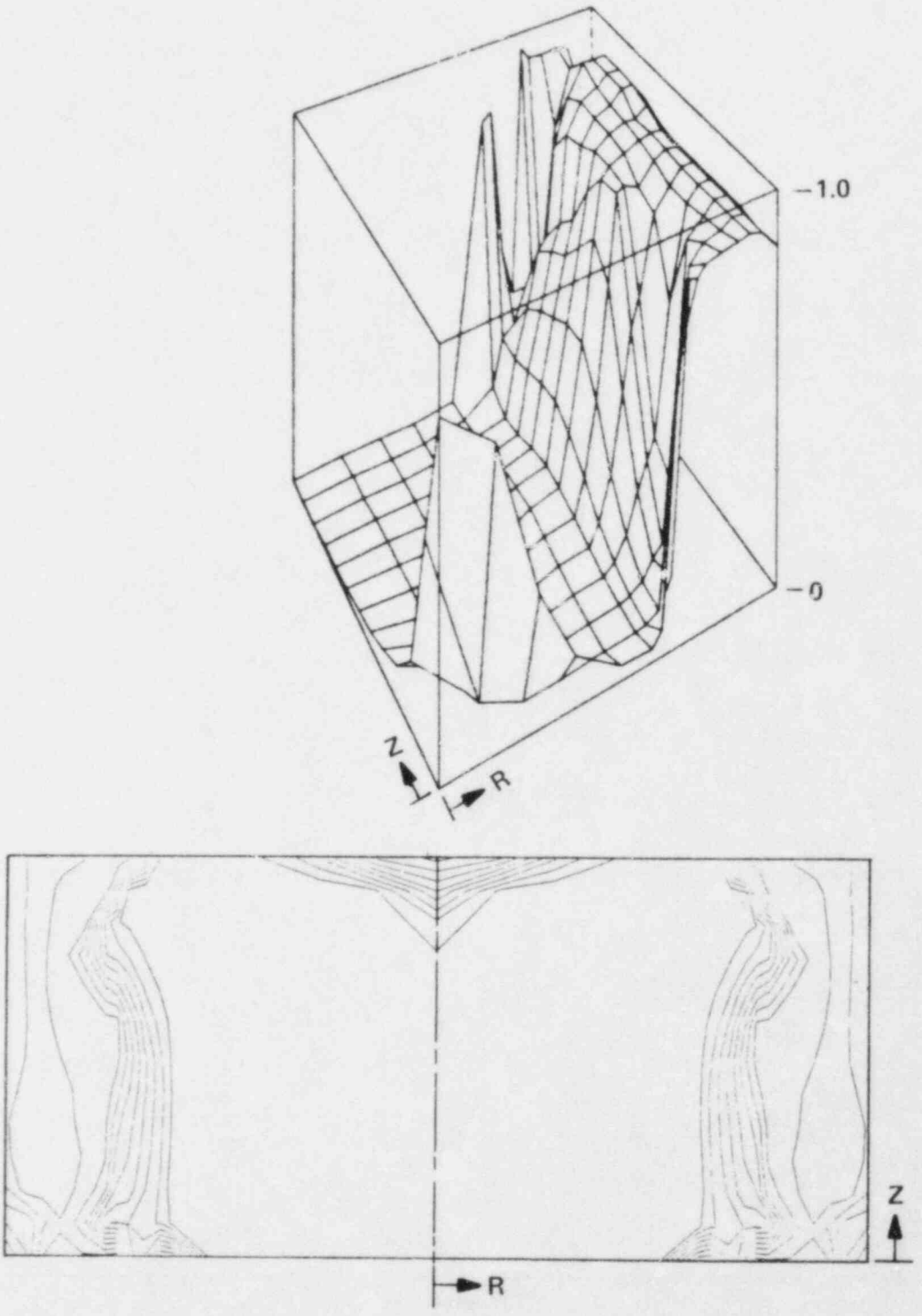

(d) Time = 0.20 s.

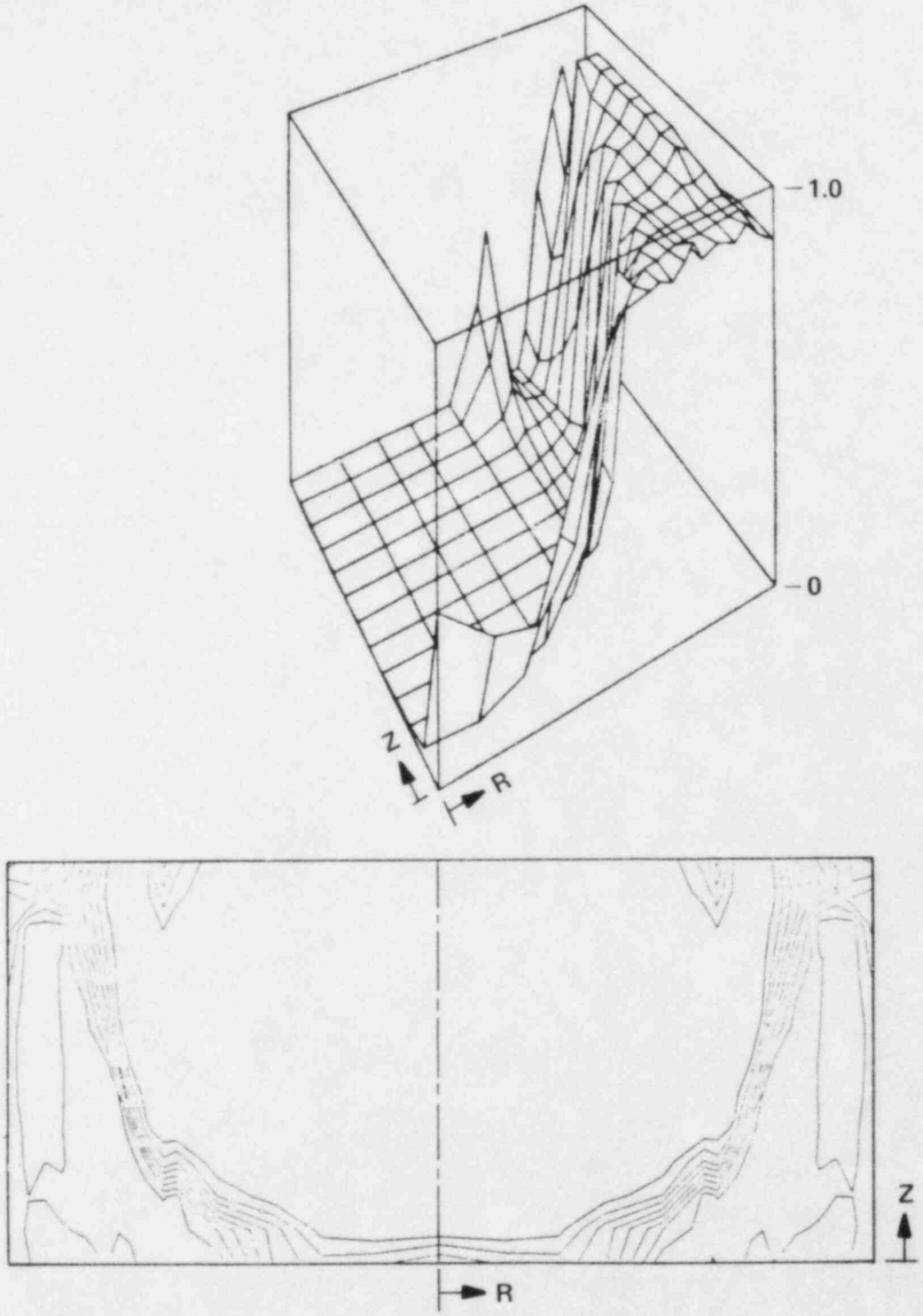

(e) Time = 0.30 s.

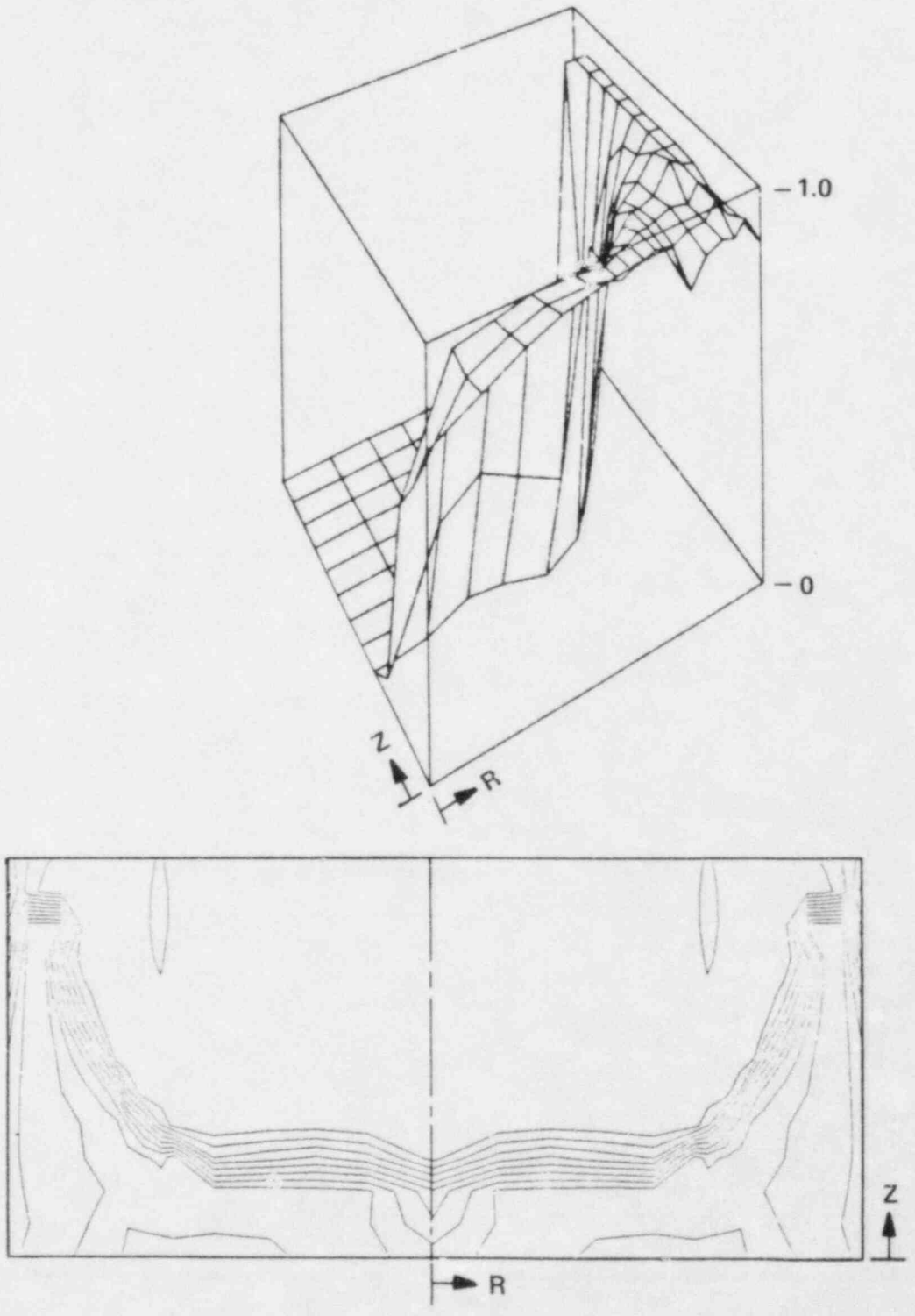

(f) Time = 0.40 s.

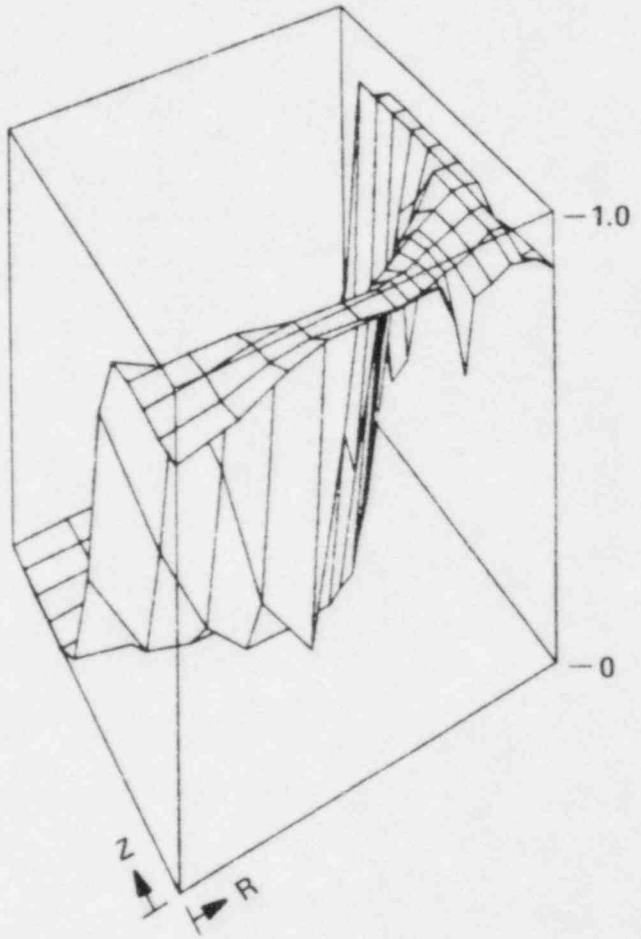

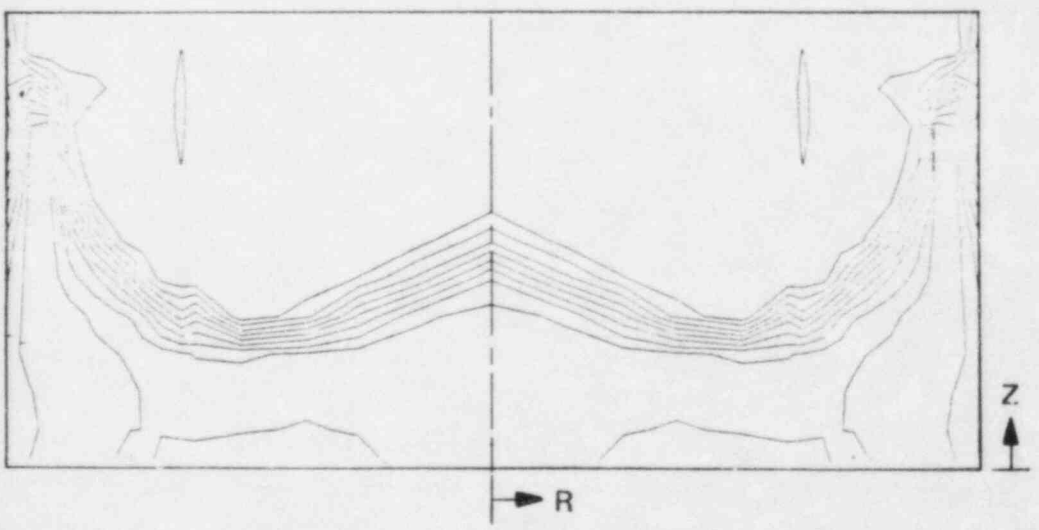

(g) Time = 0.45 s.

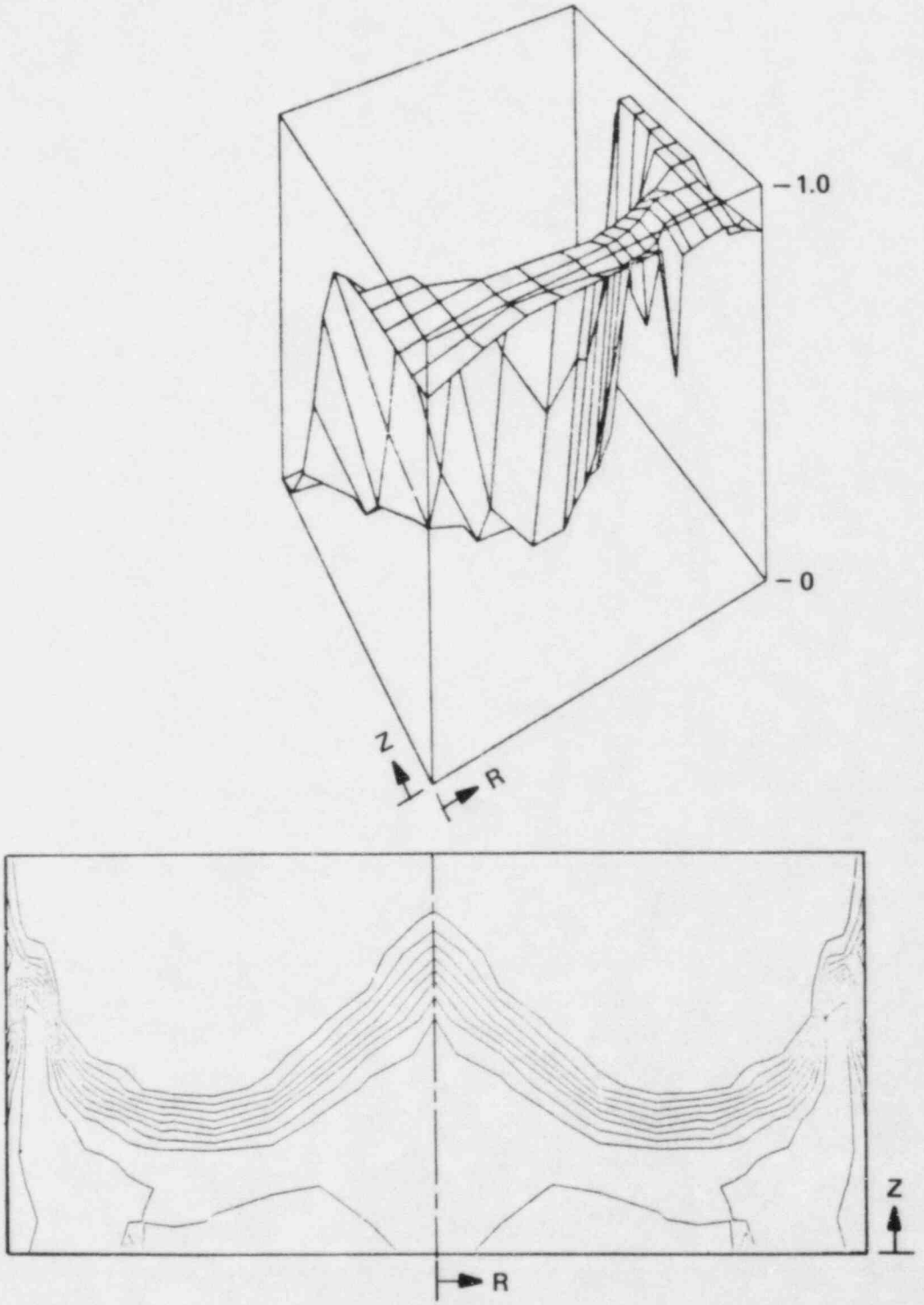

(h) Time = 0.50 s.

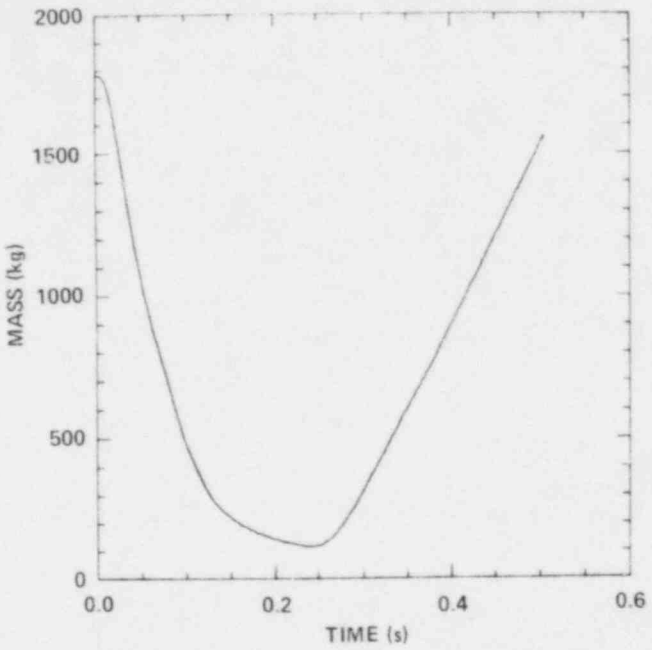

Fig. 13.
Fuel inventory transient in the central core region (radial nodes 1 through 5) for sodium induced sloshing.

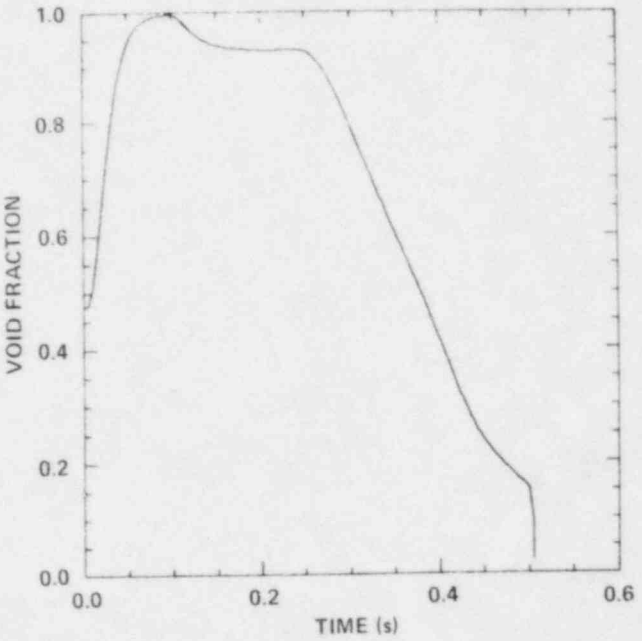

Fig. 14.
Void fraction transient in the lower central core region (axial nodes 12 through 16) for sodium induced sloshing.

4. Experimental Benchmarking

To benchmark the capability of SIMMER-II to adequately assess sloshing behavior (fluid dynamics), a series of experiments was conducted in the existing OMEGA facility [6] (see Figures 15 and 16) at Purdue University. An experiment simulating whole-core, centerline perturbed sloshing was analyzed with SIMMER-II.

The experiment was run with a 0.9-m diameter by 0.3-m deep water pool. The cover gas space above the pool was also 0.3 m. This pool depth and cover gas space represent the reactor core in full scale with a midplane (in the pool) induced slosh such as a recriticality. The diameter is about one-half of full reactor scale. The slosh was induced by introducing nitrogen gas at the bottom centerline of the pool through a rupture disc arrangement. The volume of gas (0.005 m^3) and the initial pressure (approximately 0.7 MPa) were selected to give a gentle perturbation to the pool, thereby assuring good data resolution (high speed photography) during the initial expansion phase. Indeed, this was accomplished. Very clear results for bubble growth, pool surface displacement, and bubble collapse were obtained. The bubble growth contours as a function of time are shown in Figure 17 and the upper surface displacement at the centerline is shown in Figure 18. The upper surface shape is given in Figure 19.

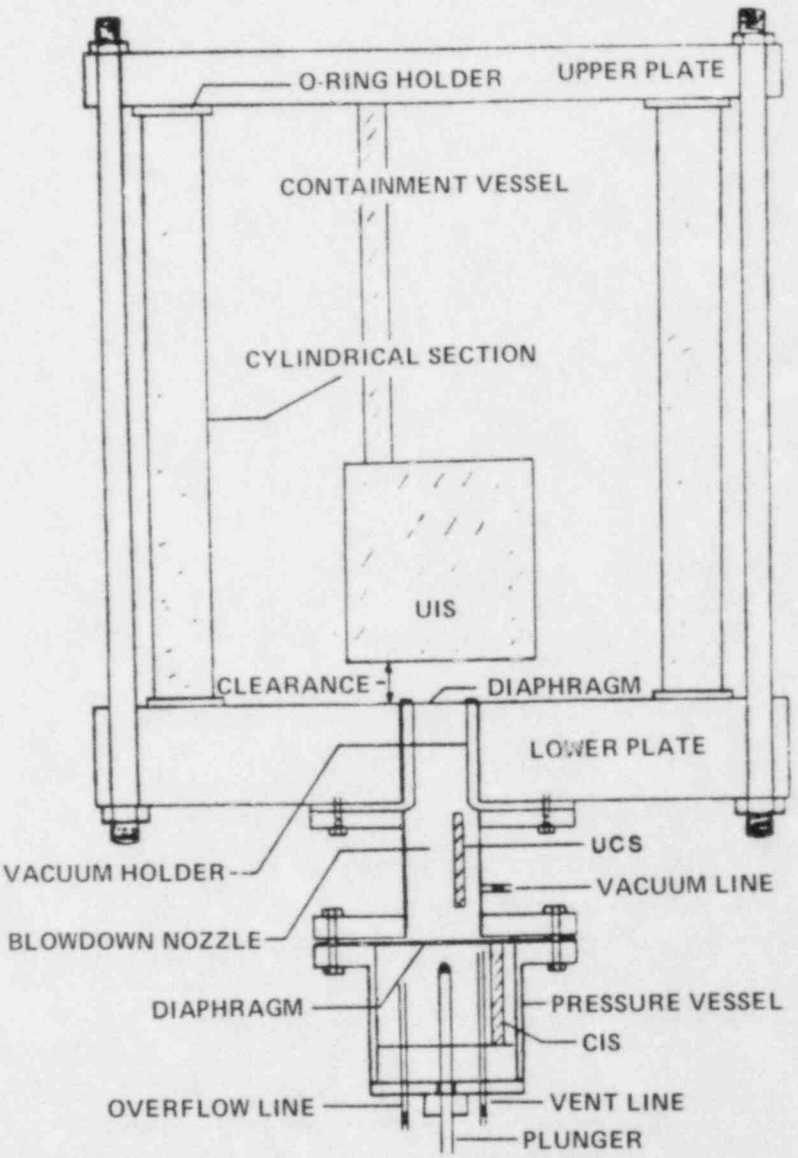

Fig. 15.
Schematic of the OMEGA test section.

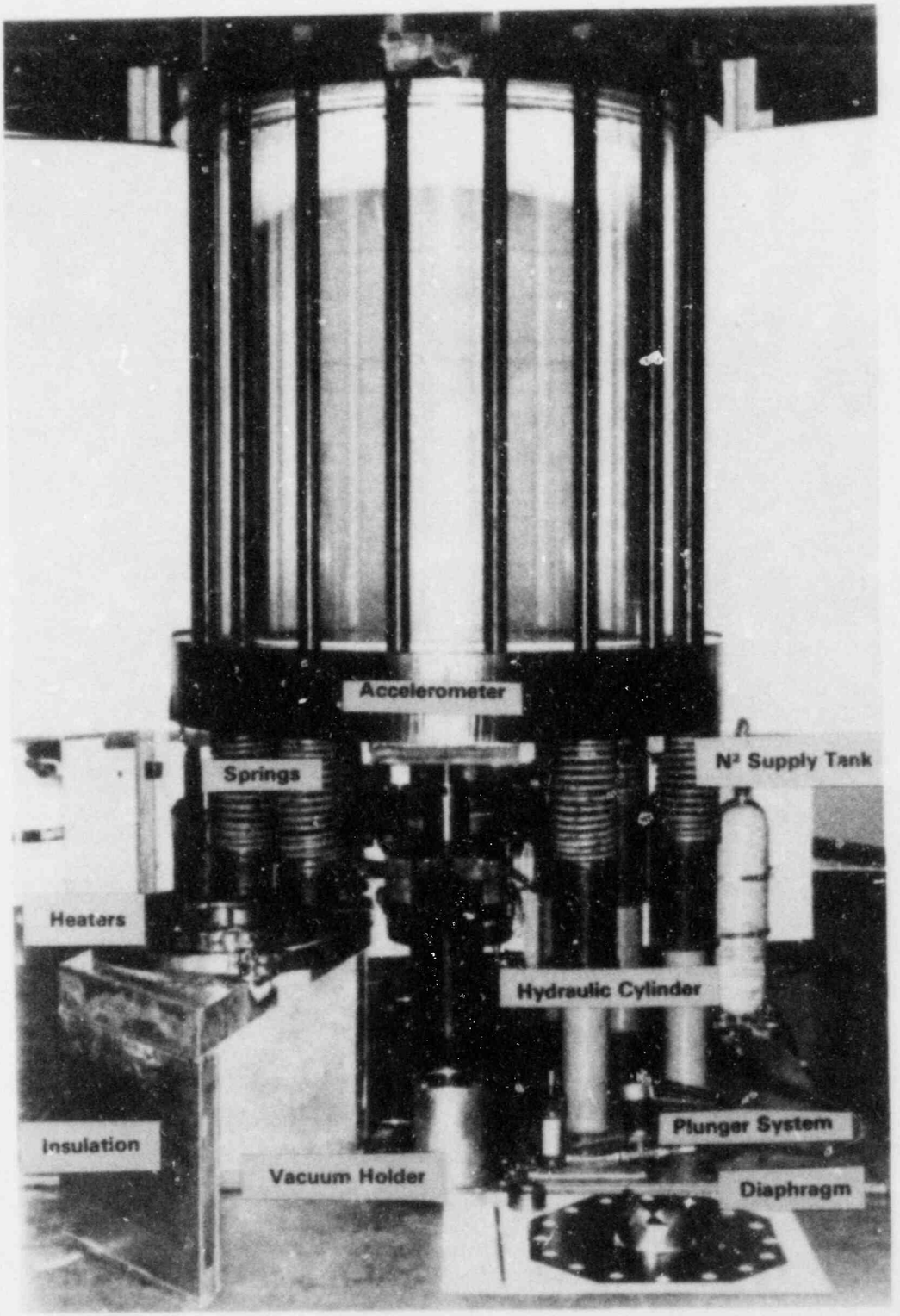

Fig. 16.
The OMEGA experimental facility.

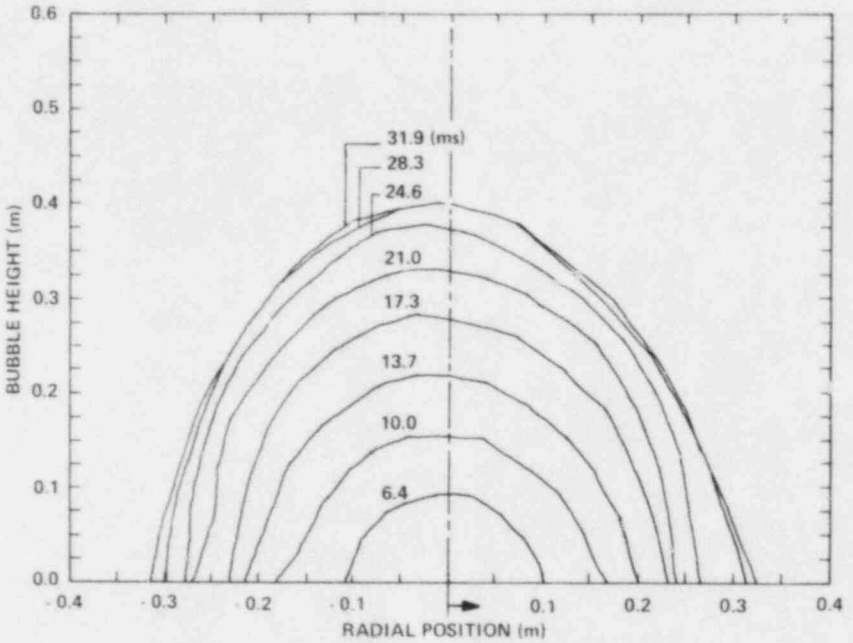

Fig. 17.
Bubble growth contours vs. time.

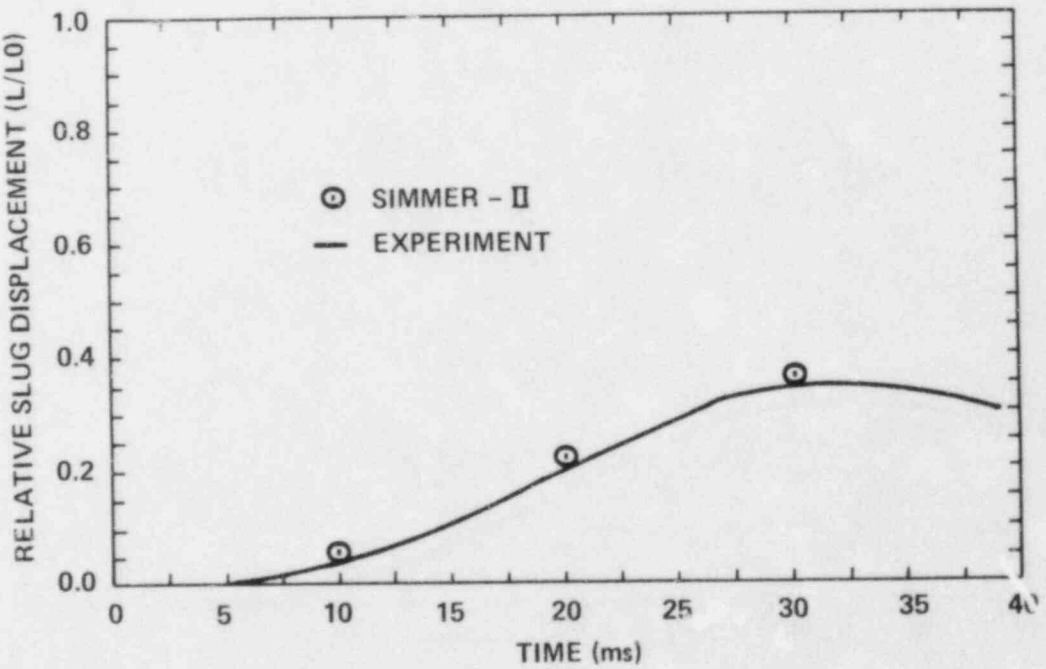

Fig. 18.
Comparison of SIMMER-II predicted pool upper surface displacement with experimental data.

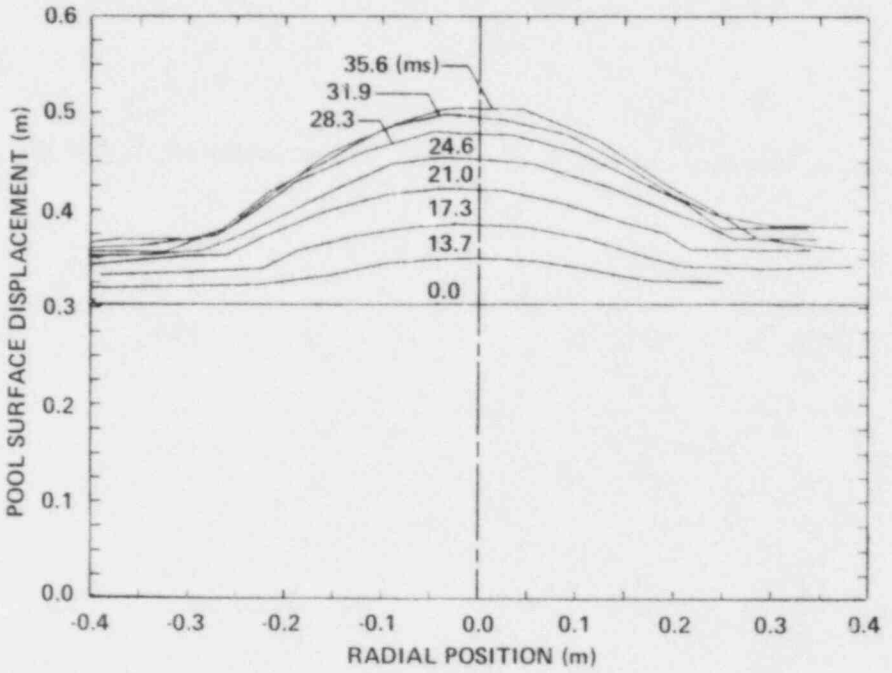

Fig. 19.
Pool upper surface contours vs. time.

A SIMMER-II model of the experiment was generated that included the nitrogen source and the complete pool (and cover gas). Node sizes in the pool and cover gas were 0.02 m axially and 0.02 m radially. The calculation was initiated at the time of rupture disc failure in the experiment.

The calculated upper surface displacement at the centerline is shown in Figure 18 as the circles. The agreement is excellent. We obtain an additional view of the agreement by comparing Figures 17 and 19 with the sequence of calculated bubble and surface contours in Figure 20. The initial state is shown in Figure 20a. The growth shape in both experiment and calculation was very close to hemispherical. The maximum growth occurred at about 30 ms in both and the bubble collapse was nearly identical in both.

These results indicate that SIMMER-II performs very well in the early bubble growth phase of a slosh. It is during this phase that the momentum is produced in the liquid, thereby setting the stage for the subsequent in-slosh.

5. Summary

Whole-core, centerline-induced sloshing does have the potential to produce high ramp rate events. The configuration and extent of the in-slosh are of major importance in determining the magnitude of the ramp rate and

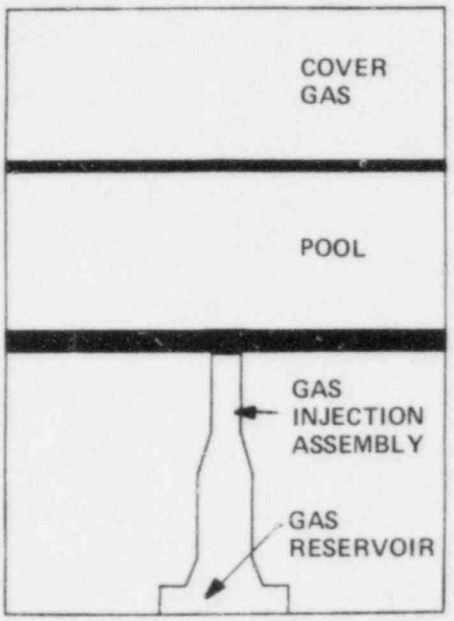

(a) Time = 0 ms.

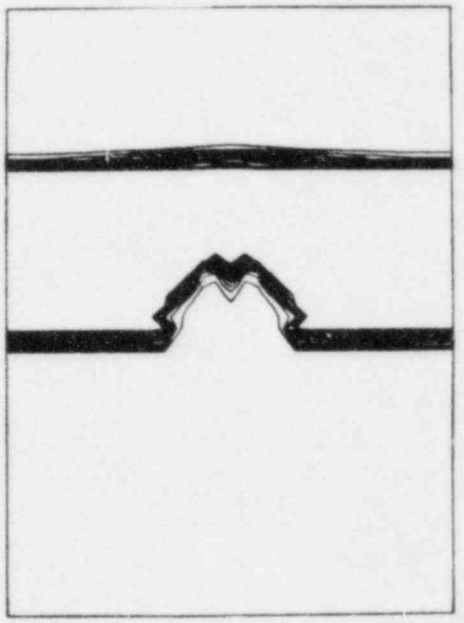

(b) Time = 10 ms.

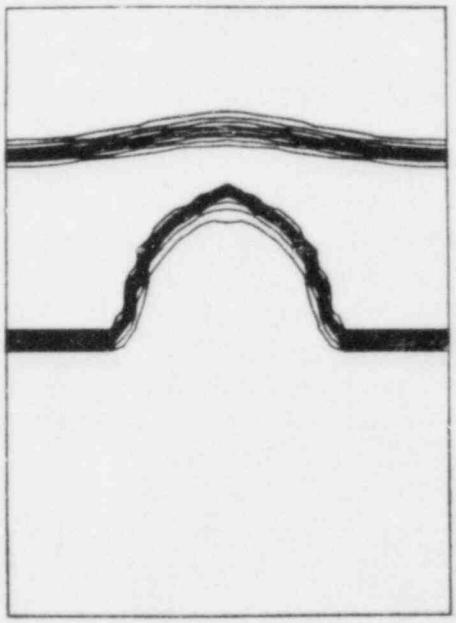

(c) Time = 20 ms.

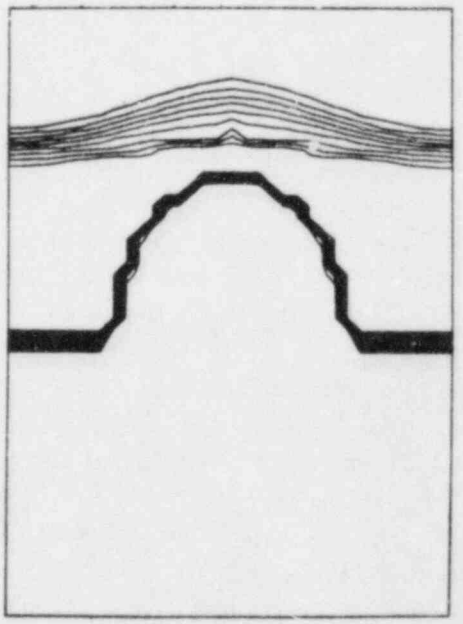

(d) Time = 30 ms.

Fig. 20.
Calculated fluid-dynamic transient for the OMEGA pool experiment.

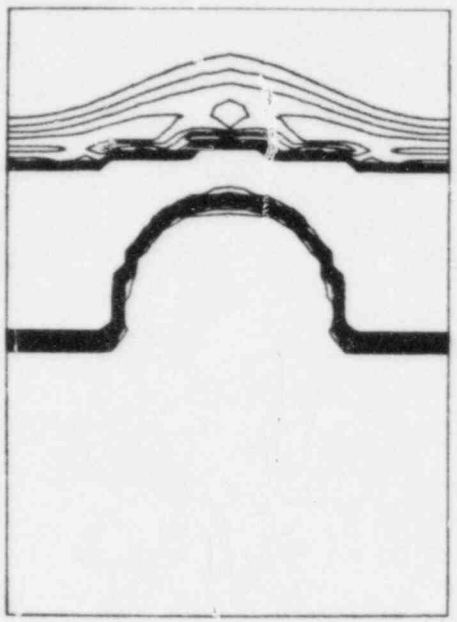

(e) Time = 40 ms.

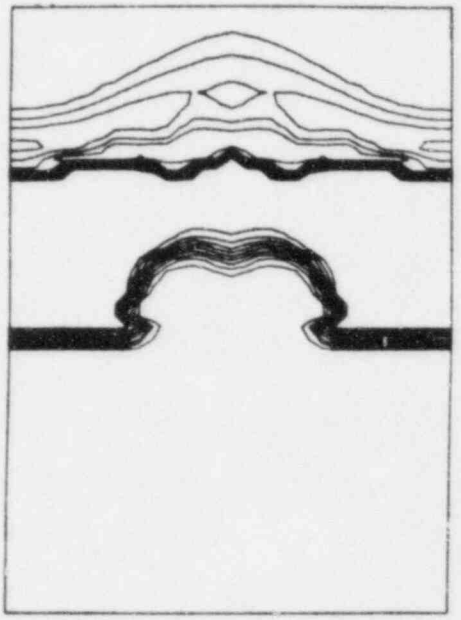

(f) Time = 50 ms.

(g) Time 60 ms.

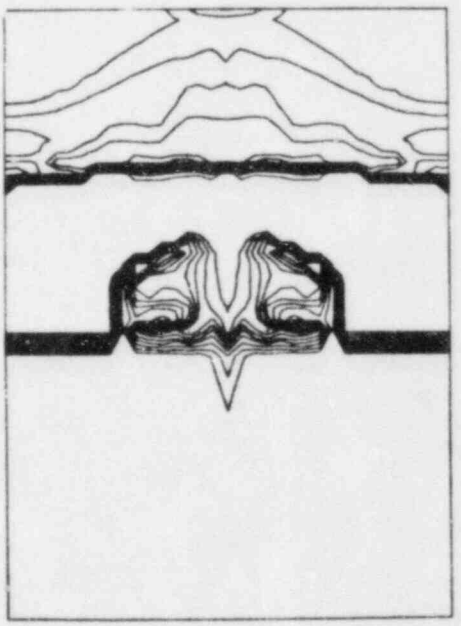

(h) Time = 70 ms.

(i) Time = 80 ms.

the energy yield. There is a connection between high ramp rates (300 $/s) and the accumulation of a dense (low void) mass of fuel at the centerline of the pool. The dense mass produces large worth gradients near the centerline region such that further influx of mass has a large reactivity effect. The existence of this dense region offsets, however, the large ramp in terms of energy yield.

The benchmarking activity performed as part of the independent assessment of CRBR energetics indicates that SIMMER-II can adequately address and quantify pool sloshing recriticalities.

6. References

1. M. G. Stevenson, "Nuclear Reactor Safety Quarterly Progress Report, April 1-June 30, 1982," Los Alamos National Laboratory report NUREG/CR-9814, LA-9556-PR (November 1982).

2. L. L. Smith, "SIMMER-II: A Computer Program for LMFBR Disrupted Core Analysis," Los Alamos National Laboratory report NUREG/CR-0453, LA-7515-M (June 1980).

3. C. R. Bell, "A Calibration of the SIMMER-II Boilup Capability," Trans. Am. Nucl. Soc. 39, 662 (1981).

4. P. E. Rexroth and V. Starkovich, "Two-Phase Momentum Exchange Experiment and Analysis," Trans. Am. Nucl. Soc. 28, 445 (1978).

5. James F. Dearing, "SIMMER-II Analysis of Short-Risetime, Two-Component, Transient Boilup-Up Pool Simulation Tests," Los Alamos National Laboratory report LA-9736-MS (May 1983).

6. J. J. Simpson, M. Saito, and T. G. Theofanous, "The Termination Phase of Core Disruptive Accidents in LMFBRS," Purdue University report PNE-81-151 (June 1981).

APPENDIX D
WHOLE-CORE DISASSEMBLY ANALYSIS

1. Introduction

In this Appendix we present the model used to assess the energy yield characteristics of whole-core disassemblies for postulated disrupted core states. We also discuss the initial conditions used and the method of reactivity insertion. The four configurations investigated are shown in Figure 9 of Section II.7. They will be described in more detail here.

2. Analysis Model

The analysis model for these disassembly calculations with SIMMER-II [1] was adapted from that used for a previous assessment of intersubassembly gap fuel removal [2]. The calculational model is the same as that shown in Figure 1 of Appendix C. The region characteristics (Table 1) are the same as in Reference 2 except for the active core regions 1 through 12. The specific characteristics of these regions were varied depending on the configuration simulated (intact pin structure, totally disrupted, or totally disrupted and partially slumped).

This model was used because it permitted a partially mechanistic representation of an advanced core state (both geometric and thermal) for a starting point. The state selected was that at 5 s into the transient of Reference 2. This state was reproduced for this investigation by generating automatically a new SIMMER-II input file from the output of that analysis. Thus, reasonable temperatures were obtained for the internal and external blankets, as well as for any intact fuel in the outermost driver regions 9 through 12. All driver regions were assumed blocked and completely voided.

The neutronic model was the same as that used in Appendix C. Before performing these analyses, a check was made on the effective Doppler feedback because it is very important in determining disassembly energy yields and because it cannot be explicitly monitored in the transport theory formulation of SIMMER-II. These checks were performed through K-effective calculations for core temperature changes of 1000 K (intact, voided core with a fuel temperature distribution typical of that at initiation of cladding melting). The results were in excellent agreement with those calculated in Appendix A of Section II.3.

TABLE 1
REGION CHARACTERISTICS IN THE SIMMER-II MODEL FOR ANALYZING WHOLE-CORE DISASSEMBLY ENERGY YIELDS

Region Number	Reactor Region	Modeling Characteristics
1 through 12	Active core	Variable per configuration
13 through 16	Internal blanket (IB)	Interconnected gaps
17 and 18	Radial blanket (RB)	Interconnected gaps
19	Radial reflector (RR)	Interconnected gaps
20 through 23	Lower axial blanket-driver	Complete blockage
24 through 27	Lower axial blanket-IB	Interconnected gaps
28	Lower axial blanket-RB	Interconnected gaps
29 through 32	Lower axial blanket-driver	Interconnected gaps
33	Lower shield	Intersubassembly gaps
34	Radial reflector nozzles	No structure
35 through 38	Upper axial blanket-IB	Interconnected gaps
39	Upper axial blanket-RB	Interconnected gaps
40 through 43	Upper axial blanket-driver	Complete blockage
44 through 47	Upper axial blanket-driver	Interconnected gaps
48 through 51	Upper axial blanket-IB load pad	Interconnected gaps
52	Upper axial blanket-RB load pad	Interconnected gaps
53 through 56	Upper axial blanket-driver load pad	Interconnected gaps
57	Radial reflector load pad	Interconnected gaps
58 through 61	Upper axial blanket-IB	Interconnected gaps
62	Upper axial blanket-RB	Interconnected gaps
63 through 66	Upper axial blanket-driver	Interconnected gaps
67	Radial reflector	Interconnected gaps

The ramp rates were generated in these calculations in a way that approximates the expected mode of recriticality during the disruption phase, namely fuel slumping into the lower part of the core. Once a slumping region was defined, a slumping velocity was determined that provided the desired ramp. By using material motion instead of a programmed ramp, a natural mitigation of the ramp was permitted from local pressure gradient development as the power rose during the approach to prompt critical. This approach worked very well and very predictably although the mitigation effects were not significant for ramp rates of 25 $/s and larger.

3. Configurations

Four configurations were used in this investigation. The reference configuration, labeled "0," was an idealized arrangement through which the classical two-phase disassembly yields were established. These yields for various ramp rates provided a baseline against which the yields of the disrupted-core situations could be related to get a relative sensitivity of yield to configuration. Configuration 0 is shown in Figure 9a of Section II.7. The driver subassembly walls were generally intact but were assumed to have little strength; therefore, they were assumed to have deformed to close the adjacent intersubassembly gaps. Thus, the driver regions consisted of about 10% S/A wall steel, 34% liquid fuel, and 56% void. The cladding and wire wraps were removed to the axial blankets. As seen in Appendix A, this material arrangement should guarantee classical two-phase disassembly mechanics. It is an idealized arrangement in that it can never develop in a neutronically active system as seen in Section II.5.

Configuration "2" represents a more realistic situation where some initial slumping has occurred in the central three driver regions (a puddle depth of about 0.14 m). This was considered as representative of the S/A disruption phase. The material above the single-phase puddle was assumed to be of the same composition as in configuration 0. This two-phase material was assigned the appropriate rainback velocity to deliver the desired reactivity ramp. The disassembly was initiated at a critical state and nominal full power. To provide a critical state, approximately 10% of the total driver fuel inventory had to be removed (~ 20% of the central three drivers). This configuration also was idealized because the rainback was uniform axially and radially, a clean interface was assumed between the single-phase and two-phase regions, the ramp rates were arbitrarily assigned, and no disruption was assumed in the outer driver regions. It is a perfect arrangement for quantifying the magnitude of any potential "boost" phenomenon.

Configuration "3" represents the situation expected in the late initiating phase or early S/A disruption phase. A small group of S/As (12 in this case) were assumed to slump to produce the driving ramp. The purpose of this configuration was to determine the extent to which very localized

slumping and radial flux shape changes could alter the yield spectrum. The arrangement was identical to configuration 0 except that the outer driver regions were intact and only driver 1 was given a uniform downward velocity to provide the desired ramp. This configuration is not highly unrealistic if lead S/As are involved as in EOC-4. The idealization in this configuration relates to the arbitrary specification of slumping velocity (24 m/s to achieve 100 $/s). This is clearly unreasonable on physical grounds for blocked S/As. However, this configuration should quantify the relative sensitivity of the yields to this configuration when compared to the others.

Configuration "5" represents a late stage of the S/A or perhaps annular-pool disruption phases. The core was uniformly slumped with a puddle depth of 0.21 m. The rainback was nearly complete. It was constituted as in configuration 0. For this configuration to be critical, about 36% of the fuel had to be removed. This situation was near the permanent neutronic shut-down condition. Again, the ramps were delivered by the velocity of the rainback. The region above the "rain" region was void. This case provides insight into the yields at the opposite configuration extreme from configuration 0.

4. Results

The results in terms of yields (FPS) are shown in Figure 15 of Section II.7 as a function of ramp rate and configuration. The results showed the existence of the boost for the high inventory configurations in which bottom puddling occurred (configurations 2 and 3). They also showed the presence of strong mitigation for low-inventory, highly puddled configurations (configuration 5) as would be expected from the single-phase disassembly dominance discussed in Appendix A. These results are in total agreement with the expectations generated from the K-effective assessments of these configurations that showed the relation between inventory, flux peak/puddle alignment, and boost potential.

Two sets of results are given in Figures 1 through 3 and Figures 4 through 6 for configuration 0 and 2, respectively. Both sets are for a 50-$/s initiating ramp. Figures 1 and 4 show the reactivity transients. The reactivity for the two-phase disassembly leveled out because of Doppler feedback and turned down rapidly because of fuel motion (classical disassembly). The reactivity history for configuration 2 differed in that it leveled out because of Doppler feedback but then spiked upward before the rapid turndown. This is characteristic of the single-phase boost phenomenon. The power transients also showed a very different character (compare Figures 2 and 5). The boost caused the power to rise to a much higher level and then to decrease very rapidly as in a single-phase disassembly. The

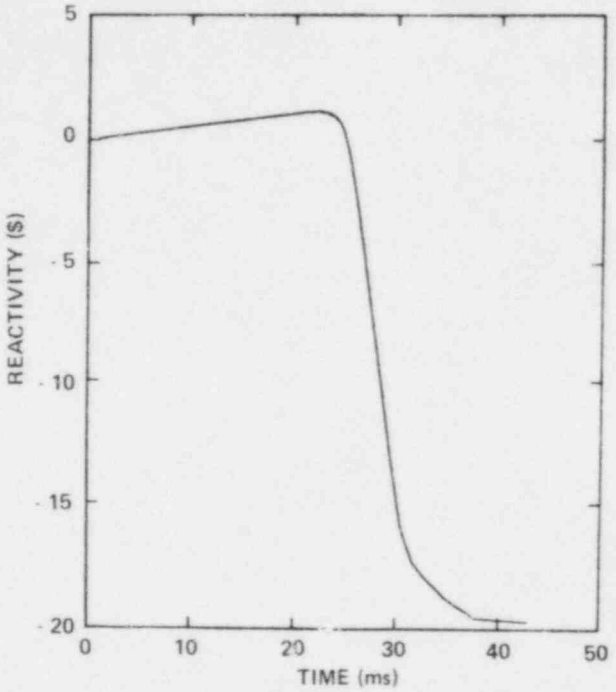

Fig. 1.
Reactivity transient for a 50 $/s disassembly with configuration 0.

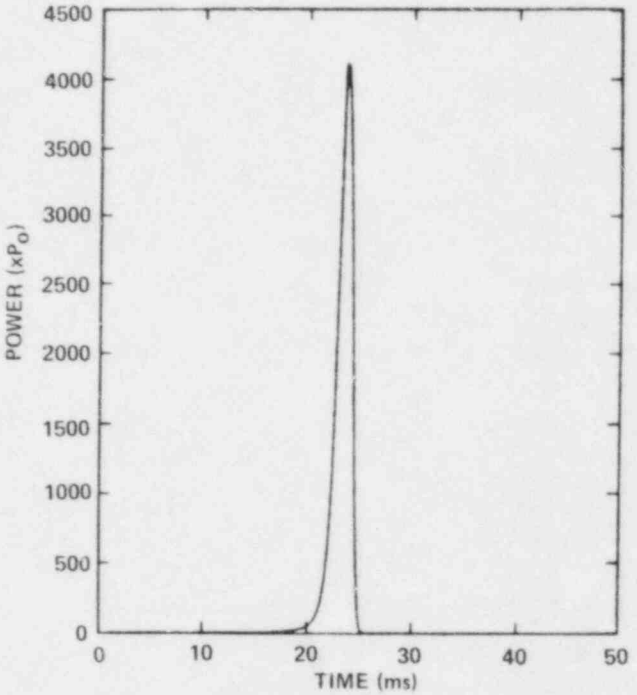

Fig. 2.
Power transient for a 50 $/s disassembly with configuration 0.

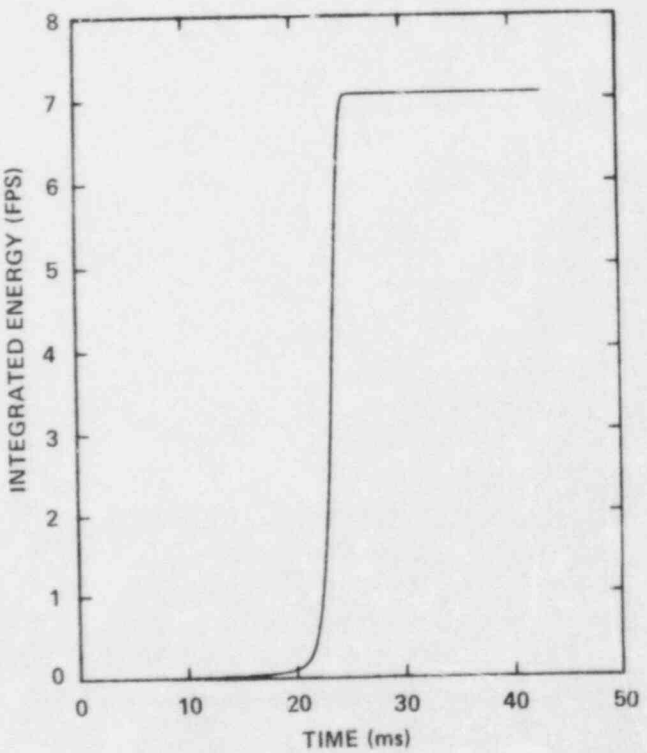

Fig. 3.
Energy yield transient for a 50 $/s disassembly with configuration 0.

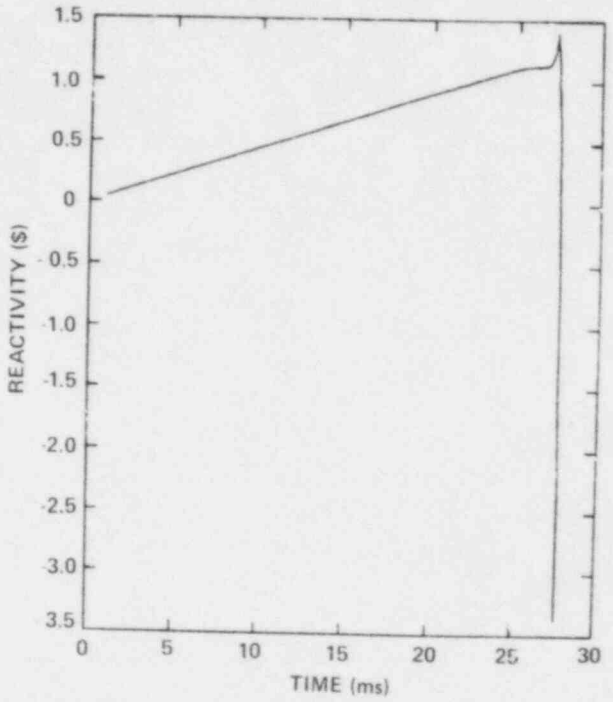

Fig. 4.
Reactivity transient for a 50 $/s disassembly with configuration 2.

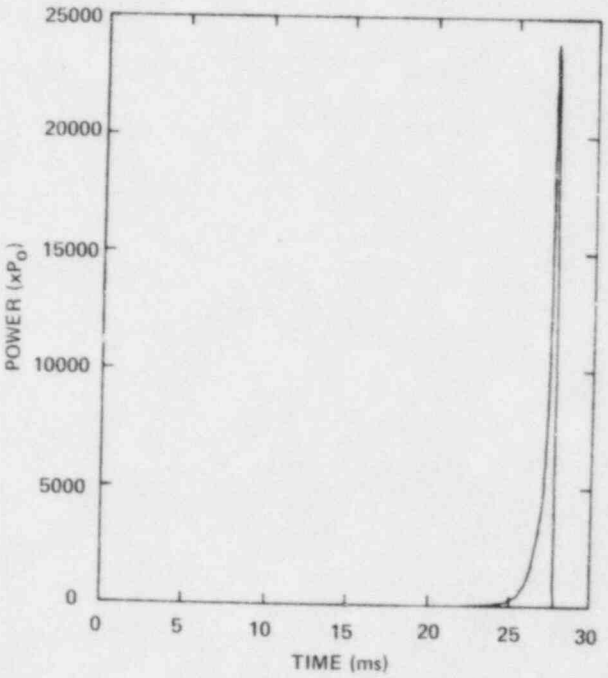

Fig. 5.
Power transient for a 50 $/s disassembly with configuration 2.

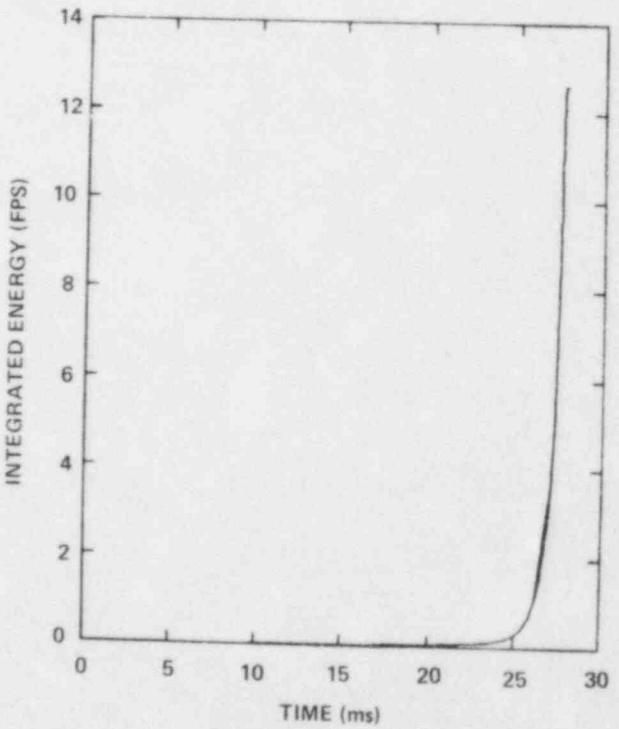

Fig. 6.
Energy yield transient for a 50 $/s disassembly with configuration 2.

difference in energy added to the materials or yield can be seen by comparing Figures 3 and 6. This difference was about a factor of 2.

5. Summary

There appears to be a significant configuration effect on disassembly yields when considering these postulated configurations. It is reasonable that these phenomena occur under the specified conditions. The major question to be addressed is the realism of these configurations in the neutronically active, disrupting core (see Section II.7, part 6).

6. References

1. L. L. Smith, "SIMMER-II: A Computer Program for LMFBR Disrupted Core Analysis," Los Alamos National Laboratory report NUREG/CR-0453, LA-7515-M (June 1980).

2. M. G. Stevenson, "Nuclear Reactor Safety Quarterly Progress Report, April 1-June 30, 1982," Los Alamos National Laboratory report NUREG/CR-9814, LA-9559-PR (November 1982).

II.8. CONCLUSIONS

Based on the technical bases developed in the previous six sections, we now proceed to assign probability split levels at each bifurcation of our generic accident sequence path (Figure 1). The procedure has been described in Section II.1. The rational for these assignments also will be briefly given. We have presumed that the Applicant will follow our recommendation for a design fix to eliminate the precipitous manifestation of the plenum fission gas pressure on the fuel columns upon disruption, and that the vessel head capability will be restored to its originally specified value of 75-MJ sodium slug impact kinetic energy. Since this probabilistic exercise is carried out on an order-of-magnitude basis, we assign only the 1, 10^{-1}, 10^{-2} and 10^{-3} levels on each branch, that is, the sum of branch probabilities from any state should add up to unity within 0.111. The discussion below relates to Figure 1.

The sodium void worth, including uncertainties, is adequately low to guarantee, presuming the design fix for the plenum fission gas compaction problem, the absence of LOF-d-TOP. The only remaining mode for energetic behavior is by fuel slumping under gravity. The assured incoherent nature of this process within the initiating phase guarantees the absence of significant energetic events at this stage. Hence, a value of 1/1000 (physically unreasonable) was assigned to path α. Having assured ourselves that no mechanisms exist to produce an energetic initiating phase, it would appear even more difficult to identify energetic events of sufficient magnitude to challenge the vessel head structure (VHS). Hence, a value of 1/1000 was assigned to path α'.

The subassembly and annular-pool stages do not favor amplification of mild recriticalities to substantial energetic events. This statement is based on inherent physical behavior and analysis, and it is insensitive to gross uncertainties in the detailed phenomenology that controls fuel motions. Because significant amplification is not likely, VHS failure is considered physically unreasonable and the value of 1/1000 was assigned to paths β' and γ'. For the same reasons, in fact, it is difficult to achieve recriticalities of magnitude greater than that of a 30-$/s two-phase disassembly, which we chose to define as the lower limit for this path. Clearly, the events here are of more detailed nature, and we hesitate to claim that an out-of-spectrum characterization would be adequately conservative. Hence, an edge-of-spectrum value of 1/10 is assigned to both path β and γ.

For the whole core pool we have identified mechanisms that produce amplification of mild recriticalities and the associated energetic releases

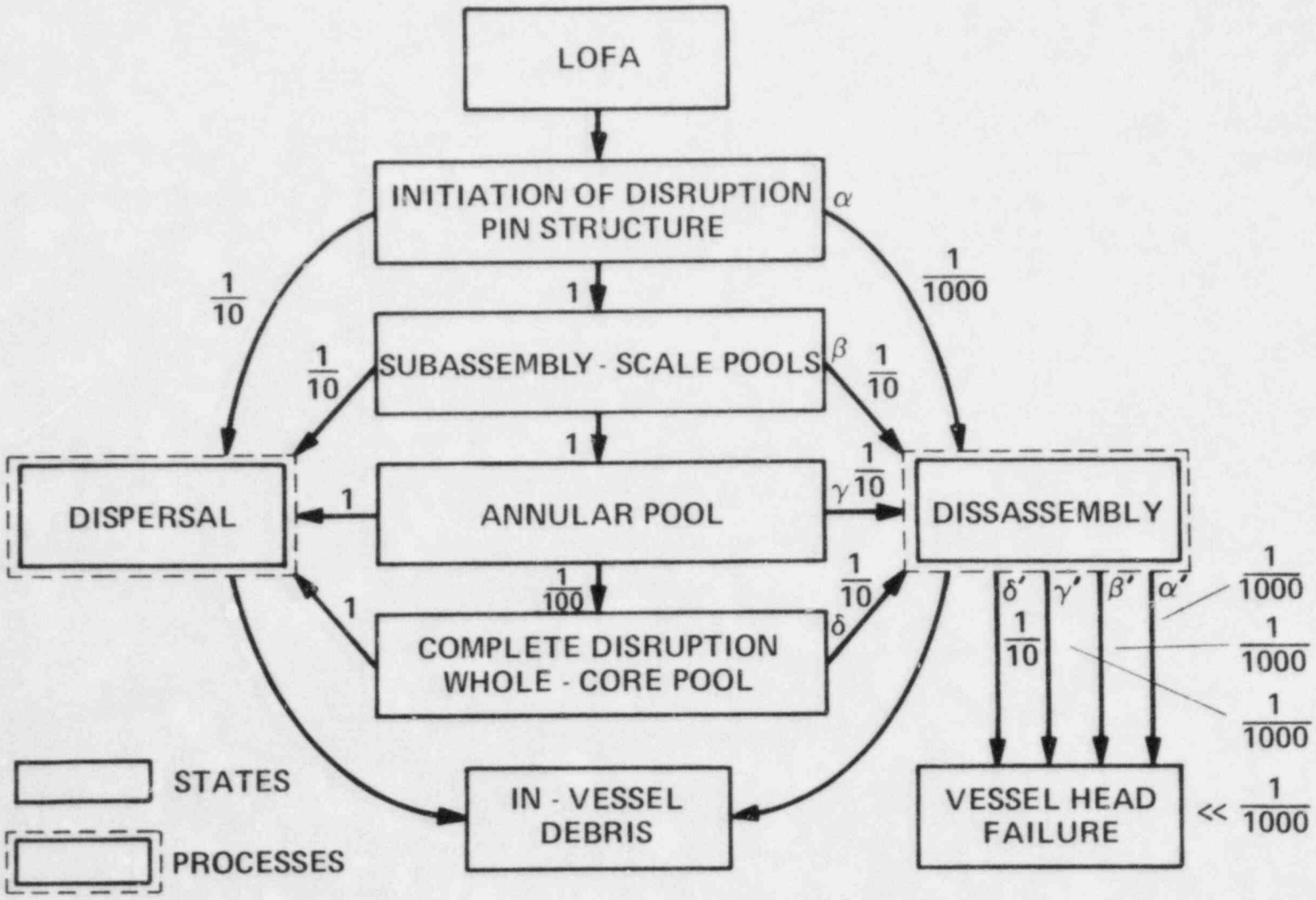

Fig. 1.
Probability assignments to the branches of the generic LOFA sequence.

approaching the structural capability of the VHS. Although the conditions under which these mechanisms may become operative are highly idealized, that is, a perfectly symmetric and homogeneous pool, we cannot at present rule out such behavior. However, we also found that only special pool configurations are potentially susceptible, that only short time intervals are required to obtain the incremental fuel removal through the radial blanket gaps for termination, and that the strongly nonhomogeneous and chaotic character of this pool following its initial formation dampen its neutronic response. Therefore, its tendency for energetic termination is not midspectrum but clearly edge of spectrum. Thus, we assign to the path δ a value of 1/10. However, recognizing that even our idealized calculations have failed to produce energetic releases exceeding the capability of the VHS, we cannot assign a high conditional probability for head failure. We hesitate claiming anything less than end of spectrum, however, primarily because we wish to maintain the high level of confidence in the conservative estimation of these numbers as specified. Thus, a value of 1/10 is chosen for path δ'.

We quantified the transient pressure histories that drive the dispersal as well as the associated fuel removal rates. Due to codisruption and sustained neutronic activity, we believe favorable conditions exist for mild dispersal termination throughout the core disruption phases. For such termination from the initiating phase, we remain skeptical, primarily because the judgement depends on details of behavior with substantial uncertainties. However, such an evolution should not be considered completely outside of expectation. Hence, a value of 1/10 is assigned. Termination from the S/A-scale pool phase is similarly uncertain. The reason is that at this stage the competition between opening up into the annular-pool phase and expelling fuel for termination is still strong. In the absence of sustained pressures to drive fuel removal (an oscillatory character is expected), we hesitate to call the expectation for such termination any more likely than edge of spectrum. However, as the core disruption develops further, clearly more escape paths open; new ones into the radial blankets and the control rod assemblies and old ones by remelting blockages (especially those formed in many of the axial blanket regions due to codisruption). The process of dispersal becomes overwhelming because of the continuously increasing path availability, especially in the time interval between destruction of internal blankets (entry into the cylindrical pool) and mixing of this material that is required to yield the homogeneous whole-core pool. Hence, an out-of-spectrum choice is made for the path to homogeneous whole-core pool formation with a potentially critical inventory (1/100) while termination from both of these advanced core-disruption states (annular and whole-core pools) is assigned a probability of unity.

Based on the above, the total vessel head failure probability, conditional on the occurrence of the LOFA, is approximately 3×10^{-4}. Returning to our definitions, this number indicates that such an event should be considered

physically unreasonable. Recall that the assignment of numbers for each path was intended as a high confidence, conservative bound with regard to the key accident branch points (virtual assurance that the assigned probability number would not be exceeded). Still, this final result indicates considerable margin before the "physically unreasonable" threshold in probability is exceeded.

It is emphasized that these probabilistic estimates are an integral part of the primary definitions utilized in assigning branch probabilities, and they should only be utilized in conjunction with these definition. An example was provided above, whereby the final probability for energetic head failure was converted back to a physical meaning of expectation. As another example, the probability of experiencing a whole-core, homogeneous, pool given a LOFA is 10^{-2}. This number is converted to words to conclude that "the occurrence of a homogeneous whole-core pool with recriticality potential given a LOFA should be considered as very unlikely and outside the spectrum of reason." Also, it is important that our numbers not be used as inputs directly into PRA studies. Rather, the word interpretations mentioned above should be converted to PRA input numbers in a manner physically consistent with other PRA inputs.

III. TRANSIENT OVERPOWER INITIATED CDAs

1. Objectives and Overview

Overpower conditions (as initiating events) result from unchecked reactivity increases. Such increases may occur in step-like or continuous fashion. Mechanistically, a step-like reactivity increase may result from sudden changes in core geometry due to severe external forces (typically a severe earthquake) or from sudden changes in core composition from reductions in coolant in the core (rapid formation of fission gas bubbles or gas entrainment from the inlet plenum). A continuous reactivity insertion, however, would be the consequence of sustained removal of poison material (typically a withdrawal of control rods). In this section we are concerned with this latter mode.

Clearly, only unprotected TOP events can lead to core disruption. Inherent negative reactivity feedbacks are inadequate to compensate for the continuously imposed reactivity insertion. The power level rises quickly, typically reaching the primary and secondary scram trip levels of 115% and 130% power, respectively, in just a few seconds. For all but the smallest imposed reactivity ramps, fuel melting and pin failure occur before coolant boiling. We have already encountered a similar sequence of events in the TOP driven by the LOFA-initiated material relocations (LOF-d-TOP, Section II.4). The energetics mechanisms and concerns for autocatalysis also are similar (midplane failures and pin-internal fuel motion). The distinguishing characteristics in the present situation are full coolant flow (as opposed to approximately 20% in the LOF-d-TOP) and low reactivity insertion rates (as opposed to many $/s in the LOF-d-TOP). The lower ramp rates might be less likely to cause midplane failures and the higher coolant flow would favor sweepout (in both rate and extent). However, the potential availability of the whole core for such failures in the present case (as opposed to only a fraction in the LOF-d-TOP case) suggests that a careful delineation of the autocatalysis-prone range of conditions should be made.

Various combinations (cases) of core conditions (burnup), driving reactivity ramp rates, and parametric variations in key phenomena (Doppler feedback, failure location, etc.) were examined by the Applicant [1]. The SAS3D [2] code was used in these evaluations. The two extremes of the core burnup states, that is, BOC-1 and EOC-4, were combined with the "design ramp rate of 4.1 ¢/s" (uncontrolled withdrawal of the peak worth control rod at its design speed) and with the arbitrarily higher rates of 10 ¢/s and 50 ¢/s. In addition, parametrics with "pessimistic" Doppler and material worth

values and "forced" midplane failures (in the 4.1 ¢/s, BOC-1 and 10 ¢/s, EOC-4 cases) were considered. Only the 10 ¢/s, EOC-4 case with forced midplane failure and SAS/FCI modeling of postfailure fuel motion and fuel-coolant interactions evolved into an energetic event. Reanalysis of these events using the PLUTO2 code (uncoupled from SAS3D) did not yield such superprompt-critical conditions, however. All other cases produced benign termination by fuel sweepout (neutronic shutdown or power stabilized at some level). In fact, for the best estimate, only partial core damage was projected.

Our detailed evaluation of these analyses [3] raised a couple of important concerns in the areas of failure location and core-wide pin failure coherence. The location of pin failure under TOP conditions has always been a subject of controversy. The situation was aggravated in favor of mid-plane failures by the results of the most recent SLSF W-2 TOP-simulation test (released during the course of our review) that was intended as highly prototypic. Therefore, we took the position that midplane failures during low-ramp rate TOPs not only could not be excluded but might even represent the best-estimate choice. The subject of core-wide coherence is important, particularly if midplane failures are assumed. Specifically, the time between successive pin failures (pin failure coherence) must be long compared to the characteristic sweepout time (typically approximately 30 ms) if the escalation of the overpower condition is to be avoided. The cases examined by the Applicant did not adequately envelop the expected CRBR core-wide coherence. Specifically, we identified an intermediate-burnup core configuration, the EOC-3, in which the six highest-power fuel subassemblies in cycle 4 contain blanket material, as a more appropriate case for consideration in this respect.

An update of the Applicant's arguments in this area was provided [4] in response to our Question #1 (Table 2 of Section I) early in our independent assessment. This update addressed the above concerns and arrived at the same position; namely, that "a prompt-critical response would be very unlikely even for combinations of pessimistic assumptions" on failure location and reactivity insertion rates. The principal effort in this new documentation is to show the effectiveness of analytically predicted sweepout mechanism by comparisons to available in-pile experimental data. These results which are in reasonable agreement with those of our own independent assessment are examined and discussed in detail in [5].

Based on the above reservations, our independent assessment efforts attempted to delineate more closely the boundaries of the autocatalysis regime. Although upon closer examination the W-2 test has been found nonprototypic [6], we chose to maintain a midplane failure assumption throughout in the absence of reliable evidence to the contrary. Consequently, pin failure coherence is of central importance. Clearly, the failure time delay between any two groups of pins depends upon the relative power at the two respective locations (power distribution) as well as upon the absolute power level. As

mentioned above, the EOC-3 configuration envelops the power distribution aspect. The power level, however, will depend upon the assumed driving reactivity ramp rate. Hence, these evaluations must be placed in the proper context (probabilistic) with control system failure mode and effects analysis. We begin, therefore, the detailed considerations with this topic in Section 2. The competition between pin-internal fuel motion and sweepout dictate the essential aspects of the phenomenological progression and is discussed in Section 3. Certain peripheral issues such as the potential for achieving advanced core disruption states similar to those found in the LOFA progression also are included here. Finally, the TOP unique energetic circumstances identified on the basis of this discussion are dealt with in Section 4.

2. Driving Ramp Rates and Relative Likelihoods

Various combinations of the control-rod subsystem failures were examined [7] with the objective of ordering the relative likelihood of reactivity insertion rates. Because multilevels of overspeed protection are incorporated in different subsystems of the control-rod system, the rate of reactivity insertion may be divided into discrete levels corresponding to multifailures up to an overspeed protection failure. Starting with the rod withdrawal accidents in a group mode, the first overspeed protection is in the reactor controller system. This limiter will limit the rod withdrawal to speeds below 4 inches/min. Thus, at the first level is the control rod bank withdrawal at the speed of up to 4 inches/min. Five subsystems must fail for this occurrence; the result would be a reactivity ramp rate of 5.6 ¢/s.

The next overspeed protection is in the auto interface board which limits the rod withdrawal to 5.5 inches/min. For this accident which yields a reactivity ramp rate of 7.7 ¢/s, six subsystems must fail. The third overspeed protection is in the rod controller drawers and limits the bank withdrawal to 9 inches/min. A total of seven subsystem failures are necessary for this event which produces a ramp of 12.6 ¢/s.

There can be also single rod withdrawal events although for the same reactivity insertion rate a larger number of subsystem failures would be necessary. Thus, a single rod withdrawn at 9 inches/min requires six subsystem failures and produces only a 2.1 ¢/s ramp. Single rod withdrawal at the maximum possible mechanical speed of 45 inches/min, however, yields 10.5 ¢/s and requires the failure of eight subsystems.

Thus, rates in the 2 ¢/s or the 10-12 ¢/s ranges are already significantly less probable (at least by one order of magnitude) than those in the intermediate range of 5-8 ¢/s. In order to obtain even higher rates, additional subsystem failures must be postulated. As a scoping example the 15 ¢/s case was examined in some detail [5]. Among the several failure

combinations, the two most likely scenarios were analyzed [7]. The probability of a 15 ¢/s event was estimated to be at least three orders of magnitude lower than that for a 10-12 ¢/s event. Considering that failure of the reactor protection system is itself an extremely unlikely event, we will limit our considerations of TOP events to ramp rates up to the 10-12 ¢/s range.

In addition we examined the possibility of a pump trip (LOF) occurring concurrently with a TOP. This possibility arises since the scram systems will attempt to trip both the reactor and the primary coolant pumps. If the TOP/LOF combination were to occur, it would develop as a reactivity augmented (from the reactivity standpoint) LOF sequence with an increased potential for an LOF-d-TOP event (see Section II.4). In contrast to the electrical failures in both the primary and the secondary shutdown systems responsible for a TOP event, a TOP/LOF event would require the concurrent (a) electrical failure of the secondary reactor shutdown system, (b) mechanical failure of the secondary reactor shutdown system, and (c) failure of the interlock between the primary and secondary shutdown systems. Since the secondary shutdown system is designed to scram the reactor with the most reactive control rod stuck, mechanical failure of two or more control rods is necessary to make this system fail. Complete failure of the secondary scram system, therefore, consists of a mechanical common-mode failure of five secondary control rods. Compared to the electrical failure of the secondary system (required for the classical TOP), this common-mode mechanical failure of the secondary shutdown system is judged to be very unlikely. The combined TOP/LOF event was not, therefore, considered any further.

3. Ranges of Phenomenological Progression

All available accident analysis experience [1, 8, etc.] suggests that the energetically significant TOP phenomenology is associated with the initiating-phase events. We concur with this conclusion. The discussion in this section will follow this emphasis. As mentioned above, a central aspect of this phenomenology is the competition between pin failure coherence on the one hand and fuel sweepout on the other. In assessing the outcome, we utilized the codes PLUTO2 [9], SAS/EPIC [10], and the PLUTO2/SAS4A [11] which are the most advanced computational tools available in this area. A summary of this assessment is provided below. Additional details may be found in Reference 12. In what follows we have presupposed midplane failures. A discussion of this topic is given in Appendix A. Our rationale is that, in view of the uncertainties, such a choice is necessary to adequately explore the margins to energetic behavior. Clearly, failures well above the core midplane would be benign and, as already documented by the Applicant, would lead to early termination.

3.1. Pin Failure Coherence

Pin failure under TOP conditions is the result of thermal and mechanical loads on the cladding that in turn are driven by the overheating of the fuel contained within. That is, notwithstanding the uncertainties in failure mechanisms and hence in the prediction of failure location(s) (see Appendix A), the relative timing of pin failures for the same core and imposed transient can be quantified accurately from their respective fuel enthalpy rise histories. This method was utilized in this study.

In addition to the BOC-1 and EOC-4 cases examined by the Applicant, we studied the EOC-3 core also. The results, for an imposed 10-¢/s TOP for BOC-1 and EOC-4 and 12-¢/s TOP for EOC-3, are given in Figures 1 to 3 for these three cases. As expected, maximum coherence is observed in the EOC-3 case. The BOC-1 configuration appears only slightly more incoherent; however, the low fuel fission gas content in this fresh core could not support as extensive pin-internal fuel motion and was judged to have a significantly lower energetics potential (as compared to the EOC-3 case). The EOC-4 case clearly is highly incoherent (Channel 6 leading by more than 500 ms). In fact, even though in this calculation the negative reactivity from sweepout in Channel 6 was arbitrarily suppressed, a significant incoherence is seen (approximately 100-200 ms, that is, ample time for manifestation of the negative sweepout reactivity) between the next group of failures (Channel 7) and the remainder of the core. Thus, for the BOC-1 and EOC-4 cases, in agreement with the Applicant, we see no credible evidence for development of autocatalytic behavior. The more limiting EOC-3 scenario, however, requires more detailed discussion.

To better resolve the coherence behavior, the EOC-3 case [13] was analyzed with a 33-channel core discretization. From Figure 3 we deduce a pin failure incoherence of more than 300 ms for the first six SAS3D channels (6, 6, 3, 6, 6, and 3 subassemblies, respectively). Significant fuel sweepout must occur within about 100-200 ms of the failure of the first group of subassemblies to assure avoidance of self-accelerating trends. Furthermore, in this case the sweepout reactivity (negative) must be of sufficient magnitude to counter effectively the positive contributions caused by pin-internal fuel motion because of the presence of significant fission gas pressure. In fact, for the case shown, this additional reactivity insertion following the failure of the first 12 subassemblies may reduce the time interval to failure of the next group of subassemblies to as little as 100 ms. These sweepout requirements increase with the magnitude of the driving reactivity ramp rate. Thus, for a 4-¢/s TOP, the failure incoherence may be approximately 600 ms, while, for a 20-¢/s TOP, it may be approximately 25 ms.

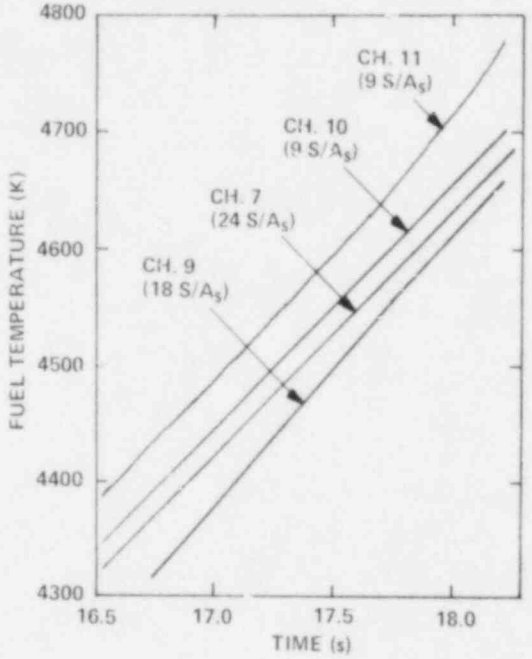

Fig. 1.
Fuel temperature transients for various channels during a 10 ¢/s TOP (BOC-1).

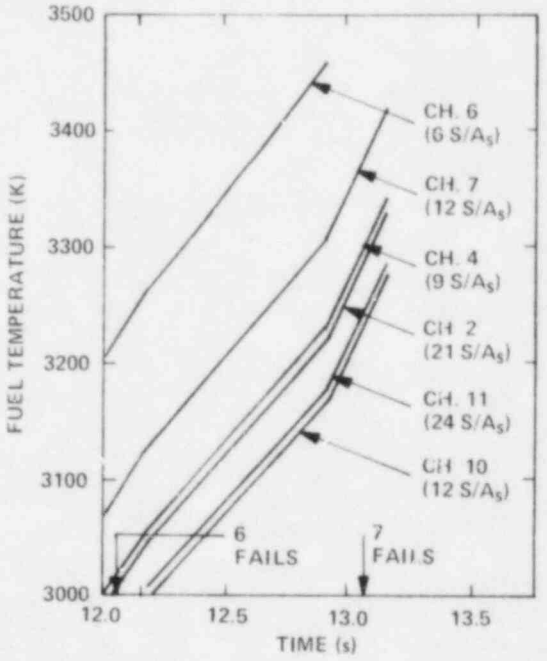

Fig. 2.
Fuel temperature transient for various channels during a 10 ¢/s TOP (EOC-4).

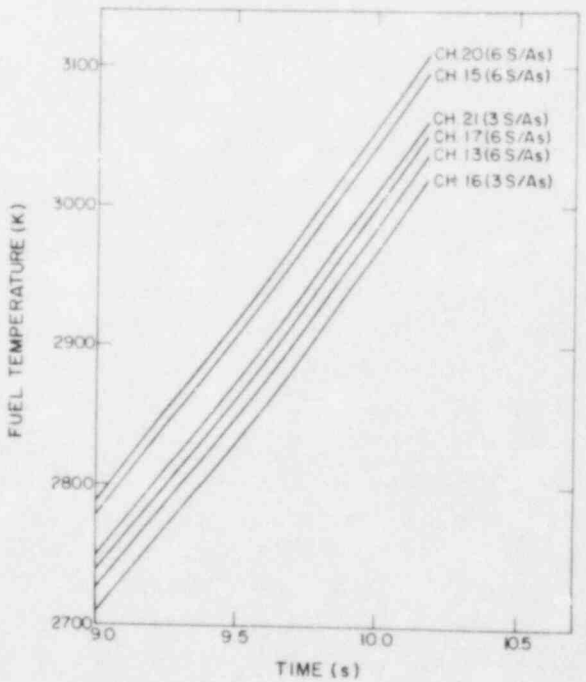

Fig. 3.
Fuel temperature transient for various channels during a 12 ¢/s TOP (EOC-3).

3.2. Sweepout Time Scales

Several in-pile and out-of-pile experiments are useful in addressing the sweepout question. In all cases, rapid and extensive sweepout was measured. However, as none of these tests adequately matched the conditions of interest here, these data could not be applied directly and quantitatively. The PLUTO2 code was utilized by the Applicant [4] to bridge this gap. With an appropriate selection of phenomenological parameters, PLUTO2 results provided a fairly good match of observed fuel sweepout for in-pile, irradiated-pin, TOP TREAT tests H6 and L8. Similarly satisfactory results were obtained for the E8 TOP test using PLUTO, the predecessor of PLUTO2. To assess how well these parameters could be determined, we utilized the PLUTO2 code for additional sensitivity studies on these parameters for the L8 test. The details of these evaluations are summarized in Appendix B. Our findings support the Applicant's position that PLUTO2, in conjunction with tests H6, E8, and L8, provides an adequate basis for predicting sweepout reactivities in CRBR TOP events.

Among the three available in-pile tests, only L8 had full-length pins, and it is therefore the best suited for supplying the fuel motion reactivity data necessary in our present evaluations. However, in this experiment a high driving reactivity ramp rate (approximately 7 $/s, initial period 0.08 s, peak power 75 x nominal) was chosen to simulate an LOF-d-TOP event. It is important, therefore, to examine the applicability of these results to the much lower ramp rate TOP cases of interest here. This was accomplished by several PLUTO2 and SAS4A/PLUTO2 simulations as follows.

The total reactivity transient from fuel motion was measured in the L8 experiment. By neglecting the contribution from in-pin motion, this same result may be taken to represent the sweepout reactivity. This assumption is based on the non-prototypic, shorter (molten) cavity found in L8 compared to that expected in CRBR at the same radial melt fraction. Furthermore, this assumption leads to a conservative measure of the sweepout reactivity. This inferred experimental sweepout reactivity is compared to the PLUTO2 simulation in Figure 4. The choice of "specific" reactivity (expressed in terms of ¢ per subassembly per gram of fuel ejected from each pin) is convenient in expressing a "removal" efficiency more or less independently of the quantity of the fuel involved. In the very early period, the calculation overestimated the data. However, in the most critical time period (first 30 to 60 ms), it produced conservative results and fair overall agreement. This early overprediction could be the result of neglecting the contribution (positive) from pin-internal motion that may be present in the L8 data. The simulation, again overpredicted the sweepout beyond 75 ms. However, the total fuel ejection (in L8) at this time was far outside the range of interest for a slow TOP. This is demonstrated in Figure 5 where the amount of fuel ejected in L8 (approximately 7 $/s), as simulated by PLUTO2, is compared with the amount that would have been ejected if the L8 experiment was run at

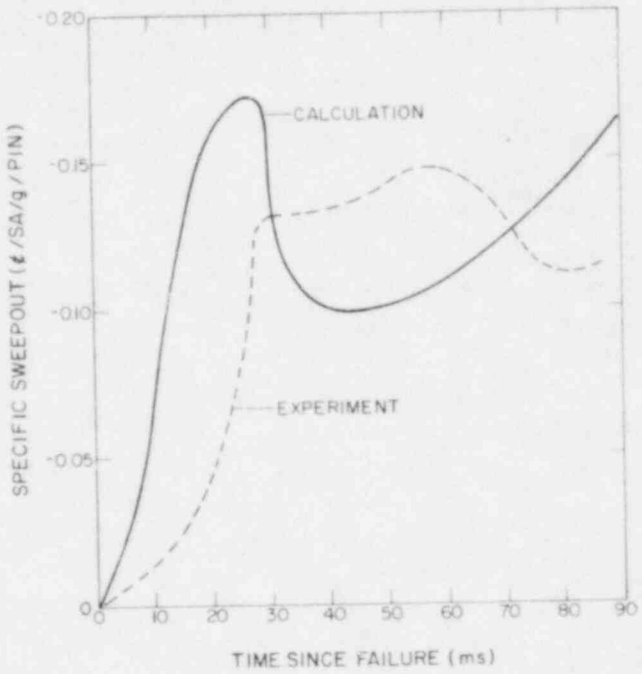

Fig. 4.
Specific sweepout inferred from the L8 experiment compared with calculated values from standalone PLUTO2.

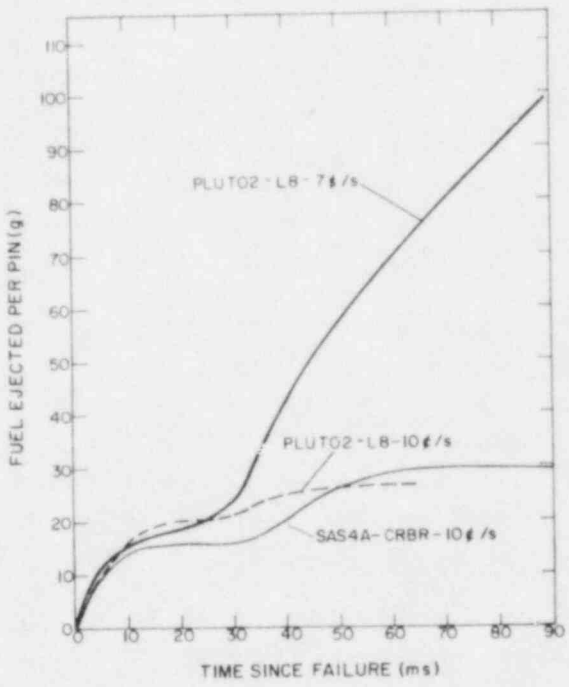

Fig. 5.
Grams of fuel ejected per pin in the L8 experiment compared to that in a 10¢/s TOP transient in L8 and CRBR geometry.

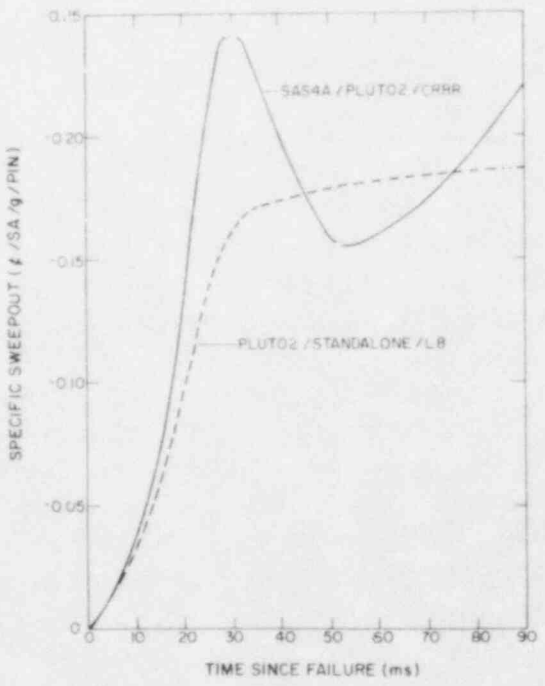

Fig. 6.
Comparison of specific sweepout for a 10¢/s TOP calculated by standalone PLUTO2 for L8 geometry and by PLUTO2 in SAS4A for CRBR geometry.

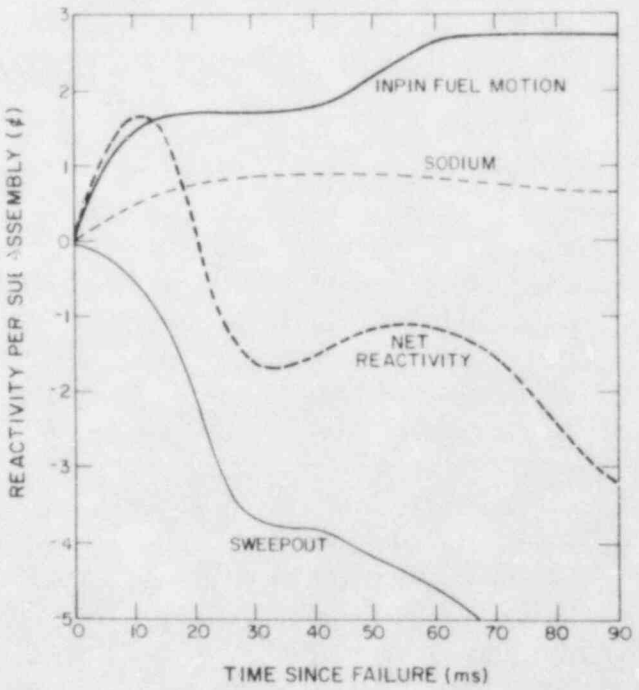

Fig. 7.
Reactivity effects in a high power subassembly for a 12¢/s TOP in the CRBR.

10 ¢/s instead. Also, as shown, this latter amount would be very close to what would be expected in a CRBR 10-¢/s TOP transient as predicted by a SAS4A/PLUTO2 simulation. Note that all cases agree up to approximately 30 ms as they should since the ejection up to this time corresponds to the fuel contained in the (molten) cavity at the time of failure. In the high-ramp TOP, melting and ejection continued whereas the 10-¢/s ramp was too slow to generate significant additional molten fuel in the time frame of interest for sweepout. This is a key point in assessing the sensitivity of the autocatalysis potential to uncertainties in the sweepout phenomena.

The effects of other L8 nonprototypic aspects on sweepout can be deduced analytically by comparing the PLUTO2 L8 simulations for a 10 ¢/s TOP to those obtained with SAS4A/PLUTO2 for the CRBR geometry. One such result is shown in Figure 6. The results agreed well up to 20 ms. Then SAS4A/PLUTO2 produced more efficient sweepout as expected because less fuel is ejected from the CRBR pin (see Figure 5). It is important, however, that in both cases major sweepout feedback (-0.15 ¢/SA/g/pin) was obtained within approximately 20-30 m/s and continued generally to rise well into the 80-90 ms time frame. This general increase in specific sweepout reactivity in the 10-¢/s case of Figure 6 should be contrasted to the leveling off observed in the 7 $/s case of Figure 4. The explanation is contained in the total amount of fuel involved as shown in Figure 5.

On the basis of this discussion, we conclude that for a 10 ¢/s TOP in the CRBR a specific sweepout reactivity of -0.15 ¢/SA/g/pin, occurring within approximately 60 ms from the time of failure, represents a reasonably conservative estimate that is consistent with available experimental data.

3.3. Accident Analysis Aspects

On the basis of the above, the TOP outcome really is determined within 50-100 ms from the time of pin failure and can be deduced rather simply as follows. With a specific sweepout reactivity of -0.15 ¢/SA/g/pin (Figure 6) and an ejected fuel mass of approximately 20 g/pin (Figure 5), a reactivity reduction of approximately 3 ¢/SA at 50 ms is estimated. The associated reactivity increase because of sodium voiding is typically ~ 1 ¢/SA and that due to pin-internal fuel motion (of approximately 20 g/pin) is approximately 2 ¢/SA. Thus, the failure of the 12 subassemblies of Channels 20 and 15 (EOC-3 core) would produce a negative feedback countering that from voiding and in-pin motion of approximately 36 ¢ within approximately 50 ms. One actual transient as depicted by SAS4A/PLUTO2 is shown in Figure 7. Even a conservative envelope above the net reactivity curve on Figure 7 indicates a subcritical state of about -30¢ at 90 ms for the 12 S/As. The next group of S/As (Channel 21 with 3 S/As) fail at about 135 ms. The projected reactivity state at that time is well below -30¢ while the maximum positive reactivity from Channel 21 is only about +5¢. It is seen that the sweepout reactivity

rate of > -5 $/s for the 12 S/As by far cancels the 12-¢/s insertion rate beyond 50 ms. Thus, ample sweepout exists in this 12 ¢/s CRBR TOP case to assure termination even under the most restrictive coherence conditions and pessimistic failure location assumptions. A large number of parametric whole-core CRBR TOP simulations were performed to support this conclusion further. Two different codes, EPIC and PLUTO2, were utilized. The effects of pin-internal fission gas pressure at failure (10 to 60 MPa) and the intensity of fuel-coolant heat transfer following failure were particularly explored. The results are documented in Reference 12 and support the simple derivation provided above.

The longer-term evolution will depend on the coolability of the disrupted and swept-away fuel. All available experimental evidence indicates that for the wire-wrapped pin design, in-core blockages are not expected. The Applicant has addressed the question of blockage formation and coolability and concluded that stable (coolable) conditions would prevail. We did not independently assess this problem. However, with the relatively small number of subassemblies affected and the relatively small degree of pin disruption predicted for the 12-¢/s TOP, we cannot visualize extensive core disruption and/or associated energetics even if noncoolable, in-core blockages were postulated arbitrarily. The so-called TOP-derived transition phase has been of some concern in the past. We chose not to pursue this topic further on the following bases: (a) The heterogeneous-core design provides fuel escape paths especially for isolated (subassembly-scale) molten regions (see Section II.6) and (b) transition-phase energetics have been adequately bounded for the LOF case (Section II.7), and no unique aspects could be identified for TOP-derived advanced core disruption.

4. Treatment of Unique Energetic Circumstances

As indicated in the previous section, an energetic TOP would occur primarily from midplane failures and inadequate sweepout. We also have established that energetic TOPs would not be expected even under the most limiting conditions consistent with physical reality and experimental evidence. Conversely, if we arbitrarily postulate the existence of such energetic behavior for consistency reasons, we should expect a self-accelerating condition (autocatalysis) at least to a certain level. Thus, although at initial escalation, the tendency would be to favor increasingly midplane failures and, of course, coherence, there may be a power level at which the pressure build-up within the pin is rapid enough to cause failure extension along its length, thus terminating the reactivity augmenting, pin-internal (towards the core mid-plane) fuel motion. However, any such inherent limits are difficult to support or quantify at this time. Thus, the unique energetic circumstances, should these be postulated, consist of autocatalytic tendencies and the presence of sodium in the core. Both of these aspects were discussed in connection with the LOF-d-TOP (Section II.4). Given that the present

context we are even further removed from that realm of possibility, we will let the discussion in Section II.4 suffice.

5. Summary

The potential for energetic TOP-initiated behavior was assessed for a limiting imposed ramp in the 10-12 ¢/s range. Even under the most limiting core-coherence conditions (EOC-3), energetic behavior is judged as an off-spectrum occurrence.

Additional work is recommended to clarify further the matters of pin failure mechanisms and location under low-ramp TOPs. This work would help clarify failure assumptions utilized herein, possibly revealing additional margins of safety.

6. References

1. S. K. Rhow, D. M. Switick, J. L. McElroy, and B. W. Joe, "An Assessment of HCDA Energetics in the CRBR Heterogeneous Reactor Core," General Electric Company report CRBRP-GEFR-00523 (December 1981).

2.[a] J. E. Cahalan and D. R. Ferguson, "A Preliminary User's Guide to Version 1.0 of the SAS3D LMFBR Accident Analysis Computer Code," Argonne National Laboratory (informal document included with code) (1977).

3. "Compendium to NUREG/CR-3224, An Assessment of CRBR Core Disruptive Accident Energetics," Section 5, Nuclear Regulatory Commission document (March 1983).

4. "Compendium to NUREG/CR-3224, An Assessment of CRBR Core Disruptive Accident Energetics," Section 6, Nuclear Regulatory Commission document (March 1983).

5. "Compendium to NUREG/CR-3224, An Assessment of CRBR Core Disruptive Accident Energetics," Section 7, Nuclear Regulatory Commission document (March 1983).

6. A. L. Pitner, D. E. Smith and G. E. Culley, "W-2 SLSF Experiment Final Report," Hanford Engineering Development Laboratory report HEDL-TME 82-49 (February 1983).

7. "Compendium to NUREG/CR-3224, An Assessment of CRBR Core Disruptive Accident Energetics," Section 8, Nuclear Regulatory Commission document (March 1983).

8. J. F. Meyer, L. Lois, J. L. Carter, and T. P. Speis, "An Analysis and Evaluation of the Clinch River Breeder Reactor Core Disruptive Accident Energetics," Nuclear Regulatory Commission report NUREG-0122 (March 1977).

9. H. U. Wider, A. M. Tentner, and P. A. Pizzica, "The PLUTO2 Overpower Excursion Code and a Comparison with EPIC," Int. Meeting on Fast Reactor Safety Technology, Seattle, WA (August 1979).

10. P. A. Pizzica, P. L. Garner, and P. B. Abramson, "A User's Guide to EPIC, a Computer Program to Calculate the Motion of Fuel and Coolant Subsequent to Pin Failure in an LMFBR," Argonne National Laboratory report NUREG/CR-1504, ANL-80-47 (October 1979).

11.[a] D. P. Weber, "Preliminary User's Guide to the SAS4A LMFBR Accident Analysis Computer Code," Argonne National Laboratory informal report (February 1981).

12. "Compendium to NUREG/CR-3224, An Assessment of CRBR Core Disruptive Accident Energetics," Section 9, Nuclear Regulatory Commission document (March 1983).

13. "Compendium to NUREG/CR-3224, An Assessment of CRBR Core Disruptive Accident Energetics," Section 10, Nuclear Regulatory Commission document (March 1983).

[a] Address requests for this document to: F. X. Gavigan, Director, Office of Breeder Demonstration Projects (NE-50), U.S. Department of Energy, Washington, DC 20545, Telephone (301) 353-3134.

APPENDIX A
TIME AND LOCATION OF MOLTEN FUEL EXPULSION

1. Status of Fuel-Rod-Failure Prediction Methods

Extensive effort has been expended on experimentation and development of predictive methods for the time and location of fuel expulsion under TOP conditions [1, 3]. The methods involve predicting expansion of the fuel relative to the cladding, predicting the interaction (load generated) between the two when they are in contact, and predicting the response of the cladding to the load that is generated. The behavior of fuel involves the temperatures characteristic of brittle ceramic material to temperatures exceeding the liquidus point. The behavior of cladding must be predicted for ranges of irradiation damage, strain rates, temperatures, and temperature rates of change. Clearly, the subject is very complex.

The current understanding is that initially the fuel expands differentially against the cladding, generating high loads until the uncracked fuel at the center of the pin creeps, thins sufficiently, or softens enough because of increasing temperature that it can no longer sustain the load. Cladding loads then decrease until the build-up of cavity pressure caused by the release of fission gas from the fuel during the transient, by reduction of cavity volume, and by buildup of fuel vapor pressure.

Empirical correlations having the form of stress-rupture formulations (Larson-Miller or Dorn parameters) are used to predict when the time-load-temperature history will cause cladding failure. These parameters collapse time and temperature into a single parameter that is correlated as a function of loading in experimental tests.

These predictive methods involve the modeling of several individual processes and properties both in the fuel and the cladding. For fuel processes and properties in particular, there are virtually no really applicable data. Accordingly, the properties and models are "calibrated" simultaneously against integral fuel pin tests. Thus, each of the predictive methods has several adjustable knobs, or correlating constants. There is no really good way to determine whether any of these methods can extrapolate correctly outside their range of correlating data. Yet, they must be extrapolated because of inadequate coverage of the data base and because of factors in the tests that are atypical to the CRBR. These deficiencies in the data base are discussed in Reference 1.

The most serious specific deficiencies in the predictive models are listed below.

- The cladding failure criteria do not specifically model the fuel adjacency effect. The fuel adjacency effect, the term given to the more severe reduction of strength in cladding irradiated near fuel as compared to cladding irradiated to the same fluence but not near fuel [4], may significantly affect the location of fuel expulsion. This is particularly true because of data that indicate the effect either does not exist or is much less severe [5, 6] above irradiation temperatures of 1050 to 1100°F.

- Current predictive methods do not address whether early cladding failures occurring before significant fuel melting may subsequently influence the location of expulsion.

- Current methods assume molten fuel expulsion is synonymous with cladding breach, probably a good assumption for TREAT tests. However, the mechanics of the molten fuel reaching the breach site, the opening or extension of the breach site from a small crack, and prerequisites for these processes may be very important for slow overpower or LOF-initiated events.

- No generally recognized integrated thermal model now exists for fuel-cladding gap conductance and fuel thermal conductivity, particularly for transient conditions.

- Cladding failure models do not now directly address the possible influence of annealing or strain rate on the location or time of expulsion.

- Wide diversity exists in the modeling of fission-gas phenomena in predictive methods, including the pretransient distribution of retained gas, if the phenomena are modeled at all.

- There is virtually no way to verify the correctness of expulsion location predictions, and no data exist for the ramp rate range of greatest concern (5 to 12 ¢/s).

2. Review of the W2 Test

The W2 test was a transient overpower test conducted by the Hanford Engineering Development Laboratory (HEDL) in the Sodium Loop Safety Facility in the Engineering Test Reactor late in 1980 [7]. The test was conducted on a bundle of seven full-length pins. The center pin was fully prototypic of the FFTF and nearly prototypic of the CRBR, except for the use of highly enriched uranium (93%) in the UO_2 portion of the mixed oxide. The peripheral pins used less highly enriched UO_2 and were designed with a

large fuel-cladding gap to minimize the possibility of a peripheral pin failing before the central pin. The test as planned was of particular interest because:

- the test transient was initiated at true steady-state conditions,
- the test simulated a credible ramp rate (5 ¢/s), and
- full-length (0.91 m fuel column) pins were used.

The test was as nearly prototypic as any conducted. Nevertheless, there were atypical factors in the test, including:

- the high enrichment caused a pronounced radial power depression in the central pin and a markedly asymmetric power distribution in the peripheral pins, and
- despite filtering to harden the neutron spectrum, it was still very soft thereby giving the cladding less than one-tenth the fluence corresponding to typical fluences for the fuel exposure.

Pretest predictions for the test with several of the available predictive methods agreed well with the observed time of expulsion in the test but did not agree at all with the location of expulsion, which was determined to be at axial midplane.

Subsequent posttest examinations and analyses by the experimentor [8] have established that for unknown reasons the flux collar was ineffective in obtaining the desired axial power distribution. The axial peak-to-average ratio was 1.39 rather than the desired 1.25. The radial power split between the central and peripheral pins was also more biased in favor of the peripheral pins than desired. These differences further accentuated an expected peripheral pin bowing tendency. The experimentor makes a good case for explaining the oscillating thermocouple temperatures that were observed in terms of peripheral pins bowing in and out. It is not obvious, however, why the pins would osciliate back and forth dynamically.

The Applicant explains the midplane fuel expulsion as resulting from a meltthrough of cladding on a peripheral pin after molten fuel contacted the cladding where it was jammed against the fluted tube and was starved of coolant. This is probably the most rational explanation of the events; however, no data were found that would prove this hypothesis.

We believe enough doubt has been cast on the applicability of the W2 midplane failure that it should not be considered in determining the propensity toward midplane failure. The following briefly reviews the principal points of why the W2 failure should not be considered.

- Severe pin bowing does appear to have occurred.

- The factors that caused a marked tendency toward outward pin bowing in W2 were more pronounced than anticipated and will not be present in CRBR.

- The maximum amount of channel constriction possible in CRBR may be comparable to that achieved in W2 by jamming a pin between flutes; however, such an eventuality would clearly be an atypical mode of failure in a CRBR TOP-initiated CDA.

3. A Criterion for Molten Fuel Expulsion

The available approaches for predicting the time of molten fuel expulsion, whatever their other problems, generally use methods that are impractical for large CDA analysis codes. Accordingly, the results obtained from these approaches need to be correlated in some simple manner for use in the CDA codes. For this reason as well as to provide a criterion with some basis in reality, we propose the use of the peak axial fuel enthalpy, with a value of 1140 kJ/kg (277 cal/g) referred to room temperature. By peak axial fuel enthalpy we mean the maximum value of the mean energy content at any radial slice along the fuel column.

Fuel enthalpy has been proposed as a failure criterion before, but never received general acceptance. This proposal is based on the discovery that the calculated values of peak fuel enthalpy at the observed time of fuel expulsion for nine TREAT tests [9-14] could be correlated by a single value (1140 kJ/kg) with a standard deviation of only 76 kJ/kg (6.7%). Calculations were performed with the LAFM [15] code. These same calculations produced good agreement with thermal data taken in the tests, and the mechanically based cladding failure predictions agreed well with observed times of fuel expulsion. The tests for which calculations were performed are tabulated in Table 1, along with the calculated enthalpies and mass fractions of fuel in the liquid phase at the time of expulsion.

These tests covered a range of burnups from 30 to 120 MWd/kg, a range of fluences from 3 to 8 x 10^{22} nvt/cm^2 ($E \geq 0.1$ Mev), a range of linear powers from 6 to 12 kW/ft, and a range of ramp rates from 50 ¢/s to 3 $/s. We believe that, because this wide range of conditions could be correlated by a single value of fuel enthalpy at expulsion, fuel conditions may be more important to fuel expulsion than previously thought and that use of the criterion for slow overpower and LOF-initiated TOP conditions may be reasonable.

TABLE 1
CALCULATED VALUES OF SELECTED PARAMETERS
AT OBSERVED TIMES OF FUEL EXPULSION

Test	Peak Fuel Enthalpy (kJ/kg)	Fraction of Fuel in Liquid Phase
HUT-37B	1127.6	0.63
HUT-36B	1121.3	0.64
HUT-32A	1221.6	0.78
HUT-57B	1073.0	0.49
HUT-55A	1169.4	0.63
HUT-52B	1228.2	0.69
E6	1197.4	0.68
E7	989.5	0.29
E8	1132.2	0.62

4. Location of Expulsion: TOP-Initiated CDA

The ramp-rate range of interest in the TOP-initiated CDA is bounded on one side by the rate below which location of expulsion is unimportant to the outcome and on the other by the maximum credible ramp rate. This range of interest is quite narrow, from about 5 ¢/s to about 12 ¢/s.

There are no reliable experimental data on the response of integral pins to ramp rates in the range of interest, and we must rely on other means of assessment. Our principal concerns about applying the predictive methods to this problem are that (1) the methods do not address the possible impact of reduced fuel adjacency effect above irradiation temperatures of 1050 to 1100 F and (2) the methods do not address what influence, if any, breaches predicted before significant fuel melting have on the location of expulsion.

Calculations were performed with the LAFM code to explore the predicted response of a peak power pin to ramp rates in the range of interest under various conditions. Fuel creep was considered in these calculations by setting the temperature at which fuel is strengthless to 2700 K, the same value as was used in the previously reported analyses of TREAT tests. Because the TREAT tests were all between 50 ¢/s to 3 $/s, use of the same threshold temperature for strengthless fuel should be conservative (overestimate cladding loading) for slower ramp rates.

The analyses were performed for a pin with a peak linear heat rating of 11 kW/ft, estimated to be the nominal peak power pin at EOC-3, and for inlet temperatures of 750 and 600 F. The peak cladding midwall temperatures corresponding to these inlet temperatures were 1220 and 1070 F, respectively. Cladding breach predictions were made using the life fraction approach with the HEDL Dorn parameter correlation [16]. This correlation assumed that damage saturated at a fluence of 6×10^{22} nvt/cm^2 ($E \geq 0.1$ Mev) and that damage was not a function of irradiation temperature.

In all cases analyzed, initial breaches occurred before significant fuel melting. By the time the peak fuel enthalpy had reached the enthalpy criterion proposed previously, life fractions had exceeded one over virtually the entire pin and had exceeded one by several orders of magnitude in the upper half. To assess the probability of midplane expulsion because of the influence of an early breach, we reviewed the axial profile of life fraction at the time of initial breach, that is, the earliest time that a life fraction of one was achieved anywhere on the pin. The location of the peak life fraction at that time, coupled with the gradient of the life fraction in either direction from the peak, provides some guidance as to the possibility of the early breach significantly affecting the subsequent site of expulsion. The life fraction profiles for the two inlet temperatures are shown in Figure 1.

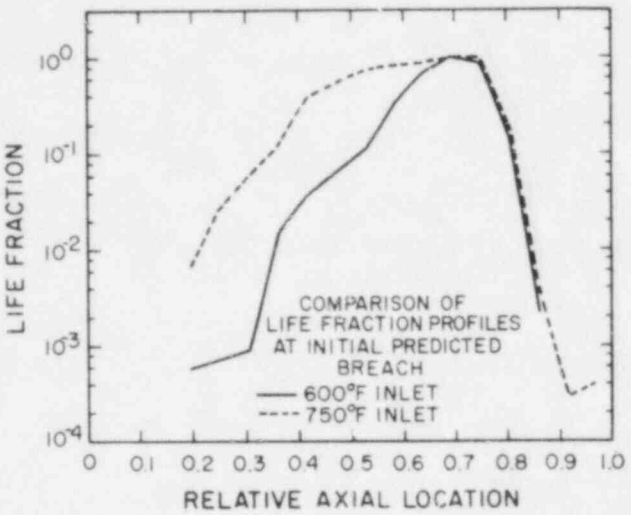

Fig. 1.
Axial profiles of calculated life fractions for two inlet temperatures.

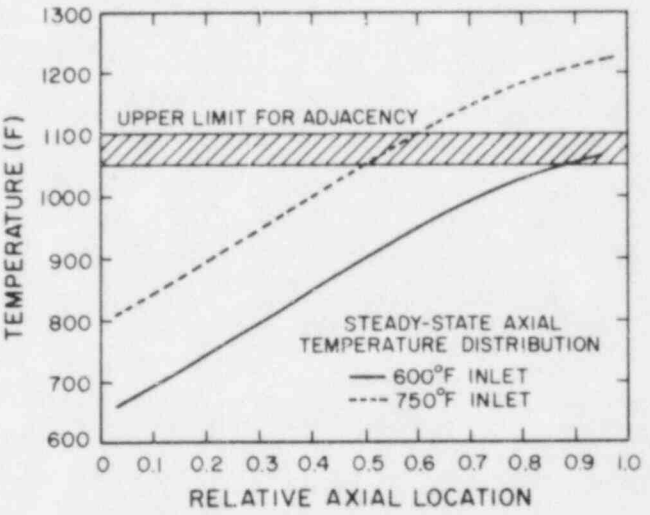

Fig. 2.
Steady-state cladding midwall temperatures as a function of axial location for two inlet temperatures.

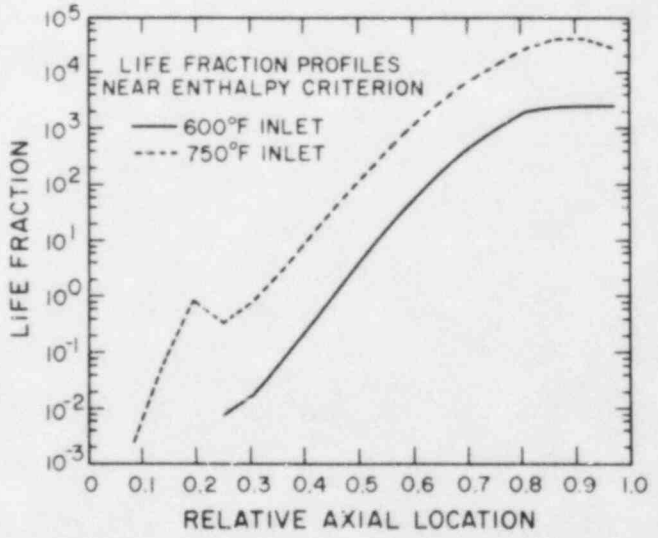

Fig. 3.
Life fraction profiles for two inlet temperatures at a time near a peak fuel enthalpy of 1140 kJ/kg.

To assess the impact of the fuel adjacency effect being markedly diminished above a particular temperature, we looked for the axial location on the cladding where the presumed threshold temperature occurred and assumed that expulsion would occur only below that location. This presumes that the effect is a cliff, that is, the effect disappears over a narrow temperature range. The steady-state temperatures are compared in Figure 2 for the two inlet temperatures.

Finally, to assess the location of expulsion in the absence of the foregoing two biases, we could consider the axial profile of the life fraction at the time the fuel enthalpy criterion is reached. This approach may be risky because it assumes that the fuel itself plays a significant role and that the actual expulsion of fuel does not occur at the instant when both molten fuel is available in the pin and the cladding has breached. Clearly, if the foregoing is true, then the mechanics of how molten fuel reaches the breach site, how the breach site opens, and what conditions are necessary for this process to proceed are all important factors, and factors about which we have essentially no knowledge. The life fraction and life fraction profile may reflect something about this process when the life fraction is orders of magnitude greater than one, but such is not guaranteed at this time. The life fraction profiles when the enthalpy criterion is met are shown in Figure 3 for the two inlet temperatures.

The life fraction profiles shown in Figure 1 indicate a clearly greater bias toward cladding breach above midplane for the 600 F inlet temperature than for the 750 F inlet temperature. If the early cladding breach or damage does influence the subsequent location of fuel expulsion, then the low inlet temperature case would clearly entail less potential reactivity gain from fuel motion toward the midplane within the pin than the high inlet temperature case. Similarly, a review of Figure 2 clearly demonstrates that if the fuel adjacency effect is markedly diminished above the 1050 to 1100 F range of irradiation temperature, the adverse impact of favoring an expulsion site low on the pin would be considerable for the high inlet temperature but not for the low inlet temperature. A review of Figure 3 indicates that both life fraction profiles appear to favor an expulsion site high on the pin. However, we have previously pointed out that if expulsion were delayed until a fuel enthalpy of 1140 kJ/kg were reached, it is not clear that accumulated life fractions of several orders of magnitude over the breach criterion of one are meaningful. Accordingly, we have not attached much significance to the results shown in Figure 3.

We conclude that (1) at the high inlet temperature (750 F) expulsion high on the fuel pin is not assured and the midplane may be the preferred site and (2) at the low inlet temperature expulsion seven to ten inches above midplane appears more likely than expulsion at midplane.

5. Location of Expulsion: LOF-Initiated TOP CDA

The LOF-initiated TOP event is primarily concerned with the behavior of low-powered pins that would not disrupt during the early LOF-initiating phase. These pins experience elevated cladding temperatures during the LOF phase, followed by a mild TOP (about five times steady-state power over a period of about two seconds), and then a very rapid burst. The concern with when and where fuel expulsion occurs from these pins relates to the reactivity consequences of their behavior during the rapid burst and to the potential for adding to the severity of the overall event.

There are very few data on integral pin responses to such specialized, extreme conditions. Available analytical methods, coupled with recent data on the response of cladding to such conditions, must be used to assess the response of these pins.

We have explored the behavior of integral fuel pins under these conditions using the LAFM and DSTRESS [17] codes. The cladding-flow stress model in LAFM was modified to provide cladding strength predictions in accordance with the data in Reference 18. In general, we assumed that the cladding in this application would behave as unirradiated because of the high temperatures experienced in the LOF phase and the evidence that such high temperatures would erase the fuel adjacency effect [5].

The calculations were performed for a pin with a 6 kW/ft peak linear heat rating and an inlet temperature of 700 F. The pin was assumed to undergo the undercooling transient described in Reference 2 out to 16 s, then begin an exponentially increasing TOP transient to five times steady-state power in two seconds followed by a rapid burst. Bursts were analyzed with periods ranging from 2 to 10 ms. Fission gas was assumed to be released during the LOF transient in accordance with the LAFM model, but to escape to the plenum. During the mild TOP, released fission gas was assumed to be retained in the central cavity. It was assumed during the rapid burst that effectively no fission gas was released because of the shortness of the event.

The DSTRESS code was used primarily because it models strain rate effects in the cladding. The code does model fuel creep. LAFM does not model fuel creep explicitly, but does allow fuel creep to be simulated by specifying a fuel temperature above which the fuel is strengthless.

We found that the pin being analyzed would not have a closed fuel-cladding gap during steady-state operation (according to the SIFAIL code [19]). The gap was just beginning to close at the start of the rapid burst, and incipient fuel melting also was reached at that time. Neither code provided reasonable predictions during the rapid burst. The gap in the top third of the pin never closed and was only barely closed at midplane in the DSTRESS calculation. The problem appeared to be caused by a combination

of cladding thermal creep and densification of the outer fuel when reasonable plenum pressures were used. Even with reduced plenum pressures we could not get significant fuel-cladding mechanical interaction, and the gaps in the upper half of the pin tended to oscillate from closed to open. The LAFM code gave similar results when the fuel creep parameter was set to the solidus temperature. However, the fuel during most of the burst was either above 2700 K or radially cracked, so that when the strengthless threshold was set to 2700 K, the fuel moved out to the cladding and the cavity pressure was applied directly to the cladding. Cladding loads were significantly increased as a result of this behavior.

We conclude that these mechanical predictive methods were never intended to be used for the type of conditions being analyzed and that the mechanical predictions are not trustworthy. We do note that all of the LAFM cladding breach predictions were for earlier times than the time at which the fuel enthalpy criterion in Section 4.2 was satisfied. This was the result whether the HEDL Dorn stress-based criterion or the strain criterion in Reference 18 was used. We believe that, under the circumstances, the fuel enthalpy criterion is the most realistic to use for predicting the time of fuel expulsion. There is no alternative, we believe, but to assume that expulsion would begin at the axial midplane.

Other studies have shown that when expulsion begins at midplane, the consequences are significantly mitigated when the expulsion site is assumed to extend upward along the top half of the fuel pin within a few milliseconds [20]. We studied this possibility for the current application and concluded that we could not now support its use, at least on the time frame necessary to mitigate the event. We reached this conclusion for the following reasons.

- Data [21] clearly show that unstable rip propagation is very unlikely at the high temperatures encountered in this application.

- Assuming that the enthalpy criterion can be applied locally, the axial rate at which additional sites reach the criterion and presumably open for expulsion (beyond the original site) exceeds the speed of the internal decompression wave only out to 0.15 m from the original site. As the extension rate falls below the decompression wave propagation rate, the site could still open, but it would be delayed. We were not in a position to evaluate that delay.

6. Conclusions

- Several predictive systems [1, 3] are available for predicting the time of expulsion from TREAT TOP tests with acceptable accuracy. Verification of prediction accuracy for the location of expulsion is not possible because that is known for only three of the TREAT tests. None of

these methods addresses how molten fuel reaches the cladding breach site, nor what conditions are required for molten fuel to be expelled once the cladding is predicted to have breached.

- No data are available to verify either time or location of expulsion for slow overpower conditions (the TOP event most likely to initiate a CDA) or for fuel pins irradiated with significant portions of the cladding above 1050 to 1100 F. The latter phenomenon could involve significant portions of the highest-powered CRBR pins. The relevance of these phenomena is identified in the following point.

- Two possibly significant phenomena not now addressed could mandate midplane failure.

  - Cladding breaches or severe damage incurred near midplane early in the transient when there is little or no molten fuel, as may occur in slow overpower transients, may subsequently influence the location of fuel expulsion [1].

  - Current data for the fuel adjacency effect (a phenomenon wherein cladding irradiated next to fuel is more severely degraded than cladding irradiated remote from fuel) indicate that the effect for fueled cladding irradiated at temperatures above 1050 to 1100 F is either not present or is much less severe [4-6]. If true, cladding breach and fuel expulsion would be virtually guaranteed below the locations on the pin corresponding to those temperatures.

- In the absence of the foregoing the influences, the major phenomenon biasing the location of fuel expulsion is believed to be cladding temperature, which would favor an expulsion site high on the pin.

- A fuel enthalpy of 1140 J/gm (272 cal/gm) is recommended as a criterion for determining the time of fuel expulsion under all TOP conditons.

- The minimum conceivable cavity driving force to cause fuel expulsion is believed to be 5 MPa. This bound is based on calculations with the LAFM code for several TREAT tests assuming that no fission gas was released so that cavity pressure increased only because of heating and compression at the observed time of expulsion.

- Based on TOP calculations for a peak-power CRBR pin in the 5 to 15 ¢/s ramp rate range, with appropriate consideration for biasing agents previously listed, we conclude that midplane failure cannot be precluded at normal CRBR operating conditions and may be the preferred location. If operating temperatures were lowered so that no more than the top ten percent of any fuel pin were irradiated above a temperature of 1050 F, the most probable location of fuel expulsion would be seven to ten inches

above the fuel column midplane. For these conditions, the probability of expulsion at midplane would definitely be less than the probability of expulsion above midplane, but would still be finite.

- LOF-induced TOP conditions involve pins of low linear heat rating (about 6 kW/ft), coupled with much higher cladding temperatures than are encountered in a straight TOP-initiated event. Our studies of this event show many similarities with the slow overpower regime in that cladding breach is likely much earlier than the availability of significant amounts of molten fuel. The time and location of molten fuel expulsion probably will be determined by processes in the fuel rather than in the cladding. All of the location biases identified for the TOP-initiated event are likely to be muted if operable at all, further supporting the likelihood of the event being dominated by fuel processes. We recommend that the fuel enthalpy criterion previously cited for use in TOP-initiated events also be used for determining when molten fuel would be expelled in a LOF-initiated TOP event, with an axial midplane location presumed.

- We cannot now support rip extensions of more than 0.15 m for the LOF-initiated TOP event, at least on a time scale that would mitigate the outcome of the event. Data have shown that unstable rip propagation is very unlikely at elevated temperatures. Calculations show that axial extension of multiple expulsion sites is unlikely beyond 0.15 m from the original site.

7. References

1.[a] R. E. Baars, "Fuel Pin Failure Mechanisms, TOP Conditions (1979)," Hanford Engineering Development Laboratory report HEDL-TME 81-38 (May 1980).

2. S. K. Rhow, D. M. Switick, J. L. McElroy, and B. W. Joe, "An Assessment of HCDA Energetics in the CRBR Heterogeneous Reactor Core," General Electric Company report CRBRP-GEFR-00523 (December 1981).

3. J. M. Kramer and T. H. Hughes, "Comparison and Evaluation of Four Transient Fuel Pin Behavior Codes," Proceedings of ANS Topical Meeting on Reactor Safety Aspects of Fuel Behavior, Sun Valley, Idaho, August 2-6, 1981.

4. C. W. Hunter and G. D. Johnson, "Fuel Adjacency Effects on Fast Reactor Cladding Mechanical Properties," Proceedings of International Conference on Fast Breeder Reactor Fuel Performance, Monterey, CA, March 5-8, 1979.

5. D. R. Duncan, N. F. Panayoyou (HEDL), and E. L. Wood, Jr. (ANL-Idaho), "Chemical Degradation Mechanisms of Fast Reactor Fuel Cladding Mechanical Properties," Trans. Am. Nuc. Soc. 38, pp. 265-266 (1981).

6. M. G. Adamson, S. Vaidyanathan, T. Lauritzen, and W. H. Reineking, "Evidence for Liquid-Metal Embrittlement of 20% Cold-Worked Type 316 by Cesium-Tellurium Fission Products, Trans. Am. Nuc. Soc. 39, pp. 385-387 (1981).

7. J. M. Henderson, S. E. Seeman, S. A. Wood, and I. L. Metcalf, "Fuel Pin Behavior Under Slow Overpower Transient Conditions: HEDL W-2 SLSF Experiment Results," Proceedings of ANS Topical Meeting on Reactor Safety Aspects of Fuel Behavior, Sun Valley, Idaho, August 2-6, 1981.

8. A. L. Pitner, D. E. Smith, and G. E. Culley, "W-2 SLSF Experiment Final Report," Hanford Engineering Development Laboratory report HEDL-TME 82-49 (February 1983).

9.[a] M. J. Blasdel, "Final Report for the Static Capsule HUT 3$/s Transient Tests," Hanford Engineering Development Laboratory report HEDL-TME 80-16 (January 1981).

10.[a] M. J. Blasdel, "Final Report for the Static Capsule HUT 50 cents/s Transient Tests," Hanford Engineering Development Laboratory report HEDL-TME 80-15 (September 1980).

11.[a] M. J. Blasdel, "Final Report for Static Capsule Tests: HUT 3-5A, HUT 3-5B, HUT 3-6A, and HUT 3-6B," Hanford Engineering Development Laboratory report HEDL-TME 81-14 (May 1982).

12.[a] R. C. Doerner, W. F. Murphy, and G. S. Stanford, "Failure of a High-Power Pin in a Simulated 3$/S TOP Accident: Test E6 Final Report," Argonne National Laboratory report ANL-78-73 (August 1978).

13.[a] R. C. Doerner, W. F. Murphy, G. S. Stanford, and P. H. Froehle, "Final Summary Report of Fuel Dynamics Test E7," Argonne National Laboratory report ANL-77-25 (April 1977).

14. R. Simms, R. K. Lo, W. F. Murphy, G. S. Stanford, and A. B. Rothman, "Transient-Overpower-Test E8 on FFTF-Type Low-Power-Irradiated Fuel," Argonne National Laboratory report ANL-77-93 (December 1977).

15. P. K. Mast, "The Los Alamos Failure Model (LAFM): A Code for the Prediction of LMFBR Fuel Pin Failure," Los Alamos National Laboratory report LA-7161-MS (March 1978).

16. G. D. Johnson, J. L. Straalsund, and C. L. Wire, "A New Approach to Stress-Rupture Data Correlation," Materials in Science and Engineering, 28, pp. 998-1006 (1976).

17. G. L. Fox, "Interim Report on Analytical Modeling used for DSTRESS, Hanford Engineering Development Laboratory report HEDL-TME 76-95 (January 1977).

18. N. S. Cannon and C. W. Hunter, "High Rate Transient Mechanical Properties of Unirradiated Fast Reactor Cladding," Proceedings of ANS Topical Meeting on Reactor Safety Aspects of Fuel Behavior, Sun Valley, Idaho, August 2-6, 1981.

19. D. R. Wilson and D. S. Dutt, "SIFAIL: A Subprogram to Calculate Cladding Deformation and Damage for Fast Reactor Fuel Pins," Hanford Engineering Development Laboratory report HEDL-TME 79-34 (May 1979).

20. P. A. Pizzica and H. H. Hummel, "The Effect of Time Delays in Fuel Pin Failure on LOF-TOP Transient Calculations for a Commercial Sized LMFBR," Nuclear Technology, 56, pp. 313-321 (February 1982).

21. W. L. Hu, R. L. Bogart and C. W. Hunter, "Cladding Rip Propagation Tests of Unirradiated 20% CW 316 Stainless Steel Cladding," Proceedings of ANS Topical Meeting on Reactor Safety Aspects of Fuel Behavior, Sun Valley, Idaho, August 2-6, 1981.

[a] Address requests for these documents to: F. X. Gavigan, Director, Office of Breeder Demonstration Projects (NE-50), U.S. Department of Energy, Washington, DC 20545, Telephone (301) 353-3134.

APPENDIX B
PLUTO2 ANALYSES OF L8 EXPERIMENT

1. Introduction

An analysis of the L8 experiment using a stand-alone version of the PLUTO2 code was presented by Bowers, Tentner, and Wider [1]. In that analysis the following parameters were adopted as best fitting the experimental results:

- Pin failure pressure of 15 MPa (adjusted by varying cavity gas volume).
- Fuel particle radius for particulate flow in coolant channel of 170 μm.
- Fuel/coolant heat transfer proportional to the square of the liquid sodium volume fraction.
- Grain boundary fission gas (instantly available on fuel melting) equal to 0.1 to 0.5 of the retained gas.
- Coalescence time constant for gas in grains at fuel melting of 60 ms.
- Initial cladding rip of 3 nodes (18.5 cm) centered at the core midplane and increasing with time.

To assess how well these parameters can be determined by the experiment, a series of variations was performed. The version of PLUTO2 used for performing these studies was made available to us by courtesy of H. Wider (ANL).

2. Parametric Variations

Parametric variations from the base case, Case 1 in Table 1, are as follows. In Case 2, all FCI heat transfer was eliminated in the particulate flow regime. Some fuel-coolant heat transfer still occurred in the annular flow regime, however. In Case 3, the transition from the original particulate flow in the coolant channel to annular flow for molten fuel and sodium/fission gas was suppressed in order to simulate the modeling in EPIC, which is restricted to particulate flow. In the base case, this transition was specified by input to occur when the liquid sodium volume fraction dropped to 0.33. In Case 4, the molten fuel/sodium heat-transfer coefficient was assumed proportional to the first power instead of to the square of the liquid sodium

volume fraction. In Case 5, the initial cavity pressure was increased by a factor of three by tripling the initial fission gas content. In Case 6, the initial cavity fission gas content was divided by three to reduce the initial cavity pressure to one third. In Case 7, the initial cavity pressure was tripled by dividing the void volume by three and in Case 8, the initial pressure was reduced by a factor of three by tripling the void volume at pin failure. In Case 9, the fraction of retained fission gas assumed to be on grain boundaries (and thus immediately available) was reduced to zero. In Case 10, the time constant for coalescence of gas entering the pin cavity and thus becoming available was reduced from 60 ms to 30 ms. In Case 11, the first power of the sodium volume fraction was assumed for the heat transfer coefficient, the initial fission gas and void fraction were both tripled, and the failure pressure was maintained at 15 MPa.

3. Results and Discussion

The new results for total fuel reactivity as a function of time following pin failure normalized to original fuel worth are given in Table 1 and also are compared to the experimental values. Comparison of experiment and Case 1 illustrates the trend found previously [2] that the calculated fuel sweepout was too large up to about 30 ms and was too small at later times.

A comparison of the results for Case 1 and Case 2 indicates that the FCI did not have much effect on fuel reactivity and that sweepout actually is greater when the heat transfer is turned off, apparently because the sodium liquid volume fraction is greater in this case so that the particulate flow regime is retained longer and the ejected fission gas moves fuel more efficiently. When the EPIC modeling was simulated by suppressing the development of annular flow in Case 3, excessive fuel sweepout developed even with the assumption of fuel/coolant heat transfer proportional to the square of the liquid volume fraction, particularly at times later than 50 ms. This excess in sweepout with EPIC becomes even larger if the heat transfer is assumed proportional to the first power of the sodium volume fraction. However, with PLUTO2 when all flow regimes are allowed, the use of the first power or the square of the volume fraction makes little difference because of the development of annular flow (compare Cases 1 and 4).

Early reactivity change is quite sensitive to the amount of initial fission gas in the cavity when the void volume is kept constant (compare Cases 5 and 6 with the base case). These effects tend to disappear at later times because of the growth of the cavity in this rapid transient, causing further fission gas release from newly melted fuel. The early reactivity change is far too negative with an initial pressure of 45 MPa but is about right at later times. With an initial pressure of 5 MPa the calculated early reactivity change is still too large up to 20 ms, after which it becomes much too small.

When the initial pressure is varied by varying the void volume rather than the gas content, as in Cases 6 and 7, the effects are smaller. Intermediate results are obtained when the gas content and void volume are varied simultaneously (compare Cases 4 and 11).

A common problem in all of these cases is the one pointed out by Bowers et al. [1] that the lower sodium slug velocity as calculated by PLUTO2 is lower than the measured one, particularly at times later than 30 ms after pin failure. None of the parametric variations was of such help in improving this situation.

On the basis of these studies, the most important factors affecting calculated fuel sweepout up to 50 ms after pin failure for the L8 experiment appear to be the transition from particulate to annular flow and the initial cavity fission-gas content. The ratio of fission gas to fuel used in the calculations of Bowers et al. [1] appears to be in a reasonable range but may be somewhat low considering the underprediction of fuel sweepout in the base-case calculation.

In addition to an increase in gas content, it might also be appropriate to use a lower sodium liquid volume fraction than the currently assumed 0.33 for the transition from particulate to annular flow. This would increase sweepout at times up to 50 ms.

Within the context of the PLUTO2 modeling, the FCI did not have a large effect on fuel sweepout for the L8 experiment and parameters relating to it were not determined with great precision. Only modest total pressures up to about 1.5 MPa were generated in these calculations, but these were sufficient to generate the required fuel velocities. Pressures of the same order were observed in experiments, except for the fourth event in H6 that indicated a stronger FCI occurred with a peak pressure measured at 12.4 MPa. In their analysis of this event with PLUTO2, Wider and Semenza [3] used a 100 μm fuel particle radius instead of 170 μm, but sodium vapor pressures were not significantly higher than in the L8 calculations. Therefore, their analysis did not reproduce the experimental pressure history.

4. Conclusions

The parametric PLUTO2 studies of the L8 experiment reveal certain modeling deficiencies; however, the benchmarking provides adequately conservative modeling of fuel motion reactivity effects for TOP accident analysis.

5. References

1. C. H. Bowers, A. M. Tentner, and H. U. Wider, "Analysis of TREAT Tests L7 and L8 with SAS3A, LEVITATE, and PLUTO2," Specialists' Workshop on Prediction Analysis of Material Dynamic in LMFBR Safety Experiments, March 13-15, 1979, Los Alamos National Laboratory report LA-7938C. 242.

2. H. U. Wider, A. M. Tentner, and P. A. Pizzica, "The PLUTO2 Overpower Excursion Code and a Comparison with EPIC," Proceedings of the ANS/ENS International Meeting on Fast Reactor Safety Technology, Seattle, WA, August 19-23, 1979.

3. H. U. Wider and L. A. Semenza, "Analysis of TREAT Transient Overpower Experiments Using the PLUTO Codes," Specialists' Workshop on Prediction Analysis of Material Dynamic in LMFBR Safety Experiments, March 13-15, 1979, Los Alamos National Laboratory report LA-7938C.

TABLE 1
TOTAL FUEL REACTIVITY IN L8 RELATIVE TO ORIGINAL

Case	Description	Time after pin failure (ms) 10	20	30	40	50	60	70	80	90	100
	Experiment	1.01	0.99	0.96	0.93	0.90	0.88	0.88	0.88	0.86	0.85
1	Base case[a]	0.984	0.961	0.951	0.951	0.948	0.935	0.918	0.901	0.886	0.866
2	No FCI	0.984	0.957	0.938	0.928	0.923	0.913	0.900	0.892	0.900	0.861
3	All particulate flow	0.984	0.959	0.942	0.929	0.905	0.874	0.835	0.803	0.779	0.757
4	FCI $\propto$ (NaVF)	0.983	0.964	0.953	0.949	0.941	0.929	0.913	0.898	0.883	0.861
5	Initial FG x 3 (P = 45 MPa)	0.977	0.929	0.919	0.918	0.912	0.903	0.894	0.890	0.883	0.863
6	Initial FG x 1/3 (P = 5 MPa)	0.993	0.979	0.972	0.970	0.961	0.949	0.936	0.924	0.906	0.882
7	1/3 Initial void (P = 45 MPa)	0.980	0.953	0.944	0.942	0.934	0.920	0.903	0.891	0.881	0.871
8	Initial void x 3 (P = 5 MPa)	0.989	0.969	0.962	0.960	0.953	0.945	0.935	0.930	0.917	0.893
9	0 Grain boundary gas	0.984	0.959	0.945	0.943	0.936	0.924	0.907			
10	30 ms coalescence time	0.984	0.957	0.948	0.943	0.931	0.915	0.898	0.887	0.883	0.882
11	FCI $\propto$ (NaVF), Initial FG x 3, Initial void x 3 (P = 15 MPa)	0.975	0.944	0.933	0.932	0.927	0.930	0.905	0.892	0.882	0.869

[a] Failure pressure 15 MPa, particle radius 170 μm, and fuel/coolant heat transfer $\propto$ $(NaVF)^2$ unless otherwise noted

IV. LOSS-OF-HEAT-SINK-INITIATED CDAs

1. Objectives and Overview

We have already examined in detail CDAs initiated by coolant overheating (LOF). We have also considered CDAs initiated by overheating of the fuel (TOP). Here we will be concerned with the consequences of a third generic CDA initiator mechanism that leads to simultaneous fuel and coolant overheating. This situation arises as a result of loss in heat rejection capability from the primary system. Such loss normally is considered in conjunction with the achievement of neutronic shutdown and is known as the Loss-of-Heat Sink (LOHS) accident.

The LOHS also may occur in conjunction with failure of the reactor protection system (unprotected accident, ULOHS) [1, 2]. However, we would expect that the phenomenological evolution of the ULOHS would contain elements of both the LOHS and the LOFA; and, in fact, it would easily revert to either of the two by tripping either the primary coolant pumps and/or the reactor shutdown system. Such transitions are particularly likely in view of the relatively long time margins available (large system heat capacity) for recovery actions. In other words, from the point of view of providing the fullest coverage of the CDA phenomenologies in a generic sense, it would appear that the "protected" aspect of the LOHS would provide the most meaningful complement to the unprotected LOFA and TOP cases covered already. On this basis we chose not to consider the ULOHS further here.

The essential character of the LOHS is that core disruption occurs at decay power levels. The relevant degradation processes occur on time scales of many minutes to many hours, as compared to the fractions of a minute associated with the unprotected CDAs. This slow evolution of disruption, together with a highly subcritical initial core state, suggests an extremely sluggish neutronic behavior at least during the first approach to criticality. The approach to criticality would appear inevitable because continuing fuel and control material degradation would yield states of increased fuel compaction and eventually, melting (or sublimation) and separation of the considerably lighter control material. Just as in the other CDAs considered previously, our objective here is to establish the LOHS core-disruption path, to identify termination mechanisms, and to explore the potential for energetic behavior during disruption.

The unique character of the LOHS CDA was emphasized by the first study of the topic appearing in 1977 [3]. A handful of others followed [4, 5] but not all unique aspects of the behavior appear to have been pursued in the past. These studies originated with the homogeneous CRBR core design and agree in concluding that eventual recriticality is to be expected, but disagree on the timing of such events.

The Applicant's CDA analyses did not address this topic specifically. Thus, our own efforts in this area will have to stand alone at this time. It is important, therefore, that we place our results in the proper perspective of this limited extent of previous work available. This is accomplished in Section 2. The possible ranges of phenomenology are examined in Section 3 and our assessment of the LOHS-unique energetic circumstances is presented in Section 4.

2. Previous Work

Previous work on LOHS CDAs has been very limited. The first such study carried out for the homogeneous CRBR core design was that of Chan, Min, and Okrent [3]. They modeled the natural circulation (assumed to continue through sodium boiling and until core uncovery with sodium escaping as vapor from primary system relief paths) between the inlet and outlet plena. They estimated times of 5.6 h and 32 h for reaching coolant boiling and upper plenum depletion, respectively. Following core uncovery and melting, S/A wall melting and fuel disruption occurred sequentially. The sodium vapor velocities were found to be inadequate to levitate the molten cladding; hence, a downward steel relocation process was projected (absence of core-exit blockages). Failure of the S/A walls was taken as the threshold for "gross fuel motion wherein fuel pellets can be arranged into a more compact geometry before they start to melt." Criticality calculations were carried out for several hypothesized core geometries including fuel compaction states with 30% and 50% void fraction and the presence or absence of steel at the upper core boundary. In the absence of control material, all cases indicated supercriticality ($k_{eff} > 1$), while a homogeneous mixture of fuel with the control materials produced a subcritical state. The view expressed in their conclusion was that further study of the core-disruption stages of this rather different class of CDAs would be worthwhile, although no projections on the potential for energetic behavior were given.

The LOHS accident also was studied by Bari and co-workers at BNL. The first study [4] appeared a little after that of Chan et al. [3]. It presented the ALOHA code modeling and preliminary results up to cladding melting and relocation. In these calculations natural convection was assumed to terminate following sodium saturation and boiling inception, that is, sodium boiloff and subsequent heatup were considered from heat capacity standpoint on a (isolated) subassembly scale. As a result, dryout was

calculated to occur in less than 10 min. Cladding melting and relocation into the lower axial blanket (plugging) followed soon after. A more complete presentation of the ALOHA predictions was given in a follow-on study [5]. However, the previous dryout concept was retained, leading again to core disruption soon after reaching sodium saturation conditions (approximately 3.3 h into the accident). The cladding is predicted to melt within 5 min after dryout and the fuel and control assembly walls were predicted to melt a few minutes later. A nonmechanistic equilibrium nodal heat capacity model was utilized to predict steel draining and plugging at the core inlet. The resulting, steel-free core was examined for recriticality events. The possible effects of core crushing and fuel compaction from the weight of the above-core structures were discounted. However, compaction by solid state toppling of fuel and/or control pellets, including the possibility of fragmentation of the fuel from retained fission gases, was identified as a very likely mechanism for recriticality. The criticality compaction boundaries were estimated for the CRBR homogeneous core design as shown in Figure 1. In conclusion, the qualitative judgement was offered that "the core-disruption process is rather slow and sluggish" and, therefore, small ramp rates (< 10 $/s) were to be anticipated.

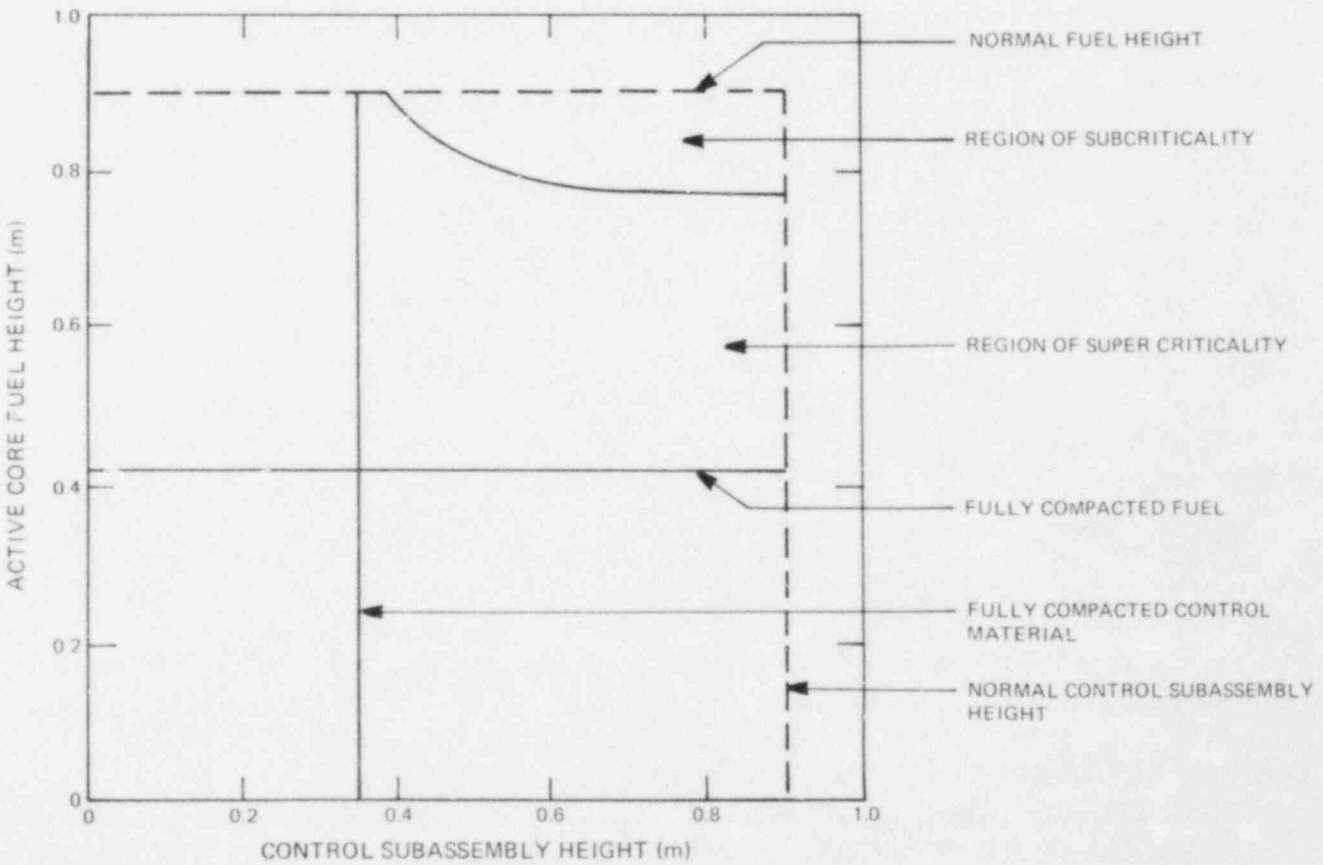

Fig. 1.
Criticality requirement for core compaction during an LOHS.

Quite a different interpretation of these results was suggested by Williams [6]. Such sluggish recriticalities were viewed as the prelude to the formation of a whole-core, transition-phase pool. Based on recent SIMMER results [7] that indicated a potent energetic behavior of such pools (but see Section II.7 for an update) and the judgement that the energetic behavior of such pools would overshadow all other aspects of the LOFA energetic behavior, he concluded that the LOHS accident consequences would be comparable to those of the LOF. This, coupled with the conclusion of another related Sandia study [2], that indicated a two orders of magnitude higher probability for the LOHS accident, led to the conclusion that the major energetics contributor to the risk had been badly neglected.

The assumptions of Chan et al. [3] and Bari et al. [4, 5] concerning the onset of dryout were examined by Perkins et al. [8] in terms of the stability of the boiling process. By comparing the two-phase (boiling) pressure drop to the available static sodium head, the coolability power limits could be established. However, uncertainties in predicting the frictional losses yielded a wide range of predicted dryout power levels. In fact, the decay heat power levels of interest to LOHS assessments fell well within the quoted dryout power uncertainty range of 0.2 to 4%. At about the same time as this study, direct experimental evidence on the subject became available [9]. An average subchannel of the Fast Test Reactor (FTR) was simulated in the radiantly heated Sodium Boiling Test Facility (SBTF) at Oak Ridge National Laboratory. With the exception of a longer inlet section, closely prototypic thermal-hydraulic characteristics were achieved. With an inlet subcooling of approximately 770 K, stable natural convection boiling was achieved up to a power level equivalent to 15% of the FTR power (17 w/cm^2 or 200 w/cm^3). These experimental coolability limit results were recently interpreted [11] in terms of the same flow stability considerations mentioned above. However, a slip flow model (for $\alpha > 0.4$) and the homogeneous friction factor was utilized as opposed to the Barockzy correlation (for two-phase friction) previously used. This study concluded that typical LMFBR subassemblies can be safely cooled under natural convection for heat fluxes corresponding to 8 to 10% of the average nominal power.

The energetics implications for these dryout requirements were recently discussed by Fauske [12]. He suggested that "the steel-blanket fuel pin structure above the core would melt almost simultaneously with the fuel and steel materials that comprise the active core, as if the subassembly structure just above the core was subjected directly to the core volumetric power level." Thus, he ruled out the possibility of core exit plugging and the bottled-up whole-core pool recriticality concerns of Williams [6]. Furthermore, he suggested that even if a severe recriticality event were postulated in the absence of the upper sodium pool, no mechanism would exist to focus the fuel expansion work into the reactor vessel head.

3. Range of Phenomenological Progression

3.1. The Pre-dryout Period

The decay power behavior of the CRBR following a full cycle of operation is shown in Figure 2. We see that within 1 s after shutdown, the power is under 10% and within 10 s it is below 6%. At these times, the inlet sodium is well subcooled and the experimental results from the SBTF directly apply indicating assured coolability. In a LOHS accident, the primary system will continue to heat and will approach coolant saturation in 3 to 5 h. In this near-saturation regime, no directly applicable experimental data are available. However, the following considerations apply: (a) Even with the 770 K subcooling utilized in the SBTF experiments, only 7% of the total power (at near dryout conditions) was absorbed as sensible heat (bringing the sodium flow to saturation) while 93% was utilized for vaporization. Thus, the subcooling should not have been a significant contributor to the coolability limits; (b) The previous conclusion is supported by analytically accounting for the effect of subcooling [11]; (c) As may be seen from Figure 2, at times where the coolant approaches saturation the decay power has declined to the value of approximately 1%. Thus, this whole order-of-magnitude margin from the measured dryout fluxes should overshadow any detail effects.

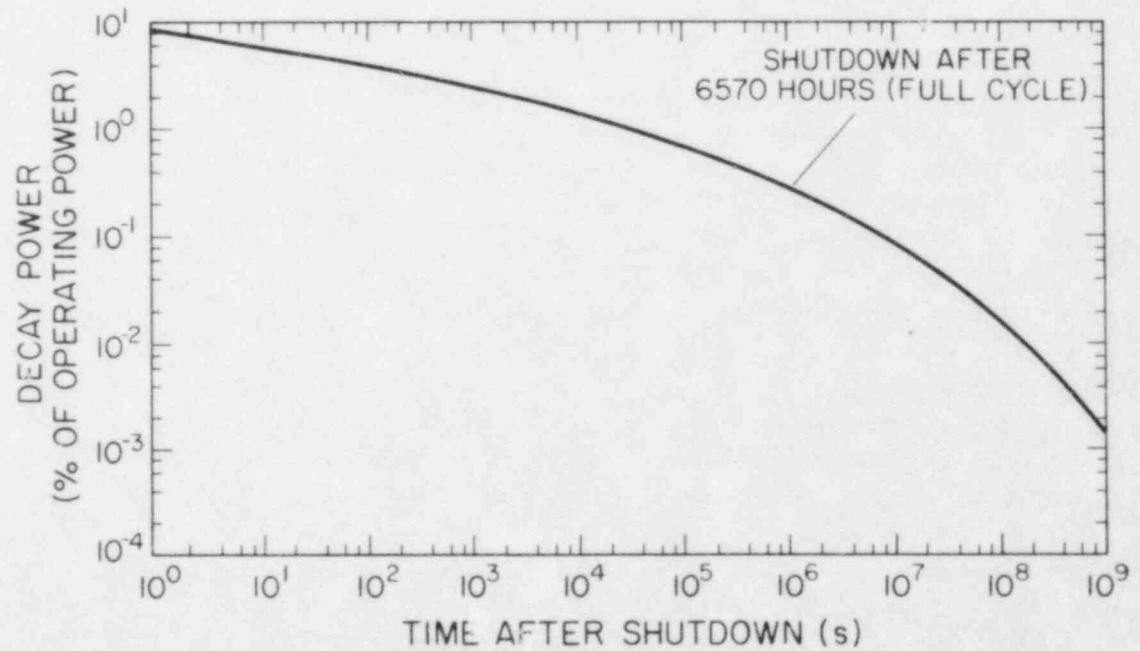

Fig. 2.
Decay power after shutdown equilibrium cycle conditions.

Clearly, we rely heavily on the SBTF experimental results in formulating the position presented above. It is worthwhile, therefore, to consider in more detail any possible limitations of their applicability to the problem at hand. The authors [9] emphasize in particular the nonprototypicality resulting from an SBTF loop inertance (proportional to inlet length) that is considerably larger than that of the fuel assembly inlet module. This would resist flow reversal and, indeed, only sporadic reversals were measured. However, at such low heat fluxes it is doubtful that flow reversals, even if possible (especially limited under inlet subcooling) would be of much consequence on coolability. The authors mention two additional limitations: (a) a relatively high (±17%) power level uncertainty (at the dryout limits), and (b) an axial temperature profile anomaly that was attributed to nonuniform (inlet peaked) power distribution that moved the saturation point upstream and into the inlet (unheated) section. This anomaly had not been resolved but was deemed as a conservative aspect of the experiment (an increased requirement in pressure drop for the two-phase flow). The potential differences in frictional characteristics between the simple tube geometry in the test and the 217-pin wire-wrapped fuel bundle also should be mentioned. Such differences are known to exist for grid-spaced bundles, where grids disrupt the wall film, causing a lower frictional pressure drop but a premature dryout [13]. Although no experimental data for wire-wrapped bundles exist for two-phase flow, experience with single-phase flows and the nonobstructing character of the wire-wrap indicates that no significant deviation from simple channel behavior should be expected.

Thus, we conclude that the core will remain coolable for as long as it is covered by sodium. Even if the LOHS initiator left the primary system intact, at the high boiling point of sodium, the shear ring seals would fail, creating a sodium vapor relief path. Under these conditions, sodium boil-off would continue with stable natural convection boiling through the core until the whole upper pool inventory was depleted. The time duration for this process was estimated by Chan et al. [3] at approximately 32 h. Indeed, at approximately 1% power level (approximately 10 MW) sodium vaporization would occur at approximately 2.7 kg/s (5.4 lbm/s), yielding depletion of the whole primary system inventory of approximately 320000 kg (mostly in the upper pool) in approximately 30 h.

Such long exposures at the high (sodium boiling) temperatures of approximately 1150 K raise the question of mechanical integrity of the load-bearing reactor vessel components. We utilized the recently available high temperature creep data of Reference 14 to evaluate the response of the reactor vessel/flange-support juncture. With a total dead-weight load of 10^6 kg, we estimated a lifetime in excess of 1000 h [10]. Similarly, the vessel sidewall would survive high temperature creep for as long as 10000 hrs. Our concern for such failures stems from the possibility of vessel slump upon the guard vessel and onto the reactor cavity floor, that is, core moving away from the still-latched control rods. Although, such failures appear

unlikely, we emphasize the need for procedures to scram the reactor, thus unlatching the control rods upon any indication of a LOHS.

Considerations quite different from those discussed above did yield a potential mode of vessel failure [10]. As the primary system heats slowly as a whole, the reactor vessel expands downward, while the surrounding guard vessel expands upward slightly in the manner indicated in Figure 3. Such differential thermal expansion may cause mechanical interference and failure at the inlet nozzle position. Such failure would occur at near-saturation conditions and would result in rapid draining of the whole primary system sodium inventory into the reactor cavity. Such a scenario would imply a considerably earlier entry into the core-disruption phase as compared to the boil-off scenario developed earlier. This would imply a somewhat higher decay power (approximately 1% vs. 0.4%, see Figure 2), however, we are still concerned with a very gradual disruption and the absence of sodium throughout this process.

3.2. Core Disruption

Following core dryout, the disruption phase would commence with cladding melting at approximately a 1% power level. Even if vessel failure and coolant draining did not occur, sodium vapor velocities clearly would be inadequate to produce cladding levitation (see Section II.3), hence, gradual draining will occur. Soon after the fuel and control subassembly walls would melt and relocate into the lower blanket space. The details of this seemingly complicated process are not important. The important point is that the control material (BC_4) melts at about 2625 K and the fuel at about 3100 K; that is, at temperatures of more than 1000 K above the steel melting temperature (1700 K). At the extremely low power levels of interest, core-internal thermal gradients would be minimal. Thus, complete melting and draining of all steel would be expected well before any fuel or absorber material melting.

This behavior also would be true for at least a portion of the above core structure (blanket and fission gas plenum cladding and corresponding S/A walls). Therefore, the upper axial blanket pellets would be released on the top of the fuel pellets which by this time, should be found in a randomly packed rubble-bed configuration. Most likely, the remaining above-core steel structure also would dislodge coming to rest on the top of the blanket rubble. The possibility of continued melt attack through conduction and radiation processes should be mentioned. The resulting molten steel would trickle down the fuel bed, providing a cooling mechanism and eventually filling the available interstitial space. However, in view of the insulating properties of the blanket layers and the large heat capacity of the steel structures (behaving in a thermally lumped manner due to its order-of-magnitude-higher thermal conductivity than that of the blanket material), the degree of this

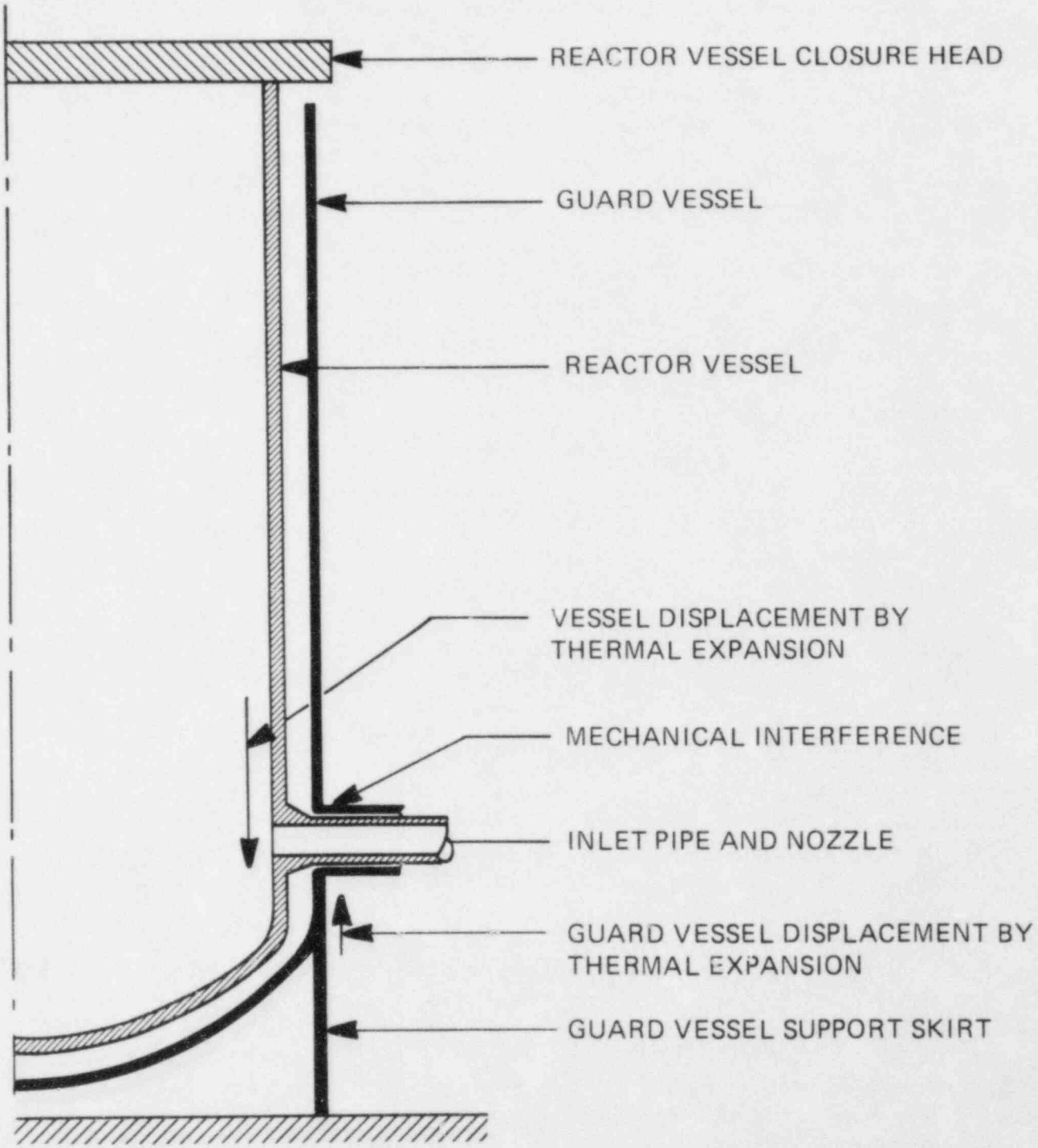

Fig. 3.
Potential inlet pipe failure mode during the LOHS accident.

additional melt attack before fuel melting may be minimal. An upper limit of the available time, assuming approximately 1% power and adiabatic core heatup, is estimated at approximately 10 min. At the other extreme, a prior recriticality would significantly shorten or essentially eliminate this time interval. Indeed, such recriticality seems entirely possible.

3.3. Recriticality Considerations

A schematic of the material configuration described above is shown in Figure 4. The lower steel plug was assumed to penetrate the whole LAB, that is, all in-core and UAB cladding and S/A wall material was taken to fill the available space, thus reaching approximately 0.2 m into the active core. With the fuel, blanket, and control materials in their respective operating positions, the pile would be approximately 30 $ subcritical. A uniform compaction of the fuel rubble (control material still in the core) by approximately 0.20 m, corresponding to an increase in the fuel volume fraction from its initial 35% to approximately 50%, as shown in Figure 4, would be required to approach criticality. These criticality calculations, carried out in the manner described in Section II.7, indicate a similar reactivity worth gradient of approximately 1.5 $/cm of compaction. That is, a uniform collapse velocity of approximately 1 m/s would be required to achieve a ramp rate of 150 $/s. Clearly, such situations would be incredible given the material configurations of interest here).

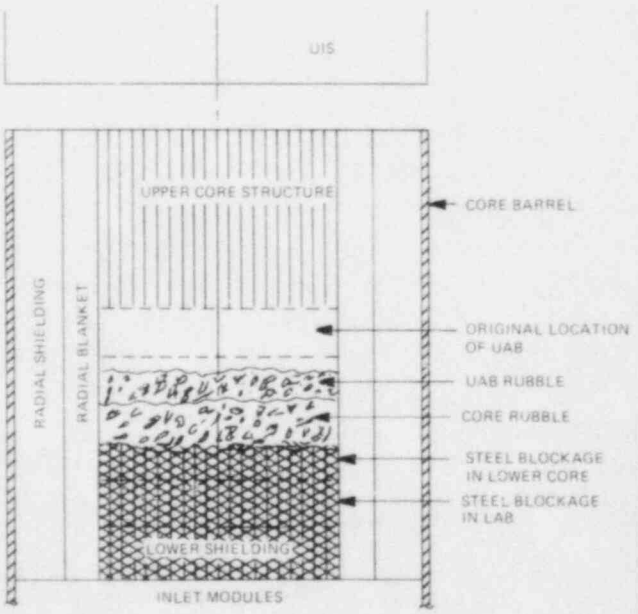

Fig. 4.
Schematic representation of core disruption during the LOHS accident.

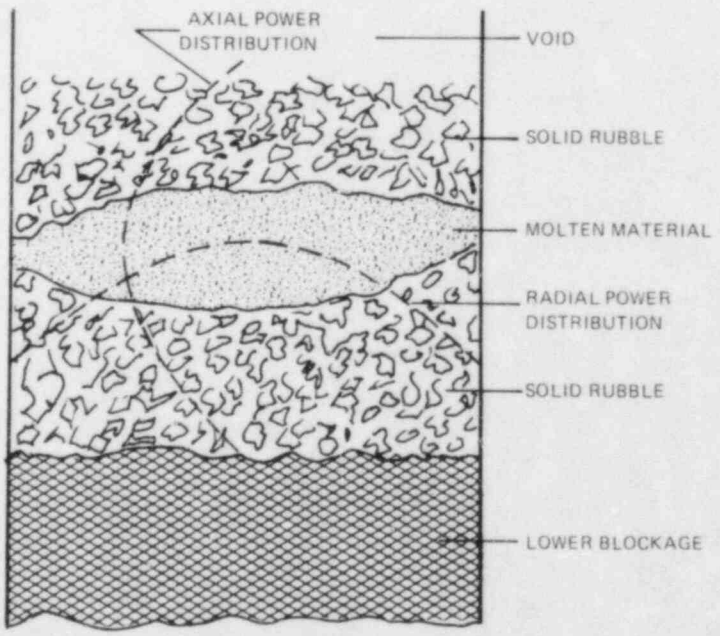

Fig. 5.
Rubble collapse under critical conditions during the LOHS accident.

However, a mild recriticality will be achieved sooner or later; if not by toppling of the unclad fuel and control pellets (sintering during power operation will tend to inhibit such topplings), then by a gradual melting and draining mechanism. Upon first reaching a fission power level (criticality), neutronic activity would accelerate with the increasing rate of fuel melting and collapse. An upper bound example of reactivity ramp rates associated with such a collapse may be obtained by assuming a freefall process uniformly across the whole rubble pile. The mechanistic concept of this collapse is illustrated in Figure 5. Starting from critical, a net displacement by only 1-2 cm would be required to achieve prompt criticality. Under free-fall conditions, the velocity at prompt critical would be approximately 0.4 m/s, which with the worth gradient of approximately 1.5 $/cm quoted above, translates into approximately 60 $/s. However, if neutron precursors are not available because of the long time after shutdown, the higher power condition might be obtained at a supercritical or perhaps a prompt critical state. In this event, even less acceleration time is available, hence a lower level of energetics is obtained.

3.4. Termination Considerations

With respect to termination, the essential aspects of the above scenario is that the plugging-prone, high-heat-capacity UAB region, would be disrupted well before the onset of neutronic activity. However, the blanket layer and plenum cladding and S/A steel shown in Figure 4 may still represent a formidable obstacle for sustained fuel blowdown and dispersal in the upward direction for a low range of recriticality intensities. Indeed, the 60-$/s estimate was presented above as an upper bound. That is, taking into account radial melting incoherencies due to blankets and the nonuniform radial power distribution, we would expect only a fraction of this upper-bound ramp rate to manifest itself. As the core became mobile by melting, the UAB would mix rapidly (greater density) to lower the reactivity state, offset control material loss, and dampen any neutronic activity. The higher energy state of the core would melt the wall and cladding steel from the radial blanket, if it hadn't occurred earlier, leading to radial blanket entrainment into the pool. At this point the core would be immune neutronically to any type of reconfiguration, homogenization, or material removal. It would be permanently subcritical.

4. Energetics Margins for LOHS

Although no significant energetics events for the LOHS accident sequence have been identified, we will discuss the characteristics of a postulated event to establish a point of reference and to highlight the generic margin in the system to accommodate events of this type.

Contrary to all cases of energetic behavior examined to this point, in the LOHS accident, the mechanical loads on the primary system from an energetics event will not involve an intervening sodium pool. As we have seen for the cases of unprotected CDAs (LOFA and TOP), the role of the pool is to provide a medium for focusing this expansion work into a sharp and, hence, potentially damaging mechanical impact on the reactor vessel head. Here we will consider an example of this energy conversion process in the absence of the sodium pool.

The methods of Section II.2 were applied, but the loss of mechanical strength of certain structural components in the high temperature LOHS environments was taken into account. Thus, we assumed that the UIS support columns offer no resistance to the upward UIS displacement driven by the core expansion process. Similarly, the core barrel is assumed to offer no resistance to core expansion in the radial direction. Thus, the conceptual picture consists of an expansion in all directions constrained only by the inertia of the intervening masses. A schematic is shown in Figure 6. The UCS also is considered to be a strengthless inertial constraint, which is visualized to crush upon contract with the UIS. With an initial void fraction (porosity) within the UCS of approximately 75%, at full compaction against the UIS core venting would be expected. Such venting would further accelerate the rate of pressure decay within the expansion zone, thus moderating the continuing acceleration of the masses. Our first order concern was to evaluate the potential for damage to the vessel and containment due to potential missile generation and subsequent impacts.

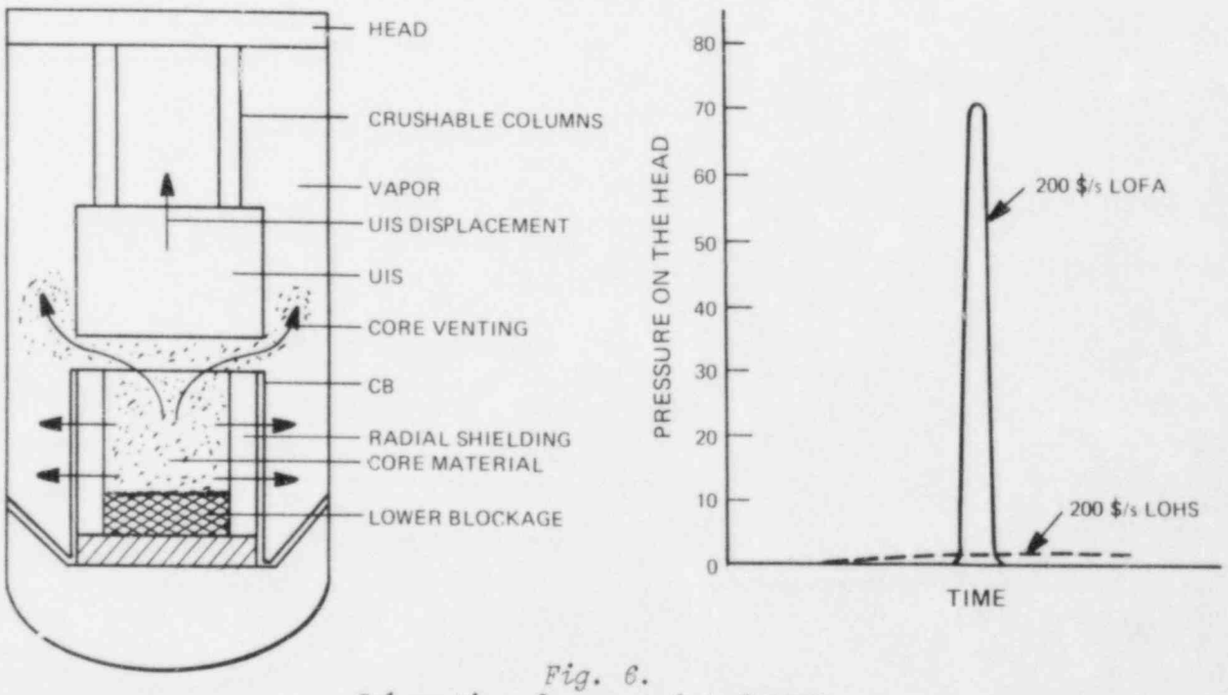

Fig. 6.
Schematic of a postulated LOHS postdisassembly expansion and comparison of calculated vessel head pressures to the 200$/s LOFA.

From the point of view of containment integrity, the question is whether the UIS impact upon the reactor vessel head could generate a secondary missile of energy sufficient to reach the containment boundary. A highly conservative upper bound on the UIS impact velocity was obtained as follows. The maximum level of energetics examined in the presence of the sodium pool (Section II.2) was chosen for this evaluation. The downward and radial components of the expansion were conservatively neglected. Early venting also was conservatively prevented by assuming that the UIS and CB do not move. A SIMMER-II expansion of the high-pressure core into the empty reactor vessel was carried out. The resulting pressure transients across the UIS are shown in Figure 7. From this figure the net impulse to the UIS may be approximated. The mass of the UIS is 4.75×10^4 kg and the area over which the pressure acts is approximately 4.5 m^2. A peak velocity of approximately 15 m/s, corresponding to a kinetic energy of approximately 5 MJ, was estimated. Such missile energies are clearly of no consequence to the reactor vessel head integrity, and, of course, to the generation of secondary missiles. Similarly, radial or downward vessel failures could be of no consequence to containment integrity.

5. Summary

Severe energetic behavior in the LOHS accident can be ruled out at this time. An evaluation of the inherent margin to accommodate such events indicates a negligible challenge to the reactor vessel head even if severe events are postulated because of the absence of the sodium pool.

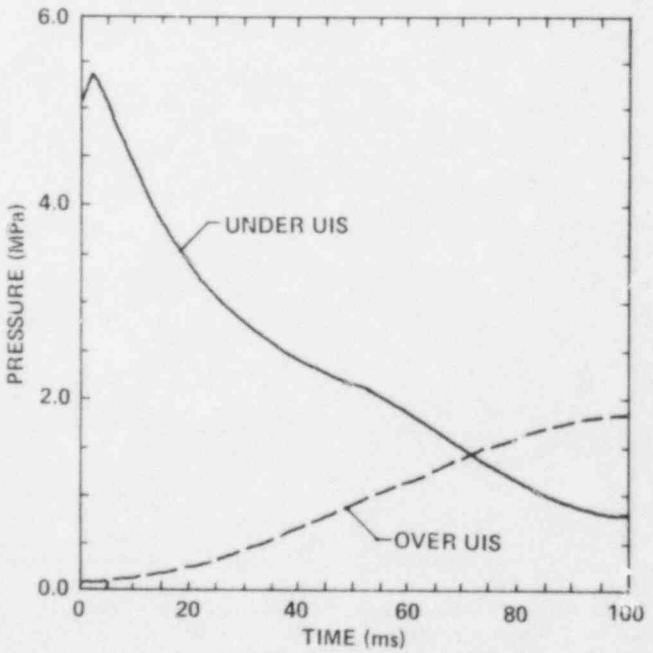

Fig. 7.
Pressures on the UIS during a postulated 200%/s LOHS postdisassembly expansion.

6. References

1. "An Estimate of Release Frequencies for CRBR Potential Core Disruptive Accidents," Phase I, Preliminary Report, Science Applications Inc. report SAI-319-82-PA (August 1982).

2. E. R. Copus, "Estimated Recurrence Frequencies for Initiating Accident Categories Associated with the Clinch River Breeder Reactor Plant Design," NUREG/CR-2681, Sandia National Laboratory report SAND 82-0720 (April 1982).

3. C. K. Clan, T. K. Min and D. O. Okrent, "A Look at Alternate Core Disruption Accidents in LMFBRs," UCLA report NUREG-0259 (May 1977).

4. R. A. Bari, M. A. Klenin, W. T. Pratt, and Y. H. Sun, "Preliminary Assessment of the Meltdown Progression of the Loss-of-Heat-Sink Accident with Scram in the LMFBR," Brookhaven National Laboratory report BNL-NUREG-23137 (August 1977).

5. R. A. Bari, H. Ludewig, W. T. Pratt, and Y. H. Sun, "Accident Progression for a Loss of Heat Sink with Scram in a LMFBR," Brookhaven National Laboratory report BNL-NUREG-50910 (October 1978).

6. D. C. Williams, J. A. Sholtis, F. W. Sciacca, D. W. Varela, M. Rios, P. W. Conrad, E. R. Copus, M. J. Clauser and P. S. Pickard, "LMFBR Accident Delineation Study, Phase I Final Report," Sandia National Laboratory report NUREG/CR-1507, SAND 80-1267 (November 1980).

7. W. R. Bohl, "Some Recriticality Studies with SIMMER-II," Proceedings of the Fast Reactor Safety Meeting, Seattle, WA, August 19-23, 1979.

8. K. R. Perkins, R. A. Bari, and D. C. Albright, "Uncertainties in the Calculated Response of the Clinch River Breeder Reactor During Natural Circulation Decay Heat Removal," Brookhaven National Laboratory report, BNL-NUREG-22715 (April 1977).

9. D. N. Garrison, "Dryout Measurements for Sodium Natural Convection in a Vertical Channel," Oak Ridge National Laboratory report ORNL/TM-7018 (December 1979).

10. "Compendium to NUREG/CR-3224, An Assessment of CRBR Core Disruptive Accident Energetics," Section 11, Nuclear Regulatory Commission document (March 1983).

11. M. Ishii and H. K. Fauske, "Boiling and Dryout Behavior in an LMFBR Subassembly Bundle Under Low Heat Flows and Low Flux Conditions," Nuclear Science and Engineering (in press).

12. H. K. Fauske, "Sodium Re-entry and Dry-out Criteria Under Decay Heat Power Conditions," Proceedings of the Fast Reactor Safety Meeting, Lyon, France, July 19-23, 1982.

13. A. Kaiser, "Two Phase Pressure Drop and Critical Cooling Conditions: Comparison of Results with Sodium in Single Channel and Multi-Channel Geometry," Liquid Metal Boiling Working Group Meeting, Petten, Holland, June 1-3, 1977.

14. M. F. Felsen, "Creep Behavior of Austenitic Stainless Steels, Base and Weld Metals Used in Liquid Metal Fast Breeder Reactors, During Temperature Variations," Proceedings of the Fast Reactor Safety Meeting, Lyon, France, July 19-23, 1982.

V. CONCLUSIONS

We have systematically evaluated the possible progression of three classes of CDAs as exemplified by the LOF, TOP, and LOHS accidents. Non-negligible energetic circumstances were identified only within the LOFA sequences and, assuming that the plenum fission gas fuel compaction mechanism becomes inoperative by design as recommended, only as a consequence of recriticalities.

Recriticality events in the S/A-scale and annular pool phases cannot be excluded. However, their magnitudes are about 50 $/s or less because of incoherence and the absence of significant amplification. Neutronic activity throughout both of these stages of core disruption is substantial and contributes to core pressurization and fuel dispersal away from the core region. Thus, benign termination before formation of the whole-core, homogeneous, pool phase is projected even under restrictive assumptions for fuel removal path availability and fuel removal mechanics.

Whole-core pool recriticalities exhibit a narrow range of significant energetic behavior. This energetic regime is associated with idealized, perfectly symmetric geometry and completely homogeneous pools. The amplification is the result of radial sloshing following a centrally located and symmetrically distributed power pulse. Even so, the resulting level of energetics did not exceed the structural capability of the primary-system boundary.

The levels of energetics required to produce significant structural damage in the CRBR were evaluated, taking into account for the first time the structural enclosure formed by the Core Barrel/Core Support Structure/ Upper Internal Structure and the pressure transmission characteristic of the expanding core medium and other materials found within. We conclude that an 1130-MJ accident (expressed as the isentropic work potential for expansion to one atmosphere) would be required to fail this inner structure, and a 2550-MJ accident would be required to substantially challenge the reactor vessel head structure, that is, produce a slug impact kinetic energy close to the CRBR vessel head design value of 75 MJ. These levels of energetics roughly correspond to two-phase whole-core disassemblies with 100-$/s and 200-$/s driving reactivity ramp rates.

Based on these results we conclude that a CDA-induced energetic vessel head failure is physically unreasonable.

Further, based on the projected absence of significant energetic events we conclude that the Applicant's energetic source term of 661 MJ (75 MJ slug impact kinetic energy) is adequate as applied by the Applicant for evaluating the structural margin beyond design basis.

ACKNOWLEDGEMENTS

We are particularly grateful to Mssrs. N. Grace, P. Check, W. Morris, and C. Allen for their support, encouragement, and understanding throughout the period of this study. We also appreciate the support of the Los Alamos National Laboratory management in making available the resources necessary for maintaining the fast pace and tight schedules of this work. We are indebted to N. Sheheen for her technical editing and coordination of the graphics work and to J. Martinez, C. Gonzales and M. Lopez for their efforts in final assembly of the document. Last, but not least, our sincere thanks to Ms. B. Douglass whose magnificent typing and perseverance removed all pain in the preparation of the final manuscript and made the meeting of the deadlines possible.

NRC FORM 335 (11-81)

U.S. NUCLEAR REGULATORY COMMISSION

BIBLIOGRAPHIC DATA SHEET

1. REPORT NUMBER (Assigned by DDC)
NUREG/CR-3224
LA-9716-MS

4. TITLE AND SUBTITLE (Add Volume No., if appropriate)
An Assessment of CRBR Core Disruptive Accident Energetics

2. (Leave blank)

3. RECIPIENT'S ACCESSION NO.

7. AUTHOR(S)
T. G. Theofanous & C. R. Bell

5. DATE REPORT COMPLETED
MONTH: March YEAR: 1983

9. PERFORMING ORGANIZATION NAME AND MAILING ADDRESS (Include Zip Code)
Los Alamos National Laboratory
P.O. Box 1663
Los Alamos, New Mexico 87545

DATE REPORT ISSUED
MONTH: March YEAR: 1984

6. (Leave blank)

8. (Leave blank)

12. SPONSORING ORGANIZATION NAME AND MAILING ADDRESS (Include Zip Code)
Clinch River Breeder Reactor Program Office
Office of Nuclear Reactor Regulation
U.S. Nuclear Regulatory Commission
Washington, D.C. 20555

10. PROJECT/TASK/WORK UNIT NO.

11. FIN NO.
A7271

13. TYPE OF REPORT
Technical

PERIOD COVERED (Inclusive dates)
January 15, 1982 - August 31, 1983

15. SUPPLEMENTARY NOTES

14. (Leave blank)

16. ABSTRACT (200 words or less)

The results of an independent assessment of core disruptive accident energetics for the Clinch River Breeder Reactor are presented in this document. This assessment was performed for the Nuclear Regulatory Commission under the direction of the CRBR Program Office within the Office of Nuclear Reactor Regulation. It considered in detail the accident behavior for three accident initiators that are representative of three different classes of events; unprotected loss of flow, unprotected reactivity insertion, and protected loss of heat sink. The primary system's energetics accommodation capability was determined in terms of core events. This accommodation capability was found to be equivalent to a ramp rate of about 200 $/s applied to a classical two-phase disassembly. This accommodation capability was contrasted to the potential for energetic behavior which was shown to arise only in the advanced core disruption states (gravity driven recriticalities). The accident behavior was found to be dominated by neutronic activity that was bounded conservatively by 100-$/s events. Based on a qualitative probabilistic approach, we concluded that massive failure of the reactor head with associated early challenge to the containment building is physically unreasonable.

17. KEY WORDS AND DOCUMENT ANALYSIS

17a. DESCRIPTORS

CRBR Core Disruptive Accident Energetics
CDA Energetics

17b. IDENTIFIERS/OPEN-ENDED TERMS

18. AVAILABILITY STATEMENT
Unlimited

19. SECURITY CLASS (This report)
Unclassified

21. NO. OF PAGES

20. SECURITY CLASS (This page)

22. PRICE
$

NRC FORM 335 (11-81)

UNITED STATES
NUCLEAR REGULATORY COMMISSION
WASHINGTON, D.C. 20555

120555078877 1 1AN
US NRC
ADM-DIV OF TIDC
POLICY & PUB MGT BR-PDR NUREG
W-501
WASHINGTON DC 20555